Journal of Applied Mechanics

Published Quarterly by The American Society of Mechanical Engineers

VOLUME 51 • NUMBER 4 • DECEMBER 1984

The Journal of Applied Mechanics (ISSN 0021-8936) is published quarterly for $100 per year by The American Society of Mechanical Engineers, 345 East 47th Street, New York, NY 10017. Second class postage paid at New York, NY and additional mailing offices. POSTMASTER: Send address changes to The Journal of Applied Mechanics, c/o THE AMERICAN SOCIETY OF MECHANICAL ENGINEERS, 22 Law Drive, Box 2300, Fairfield, NJ 07007-2300. **CHANGES OF ADDRESS** must be received at Society headquarters seven weeks before they are to be effective. Please send old label and new address.

PRICES: To members, $24.00, annually; to nonmembers, $100.00. Add $6.00 for postage to countries outside the United States and Canada.

INDEXED by the Engineering Index, Inc.

TECHNICAL PAPERS

(Contents continued on Inside Back Cover)

CONTENTS (CONTINUED)

DESIGN DATA AND METHODS

BRIEF NOTES

DISCUSSIONS

BOOK REVIEWS

D. A. Caulk
Engineering Mechanics Department,
General Motors Research Laboratories,
Warren, Mich. 48090-9055
Mem. ASME

Special Boundary Integral Equations for Potential Problems in Regions With Circular Holes

An infinite system of special boundary integral equations is derived for the solution of Laplace's equation in a general two-dimensional region with circular holes. The solution is shown to converge when the number of holes is finite and no two holes are touching. In special cases, these equations are shown to yield the same results as two more restricted methods, which are based on different approaches.

Introduction

In a recent paper, Barone and Caulk [1] proposed a new boundary integral method for solving potential problems in a general two-dimensional region with circular holes. Boundary quantities were expanded in circular harmonics on the holes and special boundary integral equations were introduced to determine the unknown coefficients. The outer boundary was treated in a conventional manner and, in principle, all integration on the holes was to be done explicitly. Approximate equations, retaining only the first harmonic on the hole boundary, have already been applied successfully in a number of problems [2-4]. However, because the integrals involving higher harmonics on the holes had not then been evaluated, the explicit set of general equations was not available. In this paper we complete the system by explicitly evaluating all the integrals on the holes and prove that the solution always converges as long as the number of holes is finite and no two holes are touching.

It turns out that the general equations proposed here contain those of Craggs [5] as a special case. They also give results equivalent to another restricted method due to Howland [6] for two different problems involving an infinite row of identical holes in an unbounded region. Since Craggs' method is also applicable to one of these problems, both Cragg's and Howland's methods give equivalent results for at least one problem where they both apply. This observation appears to be new.

Integral Equations

Consider a two-dimensional region R containing N circular holes centered at points ξ^α ($\alpha=1, 2, \ldots, N$). Let a_α denote its radius of hole α, ∂C^α its boundary, and ∂R the outer boundary of the region. Let ϕ be a regular harmonic function in R and let $\partial\phi/\partial n$ denote its outward normal derivative on the boundary. Now let ϕ and its normal derivative on ∂C^α be represented by the finite sums

$$\phi=\phi_0^\alpha+\sum_{m=1}^{M^\alpha}(\phi_{1m}^\alpha \sin m\theta^\alpha+\phi_{2m}^\alpha \cos m\theta^\alpha), \tag{1}$$

$$\frac{\partial\phi}{\partial n}=q_0^\alpha+\sum_{m=1}^{M^\alpha}(q_{1m}^\alpha \sin m\theta^\alpha+q_{2m}^\alpha \cos m\theta^\alpha), \tag{2}$$

where ϕ_0^α, $\phi_{\lambda m}^\alpha$, q_0^α, $q_{\lambda m}^\alpha$ ($\alpha=1, 2, \ldots, N$; $\lambda=1, 2$; $m=1, 2, \ldots, M^\alpha$) are constants and θ^α is the polar angle centered at ξ^α, measured relative to the x_1-axis. When (1) and (2) are used to explicitly evaluate the integrals on ∂C^α, the usual boundary integral equation for this region becomes [1]

$$G(\mathbf{y})+\int_{\partial R}\left(\phi\frac{\partial g}{\partial n}-g\frac{\partial\phi}{\partial n}\right)ds+\sum_{\alpha=1}^{N}\Bigg\{a_\alpha q_0^\alpha \log r_\alpha$$
$$-\frac{1}{2}\sum_{m=1}^{M^\alpha}b_\alpha^m\bigg[\left(\phi_{1m}^\alpha+\frac{a_\alpha}{m}q_{1m}^\alpha\right)\sin m\psi^\alpha$$
$$+\left(\phi_{2m}^\alpha+\frac{a_\alpha}{m}q_{2m}^\alpha\right)\cos m\psi^\alpha\bigg]\Bigg\}=0, \tag{3}$$

where

$$g=-\frac{1}{2\pi}\log|\mathbf{x}-\mathbf{y}|,\quad b_\alpha=a_\alpha/r_\alpha,$$
$$r_\alpha=|\mathbf{y}-\xi^\alpha|,\quad \psi^\alpha=\theta^\alpha(\mathbf{y}), \tag{4}$$

and

$$G(\mathbf{y})=\begin{cases}\phi(\mathbf{y}) \text{ when } \mathbf{y}\in\{R,\partial C^\alpha\},\\[2ex] \dfrac{1}{2}\phi(\mathbf{y}) \text{ when } \mathbf{y}\in\partial R.\end{cases} \tag{5}$$

Integral equations for the coefficients in (1) and (2) are obtained by introducing the special kernel functions

Contributed by the Applied Mechanics Division for publication in the JOURNAL OF APPLIED MECHANICS.

Discussion on this paper should be addressed to the Editorial Department, ASME, United Engineering Center, 345 East 47th Street, New York, N.Y. 10017, and will be accepted until two months after final publication of the paper itself in the JOURNAL OF APPLIED MECHANICS. Manuscript received by ASME Applied Mechanics Division, October, 1983; final revision, March, 1984.

$$g_0^\beta(\mathbf{x}) = g(\mathbf{x}, \xi^\beta), \quad g_{1m}^\beta = \frac{a_\beta^m \sin m\theta^\beta}{2\pi |\mathbf{x} - \xi^\beta|^m}, \quad g_{2m}^\beta = \frac{a_\beta^m \cos m\theta^\beta}{2\pi |\mathbf{x} - \xi^\beta|^m},$$
$$(\beta = 1, 2, \ldots, N; \; m = 1, 2, \ldots, M^\beta) \tag{6}$$

into Green's second identity for the potential ϕ. Since the singularities of the kernels (6) occur outside the region, these equations reduce to [1, 2]

$$\int_{\partial R} \left(\phi \frac{\partial g_0^\beta}{\partial n} - g_0^\beta \frac{\partial \phi}{\partial n} \right) ds + \phi_0^\beta + a_\beta q_0^\beta \log a_\beta$$
$$+ \sum_{\substack{\alpha=1 \\ \alpha \neq \beta}}^{N} \left\{ a_\alpha q_0^\alpha \log r_{\alpha\beta} \right.$$
$$- \frac{1}{2} \sum_{m=1}^{M^\alpha} b_{\alpha\beta}^m \left[\left(\phi_{1m}^\alpha + \frac{a_\alpha}{m} q_{1m}^\alpha \right) \sin m\psi^{\alpha\beta} \right.$$
$$\left. \left. + \left(\phi_{2m}^\alpha + \frac{a_\alpha}{m} q_{2m}^\alpha \right) \cos m\psi^{\alpha\beta} \right] \right\} = 0, \tag{7}$$

$$\int_{\partial R} \left(\phi \frac{\partial g_{1k}^\beta}{\partial n} - g_{1k}^\beta \frac{\partial \phi}{\partial n} \right) ds + \frac{1}{2} \left(k\phi_{1k}^\beta - a_\beta q_{1k}^\beta \right)$$
$$+ (-1)^{k-1} \sum_{\substack{\alpha=1 \\ \alpha \neq \beta}}^{N} b_{\beta\alpha}^k \left\{ a_\alpha q_0^\alpha \sin k\psi^{\alpha\beta} \right.$$
$$- \frac{1}{2} \sum_{m=1}^{M^\alpha} b_{\alpha\beta}^m \binom{m+k-1}{m} \left[\left(m\phi_{1m}^\alpha + a_\alpha q_{1m}^\alpha \right) \cos(m+k)\psi^{\alpha\beta} \right.$$
$$\left. \left. - \left(m\phi_{2m}^\alpha + a_\alpha q_{2m}^\alpha \right) \sin(m+k)\psi^{\alpha\beta} \right] \right\} = 0, \tag{8}$$

$$\int_{\partial R} \left(\phi \frac{\partial g_{2k}^\beta}{\partial n} - g_{2k}^\beta \frac{\partial \phi}{\partial n} \right) ds + \frac{1}{2} \left(k\phi_{2k}^\beta - a_\beta q_{2k}^\beta \right)$$
$$+ (-1)^{k-1} \sum_{\substack{\alpha=1 \\ \alpha \neq \beta}}^{N} b_{\beta\alpha}^k \left\{ a_\alpha q_0^\alpha \cos k\psi^{\alpha\beta} \right.$$
$$+ \frac{1}{2} \sum_{m=1}^{M^\alpha} b_{\alpha\beta}^m \binom{m+k-1}{m} \left[\left(m\phi_{1m}^\alpha + a_\alpha q_{1m}^\alpha \right) \sin(m+k)\psi^{\alpha\beta} \right.$$
$$\left. \left. + \left(m\phi_{2m}^\alpha + a_\alpha q_{2m}^\alpha \right) \cos(m+k)\psi^{\alpha\beta} \right] \right\} = 0, \tag{9}$$
$$(\beta = 1, 2, \ldots, N; \quad k = 1, 2, \ldots, M^\beta)$$

where

$$b_{\alpha\beta} = a_\alpha / r_{\alpha\beta}, \quad r_{\alpha\beta} = |\xi^\alpha - \xi^\beta|, \quad \psi^{\alpha\beta} = \theta^\alpha(\xi^\beta). \tag{10}$$

The explicit results for $k > 1$ in (8) and (9) are new. Details of the necessary integration are recorded in the appendix.

Now pass to the limit $M^\alpha \to \infty$ and consider the infinite system of equations (3) and (7)–(9) for the infinite set of coefficients in either (1) or (2). Although the proof is somewhat tedious, it is not difficult to show from the theory of infinite determinants that the solution converges (when N is finite) if the series

$$\sum_{k=1}^{\infty} \sum_{m=0}^{\infty} \binom{m+k-1}{m} b_{\beta\alpha}^k b_{\alpha\beta}^m \tag{11}$$

converges. Now

$$\sum_{k=1}^{\infty} \sum_{m=0}^{\infty} \binom{m+k-1}{m} b_{\beta\alpha} b_{\alpha\beta}^m = \sum_{k=1}^{\infty} b_{\beta\alpha}^k \left(1 - b_{\alpha\beta} \right)^{-k}$$
$$= \sum_{k=1}^{\infty} \left(\frac{a_\beta}{r_{\alpha\beta} - a_\alpha} \right)^k$$
$$= a_\beta / (r_{\alpha\beta} - a_\alpha - a_\beta) \tag{12}$$

as long as $r_{\alpha\beta} > a_\alpha + a_\beta$. Hence, the solution converges as long as no two holes are touching. Of course, these equations would be of little value unless reasonable accuracy could be achieved for relatively small values of M^α. In fact, they give exceptionally accurate results with just $M^\alpha = 1$ in several practical examples [2–4].

For the special case when all the holes have colinear centers and a constant boundary potential, equations (7)–(9) reduce to equations proposed by Craggs [5] and Craggs and Tranter [7] for calculating the capacity of systems of cylindrical conductors. Although the method in [5] and [7] can be generalized in some aspects, it is always restricted to circular or unbounded regions. Not only does the present approach place no restrictions on the outer boundary, but either numerical solutions are possible using standard quadrature methods for boundary integral equations.

A Single Hole in a Strip

To establish correspondence with Howland's method [6], we consider the example of infinite strip with a single hole in its center. Let d be the width of the strip and a the radius of the hole. The boundary of the hole has a constant potential ϕ_0 and the potential on both edges of the strip is taken to be zero.

First consider an infinite region with a row of $2N$ identical holes whose centers are a distance d apart and let the boundary potential on these holes be alternately $\pm\phi_0$. Then the solution on each hole approaches that in the strip (apart from sign) as $N \to \infty$. Let the holes be indexed by a superscript n, which takes all integer values including zero, and let

$$\xi_1^n = 0, \quad \xi_2^n = nd. \tag{13}$$

Then from symmetry

$$\phi_0^n = (-1)^n \phi_0, \quad q_0^n = (-1)^n q_0,$$

$$q_{2(2k+1)}^n = q_{1k}^n = 0, \quad q_{2(2k)}^n = (-1)^n q_{2(2k)}, \qquad (k = 1, 2, \ldots). \tag{14}$$

Now let $M^n = 2K$ and identify β with $n = 0$ so that the only nontrivial equations in (7)–(9) become

$$\phi_0 + aq_0 \log(\pi a / 2d) - \frac{1}{2} \sum_{m=1}^{K} \left(\frac{a}{d} \right)^{2m} \mu_{2m} (-1)^m \frac{a}{m} q_{2(2m)} = 0, \tag{15}$$

$$(-1)^k aq_{2(2k)} + 4 \left(\frac{a}{d} \right)^{2k} \mu_{2k} a q_0$$
$$+ 2 \sum_{m=1}^{K} \binom{2m+2k-1}{2m} \left(\frac{a}{d} \right)^{2m+2k} \mu_{2m+2k} (-1)^m a q_{2(2m)} = 0,$$
$$(k = 1, 2, \ldots K) \tag{16}$$

where

$$\mu_{2k} = \sum_{n=1}^{\infty} \frac{(-1)^n}{n^{2k}} \tag{17}$$

and we have used the fact that

$$\log a + 2 \sum_{n=1}^{\infty} (-1)^n \log nd = \log(\pi a / 2d). \tag{18}$$

Table 1 Comparison of three results for a single hole in a strip

a/d	$\phi_0/(aq_0)$		
	Knight [8]	equation (19)	Balcerzak [9]
0.05	0.3931	0.3931	0.3931
0.10	0.5403	0.5403	0.5403
0.15	0.6921	0.6921	0.6918
0.20	0.8653	0.8653	0.8637
0.25	1.0761	1.0761	1.0698
0.30	1.3498	1.3291	1.3497
0.35	1.7369	1.7360	1.6716
0.40	2.3656	2.3575	2.1519

In the limit $K\to\infty$ (15) and (16) become identical to the equations derived by Knight [8] using the method of superposed singular solutions due to Howland [6]. Knight solves the infinite system for q_0 by successive approximations and obtains results that are accurate to five significant figures. It is interesting to compare these results with the finite system (15) and (16) when $K = 1$. In this case, the latter equations have the solution

$$\phi_0/(aq_0)=\log\,(2d/\pi a)-\frac{\frac{2}{9}\left(\frac{\pi a}{2d}\right)^4}{1-\frac{14}{15}\left(\frac{\pi a}{2d}\right)^4} \tag{19}$$

This solution is compared to Knight's results in Table 1. Even for $a/d = 0.4$, the accuracy of the approximation (19) is remarkable.

Balcerzak and Raynor [9] solved the same problem using an approximate conformal mapping technique. Their result, which is equivalent to the solution of (15) when $K = 0$, is given by just the first term of (19). This approximation is also included in Table 1 for comparison.

Howland [6] used the same method to derive an infinite system of equations for potential flow around an infinite row of cylinders parallel to a uniform stream. The details will not be given, but it is possible to show that equations (3) and (7)-(9) reduce to an equivalent system in this case as well. Since Howland's method is not a general one, its correspondence with the present approach can only be considered on a case-by-case basis. But since (3) and (7)-(9) reduce to both Craggs' and Howland's results in special cases, it is possible that the latter methods may always yield equivalent results in problems where they both apply.

References

1 Barone, M. R., and Caulk, D. A., "Special Boundary Integral Equations for Approximate Solution of Laplace's Equation in Two-Dimensional Regions With Circular Holes," *Q. J. Mech. Appl. Math.*, Vol. 34, 1981, pp. 265-286.

2 Caulk, D. A., "Analysis of Elastic Torsion in a Bar With Circular Holes by a Special Boundary Integral Method," ASME Journal of Applied Mechanics, Vol. 50, 1983, pp. 101-108.

3 Caulk, D. A., "Steady Heat Conduction From an Infinite Row of Holes in a Half-Space or a Uniform Slab," *Int. J. Heat Mass Transfer*, Vol. 26, 1983, pp. 1509-1513.

4 Caulk, D. A., "Analysis of Steady Heat Conduction in Regions With Circular Holes by a Special Boundary Integral Method," *IMA J. Appl. Math.*, Vol. 30, 1983, pp. 231-246.

5 Craggs, J. W., "The Determination of Capacity for Two-Dimensional Systems of Cylindrical Conductors," *Q. J. Math.*, Vol. 17, 1946, pp. 131-137.

6 Howland, R. C. J., "Potential Functions With Periodicity in One Coordinate," *Proc. Camb. Phil. Soc.*, Vol. 30, 1934, pp. 315-326.

7 Craggs, J. W., and Tranter, C. J., "The Capacity of Two-Dimensional Systems of Conductors and Dielectrics With Circular Boundaries," *Q. J. Math.*, Vol. 17, 1946, pp. 138-144.

8 Knight, R. C., "The Potential of a Circular Cylinder Between Two Infinite Planes," *Proc. Lond. Math. Soc.*, Vol. 39, 1935, pp. 272-281.

9 Balcerzak, M. J., and Raynor, S., "Steady State Temperature Distribution and Heat Flow in Prismatic Bars With Isothermal Boundary Conditions," *Int. J. Heat Mass Transfer*, Vol. 3, 1961, pp. 113-125.

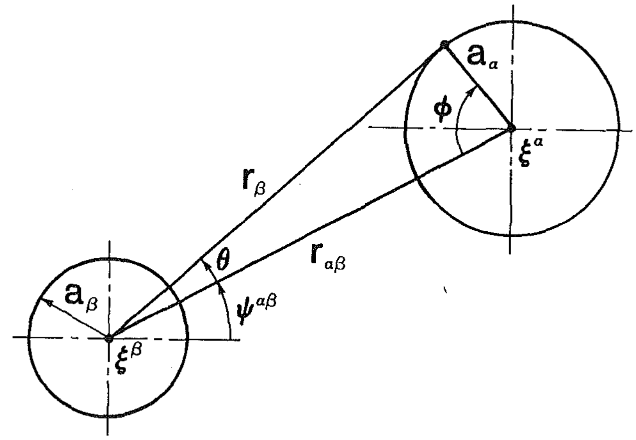

Fig. 1 Geometry and notation

APPENDIX

In this appendix we evaluate the integrals

$$\int_{\partial C^\alpha}\left(\phi\frac{\partial g^\beta_{\lambda k}}{\partial n}-g^\beta_{\lambda k}\frac{\partial\phi}{\partial n}\right)ds, \tag{A1}$$

using (1), (2), and (6). Until now, this has been done only for $k = 1$.

We first note the following geometric relationships from Fig. 1:

$$\phi=\psi^{\alpha\beta}-\theta^\alpha,\ \theta=\theta^\beta-\psi^{\beta\alpha},\ \psi^{\beta\alpha}=\psi^{\alpha\beta}+\pi, \tag{A2}$$

$$r_\beta\sin\,\theta=a_\alpha\sin\,\phi,\quad r_\beta\cos\,\theta=r_{\alpha\beta}-a_\alpha\cos\,\phi. \tag{A3}$$

Now consider the integrals

$$_1I^n_m=\int_0^{2\pi}b^n_\beta\,\sin\,n\theta\,\sin\,m\phi\,d\phi,$$

$$_2I^n_m=\int_0^{2\pi}b^n_\beta\,\cos\,n\theta\,\cos\,m\phi\,d\phi, \tag{A4}$$

and expand $\sin n\theta$ and $\cos n\theta$ in the form

$$\sin\,n\theta=\sin(n-1)\theta\,\cos\,\theta+\cos(n-1)\theta\,\sin\,\theta, \tag{A5}$$

$$\cos\,n\theta=\cos(n-1)\theta\,\cos\,\theta-\sin(n-1)\theta\,\sin\,\theta. \tag{A6}$$

Express $\sin\theta$ and $\cos\theta$ in terms of ϕ from ($A2$) and integrate by parts in ($A4$), using

$$\frac{d\theta}{d\phi}=\frac{r_{\alpha\beta}}{r_\beta}\cos\,\theta-1,\quad \frac{dr^n_\beta}{d\phi}=n\,a_\beta r_\beta{}^{+n-2}\sin\,\phi, \tag{A7}$$

to obtain the recursive relations

$$_1I^n_m=b_{\beta\alpha}\left[{}_1I^{n-1}_m+\left(\frac{m}{n-1}\right){}_2I^{n-1}_m\right], \tag{A8}$$

$$_2I^n_m=b_{\beta\alpha}\left[{}_2I^{n-1}_m+\left(\frac{m}{n-1}\right){}_1I^{n-1}_m\right],\quad (n>1). \tag{A9}$$

For $n = 1$, we have from standard integration formulas

$$_1I^1_m={}_2I^1_m=\pi b_{\beta\alpha}b^m_{\alpha\beta},\quad {}_2I^1_0=2\pi\,b_{\beta\alpha}, \tag{A10}$$

and so

$$_1I^n_m={}_2I^n_m=I^n_m=\pi b^n_{\beta\alpha}b^m_{\alpha\beta}\frac{(m+n-1)(m+n-2)\ldots(m+1)}{(n-1)!}$$

$$=\pi\binom{m+n-1}{m}b^n_{\beta\alpha}b^m_{\alpha\beta}\qquad(m,n\geq 1), \tag{A11}$$

$$I^n_0=2\pi\,b^n_{\beta\alpha}. \tag{A12}$$

Next consider

$$_1J^n_m=\int_0^{2\pi}b^n_\beta r_\beta^{-1}\sin[(n+1)\theta+\phi]\sin\,m\phi\,d\phi, \tag{A13}$$

$${}_2J_m^n = \int_0^{2\pi} b_\beta^n r_\beta^{-1} \cos[(n+1)\theta + \phi] \sin m\phi \, d\phi,$$

and note from ($A3$) that

$$a_\alpha \sin[(n+1)\theta + \phi] = r_{\alpha\beta} \sin(n+1)\theta - r_\beta \cos n\theta, \qquad (A14)$$

$$a_\alpha \cos[(n+1)\theta + \phi] = r_{\alpha\beta} \cos(n+1)\theta - r_\beta \sin n\theta. \qquad (A15)$$

From ($A4$) and ($A13$)-($A15$), it follows that

$${}_1J_m^n = {}_2J_m^n = J_m^n = \frac{1}{a_\beta}\left(b_{\beta\alpha}^{-1} I_m^{n+1} - I_m^n\right) = \frac{1}{a_\beta}\left(\frac{m}{n}\right) I_m^n, \qquad (A16)$$

where we have also used ($A8$), ($A9$), and ($A11$).

Now from (4), (6), and ($A2$)

$$g_{1k}^\beta = \frac{(-1)^k}{2\pi} b_\beta^k (\sin k\theta \cos k\psi^{\alpha\beta} + \cos k\theta \sin k\psi^{\alpha\beta}), \qquad (A17)$$

$$g_{2k}^\beta = \frac{(-1)^k}{2\pi} b_\beta^k (\cos k\theta \cos k\psi^{\alpha\beta} - \sin k\theta \sin k\psi^{\alpha\beta}), \qquad (A18)$$

and by a straightforward calculation, one can show that for $\mathbf{x} \epsilon \partial C^\alpha$

$$\frac{\partial g_{1k}^\beta}{\partial n} = \frac{k}{2\pi} b_\beta^k r_\beta^{-1} \sin[(k+1)\theta^\beta - \theta^\alpha]$$

$$= (-1)^{k+1} \frac{k}{2\pi} b_\beta^k r_\beta^{-1} \{\sin k\psi^{\alpha\beta} \cos[(k+1)\theta + \phi]$$

$$+ \cos k\psi^{\alpha\beta} \sin[(k+1)\theta + \phi]\}, \qquad (A19)$$

$$\frac{\partial g_{2k}^\beta}{\partial n} = \frac{k}{2\pi} b_\beta^k r_\beta^{-1} \cos[(k+1)\theta^\beta - \theta^\alpha]$$

$$= (-1)^{k+1} \frac{k}{2\pi} b_\beta^k r_\beta^{-1} \{\cos k\psi^{\alpha\beta} \cos[(k+1)\theta + \phi]$$

$$- \sin k\psi^{\alpha\beta} \sin[(k+1)\theta + \phi]\}. \qquad (A20)$$

Finally, by combining ($A11$), ($A12$), ($A16$)-($A20$), (1), (2), and using symmetry we obtain the desired results ($\alpha \neq \beta$):

$$\int_{\partial C^\alpha} \left(\phi \frac{\partial g_{1k}^\beta}{\partial n} - g_{1k}^\beta \frac{\partial \phi}{\partial n}\right) ds = (-1)^{k-1} b_{\beta\alpha}^k \Bigg\{ a_\alpha q_0^\alpha \sin k\psi^{\alpha\beta}$$

$$- \frac{1}{2} \sum_{m=1}^{M^\alpha} b_{\alpha\beta}^m \binom{m+k-1}{m} \Bigg[\left(m\phi_{1m}^\alpha + a_\alpha q_{1m}^\alpha\right) \cos(m+k)\psi^{\alpha\beta}$$

$$- \left(m\phi_{2m}^\alpha + a_\alpha q_{2m}^\alpha\right) \sin(m+k)\psi^{\alpha\beta} \Bigg] \Bigg\}, \qquad (A21)$$

$$\int_{\partial C^\alpha} \left(\phi \frac{\partial g_{2k}^\beta}{\partial n} - g_{2k}^\beta \frac{\partial \phi}{\partial n}\right) ds = (-1)^{k-1} b_{\beta\alpha}^k \Bigg\{ a_\alpha q_0^\alpha \cos k\psi^{\alpha\beta}$$

$$+ \frac{1}{2} \sum_{m=1}^{M^\alpha} b_{\alpha\beta}^m \binom{m+k-1}{m} \Bigg[\left(m\phi_{1m}^\alpha + a_\alpha q_{1m}^\alpha\right) \sin(m+k)\psi^{\alpha\beta}$$

$$+ \left(m\phi_{2m}^\alpha + a_\alpha q_{2m}^\alpha\right) \cos(m+k)\psi^{\alpha\beta} \Bigg] \Bigg\}. \qquad (A22)$$

A Consistent Theory for Elastic Deformations With Small Strains

R. T. Shield
Department of Theoretical and Applied Mechanics,
University of Illinois at Urbana-Champaign,
Urbana, Ill. 61801
Mem. ASME

A consistent theory is developed for linear elastic behavior in which the strains are small but in which no restriction is placed on the magnitudes of the displacements or the rotations of elements of the body. The theory reduces to the classical theory for infinitesimal deformations when the rotations are small. Pure torsion of a long cylinder and the bending of a beam by a terminal load are treated in order to illustrate the application of the theory. The bending solution agrees with the St. Venant flexure solution when the deflections are small and with the theory of the elastica when the deflections are large.

1 Introduction

The classical infinitesimal theory of elasticity treats deformations of a body composed of a linear elastic material in which the strains are small and the relative rotations of parts of the body are also small. For slender bodies, such as thin rods, the rotation of one part of the body relative to another need not be small even though the strains remain small. In 1859 Kirchhoff (see Love [1]) provided a theory for the bending and twisting of thin elastic rods and wires in which the relative displacements and rotations were not small. Love described Kirchhoff's approach as being largely kinematical and not free from difficulty, and gave an alternative description (pp. 389–393) of the nature of the strain in a bent and twisted rod in order to relate the moments applied to a section of a rod to the curvature and twist of the rod. As Love points out (p. 24), Kirchhoff's theory has been applied to problems such as the elastica, to the deflection of spiral springs, and to various problems of elastic stability, and the success of the theory is without question. Nevertheless, comments still appear in the literature (see [2], for example) to the effect that there are inconsistencies in "elementary" approaches such as Kirchhoff's and much effort has been spent on axiomatic approaches that claim to be more rational and therefore more correct. An analogous situation exists with regard to the theory of thin elastic plates and shells.

There is need, therefore, for a consistent theory for linear elastic behavior in which the strains are small enough that second-order terms in the stress-strain relation can be neglected, as in the infinitesimal theory, but in which no restriction is placed on the displacements or rotations of elements of the body. Section 2 uses a Lagrangian approach in which the Cartesian coordinates x_i of particles in the reference state are used as independent variables. Strains e_{ik} are defined for deformations with possibly large displacements and rotations which reduce to the usual infinitesimal strains when the rotations and strains are small. For deformations with small strains, the magnitudes of e_{ik} are assumed to be of the order of a dimensionless parameter ϵ which is small enough (say around 10^{-3}) so that second-order terms in ϵ can be neglected in the calculation of e_{ik}. The first and second derivatives of e_{ik} are assumed to be $0(\epsilon)/a$ and $0(\epsilon)/a^2$, where a is a reference length involved in the description of the body and the loading causing the deformation. To $0(\epsilon)$, for compatibility e_{ik} satisfy the compatibility equations of the infinitesimal theory, and locally, that is in a region of diameter $0(a)$, *virtual* displacements v_i exist such that the tensor e_{ik} is the symmetric part of the gradient $v_{i,k}$ as in the infinitesimal theory.

Section 3 considers the equilibrium equations for the small strain deformation of linearly elastic bodies. The stress-strain relation for finite elastic deformations is used to show that with neglect of second-order terms, the Kirchhoff stresses σ_{ik} are linearly related to e_{ik} through the elastic moduli c_{ikmn} for small strains. Moreover to $0(\epsilon)$ the local equations of equilibrium for σ_{ik} are those of the classical theory with a particular body force field, derived by taking the rotation of the elements into account. Thus to $0(\epsilon)$, the differential equations governing e_{ik} are formally identical with the equations of classical infinitesimal elasticity for a particular body force field. This is to be expected because by imposing a suitable rigid displacement, we can arrange that in the neighborhood of a typical particle P the displacements and rotations are small when the strains are small. For slender bodies with some dimensions large compared to a, it is also necessary to impose overall conditions of equilibrium because terms of $0(\epsilon^2)$ neglected in the local equilibrium equations or in the boundary conditions can contribute to the overall balance of force on integration over the body. In this case some of the applied loads can be second order in ϵ and therefore cannot be directly related to the stress distribution with a theory using a first-order stress-strain relation.

The pure torsion of a very long cylinder of isotropic elastic material provides a simple example of the theory (Section 4).

Contributed by the Applied Mechanics Division and presented at the Winter Annual Meeting, New Orleans, La., December 9–14, 1984 of THE AMERICAN SOCIETY OF MECHANICAL ENGINEERS.

Discussion on this paper should be addressed to the Editorial Department, ASME, United Engineering Center, 345 East 47th Street, New York, N.Y. 10017, and will be accepted until two months after final publication of the paper itself in the JOURNAL OF APPLIED MECHANICS. Manuscript received by ASME Applied Mechanics Division, July 1983. Paper No. 84-WA/APM-32.

Copies will be available until August, 1985.

The strains e_{ik} and the stresses σ_{ik} are those of St. Venant theory but they are generated by a finite displacement field in which the relative rotation of the ends can be large.

A more interesting application of the theory is given in Section 5 which considers a beam of isotropic material bent about a principal axis of the cross section so that the deformed central line lies in a plane. The beam is bent by end loads only, and it is assumed that the extension e of the beam is $0(\epsilon)$ or less where ϵ is a measure of the maximum bending strain in the beam. The reference length a is taken to be half the depth of the beam and there is no restriction on the magnitude of the ratio l/a, l being the length of the beam. Thus the approach provides solutions for all values of l/a, in contrast to the St. Venant flexure solution, valid only for beams with small deflections, and to the theory of the elastica, developed for very thin rods. To $0(\epsilon)$, the bending moment M has the Bernoulli-Euler value, and overall equilibrium determines the shape of the deformed central line, which has the shape of the elastica. A feature of the approach is that the transverse shear force S and longitudinal force T on a section are in the nature of reactions which enter into the equations of overall equilibrium. For slender enough beams, S and T can be $0(\epsilon^2)$ or less and so cannot be determined directly from stress distributions which are correct only to $0(\epsilon)$. Section 6 uses the theory of Section 5 to treat a horizontal cantilever with a vertical end load. Approximate formulas for the end deflections are given that are within 1 percent for values of $\epsilon l/a$ up to 3.

Other applications of the theory for small-strain elastic deformations will be given in subsequent papers.

2 Deformations With Small Strains

We suppose that a body occupies a region V of space in its unstrained or reference state B. In a deformation of B into a body B^*, a typical particle initially at the point x_i moves to the point y_i, referred to a fixed rectangular Cartesian coordinate system. The line element ds^* of B^* is given by

$$ds^{*2} = dy_i dy_i = C_{ik} dx_i dx_k,$$

where C_{ik} are the Cauchy strains,[1]

$$C_{ik} = y_{r,i} y_{r,k}. \tag{1}$$

A repeated Latin index implies summation over the values 1, 2, 3 and a comma is used to denote partial differentiation with respect to x_i, $y_{r,i} = \partial y_r / \partial x_i$.

We assume that the functions $y_i(x)$ and the Cauchy strain tensor C_{ik} are C_2 in V. Green's strain tensor e_{ik} is defined by

$$e_{ik} = \frac{1}{2}(C_{ik} - \delta_{ik}), \tag{2}$$

where δ_{ik} is the Kronecker delta. For deformations with small relative changes in distances between neighboring particles, e_{ik} will be small and we indicate this by writing

$$e_{ik} = 0(\epsilon), \tag{3}$$

where ϵ is a dimensionless loading parameter which is a measure of the amount of strain undergone by the body. As normally used, the 0 notation refers to limiting behavior as $\epsilon \to 0$. However, although small, ϵ will be nonzero and we use (3) to indicate the order of magnitude of e_{ik}, so that (3) means that the magnitudes of e_{ik} will not exceed several times ϵ. If the rotations as well as the strains are small, then e_{ik} are the usual infinitesimal strains.

So far as changes in length and direction of infinitesimal elements are concerned, the local deformation at a particle is equivalent to a pure strain followed by a rigid rotation (see [1], for example). In mathematical terms, we have the decomposition (see [4])

$$y_{i,k} = r_{im} s_{mk}. \tag{4}$$

Here r_{ik} is a proper orthogonal tensor,

$$r_{im} r_{km} = r_{mi} r_{mk} = \delta_{ik}, \quad |r_{ik}| = 1,$$

while the symmetric tensor s_{ik} is the positive definite square root of C_{ik},

$$s_{im} s_{mk} = C_{ik}.$$

From (2) and (3),

$$s_{ik} = \delta_{ik} + e_{ik} + 0(\epsilon^2).$$

It can be shown [5] that the rotation tensor r_{ik} satisfies linear equations of the form

$$r_{mn,k} = r_{mp} A_{pnk},$$

where A_{pnk} is antisymmetric in p,n and is determined by the strain tensor s_{ik},

$$A_{pnk} = \frac{1}{2}\{(s_{rn,k} - s_{kn,r}) s_{rp}^{-1} + (s_{kp,i} - s_{ip,k}) s_{in}^{-1} + (s_{rt,i} - s_{it,r}) s_{kt} s_{rp}^{-1} s_{in}^{-1}\}. \tag{5}$$

We denote by a the smallest reference length involved in the description of the body B and the loading causing the deformation. Thus a could be the smallest diameter of the region V or the smallest diameter of a loaded portion of the surface of B. Assuming that the first partial derivatives of e_{ik} are $0(\epsilon)/a$, we have from (5) and the definition of s_{ik}

$$A_{pnk} = e_{kp,n} - e_{kn,p} + 0(\epsilon^2)/a \tag{6}$$

and A_{pnk} is $0(\epsilon)/a$. The derivatives $r_{mn,k}$ will then be $0(\epsilon)/a$, and so will be the derivatives $y_{i,kl}$. However, when one or more dimensions of the body B are very large compared to a, the rotation of one part of the body relative to another need not be small even though the strains e_{ik} and their derivatives are small.

The compatibility conditions on the Cauchy strains C_{ik} (or equivalently the compatibility conditions [5] on A_{pnk} for r_{ik} to exist) give

$$e_{ik,mn} + e_{mn,ik} - e_{im,nk} - e_{nk,im} = 0(\epsilon^2)/a^2, \tag{7}$$

if we assume that e_{ik} are $0(\epsilon)$ and that the first and second derivatives of e_{ik} are $0(\epsilon)/a$ and $0(\epsilon)/a^2$, respectively. (If we know only that e_{ik} are $0(\epsilon)$ and $e_{ik,l}$ are $0(\epsilon)/a$, then the left-hand side of (7) is of the order of ϵ times $e_{ik,rs}$.) The left-hand side of (7) vanishes when e_{ik} are compatible strains for an infinitesimal deformation. If we consider a simply connected region in V with dimensions comparable to a and containing a typical particle P of the body, the approach for infinitesimal deformations (see [6]) and equations (7) imply the existence of functions v_i such that

$$e_{ik} = \frac{1}{2}(v_{i,k} + v_{k,i}) + 0(\epsilon^2) \tag{8}$$

in the region in question. By imposing a suitable rigid body displacement on the deformed body, we can arrange that to $0(\epsilon)$, v_i are the actual displacements in the neighborhood of the particle P. We will see later through examples that functions v_i can exist so that (8) holds throughout V even when a dimension of B is very large compared to a.

When v_i exist satisfying (8) throughout V, the deformation in which a particle at x_i goes to y_i', where

$$y_i' = x_i + v_i, \tag{9}$$

will not be, in general, a deformation with small strains, i.e., it will not have Cauchy strains near δ_{ik} in general. We therefore refer to v_i as virtual displacements for the deformation. If the antisymmetric part of $v_{i,k}$

$$\omega_{ik} = \frac{1}{2}(v_{i,k} - v_{k,i})$$

is also $0(\epsilon)$, then the deformation (9) will have small strains.

[1] We use the terminology of Prager [3] but with different notation.

A simple example is provided by the deformation for pure torsion of an isotropic cylinder of length l. The reference length a is the maximum distance of the boundary of the cross section from the axis of torsion, which is the y_3(or x_3) axis. For twist of amount $\tau = \epsilon/a$ per unit length we take

$$y_i = (x_1 \cos\tau x_3 - x_2 \sin\tau x_3, \quad x_1 \sin\tau x_3 + x_2 \cos\tau x_3, \quad x_3 + \tau w), \tag{10}$$

where $w(x_1, x_2)$ is the St. Venant torsion function. The strains e_{ik} are found from (1), (2), and (10) and we find that

$$e_{13} = e_{31} = \frac{\tau}{2}\left(\frac{\partial w}{\partial w_1} - x_2\right), \quad e_{23} = e_{32} = \frac{\tau}{2}\left(\frac{\partial w}{\partial x_2} + x_1\right) \tag{11}$$

to $0(\epsilon)$, the other components being $0(\epsilon^2)$. The virtual displacements

$$v_i = (-\tau x_2 x_3, \quad \tau x_1 x_3, \quad \tau w) \tag{12}$$

provide infinitesimal strains equal to e_{ik} to $0(\epsilon)$. However, the deformation $y_i' = x_i + v_i$ gives the Cauchy strains

$$C_{11}' = 1 + \tau^2\left\{\left(\frac{\partial w}{\partial x_1}\right)^2 + x_3^2\right\}, \quad C_{22}' = 1 + \tau^2\left\{\left(\frac{\partial w}{\partial x_2}\right)^2 + x_3^2\right\}, \quad C_{12}' = \tau^2 \frac{\partial w}{\partial x_1}\frac{\partial w}{\partial x_2},$$

$$C_{13}' = \tau\left(\frac{\partial w}{\partial x_1} - x_2\right) + \tau^2 x_1 x_3, \quad C_{23}' = \tau\left(\frac{\partial w}{\partial x_2} + x_1\right) + \tau^2 x_2 x_3, \quad C_{33}' = 1 + \tau^2(x_1^2 + x_2^2),$$

and the strains e_{ik} agree with (11) to $0(\epsilon)$ only if we restrict the length of the cylinder so that $\tau x_3 = 0(\epsilon)$.

3 Equilibrium Equations for Elastic Bodies

The Lagrangian stress tensor T_{ik} is defined so that the stress vector T_i, measured per unit area of the reference state, for a surface element with unit normal n_i in the reference state is given by

$$T_i = T_{ki} n_k.$$

When the deformed body B^* is in equilibrium, the total applied force on a portion of the body which occupied a region V' with surface S' in the reference state is zero so that

$$\int_{S'} T_{ki} n_k dS + \int_{V'} F_i dV = 0, \tag{13}$$

where F_i are the components of the body force measured per unit volume of the reference state B. Use of the divergence theorem and the arbitrariness of V' then gives the equilibrium equations

$$\frac{\partial T_{ki}}{\partial x_k} + F_i = 0. \tag{14}$$

An elastic material has a strain energy W per unit volume of the reference state which is a function of the deformation gradient $y_{i,k}$. In a quasi-static deformation of the material, it is assumed that the rate of work of the applied forces is equal to the rate of change of the strain energy, and this leads to the stress-strain relation

$$T_{ki} = \frac{\partial W}{\partial y_{i,k}}. \tag{15}$$

The function W is unchanged in value by a rigid body rotation of the deformed state and so depends on $y_{i,k}$ only through the Cauchy strains. With (2) we therefore have

$$W = W(e_{ik}), \tag{16}$$

and W also depends explicitly on x_i if the material is inhomogeneous. From (1) and (2) we then have

$$\frac{\partial W}{\partial y_{i,k}} = \frac{\partial W}{\partial e_{mk}} y_{i,m} \tag{17}$$

under the assumption that W is written as a symmetric function of e_{ik} and e_{ki} (the differentiation with respect to e_{mk} treats e_{mk} distinct from e_{km} for $k \neq m$). If we denote the (symmetric) components of the Kirchhoff stress tensor by σ_{ik}, then

$$\sigma_{ik} = T_{kr}\frac{\partial x_i}{\partial y_r} = \frac{\partial W}{\partial e_{ik}}.$$

Substituting for T_{ki} in (14) and multiplying by $\partial x_r/\partial y_i$ we find that the equilibrium equations can be written as

$$\frac{\partial \sigma_{ik}}{\partial x_k} + \sigma_{rk}\Gamma^i_{rk} + F_k \frac{\partial x_i}{\partial y_k} = 0, \tag{18}$$

where the Christoffel symbol is given by

$$\Gamma^i_{rk} = \frac{\partial^2 y_m}{\partial x_r \partial x_k}\frac{\partial x_i}{\partial y_m} = C^{-1}_{im}(e_{rm,k} + e_{km,r} - e_{rk,m}). \tag{19}$$

The symmetry relation

$$y_{i,r}\frac{\partial W}{\partial y_{k,r}} = y_{k,r}\frac{\partial W}{\partial y_{i,r}} \tag{20}$$

follows from (17) and the symmetry of e_{ik} and (20) implies that the Eulerian stress tensor is symmetric. From (20), (14), and (15) we obtain

$$\int_{S'} (y_i T_{rk} - y_k T_{ri}) n_r dS + \int_{V'} (y_i F_k - y_k F_i) dV = 0, \tag{21}$$

so that the resultant applied moment on any portion of the body is zero, as required for an equilibrium state.

We now restrict attention to deformations with small strains. Many materials such as metals are elastic only for a limited range of strain, e.g., extensional strains up to 10^{-3} approximately, and in this range of strain the stress-strain behavior is linear within the limits of experimental accuracy. We suppose that the reference state is unstressed and take

$$W = \frac{1}{2} c_{ikmn} e_{ik} e_{mn}, \quad c_{ikmn} = c_{mnik} = c_{kimn}, \tag{22}$$

where the elastic moduli c_{ikmn} may depend on x_i. The stresses σ_{ik} are

$$\sigma_{ik} = c_{ikmn} e_{mn}. \tag{23}$$

Consistent with the accuracy of the assumption of linear behavior for small strains (and the accuracy to which the moduli c_{ikmn} can be determined), second-order terms are ignored in calculating the strains e_{ik} from (2), just as second-order terms are ignored in the classical theory for infinitesimal deformations. To first order in the strains, the stresses are measured per unit area of either the reference state or the deformed state, and so are true stresses associated with directions in the deformed state of line elements which were initially parallel to the coordinate axes. For strains of the order of ϵ the stresses are of the order of $E\epsilon$, where E is a typical elastic modulus for the material, and for a consistent theory, the body force F_i must be of the order of $E\epsilon/a$ or less and any applied surface traction must be of the order of $E\epsilon$ or less.

If we assume as before that the first derivatives of e_{ik} are $0(\epsilon)/a$, then the derivatives $y_{i,kl}$ will be $0(\epsilon)/a$, as discussed in the preceding section, and the Christoffel symbol in (20) will $0(\epsilon)/a$. Thus neglecting terms of the order of $E\epsilon^2/a$, the equations of equilibrium become

$$\frac{\partial \sigma_{ik}}{\partial x_k} + F_k \frac{\partial x_i}{\partial y_k} = 0, \tag{24}$$

in which $\partial x_i/\partial y_k$ is evaluated to 0(1). To 0(1), $y_{i,k}$ is the rotation tensor r_{ik} and $\partial x_i/\partial y_k$ is r_{ki}. To our order of accuracy, it is only necessary to satisfy (24) to $0(\epsilon)$.

If the tractions are prescribed on a portion S_T of the surfaces S of V, then

$$T_{ki}n_k = \sigma_{mk} y_{i,m} n_k = \hat{T}_i \qquad \text{on} \quad S_T,$$

where $\hat{T}_i$ are the applied tractions of order $E\epsilon$. Equivalently we have

$$\sigma_{ik} n_k = \hat{T}_k \frac{\partial x_i}{\partial y_k} = \hat{\tau}_i \qquad \text{on} \quad S_T. \tag{25}$$

To our order of approximation $\partial x_i/\partial y_k$ in (25) need only be evaluated to 0(1) and $\hat{\tau}_i$ are then the components of the applied traction in the directions of line elements that were originally parallel to the coordinate axes. For zero surface tractions $\sigma_{ik}\, n_k$ must vanish to $0(\epsilon)$ on S_T. For some loadings, the components $\hat{T}_i$ depend on the deformation, e.g., for a pressure loading P,

$$\hat{T}_i = -P n_i^*,$$

where n_i^* is the unit normal to the surface in the deformed state, so that to 0(1),

$$n_i^* = n_r \frac{\partial x_r}{\partial y_i} = n_r \frac{\partial y_i}{\partial x_r}.$$

Thus for pressure P on a surface S_p we need to $0(\epsilon)$

$$\sigma_{ik} n_k = -P n_i \qquad \text{on} \quad S_p. \tag{26}$$

We note that for bodies with some dimensions very large compared to a, quantities of $0(\epsilon^2)$ which are neglected in the local equilibrium equations (24) or in the boundary conditions (25) can contribute to the overall balance of force on integration over the body. In fact, for slender bodies some of the applied loads can be second order in ϵ and their relation to the deformation is determined from overall equilibrium considerations. Such second-order loads cannot be related directly to the stress distribution because second-order effects are neglected in the stress-strain relation.

The strains e_{ik} must be such that the left-hand side of (7) is $0(\epsilon^2)$ and that the equilibrium equations (24) with the stresses (23) are satisfied to $0(\epsilon)$. To $0(\epsilon)$, the differential equations governing e_{ik} are therefore formally identical to the equations of classical infinitesimal elasticity for the strains generated by a particular body force field (zero when F_i is zero). A strain field for an equilibrium infinitesimal deformation has the potential to supply a solution for large deflections and small strains. The torsion example of the preceding section for a very long cylinder is an illustration. It is usual to satisfy the governing differential equations exactly in determining solutions in classical elasticity, but it is important here to recognize that the equations need only be satisfied to $0(\epsilon)$. For slender bodies there is then no contradiction between satisfying the local equilibrium equations (24) and in addition imposing overall equilibrium conditions when second order loads are involved.

When functions y_i have been found which generate through (1) and (2) small strains e_{ik} which satisfy the equilibrium equations (24), it must be verified that the first derivatives of e_{ik} are also small, a condition under which (24) was derived.

Materials subject to kinematic constraints can also be treated. In the case of incompressible materials, the condition of no volume change gives, to $0(\epsilon)$,

$$e_{ii} = 0$$

and the stresses are given by

$$\sigma_{ik} = c_{ikmn} e_{mn} + p\delta_{ik},$$

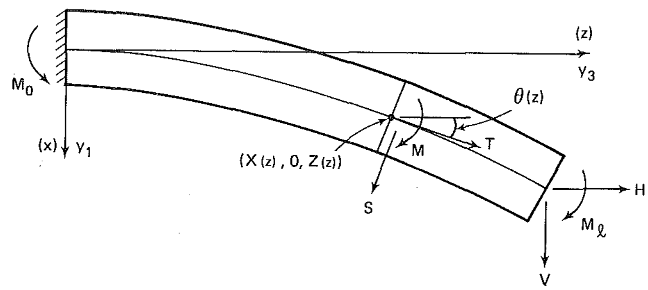

Fig. 1 Bending of a beam about a principal axis by end loads

where the pressure p is a scalar function of position of the order of $E\epsilon$.

We note that a reference state under (small) initial stress adds a linear term in e_{ik} to the form (22) for W. For modeling of nonlinear small strain behavior, a third-order term is included in (22) and a corresponding second order term occurs in the stresses σ_{ik}. For small enough strains, the linear terms will dominate (as shown in [7]), but for some materials, such as rock, at practical levels of strain the second-order terms are significant. This requires the second-order moduli to be several orders of magnitude larger than the first-order moduli c_{ikmn}.

4 Torsion of a Cylinder

The small strain solution for pure torsion of a cylinder of homogeneous isotropic material is given by (10). The twist τ per unit length is such that $\epsilon = \tau a$ is small, a being the maximum distance of particles in the cross section from the axis of torsion. To $0(\epsilon)$, the nonzero strains are given by (11) and they provide stresses σ_{ik} which satisfy the equations of equilibrium (24) with no body force and have zero traction on the lateral surface because $w(x_1, x_2)$ is the St. Venant torsion function. The Kirchhoff stresses σ_{ik} are equal to the stresses of the classical solution and the twisting moment has the St. Venant value. With the length l of the cylinder unrestricted there is no limit on the amount of rotation of one end of the cylinder relative to the other, but τa must be small in order to have small strains involved in the deformation (10). If the cylinder is not too long so that l/a is 0(1), then to $0(\epsilon)$ the deformation (10) involves displacements equal to those of the St. Venant solution and given by the virtual displacements (12).

5 Bending of a Beam About a Principal Axis

In this section we consider a beam of isotropic material bent about a principal axis of inertia of the cross section so that the deformed central line lies in a plane. The beam is bent by end loads only, there being no body forces and no tractions on the lateral surface of the beam. The approach leads to solutions valid for any value of the length to thickness ratio, within the assumption of small-strain, linear-elastic behavior.

To fix ideas, we suppose that initially the beam is horizontal. We take the y_3 axis to be the line of centroids of the sections. The y_1 axis is directed vertically downward and the y_1 and y_2 axes are principal axes of inertia of the cross section. Where convenient, we use x,y,z for the initial particle locations x_i. The end $z = 0$ is held fixed, and the loads on the end $z = l$ deform the central line into a plane curve in the $y_1 - y_3$ plane, l being the length of the beam. The tractions applied to the end $z = l$ are statically equivalent to a downward vertical force V and a horizontal force H through the centroid of the section together with a moment M_l about an axis parallel to the y_2 direction, Fig. 1. To avoid questions of instability due to flexure, we suppose that the moment of inertia of the section about the y axis is smaller than that about the x axis. The reference length a is taken to be half the depth of the beam, and we assume that the diameter of the cross section in the y direction is comparable to a.

We suppose that in the deformed state the central line becomes the curve

$$y_i = \{X(z),\ \ 0,\ \ Z(z)\}, \tag{27}$$

where the functions X,Z are to be determined. The extension of the central line is denoted by $e(z)$ so that we have

$$X'^2 + Z'^2 = (1+e)^2,$$

where a prime denotes differentiation with respect to z. We require e to be $0(\epsilon)$ or smaller. The inclination of the tangent to the deformed central line is denoted by $\theta(z)$, so that

$$\sin\theta = X'/(1+e), \quad \cos\theta = Z'/(1+e). \tag{28}$$

To have small strains, a cross section of the beam must become a surface close to a plane which is normal to the deformed central line. The deformation of the beam can be thought of as effected by first giving the particles a small displacement, then cross sections are rotated an amount θ about an axis parallel to the y_2 axis through the centroid $(0,0,z)$ of the section, and finally a translation is applied to bring the centroid to its proper location on the curve (27). Thus we take

$$y_1 = X + (x+u)\cos\theta + w\sin\theta, \quad y_2 = y + v,$$
$$y_3 = Z - (x+u)\sin\theta + w\cos\theta, \tag{29}$$

where u,v,w are functions of x,y,z which vanish with x and y. For small strains the first partial derivatives of u,v,w will be $0(\epsilon)$, and then u,v,w will be $0(\epsilon a)$ because they vanish on the central line. We also assume that the derivative θ' is $0(\epsilon)/a$; to $0(\epsilon)$, θ' is the curvature of the deformed central line. We have

$$\frac{\partial y_i}{\partial x_k} = \begin{pmatrix} \cos\theta & 0 & \sin\theta \\ 0 & 1 & 0 \\ -\sin\theta & 0 & \cos\theta \end{pmatrix} + 0(\epsilon). \tag{30}$$

From (1) and (28) we can calculate C_{ik} and we find that to $0(\epsilon)$

$$C_{11} = 1 + 2\frac{\partial u}{\partial x}, \qquad C_{22} = 1 + 2\frac{\partial v}{\partial y}, \qquad C_{33} = 1 + 2e + 2\frac{\partial w}{\partial z} - 2\theta' x,$$
$$C_{13} = \frac{\partial u}{\partial z} + \frac{\partial w}{\partial x}, \quad C_{23} = \frac{\partial v}{\partial z} + \frac{\partial w}{\partial y}, \quad C_{12} = \frac{\partial u}{\partial y} + \frac{\partial v}{\partial x}. \tag{31}$$

Guided by the St. Venant solution for flexure of a beam, we now assume that

$$u = -\nu e x + \frac{1}{2}\nu\theta'(x^2 - y^2), \quad v = -\nu e y + \nu\theta' xy,$$
$$w = \theta''(\chi + xy^2). \tag{32}$$

Here ν is Possion's ratio and the St. Venant flexure function $\chi(x,y)$ is harmonic in the cross section A of the beam and satisfies the condition

$$\frac{\partial\chi}{\partial x}n_x + \frac{\partial\chi}{\partial y}n_y = -\left\{\frac{\nu}{2}x^2 + \left(1 - \frac{\nu}{2}\right)y^2\right\}n_x - (2+\nu)xyn_y \tag{33}$$

on the boundary of the cross section, where (n_x,n_y) is the unit normal. We assume here that the center of flexure lies on the x axis; otherwise we add terms corresponding to torsion of the order of ϵ/l per unit length to the displacements (32) with a rotation of the end $z = l$ of amount $0(\epsilon)$, in order to have zero twisting moment on the section $z = l$. With (32), the strain e_{ik} can be found from (2) and (31), and we find that, to $0(\epsilon)$, $e_{12} = 0$ and

$$e_{11} = -\nu e + \nu\theta' x, \quad e_{22} = -\nu e + \nu\theta' x,$$
$$e_{33} = e - \theta' x + \theta'''(\chi + xy^2),$$
$$e_{13} = -\frac{\nu}{2}e' x + \frac{1}{2}\theta''\left\{\frac{\partial\chi}{\partial x} + \frac{\nu}{2}x^2 + \left(1 - \frac{\nu}{2}\right)y^2\right\},$$
$$e_{23} = -\frac{\nu}{2}e' y + \frac{1}{2}\theta''\left\{\frac{\partial\chi}{\partial y} + (2+\nu)xy\right\}.$$

The contribution of the term in θ''' to e_{33} will turn out to be of the second order in ϵ at most, as will the contribution from e' to e_{13} and e_{23}. Thus to $0(\epsilon)$ the nonzero components of the stresses σ_{ik} are

$$\sigma_{13} = \mu\theta''\left\{\frac{\partial\chi}{\partial x} + \frac{\nu}{2}x^2 + \left(1 - \frac{\nu}{2}\right)y^2\right\},$$
$$\sigma_{23} = \mu\theta''\left\{\frac{\partial\chi}{\partial y} + (2+\nu)xy\right\},$$
$$\sigma_{33} = E(e - \theta' x) \tag{35}$$

where E is Young's modulus and μ is the shear modulus.

With the boundary condition (33) on the flexure function χ, the tractions on the lateral surface are zero to $0(\epsilon)$. From (35)

$$\frac{\partial\sigma_{ik}}{\partial x_k} = \left(\mu\theta'''\left\{\frac{\partial\chi}{\partial x} + \frac{\nu}{2}x^2 + \left(1 - \frac{\nu}{2}\right)y^2\right\},\right.$$
$$\left.\mu\theta'''\left\{\frac{\partial\chi}{\partial y} + (2+\nu)xy\right\}, Ee'\right). \tag{36}$$

With θ''' and e' of second order in ϵ at most, the equilibrium equations (24) with F_i zero will be satisfied to $0(\epsilon)$.

We note that the forms (35) for σ_{13} and σ_{23} are correct only to $0(\epsilon)$. For a slender enough beam, θ'' becomes $0(\epsilon^2)$ and the shear stresses σ_{13}, σ_{23} are then second order in ϵ at most; in general, they will no longer be given by (35) because second-order terms in the stress-strain relations have been ignored.

Virtual displacements v_i which give the strains (34) to $0(\epsilon)$ through the infinitesimal forms (8) are given by

$$v_1 = -\nu e x + \frac{\nu}{2}\theta'(x^2 - y^2) + \int_0^z \theta dz,$$
$$v_2 = -\nu e y + \nu\theta' xy,$$
$$v_3 = \int_0^z e dz - \theta x + \theta''(\chi + xy^2).$$

The deformed shape of the central line, or equivalently the function $\theta(z)$, is determined from conditions of overall equilibrium. The resultant of the tractions on the surface which was initially the cross section $z =$ constant is statically equivalent to transverse and longitudinal forces $S(z)$ and $T(z)$ through the deformed position of the centroid of the section together with a moment $M(z)$ about an axis parallel to the y_2 axis, Fig. 1. The forces S and T act at an angle θ to the y_1 and y_3 axes, respectively, and we have

$$S\cos\theta + T\sin\theta = \int_A T_{31}dA, \; -S\sin\theta + T\cos\theta = \int_A T_{33}dA,$$
$$M = \int_A \{(y_3 - Z)T_{31} - (y_1 - X)T_{33}\}dA. \tag{37}$$

where the integrals are evaluated over the cross section $z =$ constant. With (28) and (29) and

$$T_{ki}=\sigma_{mk}\frac{\partial y_i}{\partial x_m},$$

we find that to $0(\epsilon)$ the moment is given by

$$M=-\int_A x\sigma_{33}dA. \tag{38}$$

With the value for σ_{33} given by (35) we have to $0(\epsilon)$

$$M=EI\theta', \tag{39}$$

where I is the moment of inertia of the cross section about the y axis. We also have to $0(\epsilon)$

$$S=\int_A \sigma_{13}dA, \quad T=\int_A \sigma_{33}dA. \tag{40}$$

With (35), (40) gives to $0(\epsilon)$

$$S=-EI\theta'', \quad T=EAe, \tag{41}$$

where A is the area of the cross section. The properties of the flexure function have been used in deriving the value for S, as in the St. Venant theory. We emphasize that *expressions (40) and (41) for S and T are correct only to $0(\epsilon)$*. For slender beams, S and T can be one or more orders of smallness less than $EA\epsilon$ and terms ignored in deriving (40) can contribute to S and T. For any length beam, the value (39) for M in conjunction with the equations of overall equilibrium for an arbitrary portion of the beam, will be seen to be sufficient to determine the shape of the deformed central line and the forces S and T for a given end loading within the accuracy of the theory. Thus the forces S and T can be considered to be in the nature of reactions because they can be found without direct use of the stress-strain relations. For this special case of bending about a principal axis by end loads only, we will see that equilibrium requires S to be $-dM/dz$ so that the value given by (41) for S will still be the dominant term when S is of smaller order than $EA\epsilon$.

For equilibrium of the portion of the beam between the end $z=0$ and a section $z=$ constant, we need

$$M+VZ-HX=M_0, \quad S\cos\theta+T\sin\theta=V, \quad -S\sin\theta+T\cos\theta=H, \tag{42}$$

where M_0 is the moment applied to the end $z=0$. If we differentiate these relations with respect to z and use (28), we arrive at the (exact) differential form of the equilibrium conditions,

$$M'+S(1+e)=0, \quad S'+T\theta'=0, \quad T'-S\theta'=0. \tag{43}$$

To our order of accuracy, e can be set equal to zero in the first of equations (43). Equations (43) are special cases of the general equations of equilibrium [1] for the bending and twisting of thin rods.

The first of (43), with (39) and the second and third of (42), shows that the deformed central line has the shape of the elastica [1, 8].

If we take H and V to be zero, the simple case of pure bending by terminal couples, the equilibrium equations (42) show that S and T are zero and the bending moment M has the constant value M_0. From (39), θ' is M_0/EI to $0(\epsilon)$ and the central line becomes a circle of radius $1/\theta'$. The extension e of the central line will be $0(\epsilon^2)$ in general and will depend on the second-order effects in the stress-strain relations. The second-order extension induced in an isotropic cylinder by bending has been considered by Blackburn and Green [9].

The St. Venant solution for flexure by a transverse end load, the case when H and M_l vanish, is derived on the assumption that θ is $0(\epsilon)$. If we set $M_0=Vl$ and $Z=z$ in the first of (42), use the value (39) for M and integrate using θ zero at $z=0$, we get the St. Venant value

$$\theta=\frac{\epsilon}{2}\,\frac{z}{a}\left(2-\frac{z}{l}\right), \tag{44}$$

where $\epsilon=Vla/EI$. Because the first of the overall equilibrium conditions (42) is satisfied to $0(\epsilon)$ only when θ remains $0(\epsilon)$, the St. Venant solution is valid only for moderate values of l/a.

6 Bending of a beam by a Vertical End Load

To illustrate the approach of the preceding section, we consider a horizontal cantilever beam loaded by a vertical load V at the free end. With the horizontal load H zero we suppose that e is $0(\epsilon^2)$ and verify this assumption later. We denote by L the value of Z at $z=l$ so that L is the horizontal extent of the beam in the deformed position. From (28),

$$L=Z(l)=\int_0^l \cos\theta\, dz \tag{45}$$

correct to $0(\epsilon)$. The end moment M_0 is VL and as a measure of the strain in the beam we set

$$\epsilon=M_0a/EI=VLa/EI,$$

so that ϵ (assumed positive) is essentially the magnitude of the strain in the outer fibers at the fixed end. With the value (39) for M, the first of the equilibrium equations (42) gives, after division by EI,

$$\theta'+\frac{V}{EI}Z=\frac{\epsilon}{a}. \tag{46}$$

If we differentiate (46), use (28) and ignore e in comparison with 1 we obtain

$$\theta''+\frac{\epsilon}{aL}\cos\theta=0, \tag{47}$$

which is the equation of the elastica [1, 8]. (The coefficient ϵ/aL is equal to V/EI.) Equation (47) can also be derived from the first of (43) by using $S=V\cos\theta$, which follows from the second and third of (42), and the value (39) for M. At the fixed end θ is zero and at the end $z=1$ the moment is zero so that we have

$$\theta=0 \quad \text{at} \quad z=0, \quad \theta'=0 \quad \text{at} \quad z=l. \tag{48}$$

From (46), θ' is ϵ/a at $z=0$ where $Z=0$. We see that (45) is consistent with equation (47) and the end values of θ'. One approach to determine θ is to choose a value for ϵ/a, solve (47) numerically subject to

$$\theta=0, \quad \theta'=\epsilon/a \quad \text{at} \quad z=0, \tag{49}$$

and by iteration find the value of ϵ/aL which makes θ' zero at $z=l$. The functions $X(z)$ and $Z(z)$ can then be found by integration from (28) (with e set equal to zero). The St. Venant solution (44) for small θ is obtained by setting L equal to l and $\cos\theta$ equal to 1 in (46) and using (49).

A first integral of (47) is

$$\theta'^2+\frac{2\epsilon}{aL}\sin\theta=\frac{\epsilon^2}{a^2}, \tag{50}$$

where we have used (49). If we denote the value of θ at $z=l$ by θ_l, we have from (50) and (48)

$$\sin\theta_l=\frac{1}{2}\,\frac{\epsilon L}{a}. \tag{51}$$

For θ_l to be appreciably different from zero, $\epsilon L/a$ and therefore $\epsilon l/a$ must be $0(1)$, and the beam is very long compared to its lateral dimensions. From (46) and (47) we have, using $Z\le L$,

$$|\theta'|\le\epsilon/a, \quad |\theta''|\le\epsilon/aL.$$

From the first of these inequalities and (50), we have

$$0\le\sin\theta\le\frac{1}{2}\,\frac{\epsilon L}{a}, \tag{52}$$

and after differentiating (47), we easily find that

$$|\theta'''| \leq \epsilon^3/2a^3.$$

The estimates for the derivatives of θ agree with those used in the preceding section. The fourth derivative of θ can be shown to be no greater than $\epsilon^3/a^3 L$ in magnitude.

That the extension of the beam is $0(\epsilon^2)$ as assumed follows from

$$\frac{T}{EA} = \frac{V}{EA}\sin\theta = \frac{I\epsilon}{AaL}\sin\theta,$$

which is seen to be $0(\epsilon^2)$ from (52).

If we write

$$\zeta = z/l, \quad k = \epsilon l/a,$$

then we find that

$$\theta = \frac{k}{2}\zeta(2-\zeta) - \frac{k^3}{240}\zeta^2(8 - 10\zeta^2 + 6\zeta^3 - \zeta^4) + 0(k^5),$$

$$\frac{X}{l} = \frac{k}{2}\zeta^2\left(1 - \frac{\zeta}{3}\right) - \frac{k^3}{120}\zeta^3\left(\frac{4}{3} + 5\zeta - 7\zeta^2 + 3\zeta^3 - \frac{3}{7}\zeta^4\right) + 0(k^5), \tag{53}$$

$$\frac{Z}{l} = \zeta - \frac{k^2}{120}\zeta^3(20 - 15\zeta + 3\zeta^2) + 0(k^4).$$

When $k = \epsilon l/a = 1$, the end slope is close to half a radian and (53) gives θ_l to within 0.02 percent of the value obtained by numerical integration; the corresponding errors in the approximate forms for X and Z are 0.2 and 0.4 percent, respectively. The leading terms in (53) are the values according to the St. Venant theory; for $\epsilon l/a = 1$ they overestimate θ_l and $X(l)$ by only 2.5 and 5 percent, respectively. The approximate formulas

$$\frac{X(l)}{l} \sim \frac{1}{3}\,\frac{\epsilon l}{a}\Big/\left\{1 + \frac{1}{21}\left(\frac{\epsilon l}{a}\right)^2\right\},$$

$$\frac{Z(l)}{l} = \frac{L}{l} \sim 1\Big/\left\{1 + \frac{1}{15}\left(\frac{\epsilon l}{a}\right)^2\right\} \tag{54}$$

give the end values of X and Z to within 1 percent for $\epsilon l/a$ up to 3. Because $VL = M_0$ we also have the approximate formula

$$\frac{Va^2}{EI} \sim \frac{\epsilon a}{l}\left\{1 + \frac{1}{15}\left(\frac{\epsilon l}{a}\right)^2\right\} \tag{55}$$

with the same accuracy as the approximate formulas (54).

The case of an end load at a fixed angle to the vertical can be treated similarly.

Acknowledgment

This work was begun while the author was a Sherman Fairchild Distinguished Scholar at the California Institute of Technology. Thanks are due to T. K. Caughey, J. K. Knowles, and T. W. Shield for helpful discussions.

References

1 Love, A. E. H., *A Treatise on the Mathematical Theory of Elasticity*, Cambridge Univ., 4th Ed., 1927; Reprinted by Dover, New York, 1944.

2 Antman, S. S., "The Theory of Rods," in: *Hand. Phys.*, Vol. VI*a*/2, Springer, Berlin, 1972, pp. 641–703.

3 Prager, W., *Introduction to Mechanics of Continua*, Ginn & Co., Boston, 1961.

4 Truesdell, C., and Noll, W., "The Non-Linear Field Theories of Mechanics," *Hand. Phys.*, Vol. III/3, Springer, Berlin, 1965.

5 Shield, R. T., "The Rotation Associated With Large Strains," *SIAM J. Appl. Math.*, Vol. 22, 1973, pp. 483–491.

6 Sokolnikoff, I. S., *Mathematical Theory of Elasticity*, McGraw-Hill, New York, 2nd Ed., 1956.

7 Bharatha, S., and Levinson, M., "On Physically Nonlinear Elasticity," *J. Elasticity*, Vol. 7, 1977, pp. 307–324.

8 Frisch-Fay, R., *Flexible Bars*, Butterworth, Washington, 1962.

9 Blackburn, W. S., and Green, A. E., "Second-Order Torsion and Bending of Isotropic Elastic Cylinders," *Proc. Roy. Soc. Lond.*, Series A, Vol. 240, 1957, pp. 408–422.

C. H. Wu
Professor,
Department of Civil Engineering,
Mechanics and Metallurgy,
University of Illinois at Chicago,
Chicago, Ill. 60680
Mem. ASME

Plane Anisotropic Thermoelasticity

The problem is formulated in terms of the three pairs of eigenvalues of the elasticity constants and the pair of eigenvalues of the heat conduction constants. Special attentions are given to the cases where the latter eigenvalue pair becomes equal to one or more pairs of the former group. The problem of a crack in an infinite medium is used as an example and solved exactly. This solution, however, is valid only for the case where the four pairs of eigenvalues are distinct.

1 Introduction

For plane deformations in a general anisotropic material, the most convenient and powerful approach appears to be that introduced by Stroh [1]. The approach was used to study surface waves by Barnett et al. [2], and Chadwick and Smith [3]. It was extensively used in dealing with dislocation and elasticity problems [4–6]. In the context of analyzing stress singularities, a most exhaustive and complete treatment can be found in a series of recent papers by Ting et al. (See e.g. [7–9]). A plane-stress version of the Stroh vectors was discussed by Wu [10].

A systematic use of the approach was conducted by Clements [11] in studying the thermal stress in a half space. His work was a generalization of Akoz and Tauchert [12] and Sharma [13]. In this paper the plane deformation is formulated in general terms. The basic elements are the three pairs of eigenvalues of the elasticity constants and the pair of eigenvalues of the heat conduction constants. Special attentions are given to the cases where the heat-eigenvalue becomes equal to a single or double elasticity-eigenvalue.

The governing equations, formulated in terms of several complex variables, resemble very much the structure of equations governing the forced vibrations of discrete systems in that the heat-eigenvalue plays the role of forcing frequency while the elasticity-eigenvalues may be identified with the natural frequencies. The constructions of a particular solution as a linear combination of the Stroh vectors is greatly facilitated by this observation. A direct application of the explicit result given by Ting and Hoang [9] leads to the exact solution for a crack in an infinite medium subjected to remote stresses and temperature.

2 Basic Equations

In a fixed rectangular coordinates z_i (i = 1, 2, 3), let u_i, ϵ_{ij}, σ_{ij}, T, and q_i be the displacement, strain, stress, temperature, and heat flux, respectively. The complete set of governing equations for uncoupled thermoelastic problems involving homogeneous but anisotropic materials are [14]:

$$q_i = -k_{ij} T_{,j}, \tag{2.1}$$

$$q_{i,i} = -k_{ij} T_{,ij} = 0, \tag{2.2}$$

$$\epsilon_{ij} = 1/2(u_{i,j} + u_{j,i}), \tag{2.3}$$

$$\sigma_{ij} = c_{ijke}\epsilon_{ke} - \beta_{ij} T = c_{ijke} u_{k,e} - \beta_{ij} T, \tag{2.4}$$

$$\sigma_{ij,j} = c_{ijke} u_{k,ej} - \beta_{ij} T_{,j} = 0, \tag{2.5}$$

where

$$k_{ij} = k_{ji}, \tag{2.6}$$

$$c_{ijke} = c_{jike} = c_{ijek} = c_{keij}, \tag{2.7}$$

$$\beta_{ij} = \beta_{ji} \tag{2.8}$$

are, respectively, the coefficients of heat conduction, elasticity constants of the anisotropic material, and stress-temperature coefficients. Unless otherwise stated, repeated indices imply summation. Also, Greek suffixes will be understood to take the values 1 and 2 only.

If the displacement components u_i and temperature T are independent of the z_3-coordinate, then (2.2) and (2.5) become

$$k_{\alpha\beta} T_{,\alpha\beta} = 0, \tag{2.9}$$

$$c_{i\beta k\delta} u_{k,\beta\delta} = \beta_{i\alpha} T_{,\alpha} = 0 \tag{2.10}$$

The solution to the preceding equations may be expressed in terms of new variables of the form

$$Z = z_1 + p\, z_2, \tag{2.11}$$

For the temperature distribution, we assume

$$T(z_1, z_2) = f'(Z) = \frac{df}{dZ} \tag{2.12}$$

This form will give a solution to (2.9) if p satisfies the equation

$$k_{11} + 2k_{12}p + k_{22}p^2 = 0. \tag{2.13}$$

Since the quadratic form $k_{\alpha\beta}\, q_\alpha\, q_\beta$ is positive-definite (see Carslaw and Jaeger [15]), the two roots of (2.13) are complex conjugate. We denote the roots by p_0 and $\bar{p}_0$. Hence a general form for the temperature may be written as

$$T(z_1, z_2) = f_0'(Z_0) + g_0'(\bar{Z}_0) \tag{2.14}$$

where

$$Z_0 = z_1 + p_0 z_2 \tag{2.15}$$

and overbars indicate complex conjugates.

Contributed by the Applied Mechanics Division for publication in the JOURNAL OF APPLIED MECHANICS.

Discussion on this paper should be addressed to the Editorial Department, ASME, United Engineering Center, 345 East 47th Street, New York, N.Y. 10017, and will be accepted until two months after final publication of the paper itself in the JOURNAL OF APPLIED MECHANICS. Manuscript received by ASME Applied Mechanics Division, October, 1983.

A general homogeneous solution to (2.10) may be obtained by letting

$$u_i = v_i f(Z) = v_i f(z_1 + pz_2) \tag{2.16}$$

where p and v_i are constants to be determined and f is an arbitrary function of Z. Substituting the above into the homogeneous equations defined by (2.10) we obtain

$$D_{ij} v_j = 0 \tag{2.17}$$

where

$$D_{ij} = D_{ij}(p) = c_{i1j1} + (c_{i1j2} + C_{i2j1})p + C_{i2j2}p^2 \tag{2.18}$$

It follows that for a nontrivial solution of v_i, the determinant of D_{ij} must vanish, i.e.,

$$|D_{ij}(p)| = 0. \tag{2.19}$$

Since the roots of (2.19) are all nonreal [7] there are three pairs of complex conjugates for p which will be donated by p_L and $\overline{p_L}$ $(L = 1,2,3,)$, and three pairs of associated eigenvectors.

If the p_L's are distinct, the three pairs of eigenvectors are denoted by

$$v_{Li} = v_{Li}(p_L) \quad \text{and} \quad \bar{v}_{Li} = \overline{v_{Li}(p_L)} \tag{2.20}$$

which are obtained from

$$D_{ij}(p_L) v_{Lj}(p_L) = 0 \tag{2.21}$$

The relation, together with (2.18), indicates that $\overline{v_{Li}(p_2)}$ is indeed the eigenvector associated with $\overline{p_L}$ (see (2.20)). We will implicitly assume that the eigenvectors are normalized in certain fashion so that no arbitrary constants are involved. Finally, the associated solutions will be denoted by

$$u_i = u_{Li} = v_{Li} f_L(Z_L) + \bar{v}_{Li} g_L(\bar{Z}_L) \tag{2.22}$$

$$\sigma_{ij} = \sigma_{Lij} = \tau_{Lij} \frac{d}{dZ_L} f_L(Z_L) + \bar{\tau}_{Lij} \frac{d}{d\bar{Z}_L} g_L(\bar{Z}_L), \tag{2.23}$$

where

$$Z_L = z_1 + p_L z_2, \tag{2.24}$$

$$\tau_{Lij} = (C_{ijk1} + p_L C_{ijk2}) v_{Lk}, \tag{2.25}$$

and no sum is performed on L. The coefficients τ_{Lij} also satisfy the relations [7]

$$\tau_{12} = -p\tau_{22}, \quad \tau_{11} = p^2 \tau_{22}, \quad \tau_{13} = -p\tau_{23}. \tag{2.26}$$

If p_L is a double root, then a second independent solution may be written as [7]

$$\begin{aligned} u_i = u^*_{Li} = &\left[v'_{Li} f_L(Z_L) + v_{Li} z_2 f'_L(Z_L)\right] \\ &+ \left[\bar{v}'_{Li} g_L(\bar{Z}_L) + \bar{v}_{Li} z_2 g'_L(\bar{Z}_L)\right] \end{aligned} \tag{2.27}$$

$$\begin{aligned} \sigma_{ij} = \sigma^*_{Lij} = &\left[\tau'_{Lij} f'_L(Z_L) + \tau_{Lij} z_2 f''_L(Z_L)\right] \\ &+ \left[\bar{\tau}'_{Lij} g'_L(\bar{Z}_L) + \bar{\tau}_{Lij} z_2 g''_L(\bar{Z}_L)\right] \end{aligned} \tag{2.28}$$

where

$$v'_{Li} = \frac{d}{dp_L} v_{Li}(p_L), \quad \tau'_{Lij} = \frac{d}{dp_L} \tau_{Lij}(p_L) \tag{2.29}$$

and

$$D_{ij} v'_j + D'_{ij} v_j = 0, \tag{2.30}$$

$$\tau'_{ij} = (c_{ijk1} + pc_{ijk2}) v'_k + c_{ijk2} v_k. \tag{2.31}$$

In the foregoing expressions no sum is performed on L.

For isotropic materials, $p = \pm i$ is a triple root but u_3 is uncoupled from u_1 and u_2. As it was commented by Ting and Chou [7], the existence of a triple root for a coupled deformation is not known. We will therefore discard this case in the following discussion.

We return now to the determination of a particular solution to (2.10) which, in view of (2.12)–(2.15), may be written as

$$c_{i\beta k\delta} u_{k,\beta\delta} = b_i(p_0) f''_0(Z_0) \tag{2.32}$$

where

$$b_i(p_0) = \beta_{i1} + \beta_{i2} p_0. \tag{2.33}$$

It is clear that a similar solution will be determined to pair with g_0. The structure of a particular solution is greatly affected by the root p_0 of (2.13) and roots p_L $(L = 1,2,3)$ of (2.19).

(*A*) $\quad p_0 \neq p_1 \neq p_2 \neq p_3$

This is essentially the case studied by Clements [11] for a special class of problems. The even more specialized studies given in [12,13] also belong to this case. We assume

$$u_i = u_{0i} = v_{0i} f_0(Z_0), \qquad \sigma_{0ij} = \tau_{0ij} f'_0(Z_0) \tag{2.34}$$

where τ_{0ij} are related to v_{0i} by (2.25). To determine v_{0i}, we substitute the first of (2.34) into (2.32) to obtain

$$D_{ij}(p_0) v_{0j} = b_i(p_0). \tag{2.35}$$

Since $D_{ij}(p_0)$ is nonsingular,

$$v_{0j} = v_{0j}(p_0) = D^{-1}_{ji}(p_0) b_i(p_0) \tag{2.36}$$

where D^{-1}_{ij}. is the inverse of D_{ij}. A complete particular solution may now be written as

$$u_i = u_{0i} = v_{0i} f_0(Z_0) + \bar{v}_{0i} g_0(\bar{Z}_0), \tag{2.37}$$

$$\sigma_{ij} = \sigma_{0ij} = \tau_{0ij} f'_0(Z_0) + \bar{\tau}_{0ij} g'_0(\bar{Z}_0), \tag{2.38}$$

where τ_{0ij} are again related to v_{0i} by (2.25).

The structure of the equations (2.32) parallels to that of the forced vibrations of a discrete system. In this connection, p_0 may be interpreted as the forcing frequency while p_L $(L = 1,2,3)$ the natural frequencies. It is therefore instructive to rewrite (2.34) in terms of the "natural modes" as follows:

$$u_i = u_{0i} = a_L v_{Li} f_0(Z_0) \tag{2.39}$$

where a_L are constants to be determined from

$$D_{ij}(p_0) v_{Lj} a_L = b_i. \tag{2.40}$$

The constants a_L are, of course, related to the constants v_{0i}, equation (2.36), in a trivial manner, but the mode-approach will facilitate the presentation of cases where a "reasonance" is involved.

(*B*) $\quad p_1 \neq p_2 = p_3, \quad p_0 \neq p_L$

The solution (2.39) must be modified to accommodate (2.27). We write

$$u_i = u_{0i} = (a_\alpha v_{\alpha i} + a_3 v'_{2i}) f_0(Z'_0). \tag{2.41}$$

Substituting the foregoing into (2.32), we find that the constants a_i must satisfy

$$D_{ij}(p_0)[a_\alpha v_{\alpha j} + a_3 v'_{2j}] = b_i. \tag{2.42}$$

(*C*) $\quad p_1 \neq p_2 \neq p_3 = p_0$

The linear combination must be chosen to reflect the resonance with respect to u_{3i}. Accordingly,

$$u_i = u_{0i} = a_\alpha v_{\alpha i} f_0(Z_0) + a_3 v_{3i} z_2 f'_0(Z_0). \tag{2.43}$$

Substituting the foregoing into (2.32) and noting that

$$D_{ij}(p_0) v_{3j}(p_3) = 0, \tag{2.44}$$

we obtain

$$D_{in}(p_0) v_{\alpha j} a_\alpha + D'_{ij}(p_0) v_{3j} a_3 = b_i \tag{2.45}$$

which may be solved for the constants a_i.

(*D*) $\quad p_1 = p_2 \neq p_3 = p_0$

The results for this case may be obtained from (2.43)–(2.45) by replacing $v_{2i} = v'_{1i}$.

(*E*) $p_1 \neq p_2 = p_3 = p_0$

The resonance occurs at a double root. Accordingly,

$$u_i = u_{0i} = a_1 v_{1i} f_0(Z_0) + a_2 v_{2i} z_2 f_0'(Z_0) + a_3[2v_{2i}' z_2 f_0'(Z_0) + v_{2i} z_2^2 f_0''(Z_0)]. \quad (2.46)$$

Substituting the foregoing into (2.32) and applying (2.17) and (2.30), we get

$$D_{ij}(p_0)v_{1j}a_1 + D_{ij}'(p_0)v_{2j}a_2 + 2[D_{ij}'(p_0)v_{2j}' + c_{i2j2}v_{2j}]a_3 = b_i. \quad (2.47)$$

These are the needed equations for the determination of a_i.

For case (*A*), the general solution may now be written as

$$(z_1, z_2) = f_0'(Z_0) + g_0'(\bar{Z}_0), \quad (2.48)$$

$$u_i(z_1, z_2) = \sum_{L=0}^{3} \{ v_{Li} f_L(Z_L) + \bar{v}_{Li} g_L(\bar{Z}_L) \}, \quad (2.49)$$

$$\sigma_{ij}(z_1, z_2) = \sum_{L=0}^{3} \{ \tau_{Lij} f_L'(Z_L) + \bar{\tau}_{Lij} g_L'(\bar{Z}_L) \} - \beta_{ij}[f_0'(Z_0)] + g_0'(\bar{Z}_0)]. \quad (2.50)$$

The general solutions for other cases may be formed in a similar manner.

3 A Crack in a Homogeneous Anisotropic Material

Consider a crack of length $2a$ located on the z_1-axis between $z_1 = -a$ and $z_1 = +a$ in an infinite anisotropic elastic material subjected to a state of uniform remote stresses σ_{2i}^∞ and temperature T^∞ at infinity. The surface of the crack is stress-free and also kept at zero temperature. To study the effects of the crack, it suffices to consider the associated problem in which the crack surface satisfies the conditions

$$T = -T^\infty \qquad \text{on} \qquad -a < z_1 < +a \quad (3.1)$$

$$\sigma_{2j} = -\sigma_{2j}^\infty \qquad \text{on} \qquad -a < z_1 < +a \quad (3.2)$$

and the temperature and stresses vanish at infinity. This is just the problem considered by Ting and Hoang [9] where the temperature effect was not included.

To this end, we choose in (2.48) and (2.49)

$$f_L = \bar{g}_L = 1/2\, A_L[(Z_L{}^2 - a^2)^{1/2} - Z_L] \quad (3.3)$$

where A_L ($L = 0,1,2,3$) are arbitrary complex constants. The temperature, displacements and stresses are

$$T = Re\, A_0 \left[\frac{Z_0}{(Z_0^2 - a^2)^{1/2}} - 1 \right], \quad (3.4)$$

$$u_i = Re \sum_{L=0}^{3} A_L v_{Li} [(Z_L^2 - a^2)^{1/2} - Z_L], \quad (3.5)$$

$$\sigma_{ij} = Re\left\{ \sum_{L=0}^{3} A_L \tau_{Lij} \left[\frac{Z_L}{(Z_L^2 - a^2)^{1/2}} - 1 \right] - A_0 \beta_{ij} \left[\frac{Z_0}{(Z_0^2 - a^2)^{1/2}} - 1 \right] \right\}. \quad (3.6)$$

It is noted that T and σ_{ij} vanish at infinity.

The boundary conditions (3.1) and (3.2) now become

$$-T^\infty = Re\, A_0 \left[\frac{z_1}{\pm i(a^2 - z_1^2)^{1/2}} - 1 \right], \quad (3.7)$$

$$-\sigma_{2j}^\infty = Re\left\{ \sum_{L=0}^{3} A_L \tau_{L2j} - A_0 \beta_{2j} \right\} \left[\frac{Z_1}{\pm i(a^2 - z_1^2)^{1/2}} - 1 \right] \quad (3.8)$$

for $-a < z_1 < +a$. They are satisfied if we let

$$A_0 = T^\infty, \quad (3.9)$$

$$\sum_{L=1}^{3} A_L\, \tau_{L2j} = R_{2j}^\infty = \sigma_{2j}^\infty + T^\infty(\beta_{2j} - \tau_{02j}). \quad (3.10)$$

where

$$\tau_{0ij} = (c_{ijk1} + p_0 c_{ijk2}) D_{ke}^{-1}(p_0)(\beta_{e1} + p_0 \beta_{e2}). \quad (3.11)$$

The solution follows directly from that of [9]. It is

$$u_i = \sum_{L=1}^{3} Re\left\{ J^{-1} \tau_{L2S}^* V_{Li} \left[(Z_L^2 - a^2)^{1/2} - Z_L \right] \right\} R_{2S}^\infty + Re\, T^\infty D_{ij}^{-1}(p_0)(\beta_{j1} + p_0\beta_{j2})[(Z_0^2 - a^2)^{1/2} - Z_0], \quad (3.12)$$

$$\sigma_{ij} = \sum_{L=1}^{3} Re\{ J^{-1} \tau_{L2S} \tau_{Lij} [(Z_L^2 - a^2)^{1/2} - Z_L] \} R_{2S}^\infty + Re\, T^\infty(\tau_{0ij} - \beta_{ij})[(Z_0^2 - a^2)^{1/2} - Z_0], \quad (3.13)$$

where τ_{L2i}^* and J are given in [9],

$$\sum_{L=1}^{3} \tau_{L2j} \tau_{L2S}^* = J\delta_{js}, \quad J = \det(\tau_{L2j}). \quad (3.14)$$

The stress distribution near the tip $x_1 = a$ becomes

$$\sigma_{ij} = Re \frac{\sqrt{a}}{(2r)^{1/2}} \left\{ \sum_{L=1}^{3} [J^{-1} \tau_{L2s}^* \tau_{Lij} \zeta_L^{-1/2}] R_{2s}^\infty + T^\infty(\tau_{0ij} - \beta_{ij}) \zeta_0^{-1/2} \right\} \quad (3.15)$$

where $Z_L - a = r\,\zeta_L \qquad (L = 0, 1, 2, 3). \quad (3.16)$

4 Conclusion

The exact solution obtained by Ting and Hoang [9] for a crack in an infinite anisotropic elastic material is generalized to include temperature effect. It is obtained for the case where the heat conduction property is not in reasonance with the elasticity property (see (2.13) and (2.19)).

In terms of plane anisotropic thermoelasticity, our results obtained for the resonance cases also appear to be new.

References

1 Stroh, A. N., "Steady State Problems in Anisotropic Elasticity," *J. Math. Phys.*, Vol. 41, 1962, pp. 77–103.

2 Barnett, D. M., and Lothe, J., "Synthesis of the Sextic and the Integral Formalism for Dislocation, Greens Function, and Surface Waves in Amisotropic Elastic Solids," *Phys. Norv.*, Vol. 7, 1973, pp. 12–19.

3 Chadwick, P., and Smith, G. D., "Foundations of the Theory of Surface Waves in Amisotropic Elastic Materials," *Adv. in Appl. Mech.*, Vol. 17, 1977, pp. 703–736.

4 Eshelby, J. D., Read, W. T., and Shockley, W., "Anisotropic Elasticity With Applications to Dislocation Theory," *Acta Met.*, Vol. 1, 1953, pp. 251–259.

5 Stroh, A. N., "Dislocations and Cracks in Anisotropic Elasticity," *Philos. Mag.*, Vol. 3, 1958, pp. 625–646.

6 Clements, D. L., "The Response of an Anisotropic Elastic Half-Space to a Rolling Cylinder," *Proc. Cambridge Philos. So.*, Vol. 70, 1971, pp. 467–484.

7 Ting, T. C. T., and Chou, S. C., "Edge Singularities in Anisotropic Composites," *Int. J. Solids Structures*, Vol. 17, 1981, pp. 1057–1068.

8 Ting, T. C. T., "Effects of Change of Reference Coordinates on the Stress Analysis of Anisotropic Elastic Materials," *Int. J. Solids Structures*, Vol. 18, 1982, pp. 139–152.

9 Ting, T. C. T., and Hoang, P. H., "Singularities at the Edge of a Crack Normal to the Interface of an Anisotropic Layered Composite," private communication, to be published.

10 Wu, C. H., "Plane-Stress Approximation for Anisotropic Plates Without a Plane of Symmetry," submitted for publication.

11 Clements, D. L., "Thermal Stress in Anisotropic Elastic Half-Space," *SIAM J. Appl. Math.*, Vol. 24, 1973, pp. 332–337.

12 Akoz, A. Y., and Tauchert, T. R., "Thermal Stresses in an Orthotropic Elastic Semispace," ASME JOURNAL OF APPLIED MECHANICS, Vol. 39, 1972, pp. 87–90.

13 Sharma, B., "Thermal Stresses in Transversely Isotropic Semi-Infinite Elastic Solids," ASME JOURNAL OF APPLIED MECHANICS, Vol. 25, 1958, pp. 86–88.

14 Nowacki, W., *Thermoelasticity*, Addison-Wesley, Reading, Mass., 1962.

15 Carslaw, H. S., and Jaeger, J. C., *Conduction of Heat in Solids*, Clarendon Press, Oxford, 1959.

Y. Sugano
Research Associate,
Department of Mechanical Engineering,
College of Engineering,
University of Osaka Prefecture,
Osaka, Japan 591

On a Stress Function Method of Plane-Stress Thermoelastic Problem in a Multiply Connected Region of Variable Thickness

A plane-stress thermoelastic problem in a multiply connected region of variable thickness is formulated in terms of a stress function by deriving new Michell integral conditions necessary for the assurance of single-valuedness of rotation and displacements. The system of fundamental equations is solved by means of a finite difference method and numerical calculations are carried out for the cases of a rectangular plate of variable thickness with a rectangular hole.

1 Introduction

The plane thermal-stress problem in a multiply connected region has attracted the attention of numerous investigators [1–4]. However, no solutions to plane-stress thermoelastic problems in a multiply connected region of variable thickness necessitating an assurance of single-valuedness of rotation and displacements have been reported. The determination of the thermal stresses in a multiply connected region of variable thickness plays an important role in the design of structural elements such as fins, cylinder heads, and rotating disks.

The aim of this paper is to present the formulation of the plane-stress thermoelastic problem in a multiply connected region of variable thickness in terms of Airy's stress function. New Michell integral conditions necessary for the assurance of single-valuedness of the rotation and displacements are derived taking into account the variation in thickness in both the x and y directions. The resulting system of governing equations obtained here is solved numerically by means of a finite difference method. Although the numerical method possesses some drawbacks, which are immediately apparent when problems with two distinct boundary geometries are considered, the application of this method will enable one to obtain a system of simultaneous linear equations with respect to stress functin to be solved directly by replacing each partial differential term in the governing equations of the problem with the corresponding finite difference operator. Furthermore, an application of some weighted residual technique or variational principle (such as energy minimization) necessary for application of the finite element method is unnecessary for finite difference method.

The effect of the variation of the thickness on the distributions of the temperature and the thermal stresses are discussed from the numerical results for a finite thin rectangular plate with a rectangular hole and having a decreasing thickness from the inner boundary toward the outer boundary.

2 The Plane-Stress Thermoelastic Problem for a Multiply Connected Region of Variable Thickness

2.1 Temperature Field. Consider a multiply connected region of variable thickness (i.e., a finite plate of variable thickness with many holes) bounded by $M+1$ nonintersecting contours $C_0, C_1, \ldots, C_M$ of which C_0 contains all the others as shown in Fig. 1(*a*). It is assumed that the multiply connected region, initially at the same uniform temperature T_0 as the surrounding media, is exposed to abrupt changes $T_{1i}(i=0,1,2, \ldots, M)$ in the surrounding temperatures adjacent to the boundaries C_i and that there is a heat loss into the surrounding media at the constant temperature T_0 on the upper and lower surfaces of the finite region. Now we take an elemental volume with variations of thickness in both the x and y directions as shown in Fig. 1(*b*). If the thickness of the position of the coordinates (x,y) is expressed by $D(x,y)$, then the following heat-conduction equation from the consideration of the equilibrium of heat for the elemental volume may be obtained:

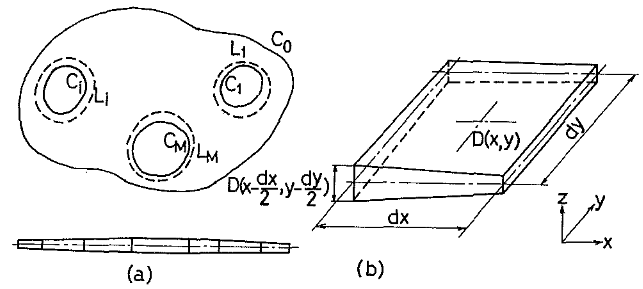

Fig. 1 Multiply connected region of variable thickness

Contributed by the Applied Mechanics Division for publication in the Journal of Applied Mechanics.

Discussion on this paper should be addressed to the Editorial Department, ASME, United Engineering Center, 345 East 47th Street, New York, N.Y. 10017, and will be accepted until the month after final publication of the paper itself in the Journal of Applied Mechanics. Manuscript received by ASME Applied Mechanics Division, May, 1983; final revision, January, 1984.

$$c\rho \frac{\partial T}{\partial t} = \lambda\left(\frac{\partial^2 T}{\partial x^2} + \frac{\partial^2 T}{\partial y^2}\right) + \frac{\lambda}{D}\left(\frac{\partial D}{\partial x}\frac{\partial T}{\partial x} + \frac{\partial D}{\partial y}\frac{\partial T}{\partial y}\right)$$

$$-\frac{2h_0}{D}(T-T_0)\sqrt{1+\left(\frac{\partial D}{\partial x}\right)^2 + \left(\frac{\partial D}{\partial y}\right)^2} \qquad (1)$$

where c, ρ, and λ denote the specific heat, density, and thermal conductivity, respectively, and h_0 is the heat transfer coefficient of the upper and lower surfaces of the region.

From the preceding description, the initial and boundary conditions may be expressed as

$$T = T_0, \quad \text{at} \quad t = 0 \qquad (2)$$

$$\lambda \frac{\partial T}{\partial n_i} + h_{1i}(T - T_{1i}) = 0, \quad \text{on} \quad C_i \qquad (3)$$

where n_i is the outward normal at the point p_i on the ith boundary C_i and h_{1i} is the heat transfer coefficient on the boundary.

2.2 Plane-Stress Thermoelastic Problem. The plane-stress thermoelastic problem in the multiply connected region of variable thickness associated with the heat-conduction problem described in the foregoing is formulated in terms of Airy's stress function, assuming that both the thickness itself and the change in thickness are small, and that the method of analysis to the plane-stress problem of constant thickness can be extended to the same problem of variable thickness.

First, the equations of equilibrium of stress components for the element as shown in Fig. 1(b) are

$$\frac{\partial(D\sigma_{xx})}{\partial x} + \frac{\partial(D\sigma_{xy})}{\partial y} = 0, \quad \frac{\partial(D\sigma_{xy})}{\partial x} + \frac{\partial(D\sigma_{yy})}{\partial y} = 0. \qquad (4)$$

These equilibrium equations are identically satisfied by Airy's stress function defined by the following equations similar to those in the constant-thickness case:

$$\sigma_{xx} = \frac{1}{D}\frac{\partial^2\chi}{\partial y^2}, \quad \sigma_{yy} = \frac{1}{D}\frac{\partial^2\chi}{\partial x^2}, \quad \sigma_{xy} = -\frac{1}{D}\frac{\partial^2\chi}{\partial x\partial y}. \qquad (5)$$

The stress-strain relations for the plane-stress thermoelastic problem are

$$\epsilon_{xx} = \frac{1}{E}(\sigma_{xx} - \nu\sigma_{yy}) + \alpha T, \quad \epsilon_{yy} = \frac{1}{E}(\sigma_{yy} - \nu\sigma_{xx}) + \alpha T,$$

$$\epsilon_{xy} = \frac{1}{E}(1+\nu)\sigma_{xy} \qquad (6)$$

where E, α, and ν are the Young's modulus, the linear thermal expansion coefficient, and the Poisson's ratio, respectively. The compatibility condition for these strain components is

$$\frac{\partial^2\epsilon_{xx}}{\partial y^2} + \frac{\partial^2\epsilon_{yy}}{\partial x^2} = 2\frac{\partial^2\epsilon_{xy}}{\partial x\partial y}. \qquad (7)$$

Substituting equations (6) into equation (7) and expressing by equations (5) the stress components in the resulting equation, yield the following compatibility equation of Airy's stress function representation.

$$\frac{\partial^4\chi}{\partial x^4} + 2\frac{\partial^4\chi}{\partial x^2\partial y^2} + \frac{\partial^4\chi}{\partial y^4} - \frac{2}{D}\frac{\partial D}{\partial x}\frac{\partial^3\chi}{\partial x^3} - \frac{2}{D}\frac{\partial D}{\partial y}\frac{\partial^3\chi}{\partial y^3}$$

$$-\frac{2}{D}\frac{\partial D}{\partial y}\frac{\partial^3\chi}{\partial x^2\partial y} - \frac{2}{D}\frac{\partial D}{\partial x}\frac{\partial^3\chi}{\partial x\partial y^2} + \frac{1}{D}\left[\frac{2}{D}\left(\frac{\partial D}{\partial x}\right)^2 - \frac{2\nu}{D}\left(\frac{\partial D}{\partial y}\right)^2\right.$$

$$\left.-\frac{\partial^2 D}{\partial x^2} + \nu\frac{\partial^2 D}{\partial y^2}\right]\frac{\partial^2\chi}{\partial x^2} + \frac{1}{D}\left[\frac{2}{D}\left(\frac{\partial D}{\partial y}\right)^2 - \frac{2\nu}{D}\left(\frac{\partial D}{\partial x}\right)^2\right.$$

$$\left.-\frac{\partial^2 D}{\partial y^2} + \nu\frac{\partial^2 D}{\partial x^2}\right]\frac{\partial^2\chi}{\partial y^2} + \frac{2(1+\nu)}{D}\left(\frac{2}{D}\frac{\partial D}{\partial x}\frac{\partial D}{\partial y} - \frac{\partial^2 D}{\partial x\partial y}\right)\frac{\partial^2\chi}{\partial x\partial y}$$

$$= -E\alpha D\left(\frac{\partial^2 T}{\partial x^2} + \frac{\partial^2 T}{\partial y^2}\right) \qquad (8)$$

Now the traction-free boundary conditions on the ith boundary C_i may be expressed in terms of Airy's stress function as follows:

$$\left.\begin{aligned} (\chi)_{p_i} &= c_{1i}x_{p_i} + c_{2i}y_{p_i} + c_{3i} \\ (\partial\chi/\partial n')_{p_i} &= c_{1i}\cos(x,n')_{p_i} + c_{2i}\cos(y,n')_{p_i} \end{aligned}\right\} \qquad (9)$$

where p_i is an arbitrary point on C_i and n' is an arbitrary direction which does not coincide with the tangential direction to C_i. Since the addition of a linear function to χ does not affect the stress distribution, one set of these constants c_{ji} ($j=1,2,3$; $i=0, 1, \ldots, M$) in the multiply connected region may be taken to be zero and it is usually convenient to take $c_{j0}=0$. The remaining $3M$ constants c_{jk} ($k=1,2,\ldots,M$) must be determined from the following conditions necessary for the assurance of single-valuedness of the rotation and displacements pointed out by Michell [5]:

$$\oint d\omega_z = 0, \quad \oint du_x = 0, \quad \oint du_y = 0. \qquad (10)$$

But there seems to be no known results on the conditions that must be considered to ensure the single-valuedness of the rotation and displacements in the multiply connected region of variable thickness. In this paper, therefore, we derive the conditions necessary for the assurance of single-valuedness of the rotation and displacements, taking into account the variation of thickness in both the x and y directions in terms of Airy's stress function as follows:

$$\oint_{L_i}\frac{\partial}{\partial n}\left(\frac{1}{D}\nabla^2\chi + E\alpha T\right)ds + (1+\nu)\oint_{L_i}\frac{\partial}{\partial y}\left(\frac{1}{D}\right)d\left(\frac{\partial\chi}{\partial x}\right)$$

$$-(1+\nu)\oint_{L_i}\frac{\partial}{\partial x}\left(\frac{1}{D}\right)d\left(\frac{\partial\chi}{\partial y}\right) = 0 \qquad (11)$$

$$\oint_{L_i}\left(y\frac{\partial}{\partial n} - x\frac{\partial}{\partial s}\right)\left(\frac{1}{D}\nabla^2\chi + E\alpha T\right)ds + (1+\nu)\oint_{L_i}y\frac{\partial}{\partial y}\left(\frac{1}{D}\right)$$

$$\times d\left(\frac{\partial\chi}{\partial x}\right) - (1+\nu)\oint_{L_i}y\frac{\partial}{\partial x}\left(\frac{1}{D}\right)d\left(\frac{\partial\chi}{\partial y}\right) = 0 \qquad (12)$$

$$\oint_{L_i}\left(x\frac{\partial}{\partial n} + y\frac{\partial}{\partial s}\right)\left(\frac{1}{D}\nabla^2\chi + E\alpha T\right)ds + (1+\nu)\oint_{L_i}x\frac{\partial}{\partial x}\left(\frac{1}{D}\right)$$

$$\times d\left(\frac{\partial\chi}{\partial y}\right) - (1+\nu)\oint_{L_i}x\frac{\partial}{\partial y}\left(\frac{1}{D}\right)d\left(\frac{\partial\chi}{\partial x}\right) = 0 \qquad (13)$$

where L_i is a closed integral path including the boundary curve C_i in the interior of the multiply connected region, n is the normal direction to L_i, and s represents the arc length along the curve L_i.

Finally, the formulation of the plane-stress thermoelastic problem in the multiply connected region of variable thickness in terms of Airy's stress function has been established by the equations (5), (8), (9), and (11)–(13).

In general, there are no exact solutions to the plane-stress thermoelastic problems in bodies with two-dimensional temperature fields when the thickness varies in both the x and y directions, or when the boundary curves are irregular, that is, not parallel to coordinates of a system. Hence we now describe how the resulting governing equations previously formulated are solved by means of the finite difference method.

3 Finite Difference Representation of the Governing Equations

We take the finite difference grids with spatial intervals Δx and Δy in the x and y directions, respectively, and Δt as the time interval, and use the subscripts i, j and the superscript k to denote the ith and jth discrete points in the x and y directions, respectively, and the kth discrete time. Then the transient heat-conduction equation (1) in the multiply connected region of variable thickness may be expressed in the finite difference form as follows:

$$\left[\frac{1}{\Delta\tau}+\frac{2}{(\Delta\xi)^2}+\frac{2}{(\Delta\eta)^2}+\frac{2m_0}{\bar{D}_{i,j}}\sqrt{1+\frac{(\bar{D}_{i+1,j}-\bar{D}_{i-1,j})^2}{4(\Delta\xi)^2}+\frac{(\bar{D}_{i,j+1}-\bar{D}_{i,j-1})^2}{4(\Delta\eta)^2}}\right]\times\bar{T}^k_{i,j}-\left[\frac{1}{(\Delta\xi)^2}+\frac{\bar{D}_{i+1,j}-\bar{D}_{i-1,j}}{4\bar{D}_{i,j}(\Delta\xi)^2}\right]\bar{T}^k_{i+1,j}$$
$$-\left[\frac{1}{(\Delta\xi)^2}-\frac{\bar{D}_{i+1,j}-\bar{D}_{i-1,j}}{4\bar{D}_{i,j}(\Delta\xi)^2}\right]\bar{T}^k_{i-1,j}-\left[\frac{1}{(\Delta\eta)^2}+\frac{\bar{D}_{i,j+1}-\bar{D}_{i,j-1}}{4\bar{D}_{i,j}(\Delta\eta)^2}\right]\bar{T}^k_{i,j+1}$$
$$-\left[\frac{1}{(\Delta\eta)^2}-\frac{\bar{D}_{i,j+1}-\bar{D}_{i,j-1}}{4\bar{D}_{i,j}(\Delta\eta)^2}\right]\bar{T}^k_{i,j-1}=\frac{\bar{T}^{k-1}_{i,j}}{\Delta\tau} \tag{14}$$

where $\bar{T}^k_{i,j}$ is the unknown temperature at the grid point (i, j) at the current time $\tau=\tau_k$, $\bar{T}^{k-1}_{i,j}$ denotes the known temperature at $\tau=\tau_{k-1}$, and in equation (14) the following dimensionless quantities, with T_1, l_0 taken as a reference temperature and a reference length, respectively, were introduced:

$$\xi=\frac{x}{l_0},\quad \eta=\frac{y}{l_0},\quad \tau=\frac{\lambda t}{c\rho l_0^2},\quad m_0=\frac{h_0 l_0}{\lambda},\quad \bar{D}(\xi,\eta)=\frac{D(x,y)}{l_0},$$
$$\bar{T}=\frac{T-T_0}{T_1-T_0}. \tag{15}$$

The values of temperature at each time step are determined by solving the simultaneous linear equations obtained from the application of equation (14) to all the grid points including the grid points on the $M+1$ boundary curves.

Now we can express the governing differential equation (8) for the plane-stress thermoelastic problem, taking into account the variation of thickness in both the x and y directions, as follows:

$$(6c_1+4c_2+6c_3-2c_8-2c_9)\bar{\chi}_{i,j}-(4c_1+2c_2-2c_4-2c_7-c_8)\bar{\chi}_{i+1,j}-(4c_1+2c_2+2c_4+2c_7-c_8)\bar{\chi}_{i-1,j}$$
$$-(2c_2+4c_3-2c_5-2c_6-c_9)\bar{\chi}_{i,j+1}-(2c_2+4c_3+2c_5+2c_6-c_9)\bar{\chi}_{i,j-1}+(c_2-c_6-c_7+c_{10})\bar{\chi}_{i+1,j+1}$$
$$+(c_2+c_6-c_7-c_{10})\bar{\chi}_{i+1,j-1}+(c_2-c_6+c_7-c_{10})\bar{\chi}_{i-1,j+1}+(c_2+c_6+c_7+c_{10})\bar{\chi}_{i-1,j-1}$$
$$+(c_1-c_4)\bar{\chi}_{i+2,j}+(c_1+c_4)\bar{\chi}_{i-2,j}+(c_3-c_5)\bar{\chi}_{i,j+2}+(c_3+c_5)\bar{\chi}_{i,j-2}+c_{11}=0 \tag{16}$$

where $\bar{\chi}_{i,j}=\chi_{i,j}/[E\alpha(T_1-T_0)l_0^3]$ and c_1-c_{11} are:

$$c_1=1/(\Delta\xi)^4,\ c_2=2/(\Delta\xi)^2(\Delta\eta)^2,\ c_3=1/(\Delta\eta)^4,$$
$$c_4=(\bar{D}_{i+1,j}-\bar{D}_{i-1,j})/[2\bar{D}_{i,j}(\Delta\xi)^4],$$
$$c_5=(\bar{D}_{i,j+1}-\bar{D}_{i,j-1})/[2\bar{D}_{i,j}(\Delta\eta)^4],\ c_6=(\bar{D}_{i,j+1}-\bar{D}_{i,j-1})/[2\bar{D}_{i,j}(\Delta\xi)^2(\Delta\eta)^2],$$
$$c_7=(\bar{D}_{i+1,j}-\bar{D}_{i-1,j})/[2\bar{D}_{i,j}(\Delta\xi)^2(\Delta\eta)^2]$$
$$c_8=\{(\bar{D}_{i+1,j}-\bar{D}_{i-1,j})^2/[2\bar{D}_{i,j}(\Delta\xi)^2]-\nu_{i,j}(\bar{D}_{i,j+1}-\bar{D}_{i,j-1})^2/[2\bar{D}_{i,j}(\Delta\eta)^2]-(\bar{D}_{i+1,j}+\bar{D}_{i-1,j}-2\bar{D}_{i,j})/(\Delta\xi)^2+\nu_{i,j}(\bar{D}_{i,j+1}+\bar{D}_{i,j-1}-2\bar{D}_{i,j})/(\Delta\eta)^2\}/[\bar{D}_{i,j}(\Delta\xi)^2], \tag{17}$$
$$c_9=\{(\bar{D}_{i,j+1}-\bar{D}_{i,j-1})^2/[2\bar{D}_{i,j}(\Delta\eta)^2]-\nu_{i,j}(\bar{D}_{i+1,j}-\bar{D}_{i-1,j})^2/[2\bar{D}_{i,j}(\Delta\xi)^2]-(\bar{D}_{i,j+1}+\bar{D}_{i,j-1}-2\bar{D}_{i,j})/(\Delta\eta)^2-\nu_{i,j}(\bar{D}_{i+1,j}+\bar{D}_{i-1,j}-2\bar{D}_{i,j})/(\Delta\xi)^2\}/[\bar{D}_{i,j}\times(\Delta\eta)^2],$$
$$c_{10}=(1+\nu_{i,j})\times[2(\bar{D}_{i+1,j}-\bar{D}_{i-1,j})(\bar{D}_{i,j+1}-\bar{D}_{i,j-1})/\bar{D}_{i,j}-\bar{D}_{i+1,j+1}+\bar{D}_{i+1,j-1}+\bar{D}_{i-1,j+1}-\bar{D}_{i-1,j-1}]/[8\bar{D}_{i,j}(\Delta\xi)^2(\Delta\eta)^2],$$
$$c_{11}=\bar{D}_{i,j}[(\bar{T}_{i+1,j}+\bar{T}_{i-1,j}-2\bar{T}_{i,j})/(\Delta\xi)^2+(\bar{T}_{i,j+1}+\bar{T}_{i,j-1}-2\bar{T}_{i,j})/(\Delta\eta)^2].$$

Finally, the new Michell integral conditions (11)-(13) may be expressed in the following finite difference forms:

$$\oint_{L_i}(W_{1m}\bar{\chi}_{i,j}+W_{2m}\bar{\chi}_{i+1,j}+W_{3m}\bar{\chi}_{i-1,j}+W_{4m}\bar{\chi}_{i,j+1}+W_{5m}\bar{\chi}_{i,j-1}+W_{6m}\bar{\chi}_{i+2,j}+W_{7m}\bar{\chi}_{i-2,j}+W_{8m}\bar{\chi}_{i,j+2}+W_{9m}\bar{\chi}_{i,j-2}$$
$$+W_{10m}\bar{\chi}_{i+1,j+1}+W_{11m}\bar{\chi}_{i+1,j-1}+W_{12m}\bar{\chi}_{i-1,j+1}+W_{13m}\bar{\chi}_{i-1,j-1}+W_{14m})d\bar{s}=0\quad(m=1,2,3) \tag{18}$$

where $d\bar{s}=ds/l_0$, the subscripts $m=1$, 2, 3 denote the conditions necessary for the assurance of single-valuedness of the rotation and the displacements in the x and y directions, respectively and $W_{1m}-W_{14m}$ are:

$$W_{1m}=2(b_{1m}+b_{2m}),\quad W_{2m}=-(b_{1m}+b_{3m}),$$
$$W_{3m}=b_{3m}-b_{1m},\ W_{4m}=-(b_{2m}+b_{4m}),\ W_{5m}=b_{4m}-b_{2m},$$
$$W_{6m}=-W_{7m}=b_{8m},\quad W_{8m}=-W_{9m}=b_{9m},$$
$$W_{10m}=b_{5m}-b_{7m},$$
$$W_{11m}=b_{6m}+b_{7m},\quad W_{12m}=-b_{6m}+b_{7m},$$
$$W_{13m}=-(b_{5m}+b_{7m}),\quad W_{14m}=d_{1m}(\bar{T}_{i+1,j}-\bar{T}_{i-1,j})/(2\Delta\xi)+d_{2m}(\bar{T}_{i,j+1}-\bar{T}_{i,j-1})/(2\Delta\eta)$$
$$b_{11}=[b_{101}(D_{i+1,j}-D_{i-1,j})/(2\Delta\xi)-b_{111}\nu_{i,j}(\bar{D}_{i,j+1}-\bar{D}_{i,j-1})/(2\Delta\eta)]/(\bar{D}_{i,j}\Delta\xi)^2,\ b_{21}=[-b_{101}\nu_{i,j}(\bar{D}_{i+1,j}-\bar{D}_{i-1,j})/(2\Delta\xi)+b_{111}(\bar{D}_{i,j+1}-\bar{D}_{i,j-1})/(2\Delta\eta)]/(\bar{D}_{i,j}\Delta\eta)^2,$$
$$b_{31}=b_{101}[(\Delta\xi)^{-2}+(\Delta\eta)^{-2}]/(\bar{D}_{i,j}\Delta\xi),\ b_{41}=b_{111}[(\Delta\xi)^{-2}+(\Delta\eta)^{-2}]/(\bar{D}_{i,j}\Delta\eta),\ b_{51}=(b_{111}/\Delta\xi+b_{101}/\Delta\eta)/(2\bar{D}_{i,j}\Delta\xi\Delta\eta),$$
$$b_{61}=(b_{101}/\Delta\eta-b_{111}/\Delta\xi)/(2\bar{D}_{i,j}\Delta\xi\Delta\eta),\ b_{71}=(1+\nu_{i,j})\times[b_{111}(\bar{D}_{i+1,j}-\bar{D}_{i-1,j})/(2\Delta\xi)+b_{101}(\bar{D}_{i,j+1}-\bar{D}_{i,j-1})/(2\Delta\eta)]/(4\bar{D}^2_{i,j}\Delta\xi\Delta\eta),$$
$$b_{81}=b_{101}/[2\bar{D}_{i,j}(\Delta\xi)^3],\ b_{91}=b_{111}/[2\bar{D}_{i,j}(\Delta\eta)^3],$$
$$b_{101}=\cos(\xi,n)_{i,j},\ b_{111}=\cos(\eta,n)_{i,j}$$
$$b_{12}=\eta_j b_{11}+\xi_i b_{122}/(\Delta\xi)^2,\ b_{22}=\eta_j b_{21}+\xi_i b_{122}/(\Delta\eta)^2,\ b_{32}=b_{102}\times[(\Delta\xi)^{-2}+(\Delta\eta)^{-2}]/(\bar{D}_{i,j}\Delta\xi),\ b_{42}=b_{112}[(\Delta\xi)^{-2}+(\Delta\eta)^{-2}]/(\bar{D}_{i,j}\Delta\eta),$$
$$b_{52}=(b_{102}/\Delta\eta+b_{112}/\Delta\xi)/(2\bar{D}_{i,j}\Delta\xi\Delta\eta),\ b_{62}=(b_{102}/\Delta\eta-b_{112}/\Delta\xi)/(2\bar{D}_{i,j}\Delta\xi\Delta\eta),\ b_{72}=\eta_j b_{71},\ b_{82}=b_{102}/[2\bar{D}_{i,j}(\Delta\xi)^3],\ b_{92}=b_{112}/[2\bar{D}_{i,j}(\Delta\eta)^3],$$
$$b_{102}=\eta_j b_{101}+\xi_i b_{111},\ b_{112}=\eta_j b_{111}-\xi_i b_{101},$$
$$b_{122}=[b_{111}(\bar{D}_{i+1,j}-\bar{D}_{i-1,j})/(2\Delta\xi)-b_{101}(\bar{D}_{i,j+1}-\bar{D}_{i,j-1})/(2\Delta\eta)]/\bar{D}^2_{i,j} \tag{19}$$
$$b_{13}=\xi_i b_{103}-\eta_j b_{122}/(\Delta\xi)^2,\ b_{23}=\xi_i b_{113}-\eta_j b_{122}/(\Delta\xi)^2,\ b_{33}=-b_{42}\Delta\eta/\Delta\xi,\ b_{43}=b_{32}\Delta\xi/\Delta\eta,\ b_{53}=(b_{102}/\Delta\xi-b_{112}/\Delta\eta)/(2\bar{D}_{i,j}\Delta\xi\Delta\eta)$$
$$b_{63}=-(b_{102}/\Delta\xi+b_{112}/\Delta\eta)/(2\bar{D}_{i,j}\Delta\xi\Delta\eta),$$
$$b_{73}=-\xi_i b_{71},\ b_{83}=-b_{112}/[2\bar{D}_{i,j}(\Delta\xi)^3],$$
$$b_{93}=b_{102}/[2\bar{D}_{i,j}(\Delta\eta)^3],\ b_{103}=[b_{101}(\bar{D}_{i+1,j}-\bar{D}_{i-1,j})/(2\Delta\xi)+b_{111}(2+\nu_{i,j})(\bar{D}_{i,j+1}-\bar{D}_{i,j-1})/(2\Delta\eta)]/(\bar{D}_{i,j}\Delta\xi)^2$$
$$b_{113}=[b_{101}(2+\nu_{i,j})(\bar{D}_{i+1,j}-\bar{D}_{i-1,j})/(2\Delta\xi)+b_{111}(\bar{D}_{i,j+1}-\bar{D}_{i,j-1})/(2\Delta\eta)]/(\bar{D}_{i,j}\Delta\eta)^2$$
$$d_{11}=b_{101},$$
$$d_{21}=b_{111},$$

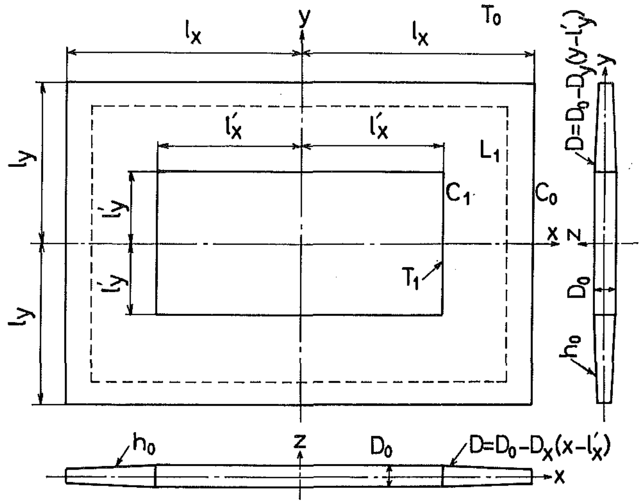

Fig 2 Rectangular plate of variable thickness with a rectangular hole

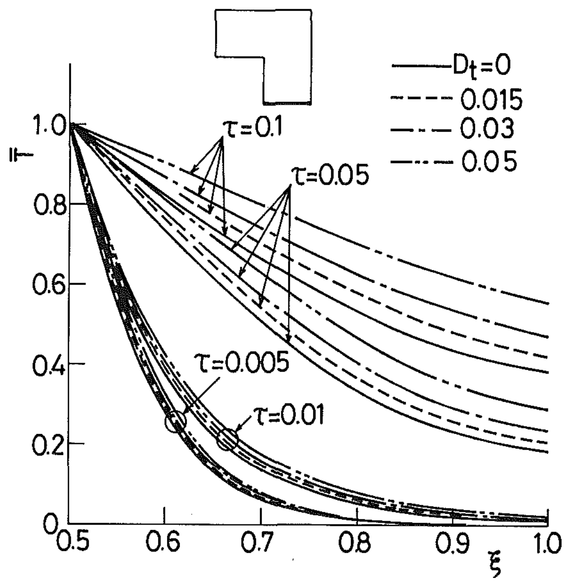

Fig. 3 Effect of variation of thickness on temperature distribution on x axis ($m_0 = 0$)

$d_{12} = d_{23} = b_{102}$,

$d_{22} = -d_{13} = b_{112}$,

The integrations of equations (18) are evaluated by the use of numerical integration methods (for example, Simpson's rule). The numerical analysis of the plane-stress thermoelastic problem formulated in terms of Airy's stress function in the multiply connected region with the variation in the thickness in both the x and y directions by the finite difference method is reduced to determination of the values of the stress function at the grid points in the interior of the region and the unknown constants c_{jk} ($j-1$, 2, 3; $k=1$, 2, ... , M) in equation (9) by solving the simultaneous equations obtained from application of equation (16) to the same grid points and the numerical integrations of equations (18). Then, the values of the stress function at the grid points on the boundary curves C_i are readily determined by the use of equations (9). Once the values of the stress function at all grid points including those on the boundary curves at each time step are determined, the desired plane thermal stress components are readily obtained by substituting the values into the finite difference representations of equations (5).

4 Numerical Calculations and Discussion

Consider the distributions of the transient temperature and plane thermal stress in a thin rectangular plate of dimension

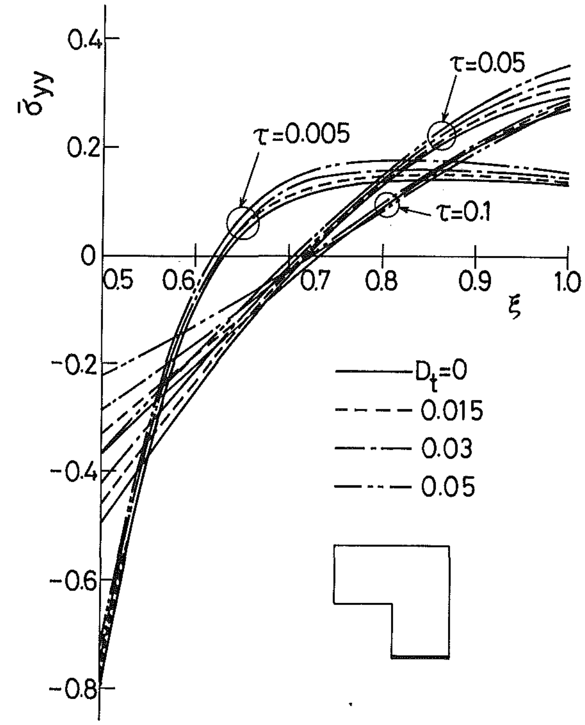

Fig. 4 Effect of variation of thickness on $\bar{\sigma}_{yy}$ on x axis ($m_0 = 0$)

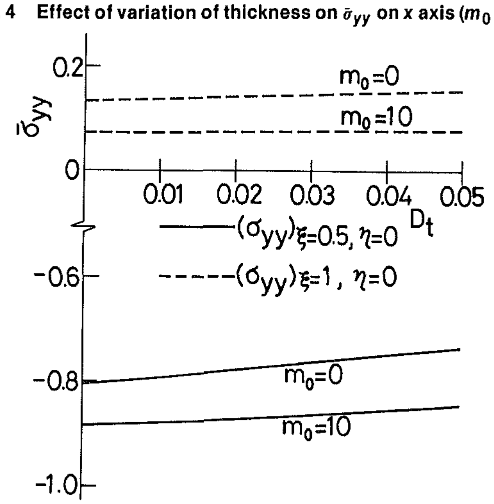

Fig. 5 Effect of variation of thickness on $(\bar{\sigma}_{yy})_{\xi=0.5,\,\eta=0}$ and $(\bar{\sigma}_{yy})_{\xi=1,\,\eta=0}$ for $m_0 = 0$ and $m_0 = 10$

$2l_x \times 2l_y$ and variable thickness with a rectangular hole of dimension $2l_x' \times 2l_y'$ as a case of a multiply connected region as shown in Fig. 2, assuming that the variable-thickness plate, initially at the same uniform temperature T_0 as the surrounding media, is heated by an abrupt temperature change T_{11} of the inner surrounding temperature and that there is a heat loss into the surrounding medium at constant temperature T_0 on the outer boundary and the upper and lower surfaces of the plate. As an example of such small thickness and small variation of thickness in which the method of analysis to the plane-stress thermoelastic problem of constant thickness can be extended, we took the following linearly decreasing thickness in both the x and y directions from the inner boundary of constant thickness D_0 toward the outer boundary:

$$D=D_0-D_x(x-l_x'),\quad D=D_0-D_y(y-l_y') \qquad (20)$$

where D_x and D_y denote the constant gradients of thickness in the x and y directions, respectively. We also took the half length l_x and the inner surrounding temperature T_{11} as the reference length l_0 and the reference temperature T_1,

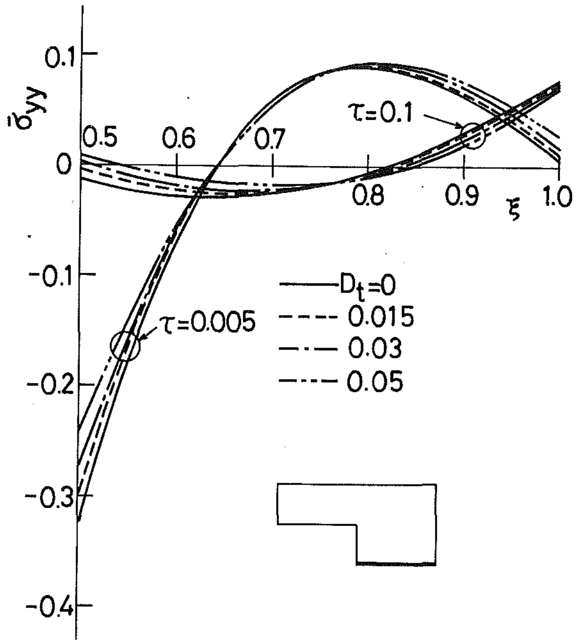

Fig. 6 Effect of variation of thickness on $\bar{\sigma}_{yy}$ on x axis ($m_0 = 0$)

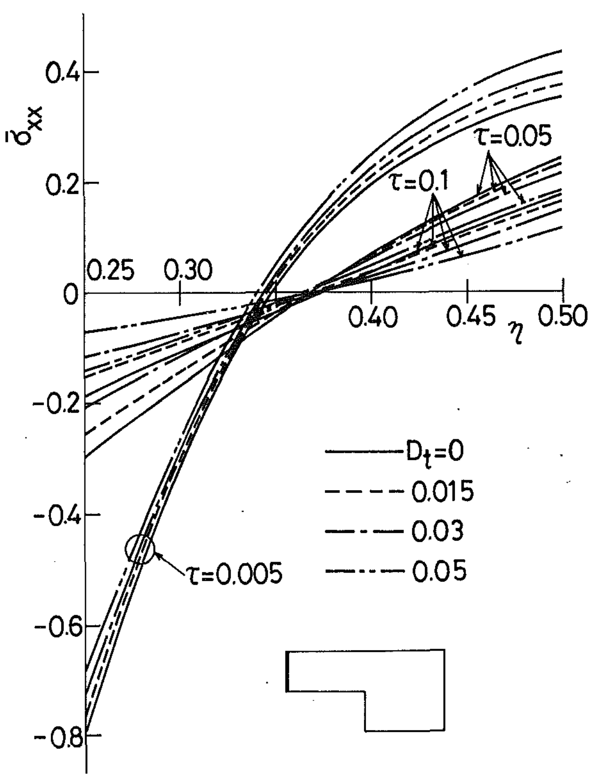

Fig. 7 Effect of variation of thickness on $\bar{\sigma}_{xx}$ on y axis ($m_0 = 0$)

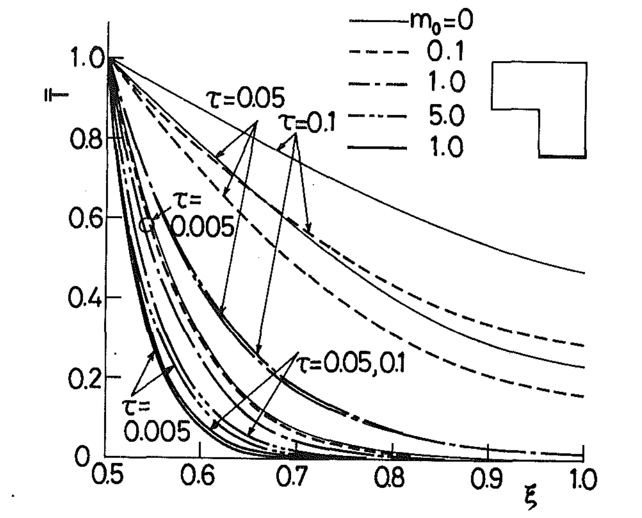

Fig. 8 Effect of Biot's number on upper and lower surfaces on temperature distribution on x axis ($D_t = 0.03$)

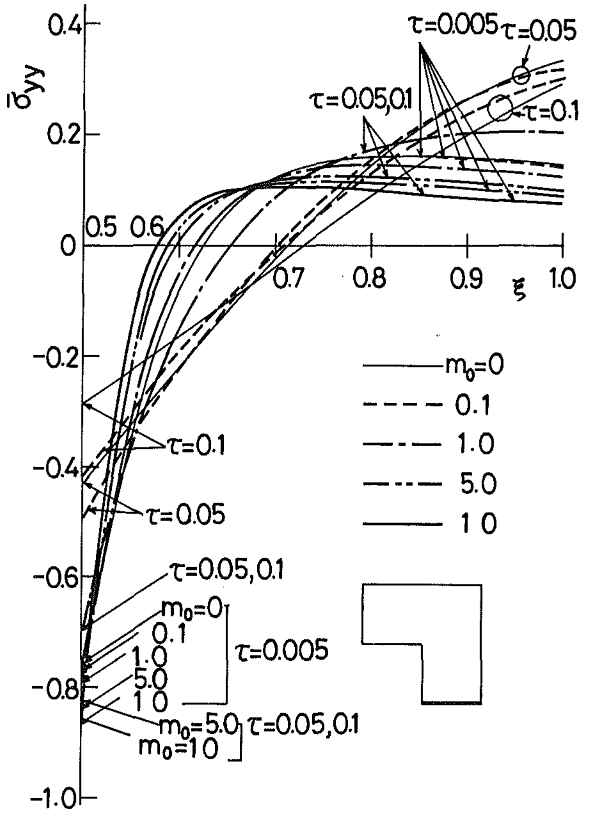

Fig. 9 Effect of Biot's number on upper and lower surfaces on $\bar{\sigma}_{yy}$ on x axis ($D_t = 0.03$)

respectively, and used the following values in the numerical calculations of the temperature and plane thermal stress:

$$\bar{l}_y = l_y/l_x = 0.5, 1,\ \bar{l}_x' = l_x'/l_x = 0.5,\ \bar{l}_y' = l_y'/l_x = 0.25, 0.5,\ \bar{D}_0 = D_0/l_x = 0.05,\ D_x = D_y = 0, 0.015, 0.03, 0.05,\ m_{10} = h_{10} l_x/\lambda = 1,\ m_{11} = h_{11} l_x/\lambda = \infty,\ m_0 = 0, 0.1, 1.0, 5.0, 10,\ T_{10} = 0,\ \bar{T}_{11} = 1$$

The spatial and time intervals for all cases considered were taken to be smaller than $\Delta\xi = \Delta\eta = 0.03125$ and $\Delta\tau = 0.0025$. For this numerical example, neither results obtained by exact solution nor by finite element method have so far been reported. So, to verify the effect of mesh size on the convergence, the calculation was also done with mesh systems of $\Delta\xi = \Delta\eta = 0.05$, $\Delta\tau = 0.0025$ and $\Delta\xi = \Delta\eta = 0.025$, $\Delta\tau = 0.002$. The absolute values of $\bar{\sigma}_{yy} = \sigma_{yy}/[E\alpha(T_1 - T_0)]$ at $\xi = 0.5$, $\eta = 0$ and $\tau = 0.005$ of Fig. 4 obtained by taking the mesh systems of $\Delta\xi = \Delta\eta = 0.05$, $\Delta\xi = \Delta\eta = 0.03125$ and $\Delta\xi = \Delta\eta = 0.025$ were 0.699, 0.721 and 0.726, respectively. It can be seen from these results that the mesh system of $\Delta\xi = \Delta\eta = 0.03125$ and $\Delta\tau = 0.0025$ produces satisfactory results.

First, Figs. 3 and 4 show the distributions of the temperature and $\bar{\sigma}_{yy}$, respectively, on the x axis in the square plate ($\bar{l}_y = 1$, $\bar{l}_x' = \bar{l}_y' = 0.5$). It is noted from Fig. 3 that the temperature distribution during the short period after the abrupt change in the inner surrounding temperature is roughly the same whether the variation of thickness in both the x and y

directions is taken into account or not, but the temperture increases become much larger and the temperature gradients become considerably smaller with an increase in the gradient of thickness $D_t = D_x = D_y$ at the approximate steady state $\tau = 0.1$. As illustrated in Fig. 4, the absolute values of the compressive thermal stress $\bar{\sigma}_{yy}$ at the inner boundary become smaller with an increase in the gradient of thickness because the increase in the gradient of thickness D_t causes a drop in the temperature gradient; while the values of the tensile thermal stress $\bar{\sigma}_{yy}$ at the outer boundary become larger with the increase except for the values at $\tau = 0.1$. Figure 5 shows the effect of the gradient of thickness on $\bar{\sigma}_{yy}$ at $\xi = 0.5$, $\eta = 0$ and $\xi = 1$, $\eta = 0$ for the two cases of the Biot's number on the upper and lower surfaces. It is clear from this figure that the effect of the gradient of thickness D_t on $\bar{\sigma}_{yy}$ becomes smaller with an increase in the Biot's number on the upper and lower surfaces because a change in the temperature gradient on the x axis for the large value of Biot's number becomes quite small regardless of the value of D_t. Figures 6 and 7 show the effect of the gradient of thickness on $\bar{\sigma}_{yy}$ on the x axis and $\bar{\sigma}_{xx}$ on the y axis in the rectangular plate ($\bar{l}_y = \bar{l}_x' = 0.5$, $\bar{l}_y' = 0.25$) for the thermally insulated case of the upper and lower surfaces, respectively. It is noted from these figures that both $\bar{\sigma}_{yy}$ on the x axis and $\bar{\sigma}_{xx}$ on the y axis in the rectangular plate are smaller than $\bar{\sigma}_{yy}$ on the x axis in the square plate illustrated in Fig 4, but the effect of the gradient of thickness on the distribution of the these stresses is quite similar to the case of the square plate. Finally, Figs. 8 and 9 show the effect of the Biot's number of the upper and lower surfaces on the distributions of the temperature and $\bar{\sigma}_{yy}$ on the x axis in the square plate for the case of $D_t = 0.03$. It is of practical interest to note that the effect of the Biot's number on the upper and lower surfaces of the perforated plate of variable thickness on the distributions of the temperature and $\bar{\sigma}_{yy}$ on the x axis is much more important than the gradient of thickness and that as the value of the Biot's number m_0 increases, the absolute value of $\bar{\sigma}_{yy}$ at the inner boundary apparently increases.

References

1 Takeuti, Y., and Sekiya, T., "Thermal Stresses in a Polygonal Cylinder With a Circular Under Internal Heat Generation," *Zeitschrift fur angewandte Mathematik und Mechanik*, Vol. 48, 1968, pp. 237–246.

2 Hulbert, L. E., "Solution of Thermal Stress Problems in Tube Sheets by the Boundary Point Least Squares Method," ASME *Journal of Engineering for Industry*, Vol. 92, 1970, pp. 339–349.

3 Takeuti, Y., and Noda, N., "Transient Themoelastic Problem in a Polygonal Cylinder With a Circular Hole," ASME Journal of Applied Mechanics, Vol. 40, 1973, pp. 935–940.

4 Kettleborough, C. F., "Non-Axial-Symmetric Thermal Stresses in Circular Discs or Cylinders," *International Journal for Numerical Methods in Engineering*, Vol. 3, 1971, pp. 53–61.

5 Michell, J. H., "On the Direct Determination of Stress in an Elastic Solid, With Application to the Theory of Plates," *Proceedings of the London Mathematical Society*, Vol. 31, 1899, pp. 100–124.

B. Budiansky
Fellow ASME

G. F. Carrier
Honorary Mem. ASME

Division of Applied Sciences,
Harvard University,
Cambridge, Mass. 02138

High Shear Stresses in Stiff-Fiber Composites

Elastic analysis of two parallel fibers in an infinite matrix subjected to longitudinal shear leads to some exact results for stress concentrations between the fibers. High shear stresses occur when stiff fibers are in close proximity.

Introduction

Unexpectedly low strengths in longitudinal shear have been reported for brittle-matrix, fiber-reinforced composites, and it has been suggested that this might be explained by high stress concentrations in the matrix between neighboring fibers [1]. In 1967, an analysis of two elastic fibers in an infinite elastic matrix under longitudinal shear was presented by Goree and Wilson [2], and for the case of rigid fibers in close proximity high shear stresses were indeed found numerically.

In this paper the Goree-Wilson solution is rederived succinctly in a way that leads to the deduction of some exact results for matrix shear stresses near elastic as well as rigid fibers. Key results will first be displayed, followed by the analysis.

Results

We consider two identical elastic fibers of diameter d embedded in an infinite elastic matrix (Fig. 1) subjected to shear loading $\tau_{xz} = \tau_0$ at infinity. The fiber shear modulus is G_F, the matrix modulus is G_M, and the separation distance between the fibers is s.

(*i*) For rigid fibers ($G_F = \infty$) the average matrix shear stress $\bar{\tau}_{xz}$ between the fibers is given exactly by

$$\bar{\tau}_{xz}/\tau_0 = \sqrt{(2+\epsilon)/\epsilon} \qquad (1)$$

where

$$\epsilon = s/d$$

(*ii*) If the fibers are not rigid but touch each other ($\epsilon = 0$), the stress τ_{xz} at the point of contact satisfies

$$\tau_{xz}/\tau_0 = G_F/G_M \qquad (2)$$

(*iii*) Numerical results for the average stress concentration $\bar{\tau}_{xz}/\tau_0$ between the fibers as a function of ϵ are shown in Fig. 2 for several values of G_F/G_M.

On the basis of their numerical calculations Goree and Wilson surmised that the maximum shear stress between the fibers would become infinite for rigid fibers approaching zero separation. This is corroborated by the exact result (1), which shows that the shear stress becomes infinite like the reciprocal square root of the separation distance. The exact result (2) shows that an intense stress concentration can also occur for a finite fiber modulus that is substantially higher than that of the matrix. On the other hand, the curves in Fig. 2 indicate that such stress concentrations may be very considerably diminished when the fibers do not quite touch. Nevertheless, fiber contact or near contact may well be a frequent occurrence in high-fiber-density composites, and the consequent shear stress concentrations could still be responsible for the reported low shear strengths of brittle-matrix composites.

Analysis

As in [2], we can write the longitudinal displacement w as

$$w = (\tau_0/G_M)\,Re\,f \qquad (3)$$

where f is a complex function of $Z = x + iy$, piecewise analytic within the matrix and the fibers. The shear stresses are given by

$$\tau_{xz} - i\tau_{yz} = \tau_0 \frac{df}{dZ} \quad \text{in the matrix,} \qquad (4a)$$

$$= \lambda\tau_0 \frac{df}{dZ} \quad \text{in the fibers,} \qquad (4b)$$

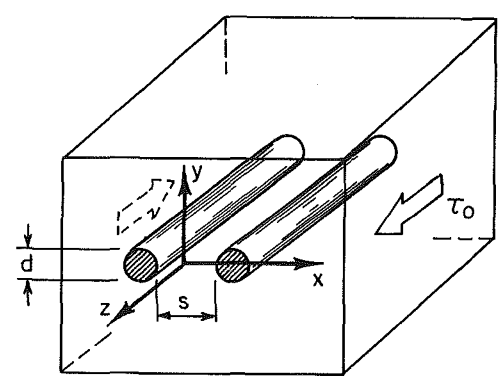

Fig. 1 Two-fiber configuration

Contributed by the Applied Mechanics Division for publication in the Journal of Applied Mechanics.

Discussion on this paper should be addressed to the Editorial Department, ASME, United Engineering Center, 345 East 47th Street, New York, N.Y. 10017, and will be accepted until two months after final publication of the paper itself in the Journal of Applied Mechanics. Manuscript received by ASME Applied Mechanics Division, April, 1984.

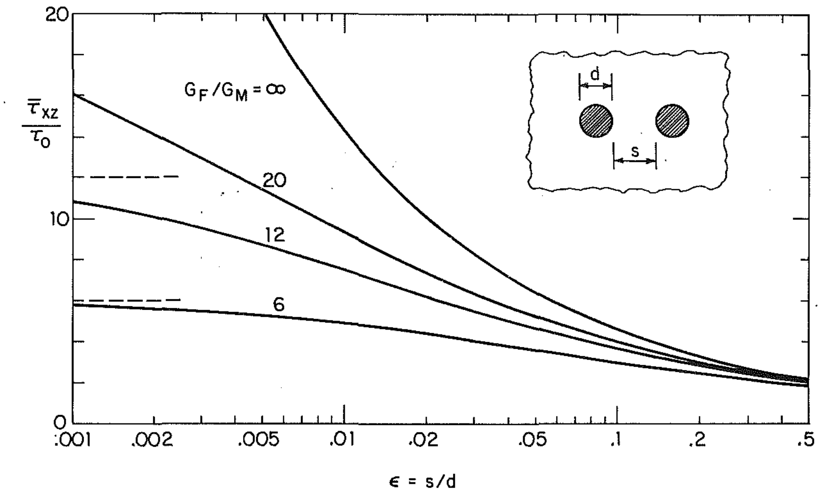

Fig. 2 Average interfiber shear stress versus fiber spacing

where $\lambda = G_F/G_M$. Single-valued displacements, and the absence of net force on each fiber imply that f is single-valued in the matrix as well as the fibers. Without loss, let $w(0, y) = \partial w/\partial y\ (x, 0) = 0$ and pick $Im\, f(0) = 0$; then, by symmetry,

$$f(Z) = \bar{f}(Z) = -f(-Z) \tag{5}$$

The prescribed loading gives

$$f \sim Z \qquad \text{for} \qquad |Z| \to \infty \tag{6}$$

Let f_M, f_F denote the values of f in the matrix and the right-hand fiber, respectively. The conditions of displacement and traction continuity along the fiber-matrix interface then imply

$$Re\, f_M + i \quad Im\, f_M = Re\, f_F + i\lambda\, Im\, f_F \tag{7}$$

along the fiber boundary.

Let the fibers have unit radius and separation distance 2ϵ. Following [2], map the Z-plane (Fig. 3a) into the ζ-plane (Fig. 3b) via

$$\begin{cases} \zeta = (Z-a)(Z+a)^{-1} \\ Z = a(1+\zeta)(1-\zeta)^{-1} \end{cases}$$

where

$$a = \sqrt{\epsilon(2+\epsilon)} \tag{8}$$

This maps the right-hand fiber into the interior of the circle C_1 of radius

$$\rho = (a-\epsilon)(a+\epsilon)^{-1} \tag{9}$$

and the matrix is transformed into the annulus $\rho < |\zeta| < \rho^{-1}$, bounded by C_1 and C_2.

In accordance with (6) we can write

$$f_M = a(1+\zeta)(1-\zeta)^{-1} + g_M(\zeta) \tag{10}$$

where $g_M(\zeta)$ is analytic in the annulus. By the Cauchy integral formula

$$g_M(\zeta) = g_1(\zeta) + g_2(\zeta)$$

where

$$g_1(\zeta) = \frac{1}{2\pi i} \oint_{C_2} \frac{g_M(\sigma)d\sigma}{\sigma - \zeta} \tag{11}$$

$$g_2(\zeta) = -\frac{1}{2\pi i} \oint_{C_1} \frac{g_M(\sigma)d\sigma}{\sigma - \zeta} \tag{12}$$

The symmetry conditions (5) imply $g_M(\zeta) = \bar{g}_M(\zeta) = -g_M(1/\zeta)$, and it follows directly from (11) and (12) that $\bar{g}_1(\zeta) = g_1(\zeta)$, $\bar{g}_2(\zeta) = g_2(\zeta)$, and $g_1(\zeta) = -g_1(1/\zeta)$, with $g_1(0) = g_2(\infty) = 0$. Hence

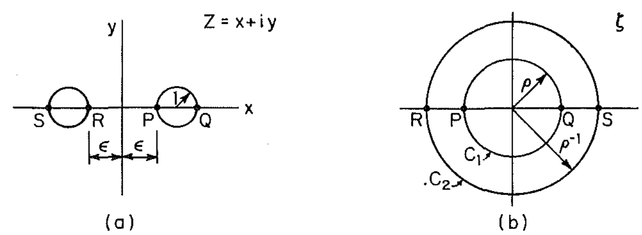

Fig. 3 Mapping geometry

$$f_M = a(1+\zeta)(1-\zeta)^{-1} + g_1(\zeta) - g_1(1/\zeta) \tag{13}$$

Note that $g_1(\zeta)$ is analytic for $|\zeta| < \rho^{-1}$.

In the ζ-plane, denote f_F by the function $g_F(\zeta) = \bar{g}_F(\zeta)$ analytic for $|\zeta| < \rho$. Then the interface conditions (7) may be written as

$$a[(1+\zeta)(1-\zeta)^{-1} + (1+\bar{\zeta})(1-\bar{\zeta})^{-1}] + g_1(\zeta) + g_1(\bar{\zeta}) - g_1(1/\zeta) - g_1(1/\bar{\zeta}) = g_F(\zeta) + g_F(\bar{\zeta}) \tag{14a}$$

$$a[(1+\zeta)(1-\zeta)^{-1} - (1+\bar{\zeta})(1-\bar{\zeta})^{-1}] + g_1(\zeta) - g_1(\bar{\zeta}) - g_1(1/\zeta) + g_1(1/\bar{\zeta}) = \lambda[g_F(\zeta) - g_F(\bar{\zeta})] \tag{14b}$$

on C_1. Since $\bar{\zeta} = \rho^2/\zeta$ on C_1, we get

$$\begin{cases} a(1+\zeta)(1-\zeta)^{-1} + g_1(\zeta) - g_1(\zeta/\rho^2) - g_F(\zeta) \\ = -a(\zeta+\rho^2)(\zeta-\rho^2)^{-1} + g_1(1/\zeta) - g_1/\rho^2(\zeta) + g_F(\rho^2/\zeta) \quad (15a) \\ a(1+\zeta)(1-\zeta)^{-1} + g_1(\zeta) + g_1(\zeta/\rho^2) - \lambda g_F(\zeta) \\ = a(\zeta+\rho^2)(\zeta-\rho^2)^{-1} + g_1(1/\zeta) + g_1(\rho^2/\zeta) - \lambda g_F(\rho^2/\zeta) \quad (15b) \end{cases}$$

for $|\zeta| = \rho$.

The left and right-hand sides of (15a) are analytic for $|\zeta| < \rho$ and $|\zeta| > \rho$, respectively. Consequently, each is the same entire function, namely the constant

$$[-a + g_F(0)] \tag{16}$$

approached on the right for $\zeta \to \infty$. But the left-hand side of (15a) equals $[a - g_F(0)]$ for $\zeta = 0$; hence

$$g_F(0) = a \tag{17}$$

This immediately provides the exact result (1). The average matrix stress between the fibers is given by

$$\bar{\tau}_{xz} = G_M w(\epsilon, 0)/\epsilon$$

or

$$\bar{\tau}_{xz}/\tau_0 = g_F(-\rho)/\epsilon \qquad (18)$$

But in the case of rigid fibers, $g_F(\zeta) \equiv g_F(0) = a$, and (1) follows.

A similar analytic-continuation argument may be applied to equation (15*b*), each side of which must equal $a(1-\lambda)$. From the left sides of equations (15) we then find that

$$\begin{cases} g_1(\zeta) - g_1(\zeta/\rho^2) - [g_F(\zeta) - a] = -2a\zeta(1-\zeta)^{-1} \\ g_1(\zeta) + g_1(\zeta/\rho^2) - \lambda[g_F(\zeta) - a] = -2a\zeta(1-\zeta)^{-1} \end{cases} \qquad (19)$$

The series solutions

$$\begin{cases} g_F(\zeta) = a + \sum_{n=1}^{\infty} a_n \zeta^n \qquad |\zeta| \leqq \rho & (20) \\ g_1(\zeta) = \sum_{n=1}^{\infty} b_n \zeta^n \qquad |\zeta| \leqq \rho^{-1} & (21) \end{cases}$$

follow, with

$$\begin{cases} a_n = 4a[\lambda + 1 - (\lambda - 1)\rho^{2n}]^{-1} & (22) \\ b_n = 2(\lambda - 1)a\rho^{2n}[\lambda + 1 - (\lambda - 1)\rho^{2n}]^{-1} & (23) \end{cases}$$

The interfiber average shear stress can now be calculated directly from (18), but alternative forms are available. With

$$\alpha = (\lambda - 1)(\lambda + 1)^{-1} \qquad (24)$$

each a_n can be expanded into a power series in α, and the summation over n in (20) can be performed to give

$$g_F(\zeta) = 2(\lambda + 1)^{-1} \sum_{m=0}^{\infty} [(1 - \rho^{2m+1})/(1 + \rho^{2m+1})]\alpha^m \qquad (25)$$

Since $a/\epsilon = (1+\rho)/(1-\rho)$, we find from (18) that for $\epsilon \to 0$,

$$\bar{\tau}_{xz}/\tau_0 = 2(\lambda+1)^{-1} \lim_{\rho \to 1} \sum_{m=0}^{\infty} [(1 - \rho^{2m+1})(1-\rho)^{-1}]\alpha^m$$

$$= 2(\lambda + 1)^{-1} \sum_{m=0}^{\infty} (2m+1)\alpha^m$$

$$= \lambda$$

as stated in equation (2).

We could also use the fact that $g_F = f_M$ at $\zeta = -\rho$ to get, via (13) and (18),

$$\bar{\tau}_{xz}/\tau_0 = 1 + [g_1(-\rho) - g_1(-1/\rho)]/\epsilon$$

Using (23) and (21) here, expanding into powers of α, and inverting orders of summation, leads to

$$\bar{\tau}_{xz}/\tau_0 = 1 + 2(1+\rho)^2 \sum_{m=0}^{\infty} \alpha^{m+1}\rho^{2m+1}(1+\rho^{2m+1})^{-1}(1+\rho^{2m+3})^{-1} \qquad (26)$$

This also gives λ for $\rho \to 1$. Equation (26) is convenient for calculating $\bar{\tau}_{xz}/\tau_0$ for arbitrary values of λ and ϵ, and was used to generate Fig. 2. (Since $\alpha \to 1$ for $\lambda \to \infty$, the interesting identity

$$\sum_{m=0}^{\infty} \rho^{2m+1}(1+\rho^{2m+1})^{-1}(1+\rho^{2m+3})^{-1} = \rho(1+\rho)^{-1}(1-\rho^2)^{-1}$$

follows from equations (1) and (26)).

Similar manipulations provide the asymptotic result

$$\bar{\tau}_{xz}/\tau_0 \approx \lambda[1 - (\lambda^2 - 1)\epsilon + \ldots]$$

for finite λ and small ϵ, which suggests the very rapid decrease in the stress concentration with small fiber separation seen in Fig. 2. Unfortunately, an approximation for $\bar{\tau}_{xz}$ that is uniformly valid in the vicinity of $\lambda = \infty$ and $\epsilon = 0$ has not been found.

Finally, we note that the rigid-fiber problem is mathematically equivalent to that of uniform potential flow past two cylinders, with no circulation around either cylinder. The analogue of τ_0 is the velocity V_0 in the y direction at infinity, and the average velocity between the cylinders becomes $\bar{V}_y = V_0\sqrt{(2+\epsilon)/\epsilon}$. When the cylinders actually touch, there is, of course, no flow between them, but the velocity nevertheless becomes infinite for $\epsilon \to 0$.

Acknowledgments

Tony Evans provoked our interest in this problem, and we discussed it with Fred Abernathy, Jim Goree, John Hutchinson, Dick Kronauer, Max Krook, Lyell Sanders, and Eli Sternberg. This work was supported in part by DARPA Materials Research Council under Contract MDA903-82-C-0428 with the University of Michigan, the National Science Foundation under Grant MEA-82-13925, and by the Division of Applied Sciences, Harvard University.

References

1 Evans, A. G., Private communication, July 1983.

2 Goree, J. G., and Wilson, A. B., Jr., "Transverse Shear Loading in an Elastic Matrix Containing Two Circular Cylindrical Inclusions," ASME JOURNAL OF APPLIED MECHANICS, Vol. 34, 1967, pp. 511–513.

Theory of Orthotropic and Composite Cylindrical Shells, Accurate and Simple Fourth-Order Governing Equations[1]

Shun Cheng
Professor.

F. B. He
Visiting Scholar.

Department of Engineering Mechanics,
University of Wisconsin,
Madison, Wis. 53706

A pair of complex conjugate fourth-order differential equations that govern the deformation of orthotropic circular cylindrical shells is presented. As shown in the paper, this pair of equations is as accurate as equations can be within the scope of the Kirchhoff assumptions. Also presented for the first time are several pairs of accurate and simple fourth-order equations which can be systematically and explicitly deduced from the previously mentioned pair of equations. Because of their accuracy and simplicity, these simple equations are of practical importance. The advantage in applying those fourth-order equations presented herein is that their solutions can be easily found in simple closed forms. This considerably simplifies calculations for solving problems of orthotropic and composite cylindrical shells as well as isotropic shells as a special case. Unlike other equations known in the literature, their general solutions remain unknown because of the algebraic complexities involved. The present method of deducing simple fourth-order equations improves upon the one used for isotropic shells in the first author's previous paper entitled "Accurate Fourth-Order Equations for Circular Cylindrical Shells," Journal of the Engineering Mechanics Division, *ASCE, 1972.*

Introduction

Considerable attention has been devoted to the study of general shell theory. Literature on this subject is quite extensive. In contrast, relatively little work has been done on the formulation of the basic equations for orthotropic cylindrical shells, although they are frequently employed as structural elements in industry [1–7]. Examples of such shells include laminated composite, reinforced, perforated, and stiffened cylindrical shells whose material behavior can be considered as orthotropic. Composite cylindrical shells [4–7] constitute an example of great practical importance in recent years.

As is known in the literature, the classical shell theory is based on the same basic asumptions employed in the theory of thin plates, known as Kirchhoff assumptions. In developing the theory of thin shells, further simplifications or approximations beyond these basic assumptions have been introduced since the inception of Love's first approximation. As the abundance of literature indicates, many versions of shell theories have been formulated, each depending on different versions of the various approximations. This has confronted engineers as well as researchers with a controversial problem with regard to the consistency of the theory and accuracy of the resulting equations. Many sets of resulting equations have been proposed for isotropic shells [8–12] and especially, due to their importance in application and the fact that they display nearly every type of behavior found in general shell theory, for cylindrical shells [8–16]. Many other publications are readily available.

As for orthotropic cylindrical shells, two types of basic equations, corresponging either to Flügge's or Donnell's equations for isotropic shells, have been formulated in the literature [1–7]. In either case, a resulting single eighth-order differential equation may be deduced. However, the eighth-order equation for orthotropic shells is more complicated than the corresponding ones for isotropic shells. A common difficulty with these eighth-order equations in isotropic or orthotropic shell theory is that their general solutions remain unknown because of the algebraic complexities involved. These unnecessarily complicated equations hamper the analysis and hence bury essential features beneath a mound of algebra. For orthotropic cylindrical shells, even the simpler eighth-order equation based on Donnell approximations as seen in [2] suffers from the same complexity. In computing the characteristic roots arising from solving these eighth-order equations by means of eigenfunctions, it is found that the two large roots and the two small roots in the same set of solutions

[1] Report No. 2580, Mathematics Research Center, University of Wisconsin, Madison, Wis., Oct. 1983. Presented at the XVIth International Congress of Theoretical and Applied Mechanics, Aug. 19–25, 1984, Lyngby, Denmark.

Contributed by the Applied Mechanics Division and presented at the Winter Annual Meeting, New Orleans, La., December 9–14, 1984 of The American Society of Mechanical Engineers.

Discussion on this paper should be addressed to the Editorial Department, ASME, United Engineering Center, 345 East 47th Street, New York, N.Y. 10017, and will be accepted until two months after final publication of the paper itself in the Journal of Applied Mechanics. Manuscript received by ASME Applied Mechanics Division, January, 1983; final revision, March, 1984. Paper No. 84-WA/APM-29.

Copies will be available until February, 1985.

for the characteristic equation are far apart and of different orders of magnitude. This makes the computation more tedious and time-consuming, even with present-day numerical techniques. Using an approach identical to that of Donnell [13], a fourth-order equation is presented in [3]. Since in Donnell's derivation a number of terms in the relationships between the changes of curvature and twist and the displacements, and in the relations of stress resultants and moment resultants in terms of displacements are simply neglected, it cannot be easily followed. It is also difficult to visualize the effect of so many reductions on the final solutions [14, 15]. Furthermore in [3], no justification is given for replacing the shear modulus by other material coefficients. In addition to the shortcomings cited in the foregoing, only a specific numerical problem is treated in [3]. This signifies that a general investigation of the accuracy of the fourth-order equation is still lacking. This paper attempts to provide such an investigation as well as among other things, a systematic and explicit deduction of the fourth-order equation.

Recently a general theory for thin isotropic shells, which makes no simplifications or approximations beyond a clear set of fundamental hypotheses, was developed by Markov [17]. Other advantages of the method of derivation as applied to shells of general curvature have also been illustrated in [17]. Results obtained herein illustrate that the method developed in [15, 16] can also be useful for orthotropic shells.

In the present paper, a pair of complex conjugate fourth-order partial differential equations that govern the deformation of orthotropic circular cylindrical shells is proposed. This pair of equations is deduced from a set of basic equations that is based on the following Kirchhoff hypotheses:

(*a*) The transverse normal stress is negligibly small, and

(*b*) normal-to-the-middle surface of the shell remain normal to it and undergo no change in length during deformation.

The set of basic equations (8) is exact in the sense that in deriving these equations all terms have been retained without introducing further simplifications or approximations beyond these fundamental hypotheses. Even those terms that are of higher-order are kept since they can be summed in closed form.

Because the pair of equations deduced herein is complex conjugates, only one of the equations needs to be considered. Further, closed-form solutions of the characteristic equations that arise from solving the pair of governing equations by means of eigenfunctions can be easily obtained. The technique used is an extension of the one for isotropic shells presented in [15, 16]. From the pair of equations, a number of simplified fourth-order governing equations can be systematically and explicitly deduced, as shown in the paper. These fourth-order equations for orthotropic cylindrical shells are new in the literature and of definite technical importance because these equations can be easily solved in closed forms and yet retain practically the same accuracy as the original eighth-order equation.

Basic Equations

In accordance with the fundamental hypotheses stated previously, the following basic equations can be deduced for orthotropic circular cylindrical shells. Let a be the radius of the midsurface of the shell, x, y, z the axial, circumferential, and radial coordinates, and α, β the dimensionless midsurface coordinates along lines of curvatures ($\alpha = x/a$, $\beta = y/a$). The three displacement components u_α, u_β, and u_z of an arbitrary point of the shell can be expressed in terms of midsurface displacements u, v, and w as follows [8, 16]

$$u_\alpha = u + z\omega_\beta, \quad u_\beta = v - z\omega_\alpha, \quad u_z = w \tag{1}$$

where

$$\omega_\alpha = \frac{1}{a}\left(\frac{\partial w}{\partial \beta} - v\right), \quad \omega_\beta = -\frac{1}{a}\frac{\partial w}{\partial \alpha}$$

The stress-strain relations for orthotropic materials [5, 18, 19] are

$$\sigma_\alpha = \frac{E_1}{1-\nu_1\nu_2}(e_\alpha + \nu_1 e_\beta), \quad \sigma_\beta = \frac{E_2}{1-\nu_1\nu_2}(\nu_2 e_\alpha + e_\beta),$$
$$\tau_{\alpha\beta} = G e_{\alpha\beta} \tag{2}$$

where E_1, E_2 are the moduli of elasticity along the principal directions α and β, respectively, G is the shear modulus that characterizes the change of angles between principal directions α and β, $\nu_1 = \nu_{\beta\alpha}$ is the Poisson's ratio that characterizes the decrease in α-direction due to tension applied in β-direction, and $\nu_2 = \nu_{\alpha\beta}$ is the Poisson's ratio that characterizes the decrease in β-direction due to tension applied in α-direction. Among these material constants there exists the relation [5, 18, 19]:

$$E_1\nu_1 = E_2\nu_2 \tag{3}$$

The components of strain at an arbitrary point of the shell are related to the midsurface displacements by [8, 15, 16]

$$e_\alpha = \frac{1}{a}\left(\frac{\partial u}{\partial \alpha} - \frac{z}{a}\frac{\partial^2 w}{\partial \alpha^2}\right), \quad e_\beta = \frac{1}{a}\left(\frac{\partial v}{\partial \beta} + w\right) - \frac{z}{a(a+z)}\left(\frac{\partial^2 w}{\partial \beta^2} + w\right) \tag{4}$$

$$e_{\alpha\beta} = \frac{1}{a+z}\left[\frac{\partial u}{\partial \beta} + \frac{\partial v}{\partial \alpha} + 2\frac{z}{a}\left(\frac{\partial v}{\partial \alpha} - \frac{\partial^2 w}{\partial\alpha\partial\beta}\right) + \left(\frac{z}{a}\right)^2\left(\frac{\partial v}{\partial \alpha} - \frac{\partial^2 w}{\partial\alpha\partial\beta}\right)\right]$$

The bending (η_α, η_β) and twisting (τ) strains are

$$\eta_\alpha = -\frac{1}{a^2}\frac{\partial^2 w}{\partial \alpha^2}, \quad \eta_\beta = -\frac{1}{a^2}\left(\frac{\partial^2 w}{\partial \beta^2} + w\right),$$
$$\tau = -\frac{1}{2a^2}\left(\frac{\partial u}{\partial \beta} - \frac{\partial v}{\partial \alpha} + 2\frac{\partial^2 w}{\partial\alpha\partial\beta}\right) \tag{5}$$

Let h be the wall thickness, K_1, K_2 the extensional rigidity, D_1 and D_2 the flexural rigidity,

$$K_1 = \frac{E_1 h}{1-\nu_1\nu_2}, \quad K_2 = \frac{E_2 h}{1-\nu_1\nu_2}, \quad D_1 = \frac{h^2}{12}K_1, \quad D_2 = \frac{h^2}{12}K_2 \tag{6}$$

and define

$$k = \frac{E_2}{E_1}, \quad k_1 = \frac{G(1-\nu_1\nu_2)}{E_1} \tag{7}$$

Let N_α and N_β be the normal stress resultants, S_α and S_β the shear stress resultants, M and M_β the bending moments, $M_{\alpha\beta}$ and $M_{\beta\alpha}$ the twisting moments, and Q_α and Q_β the transverse stress resultants [15]. These are stress resultants (N, S, Q) and couples (M) per unit length of the middle surface and are related to the midsurface displacements through the stress-strain relations as

$$N_\alpha = \frac{K_1}{a}\left[\frac{\partial u}{\partial \alpha} + \nu_1\left(\frac{\partial v}{\partial \beta} + w\right) - c^2\frac{\partial^2 w}{\partial \alpha^2}\right],$$

$$N_\beta = \frac{K_2}{a}\left[\frac{\partial v}{\partial \beta} + \nu_2\frac{\partial u}{\partial \alpha} + w + c^2\left(\frac{\partial^2 w}{\partial \beta^2} + w\right)(1+\delta)\right]$$

$$S_\alpha = \frac{Gh}{a}\left[\frac{\partial u}{\partial \beta} + \frac{\partial v}{\partial \alpha} - c^2\left(\frac{\partial^2 w}{\partial\alpha\partial\beta} - \frac{\partial v}{\partial \alpha}\right)\right]$$

$$S_\beta = \frac{Gh}{a}\left[\frac{\partial u}{\partial \beta} + \frac{\partial v}{\partial \alpha} + c^2\left(\frac{\partial^2 w}{\partial\alpha\partial\beta} + \frac{\partial u}{\partial \beta}\right)(1+\delta)\right]$$

$$M_\alpha = -\frac{D_1}{a^2}\left[\frac{\partial u}{\partial \alpha} + \nu_1\frac{\partial v}{\partial \beta} - \left(\frac{\partial^2 w}{\partial \alpha^2} + \nu_1\frac{\partial^2 w}{\partial \beta^2}\right)\right],$$

$$M_\beta=\frac{D_2}{a^2}\left[\left(\frac{\partial^2 w}{\partial\beta^2}+w\right)(1+\delta)+\nu_2\frac{\partial^2 w}{\partial\alpha^2}\right] \tag{8}$$

$$M_{\alpha\beta}=\frac{Gh^3}{6a^2}\left(\frac{\partial v}{\partial\alpha}-\frac{\partial^2 w}{\partial\alpha\partial\beta}\right),$$

$$M_{\beta\alpha}=-\frac{Gh^3}{12a^2}\left[\frac{\partial u}{\partial\beta}-\frac{\partial v}{\partial\alpha}+2\frac{\partial^2 w}{\partial\alpha\partial\beta}+\delta\left(\frac{\partial u}{\partial\beta}+\frac{\partial^2 w}{\partial\alpha\partial\beta}\right)\right]$$

$$Q_\alpha=\frac{D_1}{a^3}\left[\frac{\partial^2 u}{\partial\alpha^2}-k_1(1+\delta)\frac{\partial^2 u}{\partial\beta^2}+(k_1+\nu_1)\frac{\partial^2 v}{\partial\alpha\partial\beta}\right.$$
$$\left.-\frac{\partial^3 w}{\partial\alpha^3}-(2k_1+\nu_1+\delta k_1)\frac{\partial^3 w}{\partial\alpha\partial\beta^2}\right]$$

$$Q_\beta=\frac{D_2}{a^3}\left[2\frac{k_1}{k}\frac{\partial^2 v}{\partial\alpha^2}-(1+\delta)\left(\frac{\partial^3 w}{\partial\beta^3}+\frac{\partial w}{\partial\beta}\right)\right.$$
$$\left.-\left(2\frac{k_1}{k}+\nu_2\right)\frac{\partial^3 w}{\partial\alpha^2\partial\beta}\right]$$

in which

$$c^2=\frac{h^2}{12a^2}$$

and

$$\delta=\frac{(\tanh^{-1}\sqrt{3}c-\sqrt{3}c)}{\sqrt{3}\cdot c^3}-1$$
$$=9c^2\left[\frac{1}{5}+\frac{1}{7}(\sqrt{3}c)^2+\frac{1}{9}(\sqrt{3}c)^4+\ldots\ldots\right].$$

The equations of static equilibrium are

$$\frac{\partial N_\alpha}{\partial\alpha}+\frac{\partial S_\beta}{\partial\beta}+aX=0,\quad \frac{\partial N_\beta}{\partial\beta}+\frac{\partial S_\alpha}{\partial\alpha}+Q_\beta+aY=0;$$

$$N_\beta-\frac{\partial Q_\alpha}{\partial\alpha}-\frac{\partial Q_\beta}{\partial\beta}-aZ=0 \tag{9}$$

$$\frac{\partial M_{\alpha\beta}}{\partial\alpha}-\frac{\partial M_\beta}{\partial\beta}-aQ_\beta=0,\quad \frac{\partial M_{\beta\alpha}}{\partial\beta}-\frac{\partial M_\alpha}{\partial\alpha}-aQ_\alpha=0$$

in which X, Y, and Z are surface loads per unit area in x, y and z directions, respectively.

Pair of Accurate Complex Conjugate Fourth-Order Equations for Normal Deflection

Substituting equation (8) into equation (9), a system of three differential equations is obtained for the three basic functions. This system is presented in Table 1 and possesses a symmetrical structure. The three linear partial differential equations with constant coefficients can be reduced to a single differential equation of higher order that is more convenient to solve and/or analyze with regard to the present problem. These three equations presented in Table 1 will be considered as algebraic equations in u, v, and w having coefficients that are constants (elastic constants and c^2) and the symbols of differentiations. Let D_o be the 3×3 determinant of Table 1 and calculate its cofactors $D_{11}, D_{12}, \ldots . D_{33}$. Let

$$u=D_{i1}\phi_i,\quad v=D_{i2}\phi_i,\quad w=D_{i3}\phi_i\quad \text{(Sum on } i,\ i=1,2,3) \tag{10}$$

and substitute these expressions in the three equations in Table 1. Then, in accordance with the theory of linear algebra

$$D_0\phi_i+\frac{1-\nu_1\nu_2}{E_1 h}a^2X_i=0,\quad (i=1,2,3) \tag{11}$$

are obtained, in which $X_1=X$, $X_2=Y$, $X_3=Z$. If only a normal surface load Z is applied on the shell, ϕ_1 and ϕ_2 can be set equal to zero in equations (10) and (11). Calculating cofactors D_{31}, D_{32}, D_{33}, and D_0 from Table 1 and replacing ϕ_3 by ϕ/k_1, the following are obtained from equations (10) and (11)

$$u=\frac{\partial}{\partial\alpha}\left\{k\frac{\partial^2}{\partial\beta^2}-\nu_1\frac{\partial^2}{\partial\alpha^2}\right.$$
$$\left.+c^2\left[\frac{\partial^4}{\partial\alpha^4}-k\frac{\partial^4}{\partial\beta^4}+(2K-8k_1-4\nu_1)\frac{\partial^4}{\partial\alpha^2\partial\beta^2}\right]\right\}\phi$$

$$v=\frac{\partial}{\partial\beta}\left\{-k\frac{\partial^2}{\partial\beta^2}-\frac{1}{k_1}(k-\nu_1k_1-\nu_1^2)\frac{\partial^2}{\partial\alpha^2}\right. \tag{12}$$
$$\left.+2c^2\left[\frac{\partial^4}{\partial\alpha^4}+(2k_1+\nu_1)\frac{\partial^4}{\partial\alpha^2\partial\beta^2}\right]\right\}\phi$$

$$w=\left[\frac{\partial^4}{\partial\alpha^4}+\frac{1}{k_1}(k-2\nu_1k_1-\nu_1^2)\frac{\partial^4}{\partial\alpha^2\alpha\beta^2}+k\frac{\partial^4}{\partial\beta^4}\right]\phi \tag{13}$$

$$\frac{1}{c^2}D_0\phi=\left\{\frac{\partial^8}{\partial\alpha^8}+2K\frac{\partial^8}{\partial\alpha^6\partial\beta^2}+k_2\frac{\partial^8}{\partial\alpha^4\partial\beta^4}\right.$$
$$+2kK\frac{\partial^8}{\partial\alpha^2\partial\beta^6}+k^2\frac{\partial^8}{\partial\beta^8}+2\nu_1\frac{\partial^6}{\partial\alpha^6}$$
$$+k_2\frac{\partial^6}{\partial\alpha^4\partial\beta^2}+2k(2K-\nu_1)\frac{\partial^6}{\partial\alpha^2\partial\beta^4}$$
$$+2k^2\frac{\partial^6}{\partial\beta^6}+\left[\frac{(k-\nu_1^2)}{c^2}+4k-3\nu_1^2\right]\frac{\partial^4}{\partial\alpha^4}$$
$$\left.+2k(K-\nu_1)\frac{\partial^4}{\partial\alpha^2\partial\beta^2}+k^2\frac{\partial^4}{\partial\beta^4}\right\}\phi=\frac{a^4}{D_1}Z \tag{14}$$

Table 1

u	v	w	Loads terms	
$\frac{\partial^2}{\partial\alpha^2}+k_1[1+c^2(1+\delta)]\frac{\partial^2}{\partial\beta^2}$	$(k_1+\nu_1)\frac{\partial^2}{\partial\alpha\partial\beta}$	$\nu_1\frac{\partial}{\partial\alpha}-c^2\left[\frac{\partial^3}{\partial\alpha^3}-k_1(1+\delta)\frac{\partial^3}{\partial\alpha\partial\beta^2}\right]$	$+\frac{1-\nu_1\nu_2}{E_1h}a^2X$	$=0$
$(k_1+\nu_1)\frac{\partial^2}{\partial\alpha\partial\beta}$	$k\frac{\partial^2}{\partial\beta^2}+k_1(1+3c^2)\frac{\partial^2}{\partial\alpha^2}$	$k\frac{\partial}{\partial\beta}-c^2(3k_1+\nu_1)\frac{\partial^3}{\partial\alpha^2\partial\beta}$	$+\frac{1-\nu_1\nu_2}{E_1h}a^2Y$	$=0$
$\nu_1\frac{\partial}{\partial\alpha}-c^2\left[\frac{\partial^3}{\partial\alpha^3}-k_1(1+\delta)\frac{\partial^3}{\partial\alpha\partial\beta^2}\right]$	$k\frac{\partial}{\partial\beta}-c^2(3k_1+\nu_1)\frac{\partial^3}{\partial\alpha^2\partial\beta}$	$k+c^2\left[\frac{\partial^4}{\partial\alpha^4}+(4k_1+2\nu_1+\delta k_1)\frac{\partial^4}{\partial\alpha^2\partial\beta^2}+k(1+\delta)\left(\frac{\partial^2}{\partial\beta^2}+1\right)^2\right]$	$-\frac{1-\nu_1\nu_2}{E_1h}a^2Z$	$=0$

Table 2 Mechanical properties of materials

Species	$k=E_2/E_1$	G/E_1	ν_1	ν_2
Glass/epoxy	0.3333	0.1666	0.0833	0.2500
Boron/epoxy	0.1000	0.0333	0.0300	0.3000
Graphite/epoxy	0.0250	0.0125	0.0063	0.2500
Douglas-fir	0.0500	0.0780	0.0220	0.4490

in which

$$K=\frac{k}{2k_1}(1-\nu_1\nu_2)+2k_1, \quad k_2=6k+4\nu_1(K-4k_1)-8\nu_1^2 \tag{15}$$

The constant coefficients in equations (12), (13), and (14) may contain coefficients higher than those shown (of the order c^2 or higher). These coefficients have been omitted since, in thin shell theory, $h/a \leq 1/20$, thus $c^2 \leq 2\times10^{-4}$ is a very small number. The complete expression of D_0 is given in the Appendix. Comparison of the magnitude of the coefficients of the terms that were omitted with the coefficients of the terms (having the same partial differentiations) which were retained in equations (14), (13), and (12) reveals that these omitted terms are truly of smaller orders of magnitude. This fact has been further verified through the actual computation of these coefficients using available numerical data drawn from elastic constants of many orthotropic materials. In Table 2, the elastic constants of a few materials are presented. Thus, equation (14) is an accurate governing equation for orthotropic cylindrical shells because this equation is derived from the basic hypotheses without introducing further approximations in its derivation except that, as just stated, some negligibly small terms have been omitted. These small terms have been totally dropped in all the known equations of orthotropic shells. In some publications, even certain terms in equation (14) are neglected. In the following analysis, some of these negligibly small terms will be retained so that equation (14) can be reduced to a pair of fourth-order complex conjugate equations. This not only tremendously simplifies calculaton of the roots of the characteristic equation that arise from solving the equation by separation of variables but it also facilitates obtaining solutions in simple explicit forms. As stated previously, finding solutions to equation (14) in explicit forms is almost prohibitively difficult due to the algebraic complexity involved. In addition to keeping some small terms, the following approximate relation as given in [20, 21] is employed:

$$G=\frac{\sqrt{E_1E_2}}{2(1+\sqrt{\nu_1\nu_2})} \tag{16}$$

in which $\sqrt{E_1E_2}$ and $\sqrt{\nu_1\nu_2}$ are geometric mean values for the modulus E and Poisson's ratio ν, respectively. It should be noted that unlike [20], in [18, 23] relation (16) is presented only as a special case and no justification or proof is given to establish its validity. From equations (3), (7), (15), and (16), we obtain

$$2k_1=\sqrt{k}(1-\sqrt{\nu_1\nu_2}), \quad K=2(2k_1+\nu_1)=2\sqrt{k}, k_2=6k \tag{17}$$

If, in equation (14), the coefficient k_2 of the middle term $\partial^8/\partial\alpha^4\partial\beta^4$ (*only in this term*) is replaced by $6k$ (17) and some of these omitted small terms are kept as explained previously, then from equations (13) and (14), the governing differential equation for normal deflection w may be written as

$$L\bar{L}w=\frac{a^4}{D_1}\left[\frac{\partial^4}{\partial\alpha^4}+\frac{1}{k_1}(k-2\nu_1k_1-\nu_1^2)\frac{\partial^4}{\partial\alpha^2\partial\beta^2}+k\frac{\partial^4}{\partial\beta^4}\right]Z \tag{18}$$

in which

$$L=\frac{\partial^4}{\partial\alpha^4}+K\frac{\partial^4}{\partial\alpha^2\partial\beta^2}+k\left(\frac{\partial^4}{\partial\beta^4}+\frac{\partial^2}{\partial\alpha^2}+\frac{\partial^2}{\partial\beta^2}\right)$$
$$+i\left[\frac{1}{c_1}\frac{\partial^2}{\partial\alpha^2}+c_1\left(k_3\frac{\partial^4}{\partial\alpha^4}+k_4\frac{\partial^4}{\partial\alpha^2\partial\beta^2}+k_5\frac{\partial^4}{\partial\beta^4}+k_5\frac{\partial^2}{\partial\beta^2}+k_6\frac{\partial^2}{\partial\alpha^2}\right)\right] \tag{19}$$

and $\bar{L}$ is the complex conjugate linear differential operator of L, $i=\sqrt{-1}$, and

$$c_1=\frac{c}{\sqrt{k(1-\nu_1\nu_2)}}, \quad k_3=\nu_1-k, \quad k_4=\frac{1}{2}(k_2-2kK-2k),$$
$$k_5=k(K-k-\nu_1), \quad k_6=\frac{1}{2}(4k-k^2-3\nu_1^2) \tag{20}$$

K, k, k_1, and k_2 in equations (18), (19), and (20) have been defined previously in expressions (7) and (15). As will be shown later, the replacement of coefficient k_2 of the middle term in equation (14) by $6k$ has only an insignificant effect on the solutions of the problem. Table 3–7 show that the differences between either the real or imaginary parts of the characteristic roots of the homogeneous equations (14) and (18) are negligibly small (less than 0.5 percent). In equation (19), it is seen that the last term c_1k_6 $(\partial^2/\partial\alpha^2)$ is very small as compared with the term $(1/c_1)/(\partial^2/\partial\alpha^2)$ and hence can be dropped. This should not yield any noticeable effect on the accuracy of the equation as will be further elaborated later. The homogeneous solutions of equation (18) are obtained from

$$Lw=0, \quad \bar{L}w=0 \tag{21}$$

From equations (12) and (13), we can express u and v in terms of w [15]. Equations (18) reduces to the same governing equation for isotropic cylindrical shells as deduced in [15]. The terms of eighth-order derivatives in equation (14) can be written as

$$\left[\frac{\partial^4}{\partial x^4}+2(2k_1+\nu_1)\frac{\partial^4}{\partial x^2\partial y^2}+k\frac{\partial^4}{\partial y^4}\right]\left[\frac{\partial^4}{\partial x^4}+\frac{1}{k_1}(k-\nu_1^2-2\nu_1k_1)\frac{\partial^4}{\partial x^2\partial y^2}+k\frac{\partial^4}{\partial y^4}\right]a^8\phi \tag{22}$$

Having obtained the preceding expression, we can readily obtain the orthotropic plate equation from (14) and (13) as the radius of the shell goes to infinity:

$$\left[\frac{\partial^4}{\partial x^4}+2(2k_1+\nu_1)\frac{\partial^4}{\partial x^2\partial y^2}+k\frac{\partial^4}{\partial y^4}\right]w=\frac{Z}{D_1} \tag{23}$$

Using the relation (16), equation (18) can also be reduced to the preceding orthotropic plate equation.

Solutions by Eigenfunctions

It may be shown that homogeneous equation (21) and suitable boundary conditions are satisfied by making use of the following solution when the eigenfunctions are trigonometric along a generator:

$$w=e^{p\beta}\cos n\alpha \tag{24}$$

in which $n=(m\pi a)/(l)$, m is an arbitrary integer, l represents the length of the shell, and e is the base of natural logarithms. When the eigenfunctions are trigonometric in the circumferential direction, w can be taken as

$$w=e^{p\alpha}\cos n\beta \tag{25}$$

in which n is a real number. It is an integer value when the cylinder is closed and a noninteger value when the shell is open. Substituting expressions (24) and (25) into the governing equation (21) yields characteristic equations for the determination of the roots p. Four complex roots are obtained and the other four roots are the complex conjugate numbers to these four roots. The characteristic equations are quadratic

Table 3 Characteristic roots ($w = e^{p\beta}\cos n\alpha$) (boron/epoxy)

$1/c$	n	Equation	p_1, p_2	p_3, p_4
50	0.001	(14)	$0.009297+0.008429i$	$0.000079+1.000000i$
		(18)	$0.009278+0.008414i$	$0.000079+1.000000i$
		(26)	$0.009278+0.008414i$	$0.000079+1.000000i$
		(29)	$0.008900+0.008843i$	$0.000079+0.999997i$
		(27)	$0.008872+0.008871i$	$0.000079+0.999992i$
		(30)	$0.008872+0.008871i$	$0.000079+0.999997i$
		(28)	$0.103515+0.042850i$	$0.042877+0.103450i$
		(31)	$0.103496+0.042858i$	$0.042869+0.103469i$
50	0.010	(14)	$0.093577+0.083514i$	$0.007852+1.000139i$
		(18)	$0.093411+0.083407i$	$0.007857+1.000138i$
		(26)	$0.093414+0.083402i$	$0.007857+1.000138i$
		(29)	$0.089696+0.087736i$	$0.007870+0.999889i$
		(27)	$0.089463+0.088064i$	$0.007883+0.999372i$
		(30)	$0.089420+0.088024i$	$0.007872+0.999839i$
		(28)	$0.328262+0.135123i$	$0.135969+0.326220i$
		(31)	$0.327653+0.135377i$	$0.135719+0.326828i$
5000	0.100	(14)	$3.217938+1.376923i$	$1.331418+3.327954i$
		(18)	$3.217917+1.376970i$	$1.331469+3.327934i$
		(26)	$3.217926+1.376965i$	$1.331472+3.327925i$
		(29)	$3.211572+1.380148i$	$1.329567+3.333750i$
		(27)	$3.217595+1.377790i$	$1.332245+3.327594i$
		(30)	$3.211551+1.380201i$	$1.329618+3.333728i$
		(28)	$3.282622+1.351234i$	$1.359694+3.262197i$
		(31)	$3.276528+1.353769i$	$1.357185+3.268280i$

Table 4 Characteristic roots ($w = e^{p\alpha}\cos n\beta$) (boron/epoxy)

$1/c$	n	Equation	p_1, p_2	p_3, p_4
50	0	(14)	$2.802685+2.808032i$	0
		(18)	$2.803801+2.809136i$	0
		(26)	$2.803801+2.809136i$	0
		(29)	$2.796462+2.814284i$	0
		(27)	$2.805359+2.805359i$	0
		(30)	$2.805359+2.805359i$	0
		(28)	$2.805359+2.805359i$	0
		(31)	$2.805359+2.805359i$	0
50	1	(14)	$2.939060+2.664959i$	0
		(18)	$2.945199+2.671730i$	0
		(26)	$2.945332+2.671609i$	0
		(29)	$2.853203+2.758317i$	0
		(27)	$2.948208+2.669431i$	0
		(30)	$2.862275+2.749575i$	0
		(28)	$2.948680+2.670070i$	$0.058927+0.053359i$
		(31)	$2.862805+2.750173i$	$0.057446+0.055186i$
5000	2	(14)	$28.109116+27.998002i$	$0.019553+0.019495i$
		(18)	$28.109206+27.998089i$	$0.019553+0.019495i$
		(26)	$28.109254+27.998038i$	$0.019553+0.019495i$
		(29)	$28.075257+28.031950i$	$0.019539+0.019509i$
		(27)	$28.109475+27.997827i$	$0.019563+0.019485i$
		(30)	$28.076149+28.031060i$	$0.019540+0.019508i$
		(28)	$28.109477+27.997829i$	$0.022589+0.022500i$
		(31)	$28.076151+28.031062i$	$0.022563+0.022526i$

equations in p^2; hence solutions can be easily found in closed forms.

Simple Equations

The accurate fourth-order equation (21) can be used to obtain a number of simplified equations which are new in the literature and are of importance in practice. Considering the actual values of elastic constants of various known orthotropic materials and the smallness of c^2, it can be easily shown that the last term in equation (19) $c_1 k_6\ (\partial^2)/(\partial\alpha^2)$ is much smaller than the term $1/c_1\ (\partial^2)/(\partial\alpha^2)$, hence this term can be dropped in equation (19) as previously stated. When the same considerations and solutions by eigenfunctions are applied, terms with coefficients k_3, k_4, and k_5 in equation (19) can also be neglected because they are of a smaller order of magnitude in comparison with other terms that have the same partial differentiations in the equation. Dropping these terms in equation (19) yields the following simplified equation

$$Lw = \left[\frac{\partial^4}{\partial\alpha^4} + K\frac{\partial^4}{\partial\alpha^2\partial\beta^2} + k\frac{\partial^4}{\partial\beta^4} + k\left(\frac{\partial^2}{\partial\alpha^2} + \frac{\partial^2}{\partial\beta^2}\right) \pm \frac{i}{c_1}\frac{\partial^2}{\partial\alpha^2}\right] w = 0 \tag{26}$$

which has practically the same accuracy as equation (14) (less than 0.5 percent difference as shown in Talbe 3-8). Following the same reasoning, the fourth term is small as compared with the last term $1/c_1\ (\partial^2/\partial\alpha^2)$ and hence has little effect on the characteristic roots. Therefore this term can be dropped in equation (26) and another simple equation

$$Lw = \left(\frac{\partial^4}{\partial\alpha^4} + K\frac{\partial^4}{\partial\alpha^2\partial\beta^2} + k\frac{\partial^4}{\partial\beta^4} + k\frac{\partial^2}{\partial\beta^2} \pm \frac{i}{c_1}\frac{\partial^2}{\partial\alpha^2}\right) w = 0 \tag{27}$$

is obtained. If the fourth term in equation (27) is also dropped, one obtains

Table 5 **Characteristic roots ($w = e^{p\beta}\cos n\alpha$) (glass/epoxy)**

$1/c$	n	Equation	p_1, p_2	p_3, p_4
		(14)	$0.006679+0.006393i$	$0.000043+1.000000i$
		(18)	$0.006684+0.006406i$	$0.000043+1.000000i$
		(26)	$0.006688+0.006403i$	$0.000043+1.000000i$
50	0.001	(29)	$0.006585+0.006508i$	$0.000043+0.999999i$
		(27)	$0.006546+0.006546i$	$0.000043+0.999998i$
		(30)	$0.006546+0.006546i$	$0.000043+0.999998i$
		(28)	$0.088900+0.036816i$	$0.036824+0.088881i$
		(31)	$0.088900+0.036817i$	$0.036824+0.088833i$
		(14)	$0.067138+0.063729i$	$0.004278+1.000033i$
		(18)	$0.067147+0.063739i$	$0.004284+1.000033i$
		(26)	$0.067149+0.063741i$	$0.004285+1.000033i$
50	0.010	(29)	$0.066126+0.064801i$	$0.004285+0.999923i$
		(27)	$0.065748+0.065187i$	$0.004287+0.999847i$
		(30)	$0.065748+0.065187i$	$0.004286+0.999873i$
		(28)	$0.281398+0.116309i$	$0.116559+0.280794i$
		(31)	$0.281363+0.116327i$	$0.116545+0.280837i$
		(14)	$2.738576+1.193250i$	$1.132930+2.884387i$
		(18)	$2.738575+1.193251i$	$1.132931+2.884387i$
		(26)	$2.738617+1.193267i$	$1.132948+2.884425i$
5000	0.100	(29)	$2.738139+1.193649i$	$1.132994+2.884726i$
		(27)	$2.738452+1.193565i$	$1.133228+2.884256i$
		(30)	$2.738106+1.193733i$	$1.133074+2.884691i$
		(28)	$2.813983+1.163089i$	$1.165591+2.807942i$
		(31)	$2.813632+1.163268i$	$1.165446+2.808373i$

Table 6 **Characteristic roots ($w = e^{p\alpha}\cos n\beta$) (glass/epoxy)**

$1/c$	n	Equation	p_1, p_2	p_3, p_4
		(14)	$3.773718+3.784743i$	0
		(18)	$3.775179+3.786174i$	0
		(26)	$3.775101+3.786093i$	0
50	0	(29)	$3.757170+3.801267i$	0
		(27)	$3.779234+3.779234i$	0
		(30)	$3.779154+3.779154i$	0
		(28)	$3.779234+3.779234i$	0
		(31)	$3.779154+3.779154i$	0
		(14)	$3.860588+3.696090i$	0
		(18)	$3.862294+3.697873i$	0
		(26)	$3.862230+3.697778i$	0
50	1	(29)	$3.833873+3.725216i$	0
		(27)	$3.867971+3.692534i$	0
		(30)	$3.856292+3.703559i$	0
		(28)	$3.868686+3.693356i$	$0.078077+0.074538i$
		(31)	$3.857015+3.704375i$	$0.077861+0.074779i$
		(14)	$37.826903+37.757812i$	$0.026479+0.026442i$
		(18)	$37.826902+37.757811i$	$0.026479+0.026442i$
		(26)	$37.826113+37.757011i$	$0.026478+0.026441i$
5000	2	(29)	$37.819909+37.763213i$	$0.026479+0.026440i$
		(27)	$37.827467+37.757273i$	$0.026485+0.026436i$
		(30)	$37.822116+37.761010i$	$0.026481+0.026438i$
		(28)	$37.827470+37.757277i$	$0.030582+0.030525i$
		(31)	$37.822119+37.761013i$	$0.030578+0.030528i$

$$Lw = \left(\frac{\partial^4}{\partial\alpha^4} + K\frac{\partial^4}{\partial\alpha^2\partial\beta^2} + k\frac{\partial^4}{\partial\beta^4} \pm \frac{i}{c_1}\frac{\partial^2}{\partial\alpha^2}\right)w = 0 \qquad (28)$$

Unlike other equations presented in this section, the preceding equation is obtained by dropping a term in equation (27) without the usual presence in that equation of a similar term having a much larger coefficient with which, as a justification for the resulting simplification, the dropped term can be compared. A justification of this procedure would be provided if the accuracy of the equation could be established. In the final section, it is shown that this equation and its simplified form, equation (31), are inaccurate in the case $w = e^{p\beta}\cos n\alpha$ and, for long shells, in the case of shells under distributed surface normal loads Z. Hence this procedure does in effect affect the accuracy of the equation.

In deducing the fourth-order equations (21), (26)–(28) from the original equation (14) only the coefficient k_2 of the term $\partial^8/\partial\alpha^4\partial\beta^4$ in equation (14) is replaced by its approximate value $6k$ (17). If the same approximation (17) is also used for the coefficient K in equation (19), then equations (26)–(28) become, respectively,

$$\left(\nabla_0^4 + k\nabla^2 \pm \frac{i}{c_1}\frac{\partial^2}{\partial\alpha^2}\right)w = 0 \qquad (29)$$

$$\left(\nabla_0^4 + k\frac{\partial^2}{\partial\beta^2} \pm \frac{i}{c_1}\frac{\partial^2}{\partial\alpha^2}\right)w = 0 \qquad (30)$$

$$\left(\nabla_0^4 \pm \frac{i}{c_1}\frac{\partial^2}{\partial\alpha^2}\right)w = 0 \qquad (31)$$

in which

$$\nabla_0^2 = \frac{\partial^2}{\partial\alpha^2} + \sqrt{k}\frac{\partial^2}{\partial\beta^2}, \quad \nabla^2 = \frac{\partial^2}{\partial\alpha^2} + \frac{\partial^2}{\partial\beta^2},$$

$$k = \frac{E_2}{E_1} \quad \text{and} \quad c_1 = \frac{h}{2a\sqrt{3k(1-\nu_1\nu_2)}}.$$

As deflections and stresses depend on the characteristic roots,

Table 7 Characteristic roots ($w = e^{p\beta}\cos n\alpha$) (graphite/epoxy)

$1/c$	n	Equation	p_1, p_2	p_3, p_4
		(14)	0.013357 +0.011729 i	0.000158 + 1.000000i
		(18)	0.013303 +0.011695 i	0.000158 + 1.000000i
		(26)	0.013304 +0.011694 i	0.000158 + 1.000000i
50	0.001	(29)	0.012591 +0.012548 i	0.000158 + 0.999994i
		(27)	0.012572 +0.012568 i	0.000158 + 0.999980i
		(30)	0.012571 +0.012567 i	0.000158 + 0.999994i
		(28)	0.123248 +0.050992 i	0.051051 + 0.123106i
		(31)	0.123199 +0.051012 i	0.051031 + 0.123155i
		(14)	0.135291 +0.115102 i	0.015698 + 1.000601i
		(18)	0.134745 +0.114782 i	0.015702 + 1.000595i
		(26)	0.134744 +0.114782 i	0.015702 + 1.000595i
50	0.010	(29)	0.127835 +0.123473 i	0.015784 + 1.000040i
		(27)	0.127839 +0.123844 i	0.015855 + 0.998577i
		(30)	0.127646 +0.123680 i	0.015787 + 0.999991i
		(28)	0.391769 +0.160409 i	0.162270 + 0.387268i
		(31)	0.390212 +0.161058 i	0.161632 + 0.388826i
		(14)	3.863535 +1.625197 i	1.598486 + 3.928208i
		(18)	3.863438 +1.625419 i	1.598720 + 3.928115i
		(26)	3.863425 +1.625414 i	1.598715 + 3.928103i
5000	0.100	(29)	3.847469 +1.632947 i	1.593312 + 3.943178i
		(27)	3.862934 +1.626713 i	1.599938 + 3.927580i
		(30)	3.847456 +1.632978 i	1.593343 + 3.943165i
		(28)	3.917688 +1.604092 i	1.622698 + 3.872768i
		(31)	3.902121 +1.161058 i	1.616319 + 3.888262i

Table 8 Characteristic roots ($w = e^{p\alpha}\cos n\beta$) (graphite/epoxy)

$1/c$	n	Equation	p_1, p_2	p_3, p_4
		(14)	1.986613 + 1.988186i	0
		(18)	1.987408 + 1.988976i	0
		(26)	1.987389 + 1.988970i	0
50	0	(29)	1.984245 + 1.990535i	0
		(27)	1.987400 + 1.987400i	0
		(30)	1.987387 + 1.987387i	0
		(28)	1.987400 + 1.987400i	0
		(31)	1.987387 + 1.987387i	0
		(14)	2.111661 + 1.854832i	0
		(18)	2.119304 + 1.863529i	0
		(26)	2.119284 + 1.863523i	0
50	1	(29)	2.024353 + 1.951096i	0
		(27)	2.120223 + 1.862897i	0
		(30)	2.027557 + 1.948014i	0
		(28)	2.120533 + 1.863358i	0.042075 + 0.036972i
		(31)	2.027929 + 1.948434i	0.040542 + 0.038953i
		(14)	19.925442 + 19.822453i	0.013807 + 0.013753i
		(18)	19.925560 + 19.822572i	0.013807 + 0.013753i
		(26)	19.925434 + 19.822448i	0.013807 + 0.013753i
5000	2	(29)	19.889481 + 19.858286i	0.013791 + 0.013769i
		(27)	19.925642 + 19.822496i	0.013815 + 0.013744i
		(30)	19.889795 + 19.857972i	0.013791 + 0.013769i
		(28)	19.925643 + 19.822498i	0.015953 + 0.015870i
		(31)	19.889797 + 19.857973i	0.015924 + 0.015899i

the amount of difference between the characteristic roots of an equation under consideration and those of the accurate equation (14) should be an indication of the accuracy of the former. A comparison of the closeness of the characteristic roots of all the equations deduced herein with that of equation (14) is given in the final section. It is found that the characteristic roots of equations (26), (27), (29), and (30) are very close, well within engineering accuracy, to those of equation (14). Hence the replacement of k_2 by $6k$ in equation (14) and K by $2\sqrt{k}$ (17) in equations (26), and (27) can be justified and the accuracy as well as the validity of these equations (26), (27), (29), and (30) can be established. Equation (31) has the simplest possible form and hence may be, in some cases, preferred in practice. However, it is found herein that this equation and also equation (28) are not always as accurate and dependable as equations (26), (27), (29), and (30) and hence their use requires special care. The details are provided in the final section. By substituting the differential operators L given by equations (26)–(31) into the left-hand side of equation (18), the complete version of these equations including the load term can be written as

$$L\bar{L}w = \frac{a^4}{D_1}\left[\frac{\partial^4}{\partial\alpha^4} + \frac{1}{k_1}(k - 2\nu_1 k_1 - \nu_1^2)\frac{\partial^4}{\partial\alpha^2\partial\beta^2} + k\frac{\partial^4}{\partial\beta^4}\right]Z = \frac{a^4}{D_1}L_0 Z \qquad (32)$$

in which L represents any one of the six linear differential operators of equations (26)–(31). We rewrite equations (12) and (13) as

$$u = L_1\phi, \quad v = L_2\phi, \quad w = L_0\phi \qquad (33)$$

in which L_1, L_2, and L_0 represent the linear differential operators as given on the right-hand side of equations (12) and (13). Having obtained the governing differential equations (26)–(31) for w, the other two displacements u and v can be obtained in terms of w from equation (33) as

$$L_0 u = L_1 w, \quad L_0 v = L_2 w \qquad (34)$$

The Morley, Novozhilov, and Donnell equations for isotropic shells [15] are special cases of the equations (29), (30), and (31). The present method of deducing simple fourth-order equations improves upon the one used for isotropic cylindrical shells in a previous paper [15] by the first author.

Axially Symmetric Case

In this case the following equation is obtained from equations (14) and (13):

$$\left[\left(\frac{d^2}{d\alpha^2}+\nu_1\right)^2+\frac{k(1-\nu_1\nu_2)}{c^2}\right]w=\frac{(1-\nu_1\nu_2)h}{12E_1c^4}Z \tag{35}$$

which can be further simplified to

$$\left[\frac{d^2}{d\alpha^2}+i\frac{\sqrt{k(1-\nu_1\nu_2)}}{c}\right]\left[\frac{d^2}{d\alpha^2}-i\frac{\sqrt{k(1-\nu_1\nu_2)}}{c}\right]w=\frac{(1-\nu_1\nu_2)h}{12E_1c^4}Z \tag{36}$$

Problems of Thin Rings and Long Tubes

When a ring is loaded by forces applied at the boundary, parallel to the plane of the ring, the stress components are zero on both faces of the ring. Such a state of stress is called plane stress. Following the procedures presented in [22], the following basic equations for bending of thin rings of orthotropic materials are obtained:

$$\begin{aligned}&\frac{d^2w}{d\beta^2}+w=\frac{a^2M}{E_2I}\\&\frac{dv}{d\beta}+w=0\\&\omega=\frac{1}{a}\left(\frac{dw}{d\beta}-v\right)\end{aligned} \tag{37}$$

where $I = bh^3/12$, b = width of the ring, M is the bending moment ($M = bM_2$), and ω represents the rotation of radial cross sections of the ring. For an infinitely large radius a the preceding equations coincide with that for a straight beam.

When a long circular tube is under the action of lateral loads uniformly distributed along the axis of the cylinder, we have a state of plane strain. In this case, displacement along the axis of the tube u is zero and v and w are functions of β only. Following the procedures similar to the deductions of the basic equations for thin rings, the following basic equations for the bending of long tubes of orthotropic materials can be obtained:

$$\begin{aligned}&\frac{d^2w}{d\beta^2}+w=\frac{12(1-\nu_1\nu_2)a^2M_2}{E_2h^3}\\&\frac{dv}{d\beta}+w=0\\&\omega=\frac{1}{a}\left(\frac{dw}{d\beta}-v\right)\end{aligned} \tag{38}$$

Thus the basic equations of the present theory contain both ring bending and bending of long circular tubes as special cases. However, as stated in [16], the equations for bending of thin rings and long tubes cannot be deduced from the Donnell equations.

Comparisons and Conclusions

By means of computer, the relative accuracy of the differential equations presented previously can be further studied through numerical techniques. This can be done by calculating the numerical values of the characteristic roots of the equations and making a comparison of the closeness of these roots [16]. The accurate original equation (14) is used as the standard for comparison. The elastic constants of several typical orthotropic materials are collected in Table 2. Using these values, the roots calculated from homogeneous equations of (14) and (18) and equations (26)–(31) are obtained. Many roots for other orthotropic materials have also been calculated. Similarities in the properties of these roots for different materials can be observed. However, due to space limitations and the fact that the same conclusions can be drawn from different materials, only boron-epoxy, glass-epoxy, and graphite-epoxy are presented in Table 3–Table 8 for a range of significant parameters. From all the numerical results, it may be concluded that the differences between either the real or imaginary parts of the roots of the homogeneous equations (14), (18), and (26) are negiligibly small (less than 0.5 percent) for all values of n and c. Numerical results similarly show that simplified equations (27), (29), and (30) can also yield accurate solutions well within engineering accuracy as seen from the closeness of the characteristic roots of these equations to those of equations (14), (18), or (26). The simplified equations (28) or (31), which are only one term less than equations (27) or (30), are not always as accurate and dependable as other equations. We note that the accuracy of equations (31) and (28) are affected by the constants k and K, which is not the case for isotropic shells. These two equations are apparently inaccurate in the case $w = e^{p\beta}\cos n\alpha$ when n ($n = m\pi a/l$ (24)) is small, that is, for long shells. In the analysis of cylindrical shells under distributed loads Z ($Z = \cos m\pi a\alpha/l \cos n\beta$, $m, n = 0, 1, 2, \ldots$), similar conclusion may be made that equations (31), (28) lead to reliable results only for short shells. Hence, special care is needed when these two equations are employed. All the preceding conclusions hold also for the cases when E_1 and E_2, ν_1, and ν_2 are interchanged in the calculations and hence the preceding equations deduced in the paper may be applied to composite shells.

In conclusion, equations (26), (27), (29), and (30) deduced herein have the two essential properties of accuracy and simplicity that makes them of practical importance.

References

1 Ambartsumyan, S. A., "Theory of Anisotropic Shells," NASA TT F-118, Washington, D. C., May 1964.

2 Dong, S. B., Pister, K. S., and Taylor, R. L., "On the Theory of Laminated Anisotropic Shells and Plates," *Journal of the Aerospace Sciences*, Vol. 29, Aug. 1962, pp. 969–975.

3 Schwaighofer, J., and Microys, H. F., "Orthotropic Cylindrical Shells Under Line Load," ASME Journal of Applied Mechanics, Vol. 46, 1979, pp. 356–362.

4 Bert, C. W., "Structural Theory for Laminated Anisotropic Elastic Shells," *Journal of Composite Materials I*, 1967, pp. 414–423.

5 Calcote, L. R., *The Analysis of Laminated Composite Structures*, Van Nostrand Reinhold, New York, 1969.

6 Cheng, Shun, and Ho, B. P. C., "Stability of Heterogeneous Aeolotropic Cylindrical Shells Under Combined Loading," *AIAA Journal*, Vol. 1, No. 4, April 1963, pp. 892–898; also Forest Products Laboratory Report, Madison, Wis., July, 1962.

7 Lei, M. M., and Cheng, Shun, "Buckling of Composite and Homogeneous Isotropic Cylindrical Shells Under Axial and Radial Loading," ASME Journal of Applied Mechanics, Vol. 36, 1969, pp. 791–798.

8 Flugge, W., *Stress in Shells*, Springer-Verlag, Berlin, 1967.

9 Vlasov, V. Z., "General Theory of Shells and Its Applications in Engineering," NASA TTF-99, 1964.

10 Lure, A. I., "Statistics of Thin-Walled Elastic Shells," National Technical Information Service, U.S. Department of Commerce, 1947.

11 Love, A. E. H., *A Treatise on the Mathematical Theory of Elasticity*, 4th Ed., Dover, New York, 1944.

12 Novozhilov, V. V., *The Theory of Thin Shells*, Noordhoff, Gröningen, The Netherlands, 1959.

13 Donnell, L. H., "Stability of Thin-Walled Tubes Under Torsion," NACA, TR 479, 1933.

14 Hoff, N. J., "The Accurcy of Donnell's Equations," ASME Journal of Applied Mechanics, Vol. 22, 1955, pp. 329–334.

15 Cheng, Shun, "Accurate Fourth-Order Equation for Circular Cylindrical Shells," *Journal of the Engineering Mechanics Division, Proceedings of the ASCE*, Vol. 98, No. EM3, June 1972, pp. 641-656, also, Report No. 1198, Mathematics Research Center, University of Wisconsin, Madison, Wis., 1971.

16 Cheng, Shun, "On an Accurate Theory for Circular Cylindrical Shells," ASME JOURNAL OF APPLIED MECHANICS, 1973, pp. 583-588.

17 Markov, P., "Cheng's Theory for Shells of General Curvature," (in Czech.), *Strojnicky Casopis*, Vol. 32, No. 2, 1981, pp. 225-244, an in-depth review of Markov's paper is given by Jira, J. in *Applied Mechanics Review*, Vol. 35, Nov. 1982, pp. 1088-1089.

18 Lekhnitskii, S. G., *Theory of Elasticity of an Anisotropic Body*, translated by Fern, P., and Brandstatter, J. J., Holden-Day, San Francisco, Calif., 1963.

19 Lekhnitskii, S. G., *Anisotropic Plates*, translated by Tsai, S. W., and Cheron, T., Gordon and Breach, New York, 1968.

20 Panc, V., *Theories of Elastic Plates*, Noordhoff International, The Netherlands, 1975.

21 Huber, M. T., "Die Theories der Kreuzweise bewehrten Eisenbetonplatten nebst Anwendungen auf mehrere bautechnisch wichtige Aufgaben uber Rechteckplaten," *Bauing*, No. 4, 1923.

22 Cheng, Shun, and Hoff, N. J., "Bending of Thin Circular Rings," *International Journal of Solids and Structures*, Vol. 11, Feb. 1975, pp. 139-152.

23 Saint-Venant, B., "Mémoire sur la distribtuion d'elasticité." *Journal de Math. Pures et Appl. (Liouville)*, Ser. 2, t. 8, 1863.

APPENDIX

$$
\begin{aligned}
D_0 = k_1 \Big\{ & (k-\nu_1^2)\frac{\partial^4}{\partial\alpha^4} \\
& + c^2 \Big\{ \frac{\partial^8}{\partial\alpha^8} + \frac{1}{k_1}(k-\nu_1^2+4k_1^2+\delta k_1^2)\frac{\partial^8}{\partial\alpha^6\partial\beta^2} \\
& + \frac{1}{k_1}[4k_1k-7k_1\nu_1^2-6\nu_1k_1^2+2\nu_1k-2\nu_1^3 \\
& -(\nu_1^2k_1+2\nu_1k_1^2-2kk_1)(1+\delta)]\frac{\partial^8}{\partial\alpha^4\partial\beta^4} \\
& + \frac{1}{k_1}[3k_1^2k+2\nu_1k_1k+(k^2-\nu_1^2k-2\nu_1kk_1 \\
& + k_1^2k)(1+\delta)]\frac{\partial^8}{\partial\alpha^2\partial\beta^6} + k^2(1+\delta)\frac{\partial^8}{\partial\beta^8} \\
& + 2\nu_1\frac{\partial^6}{\partial\alpha^6} + [4k+\frac{2\nu_1}{k_1}(k-\nu_1^2)-\nu_1(6k_1+8\nu_1) \\
& + (2k-2k_1\nu_1)(1+\delta)]\frac{\partial^6}{\partial\alpha^4\partial\beta^2} \\
& + \Big[(6k_1+2\nu_1)k \\
& + \Big(\frac{2k^2}{k_1}-\frac{2k\nu_1^2}{k_1}-4\nu_1k+2kk_1)(1+\delta)\Big]\frac{\partial^6}{\partial\alpha^2\partial\beta^4} \\
& + 2k^2(1+\delta)\frac{\partial^6}{\partial\beta^6} + [3k-3\nu_1^2+k(1+\delta)]\frac{\partial^4}{\partial\alpha^4} \\
& + \frac{k}{k_1}[3k_1^2+(k-\nu_1^2-2\nu_1k_1 \\
& + k_1^2)(1+\delta)]\frac{\partial^4}{\partial\alpha^2\partial\beta^2} + k^2(1+\delta)\frac{\partial^4}{\partial\beta^4}\Big\} \\
& + c^4\Big\{2\frac{\partial^8}{\partial\alpha^8} + \Big[9k_1+8\nu_1-\frac{1}{k_1}(k-\nu_1^2)+6k_1(1+\delta)\Big]\frac{\partial^8}{\partial\alpha^6\partial\beta^2} \\
& + [-\nu_1^2+(6k-6k_1\nu_1-2\nu_1^2)(1+\delta)]\frac{\partial^8}{\partial\alpha^4\partial\beta^4} \\
& + [(6kk_1+2\nu_1k)(1+\delta) \\
& + kk_1(1+\delta)^2]\frac{\partial^8}{\partial\alpha^2\partial\beta^6} + k^2(1+\delta)^2\frac{\partial^8}{\partial\beta^8} \\
& + 6\nu_1\frac{\partial^6}{\partial\alpha^6} + 6(k-k_1\nu_1)(1+\delta)\frac{\partial^6}{\partial\alpha^4\partial\beta^2} \\
& + [12kk_1+2k\nu_1+2kk_1(1+\delta)](1+\delta)\frac{\partial^6}{\partial\alpha^2\partial\beta^4} \\
& + 2k^2(1+\delta)^2\frac{\partial^6}{\partial\beta^6} + 3k(1+\delta)\frac{\partial^4}{\partial\alpha^4} \\
& + [(6kk_1+kk_1(1+\delta)](1+\delta)\frac{\partial^4}{\partial\alpha^2\partial\beta^2} + k^2(1+\delta)^2\frac{\partial^4}{\partial\beta^4}\Big\}\Big\}
\end{aligned}
$$

J. N. Reddy
Professor,
Department of Engineering
Science and Mechanics,
Virginia Polytechnic Institute
and State University,
Blacksburg, Va. 24061
Mem. ASME

A Simple Higher-Order Theory for Laminated Composite Plates

A higher-order shear deformation theory of laminated composite plates is developed. The theory contains the same dependent unknowns as in the first-order shear deformation theory of Whitney and Pagano [6], but accounts for parabolic distribution of the transverse shear strains through the thickness of the plate. Exact closed-form solutions of symmetric cross-ply laminates are obtained and the results are compared with three-dimensional elasticity solutions and first-order shear deformation theory solutions. The present theory predicts the deflections and stresses more accurately when compared to the first-order theory.

1 Introduction

The classical theory of plates, in which it is assumed that normals to the midplane before deformation remain straight and normal to the plane after deformation, underpredicts deflections and overpredicts natural frequencies and buckling loads. These results are due to the neglect of transverse shear strains in the classical theory. The errors in deflections, stresses, natural frequencies, and buckling loads are even higher for plates made of advanced composites like graphite-epoxy and boron-epoxy, whose elastic modulus to shear modulus ratios are very large (e.g., of the order of 25 to 40, instead of 2.6 for typical isotropic materials). These high ratios render classical theories inadequate for the analysis of composite plates. An adequate theory must account for transverse shear strains.

Many plate theories exist that account for transverse shear strains. Of these, the theories based on assumed displacement fields provide a background for the present theory [1-8]. In Reissner-Mindlin type-theories, the displacement field accounts for linear or higher-order variations of midplane displacements through thickness (see [1-8]). In higher-order theories, an additional dependent unknown is introduced into the theory with each additional power of the thickness coordinate. In addition, these shear deformation theories do not satisfy the conditions of zero transverse shear stresses on the top and bottom surfaces of the plate, and require a shear correction to the transverse shear stiffnesses. The three-dimensional theories of laminates, in which each layer is treated as homogeneous anisotropic medium (see Green and Naghdi [9], Rehfield and Valisetty [10], and Pagano and Soni [11]), are intractable as the number of layers becomes moderately large. Thus, a simple two-dimensional theory of plates that accurately describes the global behavior of laminated plates seems to be a compromise between accuracy and ease of analysis. The present study deals with such a theory.

The present theory accounts not only for transverse shear strains, but also for a parabolic variation of the transverse shear strains through thickness, and consequently, there is no need to use shear correction coefficients in computing the shear stresses. During the course of the development of the present theory, it was brought to the attention of the author [12] that Levinson [13] and Murthy [14] presented similar theories for isotropic and laminated plates, respectively. The displacement fields used by these two researchers are different from each other and therefore the final equations are different. Although the displacement fields used in the present theory and that of Levinson [13] are the same, the equations of motion differ from those of both Levinson and Murthy. Both Levinson and Murthy used the equilibrium equations of the first-order shear deformation theory (see Whitney and Pagano [6]). These equations are variationally inconsistent, for the displacement field used, with those derived from the principle of virtual displacements. These authors justify their approach merely because the variational approach is algebraically more complicated. Such justifications are not only unwarranted but they lead to technically wrong theories. The correct forms of differential equations and boundary conditions for any theory based on assumed displacement field are not known without using the virtual work principles.

The present development is novel in two respects: first a consistent derivation of the displacement field and associated equilibrium equations is presented. Second, the theory is developed for laminated anisotropic composite plates. To illustrate the accuracy of the present theory, exact solutions are also presented for symmetrically laminated cross-ply rectangular plates.

Kinematics

The present theory uses a displacement approach, much like in the Reissner-Mindlin type theories. However, the

Contributed by the Applied Mechanics Division and presented at the Winter Annual Meeting, New Orleans, La., December 9-14, 1984 of THE AMERICAN SOCIETY OF MECHANICAL ENGINEERS.

Discussion on this paper should be addressed to the Editorial Department, ASME, United Engineering Center, 345 East 47th Street, New York, N.Y. 10017, and will be accepted until two months after final publication of the paper itself in the JOURNAL OF APPLIED MECHANICS. Manuscript received by ASME Applied Mechanics Division, July 1983; final revision, April, 1984. Paper No. 84-WA/APM-34.

Copies will be available until August, 1985.

displacement field chosen is of a special form. The form is dictated by the satisfaction of the conditions that the transverse shear stresses vanish on the plate surfaces and be nonzero elsewhere. This requires the use of a displacement field in which the inplane displacements are expanded as cubic functions of the thickness coordinate and the transverse deflection is constant through plate thickness. Any other choice would either not satisfy the stress-free boundary conditions or lead to a theory that would involve more dependent unknowns than those in the first-order shear deformation theory. Since the transverse normal stress is of the order $(h/a)^2$ times the inplane normal stresses, the assumption that w is not a function of the thickness coordinate is justified.

We begin with the displacement field,

$$\begin{aligned} u_1(x,y,z) &= u(x,y)+z\psi_x(x,y)+z^2\xi_x(x,y)+z^3\zeta_x(x,y) \\ u_2(x,y,z) &= v(x,y)+z\psi_y(x,y)+z^2\xi_y(x,y)+z^3\zeta_y(x,y) \\ & u_3(x,y)=w(x,y) \end{aligned} \tag{1}$$

where u,v, and w denote the displacements of a point (x,y) on the midplane, and ψ_x and ψ_y are the rotations of normals to midplane about the y and x axes, respectively. The functions ξ_x, ζ_x, ξ_y, and ζ_y will be determined using the condition that the transverse shear stresses, $\sigma_{xz}=\sigma_5$ and $\sigma_{yz}=\sigma_4$ vanish on the plate top and bottom surfaces.

$$\sigma_5\left(x,y,\pm\frac{h}{2}\right)=0, \quad \sigma_4\left(x,y,\pm\frac{h}{2}\right)=0 \tag{2}$$

For orthotropic plates or plates laminated of orthotropic layers, these conditions are equivalent to the requirement that the corresponding strains be zero on these surfaces. We have

$$\begin{aligned} \epsilon_5 &= \frac{\partial u_1}{\partial z}+\frac{\partial u_3}{\partial x}=\psi_x+2z\xi_x+3z^2\zeta_x+\frac{\partial w}{\partial x} \\ \epsilon_4 &= \frac{\partial u_2}{\partial z}+\frac{\partial u_3}{\partial y}=\psi_y+2z\xi_y+3z^2\zeta_y+\frac{\partial w}{\partial y} \end{aligned} \tag{3}$$

Setting $\epsilon_5(x,y,\pm h/2)$ and $\epsilon_4(x,y,\pm h/2)$ to zero, we obtain

$$\xi_x=0, \quad \xi_y=0$$

$$\zeta_x=-\frac{4}{3h^2}\left(\frac{\partial w}{\partial x}+\psi_x\right), \quad \zeta_y=-\frac{4}{3h^2}\left(\frac{\partial w}{\partial y}+\psi_y\right) \tag{4}$$

The displacement field in equation (1) becomes

$$\begin{aligned} u_1 &= u+z\left[\psi_x-\frac{4}{3}\left(\frac{z}{h}\right)^2\left(\psi_x+\frac{\partial w}{\partial x}\right)\right] \\ u_2 &= v+z\left[\psi_y-\frac{4}{3}\left(\frac{z}{h}\right)^2\left(\psi_y+\frac{\partial w}{\partial y}\right)\right] \\ & u_3=w \end{aligned} \tag{5}$$

This displacement field is the same as that chosen by Levinson [13] (the inplane displacements were not considered by Levinson), but is different from that derived by Murthy [14]. Except for the similarity between the form of the displacement field in equation (5) and that of Levinson [13] and Murthy [14], the remaining development, especially the derivation of the equilibrium equations for laminated plates, is novel with the present study.

The strains associated with the displacements in equation (1) are

$$\begin{aligned} \epsilon_1 &= \epsilon_1^0+z(\kappa_1^0+z^2\kappa_1^2) \\ \epsilon_2 &= \epsilon_2^0+z(\kappa_2^0+z^2\kappa_2^2) \\ \epsilon_3 &= 0 \\ \epsilon_4 &= \epsilon_4^0+z^2\kappa_4^2 \\ \epsilon_5 &= \epsilon_5^0+z^2\kappa_5^2 \\ \epsilon_6 &= \epsilon_6^0+z(\kappa_6^0+z^2\kappa_6^2) \end{aligned} \tag{6}$$

where

$$\begin{aligned} \epsilon_1^0 &= \frac{\partial u_0}{\partial x}, \quad \kappa_1^0=\frac{\partial \psi_x}{\partial x}, \quad \kappa_1^2=-\frac{4}{3h^2}\left(\frac{\partial \psi_x}{\partial x}+\frac{\partial^2 w}{\partial x^2}\right) \\ \epsilon_2^0 &= \frac{\partial u_0}{\partial y}, \quad \kappa_2^0=\frac{\partial \psi_y}{\partial y}, \quad \kappa_2^2=-\frac{4}{3h^2}\left(\frac{\partial \psi_y}{\partial y}+\frac{\partial^2 w}{\partial y^2}\right) \\ \epsilon_4^0 &= \psi_y+\frac{\partial w}{\partial y}, \quad \kappa_4^2=-\frac{4}{h^2}\left(\psi_y+\frac{\partial w}{\partial y}\right) \\ \epsilon_5^0 &= \psi_x+\frac{\partial w}{\partial x}, \quad \kappa_5^2=-\frac{4}{h^2}\left(\psi_x+\frac{\partial w}{\partial x}\right) \\ \epsilon_6^0 &= \frac{\partial u_0}{\partial y}+\frac{\partial v_0}{\partial x}, \quad \kappa_6^0=\frac{\partial \psi_x}{\partial y}+\frac{\partial \psi_y}{\partial x}, \\ \kappa_6^2 &= -\frac{4}{3h^2}\left(\frac{\partial \psi_x}{\partial y}+\frac{\partial \psi_y}{\partial x}+2\frac{\partial^2 w}{\partial x \partial y}\right) \end{aligned} \tag{7}$$

Constitutive Equations

For a plate of constant thickness h and composed of thin layers of orthotropic material, the constitutive equations can be derived as discussed in [6]. Under the assumption that each layer possesses a plane of elastic symmetry parallel to the x-y plane, the constitutive equations for a layer can be written as

$$\begin{Bmatrix} \bar\sigma_1 \\ \bar\sigma_2 \\ \bar\sigma_6 \end{Bmatrix} = \begin{bmatrix} \bar Q_{11} & \bar Q_{12} & 0 \\ \bar Q_{12} & \bar Q_{22} & 0 \\ 0 & 0 & \bar Q_{66} \end{bmatrix} \begin{Bmatrix} \bar\epsilon_1 \\ \bar\epsilon_2 \\ \bar\epsilon_6 \end{Bmatrix},$$

$$\begin{Bmatrix} \bar\sigma_4 \\ \bar\sigma_5 \end{Bmatrix} = \begin{bmatrix} \bar Q_{44} & 0 \\ 0 & \bar Q_{55} \end{bmatrix} \begin{Bmatrix} \bar\epsilon_4 \\ \bar\epsilon_5 \end{Bmatrix} \tag{8}$$

where $\bar Q_{ij}$ are the plane-stress-reduced elastic constants in the material axes of the layer, and the bar over the quantities implies that the quantities are referred to the material axes of the layer. Upon transformation, the lamina constitutive equations can be expressed in terms of stresses and strains in the plate (laminate) coordinates as

$$\begin{Bmatrix} \sigma_1 \\ \sigma_2 \\ \sigma_6 \end{Bmatrix} = \begin{bmatrix} Q_{11} & Q_{12} & Q_{16} \\ Q_{12} & Q_{22} & Q_{26} \\ Q_{16} & Q_{26} & Q_{66} \end{bmatrix} \begin{Bmatrix} \epsilon_1 \\ \epsilon_2 \\ \epsilon_6 \end{Bmatrix}$$

$$\begin{Bmatrix} \sigma_4 \\ \sigma_5 \end{Bmatrix} = \begin{bmatrix} Q_{44} & Q_{45} \\ Q_{45} & Q_{55} \end{bmatrix} \begin{Bmatrix} \epsilon_4 \\ \epsilon_5 \end{Bmatrix} \tag{9}$$

where Q_{ij} are the transformed material constants.

Equilibrium Equations

Here we use the principle of virtual displacements to derive the equilibrium equations appropriate for the displacement field in equation (1) and constitutive equations in equation (9). The principle of virtual displacements can be stated in analytical form as (see Reddy [15])

$$0 = \int_{-h/2}^{h/2}\int_\Omega (\sigma_1\delta\epsilon_1+\sigma_2\delta\epsilon_2+\sigma_6\delta\epsilon_6+\sigma_4\delta\epsilon_4+\sigma_5\delta\epsilon_5)dAdz$$

$$+\int_\Omega q\delta w\,dxdy$$

$$= \int_\Omega \Big\{ N_1 \frac{\partial \delta u_0}{\partial x} + M_1 \frac{\partial \delta \psi_x}{\partial x} + P_1 \Big[-\frac{4}{3h^2}\Big(\frac{\partial \delta\psi_x}{\partial x} + \frac{\partial^2 \delta w}{\partial x^2}\Big)\Big]$$

$$+ N_2 \frac{\partial \delta v_0}{\partial y} + M_2 \frac{\partial \delta \psi_y}{\partial y} + P_2 \Big[-\frac{4}{3h^2}\Big(\frac{\partial \delta\psi_y}{\partial y} + \frac{\partial^2 \delta w}{\partial y^2}\Big)\Big]$$

$$+ N_6 \Big(\frac{\partial \delta u_0}{\partial y} + \frac{\partial \delta v_0}{\partial x}\Big) + M_6 \Big(\frac{\partial \delta\psi_x}{\partial y} + \frac{\partial \delta \psi_y}{\partial x}\Big)$$

$$+ P_6 \Big[-\frac{4}{3h^2}\Big(\frac{\partial \delta\psi_x}{\partial y} + \frac{\partial \delta\psi_y}{\partial x} + 2\frac{\partial^2 \delta w}{\partial x \partial y}\Big)\Big]$$

$$+ Q_2 \Big(\delta\psi_y + \frac{\partial \delta_w}{\partial y}\Big) + R_2 \Big[-\frac{4}{h^2}\Big(\delta\psi_y + \frac{\partial \delta w}{\partial y}\Big)\Big]$$

$$+ Q_1 \Big(\delta\psi_x + \frac{\partial \delta w}{\partial x}\Big) + R_1 \Big[-\frac{4}{h^2}\Big(\delta\psi_x + \frac{\partial \delta w}{\partial x}\Big)\Big] q\delta w \Big\} dxdy \quad (10)$$

where in arriving at the second step, we used the strains from equations (6) and (7), and the following definitions of the stress resultants N_i, M_i, P_i, Q_i and R_i:

$$(N_i, M_i, P_i) = \int_{-h/2}^{h/2} \sigma_i (1, z, z^3) dz \quad (i = 1,2,6)$$

$$(Q_2, R_2) = \int_{-h/2}^{h/2} \sigma_4 (1, z^2) dz$$

$$(Q_1, R_1) = \int_{-h/2}^{h/2} \sigma_5 (1, z^2) dz \quad (11)$$

Integrating the expressions in equation (10) by parts, and collecting the coefficients of δu, δv, δw, $\delta\psi_x$, and $\delta\psi_y$, we obtain the following equilibrium equations in the domain Ω:

$$\delta u: \quad \frac{\partial N_1}{\partial x} + \frac{\partial N_6}{\partial y} = 0$$

$$\delta v: \quad \frac{\partial N_6}{\partial x} + \frac{\partial N_2}{\partial y} = 0$$

$$\delta w: \quad \frac{\partial Q_1}{\partial x} + \frac{\partial Q_2}{\partial y} + q - \underline{\frac{4}{h^2}\Big(\frac{\partial R_1}{\partial x} + \frac{\partial R_2}{\partial y}\Big)}$$

$$+ \underline{\frac{4}{3h^2}\Big(\frac{\partial^2 P_1}{\partial x^2} + 2\frac{\partial^2 P_6}{\partial x \partial y} + \frac{\partial^2 P_2}{\partial y^2}\Big)} = 0 \quad (12)$$

$$\delta\psi_x: \quad \frac{\partial M_1}{\partial x} + \frac{\partial M_6}{\partial y} - Q_1 + \underline{\frac{4}{h^2} R_1}$$

$$- \underline{\frac{4}{3h^2}\Big(\frac{\partial P_1}{\partial x} + \frac{\partial P_6}{\partial y}\Big)} = 0$$

$$\delta\psi_y: \quad \frac{\partial M_6}{\partial x} + \frac{\partial M_2}{\partial y} - Q_2 + \underline{\frac{4}{h^2} R_2}$$

$$- \underline{\frac{4}{3h^2}\Big(\frac{\partial P_6}{\partial x} + \frac{\partial P_2}{\partial y}\Big)} = 0$$

The boundary conditions are of the form: specify

$$\left.\begin{array}{r} u_n \text{ or } N_n \\ u_{ns} \text{ or } N_{ns} \\ w \text{ or } Q_n \\ \dfrac{\partial w}{\partial n} \text{ or } P_n \\ \psi_n \text{ or } M_n \\ \psi_{ns} \text{ or } M_{ns} \end{array}\right\} \quad (13)$$

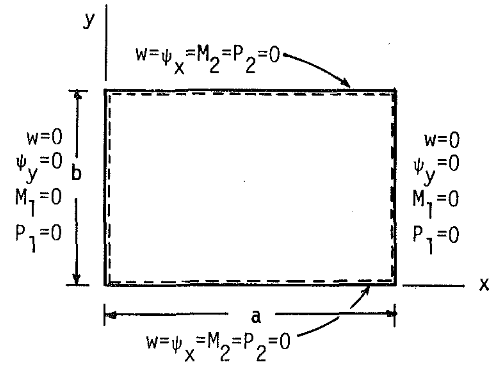

Fig. 1 Geometry of a rectangular plate

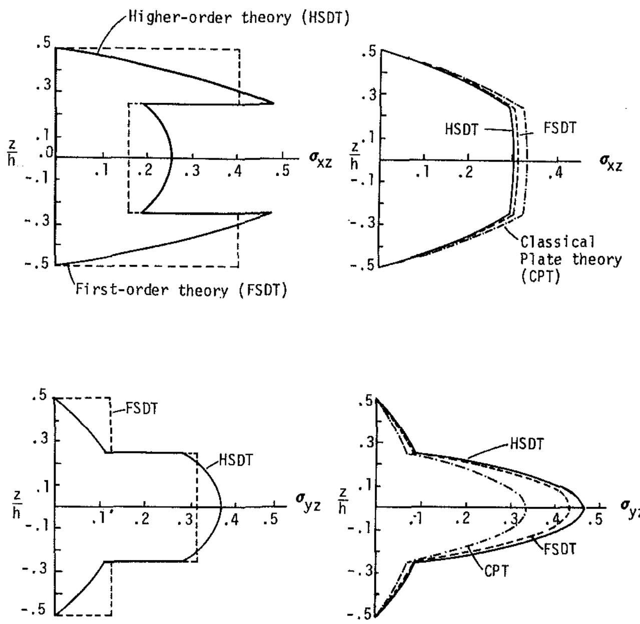

(a) From constitutive equations (b) From equilibrium equations

Fig. 2 The distribution of transverse shear stresses through the thickness of four-layer cross-ply [0/90/90/0 deg] laminate under sinusoidal load (a/b = 1; a/h = 10)

where Γ is the boundary of the plate midplane Ω, and

$$u_n = u n_x + v n_y, \quad u_{ns} = -u n_y + v n_x$$

$$N_n = N_1 n_x^2 + N_2 n_y^2 + 2N_6 n_x n_y$$

$$N_{ns} = (N_2 - N_1) n_x n_y + N_6 (n_x^2 - n_y^2)$$

$$M_n = \hat{M}_i n_x^2 + \hat{M}_2 n_y^2 + 2\hat{M}_6 n_x n_y$$

$$M_{ns} = (\hat{M}_2 - \hat{M}_1) n_x n_y + \hat{M}_6 (n_x^2 - n_y^2)$$

$$Q_n = \hat{Q}_1 n_x + \hat{Q}_2 n_y - \frac{4}{3h^2}\frac{\partial P_{ns}}{\partial s} \quad (14)$$

$$\hat{M}_i = M_i - \frac{4}{3h^2} P_i \quad (i = 1,2,6)$$

$$\hat{Q}_i = Q_i - \frac{4}{h^2} R_i \quad (i = 1,2)$$

$$\frac{\partial}{\partial n} = n_x \frac{\partial}{\partial x} + n_y \frac{\partial}{\partial s}, \quad \frac{\partial}{\partial s} = n_x \frac{\partial}{\partial y} - n_y \frac{\partial}{\partial x}$$

and P_n and P_{ns} are defined by expressions analogous to N_n and N_{ns}, respectively.

It is informative to relate the resultants defined in equation (11) to the total strains in equation (6). From equations (6), (9), and (11) we obtain

$$
\begin{Bmatrix} \begin{Bmatrix} N_1 \\ N_2 \\ N_6 \end{Bmatrix} \\ \begin{Bmatrix} M_1 \\ M_2 \\ M_6 \end{Bmatrix} \\ \begin{Bmatrix} P_1 \\ P_2 \\ P_6 \end{Bmatrix} \end{Bmatrix} = \begin{bmatrix} \begin{bmatrix} A_{11} & A_{12} & A_{16} \\ & A_{22} & A_{26} \\ \text{sym.} & & A_{66} \end{bmatrix} & \begin{bmatrix} B_{11} & B_{12} & B_{16} \\ & B_{22} & B_{26} \\ \text{sym.} & & B_{66} \end{bmatrix} & \begin{bmatrix} E_{11} & E_{12} & E_{16} \\ & E_{22} & E_{26} \\ \text{sym.} & & E_{66} \end{bmatrix} \\ & \begin{bmatrix} D_{11} & D_{12} & D_{16} \\ & D_{22} & D_{26} \\ \text{sym.} & & D_{66} \end{bmatrix} & \begin{bmatrix} F_{11} & F_{12} & F_{16} \\ & F_{22} & F_{26} \\ \text{sym.} & & F_{66} \end{bmatrix} \\ \text{symmetric} & & \begin{bmatrix} H_{11} & H_{12} & H_{16} \\ & H_{22} & H_{26} \\ \text{sym.} & & H_{66} \end{bmatrix} \end{bmatrix} \begin{Bmatrix} \begin{Bmatrix} \epsilon_1^0 \\ \epsilon_2^0 \\ \epsilon_6^0 \end{Bmatrix} \\ \begin{Bmatrix} \kappa_1^0 \\ \kappa_2^0 \\ \kappa_6^0 \end{Bmatrix} \\ \begin{Bmatrix} \kappa_1^2 \\ \kappa_2^2 \\ \kappa_6^2 \end{Bmatrix} \end{Bmatrix} \tag{15a}
$$

$$
\begin{Bmatrix} Q_2 \\ Q_1 \\ R_2 \\ R_1 \end{Bmatrix} = \begin{bmatrix} A_{44} & A_{45} & D_{44} & D_{45} \\ & A_{55} & D_{45} & D_{55} \\ & & F_{44} & F_{45} \\ \text{sym.} & & & F_{55} \end{bmatrix} \begin{Bmatrix} \epsilon_4^0 \\ \epsilon_5^0 \\ \kappa_4^2 \\ \kappa_5^2 \end{Bmatrix} \tag{15b}
$$

where A_{ij}, B_{ij}, etc., are the plate stiffnesses, defined by

$$
(A_{ij},B_{ij},D_{ij},E_{ij},F_{ij},H_{ij}) = \int_{-h/2}^{h/2} Q_{ij}(1,z,z^2,z^3,z^4,z^6)dz \quad (i,\ j=1,2,6)
$$

$$
(A_{ij},D_{ij},F_{ij}) = \int_{-h/2}^{h/2} Q_{ij}(1,z^2,z^4)dz \quad (i,\ j=4,5) \tag{16}
$$

This completes the derivation of the governing equations. It should be noted that Levinson [13] and Murthy [14] did not account for the underlined terms in equations (12).

Exact Solutions for Symmetric Cross-Ply Plates

Here we consider the exact solutions of equations (12) and (13) for simply supported, symmetric cross-ply rectangular plates. The Navier approach is used (see [15]). For symmetric (about the midplane) cross-ply plates, the following plate stiffnesses are identically zero:

$$
\begin{gathered}
B_{ij} = E_{ij} = 0 \quad \text{for} \quad i,\ j=1,2,4,5,6 \\
A_{16} = A_{26} = D_{16} = D_{26} = F_{16} = F_{26} = H_{16} = H_{26} = 0 \\
A_{45} = D_{45} = F_{45} = 0.
\end{gathered} \tag{17}
$$

Thus, the coupling between stretching and bending is zero. The following "simply-supported" boundary conditions are assumed (a and b are the plane-form dimensions of the plate; see Fig. 1):

$$
\begin{aligned}
&w(x,0) = w(x,b) = w(0,y) = w(a,y) = 0 \\
&P_2(x,0) = P_2(x,b) = P_1(0,y) = P_1(a,y) = 0 \\
&M_2(x,0) = M_2(x,b) = M_1(0,y) = M_1(a,y) = 0 \\
&\psi_x(x,0) = \psi_x(x,b) = \psi_y(0,y) = \psi_y(a,y) = 0
\end{aligned} \tag{18}
$$

The resultants of equation (15) can be expressed, for symmetric cross-ply laminates, in terms of the generalized displacements as

$$
N_1 = A_{11}\frac{\partial u}{\partial x} + A_{12}\frac{\partial v}{\partial y}
$$

$$
N_2 = A_{12}\frac{\partial u}{\partial x} + A_{22}\frac{\partial v}{\partial y}
$$

$$
N_6 = A_{66}\left(\frac{\partial u}{\partial y} + \frac{\partial v}{\partial x}\right)
$$

$$
\begin{aligned}
M_1 = {} & D_{11}\frac{\partial \psi_x}{\partial x} + D_{12}\frac{\partial \psi_y}{\partial y} + F_{11}\left(-\frac{4}{3h^2}\right)\left(\frac{\partial \psi_x}{\partial x} + \frac{\partial^2 w}{\partial x^2}\right) \\
& + F_{12}\left(-\frac{4}{3h^2}\right)\left(\frac{\partial \psi_y}{\partial y} + \frac{\partial^2 w}{\partial y^2}\right)
\end{aligned}
$$

$$
\begin{aligned}
M_2 = {} & D_{12}\frac{\partial \psi_x}{\partial x} + D_{22}\frac{\partial \psi_y}{\partial y} + F_{12}\left(-\frac{4}{3h^2}\right)\left(\frac{\partial \psi_x}{\partial x} + \frac{\partial^2 w}{\partial x^2}\right) \\
& + F_{22}\left(-\frac{4}{3h^2}\right)\left(\frac{\partial \psi_y}{\partial y} + \frac{\partial^2 w}{\partial y^2}\right)
\end{aligned}
$$

$$
M_6 = D_{66}\left(\frac{\partial \psi_x}{\partial y} + \frac{\partial \psi_y}{\partial x}\right) + F_{66}\left(-\frac{4}{3h^2}\right)\left(\frac{\partial \psi_x}{\partial y} + \frac{\partial \psi_y}{\partial x} + 2\frac{\partial^2 w}{\partial x \partial y}\right)
$$

$$
Q_2 = A_{44}\left(\psi_y + \frac{\partial w}{\partial y}\right) + D_{44}\left(-\frac{4}{h^2}\right)\left(\psi_y + \frac{\partial w}{\partial y}\right)
$$

$$
Q_1 = A_{55}\left(\psi_x + \frac{\partial w}{\partial x}\right) + D_{55}\left(-\frac{4}{h^2}\right)\left(\psi_x + \frac{\partial w}{\partial x}\right)
$$

$$
\begin{aligned}
P_1 = {} & F_{11}\frac{\partial \psi_x}{\partial x} + H_{11}\left(-\frac{4}{3h^2}\right)\left(\frac{\partial \psi_x}{\partial x} + \frac{\partial^2 w}{\partial x^2}\right) \\
& + F_{12}\frac{\partial \psi_y}{\partial y} + H_{12}\left(-\frac{4}{3h^2}\right)\left(\frac{\partial \psi_y}{\partial y} + \frac{\partial^2 w}{\partial y^2}\right)
\end{aligned}
$$

$$
\begin{aligned}
P_2 = {} & F_{12}\frac{\partial \psi_x}{\partial x} + H_{12}\left(-\frac{4}{3h^2}\right)\left(\frac{\partial \psi_x}{\partial x} + \frac{\partial^2 w}{\partial x^2}\right) \\
& + F_{22}\frac{\partial \psi_y}{\partial y} + H_{22}\left(-\frac{4}{3h^2}\right)\left(\frac{\partial \psi_y}{\partial y} + \frac{\partial^2 w}{\partial y^2}\right)
\end{aligned}
$$

$$
\begin{aligned}
P_6 = {} & F_{66}\left(\frac{\partial \psi_y}{\partial x} + \frac{\partial \psi_x}{\partial y}\right) + \left(-\frac{4}{3h^2}\right)H_{66}\left(\frac{\partial \psi_x}{\partial y}\right. \\
& \left. + \frac{\partial \psi_y}{\partial x} + 2\frac{\partial^2 w}{\partial x \partial y}\right)
\end{aligned}
$$

$$
R_2 = D_{44}\left(\frac{\partial w}{\partial y} + \psi_y\right) + F_{44}\left(-\frac{4}{h^2}\right)\left(\psi_y + \frac{\partial w}{\partial y}\right)
$$

$$R_1 = D_{55}\left(\frac{\partial w}{\partial x}+\psi_x\right)+F_{55}\left(-\frac{4}{h^2}\right)\left(\psi_x+\frac{\partial w}{\partial x}\right) \tag{19}$$

Following the Navier solution procedure, we assume the following solution form for (w,ψ_x,ψ_y) that satisfies the boundary conditions,

$$\begin{aligned} w &= \sum_{m,n=1}^{\infty} W_{mn}\sin\alpha x\,\sin\beta y \\ \psi_x &= \sum_{m,n=1}^{\infty} X_{mn}\cos\alpha x\,\sin\beta y \\ \psi_y &= \sum_{m,n=1}^{\infty} Y_{mn}\sin\alpha x\,\cos\beta y \end{aligned} \tag{20}$$

where $\alpha = m\pi/a$ and $\beta = n\pi/b$. The last three equations in equation (12) can be expressed in terms of the displacements as

$$\begin{aligned} &\frac{4}{3h^2}\Bigg[F_{11}\frac{\partial^3\psi_x}{\partial x^3}+H_{11}\left(-\frac{4}{3h^2}\right)\left(\frac{\partial^3\psi_x}{\partial x^3}+\frac{\partial^4 w}{\partial x^4}\right)+F_{12}\frac{\partial^3\psi_y}{\partial x^2\partial y} \\ &+H_{12}\left(-\frac{4}{3h^2}\right)\left(\frac{\partial^3\psi_y}{\partial x^2\partial y}+\frac{\partial^4 w}{\partial x^2\partial y^2}\right)+F_{12}\frac{\partial^3\psi_x}{\partial y^2\partial x} \\ &+H_{12}\left(-\frac{4}{3h^2}\right)\left(\frac{\partial^3\psi_x}{\partial y^2\partial x}+\frac{\partial^4 w}{\partial x^2\partial y^2}\right)+F_{22}\frac{\partial^3\psi_y}{\partial y^3} \\ &+H_{22}\left(-\frac{4}{3h^2}\right)\left(\frac{\partial^3\psi_y}{\partial y^3}+\frac{\partial^4 w}{\partial y^4}\right) \\ &+2F_{66}\left(\frac{\partial^3\psi_y}{\partial x^2\partial y}+\frac{\partial^3\psi_x}{\partial y^2\partial x}\right) \\ &+2H_{66}\left(-\frac{4}{3h^2}\right)\left(\frac{\partial^3\psi_x}{\partial y^2\partial x}+\frac{\partial^3\psi_y}{\partial x^2\partial y}+2\frac{\partial^4 w}{\partial x^2\partial y^2}\right)\Bigg] \\ &-\frac{4}{h^2}\Bigg[D_{55}\left(\frac{\partial^2 w}{\partial x^2}+\frac{\partial\psi_x}{\partial x}\right)+F_{55}\left(-\frac{4}{h^2}\right)\left(\frac{\partial\psi_x}{\partial x}+\frac{\partial^2 w}{\partial x^2}\right) \\ &+D_{44}\left(\frac{\partial^2 w}{\partial y^2}+\frac{\partial\psi_y}{\partial y}\right)+F_{44}\left(-\frac{4}{h^2}\right)\left(\frac{\partial\psi_y}{\partial y}+\frac{\partial^2 w}{\partial y^2}\right)\Bigg] \\ &+\Bigg[A_{55}\left(\frac{\partial\psi_x}{\partial x}+\frac{\partial^2 w}{\partial x^2}\right)+D_{55}\left(-\frac{4}{h^2}\right)\left(\frac{\partial\psi_x}{\partial x}+\frac{\partial^2 w}{\partial x^2}\right) \\ &+A_{44}\left(\frac{\partial\psi_y}{\partial y}+\frac{\partial^2 w}{\partial y^2}\right)+D_{44}\left(-\frac{4}{h^2}\right)\left(\frac{\partial\psi_y}{\partial y}+\frac{\partial^2 w}{\partial y^2}\right)\Bigg]+q=0 \end{aligned} \tag{21a}$$

$$\begin{aligned} &D_{11}\frac{\partial^2\psi_x}{\partial x^2}+D_{12}\frac{\partial^2\psi_y}{\partial x\partial y}+F_{11}\left(-\frac{4}{3h^2}\right)\left(\frac{\partial^2\psi_x}{\partial x^2}+\frac{\partial^3 w}{\partial x^3}\right) \\ &+F_{12}\left(-\frac{4}{3h^2}\right)\left(\frac{\partial^2\psi_y}{\partial x\partial y}+\frac{\partial^3 w}{\partial x\partial y^2}\right)+D_{66}\left(\frac{\partial^2\psi_x}{\partial y^2}+\frac{\partial^2\psi_y}{\partial x\partial y}\right) \\ &+F_{66}\left(-\frac{4}{3h^2}\right)\left(\frac{\partial^2\psi_x}{\partial y^2}+\frac{\partial^2\psi_y}{\partial x\partial y}+2\frac{\partial^3 w}{\partial x\partial y}\right) \\ &-\Bigg[A_{55}\left(\psi_x+\frac{\partial w}{\partial x}\right)+D_{55}\left(-\frac{4}{h^2}\right)\left(\psi_x+\frac{\partial w}{\partial x}\right)\Bigg] \\ &-\frac{4}{3h^2}\Bigg[F_{11}\frac{\partial^2\psi_x}{\partial x^2}+H_{11}\left(-\frac{4}{3h^2}\right)\left(\frac{\partial^2\psi_x}{\partial x^2}+\frac{\partial^3 w}{\partial x^3}\right) \\ &+F_{12}\frac{\partial^2\psi_y}{\partial x\partial y} \\ &+H_{12}\left(-\frac{4}{3h^2}\right)\left(\frac{\partial^2\psi_y}{\partial x\partial y}+\frac{\partial^3 w}{\partial x\partial y^2}\right)+F_{66}\left(\frac{\partial^2\psi_y}{\partial x\partial y}+\frac{\partial^2\psi_x}{\partial y^2}\right) \\ &+H_{66}\left(-\frac{4}{3h^2}\right)\left(\frac{\partial^2\psi_x}{\partial y^2}+\frac{\partial^2\psi_y}{\partial x\partial y}+2\frac{\partial^3 w}{\partial x\partial y^2}\right)\Bigg] \\ &+\frac{4}{h^2}\Bigg[D_{55}\left(\frac{\partial w}{\partial x}+\psi_x\right)+F_{55}\left(-\frac{4}{h^2}\right)\left(\psi_x+\frac{\partial w}{\partial x}\right)\Bigg]=0 \end{aligned} \tag{21b}$$

$$\begin{aligned} &D_{66}\left(\frac{\partial^2\psi_x}{\partial x\partial y}+\frac{\partial^2\psi_y}{\partial x^2}\right)+F_{66}\left(-\frac{4}{3h^2}\right)\left(\frac{\partial^2\psi_x}{\partial x\partial y}\right. \\ &\left.+\frac{\partial^2\psi_y}{\partial x^2}+2\frac{\partial^3 w}{\partial x^2\partial y}\right) \\ &+D_{12}\frac{\partial^2\psi_x}{\partial x\partial y}+D_{22}\frac{\partial^2\psi_y}{\partial y^2}+F_{12}\left(-\frac{4}{3h^2}\right)\left(\frac{\partial^2\psi_x}{\partial x\partial y}+\frac{\partial^3 w}{\partial x^2\partial y}\right) \\ &+F_{22}\left(-\frac{4}{3h^2}\right)\left(\frac{\partial^2\psi_y}{\partial y^2}+\frac{\partial^3 w}{\partial y^3}\right)-\Bigg[A_{44}\left(\psi_y+\frac{\partial w}{\partial y}\right) \\ &+D_{44}\left(-\frac{4}{h^2}\right)\left(\psi_y+\frac{\partial w}{\partial y}\right)\Bigg] \\ &-\frac{4}{3h^2}\Bigg[F_{66}\left(\frac{\partial^2\psi_y}{\partial x^2}+\frac{\partial^2\psi_x}{\partial y\partial x}\right)+H_{66}\left(\frac{\partial^2\psi_x}{\partial x\partial y}\right. \\ &\left.+\frac{\partial^2\psi_y}{\partial x^2}+2\frac{\partial^3 w}{\partial x^2\partial y}\right)\left(-\frac{4}{3h^2}\right) \\ &+F_{12}\frac{\partial^2\psi_x}{\partial x\partial y}+H_{12}\left(-\frac{4}{3h^2}\right)\left(\frac{\psi_x}{\partial x\partial y}+\frac{\partial^3 w}{\partial x^2\partial y}\right) \\ &+F_{22}\frac{\partial^2\psi_y}{\partial y^2}+H_{22}\left(-\frac{4}{3h^2}\right)\left(\frac{\partial^2\psi_y}{\partial y^2}+\frac{\partial^3 w}{\partial y^3}\right)\Bigg] \\ &+\frac{4}{h^2}\Bigg[D_{44}\left(\frac{\partial w}{\partial y}+\psi_y\right)+F_{44}\left(-\frac{4}{h^2}\right)\left(\frac{\partial w}{\partial y}+\psi_y\right)\Bigg]=0 \end{aligned} \tag{21c}$$

We assume that the applied transverse load, q, can be expanded in the double-Fourier series as

$$q=\sum_{m,n=1}^{\infty} Q_{mn}\sin\alpha x\,\sin\beta y \tag{22}$$

Substituting equations (19) and (21) into equation (20), collecting the coefficients, we obtain

$$\begin{bmatrix} c_{11} & c_{12} & c_{13} \\ c_{12} & c_{22} & c_{23} \\ c_{13} & c_{23} & c_{33} \end{bmatrix} \begin{Bmatrix} W_{mn} \\ X_{mn} \\ Y_{mn} \end{Bmatrix} = \begin{Bmatrix} Q_{mn} \\ 0 \\ 0 \end{Bmatrix} \tag{23}$$

for any fixed values of m and n. The elements c_{ij} of the coefficient matrix $[c]$ are given by

$$\begin{aligned} c_{11} &= \alpha^2 A_{55}+\beta^2 A_{44}-\frac{8}{h^2}(\alpha^2 D_{55}+\beta^2 D_{44}) \\ &+\left(\frac{4}{h^2}\right)^2(\alpha^2 F_{55}+\beta^2 F_{44})+\left(\frac{4}{3h^2}\right)^2 \\ &[\alpha^4 H_{11}+2(H_{12}+2H_{66})\alpha^2\beta^2+\beta^4 H_{22}] \\ c_{12} &= \alpha A_{55}-\frac{8}{h^2}\alpha D_{55}+\left(\frac{4}{h^2}\right)^2\alpha F_{55} \\ &-\frac{4}{3h^2}[\alpha^3 F_{11}+\alpha\beta^2(F_{12}+2F_{66})] \end{aligned}$$

Table 1 **Nondimensionalized[a] deflections and stresses in three-layer (0/90/0 deg) square laminates under sinusoidal loads**

a/h	variable	three-dimensional elasticity theory [16]	Present theory	First-order shear deformation theory [18]			
				$k_1^2=k_2^2=1$	$k_1^2=k_2^2=\frac{5}{6}$	$k_1^2=k_2^2=\frac{3}{4}$	$k_1^2=k_2^2=\frac{1}{2}$
	w	–	1.9218	1.5681	1.7763	1.9122	2.5769
4	σ_1	0.755	0.7345	0.4475	0.4369	0.4308	0.4065
	σ_4	0.217	0.1832	0.1227	0.1562	0.1793	0.3030
	w	–	0.7125	0.6306	0.6693	0.6949	0.8210
10	σ_1	0.590	0.5684	0.5172	0.5134	0.5109	0.4993
	σ_4	0.123	0.1033	0.0735	0.0915	0.1039	0.1723
	w	–	0.4342	0.4333	0.4337	0.4340	0.4353
100	σ_1	0.552	0.5390	0.5385	0.5384	0.5384	0.5382
	σ_4	0.0938	0.0750	0.0586	0.0703	0.0782	0.0117

[a] $\bar{w}=\left(\frac{wh^3E_2}{q_0a^4}\right)10,\ w=w\left(\frac{a}{2},\frac{b}{2}\right)$

$$\bar{\sigma}_1=\sigma\left(\frac{a}{2},\frac{b}{2},\frac{h}{2}\right)\frac{h^2}{q_0a^2},\ \bar{\sigma}_2=\sigma_2\left(\frac{a}{2},\frac{b}{2},\frac{h}{6}\right)\frac{h^2}{q_0a^2}$$

$$\bar{\sigma}_4=\sigma_4\left(\frac{a}{2},0,0\right)\frac{h}{q_0a},\ \bar{\sigma}_5=\sigma_5\left(0,\frac{b}{2},0\right)\frac{h}{q_0a}$$

$$\bar{\sigma}_6=\sigma_6\left(0,0,\frac{h}{2}\right)\frac{h^2}{q_0a^2}$$

Table 2 **Nondimensionalized[a] deflections and stresses in a rectangular, cross-ply laminate under sinusoidal load ($h_i=h/3$)**

a/h	Source	$\bar{w}$	$\bar{\sigma}_1$	$\bar{\sigma}_2$	$\bar{\sigma}_4$	$\bar{\sigma}_5$	$\bar{\sigma}_6$
	Pagano [16]	2.82	1.10	0.119	0.0334	0.387	0.0281
4	Present	2.6411	1.0356	0.1028	0.0348	0.2724	0.0263
	FSDT [18][b]	2.3626	0.6130	0.0934	0.0308	0.1879	0.0205
	Pagano	0.919	0.725	0.0435	0.0152	0.420	0.0123
10	Present	0.8622	0.6924	0.0398	0.0170	0.2859	0.0115
	FSDT	0.803	0.6214	0.0375	0.0159	0.1894	0.0105
	Pagano	0.610	0.650	0.0299	0.0119	0.434	0.0093
20	Present	0.5937	0.6407	0.0289	0.0139	0.2880	0.0091
	FSDT	0.5784	0.6228	0.0283	0.0135	0.1896	0.0088
	Pagano	0.508	0.624	0.0253	0.0108	0.439	0.0083
100	Present	0.507	0.624	0.0253	0.0129	0.2886	0.0083
	FSDT	0.5064	0.6233	0.0253	0.0127	0.1897	0.0083
	CPT	0.503	0.623	0.0252	–	–	0.0083

[a]See Table 1 for the nondimensionalized quantities
[b]The values were obtained using shear correction factors $k_1^2=k_2^2=5/6$

Table 3 **Nondimensionalized[a] deflections and stresses in four-layer cross-ply (0/90/90/0 deg) square laminates under sinusoidal transverse loads**

a/h	Source	$\bar{w}$	$\bar{\sigma}_1$	$\bar{\sigma}_2$	$\bar{\sigma}_4$	$\bar{\sigma}_5$	$\bar{\sigma}_6$
	Elasticity [17]	1.954	0.720	0.663	0.292	0.291	0.0467
4	Present theory	1.8937	0.6651	0.6322	0.2389	0.2064	0.0440
	FSDT [18][b]	1.7100	0.4059	0.5765	0.1963	0.1398	0.0308
	Three-dimensional elasticity	0.743	0.559	0.401	0.196	0.301	0.0275
10	Present theory	0.7147	0.5456	0.3888	0.1531	0.2640	0.0268
	FSDT	0.6628	0.4989	0.3615	0.1292	0.1667	0.0241
	Three-dimensional elasticity	0.517	0.543	0.308	0.156	0.328	0.0230
20	Present theory	0.5060	0.5393	0.3043	0.1234	0.2825	0.0228
	FSDT	0.4912	0.5273	0.2957	0.1087	0.1749	0.0221
	Three-dimensional elasticity	0.4385	0.539	0.276	0.141	0.337	0.0216
100	Present theory	0.4343	0.5387	0.2708	0.1117	0.2897	0.0213
	FSDT	0.4337	0.5382	0.2705	0.1009	0.1780	0.0213

[a] Same nondimensionalization as used in Table 1, except $\bar{\sigma}_2$ is evaluated at $(x,y,z)=(a/2,a/2,h/4)$.
[b] Shear correction factors, $k_1^2=k_2^2=5/6$.

Table 4 Nondimensionalized deflections in three-layer cross-ply (0/90/0 deg) square laminates under uniform loading

a/h	Present theory $N=9$[a]	$N=29$	$N=29$	First-order shear deformation theory $N=9$	$N=29$	$N=49$
2	7.7681	7.7661	7.7661	7.7170	7.7066	7.7062
4	2.9103	2.9091	2.9091	2.6623	2.6597	2.6596
10	1.0903	1.0900	1.0900	1.0224	1.0220	1.0219
20	0.7761	0.7760	0.7760	0.7574	0.7573	0.7573
50	0.6839	0.6838	0.6838	0.6808	0.6807	0.6807
100	0.6705	0.6705	0.6705	0.6697	0.6697	0.6697

[a]Number of terms in the series, $w=\Sigma_{m,n=1,3,\ldots,N} W_{mn}\sin\alpha x \sin\beta y$.

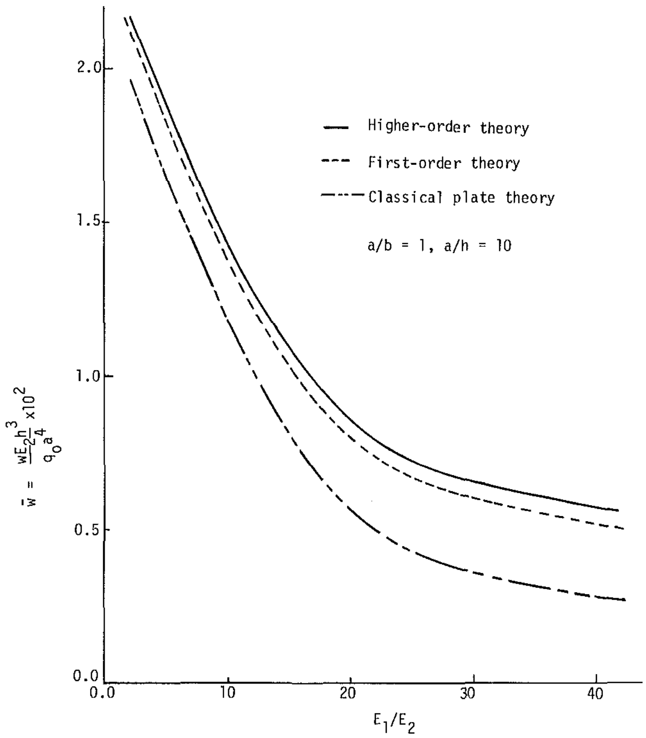

Fig. 3 The effect of material anisotropy on the nondimensionalized center deflection of a four-layer [0/90/90/0 deg] square plate under sinusoidal load

$$+\left(\frac{4}{3h^2}\right)^2[\alpha^3H_{11}+\alpha\beta^2(H_{12}+2H_{66})]$$

$$c_{13}=\beta A_{44}-\frac{8}{h^2}\beta D_{44}+\left(\frac{4}{h^2}\right)^2\beta F_{44}$$

$$-\frac{4}{3h^2}[\alpha^2\beta(F_{12}+2F_{66})+\beta^3F_{22}]$$

$$+\left(\frac{4}{3h^2}\right)^2[\alpha^2\beta(H_{12}+2H_{66})+\beta^3H_{22}]$$

$$c_{22}=A_{55}+\alpha^2D_{11}+\beta^2D_{66}-\frac{8}{h^2}D_{55}+\left(\frac{4}{h^2}\right)^2F_{55}$$

$$-\frac{8}{3h^2}(\alpha^2F_{11}+\beta^2F_{66})+\left(\frac{4}{3h^2}\right)^2(\alpha^2H_{11}+\beta^2H_{66})$$

$$c_{23}=\alpha\beta\left[D_{12}+D_{66}-\frac{8}{3h^2}(F_{12}+F_{66})+\left(\frac{4}{3h^2}\right)^2(H_{12}+H_{66})\right]$$

$$c_{33}=A_{44}+\alpha^2D_{66}+\beta^2D_{22}-\frac{8}{h^2}D_{44}+\left(\frac{4}{h^2}\right)^2F_{44}$$

$$-\frac{8}{3h^2}(\alpha^2F_{66}+\beta^2F_{22})+\left(\frac{4}{3h^2}\right)^2(\beta^2H_{22}+\alpha^2H_{66}) \quad (24)$$

The solution to equation (23), in conjunction with equation (20) gives the exact solution for any load that can be expanded in terms of the double-Fourier series. For example, for sinusoidally distributed load,

$$q(x,y)=q_0\sin\frac{\pi x}{a}\sin\frac{\pi y}{b} \quad (25)$$

we have $m=n=1$, and $Q_{11}=q_0$. For uniformly distributed load of intensity q_0, the coefficients Q_{mn} are given by

$$Q_{mn}=\frac{16q_0}{\pi^2 mn} \quad (26)$$

Numerical Results

Here we present numerical results for a couple of symmetric cross-ply plate problems, and discuss the improvement in the prediction of displacements and stresses by the present theory. The three-dimensional elasticity solutions of Pagano [16] and Pagano and Hatfield [17] for simply supported rectangular plates under sinusoidal loading are used to assess the improvement. The following four laminated plate problems are considered:

1. A three-ply square laminate with layers of equal thickness and subject to sinusoidally distributed transverse load.
2. The same lamination geometry and loading as in Problem 1, except the laminate is of rectangular geometry ($b/a=3$).
3. A four-ply square laminate with layers of equal thickness and subjected to sinusoidally distributed transverse load.
4. The same geometry and lamination scheme as in Problem 1 except the load is uniformly distributed.

In all problems, the lamina properties are assumed to be

$$E_1=25\times10^6\text{ psi (174.6 GPa)},\quad E_2=10^6\text{ psi (7 GPa)}$$
$$G_{12}=G_{13}=0.5\times10^6\text{ psi (3.5 GPa)} \quad (27)$$
$$G_{23}=0.2\times10^6\text{ psi (1.4 GPa)},\quad \nu_{12}=\nu_{13}=0.25$$

Tables 1–4 contain nondimensionalized deflections and stresses for the four problems. For Problems 1, and 2, the results obtained using the present theory are compared with those obtained by the three-dimensional elasticity theory (see [16, 17]) and the first-order shear deformation theory (FSDT) (see Reddy and Chao [18]). In Table 1 the results obtained using various shear correction coefficients in the first-order shear deformation theory are also included. Note that the shear correction factor of 5/6 can also be arrived from the present theory. For example, the average shear force per unit length of an edge prependicular to the x-axis is given by

$$(Q_5)_{avg}=\frac{1}{2}\int_{-h/2}^{h/2}\sigma_5\,dz$$

$$=\frac{1}{2}\int_{-h/2}^{h/2}\left(1-\frac{4z^2}{h^2}\right)dz\left[Q_{45}\left(\frac{\partial w}{\partial y}+\psi_y\right)\right.$$

$$+ Q_{55}\left(\frac{\partial w}{\partial x}+\psi_x\right)\Big]$$

$$= \frac{5}{6}h\left[Q_{45}\left(\frac{\partial w}{\partial y}+\psi_y\right)+Q_{55}\left(\frac{\partial w}{\partial x}+\psi_x\right)\right]$$

$$= A_{45}\left(\frac{\partial w}{\partial y}+\psi_y\right)+A_{55}\left(\frac{\partial w}{\partial x}+\psi_x\right) \quad (28)$$

from which it follows that the shear correction factors are given by

$$k_1 k_2 = \frac{5}{6}, \quad k_2^2 = \frac{5}{6} \quad (29)$$

For Problem 3, the exact stresses σ_1, σ_2, and σ_6 computed using the constitutive equations of the higher-order theory, are greatly improved over the results obtained using the first-order and classical plate theories (see Fig. 2*a*). The shear stresses obtained using constitutive equations are on the low side of the three-dimensional elasticity solutions. This error might be due to the fact that the stress continuity across each layer interface is not imposed in the present theory. As in the case of the Classical Plate Theory (CPT), the transverse shear stresses can also be determined by integrating equilibrium equations (of three-dimensional elasticity in the absence of body forces) with respect to the thickness coordinate:

$$\begin{aligned}\sigma_5 &= -\int_{-h/2}^{z}(\sigma_{x,x}+\sigma_{xy,y})dz\\ \sigma_4 &= -\int_{-h/2}^{z}(\sigma_{xy,x}+\sigma_{y,y})dz\end{aligned} \quad (30)$$

The foregoing approach not only gives single-valued shear stresses at the interfaces but yields excellent results for all theories in comparison with the three-dimensional solutions. Despite its apparent advantage, the use of stress equilibrium conditions in the analysis of laminated plates is quite cumbersome. Typical stress distributions of $\sigma_5=\sigma_{xz}$ and $\sigma_4=\sigma_{yz}$ through the thickness ($a/h=10$) are shown in Fig. 2(*b*).

According to Whitney and Pagano [6], the severity of shear deformation effects also depends on the material anisotropy of the layers. The exact maximum deflections of simply supported four-layer [0/90/90/0] cross-ply laminates are compared in Fig. 3 for various ratios of moduli, E_1/E_2 (for a given thickness, $a/h = 10$). The CPT underpredicts the deflections even at lower ratios of moduli. The disagreement between the higher-order and first-order theory is, in parts, owing to the higher-order contributions of the present theory and the fact that the shear correction factors depend on the lamina properties and the lamination scheme.

Summary and Conclusions

An improved shear deformation theory that gives parabolic distribution of the transverse shear strains is developed. The theory contains the same number of dependent variables as in the first-order shear deformation theory, but results in more accurate prediction of deflections and stresses, and satisfies the zero tangential traction boundary conditions on the surfaces of the plate. Exact closed-form solutions of the equations presented herein can also be derived for antisymmetric cross-ply and angle-ply laminates (see [19]).

From the results in Tables 1–4, one can conclude that the present theory, in general, gives more accurate results than the first-order shear deformation theory when compared to the three-dimensional elasticity solution. Although an adjustment of the shear correction factors seem to improve the results obtained by FSDT (see Table 1), too low a value of k_1 and k_2 overpredicts the solution. In Problems 2–4, a value of 5/6 is used in obtaining the FSDT results. The present theory also gives, relatively speaking, faster convergent solution when compared to the FSDT theory, as can be seen from Table 4. The results for uniform loading should serve as reference for finite-element analyses.

Acknowledgment

The research reported in this paper was conducted under a research grant from NASA-Langley Research Center under Grant NG-1-459. The author is grateful to Dr. Norman Knight, Jr. for the support. Also, it is a pleasure to acknowledge the typing of this manuscript by Mrs. Vanessa McCoy.

References

1 Bolle, L., "Contribution an Problème Lineare de Flexion d'une Plaque Elastique," *Bull. Technique de la Suisse Romade*, Parts 1 and 2, Vol. 73, 1947, pp. 281–285; 293–298.

2 Hildebrand, F. B., Reissner, E., and Thomas, G. B., "Note on the Foundations of the Theory of Small Displacements of Orthotropic Shells," IVACA Technical Note No. 1833, Mar. 1949.

3 Hencky, H., "Über die Berucksichtgung der Schubverzerrungen in ebenen Platten," *Ing.-Arch.*, Vol. 16, 1947.

4 Mindlin, R. D., "Influence of Rotary Inertia and Shear on Flexural Motions of Isotropic, Elastic Plates," ASME JOURNAL OF APPLIED MECHANICS, Vol. 18, 1951.

5 Librescu, L., *Elastostatics and Kinetics of Anisotropic and Heterogeneous Shell-Type Structures*, Noordhoff, Leyden, GDR, 1975.

6 Whitney, J. M., and Pagano, N. J., "Shear Deformation in Heterogeneous Anisotropic Plates," ASME JOURNAL OF APPLIED MECHANICS, Vol. 37, Dec. 1970, pp. 1031–1036.

7 Whitney, J. M., and Sun, C. T., "A Higher Order Theory for Extensional Motion of Laminated Composites," *J. Sound and Vibration*, Vol. 30, Sept. 1973, pp. 85–97.

8 Lo, K. H., Christensen, R. M., and Wu, E. M., "A Higher-Order Theory of Plate Deformation, Part 2: Laminated Plates," ASME JOURNAL OF APPLIED MECHANICS, Vol. 44, 1977, pp. 669–676.

9 Green, A. E., and Naghdi, P. M., "A Theory of Laminated Composite Plates," *IMA J. Appl. Mathematics*, Vol. 29, 1982, p. 1.

10 Rehfield, L. W., and Valisetty, R. R., "A Comprehensive Theory for Planar Bending of Composite Laminates," *Computers Structures*, Vol. 16, 1983, p. 441.

11 Pagano, N. J., and Soni, S. R., "Global-Local Laminate Variational Model," *Int. J. Solids & Struct.*, Vol. 19, 1983, p. 207.

12 Bert, C. W., Private Communication, June 1983.

13 Levinson, M., "An Accurate Simple Theory of the Statics and Dynamics of Elastic Plates," *Mechanics Research Communications*, Vol. 7, 1980, pp. 343–350.

14 Murthy, M. V. V., "An Improved Transverse Shear Deformation Theory for Laminated Anisotropic Plates," NASA Technical Paper 1903, Nov. 1981.

15 Reddy, J. N., *Energy and Variational Methods in Applied Mechanics*, Wiley, New York, 1984.

16 Pagano, N. J., "Exact Solutions for Rectangular Bidirectional Composites and Sandwich Plates," *J. Comp. Materials*, Vol. 4, January 1970, pp. 20–34.

17 Pagano, N. J., and Hatfield, S. J., "Elastic Behavior of Multilayered Bidirectional Composites," *AIAA Journal*, Vol. 10, July 1972, pp. 931–933.

18 Reddy, J. N., and Chao, W. C., "A Comparison of Closed-Form and Finite-Element Solutions of Thick, Laminated, Anisotropic Rectangular Plates, *Nuclear Engineering and Design*, Vol. 64, 1981, pp. 153–167.

19 Phan, N. D., and Reddy, J. N., "Analysis of Laminated Composite Plates Using a Higher-Order Shear Deformation Theory," in review.

X. Markenscoff
Mem. ASME

L. Ni[1]

Department of Mechanical
and Environmental Engineering,
University of California,
Santa Barbara, Calif. 93106

On the Effect of Dislocation Loop Curvature on Elastic Precursor Decay

The exact solution for the fields radiated from a circular dislocation loop expanding in its own plane with constant velocity is obtained in terms of elliptic functions of different kinds. The solution is used to obtain the contribution of small disloction loops to the decay of the leading wave front of a wave propagating in an elastic solid containing dislocations. It is found that the loop curvature can contribute to the decay in the leading term.

Introduction

In two recent publications Clifton and Markenscoff [1] and Markenscoff and Clifton [2] studied the effect of radiation from moving dislocations to the elastic precursor decay, i.e., the decay of the leading elastic wave front of a pulse propagating in an elastoplastic material. These analyses lead to the same result: that the precursor decay per unit distance of propagation is proportional to the product of the average mobile dislocation density and dislocation velocity at the wave front. The difficulty, however, with this phenomenon is that comparison of measured and predicted precursor amplitudes indicates that the measured amplitudes are much less than those predicted using the initial dislocation density and reasonable estimates of dislocation velocity. For a discussion of the explanation proposed to reconcile this discrepancy the reader is referred to [1] and the references cited there. The fundamental difficulty is that the dislocation density must be increased by two to three orders of magnitude to account for the order of the measured decay, and this is considered unlikely. One possibility, however, can be that dislocation loops are expanding from a sufficiently small initial radius. In the analysis in [2] Markenscoff and Clifton assumed large initial dislocation loop radii, so the analysis did not show any loop curvature (radius) effect on the wave front itself. However the finite response time Δt (of the order of a few nanoseconds) of the detectors can be a critical factor. In this analysis we assume that the loop radii are of the order of $c_2 \Delta t$ (where c_2 is the shear-wave speed), which is plausible, and obtain an effect of loop curvature on the precursor decay which is of the same order as the leading term previously obtained in [1 and 2].

[1] Permanent Address: Institute of Mathematics, Academia Sinica, Beijing, China.

Contributed by the Applied Mechanics Division and presented at the Winter Annual Meeting, New Orleans, La., December 9–14, 1984 of THE AMERICAN SOCIETY OF MECHANICAL ENGINEERS.

Discussion on this paper should be addressed to the Editorial Department, ASME, United Engineering Center, 345 East 47th Street, New York, N.Y. 10017 and will be accepted until two months after final publication of the paper itself in the JOURNAL OF APPLIED MECHANICS. Manuscript received by ASME Applied Mechanics-Division, December, 1983. Paper No. 84-WA/APM-40.

Copies will be available until August, 1984.

Radiation From an Expanding Dislocation Loop

Here we consider a circular dislocation loop in an isotropic solid with Burgers vector b_1 in the plane of the loop and without loss of generality taken along the x_1-direction. The loop is at rest until time $t' = 0$ when it starts expanding with a constant radial velocity V. In the sequel the exact solution for the velocity field of this problem is obtained. In [2] only the wave-front asymptotic behavior was obtained.

The velocity field of a dislocation loop $\mathcal{L}(t)$ moving with a velocity $V(\mathbf{x}', t')$ where $\mathbf{x}'$ denotes a point on the loop is given by [3]

$$\dot{U}_m(\mathbf{x}, t) = \frac{\partial}{\partial x_l} \int_{-\infty}^{t} dt' \int_{\mathcal{L}(t')} C_{ijkl} G_{km}(\mathbf{x}-\mathbf{x}', t-t') V_r(\mathbf{x}', t') b_l \epsilon_{jrs} dl_s'(t') \quad (1)$$

where C_{ijkl} denote the elastic coefficients, G_{km} is the Green's function for a unit impulse in a full space [4], V_r is the velocity vector at any point on the loop, b_l is the Burgers vector, dl_s' is a line element a long the loop, and ϵ_{jrs} is the permutation symbol. The expression (1) differs from the one given by Mura [5] in that the differentiation is outside the integral. For a discussion of this issue we refer to [3].

For isotropic materials, the Green's function is given by Love [4]

$$G_{ij}(x-x', t-t') = \frac{1}{4\pi\rho} \left\{ \frac{\bar{t}}{\bar{r}^2} \left(\frac{3\bar{r}_i \bar{r}_i}{\bar{r}^3} - \frac{\delta_{ij}}{\bar{r}} \right) H\left(\bar{t} - \frac{\bar{r}}{c_1}\right) H\left(\frac{\bar{r}}{c_2} - \bar{t}\right) + \frac{\bar{r}_i \bar{r}_j}{\bar{r}^3} \left[\frac{1}{c_1^2} \delta\left(\bar{t} - \frac{\bar{r}}{c_1}\right) - \frac{1}{c_2^2} \delta\left(\bar{t} - \frac{\bar{r}}{c_2}\right) \right] + \frac{\delta_{ij}}{\bar{r} c_2^2} \delta\left(\bar{t} - \frac{\bar{r}}{c_2}\right) \right\} \quad (2)$$

where ρ is the density, $\bar{t} = t - t'$, $\bar{r}_i = x_i - x_i'$, $r^2 = x_1^2 + x_2^2 + x_3^2$, $\bar{r}^2 = (x_1 - x_1')^2 + (x_2 - x_2')^2 + (x_3 - x_3')^2$; c_1 and c_2 are the longitudinal and shear wave speeds, $H(\ )$ denotes the Heaviside step function, $\delta(\ )$ denotes the delta function, and δ_{ij} is the Kronecker delta. For the loop geometry in consideration and for isotropic materials, the only nonzero terms in (1) are obtained from the terms containing

$$C_{1313} G_{11} \quad \text{and} \quad C_{1331} G_{31} \quad (3)$$

The coordinates of a point on a circular loop with initial radius α_0 that begins to expand on its own plane with constant radial velocity V at time $t' = 0$ are

$$\begin{aligned} x_1' &= \tilde{x}_1 + \alpha(t')\cos\theta \\ x_2' &= \tilde{x}_2 + \alpha(t')\sin\theta \\ x_3' &= 0, \end{aligned} \tag{4}$$

where $\tilde{x}_i$ are the coordinates of the center of the loop and

$$\alpha(t') = \alpha_0 + Vt'H(t').$$

From (1)-(4) the velocity component $\dot{U}_1$ can be written as

$$\dot{U}_1(x_1,x_2,x_3,t) = \frac{\partial}{\partial x_3}\int_{-\infty}^{t} dt' \int_0^{2\pi} b_1 \frac{C_{1313}}{4\pi\rho}\Bigg[\Bigg(-\frac{\bar{r}_1^2}{\bar{r}^3} + \frac{1}{\bar{r}}\Bigg)$$

$$\frac{1}{c_2^2}\delta\Big(t - \frac{\bar{r}}{c_2}\Big)$$

$$+ \frac{\bar{r}_1^2}{\bar{r}^3}\frac{1}{c_1^2}\delta\Big(\bar{t} - \frac{\bar{r}}{c_1}\Big)$$

$$+\bar{t}\Big(\frac{3\bar{r}_1^2 - \bar{r}^2}{\bar{r}^5}\Big)H\Big(\bar{t} - \frac{\bar{r}}{c_1}\Big)H\Big(\frac{\bar{r}}{c_2} - \bar{t}\Big)\Bigg]V\alpha(\bar{t}')\Big)d\theta$$

$$+ \frac{\partial}{\partial x_1}\int_{-\infty}^{t} dt' \int_0^{2\pi} b_1 \frac{C_{1331}}{4\pi\rho}\Bigg[-\frac{\bar{r}_1\bar{r}_3}{c^2{}_2\bar{r}^3}\delta\Big(\bar{t} - \frac{\bar{r}}{c_2}\Big)$$

$$+ \frac{\bar{r}_1\bar{r}_3}{c^2{}_1\bar{r}^3}\delta\Big(\bar{t} - \frac{\bar{r}}{c_1}\Big)$$

$$+ \frac{3\bar{t}\bar{r}_1\bar{r}_3}{\bar{r}^5}H\Big(\bar{t} - \frac{\bar{r}}{c_1}\Big)H\Big(\frac{\bar{r}}{c_2} - \bar{t}\Big)\Bigg]V\alpha(t')d\theta. \tag{5}$$

First we consider the integral

$$\frac{\partial}{\partial x_3}\int_{-\infty}^{t} dt' \int_0^{2\pi} b_1 \frac{C_{1313}}{4\pi\rho} \bullet \frac{1}{\bar{r}} \bullet \frac{1}{c_2^2}\delta\Big(\bar{t} - \frac{\bar{r}}{c_2}\Big)V\alpha(t')d\theta \tag{6}$$

and carry out the integration with respect to θ:

$$\int_0^{2\pi} \frac{1}{\bar{r}}\delta\Big(\bar{t} - \frac{\bar{r}}{c_2}\Big)d\theta = \sum_{\theta_0}\Big(\Big|\frac{df}{d\theta}\Big|\bar{r}\Big)\Big|_{\theta=\theta_0}^{-1} \tag{7}$$

where

$$f = f(\theta;t') \equiv \bar{t} - \frac{\bar{r}}{c_2} \tag{8}$$

and θ_0 are the zeros of $f(\theta;t')$. These zeros correspond to the points where the domain of dependence of the solution at (x, t) intersects the loop at time t'. From (4) and (8) the values θ_0 satisfy

$$\cos\phi\cos\theta_0 + \sin\phi\sin\theta_0 = C \tag{9}$$

in which

$$\phi = \tan^{-1}\Big(\frac{x_2 - \tilde{x}_2}{x_1 - \tilde{x}_1}\Big) \tag{10a}$$

and

$$C = [\alpha(t')^2 + a^2 + x_3^2 - c_2^2\bar{t}^2]/2\alpha(t')a, \tag{10b}$$

where

$$a \equiv [(x_1 - \tilde{x}_1)^2 + (x_2 - \tilde{x}_2)^2]^{1/2}. \tag{10c}$$

The two values of θ_0 that satisfy (9) are

$$\theta_{01,02} = \phi \pm \cos^{-1}C \tag{11}$$

The angle ϕ corresponds to the angle that the plane normal to $x_3 = 0$ and containing (x_1, x_2, x_3) and the center of the loop makes with the x_1 axis. The angles $\theta_{01,02}$ locate the intersection of the sphere with center (x_1, x_2, x_3) and radius $c_2\bar{t}$ with the loop at time $\bar{t}$.

From (4) and (8) we obtain

$$df/d\theta\Big|_{\theta=\theta_0} = \frac{-\alpha(t')}{c_2\bar{r}}\{(x_1 - \tilde{x}_1)\sin\theta_0 - (x_2 - \tilde{x}_2)\cos\theta_0\}$$

which, by means of (10*a*) and (10*b*), can be rewritten as

$$df/d\theta\Big|_{\theta=\theta_0} = \frac{\alpha(t')a}{c_2^2\bar{t}}\sin(\theta_0 - \phi).$$

Finally, using (11) we obtain

$$df/d\theta\Big|_{\theta=\theta_0} = \frac{\alpha(t')a}{c_2^2\bar{t}}\sqrt{1 - C^2} \tag{12}$$

For the angles θ_0 in (11) to be real, the values of C in (10*b*) must satisfy

$$-1 \le C \le 1 \tag{13}$$

The limits of integration in t' are defined by the inequalities (13). The motion of the loop from this point on is assumed subsonic, i.e., $V < c_2 < c_1$.

From $1 - C \ge 0$, or equivalently:

$$-c_2^2(t - t') + (\alpha_0 + Vt')^2 + a^2 + x_3^2 - 2(\alpha_0 + Vt')a \le 0,$$

it follows that $t' \le t_1$, $t' \ge t_2$

where

$$t_1 = \frac{1}{D}\{c_2^2 t + V(\alpha_0 - a) - \beta_1\} \tag{14$_1$}$$

$$t_2 = \frac{1}{D}\{c_2{}^2 t + V(\alpha_0 - a) + \beta_1\}, \tag{14$_2$}$$

with

$$\beta_1 = c_2\sqrt{(a - \alpha_0 - Vt)^2 + \Big(1 - \frac{V^2}{c_2^2}\Big)x_3^2} \tag{14$_3$}$$

and

$$D = c_2^2 - V^2$$

Moreover, it may be also seen that $t_1 \le t \le t_2$.

From $1 + C \ge 0$, or equivalently:

$$-c_2^2(t - t')^2 + (\alpha_0 + Vt')^2 + a^2 + x_3^2 + 2(\alpha_0 + Vt') \ge 0,$$

it follows that

$$t_3 \le t' \le t_4,$$

where

$$t_3 = \frac{1}{D}\{c_2^2 t + V(\alpha_0 + a) - \beta_2\} \tag{15$_1$}$$

$$t_4 = \frac{1}{D}\{c_2^2 t + V(\alpha_0 + a) + \beta_2\}, \tag{15$_2$}$$

with

$$\beta_2 = c_2\sqrt{(a + \alpha_0 - Vt)^2 + \Big(1 - \frac{V^2}{c_2^2}\Big)x_3^2}. \tag{15$_3$}$$

We can also easily prove the following ordering of the roots

$$t_3 \le t_1 \le t \le t_2 \le t_4$$

and obtain the following signs for t_1 and t_3 according to the cases:

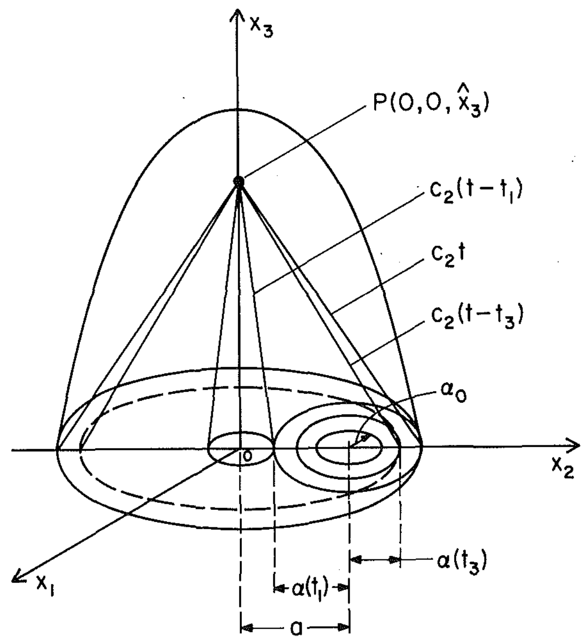

Fig. 1(*a*) Upper and lower limits t_1 and t_3 for contribution to the solution at *P* (for the case: $c_2^2t^2 > x_3^2 + (a + \alpha_0)^2$)

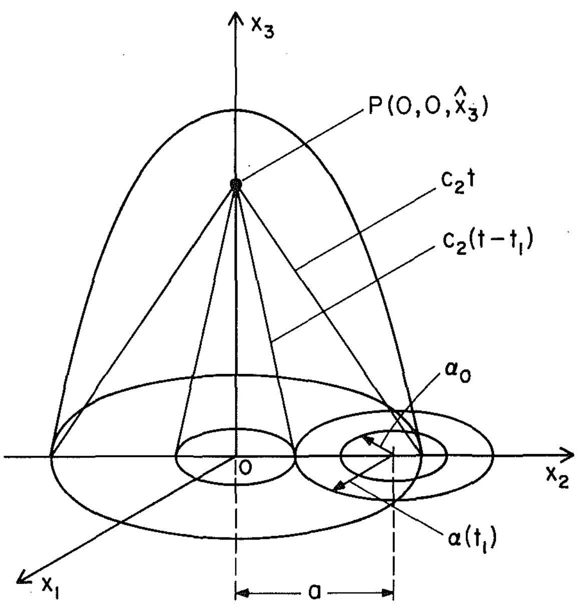

Fig. 1(*b*) Upper and lower limits t_1 and 0 for contribution to the solution at *P* (for the case: $x_3^2 + (a-\alpha_0)^2 \le c_2^2t^2 \le x_3^2 + (a+\alpha_0)^2$)

Fig. 1

(*a*) If $c_2^2t^2 > x_3^2 + (a+\alpha_0)^2$ then $t_3 > 0$ $\quad (16_1)$

(*b*) If $c_2^2t^2 < x_3^2 + (a-\alpha_0)^2$ then $t_1 < 0$ $\quad (16_2)$

(*c*) If $x_3^2 + (a-\alpha_0)^2 \le c_2^2t^2 \le x_3^2 + (a+\alpha_0)^2$ then $t_1 \ge 0$ and $t_3 \le 0$ $\quad (16_3)$

Therefore the limits of integration in case (*a*) are: $t_3 \le t' \le t_1$, and in case (*c*): $0 \le t' \le t_1$. These limits are illustrated in Figs. 1(*a*), (*b*), respectively. Case (*b*) obviously indicates that the field point lies outside the wave front.

The main contribution to $\dot{U}_1$ is due to the term

$$\frac{\partial}{\partial x_3}\int_0^t dt'\int_0^{2\pi}\frac{b_1}{c_2^2}\frac{C_{1313}}{4\pi\rho}\frac{1}{\bar{r}}\delta\left(\bar{t}-\frac{\bar{r}}{c_2}\right)V\alpha(t')d\theta$$

$$=\frac{C_{1313}}{2\pi\rho}\frac{b_1}{a}\frac{V}{c_2}\frac{\partial}{\partial x_3}\int_{\max(t_3,0)}^{t_1}\frac{dt'}{(1-C^2)^{1/2}} \tag{17}$$

and we proceed to evaluate the integral for the two cases $t_3 > 0$ and $t_3 \le 0$ in (17).

For $t_3 > 0$: $\quad I_1 \equiv \dfrac{M}{a}\displaystyle\int_{t_3}^{t_1}\frac{dt'}{(1-C^2)^{1/2}}$

$$=\frac{M}{2a}\int_{t_3}^{t_1}\left\{\sqrt{\frac{X(t')}{Y(t')}}+\sqrt{\frac{Y(t')}{X(t')}}\right\}dt'$$

where

$$M=\frac{C_{1313}b_1V}{2\pi\rho c_2}$$

where

$$X(t')=2a\alpha(t')(1-C)\equiv D(t_1-t')(t_2-t')$$
$$Y(t')=2a\alpha(t')(1+C)\equiv D(t'-t_3)(t_4-t')$$

so that

$$I_1=\frac{M}{2a}\int_{t_3}^{t_1}\left[\sqrt{\frac{(t_1-t')(t_2-t')}{(t'-t_3)(t_4-t')}}+\sqrt{\frac{(t'-t_3)(t_4-t')}{(t_1-t')(t_2-t')}}\right]dt'$$

The preceding integral can be found in the Handbook of Elliptic Integrals [6, p. 109] and is equal to:

$$\frac{M}{2a}\left[(t_2-t_1)^2\alpha^2g\int_0^{u_1}\frac{dn^2u\,du}{(1-\xi^2sn^2u)^2}\right.$$
$$\left.+(t_4-t_1)(t_1-t_3)g\int_0^{u_1}\frac{cn^2u\,dn^2u\,du}{(1-\xi^2sn^2u)^2}\right] \tag{18}$$

where

$$0<\xi^2\equiv\frac{t_1-t_3}{t_2-t_3}<1, \qquad g=\frac{2}{\sqrt{(t_4-t_1)(t_2-t_3)}}$$

and $sn\,u$, $cn\,u$, and $dn\,u$ are the Jacobian elliptic functions [6, p. 18] and $u_1 = sn^{-1}(1)$.

The expression (18) can be further simplified by use of the Tables of Elliptic Integrals [6, pp. 218–219] to yield:

$$I_1=\frac{M}{2a}g\{(t_2-t_3)(t_4-t_2)K(k)+(t_1-t_2)\frac{4Va}{D}\Pi(\xi^2,k)\} \tag{19}$$

with

$$k^2\equiv\frac{(t_4-t_2)(t_1-t_3)}{(t_4-t_1)(t_2-t_3)}, \tag{20}$$

where $K(k)$ and $\Pi(\xi^2, k)$ are the complete elliptic integrals of the first and third kind, respectively [6, p. 8]. Similarly, for $t_3 \le 0$, the integral in (17) takes the form:

$$I_2\equiv\frac{M}{a}\int_0^{t_1}\frac{dt'}{(1-C^2)^{1/2}}=\frac{M}{2a}g\{(t_2-t_3)(t_4-t_2)F(\phi,k)$$
$$+(t_1-t_2)\frac{4Va}{D}\Pi(\phi,u^2,k)\}$$

where

$$\phi=\sin^{-1}\sqrt{\frac{t_1(t_2-t_3)}{t_2(t_1-t_3)}}$$

and $F(\phi, k)$ and $\Pi(\phi, \xi^2, k)$ are the incomplete elliptic integrals of the first and third kind, respectively [6, p. 8].

Having obtained the expressions for the integrals I_1, and I_2 we will now differentiate them with respect to x_3, i.e., evaluate

$$\frac{M}{a}\frac{\partial}{\partial x_3}\int_{\max(t_3,0)}^{t_1}\frac{dt'}{(1-C^2)^{1/2}}$$

on the right-hand side of equation (17).

We have from (19):

$$J_1 \equiv \frac{\partial}{\partial x_3} I_1 = \frac{M}{2a}\frac{\partial}{\partial x_3}\{g(t_2-t_3)(t_4-t_2)K(k) + (t_1-t_2)\frac{4Va}{D}\Pi(\xi^2,k)\}$$

in which we can substitute the derivatives:

$$\frac{\partial}{\partial x_3}t_1 = \frac{-1}{D}\frac{\partial}{\partial x_3}\beta_1 = -\frac{x_2}{\beta_1}$$

$$\frac{\partial}{\partial x_3}t_2 = \frac{x_3}{\beta_1}$$

$$\frac{\partial}{\partial x_3}t_3 = -\frac{x_3}{\beta_2}$$

$$\frac{\partial}{\partial x_3}t_4 = \frac{x_3}{\beta_2}$$

$$\frac{\partial}{\partial x_3}g = -\frac{x_3}{D}\frac{(\beta_1+\beta_2)^2}{\beta_1\beta_2}\frac{g}{(t_4-t_1)(t_2-t_3)}$$

$$\frac{\partial}{\partial x_3}\xi^2 = \frac{x_3}{(t_2-t_3)^2}\left[\frac{1}{\beta_2}(t_2-t_1)-\frac{1}{\beta_1}(t_2+t_1-2t_3)\right]$$

$$\frac{\partial}{\partial x_3}K = \frac{x_3K}{D\beta_1\beta_2}\left\{\frac{-(\beta_1-\beta_2)^2}{(t_1-t_3)(t_4-t_2)}-\frac{(\beta_1+\beta_2)^2}{(t_2-t_3)(t_4-t_1)}\right\},$$

and the expressions for the derivatives of the elliptic functions [6, p. 282] to obtain the final result:

$$J_1 = \frac{2Mc_2^2x_3g(\alpha_0+Vt)}{D\beta_1\beta_2}\left\{K(k)-\frac{(t_2-t_3)(t_4-t_1)D^2}{2\beta_1\beta_2}E(k)\right\}$$

$$= \frac{2Mc_2^2g^3(\alpha_0+Vt)x_3}{D^3(1-k^2)}\{K(k)-2E(k)\}, \tag{21}$$

where $E(k)$ is the complete elliptic function of the second kind [6, p. 8].

Similarly for $t_3 < 0$ have

$$J_2 \equiv \frac{\partial}{\partial x_3}I_2 = \frac{2Mc_2^2x_3g^3(\alpha_0+Vt)}{D^3(1-k^2)}\{F(\phi,k)-2E(\phi,k)\}$$

$$+\frac{2M\alpha_0x_3}{D}\sqrt{\frac{t_1t_2}{t_4(-t_3)}}\frac{1}{(t_2-t_1)}\left\{\frac{1}{\beta_1}\left(\frac{t_3}{t_1(t_1-t_3)}+\frac{t_3}{t_2(t_2-t_3)}\right)-\frac{1}{\beta_2}\frac{(t_2-t_1)}{(t_2-t_3)(t_1-t_3)}\right\}$$

$$-\frac{Mx_3}{aD}\sqrt{\frac{t_1(-t_3)}{t_2t_4}}\frac{(t_4-t_2)}{(t_2-t_1)(t_4-t_3)}\left\{\frac{-(\beta_1-\beta_2)^2(t_4-t_1)}{\beta_1\beta_2(t_4-t_3)}-\frac{(\beta_1+\beta_2)^2}{\beta_1\beta_2}\frac{(t_4-t_2)}{(t_2-t_3)}\right\}+\frac{2MVx_3}{D}\frac{1}{(t_2-t_1)(t_2-t_3)(t_1-t_3)}$$

$$\sqrt{\frac{t_1t_4(-t_3)}{t_2}}\left(\frac{t_2-t_1}{\beta_2}-\frac{t_2+t_1-2t_3}{\beta_1}\right) \tag{22}$$

where $E(\phi,k)$ is the incomplete elliptic function of the second kind [6, p. 8].

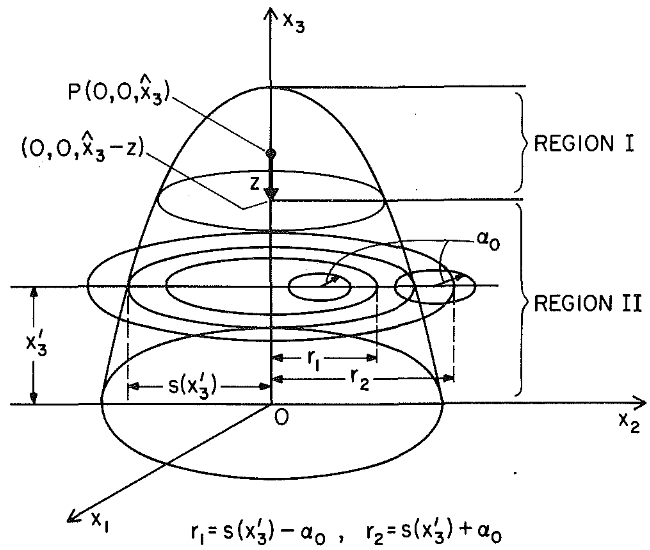

Fig. 2 Range of dislocation loops contributing to the solution at (0, 0, $\hat{x}_3$, $\hat{x}_3/c_2 + \Delta t$)

Contribution to Elastic Precursor Decay

For the elastic precursor analysis we are interested, as in [2], in evaluating the particule velocity $\dot{U}_1$ at (0, 0, $\hat{x}_3$, $\hat{x}_3/c_2 + \Delta t$) due to a dislocation loop that began expanding on the plane $x_3 = x_3'$ at the time $t = x_3'/c_2$, that is, when it was hit by the propagating pulse. The segments of the loops that contribute to the solution at (0, 0, $\hat{x}_3$, $\hat{x}_3/c_2 + \Delta t$) must lie inside a paraboloid of revolution about the x_3 axis, shown in Fig. 2, which satifies the equation (see [2]):

$$2(\hat{x}_3-x_3)c_2\Delta t = (x_1^2+x_2^2)-c_2^2(\Delta t)^2. \tag{23}$$

For the end result we need to superpose the effects on point P due to all the dislocation loops or segments of loops that lie inside the paraboloid. Analogously as in [1, 2], we may divide the paraboloid into two regions, defined as follows:

$$\text{Region } I: \quad \hat{x}_3 - z \le x_3' \le \hat{x}_3 + \frac{c_2\Delta t}{2} \tag{24}$$

$$\text{Region } II: \quad 0 \le x_3' \le \hat{x}_3 - z \tag{25}$$

where z is $0((c_2\Delta t)^{n/n+1})$ with $n > 3/2$ and is measured from the point $P(0,0,\hat{x}_3)$. We will treat Region II first since it is the one that gives the main contribution and leave Region I for the end.

In Region II we can approximate the expressions J_1 and J_2 (given by (21) and (22), respectively) asymptotically by considering (25) and making the assumption that

$$\alpha_0 \sim 0(c_2\Delta t), \tag{26}$$

which implies that we neglect loops smaller than $0(c_2\Delta t)$ as physically too small, given the magnitude of Δt to be of the order of 10^{-9} sec.

Under (25) and (26) the limits of integration t_1, t_2, t_3, and t_4 have the aproximations

$$t_1, t_3 = \Delta t + h.o.t. \tag{27$_1$}$$

$$t_2, t_4 = \frac{2c_2(\hat{x}_3-x_3')}{D} + h.o.t. \tag{27$_2$}$$

so that k^2, given by (20), is at most $0((\Delta t)^{1/n+1})$ and $K(k) \sim \pi/2$, $E(k) \sim \pi/2$. For these values of $K(k)$, $E(k)$, and t_1, t_2, t_3, t_4, the expression J_1 of equation (21) assumes the following expansion

$$J_1 \sim \frac{2Mc_2^2(\alpha_0+Vt)(\hat{x}_3-\hat{x}_3')}{(c_2(\hat{x}_3-x_3'))^3}\left(-\frac{\pi}{2}\right)+h.o.t.$$

$$\sim \frac{-\pi VM}{c_2(\hat{x}_3 - x_3')} + h.o.t. \tag{28}$$

Also under the restrictions (25) and (26), J_2, given by equation (22), assumes the expansion

$$J_2 \sim \frac{-2\alpha_0 M}{c_2\sqrt{c_2^2t^2 - (\hat{x}_3 - x_3')^2 - (a-\alpha_0)^2}\sqrt{(a+\alpha_0)^2 - c_2^2t^2 - (\hat{x}_3 - x_3')^2}} + h.o.t. \tag{29}$$

The dislocation loops that lie initially entirely inside the paraboloid (Fig. 2) have centers located at a distance a: $0 \le a \le r_1 = s(x_3') - \alpha_0$, i.e., they lie inside a circle of radius $s - \alpha_0$, while the dislocation loops that initially intersect the paraboloid have centers located in an annulus $r_1 = s(x_3') - \alpha_0 \le a \le r_2 = s(x_3') + \alpha_0$ (Fig. 2) where $s(x_3') = \sqrt{c_2^2t^2 - (\hat{x}_3 - x_3)^2}$.

For the superposition of the effect of all dislocation loops in Region II to the point P, we integrate over the range of the location of the centers described in the foregoing. Thus from loops lying either totally inside the paraboloid (initially) or intersecting the paraboloid, the contribution at P from Region II is:

$$\int_0^{\hat{x}_3 - z} dx_3' \int_0^{s(x_3')-\alpha_0} J_1 2\pi N_L\, ada + \int_0^{\hat{x}_3 - z} dx_3' \int_{s(x_3')-\alpha_0}^{s(x_3')+\alpha_0} J_2\, 2\pi N_L\, ada \tag{30}$$

where N_L denotes the number of dislocation loops per unit volume. Substituting (28) for J_1 into the first term of (30) we have

$$\int_0^{\hat{x}_3 - z} dx_3' \int_0^{s(x_3')-\alpha_0} - \frac{C_{1313} b_1 V}{2\pi\rho\, c_2} \frac{V\pi}{c_2^2(\hat{x}_3 - x_3')} 2\pi N_L\, ada$$

$$= \int_0^{\hat{x}_3 - z} \frac{-\pi N_L\, C_{1313} b_1\, V^2}{2\rho\, c_2^3(\hat{x}_3 - x_3')} (s(x_3') - \alpha_0)^2 dx_3' + h.o.t \tag{31}$$

If we substitute (29) for J_2 into the second term of (30) we obtain

$$\int_0^{\hat{x}_3 - z} dx_3' \int_{s(x_3')-\alpha_0}^{s(x_3')+\alpha_0} - \frac{2N_L C_{1313} b_1 V\, \alpha_0 ada}{\rho c_2^2 \sqrt{s(x_3')^2 - (a-\alpha_0)^2}\ \sqrt{(a+\alpha_0)^2 - s(x_3')^2}} + h.o.t.$$

$$= \int_0^{\hat{x}_3 - z} - \frac{C_{1313}\ b_1\ V N_L \pi\alpha_0}{\rho\ c_2^2} dx_3' + h.o.t. \tag{32}$$

In Region I those loops, which after time Δt are near the point P, can create singular fields. The centers Q of these loops are initially located at $x_3' = \hat{x}_3$ and $a = a_0 \equiv \alpha_0 + V\Delta t$. For these loops the contribution at P is singular since $t_2 - t_1 = 0$ in expressions (21) and (22). From (22) it follows that for $t_1 = 0$ or $t_3 = 0$, or $t_1 = t_3$, J_2 is singular, but it can be easily seen that these singularities are integrable and give negligible contribution in superposition.

We will prove that when superposing over all the loops in the neighborhood of Q the singularity is integrable and in fact there is no contribution to the present decay from these points. Consider a loop centered at (a, x_3') such that

$$a_0 - \epsilon \le a \le a_0 + \epsilon, \qquad \hat{x}_3 - \epsilon \le x_3' \le \hat{x}_3 + \epsilon$$

where $\epsilon \sim 0(c_2\Delta t)$. The contribution of this loop can be either of the J_1 or J_2 type according to the magnitude of α_0 (here we suppose $s(\hat{x}_3) \ge \alpha_0$; the $s(\hat{x}_3) < \alpha_0$ case can be treated similarly).

By superposing the loops centered in the neighborhood of Q we have

$$\int_{\hat{x}_3 - \epsilon\, \min(a_0 - \epsilon, s(x_3') - \alpha_0)}^{\hat{x}_3 + \epsilon\, \max(a_0 + \epsilon, s(x_3') - \alpha_0)} J_1\ 2\pi\ a\ dadx_3' \tag{33$_1$}$$

or

$$\int_{\hat{x}_3 - \epsilon\, \max(a_0 - \epsilon, s(x_3') - \alpha_0)}^{\hat{x}_3 + \epsilon\, \min(a_0 + \epsilon, s(x_3') - \alpha_0)} J_2\ 2\pi\ a\ dadx_3' \tag{33$_2$}$$

In this region of integration it may be seen from (20) that $k \to 1$, so that $K(k) \sim ln(1-k^2)$ [6, p. 299] and the integrals (33$_1$) and (33$_2$) may be seen to be at most of $0(\alpha_0(\Delta t)^r)$ (with $r > 0$).

For the contribution coming from the rest of Region I the corresponding integrals may be also shown to give contributions at most of order $0(\alpha_0(\Delta t)^r)$ $(r > 0)$, since $K(k)$ is at most $ln(\Delta t)$ and $1/1-k^2$ is at most $1/\Delta t$.

Thus dislocation segments or loops lying inside Region I give negligible contributions as $\Delta t \to 0$.

To obtain the precursor decay relationship we need to differentiate (31) and (32) with respect to $\hat{x}_3$:

$$\frac{\partial}{\partial \hat{x}_3} \int_0^{\hat{x}_3 - z} \frac{-\pi N_L(x_3')C_{1313}\ b_l\ V^2}{2\rho\ c_2^3(\hat{x}_3 - x_3')} (s(x_3') - \alpha_0)^2 dx_3'$$

$$= \frac{-\pi N_L\,|_{x_3' = \hat{x}_3 - z}(\hat{x}_3 - z) C_{1313} b_1\ V_2}{2\rho\ c_2^3\ z} (\sqrt{2\ c_2 z\Delta t + c_2^2\Delta t^2 - \alpha_0^2})$$

$$+ \int_0^{\hat{x}_3 - z} N_L(x_3') \frac{\partial}{\partial \hat{x}_3}\left[\frac{(s(x_3') - \alpha_0)^2}{\hat{x}_3 - x_3'}\right] dx_3' \tag{34}$$

The main contribution of (34) comes from the first term while the integral may be seen to be bounded by a term of smaller order in Δt. Thus the leading term in (34) is

$$\frac{-\pi\ C_{1313}\ b_1\ V^2}{\rho\ c_2^2} \Delta t\ N_L|_{x_3' = \hat{x}_3 - z} = \frac{-N\, b_1 V^2}{2}\left(\frac{\Delta t}{\alpha_0}\right), \tag{35}$$

where $C_{1313} = \rho\ c_2^2$ and N denote the dislocation line length per unit volume and is equal to $2\pi\ \alpha_0\ N_L$.

Proceeding with differentiation of (32) we obtain

$$\frac{\partial}{\partial \hat{x}_3} \int_0^{\hat{x}_3 - z} - \frac{C_{1313} b\ V N_L\ \pi\ \alpha_0}{\rho\ c_2^2} dx_3' = - \frac{b_1\ V N}{2}\Big|_{x_3' = \hat{x}_3 - z} \tag{36}$$

We have therefore obtained the leading term in the precursor decay, which by adding (35) and (36) is

$$\frac{D\dot{U}_1}{D\hat{x}_3} = - \frac{b_1\ V N}{2}\left(1 + \frac{V\Delta t}{\alpha_0}\right) \tag{37}$$

where N and V are evaluated immediately behind the wave front since $z \to 0$ as $\Delta t \to 0$. For loops of radius $\alpha_0 \sim 0(c_2\Delta t)$ we can have additional contributions to the precursor decay and this may explain – partly at least – the increased value of the decay. Any other terms in $(c_2\Delta t)$ will give contributions of smaller order, and this analysis has only been carried to the leading order.

Acknowledgment

This research was supported by the National Science Foundation through a grant to the University of California, Santa Barbara.

References

1 Clifton, R. J., and Markenscoff, X., "Elastic Precursor Decay and Radiation From Nonuniformly Moving Dislocations," *Journal of the Mechanics and Physics of Solids*, Vol. 29, 1981, pp. 227-252.

2 Markenscoff, X., and Clifton, R. J., "Radiation From Expanding Circular Dislocation Loops and Elastic Precursor Decay," ASME JOURNAL OF APPLIED MECHANICS, Vol. 49, 1982, pp. 792-796.

3 Markenscoff, X., "On the Dislocation Fields in Terms of the Dynamic Green's Function," *Journal of Elasticity*, Vol. 13, 1983, pp. 237-241.

4 Love, E. H., *The Mathematical Theory of Elasticity*, Dover, New York, 1944, p. 305.

5 Mura, T., "Continuous Distribution of Moving Dislocations," *Philosophical Magazine*, Vol. 8, 1963, pp. 843-857.

6 Byrd, P. F., and Friedman, M. D., *Handbook of Elliptic Integrals for Engineers and Scientists*, 2nd Ed., Springer-Verlag, Berlin, 1971.

Neck Propagation in Tensile Tests: A Study Using Rate-Independent, Strain Hardening Plasticity

R. P. Nimmer
Mechanical Engineer.

L. C. Miller
Mechanical Engineer.

General Electric Company,
Corporate Research and Development,
Schenectady, N.Y. 12301

A J_2 yield criterion and time and temperature-independent flow theory of plasticity have been applied to study characteristic phenomena observed in tensile tests of some ductile polymers: namely a load drop immediately after yield and stable propagation of a neck along the entire length of the specimen. A trilinear stress-strain curve is used to quantify the effect of material model data on these physical observations.

Introduction

Although many polymers exhibit ductile behavior in tensile tests, the characteristics of that behavior may often be quite different than those observed for metals. During a tensile test on polycarbonate, for example, yield and neck initiation occur simultaneously at a strain of about 6.0 percent. Although Vincent [1] notes that in some polymers the cross-sectional area in such a neck may steadily decrease until failure (as is often observed in metals), in many polymers like polycarbonate the cross-sectional area actually reaches a finite minimum. After reaching this minimum, the shoulders of the neck propagate along the length of the specimen, as shown by the sequence of photos in Fig. 1, until they are finally inhibited from additional movement by the enlarged cross section near the specimen grips. The mechanics of this phenomenon, known as "cold-drawing," will be the general subject of the discussion that follows.

Robertsen [2] suggests that the cold-drawing of plastics is often characterized by two features: the shape of the load extension curve in tension and the shape of the drawn test specimen. Both of these characteristics are exhibited for polycarbonate in Fig. 1. Most of the investigations directed at cold-drawing in polymers, references [2–4] for example, have dealt primarily with the thermodynamic and molecular mechanisms that may initiate the yield process at point A in Fig. 1, rather than the mechanics of a stable, propagating neck. Vincent [1] appears to have been the first to discuss the mechanical aspects of propagating necks in polymers. He argues that the drop in load after yield at point A in Fig. 1 is related to the mechanical process of necking. Furthermore, he uses a one-dimensional construction originally applied by Considere to argue that a neck of finite cross-sectional area will propagate along the length of a specimen only if the local hardening modulus at large strain exceeds the true stress at that strain. This necking process is, of course, actually three-dimensional in nature. Regarding the decrease in load after yield, Brown and Ward [5] argue that the reduction observed in polymers cannot be explained purely on the basis of the mechanics of necking. They emphasize that during tensile tests of polyethylene terephthalate, a decrease in true stress was observed after yield. Other investigators have subsequently reported similar decreases in true stress in polycarbonate [6, 7] and polyvinyl chloride [7]. More recently, Hutchinson and Neale [8] have significantly expanded the mechanics of neck propagation with a three-dimensional analysis of the necking phenomenon in an axisymmetric tensile specimen. Using both nonlinear elastic and inelastic flow theory (both rate-independent and rate-dependent), Hutchinson and Neale reinforce Vincent's suggestion that an upturn in the true stress-strain curve leads to a termination of the localization and forces the neck to

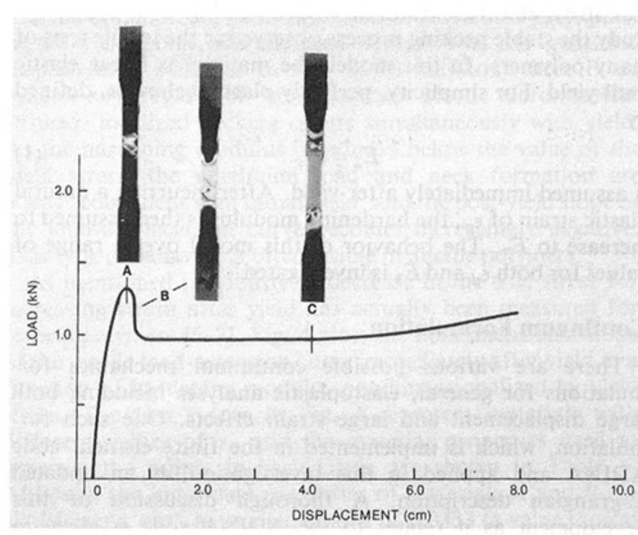

Fig. 1 Typical load-displacement behavior observed in polycarbonate tensile tests

Contributed by the Applied Mechanics Division and presented at the Winter Annual Meeting, New Orleans, La., December 9–14, 1984 of The American Society of Mechanical Engineers.

Discussion on this paper should be addressed to the Editorial Department, ASME, United Engineering Center, 345 East 47th Street, New York, N.Y. 10017, and will be accepted until two months after final publication of the paper itself in the Journal of Applied Mechanics. Manuscript received by ASME Applied Mechanics Division, September, 1983; final revision, February, 1984. Paper No. 84-WA/APM-31.

Copies will be available until August, 1985.

spread along the length of the specimen. Bagepalli [9] has also analyzed the mechanics of neck propagation in axisymmetric tensile tests of polymers and suggests a new material model which also incorporates an upturn in the true stress-strain relationship to model this behavior.

The present investigation addresses issues of mechanics with respect to two specific characteristics of cold-drawing as observed in polymers. First, immediate post-yield deformation behavior and, specifically, the drop in load which is often observed simultaneously with yield initiation in tensile tests of polymers is discussed. The relative effects of geometric (necking) instability and material (true stress versus natural strain) instability are examined. Second, rate-independent constitutive parameters governing the appearance of either an unstable, local neck or a stable, propagating neck are investigated. In addressing these issues, the finite element method including both finite deformation and plastic material behavior is applied to analyze an axisymmetric tensile specimen. With the exception of Hutchinson and Neale [8] and Bagepalli [9] previous numerical investigations [10–12] directed at the necking process have applied post-yield, hardening relationships with monotonically decreasing tangent moduli. In contrast, the current investigation provides for the appearance of an increasing tangent modulus to quantify its effect on the appearance of a propagating neck.

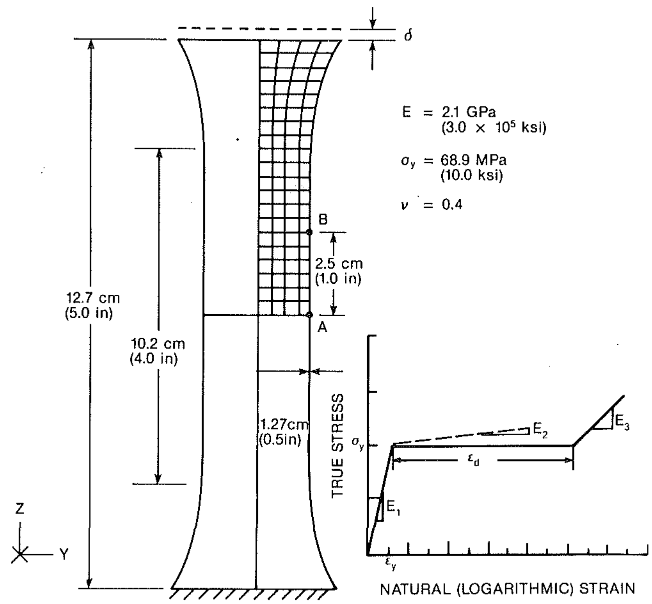

Fig. 2 Finite element model and true-stress versus natural strain relationship

Constitutive Models

Although strain rate effects are certainly important for many polymers, this investigation is limited to time and temperature-independent constitutive relations under the assumption that a clear understanding of this more simplified behavior is a logical point of depature for subsequent studies that would include these effects. The material behavior considered here is modeled as elastoplastic in nature with the yield criterion defined by a standard J_2 (von Mises) yield surface. Flow theory of plasticity is applied in the post-yield region of material behavior in conjunction with isotropic strain hardening and elastic unloading. Two simple models shown in Fig. 2 are applied to describe the relationship between effective stress and equivalent plastic strain. For the initial, post-yield stability investigation, the effective stress is related to the equivalent plastic strain through a constant hardening modulus E_2 which would be defined from uniaxial, true stress versus natural (logarithmic) strain measurements. A range of hardening moduli, E_2, varying from $-2\sigma_y$ to $+2\sigma_y$ is studied. In contrast, a trilinear relation between the true stress and true strain, also shown in Fig. 2, is applied to study the stable necking process observed in the tensile tests of many polymers. In this model, the material is linear elastic until yield. For simplicity, perfectly plastic behavior, defined by

$$E_2 = 0 \tag{1}$$

is assumed immediately after yield. After incurring a natural plastic strain of ϵ_d, the hardening modulus is then assumed to increase to E_3. The behavior of this model over a range of values for both ϵ_d and E_3 is investigated.

Continuum Formulation

There are various possible continuum mechanics formulations for general, elastoplastic analyses including both large displacement and large strain effects. One such formulation, which is implemented in the finite element code ADINA and applied in this investigation, is an updated Lagrangian description. A thorough discussion of this development as it relates to the ADINA code is given in references [13, 14]. For the purpose of describing the governing equations pertinent to the problem considered here, a more general outline is presented. The governing virtual work principle in the updated Lagrangian formulation is

$$\int_{{}^tV} ({}^{t+\Delta t}_{t}S_{ij})\,\delta({}^{t+\Delta t}_{t}\epsilon_{ij})\,dv = {}^{t+\Delta t}R \tag{2}$$

where ${}^tV$ is the volume of the body at time t, ${}^{t+\Delta t}_{t}S_{ij}$ is the second Piola-Kirchoff stress tensor at time $t+\Delta t$ referred to the configuration at time t, $\delta({}^{t+\Delta t}_{t}\epsilon_{ij})$ is the variation of the Green-Lagrange strain tensor at time $t+\Delta t$ referred to the configuration at time t, and ${}^{t+\Delta t}R$ is the external virtual work at time $t+\Delta t$. The strain at time $t+\Delta t$ with reference to the configuration at time t including large displacements can be expressed as

$${}^{t+\Delta t}_{t}\epsilon_{ij} = \frac{1}{2}\,({}_tu_{i,j} + {}_tu_{j,i}) + \frac{1}{2}\,({}_tu_{k,i})\;({}_tu_{k,j}) \tag{3}$$

where u_i are the incremental displacement components and the commas in the subscripts represent differentiation.

The elastoplastic constitutive behavior is described using the incremental flow theory of plasticity. If, for the moment, infinitesimal strains and displacements are considered, it is assumed that the total strain increment de_{ij} can be decomposed into an elastic component de^E_{ij} and a plastic component de^P_{ij}

$$de_{ij} = de^E_{ij} + de^P_{ij} \tag{4}$$

The elastic stress-strain law is then

$$d\sigma_{ij} = C^E_{ijrs}\,(de_{rs} - de^P_{rs}) \tag{5}$$

where C^E_{ijrs} represents the elastic constitutive constants. For the present problem, the von Mises yield function ${}^tF({}^t\sigma_{ij},{}^t\bar{e}^P)$ is applied with isotropic hardening where

$${}^tF({}^t\sigma_{ij},{}^t\bar{e}^P) = \frac{1}{2}\,({}^ts_{ij}\,{}^ts_{ij}) - \frac{{}^t\sigma_y\,({}^t\bar{e}^P)}{3} \tag{6a}$$

Here, s_{ij} are the deviatoric stress components, ${}^t\sigma_y$ is the current yield stress at time t and ${}^t\bar{e}^P$ is the accumulated effective plastic strain at time t

$${}^t\bar{e}^P = \int_0^t d\bar{e}^P \tag{6b}$$

For elastic behavior

$${}^tF({}^t\sigma_{ij},{}^t\bar{e}^P) < 0 \tag{7}$$

and

$$de_{ij}^P \equiv 0 \tag{8}$$

During plastic flow, the stress state must stay on the yield surface and

$$\frac{\partial^t F}{\partial^t \sigma_{ij}} \partial \sigma_{ij} + \frac{\partial^t F}{\partial e_{ij}^P} \partial e_{ij}^P \equiv 0 \tag{9}$$

The associated flow rule is then

$$\partial e_{ij}^P = {}^t\partial\lambda \frac{\partial^t F}{\partial^t \sigma_{ij}} \tag{10}$$

where ${}^t\partial\lambda$ is an infinitesimal scalar factor. Using equations (4), (5), and (9) an expression can be derived for ${}^t\partial\lambda$. Equations (5) and (10) can then be used to write an incremental constitutive relationship which can be expressed symbolically as

$$\partial\ \sigma_{ij} = {}^t C_{ijrs}^{EP} \partial\ e_{rs} \tag{11}$$

Differentiation between plastic loading and elastic unloading is made during each incremental solution by calculating a set of incremental stresses, $d\sigma'_{ij}$, using the linearized solution for the incremental displacements and the linear-elastic constitutive relation. If the total stress state ${}^{t+\Delta t}\sigma'_{ij}$ calculated by adding $d\sigma'_{ij}$ to the known stress at time t leads to the condition

$${}^{t+\Delta t}F({}^{t+\Delta t}\sigma'_{ij}, {}^t\bar{e}^P) \leq 0 \tag{12}$$

then elastic constitutive relations can be applied. If, on the other hand

$${}^{t+\Delta t}F({}^{t+\Delta t}\sigma'_{ij}, {}^t\bar{e}^P) > 0 \tag{13}$$

then plastic deformation will occur and the constitutive relations must be modified to reflect this behavior. Reference [15] outlines this procedure in detail. In the analysis that follows, this process is the same regardless of whether the hardening modulus after yield is positive or negative. For a positive hardening modulus the yield surface expands, and for a negative hardening modulus it contracts. Although this discussion has been developed for infinitesimal strains and displacements, it is directly applicable to the more general case of large deformation, elastic-plastic analysis if ${}^t\sigma_{ij}$ is replaced by the Cauchy stress tensor at time t, ${}^t\tau_{ij}$, and ∂e_{ij} is replaced by a logarithmic (or true) strain increment [14]. In this analysis, the material behavior is approximated by a multilinear stress-strain curve with an initial Young's modulus, yield point, and post-yield strain hardening modulus. Equations (2), (3), and (11) represent the equilibrium, strain-displacement, and constitutive relations, respectively, which are applied within the context of the finite element formulation for problem solution.

Finite Element Model

An axisymmetric, tensile specimen with applied displacement loading shown in Fig. 2 is modeled in this analysis using eight-noded, two-dimensional isoparametric finite elements and the nonlinear finite element code ADINA which includes the effects of finite deformation. To insure accurate results for the load-displacement and neck contraction predictions made here, the finite element size, applied, incremental displacement size and convergence tolerances were all reduced until no variation in results was observed. Figure 2 illustrates the finite element mesh used for the numerical results presented here. As can be seen in Fig. 2, the shoulder of the tensile specimen was included in the model. As a by-product of this geometry, necking was always initiated at the center of the specimen without the necessity of including any geometric or material imperfection. Except where explicitly stated in the text, the material properties used for these analyses are also listed in Fig. 2 and are representative of a ductile polymer such as polycarbonate.

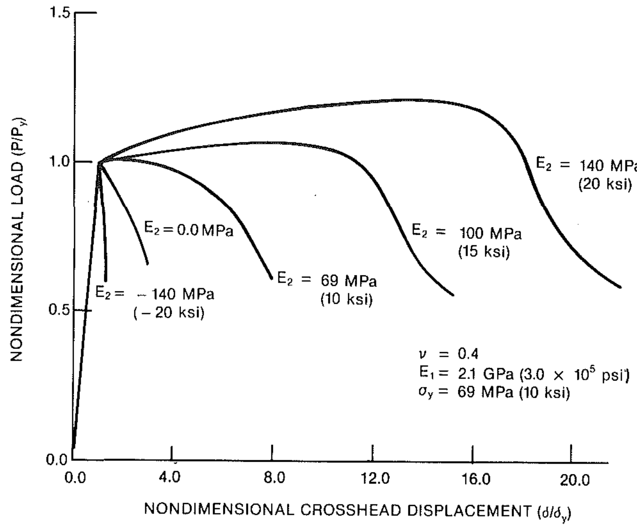

Fig. 3 Nondimensional, load-displacement curves as a function of bilinear model hardening modulus

Results and Discussion

The mechanical relationships between constitutive behavior, onset of necking, and post-yield stability of the axisymmetric tensile specimen can be studied with the simple bilinear constitutive model shown in Fig. 2. Figure 3 illustrates the load versus crosshead displacement behavior which is predicted as a function of the hardening modulus, E_2, in the bilinear constitutive model. With elastic modulus and yield stress held constant at the values listed in Fig. 2, there is a significant difference in the post-yield, load-displacement behavior as the value of E_2 is varied from $+\ 2\sigma_y$ to $-\ 2\sigma_y$. For a hardening modulus of 140 MPa (20 ksi), a value twice the yield stress, the load-displacement behavior in Fig. 3 is similar to that seen in many metals (titanium for example). As the load increases after yield, the deformation in the tensile specimen is homogeneous and plastic in nature. Based on the principal of incompressible plastic strain, it is well-known that a maximum in the load-displacement curve is expected when the true stress in the specimen reaches a value equal to the hardening modulus, $\partial(\sigma_t)/\partial(\epsilon_t)$. At that point a neck initiates and the load begins to decrease. When the hardening modulus, E_2, is reduced to 69 MPa (10 ksi), a value equal to the material's yield stress, both the load-displacement and the deformation behavior are characteristically different. The maximum in the load-displacement curve now takes place at the yield point and the load decreases as the crosshead displacement increases in Fig. 3. In addition, there is no longer any region of homogeneous plastic deformation. Instead, localized necking occurs simultaneously with yield. As the hardening modulus is reduced below the value of the yield stress, the maximum load and neck formation are always coincident with initial yield, and the post-yield slope of the load-displacement curve becomes increasingly negative. This type of behavior is often visible in ductile polymers.

As mentioned previously, a decrease in the true stress for increasing strain after yield has actually been measured for several polymers [5–7]. Fig. 4 plots the nondimensional slope of the tensile load-extension curve immediately after yield as a function of hardening modulus nondimensionalized by yield stress. The two curves in Fig. 4 represent materials with different values of ϵ_y and the material properties used to generate the points in each curve are shown in Table 1. Although the individual properties of materials A and B are all different, both have yield strains of 0.0333 (a value typical of many ductile polymers like polycarbonate). The points relating nondimensional post-yield slope $((\Delta P)\delta_y/(\Delta\delta)/P_y)$ to nondimensional, hardening modulus E_2/σ_y for materials A and B fall on the same curve. In contrast, materials C and D both have yield strains of 0.002, a magnitude more typical of metals. The data relating $((\Delta P)\delta_y/(\Delta\delta)P_y)$ to E_2/σ_y for these two materials also fall on the same curve. However, the curve for materials C and D is significantly different than the one for materials A and B. Over the range of values shown in Fig. 4, the nondimensional slope of the load-extension curve associated with a yield strain of 0.033 is much more negative than the slope of the curve for materials with a yield strain of 0.002. Regardless of yield strain value, the slope of the load-extension curve at yield is zero when E_2/σ_y is equal to one. As the nondimensional hardening modulus decreases below one, the post-yield slope of the load-extension curve becomes increasingly negative. Therefore, under the assumptions of rate-independent flow theory, there will be a decrease in load initiated simultaneously with yield for any material with a hardening modulus at yield which is less than the yield stress. For those polymers that exhibit an actual decrease in true stress after yield [5-7] the decrease in load will be even more pronounced.

Table 1 Material properties used in Fig. 4

	Material A	Materials B	Material C	Material D
E_1	2.07 GPa (3.0×10^5 psi)	20.7 GPa (3.0×10^6 psi)	207.0 GPa (3.0×10^7 psi)	20.7 GPa (3.0×10^6 psi)
ν	0.4	0.4	0.3	0.3
σ_y	68.9 MPa (10 ksi)	689.0 MPa (100 ksi)	414.0 MPa (60 ksi)	41.4 MPa (6.0 ksi)
σ_y/E_1	0.0333	0.0333	0.0020	0.0020

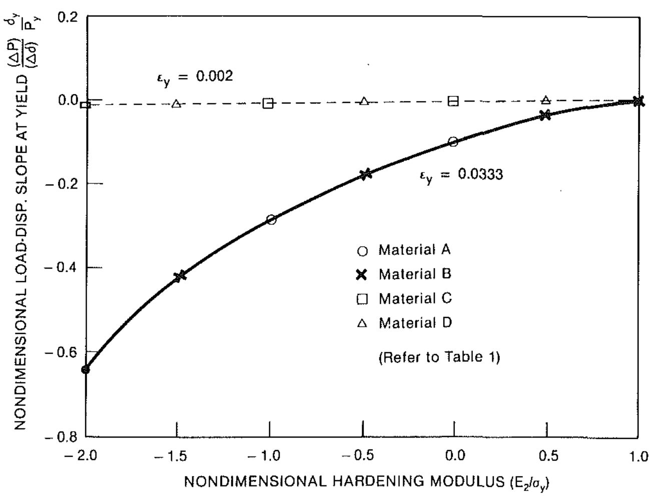

Fig. 4 Nondimensional load-displacement slope immediately following yield as a function of nondimensional hardening modulus (E_2/σ_y) and yield strain ϵ_y

For all values of E_2 considered in Fig. 3, the load decreases monotonically after initiation of a neck, the necked region remains local and the cross-sectional area of the neck decreases continuously. As previously mentioned, both Vincent [1] and Hutchinson and Neale [8] point out that an upturn in the true stress-strain relationship is necessary for a neck to stabilize and propagate. To quantify the effects of this mechanism, a trilinear relationship between the true stress and natural strain shown in Fig. 2 is applied to the axisymmetric tensile test. For this investigation, values for Young's modulus (E_1 = 2.1 GPa) and yield stress (σ_y = 69 MPa) characteristic of polycarbonate were chosen and the secondary modulus was fixed at E_2 = 0.0. The third stage modulus E_3 and the amount of natural strain between yield and third stage hardening, ϵ_d, were varied parametrically.

Figure 5 illustrates the predicted load-displacement behavior in the axisymmetric tensile specimen illustrated in Figure 2 for ϵ_d = 0.40 and a range of third stage moduli from E_3 = 0.0 to E_3 = 410 MPa (60 ksi). The case of E_3 = 0.0 corresponds to the linear elastic, perfectly plastic, bilinear case discussed earlier in Fig. 3 and shows a monotonically decreasing load associated with local unstable necking after yield. However, as E_3 is increased to values of 140 MPa and greater, the load reaches a finite minimum and then remains constant for the crosshead displacements plotted in Fig. 5. Figure 6 illustrates the effect of third-stage hardening modulus (E_3) in limiting the decrease in cross-sectional area at the neck. Here, nondimensional lateral contraction at the location of neck initiation (point A, Fig. 2) is shown as a function of nondimensional crosshead displacement. For values of E_3 less than or equal to 100 MPa (15 ksi), the lateral contraction at point A increases without bound. However, for values of E_3 greater than or equal to 140 MPa (20 ksi), there is a limiting value for the lateral contraction of the neck. For values of E_3 greater than 280 MPa (40 ksi), neither the load-displacement curve in Fig. 5, nor the lateral contraction versus displacement curve in Fig. 6 shows much variation until the

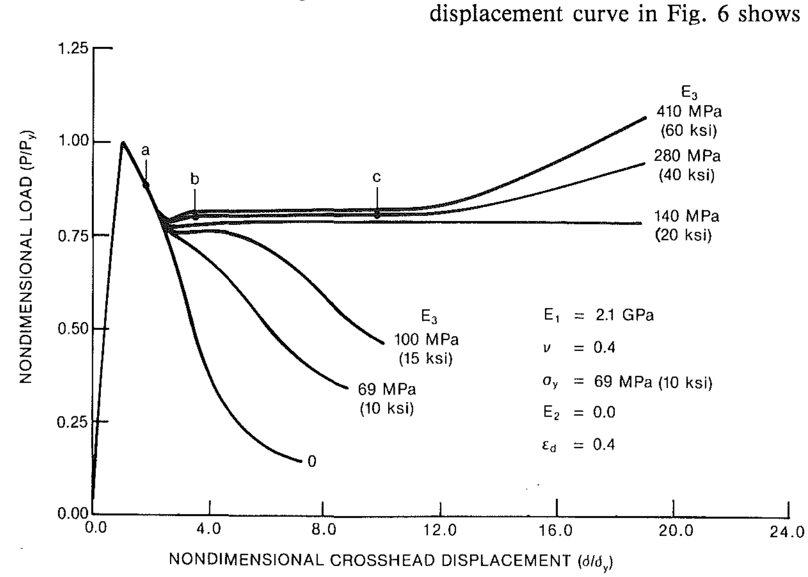

Fig. 5 Nondimensional load-displacement curves as a function of trilinear model, final-stage hardening modulus E_3

neck has propagated the entire gage length and the load begins to increase. Figures 7(*a*)–(*c*) illustrate the deformation of the specimen as predicted with the trilinear curve in Fig. 2 at three points in the load history of a material with $E_3 = 40$ ksi. The crosshead displacements and loads corresponding to these points are defined in Fig. 5. In Fig. 7(*a*), the specimen has yielded, the neck is just beginning to form, and the load is decreasing. The necking process continues with local decrease in the neck cross-sectional area until natural strains larger than $\epsilon_y + \epsilon_d$ are incurred and third-stage hardening begins in the original neck area as illustrated in Fig. 7(*b*). The increased stiffness of the material in the original neck cross section stabilizes the necking process there and forces adjacent material to yield. As this process continues, the neck propagates along the length of the specimen as shown in Fig. 7(*c*). When the neck covers the entire gage section of the specimen, the final increase in load visible in Fig. 5 will occur prior to failure.

Although there is an "upturn" in the true stress-strain relationship for any finite, positive value of E_3 in the trilinear model applied here, there is a threshold value of E_3 below which neck propagation still does not occur. For $E_3 = 69$ MPa (the yield stress of this material) the load still monotonically decreases with increasing crosshead displacement. Vincent's one-dimensional arguments suggest that a neck will begin to propagate when the tangent modulus at a given strain exceeds the true stress value at that same strain. In the present three-dimensoinal analysis of the necking process, a local minimum in the load-extension curve does appear for $E_3 = 100$ MPa (1.5 times the yield stress), as can be seen in Fig. 5. However, the reduction in cross-sectional area shown in Fig. 6 is never limited and as additional crosshead displacement is applied, the load again begins to decrease. Finally, when $E_3 \geq 140$ MPa (twice the yield stress) the load-extension behavior predicted for this test retains stability over the entire range of crosshead displacement plotted.

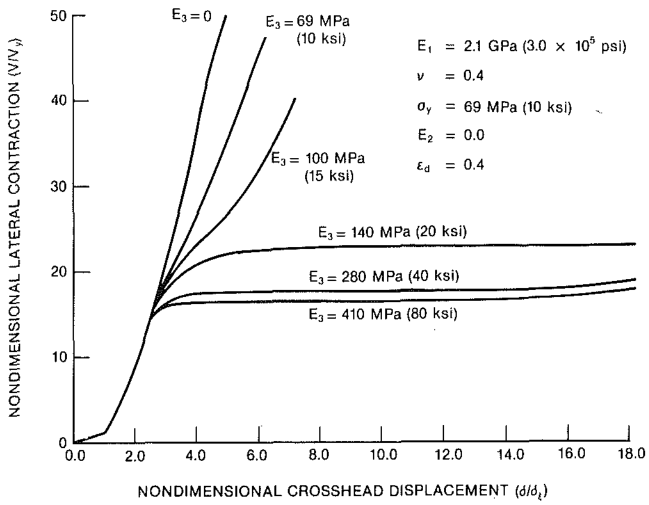

Fig. 6 Nondimensional lateral contraction at point *A* of Fig. 2 as a function of trilinear, final-stage hardening modulus E_3

Figure 4 illustrated the dependence of the post-yield slope of the nondimensional load-diplacement curve on the ratio of the hardening modulus to yield stress of a bilinear material model. In a similar manner, the ratio of the third-stage hardening modulus to yield stress is a controlling factor in establishing the stable or unstable nature of the necking process. Figure 8 shows the nondimensional load (P/P_y) as a function of nondimensional displacement (δ/δ_y). The two curves shown in Fig. 8 were predicted using the material properties shown in Fig. 2 with third-stage hardening moduli of 100 MPa (15 ksi) and 140 MPa (20 ksi). Also shown in Fig. 8 are data points predicted numerically using a trilinear material representation defined by

$$E = 4.1 \text{ Gpa } (6.0 \times 10^5 \text{ psi}) \tag{14a}$$

$$\sigma_y = 140 \text{ MPa (20 ksi)} \tag{14b}$$

$$\nu = 0.4 \tag{14c}$$

$$E_2 \equiv 0 \tag{14d}$$

$$\epsilon_d = 0.40 \tag{14e}$$

$$E_3 = \begin{cases} 210 \text{ Mpa (30 ksi)} \\ 280 \text{ MPa (40 ksi)} \end{cases} \tag{14f}$$

Since the values of yield strain and the ratio of initial hardening modulus to yield stress (E_2/σ_y) are idenical for these four materials defined in Fig. 8, the immediate post-yield slopes associated with these four different sets of material

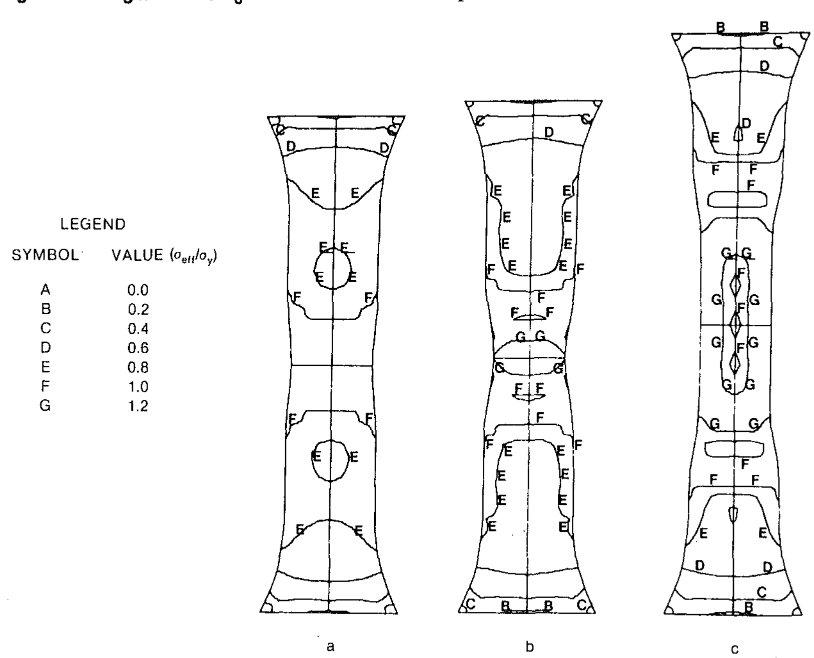

Fig. 7 Effective-stress contours during stable neck propagation

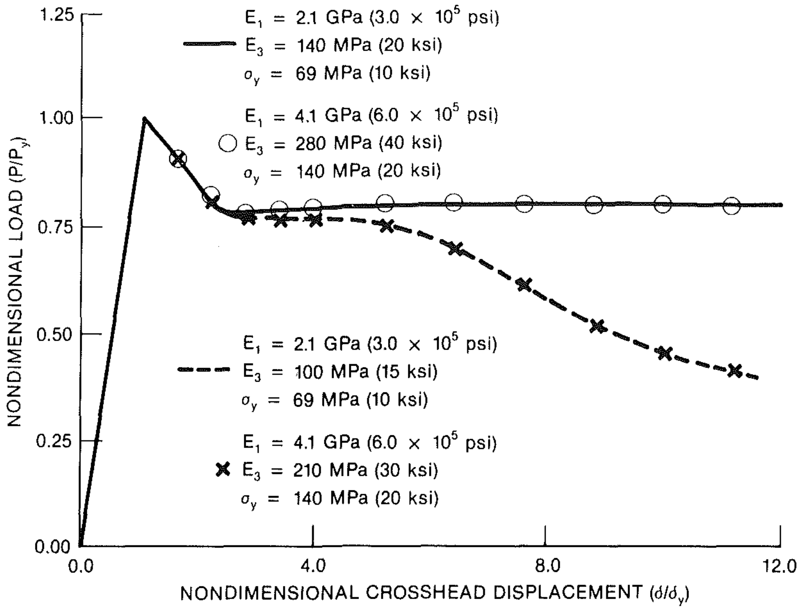

Fig. 8 Nondimensional load-displacement behavior as a function of nondimensional, final stage hardening (E_3/σ_y)

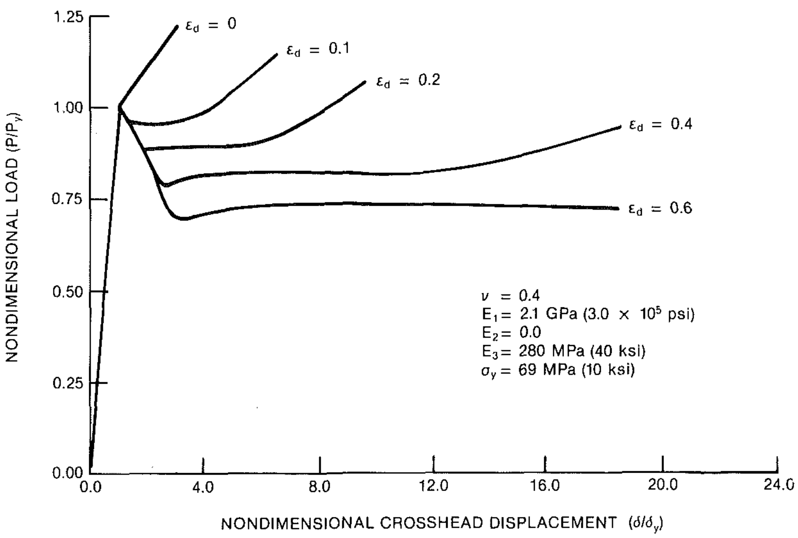

Fig. 9 Nondimensional load-displacement behavior as a function of draw strain ϵ_d

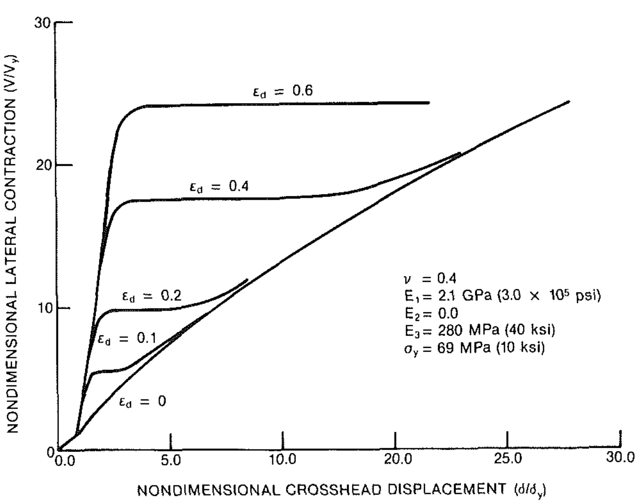

Fig. 10 Nondimensional lateral contraction as a function of draw strain ϵ_d

properties are identical. In addition, for materials with equal values of ϵ_y and E_2/σ_y, it is also clear from Fig. 8 that the very large strain, post-yield, load-displacement performance will be identical for equal values of E_3/σ_y.

Finally, Fig. 9 illustrates the effect of draw strain, ϵ_d, defined in Fig. 2, on the nondimensional load-displacement behavior of a tensile test. The curves in Fig. 9 are based on a trilinear material model defined by E_1 = 2.1 GPa, σ_y = 69 MPa, E_2 = 0, and E_3 = 280 MPa. The draw strain, ϵ_d, is varied between 0.00 and 0.60. Lower values of ϵ_d result in smaller load reductions prior to stabilization and less overall crosshead displacement prior to final stiffening. The reduced crosshead displacement at stabilization is, of course, associated with less cross-sectional area reduction in the neck, as can be seen from the curves of nondimensional lateral contraction versus nondimensional displacement in Fig. 10. For the case ϵ_d = 0, the trilinear model degenerates to a bilinear nature. Since

$$E_2 = E_3 > \sigma_y \tag{15}$$

in this case, there is neither a decrease in load nor formation of a neck immediately after yield. Instead, there is a region of homogeneous yielding which would continue until

$$\sigma_t = E_2 \tag{16}$$

at which time a maximum in the load-displacement curve would appear.

Conclusions

A J_2 yield criterion and time and temperature-independent flow theory of plasticity have been applied to study characteristic phenomena observed in tensile tests of some ductile polymers. The use of a simple, trilinear relationship between true stress and natural strain provides the advantage of a clear investigation into the mechanical effects of the parameters which govern the general shape of the constitutive relation. It is shown that for this constitutive model a decrease in load after yield does not require a negative slope in the curve relating the true stress to natural (logarithmic) strain after yield. The slope of the nondimensional load-displacement curve immediately after yield is governed by the yield strain (ϵ_y) and the ratio of true stress after yield, the slope of the load-displacement curve after yield will be more negative. Insight into whether the neck formed after yield will remain local and unstable or propagate stably along the length of the specimen requires consideration of potential increases in the hardening modulus for large strains. For simple trilinear, elastoplastic material models considered here, the local or propagating nature of a neck is determined by the ratio of third-stage hardening modulus to yield stress, E_3/σ_y. Finally, the draw strain, ϵ_d, between yield and final hardening in such a model will determine the magnitude of the drop in tensile load as well as the total amount of elongation at constant load observed in the test.

Some aspects of polymer behavior are clearly not included in the present study. For example, many polymers are associated with yield criteria that show hydrostatic stress dependence. In addition, time and temperature effects are often substantial. Finally, the third stage-hardening, which has been shown to be so important in this study, has been explained elsewhere using a mechanism of polymer chain orientation raising questions of anisotropy which are not treated within the context of this model. However, it is clear that many of the characteristic phenomena associated with yield, neck formation, and cold drawing of ductile plastics can be predicted within the context of time and temperature-independent flow theory of plasticity. The basic mechanisms behind this observed behavior in tensile tests will also have significant effects on performance in energy absorption applications as well as suitability for cold forming processes.

References

1 Vincent, P. I., "The Necking and Cold-Drawing of Rigid Plastics," *Polymer*, Vol. 1, Mar. 1960, pp. 7–19.

2 Robertsen, R. E., "On the Cold-Drawing of Plastics," *Journal of Applied Polymer Science*, Vol. 7, No. 2, Mar.–Apr. 1963, pp. 443–450.

3 Müller, I. H., and Jäckel, "Energie-Bilanz bei Kallverstreckung," *Kolloid Zeit*, Vol. 129, Dec. 1952, pp. 145–146.

4 Marshall, I., and Thompson, A. B., "The Cold-Drawing of High Polymers," *Proc. R. Soc. London*, Series A, Vol. 221, Feb. 1954, pp. 541–557.

5 Brown, N., and Ward, J. M., "Load Drop at the Upper Yield Point of a Polymer," *Journal of Polymer Science: Part A-2*, Vol. 6, No. 3, Mar. 1968, pp. 607–620.

6 Theocaris, P. S., and Hajiiossiph, C., "Strain Analysis of Neck Formation and Propagation in Glassy Polymers," *Engineering Fracture Mechanics*, Vol. 12, No. 2, 1979, pp. 241–252.

7 Halden, G. W., and Lo, Y. C., "The Solid-Phase Flow Behavior of Ductile Thermoplastics," *Proceedings of the 1983 ANTEC*, Chicago, May 2–5, Society of Plastics Engineers, Brookfield Center, Conn., 1983, pp. 366–367.

8 Hutchinson, J. W., and Neale, K. W., "Neck Propagation," *Journal of Mech. Phys. Solids*, Vol. 31, No. 5, 1983, pp. 405–426.

9 Bagepalli, B. S., "Finite Strain, Elastic-Plastic Deformation of Glassy Polymers," Doctor of Science Thesis, Department of Mechanical Engineering, Massachusetts Institute of Technology, Cambridge, Mass., Feb., 1984.

10 Chen, W. H., "Necking of a Bar," *International J. of Solids and Structures*, Vol. 7, No. 7, July 1971, pp. 685–717.

11 Needleman, A., "A Numerical Study of Necking in Circular Cylindrical Bars," *J. of Mech. Phys. Solids*, Vol. 20, No. 2, May 1972, pp. 111–127.

12 Norris, D. M., Jr., Moran, B., Scudder, J. K., and Quinones, D. F., "A Computer Simulation of the Tension Test," *J. of Mech. Phys. Solids*, Vol. 26, No. 1, Feb. 1978, pp. 1–19.

13 Bathe, K. J., Ramm, E., and Wilson, E. L., "Finite Element Formulations for Large Deformation Dynamic Analysis," *International J. for Num. Meth. in Eng.*, Vol. 9, No. 2, 1975, pp. 353–386.

14 Bathe, K. J., Snyder, M. D., Cimento, A. P., and Rolph, W. D., III, "On Some Current Procedures and Difficulties in Finite Element Analysis of Elasto-Plastic Response," *Computers and Structures*, Vol. 12, No. 4, 1980, pp. 607–624.

15 Bathe, K. J., "Inelastic Material Behavior With Special Reference to Elasto-Plasticity and Creep," *Finite Element Procedures in Engineering Analysis*, Prentice-Hall, Englewood Cliffs, N.J. 1982, pp. 386–396.

N. Sugimoto
Research Associate.

Y. Yamane
Graduate Student.

T. Kakutani
Professor.

Department of Mechanical Engineering,
Faculty of Engineering Science,
Osaka University,
Toyonaka, Osaka 560, Japan

Oscillatory Structured Shock Waves in a Nonlinear Elastic Rod With Weak Viscoelasticity[1]

The propagation of longitudinal shock waves in a thin circular viscoelastic rod is investigated theoretically as the counterpart of the torsional shock waves previously considered in [1, 2]. Assuming a "nearly elastic" rod, the approximate equation is first derived by taking account of not only the finite deformation but also the lateral contraction or dilatation of rod. The latter gives rise to the geometrical dispersion, which is taken in the form of Love's theory for an elastic rod. Taking two typical relaxation functions, the structures of the steady shock waves are investigated in detail, one being the exponential function type and the other the power function type. The effect of geometrical dispersion is emphasized. Finally a brief discussion is included on the simplified evolution equations for a far field behavior.

1 Introduction

Viscoelastic waves exhibit not only dissipation but also dispersion.[2] In an unbounded body, this dispersion results from the viscoelastic properties of materials themselves. In a bounded body, however, there appears the geometrical dispersion in addition to the material one. The former dispersion, which results from the presence of a boundary, plays an important role different from the material dispersion. This paper considers the propagation of longitudinal shock waves in a thin circular viscoelastic rod as the counterpart of the torsional shock waves previously treated in [1, 2].[3] Emphasis is placed on the effect of geometrical dispersion which does not appear in the torsional case. It is considered rather exceptional that the torsional waves are geometrically nondispersive in spite of the presence of the boundary.[4]

Suppose the same thin circular viscoelastic rod as considered in [1, 2] is subject to a small but finite longitudinal deformation along its axis. The "nearly elastic" behavior is stipulated by the constitutive equations in which the elastic response is taken up to the second order in strain, while the viscoelastic one is taken in the form of the linear hereditary integral. After the similar procedure to that developed in [1], the approximate equation is first derived. The free lateral surface of the rod allows a contraction or dilatation of a cross section, which gives rise to the geometrical dispersion. This effect is included in the form of Love's theory for an elastic rod [4].

Assuming the same two types of relaxation functions as those considered in [2], the structures of the steady shock waves are investigated in detail; one is the exponential function type corresponding to the Maxwell-Voigt model and the other the power function type. A comparison is made between the effect of geometrical dispersion and that of material one on the shock profiles. Finally the derivation of the simplified evolution equations for a far field behavior is discussed. Appendix 3 includes a brief discussion on the plausible experimental conditions for the shock wave propagation.

2 Formulation of the Problem

The formulation of the present problem is the same as that used in [1]. But since no circumferential displacement is assumed here, the basic equations are simplified considerably. Using the same notation as in [1], the dimensionless equations of motion are given in the r, θ, z cylindrical coordinates by

$$u_{r,tt} = (rL_{rr})_{,r}/r - L_{\theta\theta}/r + L_{rz,z}, \tag{1}$$

$$u_{z,tt} = (rL_{zr})_{,r}/r + L_{zz,z}, \tag{2}$$

with

$$\begin{bmatrix} L_{rr} & 0 & L_{rz} \\ 0 & L_{\theta\theta} & 0 \\ L_{zr} & 0 & L_{zz} \end{bmatrix} = \begin{bmatrix} 1+u_{r,r} & 0 & u_{r,z} \\ 0 & 1+u_r/r & 0 \\ u_{z,r} & 0 & 1+u_{z,z} \end{bmatrix} \begin{bmatrix} K_{rr} & 0 & K_{rz} \\ 0 & K_{\theta\theta} & 0 \\ K_{rz} & 0 & K_{zz} \end{bmatrix}, \tag{3}$$

[1] A part of this paper was presented at the IUTAM symposium on "Nonlinear Deformation Waves" held at Tallinn, Estonia U.S.S.R. in 1982.

[2] Waves are said, in a wide sense, to exhibit dispersion when a phase velocity depends on a frequency (or a wave number). Then dispersion includes both dissipation and "pure dispersion." By dispersion here, however, we mean "pure dispersion" and distingush it from dissipation.

[3] By a "shock wave" in this paper, we mean a smooth transition layer caused intrinsically by the *nonlinearity* (see also the footnote 1 in [1, 2]).

[4] Since the thin rod, i.e., long wave is concerned, only the lowest mode is selected in [1, 2]. In addition to this nondispersive mode, of course, there exist the dispersive higher modes [3].

Contributed by the Applied Mechanics Division for publication in the JOURNAL OF APPLIED MECHANICS.

Discussion on this paper should be addressed to the Editorial Department, ASME, United Engineering Center, 345 East 47th Street, New York, N.Y. 10017 and will be accepted until two months after final publication of the paper itself in the JOURNAL OF APPLIED MECHANICS. Manuscript received by ASME Applied Mechanics Division, November, 1983; final revision, February, 1984.

where u_r and u_z are, respectively, the r and z components of the displacement vector and L_{ij} ($\neq L_{ji}$; $i \neq j$) and K_{ij} ($=K_{ji}$) (i, $j=r$, θ, z) are Lagrangian and Kirchhoff's stress tensors, respectively. A partial differentiation is designated by a comma ",", t being the time. All quantities appearing here and hereafter have been normalized by appropriate characteristic values; a density is normalized by ρ_0 in the reference state, a length scale by a characteristic length L associated with a thickness of a transition layer, and a velocity by $V = (S/\rho_0)^{1/2}$, S being a characteristic modulus. Also the time and the stress are naturally normalized by L/V and S, respectively. In Appendix 3, some possible choices for these quantities are shown. In (1)–(3), we note that $K_{r\theta}$ and $K_{\theta z}$ vanish from the axisymmetry with $u_\theta = 0$ so that $L_{r\theta}$, $L_{\theta r}$, $L_{\theta z}$, and $L_{z\theta}$ also vanish.

The constitutive equations for the "nearly elastic" solids are given in terms of Lagrangian strain tensor E_{ij} as

$$\begin{aligned} K_{ij} &= k_1 E_{mm}\delta_{ij} + k_2 E_{ij} + (l_1 E_{mm} E_{nn} \\ &\quad + l_2 E_{mn} E_{mn})\delta_{ij} + l_3 E_{mm} E_{ij} + l_4 E_{im} E_{mj} \\ &\quad + \gamma \int_{-\infty}^{t} [K_1(t-t_1) E_{mm,t_1}\delta_{ij} + K_2(t-t_1) E_{ij,t_1}] dt_1 \\ &\quad + 0(E_{ij}^3\ \gamma E_{ij}^2), (i, j = r, \theta, z), \end{aligned} \tag{4}$$

where k_i ($i=1$, 2) and l_i ($i=1$, 2, 3, 4) are the elastic moduli in the equilibrium state and γ is a small parameter ($0 < \gamma << 1$) for a measure of weak viscoelasticity. Here the summation convention is used and t_1 implies the time variable in the past. For the present problem, E_{ij} are given by

$$2E_{rr} = 2u_{r,r} + (u_{r,r})^2 + (u_{z,r})^2, \quad 2E_{\theta\theta} = 2u_r/r + (u_r/r)^2,$$

$$2E_{zz} = 2u_{z,z} + (u_{r,z})^2 + (u_{z,z})^2,$$

$$2E_{rz} = u_{r,z} + u_{z,r} + u_{r,r}u_{r,z} + u_{z,r}u_{z,z}$$

and

$$E_{r\theta} = E_{\theta z} = 0. \tag{5}$$

The relevant boundary conditions for the free lateral surface are given by

$$L_{rr} = L_{zr} = 0, \qquad \text{at} \quad r = \epsilon, \tag{6}$$

or equivalently by

$$K_{rr} = K_{rz} = 0, \qquad \text{at} \quad r = \epsilon, \tag{7}$$

where ϵ denotes the normalized radius of the rod, which is assumed to be sufficiently small compared with unity ($0 < \epsilon << 1$). The boundary conditions at both infinite ends will be specified later.

3 Derivation of Approximate Equation

A derivation of the approximate equation is quite similar to that used in [1]. In addition to the two small parameters ϵ and γ ($0 < \epsilon$, $\gamma << 1$) designating, respectively, the thinness of rod and the weakness of viscoelasticity, we introduce another small parameter δ ($0 < \delta << 1$), which measures the magnitude of characteristic axial displacement (or strain). These parameters are mutually independent and their lowest-order terms are assumed more prominent than any other cross terms among them. Making use of these parameters as a guideline in reduction of the basic equations, we seek the displacement in the power series expansion of the radial coordinate r (see Appendix 1 in [1]):

$$u_r = \delta(u_r^{(1)} r + u_r^{(3)} r^3 + \ldots),$$

$$u_z = \delta(u_z^{(0)} + u_z^{(2)} r^2 + u_z^{(4)} r^4 + \ldots), \quad 0 \le r \le \epsilon, \tag{8}$$

where the coefficients of expansion are functions of z and t and r should be regarded as $O(\epsilon)$. Now that δ indicates the order of deformation under the proper normalization, each coefficient and its derivatives with respect to z and t are assumed to be of $O(1)$. Here it should be noted that because the expansion (8) is made with respect to r, the coefficients involve the small parameters ϵ, δ, and γ in addition to z and t.

Introducing (8) into (5), (4), and (3), the terms are ordered with respect to the two parameters δ and γ together with the radial coordinate r. In Appendix 1, we only give the explicit form of K_{ij}. First, applying the boundary conditions (7), we have readily the lowest- order expressions for $u_r^{(1)}$ and $u_z^{(2)}$ in terms of $u_z^{(0)}$:

$$u_r^{(1)} = -k_1/(2k_1 + k_2) u_{z,z}^{(0)} + O(\epsilon^2, \delta, \gamma) = -\sigma u_{z,z}^{(0)} + 0(\epsilon^2, \delta, \gamma),$$

$$u_z^{(2)} = -u_{r,z}^{(1)}/2 + O(\epsilon^2, \delta, \gamma) = \sigma u_{z,zz}^{(0)}/2 + O(\epsilon^2, \delta, \gamma), \tag{9}$$

where σ [$\equiv k_1/(2k_1 + k_2)$] denotes Poisson's ratio. Substituting $u_r^{(1)}$ into L_{zz} and taking the lowest-order terms of $0(\delta)$ only, we have the equation for $u_z^{(0)}$ from (2):

$$\frac{\partial^2 u_z^{(0)}}{\partial t^2} = E \frac{\partial^2 u_z^{(0)}}{\partial z^2} + 0(\epsilon^2, \delta, \gamma), \tag{10}$$

where E denotes Young's modulus defined by $E \equiv (3k_1 + k_2)k_2/(2k_1 + k_2) = (1+\sigma)k_2$. This well-known equation describes the lowest-order behavior of $u_z^{(0)}$ in z and t.

Next evaluating the neglected terms of $O(\epsilon^2, \delta, \gamma)$ in (10), we derive the approximate equation that takes account of the effect of geometrical dispersion, finite deformation, and viscoelasticity. To do so, L_{zz} and L_{zr} in (2) are specified up to the next higher-order terms of $O(\delta\epsilon^2, \delta^2, \delta\gamma)$ and of $O(\delta\epsilon^3, \delta^2\epsilon, \delta\epsilon\gamma)$, respectively. But so far as our present purpose to derive the equation is concerned, the explicit form of L_{zr} is unnecessary if an averaged form of (2) over a cross section is used. Indeed integrating (2) from $r = 0$ to $r = \epsilon$ after multiplying by r, L_{zr} is removed by the boundary condition. Then we have the equation for the balance of the total axial momentum over the cross section:

$$\int_0^\epsilon u_{z,tt} r\, dr = \int_0^\epsilon L_{zz,z} r dr. \tag{11}$$

For the evaluation of L_{zz} and therefore K_{zz} up to $O(\delta\epsilon^2, \delta^2, \delta\gamma)$, we must specify $u_r^{(1)}$ up to the next higher-order terms and $u_r^{(3)}$ to the lowest. Although this procedure is a little involved, they are straightforwardly obtained from the equation of motion (1) and the boundary condition (7). Using (9), it is found that L_{rr} and $L_{\theta\theta}$ are of $O(\delta\epsilon^2, \delta^2, \delta\gamma)$, while L_{rz} of $O(\delta\epsilon^3, \delta^2\epsilon, \delta\epsilon\gamma)$. The lowest-order terms in (1) are of $O(\delta\epsilon)$. From this order, we have after some calculation,

$$u_r^{(3)} = -\frac{\sigma(1-2\sigma^2)}{8k_2(1-\sigma^2)} u_{z,ttz}^{(0)} + 0(\epsilon^2, \delta, \gamma), \tag{12}$$

where the relations (9) and (10) have been used to express $u_r^{(3)}$ in terms of $u_z^{(0)}$ only. Also using $K_{rr} = 0$ at $r = \epsilon$ and (12), we evaluate

$$\begin{aligned} u_r^{(1)} &= -\sigma u_{z,z}^{(0)} + \epsilon^2 \frac{\sigma(1-2\sigma)(3-2\sigma^2)}{8k_2(1-\sigma^2)} u_{z,ttz}^{(0)} \\ &\quad - \frac{\delta}{k_2}\Bigg[\frac{\sigma E}{2} + (1-2\sigma)^3 \\ &\quad l_1 + (1-2\sigma)(1+2\sigma^2) l_2 - \sigma(1-2\sigma)^2 l_3 \\ &\quad + \sigma^2(1-2\sigma) l_4\Bigg] (u_{z,z}^{(0)})^2 \\ &\quad - \frac{\gamma}{k_2}\int_{-\infty}^{t} [(1-2\sigma)^2 K_1(t-t_1) \\ &\quad - \sigma(1-2\sigma) K_2(t-t_1)] u_{z,zt_1}^{(0)} dt_1 \\ &\quad + O(\text{terms of higher order than } \epsilon^2, \delta, \gamma). \end{aligned} \tag{13}$$

By using these expressions, L_{zz} can be evaluated in terms of $u_z^{(0)}$ up to $O(\delta\epsilon^2, \delta^2, \delta\gamma)$. Substituting it into (11) and retaining the terms of $O(\epsilon^2, \delta, \gamma)$, we have finally the approximate equation for $u_z^{(0)}$:

$$\frac{\partial^2 u_z^{(0)}}{\partial t^2} = E\frac{\partial^2 u_z^{(0)}}{\partial z^2} + \frac{\epsilon^2\sigma^2}{2}\frac{\partial^4 u_z^{(0)}}{\partial t^2 \partial z^2} + \delta C\frac{\partial}{\partial z}\left(\frac{\partial u_z^{(0)}}{\partial z}\right)^2$$

$$+\gamma\frac{\partial}{\partial z}\int_{-\infty}^{t} K(t-t_1)\frac{\partial}{\partial t_1}\left(\frac{\partial u_z^{(0)}}{\partial z}\right)dt_1$$

$+O$(terms of higher order than ϵ^2, δ, γ) with

$$C = 3E/2 + (1-2\sigma)^3 l_1 + (1-2\sigma)(1+2\sigma^2)(l_2+l_3) + (1-2\sigma^3)l_4,$$

and

$$K(t) = (1-2\sigma)^2 K_1(t) + (1+2\sigma^2)K_2(t). \tag{14}$$

Here the effect of geometrical dispersion is taken in the form of the fourth-order derivative, which is nothing but Love's theory for an elastic rod [4]. The constant C is determined by the nonlinear elastic behavior which may be positive or negative depending on the magnitude of the second-order elastic moduli l_i (i = 1, 2, 3, 4), while $K(t)$ denotes the stress relaxation function. Strictly speaking, $E + \gamma K(t)$ is equivalent to the tensile stress relaxation function $Y(t)$ in the linear viscoelasticity. Indeed since $Y(t) = 9G(t)B(t)/[G(t)+3B(t)]$ where $G(t)$ and $B(t)$ are, respectively, the shear stress and the bulk relaxation functions [5], the equivalence is seen by setting $G(t) = [k_2 + \gamma K_2(t)]/2$ and $B(t) = [3k_1 + k_2 + \gamma(3K_1 + K_2)]/3$ and taking the terms up to $O(\gamma)$. In the following analysis, two types of relaxation functions treated in [2] are considered for $K(t)$:

$$\text{Type I:} \qquad K(t) = \exp(-\kappa t), \tag{15}$$

$$\text{Type II:} \qquad K(t) = t^{-\nu}, \ (0<\nu<1), \tag{16}$$

where $\kappa^{-1}(>0)$ implies a characteristic relaxation time.

Here we examine the linear dispersion relation of (14) for both types. Assuming $u_z^{(0)}$ in the form of $\exp[i(kz-\omega t)]$, k and ω being a wave number and a frequency, respectively, the phase velocity c $(=\omega/k)$ for Type I is given by $c^2 = E-(\epsilon\sigma\omega)^2/2+\gamma/(1+i\kappa/\omega)$, while for Type II, c is given by $c^2 = E-(\epsilon\sigma\omega)^2/2+\gamma\Gamma(1-\nu)(-i\omega)^\nu$, $\Gamma(1-\nu)$ being the gamma function. For the low frequency limit $\omega\to 0$, c approaches the equilibrium sound speed $E^{1/2}$ for both types. For the other high frequency limit $\omega\to\infty$, the geometrical dispersion becomes infinitely large. But within the present theory for the thin rod, a wavelength $2\pi/k$ should be sufficiently long compared with ϵ and therefore $\omega \sim E^{1/2}k << O(\epsilon^{-1})$. In other words, we are concerned with the weak geometrical dispersion and the strong case is excluded. Thus if ω is taken large but still less than ϵ^{-1}, c is given by $c^2 = E-(\epsilon\sigma\omega)^2/2+\gamma$ for Type I ($\kappa << \omega << \epsilon^{-1}$), whereas for Type II, it increases indefinitely by the material dispersion. Thus a notion of the instantaneous sound speed loses its meaning in the present theory. This should be compared with the case of the torsional waves [2].

4 Structure of Steady Shock Waves

We consider the steady shock solutions to equation (14). Let a shock wave propagate into the unstrained state far ahead ($z\to\infty$) and let a constant equilibrium strain state prevail far behind the wave ($z\to-\infty$). Assuming that $u_z^{(0)}$ depends on z and t only through $\eta = t - z/\lambda$, $\lambda(>0)$ being a constant representing a shock velocity, it follows from (14) that

$$Vw - w^2 - \mu'\frac{d^2 w}{d\eta^2} = \int_{-\infty}^{\eta} K(\eta-\eta_1)\frac{dw}{d\eta_1}d\eta_1, \tag{17}$$

with the boundary conditions

$$w\to 0 \text{ as } \eta\to-\infty, \quad \text{and} \quad w\to w_\infty \ (=\text{const.}) \text{ as } \eta\to\infty,$$

where $w \equiv -\delta C/(\gamma\lambda)du_z^{(0)}/d\eta$, $\bar{V} \equiv (\lambda^2-E)/\gamma$, and $\mu' \equiv (\epsilon\sigma)^2/(2\gamma)$. If $e_\infty \equiv -\lambda^{-1}(du_z^{(0)}/d\eta)_{\eta=\infty}$ is taken as a strength of the shock wave,[5] w_∞ is given by $(\delta/\gamma)Ce_\infty$. It should be noted that for the same w_∞, which will be shown later to be positive, the difference in sign of C results in physically the compression for $C<0$ for the expansion for $C>0$.

4.1 Existence Conditions of Steady Shock Waves. Following the same way as in [2], we first examine necessary conditions for the existence of steady shock waves. Assuming a finite equilibrium value w_∞ at $\eta=\infty$, we integrate (17) after multiplying it by $dw/d\eta$. Then we have

$$\frac{V}{2}w_\infty^2 - \frac{1}{3}w_\infty^3 = (2\pi)^{1/2}\int_{-\infty}^{\infty}\hat{K}(y)\,|\hat{w}'(y)|^2 dy = A, \tag{18}$$

where $\hat{w}'(y)$ and $\hat{K}(y)$ denote, respectively, the Fourier transform of $dw/d\eta$ and $K(|\eta|)h(\eta)$ [2], $h(\eta)$ being a unit step function, and A is given by

$$A = \int_{-\infty}^{\infty}\frac{\kappa}{y^2+\kappa^2}\,|\hat{w}'(y)|^2 dy > 0 \qquad \text{for Type I}, \tag{19}$$

and

$$A = \Gamma(1-\nu)\sin\left(\frac{\pi\nu}{2}\right)\int_{-\infty}^{\infty}|y|^{\nu-1}\,|\hat{w}'(y)|^2 dy > 0, \qquad \text{for Type II}. \tag{20}$$

On the other hand, first differentiating (17) with respect to η and multiplying it by w, we also integrate to have

$$\frac{V}{2}w_\infty^2 - \frac{2}{3}w_\infty^3 = -A. \tag{21}$$

If A remains finite, then it is found from (18) and (21) that $w_\infty = V$ and $A = V^3/6 > 0$. For the existence of A, the asymptotic behavior of $\hat{w}'(y)$ as $y\to 0$ and $|y|\to\infty$ is responsible. For the limit $y\to 0$, $\hat{w}'$ approaches $w_\infty/(2\pi)^{1/2}$ and the integral remains finite there. For the other limit as $|y|\to\infty$, $\hat{w}'(y)$ behaves at most $|y|^{-2}$ because only a smooth solution is possible in (17) owing to the second derivative. Thus A is found to exist. Since A is positive, V and w_∞ must be positive. Hence in the following analysis, it is assumed that V is positive. From this, the velocity is always greater than the equilibrium sound speed $E^{1/2}$ and it becomes faster as the strength of shock wave w_∞ (or e_∞) increases, i.e., $\lambda^2 = E + \gamma w_\infty = E + \delta C e_\infty > E$.

4.2 Exponential Function Type. In this case, equation (17) is reduced to the following differential equation:

$$\mu\frac{d^3 w}{d\zeta^3} + \mu\frac{d^2 w}{d\zeta^2} + (2w - V + 1)\frac{dw}{d\zeta} - (V-w)w = 0, \tag{22}$$

where $\zeta = \kappa\eta$ and the effects of geometrical dispersion μ' and of the characteristic relaxation time κ^{-1} are combined into one parameter defined by $\mu = \kappa^2\mu'$. Because analytical solutions of (22) are difficult to obtain, their asymptotic behavior is first discussed and numerical solutions are sought later.

The equilibrium points of (22) are $w = 0$ and $w = V = w_\infty$, which should correspond to the boundary conditions at $\eta = -\infty$ and $\eta=\infty$, respectively. To see the asymptotic behavior about $w = 0$, we linearize (22) about it and assume w in the form of $\exp(p\eta)$. Then the characteristic equation for p is readily obtained:

$$D(p) = (\mu p^2 - V)(p+1) + p = \mu p^3 + \mu p^2 - (V-1)p - V = 0. \tag{23}$$

The investigation of roots clarifies the asymptotic behavior in

[5] Note that e_∞ is not exactly equivalent to E_{zz} at $z = -\infty$ [$E_{zz} = \delta e_\infty + (\delta e_\infty)^2/2$].

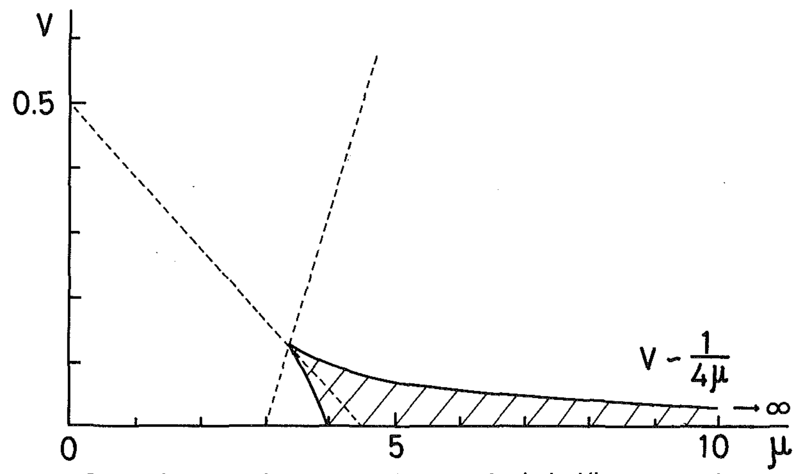

Fig. 1 Conditions for three negative roots; the dashed lines represent $\mu = 3(V+1)$ and $\mu = 9/2 - 9V$, respectively

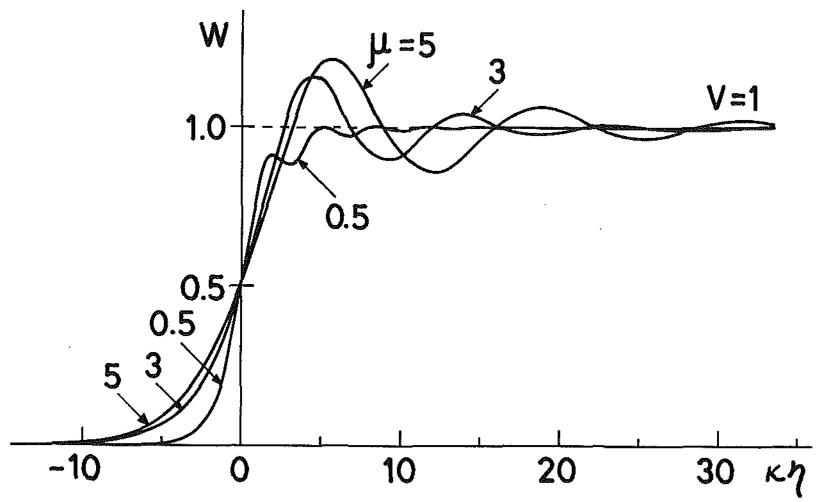

Fig. 2 Shock profiles for Type I with $V = 1$ and the various values of μ

the three-dimensional phase space (w, $dw/d\eta$, $d^2w/d\eta^2$) [6]. Since V is positive, it is clear that (23) has always one positive root and that the other two roots are both negative or complex conjugate pair. If $D(p)$ has a positive maximal value, i.e., the condition

$$\mu^{1/2}(9/2+9V-\mu) \leqq [\mu+3(V-1)]^{3/2}, \tag{24}$$

is satisfied, the two roots are negative. Then the equilibrium point $w = 0$ is a saddle point. Otherwise the two roots are complex conjugate whose real part is negative because the sum of the three roots is -1. Then the point $w = 0$ is a saddle-focus. In either case, there always exists one branch satisfying the boundary condition at $\eta = -\infty$. Here it should be remarked that if μ is set equal to zero in (22), it is easily found that there is no asymptotic branch for $V \geqq 1$. In this case, the nonuniformity between $\mu = 0$ and $\mu \to 0$ occurs. This just corresponds to the torsional case with $U \geqq 1$ in which the discontinuous solution is introduced to fit the boundary condition at $\eta = -\infty$ [2]. But when the geometrical dispersion exists, no matter how small it may be, a discontinuous solution is excluded and there always exists one asymptotic branch from $\eta = -\infty$. This is the essentially important effect of geometrical dispersion which has not met in the torsional case.

For the other equilibrium point $w = V = w_\infty$, on the other hand, linearizing of (22) about $w = V$ yields the characteristic equation:

$$D(p) = (\mu p^2 + V)(p+1) + p$$
$$= \mu p^3 + \mu p^2 + (V+1)p + V = 0. \tag{25}$$

It is found that for $V>0$, (25) has three negative roots greater than -1 or one negative root greater than -1 and complex conjugate pair whose real part is negative. If the condition

$$\mu^{1/2}\, |9/2 - 9V - \mu| \leqq [\mu - 3(V+1)]^{3/2}, \tag{26}$$

is satisfied (shaded area in Fig. 1), all the three roots are negative and greater than -1. Then the point w_∞ is a nodal point. Otherwise it becomes a focal point. In each case, all three branches can satisfy the boundary condition at $\eta = \infty$. Thus the asymptotic analysis suggests that for $V>0$, a solution increases exponentially from $\eta = -\infty$ and tends to the equilibrium value w_∞ as $\eta \to \infty$. From the behavior around w_∞, the complex roots imply the oscillatory profile, while the negative roots imply the monotonic profile. In the case with one negative root and complex conjugate pair, there may appear a monotonic profile, but an oscillatory profile appears generally because all three branches may be excited. Hence the geometrical dispersion makes profiles oscillatory. This effect should be distinguished from that of material dispersion which only makes profiles monotonic just as in torsional case [2].

We now show the numerical solutions of (22). In Fig. 2, the typical shock profiles are shown for $w_\infty = V = 1$ and $\mu = 0.5$, 3, and 5, respectively, where the coordinate axis is chosen so that w may take $w_\infty/2$ at $\eta = 0$. As is suggested from the foregoing asymptotic arguments, the oscillatory shock profiles appear. They first step up exponentially from $\eta = -\infty$, then overshoot the equilibrium value w_∞, and approach exponentially w_∞ while oscillating around it. As μ increases, the oscillation becomes prominent, while as it decreases, the

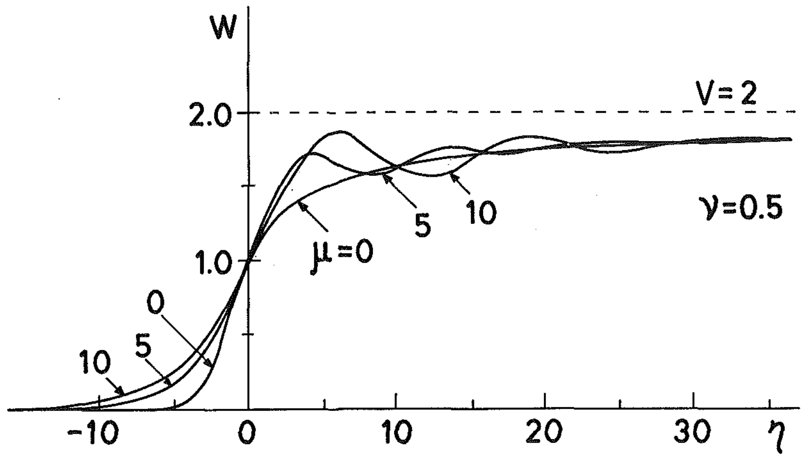

Fig. 3 Shock profiles for Type II with $V = 2$, $\nu = 0.5$, and the various values of μ

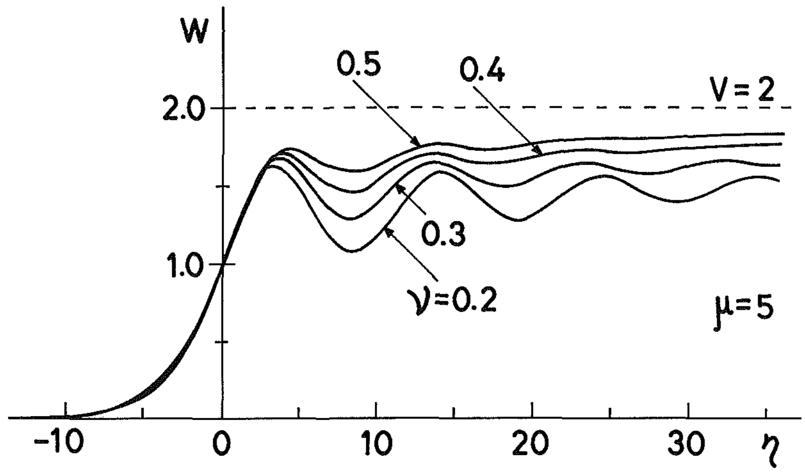

Fig. 4 Shock profiles for Type II with $V = 2$, $\mu = .5$, and the various values of ν

step-up behavior becomes steep. For greater values of V, qualitative behavior is similar and an oscillatory profile appears. As V increases, it is found from the roots of (23) and (25) that a step-up behavior becomes steep and a rapid oscillation appears. For weak shock waves ($0<V<<1$), on the other hand, a monotonic shock profile appears for $\mu \gtrsim 4$ but an oscillatory profile appears again for $O < \mu \lesssim 4$ (see Fig. 1).

4.3 Power Function Type. Equation (17) in this type remains the integrodifferential equation:

$$Vw - w^2 - \mu \frac{d^2 w}{d\eta^2} = \int_{-\infty}^{\eta} \frac{1}{(\eta-\eta_1)^\nu} \frac{dw}{d\eta_1} d\eta_1, (0<\nu<1), \quad (27)$$

here and hereafter the prime in μ' is omitted. This equation is solved numerically by the similar method of quadrature to that in [2]. For the treatment of infinite lower bound of integration, the region $(-\infty, \eta]$ is divided into two parts $(-\infty, M]$ and $(M, \eta]$, M being arbitrarily fixed, and the following asymptotic solution is assumed valid to evaluate the integral in $(-\infty, M]$.

$$w \sim w^{(1)}\exp[p(\eta-M)]$$
$$+ w^{(1)2}\exp[2p(\eta-M)]/D(2p) + O(w^{(1)3}), \quad (28)$$

where $w^{(1)}$ is a small constant ($0<w^{(1)}<<1$) and p is the unique positive root of the equation $D(p) = V - \mu p^2 - \Gamma(1-\nu)p^\nu = 0$, p^ν being defined by taking the principal value, i.e., $-\pi < \arg p \leqq \pi$. For the treatment of divergence of the integrand at the upper bound, on the other hand, the "modified Simpson's rule" is applied. But since (27) involves the second derivative, it cannot be reduced to a single integral equation by inversion unlike the case in [2]. Putting $dw/d\eta = v$, the following simultaneous equations are solved:[6]

$$Vw - w^2 - \mu \frac{dv}{d\eta} = \int_{-\infty}^{\eta} \frac{v(\eta_1)}{(\eta-\eta_1)^\nu} d\eta_1,$$

$$w = \int_{-\infty}^{\eta} v(\eta_1) d\eta_1. \quad (29)$$

The derivative $dv/d\eta$ is approximated by a finite difference. This is the main difference from [2]. The scheme to calculate w is given in Appendix 2.

In Fig. 3, the typical profiles of w are displayed with $w_\infty = V = 2$ and $\nu = 0.5$ for the various values of μ. Due to the geometrical dispersion, the shock profiles become oscillatory just as in Type I. But they do not overshoot the equilibrium value but undulate below it. Also there appears the slow relaxation region in the trail. Owing to the properties of the

[6] We note here that putting $d^2 w/d\eta^2 = v$, (27) can be rewritten by inversion as the simultaneous integral equations:

$\Gamma(1-\nu)\Gamma(\nu)w = \int_{-\infty}^{\eta} [Vw(\eta_1) - w^2(\eta_1) - \mu v(\eta_1)]/(\eta-\eta_1)^{1-\nu} d\eta_1$ and $w = \int_{-\infty}^{\eta} (\eta-\eta_1)v(\eta_1)d\eta_1$. After the same scheme as in [2], the numerical computations were carried out but the numerical instability occurred in this case.

relaxation function of Type II, the profiles are smooth themselves even if the geometrical dispersion would be neglected [2]. Consequently the effect of the second derivative in (27) does not appear so remarkably as in Type I. The asymptotic behavior of profiles as $\eta \to \infty$ is almost the same as that with $\mu = 0$ irrespective of the values of μ.

For other values of V, μ, and ν, the shock profiles are also similar. As V increases or μ decreases, the step-up behavior becomes steep. This is also understood from the asymptotic solution (28). As for the oscillation, it becomes prominent as μ increases, while as it decreases, the profiles become monotonic and tend to those with $\mu = 0$. Incidentally we remark that there is no nonuniformity between $\mu = 0$ and $\mu \to 0$. This is also seen from (28) that for any positive values of V and μ, there always exists the asymptotic branch from $\eta = -\infty$. Finally in Fig. 4, the profiles are shown for the various values of ν with $V = 2$ and $\mu = 5$. Although the step-up behavior is almost the same, it is interesting to see that the smaller ν produces a pronounced oscillation.

5 Simplified Evolution Equations

In parallel with the discussion in [2], here we derive the simplified evolution equations for a far field transient behavior. Introducing the new coordinate $\xi = t - z/E^{1/2}$ moving with the velocity $E^{1/2}$ and the stretched coordinate $\tau = \delta z/E^{1/2}$ instead of z and t, (14) is reduced by retaining the lowest-order in ϵ^2, δ, and γ to

$$\frac{\partial W}{\partial \tau} - \frac{CW}{E}\frac{\partial W}{\partial \xi} - \frac{\epsilon^2\sigma^2}{4\delta E}\frac{\partial^3 W}{\partial \xi^3} = \frac{\gamma}{2\delta E}\frac{\partial}{\partial \xi}\int_{-\infty}^{\xi} K(\xi-\xi_1)\frac{\partial W}{\partial \xi_1}d\xi_1, \tag{30}$$

where $W = -E^{-1/2}u^{(0)}_{z,\xi}$. For Type I, (30) is recast into the differential equation. Particularly if the rapid relaxation is assumed, i.e., $\kappa^{-1} \sim \delta/\gamma << 1$, we have the usual $K-d\bar{V}$-Burgers' equation with the right-hand side of (30) replaced by $\gamma W_{,\xi\xi}/(2\delta E\kappa)$ [7]. For Type II, (30) can be interpreted as a "generalized $K-d\bar{V}$-Burgers' equation" by using the definition of the derivative of real order ν [2].

Acknowledgments

The authors would like to express their thanks to the associate editor and the reviewers for their comments.

This work has been supported partially by the Grant-in-Aid for Scientific Research from the Ministry of Education. All the computations were carried out on NEAC 900 at the Computer Center of Osaka University.

References

1 Sugimoto, N., Yamane, Y., and Kakutani, T., "Approximate Equations for Torsional Waves in a Nonlinear Elastic Rod with Weak Viscoelasticity," to be published in *Wave Motion*.

2 Sugimoto, N., Yamane, Y., and Kakutani, T., "Torsional Shock Waves in a Viscoelastic Rod," to be published in ASME JOURNAL OF APPLIED MECHANICS.

3 Achenbach, J. D., *Wave Propagation in Elastic Solids*, North-Holland, Amsterdam, 1973.

4 Love, A. E. H., *A Treatise on the Mathematical Theory of Elasticity*, Dover, New York, 1944.

5 Ferry, J. D., *Viscoelastic Properties of Polymers*, Wiley, New York, 1970.

6 Hayashi, C., *Nonlinear Oscillation in Physical Systems*, McGraw-Hill, New York, 1964.

7 Nariboli, G. A., and Sedov, A., "Burgers's-Korteweg-De Vries Equation for Viscoelastic Rods and Plates," *Journal of Mathematical Analysis and Applications*, Vol. 32, 1970, pp. 661–677.

8 Schuler, K. W., Nunziato, J. W., and Walsh, E. K., "Recent Results in Nonlinear Viscoelastic Wave Propagation," *International Journal of Solids and Structures*, Vol. 9, 1973, pp. 1237–1281.

9 Nunziato, J. W., and Sutherland, H. J., "Acoustical determination of Stress Relaxation Functions for Polymers," *Journal of Applied Physics*, Vol. 44, 1973, pp. 184–187.

APPENDIX 1

Expicit form of K_{ij} $(i, j = r, \theta, z)$:

$$\begin{aligned}
K_{rr} &= \delta\{k_1 a + (2k_1+k_2)b + \delta[(k_1/2+l_2)a^2 \\
&\quad + (k_1+k_2/2+2l_2+l_4)b^2 + l_1c^2 + l_3bc] \\
&\quad + \gamma\textstyle\int_{-\infty}^{t}[K_1a_{,t_1} + (2K_1+K_2)b_{,t_1}]dt_1 \\
&\quad + [(4k_1+3k_2)u_r^{(3)} + k_1u_{z,z}^{(2)}]r^2\}, \\
K_{\theta\theta} &= K_{rr} - 2\delta k_2 u_r^{(3)}r^2, \\
K_{zz} &= \delta\{(k_1+k_2)a + 2k_1b + \delta[(k_1+k_2+2l_2+2l_4)a^2/2 \\
&\quad + (k_1+2l_2)b^2 + l_1c^2 + l_3ac] \\
&\quad + \gamma\textstyle\int_{-\infty}^{t}[(K_1+K_2)a_{,t_1} + 2K_1b_{,t_1}]dt_1 \\
&\quad + [4k_1u_r^{(3)} + (k_1+k_2)u_{z,z}^{(2)}]r^2\}, \\
K_{rz} &= \delta k_2(b_{,z} + 2u_z^{(2)})r/2, \\
K_{r\theta} &= K_{\theta z} = 0,
\end{aligned} \tag{31}$$

with $a = u^{(0)}_{z,z}$, $b = u^{(1)}_r$, and $c = a+2b$, where terms neglected in K_{rr}, $K_{\theta\theta}$, and K_{zz} are of $O(\delta\epsilon^4, \delta^3, \delta\epsilon^2\gamma)$, while those in K_{rz} of $O(\delta\epsilon^3, \delta^2\epsilon, \delta\epsilon\gamma)$.

APPENDIX 2

The numerical calculation is carried out in the region $[M, \eta]$ by taking the equidistant points $\eta^{(i)}$ $(i = 1, 2, 3, \ldots)$ separated by a small interval h, i.e., $\eta^{(i)} = M + (i-1)h$. Denoting w and v at $\eta = \eta^{(i)}$ by $w^{(i)}$ and $v^{(i)}$, respectively, the scheme to calculate unknown $w^{(i)}$ and $v^{(i)}$ from the known $w^{(j)}$ and $v^{(j)}$ $(j = 1, 2, \ldots, i-1)$ is summarized as follows:

$$\begin{aligned}
&Vw^{(i)} - w^{(i)2} - \frac{\mu}{6h} \\
&\quad (-2v^{(i-3)} + 9v^{(i-2)} - 18v^{(i-1)} + 11v^{(i)}) \\
&\quad = I_1 + I_2 + \frac{(2h)^{1-\nu}}{(2-\nu)(3-\nu)}[(1-\nu)v^{(i-2)} \\
&\quad + 4v^{(i-1)} + \frac{1+\nu}{1-\nu}v^{(i)}],
\end{aligned}$$

and

$$w^{(i)} = I_3 + I_4 + \frac{h}{3}(v^{(i-2)} + 4v^{(i-1)} + v^{(i)}), \tag{32}$$

where I_i $(i = 1, 2, 3, 4)$ are given by

$$\begin{aligned}
I_1 &= \int_{-\infty}^{M}\frac{v(\eta_1)}{(\eta-\eta_1)^{\nu}}d\eta_1 \\
&= w^{(1)}p^{\nu}\exp[p(\eta-M)]\Gamma[1-\nu, p(\eta-M)] \\
&\quad + \frac{w^{(1)2}(2p)^{\nu}}{D(2p)}\exp[2p(\eta-M)]\Gamma[1-\nu, 2p(\eta-M)] + O(w^{(1)3}),
\end{aligned}$$

$$I_2 = \int_{M}^{\eta^{(i-2)}}\frac{v(\eta_1)}{(\eta-\eta_1)^{\nu}}d\eta_1,$$

$$I_3 = \int_{-\infty}^{M} v(\eta_1)d\eta_1 = w^{(1)} + w^{(1)2}/D(2p) + O/w^{(1)3}),$$

$$I_4 = \int_{M}^{\eta^{(i-2)}} v(\eta_1)d\eta_1, \tag{33}$$

where the derivative $dv/d\eta$ is approximated by a four-point finite difference and $\Gamma\,[1-\nu, p(\eta - M)]$ denotes the incomplete gamma function. By eliminating $v^{(i)}$ from (32), the quadratic equation for $w^{(i)}$ is solved step-by-step. Here it should be remarked that the error involved in the four-point difference is of $O(h^3)$, whereas the "modified Simpson's rule" and Simpson's rule involve the error of $O(h^{4-\nu})$ and $O(h^5)$ in the $2h$ interval, respectively. The accuracy of the finite difference could be improved by adopting the five-point finite difference, etc., but it is judged unnecessary from the numerical results. In the numerical computations, h is chosen as $h = 0.001$ while the first two terms in (28) are employed with $w^{(1)} = 0.0001$.

APPENDIX 3

Plausible Experimental Conditions

Here we discuss the experimental conditions under which the propagation of shock wave is observed. A shock wave is produced by an impact loading at one end of the rod and its steady propagation is expected to be realized far downward along the rod. For this to be observed, a length of the rod is required to be sufficiently long. At the present stage, however, it is impossible to estimate quantitatively a position where the steady propagation will be achieved. To clarify this problem, an initial and boundary value problem to the equation (14) must be solved.

In the following, we show plausible experimental conditions. As a typical example of viscoelastic solids, the polymethyl methacrylate (PMMA) is considered. Many experimental data on PMMA are available from the papers [8, 9] and the papers cited therein.

diameter of the rod	: $D = 2\times 10^{-2}$ [m],
characteristic length (which corresponds to an interval $1/\lambda$ in the dimensionless η)	: $L = 5\times 10^{-2}$ [m],
characteristic velocity (equilibrium shear veocity $(S/\rho_0)^{1/2}$)[7]	: $V = 1.4\times 10^3$ [m/s],
characteristic time $T(=L/V$, which corresponds to a unit interval in the dimensionless $\eta)$	: $T = 3.6\times 10^{-5}$[s],
normalized radius $\epsilon(=D/2L)$	: $\epsilon = 2\times 10^{-1} \sim O(10^{-1})$,
characteristic axial strain	: $\delta = O(10^{-2}) \sim O(10^{-3})$,
weakness of viscoelasticity	: $\gamma = O(10^{-2})$,
Poisson's ratio (calculated from the longitudinal and shear acoustic velocities)	: $\sigma = 0.33$,
coefficient of geometrical dispersion	: $\mu' = O(1) \sim O(10^{-1})$.

Here the order of γ is roughly estimated from the data on the longitudinal relaxation function (which corresponds to $k_1 + k_2 + \gamma(K_1 + K_2)$ in our notation) [9]. In [8] and [9], the characteristic time T and the characteristic relaxation time τ are estimated, respectively, as 10^{-7} sec. and 2×10^{-7} sec. under the assumption of a single exponential function type. Then the normalized relaxation time κ^{-1} $(=\tau/T)$ becomes 2. On the other hand, we are concerned here with much slower characteristic time scale $T = 3.6\times 10^{-5}$ sec. as tabulated in the foregoing. If one measures the relaxation time τ by this slower time scale, one obtains $\kappa^{-1} = 6\times 10^{-3}$, which means that the relaxation is completed very rapidly over the present time scale. For actual solid polymers, however, there will appear subsequent slow relaxations even measured by the present slower time scale. To describe such a slow relaxation, not only a single exponential function but also even a number of exponential functions are not sufficient to cover such a wide time range. This is the reason why we introduce a new type of a relaxation function expressed by a power function which has a continuous relaxation spectrum in [2] and also in this paper.

[7] In this case, the modulus of rigidity is taken as the characteristic modulus S. It then follows that $k_1 = 2\sigma/(1-2\sigma)$, $k_2 = 2$, and $E = 2(1+\sigma)$.

Dynamic Stress Intensity Factors for an Inclined Subsurface Crack

W. Lin

L. M. Keer
Fellow ASME

J. D. Achenbach
Fellow ASME

Department of Civil Engineering,
Northwestern University,
Evanston, Ill. 60201

Stress intensity factors are computed for an inclined subsurface crack in a half space, whose surface is subjected to uniform time-harmonic excitation. The problem is analyzed by determining displacement potentials that satisfy reduced wave equations and specified boundary conditions. The formulation of the problem leads to a system of coupled integral equations for the dislocation densities. The numerical solution of the integral equations leads directly to the stress intensity factors. Curves are presented for the ratios of the elastodynamic and the corresponding elastostatic Mode-I and Mode-II stress intensity factors for various frequencies and various inclinations of the crack with the free surface. For small angles of inclination with the free surface and large crack length-to-depth ratios, strong resonance vibrations of the layer between the crack and the free surface may arise.

Introduction

The effect of the proximity of a boundary on elastodynamic stress intensity factors has been investigated in references [1] and [2] for a subsurface crack parallel and normal, respectively, to the surface of a half space. In this paper we consider a subsurface crack which is oriented under an arbitrary angle with the surface of a half space.

The configuration that is considered here, is two-dimensional with deformations in plane strain. A system of coupled singular integral equations for the Mode-*I* and Mode-*II* dislocation densities has been derived. These equations have been solved numerically for the cases of time-harmonic uniform tension and uniform shear applied at the surface of the half space. The elastodynamic stress intensity factors have been computed. The results display the dependence on the frequency, angle of inclination, and on the ratio d/a, where d is the distance from the upper crack tip to the free surface and a is the crack length. For small angles of inclination with the free surface, and for small values of d/a, time-harmonic excitations of the body may induce quite strong resonance vibrations of the layer between the crack and the free surface. Such resonance vibrations give rise to substantial increases in both the Mode-*I* and Mode-*II* stress intensity factors. These resonance effects were investigated in some detail for the parallel crack in reference [1]. Similar effects have previously been noted in papers by Mal [3] for antiplane shear and Rokhlin [4] for a crack in a layer.

Contributed by the Applied Mechanics Division and presented at the Winter Annual Meeting, New Orleans, La., December 9–14, 1984 of The American Society of Mechanical Engineers.

Discussion on this paper should be addressed to the Editorial Department, ASME, United Engineering Center, 345 East 47th Street, New York, N.Y. 10017, and will be accepted until two months after final publication of the paper itself in the Journal of Applied Mechanics. Manuscript received by ASME Applied Mechanics Division, September, 1983; final revision, February, 1984. Paper No. 84-WA/APM-35.

Copies will be available until August, 1985.

Formulation

A homogeneous isotropic linearly elastic solid, which occupies the half plane $y \geq 0$, contains a subsurface crack. The two-dimensional geometry of the traction-free crack is shown in Fig. 1. The total fields that are generated by the interactions of the incident wave(s) and the crack can be expressed as

$$u_i^t = u_i^{in} + u_i, \quad \sigma_{ij}^t = \sigma_{ij}^{in} + \sigma_{ij}, \tag{1,2}$$

where u_i^{in} and σ_{ij}^{in} are the displacement and stress components for the incident field, while u_i and σ_{ij} correspond to the scattered field. In the analysis given in this paper the time-harmonic factor $\exp(-i\omega t)$ will be suppressed.

By virtue of linear superposition, the scattered field is equivalent to the field generated in the cracked half plane by the application of tractions on the crack faces that are equal in magnitude but opposite in sign to the corresponding tractions due to the incident wave in the uncracked half plane. Thus on the faces of the crack we have

$$\sigma_{x'x'} + \sigma_{x'x'}^{in} = \sigma_{x'y'} + \sigma_{x'y'}^{in} \equiv 0 \quad x'=0,\ 0<y'<a \tag{3}$$

where the $x'y'$ coordinate system is shown in Fig. 1. Since the stresses of the incident field already satisfy the prescribed conditions on the surface of the half space, we have that

$$\sigma_{xy} = \sigma_{yy} = 0 \quad y=0, -\infty<x<\infty \tag{4}$$

For a body of arbitrary geometry, which contains a line crack on $0 \leq y' \leq a$, $x'=0$, and that is subjected to two-dimensional (in-plane) loading, a well-known elastodynamic representation theorem states (see e.g., Achenbach, et al. [5]) that the scattered displacement field can be expressed in terms of the crack-opening displacement,

$$\Delta u_i(y') = u_i(0^+, y') - u_i(0^-, y'), \tag{5}$$

as

$$u_k(x_0') = \int_0^a \sigma_{ix'\,;k}^{G}(0, y'; \mathbf{x}_0') \Delta u_i(y') dy' \tag{6}$$

Here k is the subscript referring to the coordinates x', y' and

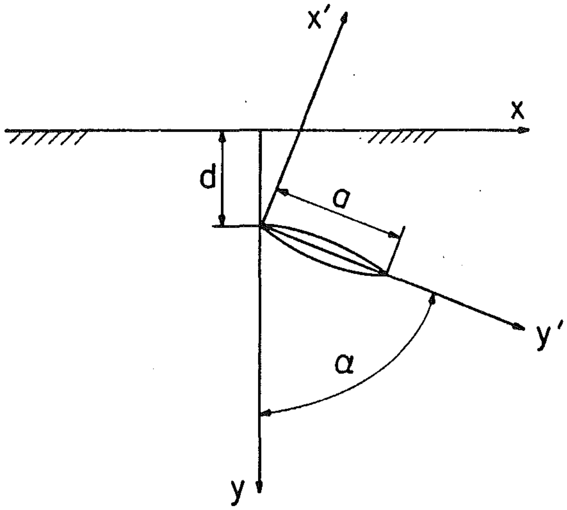

Fig. 1 Geometry of the problem

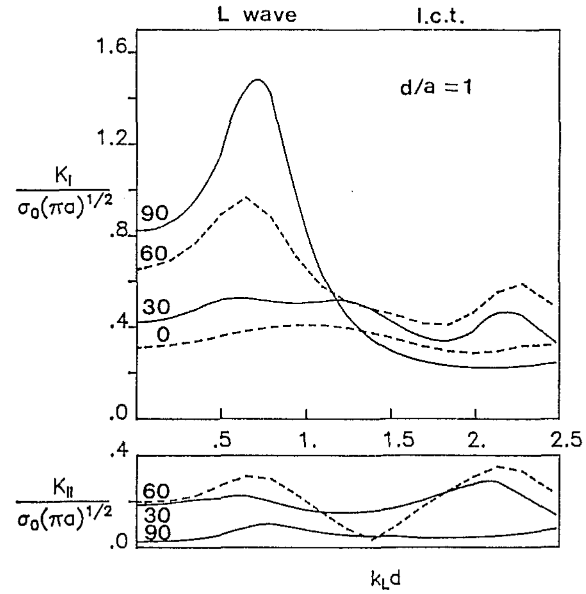

Fig. 2 Stress intensity factors at lower crack tip for $d/a=1.0$, $\alpha=0$ deg, 30 deg, 60 deg, 90 deg and time-harmonic normal loading of magnitude σ_0 applied at $y=0$

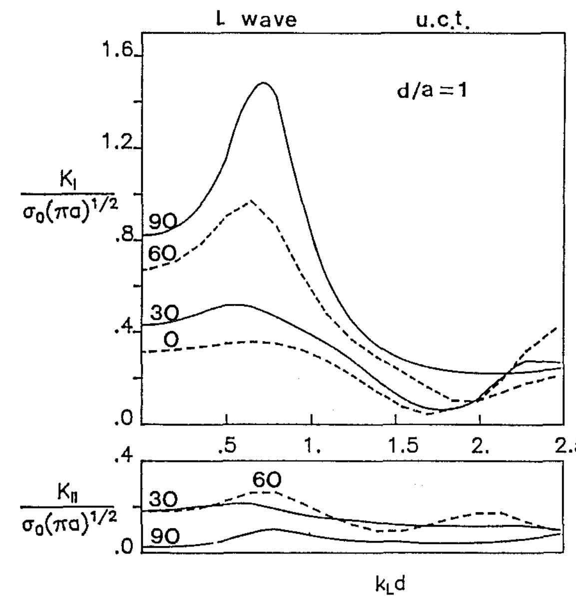

Fig. 3 Stress intensity factors at upper crack tip for $d/a=1.0$, $\alpha=0$ deg, 30 deg, 60 deg, 90 deg and time-harmonic normal loading of magnitude σ_0 applied at $y=0$.

summation is assumed to be carried out over repeated indices. In this case, summation is carried out over the index $i(i=x',y')$. The stress components $\sigma^G_{ix'};_k$ are for the field in the body with traction-free external boundary and for a time harmonic line load applied in the k-direction at $\mathbf{x}_0'$.

If we consider coordinates x_0' and y_0' and compare the following equation

$$u_{y_0'}(\mathbf{x}_0')=\partial_{y_0'}\phi-\partial_{x_0'}\psi$$
$$=\frac{-1}{\mu k_T^2}\int_0^a \Delta u_i\,(\partial_{y_0'}\sigma^L_{ix'}-\partial_{x_0'}\sigma^T_{ix'})dy', \tag{7}$$

which is obtained in reference [6] with equation (6), then the following result can be immediately obtained:

$$\sigma^G_{ix'};_{y'}=\frac{-1}{\mu k_T^2}(\partial_{y_0'}\sigma^L_{ix'}-\partial_{x_0'}\sigma^T_{ix'}) \tag{8a}$$

Similarly,

$$\sigma^G_{ix'};_{x'}=\frac{-1}{\mu k_T^2}(\partial_{x_0'}\sigma^L_{ix'}+\partial_{y'0}\sigma^T_{ix'}) \tag{8b}$$

Note that $\partial_{y_0'}=\partial/\partial y_0'$, $\partial_{x_0'}=\partial/\partial x_0'$, σ^L_{ij} and σ^T_{ij} are the components of the stress tensor derived from the fundamental potential pairs (ϕ^L, ψ^L) and (ϕ^T, ψ^T), μ is the shear modulus, and $k_T=\omega/(\mu/\rho)^{1/2}$. A proof of equation (8) is given in Appendix *I*.

Since the expressions (ϕ^L, ψ^L) and (ϕ^T, ψ^T) have already been found for the half space (reference [6]), the Green's function $\sigma^G_{ix'};_k$ can be obtained. After integrating equation (6) by parts, an integral representation of the displacement field in terms of the dislocation densities can be established as

$$u_k(\mathbf{x}_0')=-\int_0^a d_i(y')\left[\int^{y'}\sigma^G_{ix'};_k(0,\xi;\mathbf{x}_0')d\xi\right]dy' \tag{9}$$

Here,

$$d_i(y')=\partial\Delta u_i(y')/\partial y' \tag{10}$$

and the crack closure condition,

$$\int_0^a d_i(y')dy'=0 \tag{11}$$

has been applied. The stress components that correspond to equation (9) are obtained by application of Hooke's law, and lead to the set of integral equations given next:

$$\sigma_{x'x'}=\frac{\mu}{k_T^2}\int_0^a (A_{11}d_{x'}+A_{12}d_{y'})dy' \tag{12}$$

$$\sigma_{x'y'}=\frac{\mu}{k_T^2}\int_0^a (A_{21}d_{x'}+A_{22}d_{y'})dy' \tag{13}$$

Equations (12) and (13) are seen to relate the stresses on the crack faces, which are given, with the dislocation densities that are to be determined. The kernels $A_{ij}\,(i,j=1,2)$ are given in Appendix *II*.

Numerical Scheme

The coupled integral equations for the dislocation densities (12) and (13) are singular integral equations of the Cauchy type. The numerical scheme used here is the same as that given in reference [1]. It relies on the Gauss-Chebyshev quadrature formula [7]. Equations (12) and (13) are written as:

$$\sigma_{x'x'}(y_{0j}')=\frac{\mu}{k_T^2}\frac{a}{2}\frac{\pi}{m}\sum_{i=1}^{m}(\bar d_{x'}A_{11}+\bar d_{y'}A_{12}) \tag{14}$$

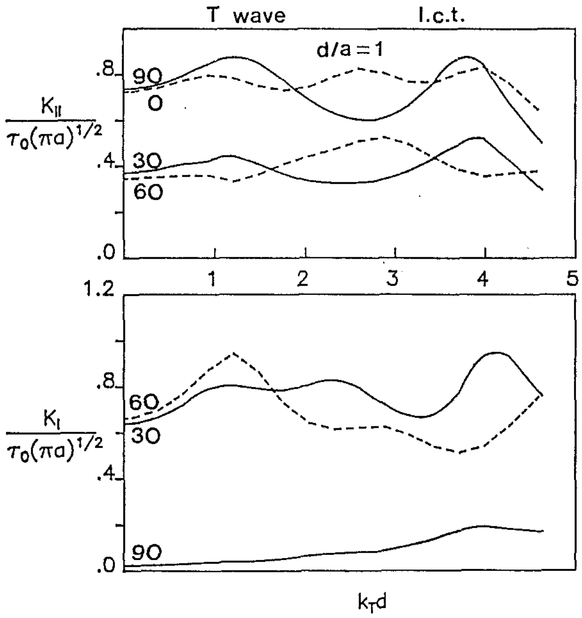

Fig. 4 Stress intensity factors at lower crack tip for $d/a = 1.0$, $\alpha = 0$ deg, 30 deg, 60 deg, 90 deg and time-harmonic shear loading of magnitude τ_0 applied at $y = 0$

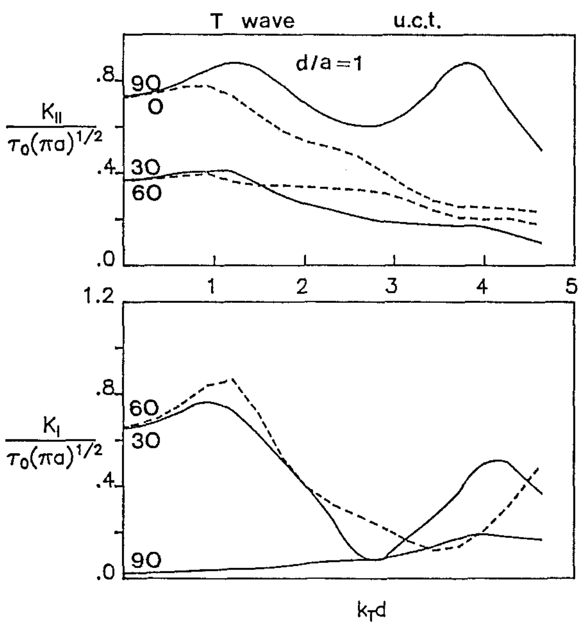

Fig. 5 Stress intensity factors at upper crack tip for $d/a = 1.0$, $\alpha = 0$ deg, 30 deg, 60 deg, 90 deg and time-harmonic shear loading of magnitude τ_0 applied at $y = 0$

$$\sigma_{x'y'}(y'_{0j}) = \frac{\mu}{k_T^2}\frac{a}{2}\frac{\pi}{m}\sum_{i=1}^{m}(\bar{d}_{x'}A_{21} + \bar{d}_{y'}A_{22}) \tag{15}$$

here $\bar{d}_{x'}(y'_i), \bar{d}_{y'}(y'_i), A_{kl}(y'_i, y'_{0j})$, $(k,l = 1,2)$ are defined as

$$z_i = \cos\frac{(i-0.5)\pi}{m}, \quad (i = 1,2, \ldots, m) \tag{16}$$

$$y'_i = (z_i + 1)a/2 \tag{17}$$

$$y'_{0j} = \left(\cos\frac{j\pi}{m} + 1\right)\frac{a}{2}, \quad (j = 1,2, \ldots, m-1) \tag{18}$$

$$\frac{\bar{d}_{x'}(y'_i)}{d_{x'}(y'_i)} = \frac{\bar{d}_{y'}(y'_i)}{d_{y'}(y'_i)} = (1 - z_i^2)^{1/2} \tag{19}$$

The crack closure condition is

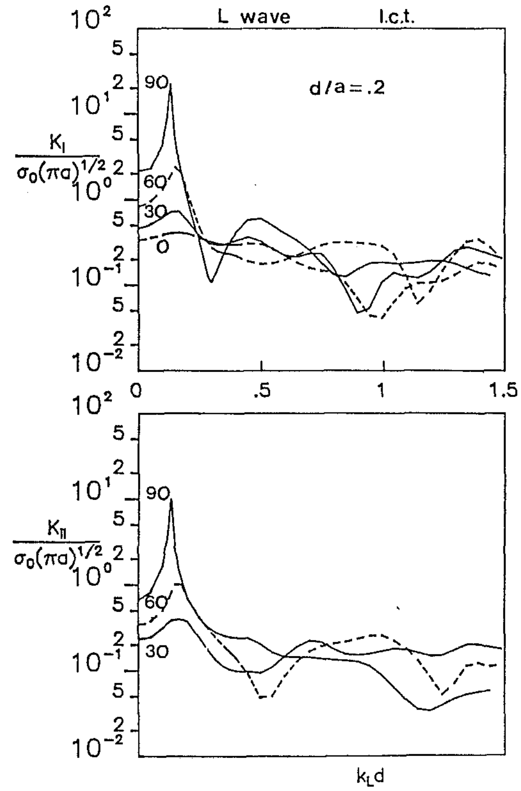

Fig. 6 Stress intensity factors at lower crack tip for $d/a = 0.2$, $\alpha = 0$ deg, 30 deg, 60 deg, 90 deg and time-harmonic normal loading of magnitude σ_0 applied at $y = 0$

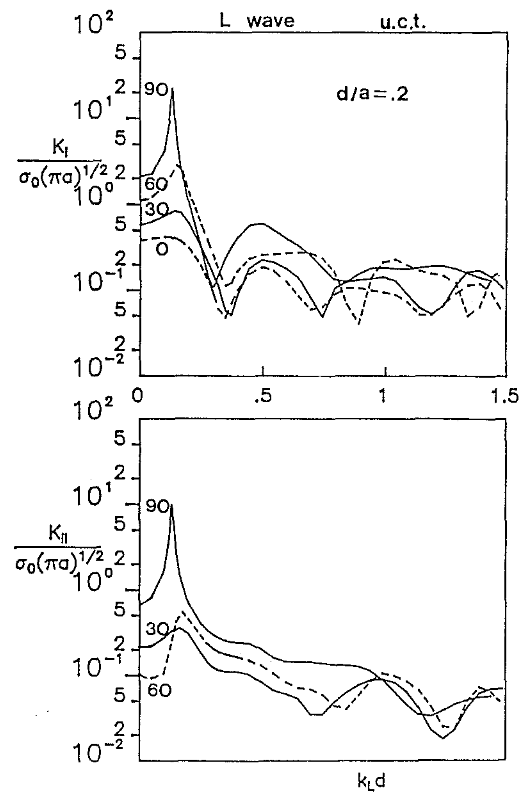

Fig. 7 Stress intensity factors at upper crack tip for $d/a = 0.2$, $\alpha = 0$ deg, 30 deg, 60 deg, 90 deg and time-harmonic normal loading of magnitude σ_0 applied at $y = 0$

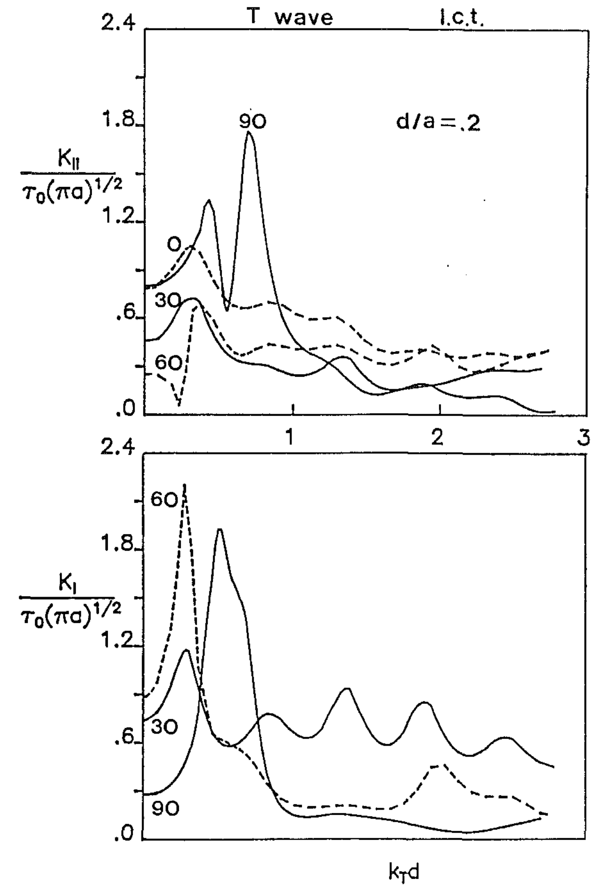

Fig. 8 Stress intensity factors at lower crack tip for $d/a = 0.2$, $\alpha = 0$ deg, 30 deg, 60 deg, 90 deg and time-harmonic shear loading of magnitude τ_0 applied to $y = 0$

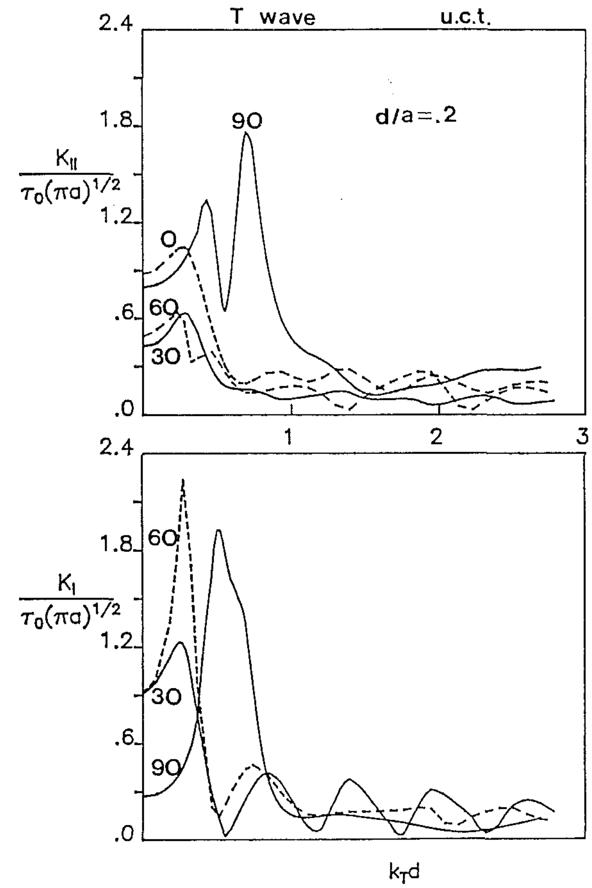

Fig. 9 Stress intensity factors at upper crack tip for $d/a = 0.2$, $\alpha = 0$ deg, 30 deg, 60 deg, 90 deg and time-harmonic shear loading of magnitude τ_0 applied at $y = 0$

$$\sum_{i=1}^{m} \bar{d}_{x'}(y_i') = \sum_{i=1}^{m} \bar{d}_{y'}(y_i') = 0 \tag{20}$$

By combining equations (14), (15), and (20) we can solve for $\mu\bar{d}_x$ and $\mu\bar{d}_{y'}$.

The stress intensity factors at the crack tips are defined as:

$$\begin{Bmatrix} K_I \\ K_{II} \end{Bmatrix} = \lim_{y' \downarrow a} [2\pi(y'-a)]^{1/2} \begin{Bmatrix} |\sigma_{x'x'}(0,y')| \\ |\sigma_{x'y'}(0,y')| \end{Bmatrix}$$
$$= \frac{\mu(k_T^2 - k_L^2)}{k_T^2} \left(\frac{a\pi}{2}\right)^{1/2} \begin{Bmatrix} |\bar{d}_x'(1)| \\ |\bar{d}_{y'}(1)| \end{Bmatrix} \tag{21}$$

$$\begin{Bmatrix} K_I \\ K_{II} \end{Bmatrix} = \lim_{y' \uparrow 0} [2\pi|y'|]^{1/2} \begin{Bmatrix} |\sigma_{x'x'}(0,y')| \\ |\sigma_{x'y'}(0,y')| \end{Bmatrix}$$
$$= \frac{\mu(k_T^2 - k_L^2)}{k_T^2} \left(\frac{a\pi}{2}\right)^{1/2} \begin{Bmatrix} |\bar{d}_x'(-1)| \\ |\bar{d}_{y'}(-1)| \end{Bmatrix} \tag{22}$$

here the argument of $\bar{d}_{x'}\bar{d}_{y'}$ in equations (21) and (22) correspond to $z = \pm 1$, and the value of $\bar{d}_{i'}(\pm 1)$ can be obtained from the extrapolation formula [8].

$$\bar{d}_{i'}\begin{pmatrix} 1 \\ -1 \end{pmatrix}$$
$$= \frac{1}{m} \sum_{k=1}^{m} \frac{\sin[(2m-1)(2k-1)\pi/4m]}{\sin[(2k-1)\pi/4m]} \bar{d}_{i'}\begin{pmatrix} y'_k \\ y'_{m+1-k} \end{pmatrix}.$$

Note that $k_L = \omega/((\lambda + 2\mu)/\rho)^{1/2}$ and λ, μ are Lamé constants.

Results

The results considered for this paper are those in which the surface of the half space ($y = 0$) is loaded harmonically by constant shear and normal stresses, i.e., $\sigma_{xy} = \tau_0 \exp(-i\omega t)$ and $\sigma_{yy} = \sigma_0 \exp(-i\omega t)$. The corresponding incident stress field is as follows:

$$\sigma^{(i)}_{x'x'} = [s^2 - c^2(2k_L^2/k_T^2 - 1)]\sigma_0 \exp(ik_L y - i\omega t)$$
$$\sigma^{(i)}_{x'y'} = -cs(2k_L^2/k_T^2)\sigma_0 \exp(ik_L y - i\omega t)$$

and

$$\sigma^{(i)}_{x'x'} = -2cs\ \tau_0 \exp(ik_T y - i\omega t)$$
$$\sigma^{(i)}_{x'y'} = (c^2 - s^2)\tau_0 \exp(ik_T y - i\omega t)$$

For all calculations Poisson's ratio is taken as 0.3. Here $c = \cos\alpha$ and $s = \sin\alpha$.

Four sets of figures are presented, two each of which give the stress intensity factors, K_I and K_{II}, for the upper and lower crack tips. Figures 2 and 3 show the results for tensile loading at $y = 0$ for a crack having a ratio of $d/a = 1.0$. As can be seen from the figures, a crack having a smaller angle of inclination with the horizontal will have a larger response with the maximum response being that of the horizontal crack. Furthermore, it is noted that K_{II} is small relative to K_I. Figures 4 and 5 give the results for the case of shear loading on $y = 0$, also with $d/a = 1.0$. As expected, K_I is small relative to K_{II} for near horizontal and vertical cracks, since the corresponding tensile tractions on the crack faces are relatively small.

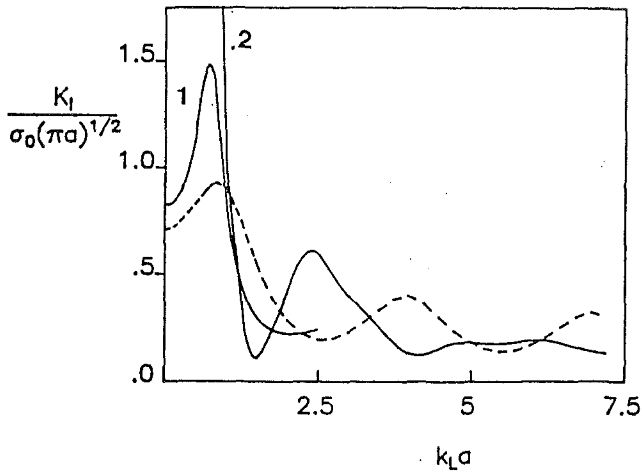

Fig. 10 Mode-*I* stress intensity factor for horizontal crack, $d/a = 0.2, 1., \infty$ (dashed line), and time-harmonic normal loading of magnitude σ_0 at $y = 0.$, $K_I/\sigma_0(\pi a)^{1/2} = 2.05$ for $d/a = 0.2$, $k_L a \to 0$ (see Fig. 6 or 7).

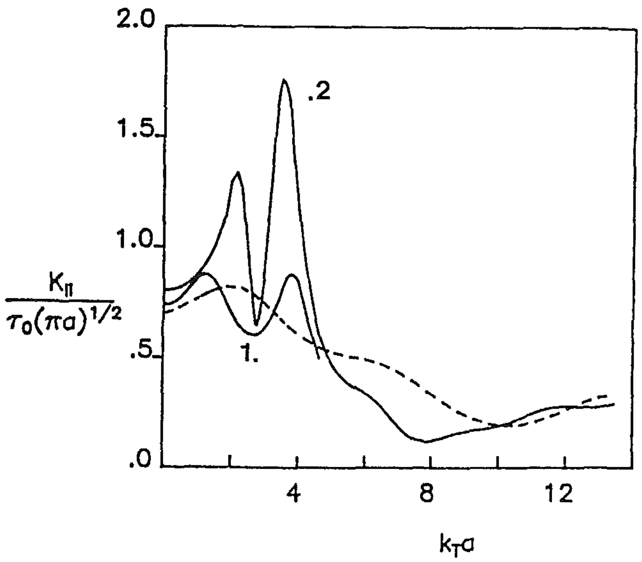

Fig. 11 Mode-*II* stress intensity factor for horizontal crack, $d/a = 0.2, 1., \infty$ (dashed line) and time-harmonic shear loading of magnitude τ_0 at $y = 0$

Figures 6 and 7 depict the case of tensile loading for a crack with $d/a = 0.2$. A very distinct resonance effect can be seen when the crack is nearly horizontal. A detailed discussion concerning this phenomenon has been given in reference [1]. It is noted that only the first peak is relatively large. Figures 8 and 9 depict the case of shear loading for $d/a = 0.2$, where it is noted that here the peak is much lower in magnitude than in the tensile loaded case.

Figures 10 and 11 allow certain conclusions to be drawn concerning the effect of the boundary. It appears that for a value of $d/a = 1.0$ the boundary has little effect for the case of shear loading. On the other hand the value of d/a should be higher for normal loading in order for the same to be true. If the frequency is sufficiently high, then the boundary effect may be small even for cracks near the surface. If the frequency is very low (static), more detailed information about the boundary effect can be found in [9].

The numerical solution of dislocation densities have been checked by calculation through power balance. The accuracy is defined by 1 – (power on crack face)/(scattered power). For $m = 15$ (equation (14)), the power balance is satisfied to within 2 percent in the numerical calculation.

Acknowledgment

The results reported in this paper were obtained in the course of research sponsored by the Air Force Office of Scientific Research under Grant AFOSR-78-3589-E. The authors are pleased to acknowledge assistance from R. J. Brind and M. K. Kuo.

References

1 Keer, L. M., Lin, W., and Achenbach, J. D., "Resonance Effects for a Crack Near a Free Surface," ASME Journal of Applied Mechanics, Vol. 51, 1984, pp. 65–70.

2 Achenbach, J. D., and Brind, R. J., "Elastodynamic Stress-Intensity Factors for a Crack Near a Free Surface," ASME Journal of Applied Mechanics, Vol. 48, 1981, pp. 539–542.

3 Mal, A. K., "Diffraction of SH Waves by a Near-Surface Crack," in: *Review of Progress in Quantitative Nondestructive Evaluation*, Thompson, D. O., and Chimenti, D. E., eds., Volume 1, Plenum Press, New York, 1981, pp. 499–509.

4 Rokhlin, S., "Diffraction of Lamb Waves by a Finite Crack in an Elastic Layer," *J. Acoust. Soc. Am.*, Vol. 67, 1980, pp. 1157–1165.

5 Achenbach, J. D., Gautesen, A. K., and McMaken, H., *Ray Methods for Waves in Elastic Solids*, Pitman Adv. Publ. Program, London, Boston, Melbourne, 1982, pp. 34–38.

6 Achenbach, J. D., and Brind, R. J., "Scattering of Surface Waves by a Sub-Surface Crack," *J. of Sound and Vibrations*, Vol. 76, 1981, pp. 43–56.

7 Erdogan, F., and Gupta, G. D., "On the Numerical Solution of Singular Integral Equations," *Quart. Appl. Math.*, Vol. 30, 1972, pp. 525–534.

8 Krenk, S., "On the Use of the Interpolation Polynomial for Functions of Singular Integral Equations," *Quart. Appl. Math.*, Vol. 33, 1975, pp. 479–484.

9 Chen, S. H., Keer, L. M., and Achenbach, J. D., "Steady Motion of a Crack Parallel to a Bond-Plane," Table 1, *Int. J. Eng. Sci.*, Vol. 18, 1981, pp. 225–238.

APPENDIX *I*

Relation Between Green's Function and Fundamental Potential Pair

In equation (8*a*) the result is stated without proof that

$$\sigma^G_{ij;y'} = \frac{-1}{\mu k_T^2}\,(\partial_{y_0'}\sigma^L_{ij} - \partial_{x_0'}\sigma^T_{ij}) \tag{I.1}$$

Here, we will now show the equivalent result that

$$\begin{Bmatrix} \phi^G \\ \psi^G \end{Bmatrix} = \frac{-1}{\mu k_T^2} \begin{Bmatrix} \partial_{y_0'}\phi^L - \partial_{x_0'}\phi^T \\ \partial_{y_0'}\psi^L - \partial_{x_0'}\psi^T \end{Bmatrix} \tag{I.2}$$

It can easily be shown that the boundary condition

$$\sigma^G_{ij;y'}(\mathbf{x}_b';\mathbf{x}_0')n_j = 0$$

is valid since we have that

$$\sigma^\beta_{ij}(\mathbf{x}_b';\mathbf{x}_0' + d\mathbf{x}_0')n_j = \sigma^\beta_{ij}(\mathbf{x}_b';\mathbf{x}_0')n_j = 0$$

where $\beta = L$ or T.

The governing equation for σ^G_{ij} is given by

$$\partial_j\sigma^G_{ij;y'} + f_i = \rho\ddot{u}^G_i \tag{I.3}$$

where ρ is the mass density and

$$f_i = \delta_{iy'}\,\delta(\mathbf{x}' - \mathbf{x}_0') \tag{I.4}$$

We will show that (1.3) follows from (*I*.1) and (*I*.2). Now if

$$\mathbf{x}' \neq \mathbf{x}'_0,$$

then

$$\begin{aligned}\partial_j\sigma^G_{ij;y'} &= \frac{-1}{\mu k_T^2}\,(\partial_j\partial y_0'\,\sigma^L_{ij} - \partial_j\partial_{x_0'}\sigma^T_{ij}) \\ &= \frac{-\rho}{\mu k_T^2}\,(\partial_{y_0'}\ddot{u}^L_i - \partial_{x_0'}\ddot{u}^T_i) = \rho\ddot{u}^G_i \end{aligned} \tag{I.5}$$

Furthermore, if $\bar{r} = |\mathbf{x}' - \mathbf{x}_0'| = \epsilon \to 0$, then only the singular term has to be considered, i.e.,

$$\phi^L \sim \frac{-i}{4} H_0^{(1)}(k_L \bar{r})$$

$$= -\int_\Gamma \frac{1}{4\pi\alpha_L} \exp[i\xi(x'-x_0') - \alpha_L |y'-y_0'|] d\xi \qquad (I.6)$$

The expression for ψ^T is identical to equation ($I.6$) with α_L replaced by α_T, see ($II.30$) (Γ is the same contour as in reference [1]).

Next, the body force is expressed in terms of the displacement potentials as

$$f_{x'} \sim \frac{1}{k_T^2}\left\{ \frac{k_T^2}{k_L^2} (\nabla^2 + k_L^2)\partial_{y_0'}\partial_{x'}\phi^L - (\nabla^2 + k_T^2)\partial_{x_0'}\partial_{y'}\psi^T \right\}$$

$$= \frac{i}{4}\nabla^2\left\{ \frac{(x'-x_0')(y'-y_0')}{\bar{r}^2} [H_2^{(1)}(k_L\bar{r}) - H_2^{(1)}(k_T\bar{r})] \right\}$$

$$+ \frac{i}{4}\frac{(x'-x_0')(y'-y_0')}{\bar{r}^2}[k_L^2 H_2^{(1)}(k_L\bar{r}) - k_T^2 H_2^{(1)}(k_T\bar{r})] \qquad (I.7)$$

$$f_{y'} \sim \frac{1}{k_T^2}\left\{ \frac{k_T^2}{k_L^2} (\nabla^2 + k_L^2)\partial_{y_0'}\partial_{y'}\phi^L + (\nabla^2 + k_T^2)\partial_{x_0'}\partial_{x'}\psi^T \right\}$$

$$= \frac{-i}{8}\nabla^2[H_0^{(1)}(k_L\bar{r}) + H_0^{(1)}(k_T\bar{r})] - \frac{i}{8}[k_L^2 H_0^{(1)}(k_L\bar{r})$$

$$+ k_T^2 H_0^{(1)}(k_T\bar{r})] + \frac{i}{8}\nabla^2\{[H_2^{(1)}(k_L\bar{r}) - H_2^{(1)}(k_T\bar{r})]$$

$$[(y_0'-y')^2 - (x'-x_0')^2]/\bar{r}^2\} + \frac{i}{8\bar{r}^2}[k_L^2 H_2^{(1)}(k_L\bar{r})$$

$$- k_T^2 H_2^{(1)}(k_T\bar{r})][(y_0'-y')^2 - (x_0'-x')^2] \qquad (I.8)$$

For the preceding calculation, the following formula (see, e.g. [6]) has been applied

$$H_n^{(1)}(k_\beta\bar{r})e^{in\bar{\theta}} = \frac{1}{\pi i}\int_{\Gamma'} \exp\{-ik_\beta\bar{x}\cosh t + k_\beta|\bar{y}|\sinh t - nt\} dt \qquad (I.9)$$

Here,

$$\cos\bar{\theta} = \frac{|\bar{y}|}{\bar{r}}, \quad \sin\bar{\theta} = \frac{-\bar{x}}{\bar{r}}, \xi = -k_\beta\cosh t,$$

and Γ' is the corresponding contour.

For those terms that do not contain the Laplace operator (∇^2), the singularity is only logarithmic; therefore, the integration over the area will be zero. For those terms that do contain the Laplace operator, we apply the formula

$$\iint_{A_\epsilon} \nabla^2 F dA = \int_{s\epsilon} \frac{\partial F}{\partial \bar{r}} ds = \epsilon\int_0^{2\pi} \frac{\partial F}{\partial \epsilon} d\theta' \qquad (I.10)$$

Thus,

$$\int_{A_\epsilon} f_{x'} dA = \lim_{\epsilon\to 0} \frac{\epsilon i}{4}\frac{d}{d\epsilon}[H_2^{(1)}(k_L\epsilon) - H_2^{(1)}(k_T\epsilon)]\int_0^{2\pi}\cos\theta'\sin\theta' d\theta' = 0$$

$$\int_{A_\epsilon} f_{y'} dA = +\frac{i}{8}\lim_{\epsilon\to 0}\left\{ -\epsilon\frac{d}{d\epsilon}[H_0^{(1)}(k_L\epsilon) + H_0^{(1)}(k_T\epsilon)]\int_0^{2\pi} d\theta' + \epsilon\frac{d}{d\epsilon}[H_2^{(1)}(k_L\epsilon) - H_2^{(1)}(k_T\epsilon)]\int_0^{2\pi}(\sin^2\theta' - \cos^2\theta')d\theta' \right\} = 1$$

and we can, therefore, construct the displacement potential of the harmonic point force from the fundamental potential pairs.

APPENDIX *II*

Tabulation of Coefficients of Kernel A_{ij}

The kernels of the coupled integral equations (12) and (13) are given by the following contour integral

$$\pi A_{ij} = \int_\Gamma \{[A_{ij1}e^{-\alpha_L(y'c+d)} + A_{ij2}e^{-\alpha_T(y'c+d)}]$$

$$[A_{ij3}e^{-\alpha_L(y_0'c+d)} + A_{ij4}e^{-\alpha_T(y_0'c+d)}]e^{i\xi(y_0'-y')s}/R(\xi)\}d\xi$$

$$+ \int_\Gamma e^{i\xi(y'-y_0')c}[A_{ij7}e^{-\alpha_L|(y'-y_0')s|} + A_{ij8}e^{-\alpha_T|(y'-y_0')s|}]d\xi$$

$$+ \int_\Gamma e^{i\xi(y'-y_0')c}[A_{ij7}e^{-\alpha_l|(y'-y_0')s|} + A_{ij8}e^{-\alpha_T|(y'-y_0')s|}]d\xi$$

$$+ \int^{y'}\int_\Gamma A_{ij9} d\xi dy' \qquad (II.1)$$

$$A_{111} = -(2\xi^2 - k_T^2)[2(\alpha_L c + i\xi s) + k_T^2/(\alpha_L c + i\xi s)]/(2\alpha_L) \qquad (II.2)$$

$$A_{112} = 2i\xi(\alpha_T s - i\xi c) \qquad (II.3)$$

$$A_{113} = (2\xi^2 - k_T^2)[k_T^2 + 2(\alpha_L c - i\xi s)^2] \qquad (II.4)$$

$$A_{114} = 4i\xi\alpha_L(\alpha_T s + i\xi c)(\alpha_T c - i\xi s) \qquad (II.5)$$

$$A_{121} = -(2\xi^2 - k_T^2)(\alpha_L s - i\xi c)/\alpha_L \qquad (II.6)$$

$$A_{122} = -i\xi\left[(\alpha_T c + i\xi s) - \frac{(\alpha_T s - i\xi c)^2}{(\alpha_T c + i\xi s)}\right] \qquad (II.7)$$

$$A_{123} = A_{113}, A_{124} = A_{114} \qquad (II.8)$$

$$A_{211} = -i\xi\left[2(\alpha_L c + i\xi s) + \frac{k_T^2}{(\alpha_L c + i\xi s)}\right] \qquad (II.9)$$

$$A_{212} = -(2\xi^2 - k_T^2)(\alpha_T s - i\xi c)/\alpha_T \qquad (II.10)$$

$$A_{213} = -4i\xi\alpha_T(\alpha_L s + i\xi c)(\alpha_L c - i\xi s) \qquad (II.11)$$

$$A_{214} = -(2\xi^2 - k_T^2)[(\alpha_T c - i\xi s)^2 - (\alpha_T s + i\xi c)^2] \qquad (II.12)$$

$$A_{221} = -2i\xi(\alpha_L s - i\xi c) \qquad (II.13)$$

$$A_{222} = (2\xi^2 - k_T^2)\left[(\alpha_T c + i\xi s) - \frac{(\alpha_T s - i\xi c)^2}{(\alpha_T c + i\xi s)}\right]\Big/(2\alpha_T) \qquad (II.14)$$

$$A_{223} = A_{213}, \ A_{224} = A_{214} \qquad (II.15)$$

$$A_{115} = \frac{[k_T^2 + 2(\alpha_L sG + i\xi c)^2](\alpha_L sG - i\xi c)}{2\alpha_L} \qquad (II.16)$$

$$A_{116} = \frac{(\alpha_T cG + i\xi s)(\alpha_T cG - i\xi s)(\alpha_T sG + i\xi c)}{-\alpha_T} \qquad (II.17)$$

$$A_{125} = \frac{(\alpha_L cG + i\xi s)[k_T^2 + 2(\alpha_L sG + i\xi c)^2]}{-2\alpha_L} \qquad (II.18)$$

$$A_{126} = \frac{(\alpha_T cG - i\xi s)(\alpha_T sG + i\xi c)(\alpha_T sG - i\xi c)}{-\alpha_T} \qquad (II.19)$$

$$A_{215} = \frac{(\alpha_L cG - i\xi s)(\alpha_L sG + i\xi c)(\alpha_L sG - i\xi c)}{\alpha_L} \qquad (II.20)$$

$$A_{216} = \frac{[(\alpha_T sG + i\xi c)^2 - (\alpha_T cG - i\xi s)^2](\alpha_T cG + i\xi s)}{2\alpha_T} \qquad (II.21)$$

$$A_{225} = \frac{(\alpha_L cG + i\xi s)(\alpha_L cG - i\xi s)(\alpha_L sG + i\xi c)}{-\alpha_L} \qquad (II.22)$$

$$A_{226} = \frac{[(\alpha_T sG + i\xi c)^2 - (\alpha_T cG - i\xi s)^2](\alpha_T sG - i\xi c)}{2\alpha_T} \qquad (II.23)$$

$$A_{117} = \frac{[k_T^2 + 2(\alpha_L sG - i\xi c)^2](\alpha_L sG - i\xi c)}{2\alpha_L} \qquad (II.24)$$

$$A_{118} = (\alpha_T cG + i\xi s)^2(\alpha_T sG - i\xi c)/\alpha_T \qquad (II.25)$$

$$A_{227} = (\alpha_L cG + i\xi s)^2(\alpha_L sG - i\xi c)/\alpha_L \qquad (II.26)$$

$$A_{228} = \frac{[2(\alpha_T sG - i\xi c)^2 + k_T^2](\alpha_T sG - i\xi c)}{2\alpha_T} \qquad (II.27)$$

$$A_{127} = A_{128} = A_{217} = A_{218} = 0 \qquad (II.28)$$

$$A_{119} = \frac{k_T^2[k_T^2 + 2(\alpha_L sG + i\xi c)^2]}{(-4\alpha_L)} e^{i\xi[(y' + y_0')c + 2d] - \alpha_L |(y' - y_0')s|}$$
$$+ \frac{k_T^2[k_T^2 + 2(\alpha_L sG - i\xi c)^2]}{(-4\alpha_L)} e^{i\xi(y' - y_0')c - \alpha_L |(y' - y_0')s|} \qquad (II.29)$$

$$A_{229} = \frac{k_T^2[k_T^2 + 2(\alpha_T sG + i\xi c)^2]}{(-4\alpha_T)} e^{i\xi[(y' + y_0')c + 2d] - \alpha_T |(y' - y_0')s|}$$
$$+ \frac{k_T^2[k_T^2 + 2(\alpha_T sG - i\xi c)^2]}{(-4\alpha_T)} e^{i\xi(y' - y_0')c - \alpha_T |(y' - y_0')s|} \qquad (II.30)$$

$$A_{129} = \frac{k_T^2(\alpha_T cG - i\xi s)(\alpha_T sG + i\xi c)}{(2\alpha_T)} e^{i\xi[(y' + y_0')c + 2d] - \alpha_T |(y' - y_0')s|}$$
$$[II.31)$$

$$A_{219} = \frac{k_T^2(\alpha_L cG - i\xi s)(\alpha_L sG + i\xi c)}{(-2\alpha_L)} e^{i\xi[(y' + y_0')c + 2d] - \alpha_L |(y' - y_0')s|}$$
$$(II.32)$$

and here

$$G = \mathrm{sign}[(y' - y_0')s] \qquad (II.33)$$

$$\alpha_\beta = (\xi^2 - k_\beta^2)^{1/2}, \quad Re(\alpha_\beta) \geq 0, \quad Im(\alpha_\beta) \leq 0 \qquad (II.34)$$

$$R(\xi) = (2\xi^2 - k_T^2)^2 - 4\xi^2 \alpha_L \alpha_T \qquad (II.35)$$

The integrals that contain $A_{ij5}, A_{ij6}, A_{ij7}, A_{ij8}$, and A_{ij9} in equation $(II.1)$ are combinations of the following:

$$\sum_{i=1}^{10} A_i I_i \equiv \frac{1}{\pi i}\int_\Gamma (A_1\alpha_\beta^2 + A_2\alpha_\beta\xi + A_3\xi^2 + A_4\xi^3/\alpha_\beta + A_5 + A_6\xi/\alpha_\beta + A_7\alpha_\beta + A_8\xi + A_9\xi^2/\alpha_\beta + A_{10}/\alpha_\beta)e^{i\xi x - \alpha_\beta |y|} d\xi \qquad (II.36)$$

By the change of variable, $\xi = -k_\beta \cosh t$, and by the use of equation $(I.9)$, these forms can be integrated as

$$I_1 = k_\beta^3 \frac{H_3\bar{C}_3 - 3H_1\bar{C}_1}{4}$$

$$I_2 = \frac{-ik_\beta^3}{4}(H_3\bar{S}_3 - H_1\bar{S}_1)$$

$$I_3 = \frac{k_\beta^3}{4}(H_3\bar{C}_3 + H_1\bar{C}_1)$$

$$I_4 = \frac{-ik_\beta^3}{4}(H_3\bar{S}_3 + 3H_1\bar{S}_1)$$

$$I_5 = k_\beta H_1\bar{C}_1$$

$$I_6 = -ik_\beta H_1\bar{S}_1$$

$$I_7 = \frac{k_\beta^2}{2}[-H_0 + H_2\bar{C}_2]$$

$$I_8 = \frac{k_\beta^2}{2}[-i\bar{S}_2 H_2]$$

$$I_9 = \frac{k_\beta^2}{2}[H_0 + H_2\bar{C}_2]$$

$$I_{10} = H_0$$

Here, $H_i = H_i^{(1)}(k_\beta\gamma)$,

$$\gamma = \sqrt{x^2 + y^2},$$

$$\bar{C}_n = \cos n\bar{\theta}, \quad \cos\bar{\theta} = \frac{|y|}{\gamma},$$

$$\bar{S}_n = \sin n\bar{\theta} \text{ and } \sin\bar{\theta} = \frac{-x}{\gamma}.$$

A.-Y. Kuo
Senior Engineer,
Structural Integrity Association,
3150 Almaden Expy.,
Suite 226
San Jose, Calif. 95118
Assoc. Mem. ASME

Transient Stress Intensity Factors of an Interfacial Crack Between Two Dissimilar Anisotropic Half-Spaces

Part 2: Fully Anisotropic Materials

Dynamic stress intensity factors for an interfacial crack between two dissimilar elastic, fully anisotropic media are studied. The mathematical problem is reduced to three coupled singular integral equations. Using Jacobi polynomials, solutions to the singular integral equations are obtained numerically. The orders of stress singularity and stress intensity factors of an interfacial crack in a $(\theta^{(1)}/\theta^{(2)})$ *composite solid agree well with the finite element solutions.*

1 Introduction

In a previous paper [1], the dynamic stress intensity factors for a Griffith crack situated at the interface of two bonded dissimilar orthotropic half-spaces were investigated. The method of solution reported in [1] is extended to the study of the transient behavior of an interfacial crack between two dissimilar, fully anisotropic, elastic solids. A typical example of interfacial cracking in anisotropic solids is the delamination of fiber-reinforced composite laminates. The interfacial cracks in composites are introduced by fabrication defects such as incomplete wetting or trapped air bubbles between layers, or by debonding of two laminas as a result of high stress concentration at geometric or material discontinuities, e.g., the well-known free edge effects [2].

Due to the highly anisotropic material properties, there exists significant coupling between three fracture modes, i.e., the simultaneous existence of mode *I*, *II*, and *III* fractures. Numerical solutions of transient stress intensity factors of interfacial cracks in composite materials have been presented in [3] by using hybrid-stress crack-tip elements. In this paper, the crack is excited by prescribed tractions suddenly applied on the crack surface. Governing differential equations, boundary conditions, and continuity conditions are transformed into a frequency domain by applying the Laplace transform. Solutions in the frequency domain are expressed as a series of Jacobi polynomials by solving three coupled singular integral equations. Inverse Laplace transform is carried out numerically with the use of Jacobi polynomials. Numerical examples for an interfacial crack between a $\pm\,\theta$ composite solid of graphite fiber-epoxy are shown. Results of the example problem are compared with finite element solutions.

2 Formulation

As shown in Fig. 1, consider a Cartesian coordinate (x, y, z) with origin at the middle of the interfacial crack between two bonded dissimilar, anisotropic solids. The z-axis is in the out-of-paper direction. All lengths are normalized with respect to the half crack length so that the crack is described by the relations: $|x| \leq 1$, $y=0$, i.e., L equals one unit length in Fig. 1.

Constitutive equations of the materials can be written in the contract notation as

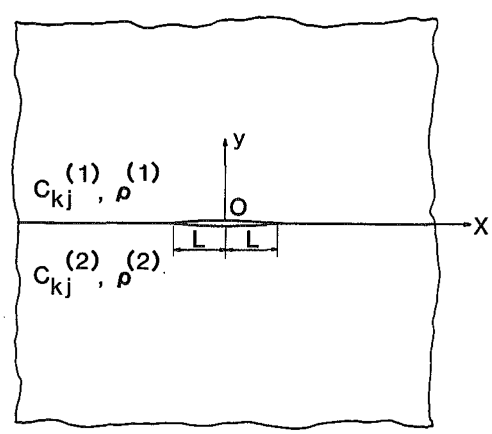

Fig. 1 Geometry of the problem

Contributed by the Applied Mechanics Division for publication in the JOURNAL OF APPLIED MECHANICS.

Discussion on this paper should be addressed to the Editorial Department, ASME, United Engineering Center, 345 East 47th Street, New York, N.Y. 10017, and will be accepted until two months after final publication of the paper itself in the JOURNAL OF APPLIED MECHANICS. Manuscript received by ASME Applied Mechanics Division, September, 1983; final revision, March, 1984.

$$\sigma_k^{(\alpha)} = C_{kj}^{(\alpha)} \epsilon_j^{(\alpha)} \qquad (k,j=1,2,3,4,5,6;\ \alpha=1,2) \tag{1}$$

where the repeated subscript indicates summation, C_{kj} is the stiffness tensor, and the superscripts 1 and 2 designate the upper and lower half-spaces, respectively. In the remainder of this paper, the Greek letter α ($\alpha = 1,2$) will be used as the index of different half-spaces, and the superscript will be dropped unless it is necessary to distinguish the upper and lower half-spaces. The repeated superscript does not imply summation, but the repeated subscript does. For a general anisotropic solid, C_{jk} is a fully populated matrix.

In equation (1), the engineering strains, ϵ_j, are defined by

$$\begin{aligned}
&\epsilon_1 = \epsilon_x = u_{1,x} \quad \epsilon_2 = \epsilon_y = u_{2,y} \quad \epsilon_3 = \epsilon_z = u_{3,z} \\
&\epsilon_4 = \gamma_{yz} = u_{3,y} + u_{2,z} \quad \epsilon_5 = \gamma_{xz} = u_{3,x} + u_{1,z} \\
&\epsilon_6 = \gamma_{xy} = u_{1,y} + u_{2,x}
\end{aligned} \tag{2}$$

where u_1, u_2, and u_3 are components of displacements in the x, y, and z-directions, respectively. The stresses, σ_k, are defined in an analogous manner in the Cartesian coordinate system. In this paper, it is assumed that all external loads are independent of the z-coordinate. Therefore, derivatives of all variables with respect to z vanish.

The equations of motion for both half-spaces are

$$[L][u] = 0 \tag{3}$$

where $[u] = (u_1, u_2, u_3)^T$ and $[L]$ is a three-by-three symmetric operational matrix defined by

$$\begin{aligned}
L_{11} &= C_{11}\frac{\partial^2}{\partial x^2} + 2C_{16}\frac{\partial^2}{\partial x \partial y} + C_{66}\frac{\partial^2}{\partial y^2} - \rho\frac{\partial^2}{\partial t^2} \\
L_{12} &= C_{16}\frac{\partial^2}{\partial x^2} + (C_{12}+C_{66})\frac{\partial^2}{\partial x \partial y} + C_{26}\frac{\partial^2}{\partial y^2} \\
L_{13} &= C_{15}\frac{\partial^2}{\partial x^2} + (C_{14}+C_{56})\frac{\partial^2}{\partial x \partial y} + C_{46}\frac{\partial^2}{\partial y^2} \\
L_{22} &= C_{66}\frac{\partial^2}{\partial x^2} + 2C_{26}\frac{\partial^2}{\partial x \partial y} + C_{22}\frac{\partial}{\partial y^2} - \rho\frac{\partial^2}{\partial t^2} \\
L_{23} &= C_{56}\frac{\partial^2}{\partial x^2} + (C_{46}+C_{25})\frac{\partial^2}{\partial x \partial y} + C_{24}\frac{\partial^2}{\partial y^2} \\
L_{33} &= C_{55}\frac{\partial^2}{\partial x^2} + 2C_{54}\frac{\partial^2}{\partial x \partial y} + C_{44}\frac{\partial^2}{\partial y^2} - \rho\frac{\partial^2}{\partial t^2}
\end{aligned} \tag{4}$$

and ρ is the density of the anisotropic material.

The initial conditions for the problem are

$$\begin{aligned}
&u_j(x,y,0) = 0 \\
&u_{j,t}(x,y,0) = 0
\end{aligned} \qquad (j=1,2,3) \tag{5}$$

The crack is excited by prescribed tractions suddenly applied at time $t=0$ on the crack surfaces. Thus, boundary conditions on the crack surface can be written as

$$\tau_{xy}(x,0,t) = -f_1(x)\ H(t) \tag{6a}$$

$$\sigma_y(x,0,t) = -f_2(x)\ H(t) \quad |x| \le 1 \tag{6b}$$

$$\tau_{yz}(x,0,t) = -f_3(x)\ H(t) \tag{6c}$$

where $H(t)$ is a Heaviside step function.

The upper and lower half-spaces are assumed to be perfectly bonded on their interface except those points in the crack region. Thus, the displacements and tractions on the uncracked interface are continuous, i.e.,

$$\tau_{xy}^{(1)}(x,0,t) - \tau_{xy}^{(2)}(x,0,t) = 0 \tag{7a}$$

$$\sigma_y^{(1)}(x,0,t) - \sigma_y^{(2)}(x,0,t) = 0 \qquad \text{all } x \tag{7b}$$

$$\tau_{yz}^{(1)}(x,0,t) - \tau_{yz}^{(2)}(x,0,t) = 0 \tag{7c}$$

and

$$u_j^{(1)}(x,0,t) - u_j^{(2)}(x,0,t) = 0 \qquad (j=1,2,3,)\ \ |x|>1 \tag{7d}$$

The problem can be simplified by treating applied tractions that are symmetric about the y-axis, i.e., $f_1(-x) = -f_1(x)$, $f_2(-x) = f_2(x)$, and $f_3(-x) = f_3(x)$.

Solutions for the asymmetric case can be obtained by following the same procedure described in this paper, and solutions of a general problem can always be decomposed into an asymmetric and a symmetric cases. This symmetric tractions on crack surfaces lead to the following relations:

$$u_j(x,0,t) = (-1)^j u_j(-x,0,t) \qquad (j=1,2,3) \tag{8}$$

3 Singular Integral Equations

The solution to the problem defined by equations (3), (5), and (6)–(8) is obtained by transforming the equations into a frequency domain by the Laplace transform. Let s be the Laplace transform parameter and a tilde over a variable, e.g., $\tilde{u}_j$, represents the corresponding transformed function in the frequency domain.

In the s-domain, the transformed equations of motion are satisfied by assuming

$$\tilde{u}_1^{(\alpha)}(x,y,s) = (2\pi)^{-1/2}\int_{-\infty}^{\infty} A_j^{(\alpha)}(\xi,s)\exp(q_j^{(\alpha)})\ d\xi \tag{9a}$$

$$\tilde{u}_2^{(\alpha)}(x,y,s) = (2\pi)^{-1/2}\int_{-\infty}^{\infty} A_j^{(\alpha)}(\xi,s)\,\omega_j^{(\alpha)}(\xi,s)\exp(q_j^{(\alpha)})\ d\xi \tag{9b}$$

$$\tilde{u}_3^{(\alpha)}(x,y,s) = (2\pi)^{-1/2}\int_{-\infty}^{\infty} A_j^{(\alpha)}(\xi,s)\,\delta_j^{(\alpha)}(\xi,s)\exp(q_j^{(\alpha)})\ d\xi \tag{9c}$$

where $j=1,2$, or 3; $q_j^{(\alpha)} = i\xi x + (-1)^\alpha p_j^{(\alpha)} y$; A_j are unknown functions of ξ and s to be determined by the boundary and continuity conditions; and p_j is the jth root with positive real part of the equation

$$|\Delta(p,\xi)| = 0 \tag{10}$$

where $[\Delta]$ is a three-by-three matrix defined by

$$\begin{aligned}
\Delta_{11} &= C_{66}p^2 - C_{11}\xi^2 - \rho s^2 \pm 2iC_{16}\xi p \\
\Delta_{12} &= C_{26}p^2 - C_{16}\xi^2 \pm i\xi p(C_{66}+C_{12}) \\
\Delta_{13} &= C_{46}p^2 - C_{15}\xi^2 \pm i\xi p(C_{14}+C_{56}) \text{“}+\text{”} \quad \text{for} \quad \alpha=1 \\
\Delta_{22} &= C_{22}p^2 - C_{66}\xi^2 - \rho s^2 \pm 2iC_{26}\xi p \quad \text{“}-\text{”} \quad \text{for} \quad \alpha=2 \\
\Delta_{23} &= C_{24}p^2 - C_{56}\xi^2 \pm i\xi p(C_{46}+C_{25}) \\
\Delta_{33} &= C_{44}p^2 - C_{55}\xi^2 - \rho s^2 \pm 2iC_{54}\xi p
\end{aligned} \tag{11}$$

For most materials of engineering interest, it can be assumed that there is no double root in equation (10). However, for the case of double root, e.g., $p_2 = p_3$, "exp (q_j)" should be replaced by "y.exp (q_j)" for $j = 3$ in equations (9a)–(9c). In equations (9b) and (9c), ω_j and δ_j are defined by

$$\omega_j = \frac{\Omega(p_j, C_{mn}, \xi, \rho)}{\Lambda(p_j, C_{mn}, \xi, \rho)} \qquad \text{(no summation)} \tag{12a}$$

$$\delta_j = \frac{-\Theta(p_j, C_{mn}, \xi, \rho)}{\Lambda(p_j, C_{mn}, \xi, \rho)} \tag{12b}$$

where

$$\Omega = \Delta_{13}\Delta_{23} - \Delta_{12}\Delta_{33} \tag{13a}$$

$$\Theta = \Delta_{13}\Delta_{22} - \Delta_{12}\Delta_{23} \tag{13b}$$

$$\Lambda = \Delta_{22}\Delta_{33} - \Delta_{23}\Delta_{23} \qquad (13c)$$

Let

$$\tilde{u}_j^{(1)}(x,0,s) - \tilde{u}_j^{(2)}(x,0,s) = (2\pi)^{-1/2}\int_{-\infty}^{\infty} G_j(\xi,s)e^{i\xi x}\frac{1}{\xi}d\xi \qquad (j=1,2,3) \qquad (14)$$

In equation (14), G_1, G_2, and G_3 can be shown to be even, odd, and even functions of ξ, respectively, by the symmetric loading conditions, equation (8). Substituting equation (14) into equations (7a)–(7c) and equations (9a)–(9c), we can rewrite $A_j^{(\alpha)}$ in terms of G_j as

$$A_j^{(\alpha)}(\xi,s) = a_{(j+3\alpha-3)k}G_k(\xi,s)/\xi \qquad (j,k=1,2,3) \qquad (15)$$

where a_{jk} is an element of the inverse matrix of a six-by-six nonsingular matrix $[D]$. Matrix $[D]$ is defined by

$$D_{1(j+3\alpha-3)} = (-1)^{\alpha+1}$$
$$D_{2(j+3\alpha-3)} = (-1)^{\alpha+1}\omega_j^{(\alpha)} \qquad (j=1,2,3) \qquad (16)$$
$$D_{3(j+3\alpha-3)} = (-1)^{\alpha+1}\delta_j^{(\alpha)}$$

$$\begin{bmatrix} D_{4(j+3\alpha-3)} \\ D_{5(j+3\alpha-3)} \\ D_{6(j+3\alpha-3)} \end{bmatrix} = (-1)^{\alpha+1}\begin{bmatrix} C_{61}^{(\alpha)} & C_{62}^{(\alpha)} & C_{64}^{(\alpha)} & C_{65}^{(\alpha)} & C_{66}^{(\alpha)} \\ C_{21}^{(\alpha)} & C_{22}^{(\alpha)} & C_{24}^{(\alpha)} & C_{25}^{(\alpha)} & C_{26}^{(\alpha)} \\ C_{41}^{(\alpha)} & C_{42}^{(\alpha)} & C_{44}^{(\alpha)} & C_{45}^{(\alpha)} & C_{46}^{(\alpha)} \end{bmatrix}.$$

$$[i\xi, (-1)^{\alpha}p_j^{(\alpha)}\omega_j^{(\alpha)}, (-1)^{\alpha}p_j^{(\alpha)}\delta_j^{(\alpha)}, i\xi\delta_j^{(\alpha)}, (-1)^{\alpha}p_j^{(\alpha)} + i\xi\omega_j^{(\alpha)}]^T$$

Substituting equations (9a)–(9c) into equations (6a)–(6c) and eliminating A_j by equation (15), we obtain three coupled integral equations:

$$\int_{-\infty}^{\infty} B_{jk}(\xi,s)G_k(\xi,s)\frac{e^{i\xi x}}{\xi}d\xi = -f_j(x)/s, |x| \le 1 \qquad (j,k=1,2,3) \qquad (17)$$

where

$$B_{1k}(\xi,s) = D_{4j}a_{jk} \qquad (18a)$$
$$B_{2k}(\xi,s) = D_{5j}a_{jk} \qquad (j,k=1,2,3) \qquad (18b)$$
$$B_{3k}(\xi,s) = D_{6j}a_{jk} \qquad (18c)$$

By Betti's reciprocal theorem, it can be shown that

$$B_{kj}(\xi,s) = B_{jk}(-\xi,s) \qquad (19)$$

Assume

$$G_1(\xi,s) = (2/\pi)^{1/2}\int_0^1 r_1'(x,s)\cos\xi x\,dx \qquad (20a)$$

$$G_2(\xi,s) = (2/\pi)^{1/2}\int_0^1 ir_2'(x,s)\sin\xi x\,dx \qquad (20b)$$

$$G_3(\xi,s) = (2/\pi)^{1/2}\int_0^1 r_3'(x,s)\cos\xi x\,dx \qquad (20c)$$

In equations (20a)–(20c), $\cos\xi x$ is used for G_1 and G_3 and $\sin\xi x$ is used for G_2 since G_1, G_2, and G_3, are, respectively, even, odd, and even functions of ξ.

Eliminating G_k from equations (20a)–(20c) and equation (17), we obtain three coupled singular integral equations:

$$M'_{jk}r_k(x,s) + (\pi i)^{-1}M''_{jk}\int_{-1}^{1} r_k(\eta,s)\frac{d\eta}{\eta - x} + \int_{-1}^{1} H_{jk}r_k(\eta,s)d\eta = -f_j(x)/s \qquad (j,k=1,2,3) \qquad (21)$$

where r_1, r_2, and r_3 are symmetric, asymmetric, and symmetric extensinos of r_1', r_2', and r_3', respectively, in $[-1, 1]$,

$$[M'] = \begin{bmatrix} 0 & im_1 & 0 \\ -im_1 & 0 & im_3 \\ 0 & -im_3 & 0 \end{bmatrix} \qquad (22)$$

$$[M''] = \begin{bmatrix} n_1 & 0 & m_2 \\ 0 & n_2 & 0 \\ m_2 & 0 & n_3 \end{bmatrix} \qquad (23)$$

and $[H]$ is a three-by-three matrix. Definitions of n_1, n_2, n_3, m_1, m_2, m_3, and elements of $[H]$ are given in Appendix 1.

Equation (21) is a standard form of a singular integral equation which can be solved numerically by the method suggested by Erdogan [4]. By the relation

$$r_j = R_{jk}\phi_k \qquad (j,k=1,2,3) \qquad (24)$$

where

$$[R] = \begin{bmatrix} T(n_3,m_2) & -T(n_3,m_2) & 1 \\ 1 & 1 & 0 \\ -T(m_2,n_1) & T(m_2,m_3) & m_1/m_3) \end{bmatrix} \qquad (25a)$$

$$T(z_1,z_2) = i(m_1z_1 + m_3z_2)/(\lambda(n_1n_3 - m_2^2)) \qquad (25b)$$

$$\lambda = \left(\frac{m_1(m_1n_3 + m_2m_3) + m_3(m_1m_2 + n_1m_3)}{n_2(n_1n_3 - m_2m_2)}\right)^{1/2}, \qquad (25c)$$

equation (21) can be transformed into a simpler form as

$$\begin{bmatrix} \lambda\phi_1(x,s) \\ -\lambda\phi_2(x,s) \\ 0 \end{bmatrix} + (\pi i)^{-1}\int_{-1}^{1}\begin{bmatrix} \phi_1(\eta,s) \\ \phi_2(\eta,s) \\ \phi_3(\eta,s) \end{bmatrix}\frac{d\eta}{\eta - x} + [\bar{M}(\eta,x,s)]\int_{-1}^{1}\begin{bmatrix} \phi_1(\eta,s) \\ \phi_2(\eta,s) \\ \phi_3(\eta,s) \end{bmatrix}d\eta = \frac{1}{s}[F] \qquad (26)$$

where

$$[F] = -[R]^{-1}[M'']^{-1}[f_1 f_2 f_3]^T \qquad (27a)$$
$$[\bar{M}] = [R]^{-1}[M'']^{-1}[H][R] \qquad (27b)$$

λ, $-\lambda$, and 0 in equation (26) are eigenvalues of the matrix $[M'']^{-1}[M']$ and $[R]$ is a three-by-three matrix containing their corresponding eigenvectors. Thus, in equation (26)

$$\phi_2(x,s) = \overline{-\phi_1(x,s)}, \qquad F_2(x,s) = \overline{F_1(x,s)} \qquad (28)$$

The first two equations of equation (26) are conjugates of each other, i.e., there are only two independent equations. The continuity of displacements, equation (7d), lead to three additional equations to be satisfied:

$$\int_{-1}^{1}\phi_j(x,s)dx = 0 \qquad (j=1,2,3) \qquad (29)$$

4 Polynomial Solutions

Solutions to equations (26) and (29) can be expressed as a series of Jacobi polynomials as [4, 6, 7]

$$\phi_1(x,s)=C_n(s)\,W_1(x)P_n^{(a,\bar{a})}(x) \qquad (n=0,1,2,\ldots,\infty) \tag{30a}$$

$$\phi_3(x,s)=D_n(s)\,W_3(x)P_n^{(-1/2,-1/2)}(x) \tag{30b}$$

where

$$W_1(x)=(1-x)^a(1+x)^{\bar{a}} \tag{31a}$$

$$W_3(x)=(1-x^2)^{-1/2} \tag{31b}$$

C_n and D_n are unknown complex constants to be determined, and

$$a=-1/2-\gamma \tag{32a}$$

$$\gamma=(\pi)^{-1}Ln((1-\lambda)/(1+\lambda)) \tag{32b}$$

$W_1(x)$ and $W_3(x)$ are weight functions of the Jacobi polynomials $p_n^{(a,\bar{a})}(x)$ and $P_n^{(-1/2,-1/2)}(x)$, respectively, and λ is defined by equation (25c).

Similar to the isotropic [5] or orthotropic [1] cases, the order of stress singularity at the interfacial crack tip has a real part of $-1/2$ and an imaginary part of γ. The imaginary part is a function of the relative material constants of the two solids. This imaginary stress singularity causes a physically unrealistic overlapping of crack surfaces near the crack tip [1, 8, 9]. However, this inadmissible phenomenon may be neglected as long as the overlapping zone is very small, e.g., 10^{-4} of the crack length.

By the relations,

$$\phi_1(-x,s)=-\overline{\phi_1(x,s)} \qquad \phi_3(-x,s)=\phi_3(x,s) \tag{33}$$

$$W_1(-x)=\overline{W_1(x)} \qquad W_3(-x)=W_3(x)$$

it can be shown that, in equations (30a) and (30b),

$$C'_{2m}=C''_{2m+1}=D'_m=0 \qquad (m=0,1,2,\ldots,\infty) \tag{34a}$$

where

$$C_n=C'_n+iC''_n \tag{34b}$$

$$D_n=D'_n+iD''_n \tag{34c}$$

Substituting equations (30a) and (30b) into equations (26) and (29) and applying the orthogonal properties of the Jacobi polynomials [1], we obtain a system of infinite linear algebra equations of C_n and D_n. If only the first $(N+1)$ terms are included in equations (29a) and (29b), i.e.,

$$\phi_1(x,s)=C_n(s)\,W_1(x)p_n^{(a,\bar{a})}(x) \qquad (n=0,1,2,\ldots,N) \tag{35a}$$

$$\phi_3(x,s)=D_n(s)\,W_3(x)p_n^{(-1/2,-1/2)}(x) \tag{35b}$$

we obtain the followng system of equations:

$$a_nC_{n+1}+b_{nj}C_j+d_{nj}\bar{C}_j+e_{nj}D_j=g_n \tag{36a}$$

$$l_nD_{n+1}+h_{nj}C_j+s_{nj}\bar{C}_j+t_{nj}D_j=\nu_n \qquad (n,j=0,1,2,\ldots,N-1) \tag{36b}$$

$$N_nC_n=0 \tag{36c}$$

$$Q_nD_n=0 \tag{36d}$$

where a_n, b_{nj}, e_{nj}, g_n, l_n, h_{nj}, s_{nj}, t_{nj}, ν_n, N_n, and Q_n are defined in Appendix 2. The $(2N+2)$ unknowns of C_n and D_n can be calculated by the $(2N+2)$ equations of (36a)–(36d).

5 Stress Intensity Factors

Both oscillatory stress singularity, $-1/2+i\gamma$, and conventional square root stress intensity exist for the present problem. The stress intensity factors are defined by

$$\begin{bmatrix}\tau_{xy}(x,0,t)\\ \sigma_y(x,0,t)\\ \tau_{yz}(x,0,t)\end{bmatrix}=\frac{1}{[\pi(x^2-1)]^{1/2}}\left\{\begin{bmatrix}K_{10}(t)\\ K_{20}(t)\\ K_{30}(t)\end{bmatrix}+\begin{bmatrix}K_{1\gamma}(t)\cos(\gamma Ln(x-1)+\beta_1(t))\\ K_{2\gamma}(t)\cos(\gamma Ln(x-1)+\beta_2(t))\\ K_{3\gamma}(t)\cos(\gamma Ln(x-1)+\beta_3(t))\end{bmatrix}\right\}+(H.O.T.) \tag{37}$$

where $|x|>1$ and $H.O.T.$ stands for higher-order terms.

It can be shown that, for $|x|>1$,

$$[G]\begin{bmatrix}\tilde{\tau}_{xy}(x,0,s)\\ \tilde{\sigma}_y(x,0,s)\\ \tilde{\tau}_{yz}(x,0,s)\end{bmatrix}=\frac{1}{\pi i}\int_{-1}^{1}\begin{bmatrix}\phi_1(\eta,0,s)\\ \phi_2(\eta,0,s)\\ \phi_3(\eta,0,s)\end{bmatrix}\frac{d\eta}{\eta-x}+\int_{-1}^{1}[\bar{M}(\eta,x,s)]\begin{bmatrix}\phi_1(\eta,0,s)\\ \phi_2(\eta,0,s)\\ \phi_3(\eta,0,s)\end{bmatrix}d\eta \tag{38}$$

where $[G]$ is a three-by-three matrix defined by

$$[G]=[R]^{-1}[M'']^{-1} \tag{39}$$

In equation (38), the second integration on the right-hand side is a higher-order term and the first integration can be evaluated by substituting the solutions, equations (35a), (35b), into it and using the relations:

$$(\pi i)^{-1}\int_{-1}^{1}p_n^{(a,\bar{a})}(\eta)\,W_1(\eta)\frac{d\eta}{\eta-x}=\frac{-2}{1+e^{-2\gamma}}[-W_1(x)p_n^{(a,\bar{a})}(x)+A_n(x)] \tag{40a}$$

$$(\pi i)^{-1}\int_{-1}^{1}p_n^{(-1/2,-1/2)}(\eta)\,W_3(\eta)\frac{d\eta}{\eta-x}=-2[-W_3(x)p_n^{(-1/2,-1/2)}(x)+B_n(x)] \tag{40b}$$

where $A_n(x)$ and $B_n(x)$ are, respectively, the principal parts of $W_1(x)p_n^{(a,\bar{a})}(x)$ and $W_3(x)p_n^{(-1/2,-1/2)}(x)$ at infinity. Thus, as $x>1$ and x approaches to 1,

$$[G]\begin{bmatrix}\tilde{\tau}_{xy}(x,0,s)\\ \tilde{\sigma}_y(x,0,s)\\ \tilde{\tau}_{yz}(x,0,s)\end{bmatrix}=\begin{bmatrix}-i(x-1)^a(x+1)^{\bar{a}}C_n(s)p_n^{(a,\bar{a})}(1)/\cosh(\pi\gamma)\\ i(x-1)^{\bar{a}}(x-1)^aC_n(s)p_n^{(a,\bar{a})}(1)/\cosh(\pi\gamma)\\ i(x-1)^{-1/2}(x+1)^{-1/2}D_n(s)p_n^{(-1/2,-1/2)}(1)\end{bmatrix} \tag{41}$$

where n is ranging 0 to N. In equation (41), higher-order terms have been neglected. From equation (41), the stress intensity factors, $\tilde{K}_{j0}(s)$ and $\tilde{K}_{j\gamma}(s)$, as well as the phase angles $\tilde{\beta}_j(s)$ $(j=1,2,3)$ can be determined.

In numerical calculation, the integrations of a_n, g_{nj}, . . . , and Q_n of equations (36a)–(36d) are performed by the use of Gaussian-Laguree quadrature, Gauss-Hermite quadrature, or Gaussian quadrature [10]. Having solutions in the frequence domain, we can do the inverse Laplace transform with the method suggested by Miller and Guy [11].

Table 1 Values of γ

$\theta^{(1)}/\theta^{(2)}$	75 deg	60 deg	45 deg	30 deg	15 deg
75 deg	0.0	0.01346	0.02886	0.04104	0.04705
60 deg	0.01346	0.0	0.01661	0.03096	0.03800
45 deg	0.02886	0.01661	0.0	0.01598	0.02480
30 deg	0.04104	0.03096	0.01597	0.0	0.01051
15 deg	0.04750	0.03800	0.02480	0.01051	0.0
−15 deg	0.04768	0.03984	0.02859	0.01617	0.00643
−30 deg	0.04402	0.03932	0.03420	0.02401	0.01617
−45 deg	0.03569	0.03513	0.03434	0.03240	0.02859
−60 deg	0.02506	0.02942	0.03513	0.03932	0.03984
−75 deg	0.01580	0.02506	0.03569	0.04402	0.04768

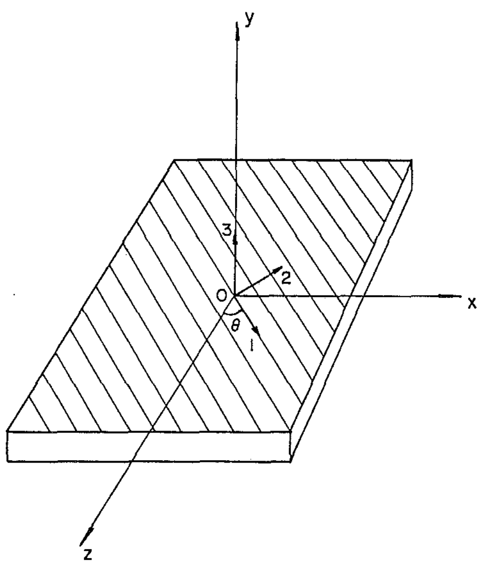

Fig. 2 Coordinates for a unidirectional fiber-reinforced composite material

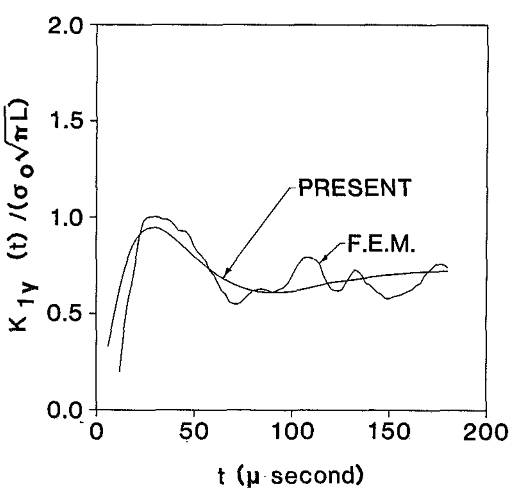

Fig. 3 Transient stress intensity factor $K_{1\gamma}(t)$ ($f_1(x) = f_3(x) = 0$, $f_2(x) = \sigma_0\delta(x)$)

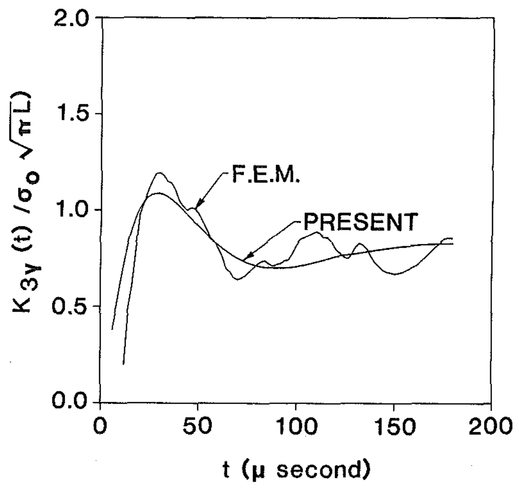

Fig. 4 Transient stress intensity factors $K_{3\gamma}(t)$ ($f_1(x) = f_3(x) = 0$, $f_2(x) = \sigma_0\delta(x)$)

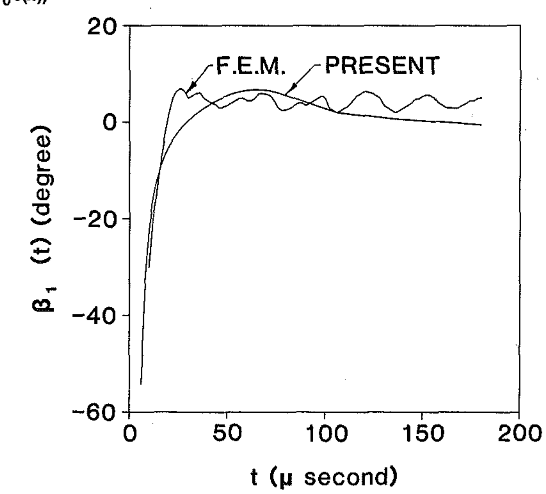

Fig. 5 Transient phase angle $\beta_1(t)$ ($f_1(x) = f_3(x) = 0$, $f_2(x) = \sigma_0\delta(t)$)

6 Numerical Results and Discussions

As shown in Fig. 1, consider a composite solid made of two dissimilar unidirectional fiber-reinforced materials. The fiber directions of the upper and lower media are $\theta^{(1)}$ and $\theta^{(2)}$, respectively, where θ is defined in Fig. 2. The following material properties of graphite fiber-epoxy composites are used:

$$\begin{aligned} \rho &= 7.44 \text{ g/cm}^3 \\ E_1 &= 137800 \text{ MPA} \\ E_2 &= E_3 = 14469 \text{ MPa} \\ G_{13} &= G_{12} = G_{23} = 5856.5 \text{ MPa} \\ \nu_{12} &= \nu_{13} = \nu_{23} = 0.21 \end{aligned} \tag{42}$$

For different combinations of $\theta^{(1)}$ and $\theta^{(2)}$, the imaginary part of the oscillatory stress singularity, γ, have been calculated and tabulated in Table 1. It is found that the γ values are the same as those calculated by the Weiner-Hopf technique [3].

For the case of $\theta^{(2)} = -\theta^{(1)}$, mode II fracture is found to be decoupled from the other two modes. As a numerical example, $\theta^{(1)}$ and $\theta^{(2)}$ are chosen to be 45 and −45 deg, respectively. The corresponding γ value is 0.03434. Two sets of loads have been applied on the crack surfaces: $f_1(x) = f_3(x) = 0$, $f_2(x) = \sigma_0\delta(x)$, and $f_1(x) = f_3(x) = 0$, $f_2(x) = \sigma_0$ where δ is a delta function and σ_0 is a positive number.

Six, five, and nine points were used in Gauss-Laguerre, Gauss-Hermite, and Gaussian quadratures, respectively. Eight terms in equations (35*a*) and (35*b*), i.e., $N=7$, were included in the solutions, and 10 Jacobi polynomials of $P_n^{(0,0)}(t)$ were used in the inverse Laplace transform [11].

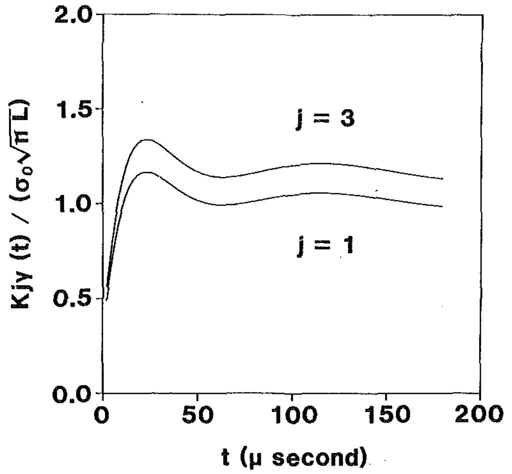

Fig. 6 Transient stress intensity factors $K_{j\gamma}(t)\,(f_1(x) = f_3(x) = 0,\ f_2(x) = \sigma_0)$

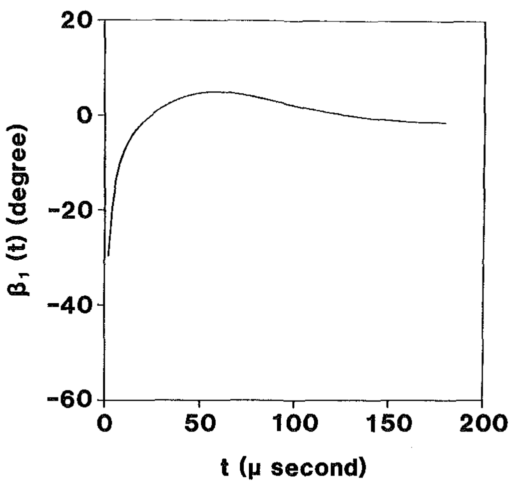

Fig. 7 Transient phase angle $\beta_1(T)\,(f_1(x) = f_3(x) = 0,\ f_2(x) = \sigma_0)$

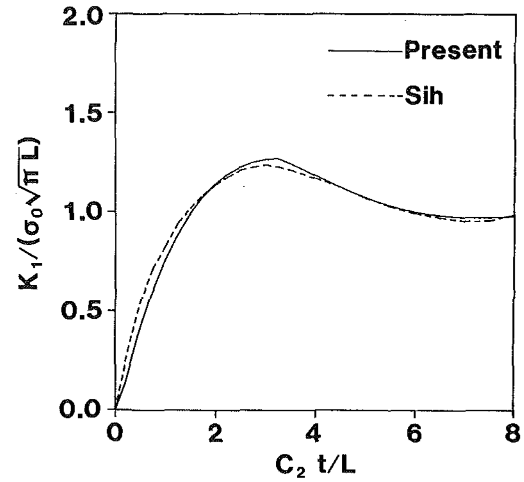

Fig. 8 Transient stress intensity factor

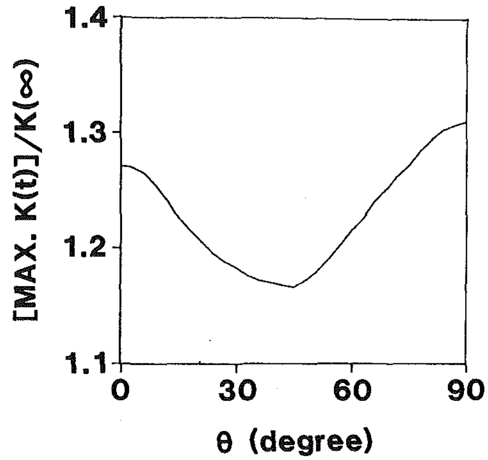

Fig. 9 Maximum overshoot of stress intensity factor

For the case of concentrate force, $f_2(x) = \sigma_0 \delta(x)$, k_{j0}, $(j = 1,2,3)$ and $K_{2\gamma}$ are all equal to zero and the transient stress intensity factors, $K_{2\gamma}(t)$, $K_{3\gamma}(t)$, and the phase angle $\beta_1(t)$ are shown in Figs. 3–5, respectively. $\beta_3(t)$ was found to be $[-\pi/2 - \beta_1(t)]$. Solutions obtained by the finite element methods [3] have also been plotted in Figs. 3–5 for comparison. Present solutions are found in very good agreement with the finite element solutions. Static solutions for this case are:

$$\frac{K_{1\gamma}(\infty)}{\sigma_0(\pi L)^{1/2}} = 0.6879(0.6876)$$

$$\frac{K_{3\gamma}(\infty)}{\sigma_0(\pi L)^{1/2}} = 0.7899(0.7893) \tag{43}$$

$$\beta_1(\infty) = 1.9978 \text{ deg } (4.5770 \text{ deg})$$

where numbers in the parentheses are static solutions of the finite element analyses. It is observed that the transient solutions converge to the static solutions very fast.

For the case of uniform tension, $f_2(x) = \sigma_0$, results have been depicted in Figs. 6 and 7. The static solutions similar to those defined in equation (43) are 1.0133, 1.1633, and 1.0529 deg, respectively. The static solutions have also been given in [3] as 0.9937, 1.1408, and 3.9700 deg, respectively. As discussed in [1], solutions during the first 10 μsec cannot be properly calculated by the numerical inverse Laplace transform due to the jump properties of the Heaviside function at $t = 0$. However, the current solutions are able to give accurate results in the range of most interest.

As a special case, the dynamic stress intensity factor of a finite crack in a homogeneous, isotropic solid is also calculated. The crack is subjected to a suddenly applied tension at the infinity, and its normalized mode I stress intensity factor is compared with the solution obtained by Sih and Embley [12] in Fig. 8. The good agreement between the present solution and Sih's solution further ensures the adequacy of the solution algorithm discussed in this paper. For an interfacial crack in $\pm\,\theta$ composites, a parametric study is conducted by changing the value of θ to see the effects of material anisotropy. The crack is subjected to uniform tension ($f_2(x) = \sigma_0$). The maximum overshoot of the stress intensity factors for different θ values are plotted in Fig. 9. It is found that the maximum overshoot of the stress intensity factor for an interfacial crack in $\pm\,\theta$ composites reaches its minimum at $\theta = 45$ deg. The maximum stress intensity factor of an interfacial crack in $\pm\theta$ composites is smaller than that of a crack in a homogeneous lamina of $\theta = 0$ deg or $\theta = 90$ deg. Thus, in a $\pm\,\theta$ composite laminate, fatigue crack growth is more likely to occur within a composite lamina than at the interfaces. The foregoing statement is not necessarily true for the composite laminate of another type.

References

1 Kuo, An-Yu, "Transient Stress Intensity Factors of An Interfacial Crack Between Two Dissimilar Anisotropic Half-Spaces, Part 1 Orthotropic Materials," ASME Journal of Applied Mechanics, Vol. 51, 1984, pp. 71–76.

2 Pipes, R. B., and Pagano, N. J., "Interlaminar Stresses in Composite Laminates Under Uniform Axial Extension," *Journal of Composite Materials*, Vol. 4, 1970, pp. 538–548.

3 Kuo, An-Yu, *Dynamic Analysis of Interfacial Cracks in Composite Laminates*, Ph.D. Dissertation, Department of Theoretical and Applied Mechanics, University of Illinois at Urbana-Champaign, 1982.

4 Erdogan, F., "Approximate Solutions of Systems of Singular Integral Equations," *SIAM Journal of Applied Mathematics*, Vol. 17, 1969, pp. 1041–1059.

5 William, M. L., "The Stress Around a Fault or Crack in Dissimilar Media," *Bulletin of the Seismological Society of America*, Vol. 49, 1959, pp. 199–204.

6 Erdogan, F., and Gupta, G. D., "On the Numerical Solution of Singular Integral Equations," *Quarterly of Applied Mathematics*, Vol. 30, 1972, pp 525–534.

7 Krenk, Steen, "Polynomial Solutions of Singular Integral Equations, With Application to Elasticity Theory," Risø National Laboratory, Denmark, 1981.

8 England, A. H., "Crack Between Dissimilar Media," ASME JOURNAL OF APPLIED MECHANICS, Vol. 32, 1965, pp. 400–402.

9 Erdogan, F., "Stress Distribution in Bonded Dissimilar Materials With Cracks," ASME JOURNAL OF APPLIED MECHANICS, Vol. 32, 1965, pp. 403–410.

10 Abramowitz, M., and Stegun, I., *Handbook of Mathematical Functions*, Dover, New York, 1965.

11 Miller, M. K., and Guy, W. T., Jr., "Numerical Inverse of Laplace Transform by Use of Jacobi Polynomials," *SIAM Journal of Numerical Analysis*, Vol. 30, 1966, pp. 624–635.

12 Sih, G. C., and Embley, G. T., "Impact Response of A Finite Element Crack in Plane Extension," *Int. J. Solids Structures*, Vol. 8, 1972, pp. 977–993.

APPENDIX 1

$$n_j = \lim_{\xi\to\infty} [B_{jj}(\xi,s)/|\xi|] \qquad (j=1,2,3,; \text{ no summation})$$

$$m_1 = -i \lim_{\xi\to\infty} [B_{12}(\xi,s)/\xi]$$

$$m_2 = \lim_{\xi\to\infty} [B_{13}(\xi,s)/|\xi|]$$

$$m_3 = -i \lim_{\xi\to\infty} [B_{23}(\xi,s)/\xi]$$

$$[H] = (i/\pi)\int_0^\infty [H_1][B'][H_2]d\xi$$

where $[H_1]$, $[H_2]$, and $[B']$ are three-by-three matrices defined by

$$(H_1)_{11} = (H_1)_{33} = (H_2)_{22} = \sin\xi x$$

$$(H_1)_{22} = (H_2)_{11} = (H_2)_{33} = \cos\xi x$$

$$(H_1)_{jk} = (H_2)_{jk} = 0, \quad j \neq k$$

$$B'_{11} = [B_{11}(\xi,s) - n_1|\xi|]/\xi$$

$$B'_{12} = iB_{12}(\xi,s)/\xi + m_1$$

$$B'_{13} = (B_{13}(\xi,s) - m_2|\xi|)/\xi$$

$$B'_{22} = [B_{22}(\xi,s) - n_2|\xi|]/\xi$$

$$B'_{23} = iB_{23}(\xi,s)/\xi + m_3$$

$$B'_{33} = [B_{33}(\xi,s) - n_3|\xi|]/\xi$$

APPENDIX 2

$$a_n = -\pi i(1-\lambda^2)^{1/2}\frac{|n+1/2+i\gamma|^2 \ldots |1/2+i\gamma|^2}{[(n+1)!]\cosh(\pi\gamma)}$$

$$b_{nj} = \int_{-1}^{1}\int_{-1}^{1} H_{11}(\eta,x,s)\, W_1(\eta)\,[W_1(x)]^{-1} p_n^{(-a,-\bar a)}(x)\, p_j^{(a,\bar a)}(\eta)\, d\eta dx$$

$$d_{nj} = -\int_{-1}^{1}\int_{-1}^{1} H_{12}(\eta,x,s)\,\overline{W_1(\eta)}\,[W_1(x)]^{-1} p_n^{(-a,-\bar a)}(x)\,\overline{p_j^{(a,\bar a)}(\eta)}\, d\eta dx$$

$$e_{nj} = \int_{-1}^{1}\int_{-1}^{1} H_{13}(\eta,x,s)\, W_3(\eta)[W_1(x)]^{-1} p_n^{(-a,-\bar a)}(x)\, p_j^{(-1/2,-1/2)}(\eta)\, d\eta dx$$

$$g_n = s^{-1}\int_{-1}^{1} p_n^{(-a,-\bar a)}(x)\,[W_1(x)]^{-1}F_1(x)\,dx$$

$$l_n = -\pi i\frac{(n+1/2)(n-1/2)^2 \ldots (1/2)^2}{[(n+1)!]^2}$$

$$h_{nj} = \int_{-1}^{1}\int_{-1}^{1} H_{31}(\eta,x,s)\, W_1(\eta)[W_3(x)]^{-1} p_j^{(-a,-\bar a)}(\eta)\, p_n^{(1/2,1/2)}(x)\, d\eta dx$$

$$s_{nj} = -\int_{-1}^{1}\int_{-1}^{1} H_{32}(\eta,x,s)\,\overline{W_1(\eta)}\,[W_3(x)]^{-1} p_n^{(1/2,1/2)}(x)\,\overline{p_j^{(-a,-\bar a)}(\eta)}\, d\eta dx$$

$$t_{nj} = \int_{-1}^{1}\int_{-1}^{1} H_{33}(\eta,x,s)\, W_3(\eta)[W_3(x)]^{-1} p_n^{(1/2,1/2)}(x) p_j^{(-1/2,-1/2)}(\eta) d\eta dx$$

$$N_n = \int_{-1}^{1} W_1(x) p_n^{(a,a)}(x) dx$$

$$Q_n = \int_{-1}^{1} W_3(x) p_n^{(-1/2,-1/2)}(x)\,dx$$

$$\nu_n = s^{-1}\int_{-1}^{1} p_n^{(1/2,1/2)}(x)\,[W_3(x)]^{-1}F_3(x)\,dx$$

where F_1 and F_3 are components of $[F]$ defined in equation (27*a*).

The integrals of b_{nj}, d_{nj}, e_{nj}, h_{nj}, s_{nj}, t_{nj}, N_n, and Q_n can be rewritten in more convenient forms with a variable transformation,

$$x = \tanh\phi, \quad \eta = \tanh\theta$$

so that the lower and upper integration limits of these numbers become ∞ and $-\infty$, respectively. For example,

$$b_{nj} = \int_{-\infty}^{\infty}\int_{-\infty}^{\infty} H_{11}(\tanh\phi,\tanh\theta,s)\, e^{-2i\gamma(\phi-\theta)} p_n^{(-a,-\bar a)}(\tanh\phi)\, p_j^{(a,\bar a)}(\tanh\theta) \quad \text{sech}^3\phi \quad \text{sech}\theta \quad d\phi d\theta$$

R. D. Gregory

I. Gladwell

Department of Mathematics,
University of Manchester,
Manchester, England M13 9PL

The Generation of Waves in a Semi-Infinite Plate by a Smooth Oscillating Piston

A semi-infinite plate is set into plane strain, time-harmonic vibration by a rigid oscillating piston, which is in smooth contact with the edge of the plate. The exact (linearized) solution to this problem is obtained as a series expansion involving the Rayleigh-Lamb modes of the plate, the coefficients being determined by a biorthogonality relation. We compute the amplitude of the resultant force exerted by the piston, the mean total rate of working of the piston, and the proportion of outgoing energy in each of the available propagating modes; resonances are observed at certain of the cut-off frequencies.

1 Introduction

In a recent paper (Gregory and Gladwell [1]) the authors investigated the reflection of a Rayleigh-Lamb wave at the free (or fixed) end of a semi-infinite plate. It was found that in general all the propagating Rayleigh-Lamb modes contributed to the relected far field, but that near the end of the plate the evanescent modes were also significant.

In the present paper we consider the *generation* of steady state, time-harmonic waves in the semi-infinite plate $x \geq 0$, $|y| \leq h$, $|z| < \infty$ by a smooth rigid piston which is in permanent contact with the end $x = 0$. The piston is made to execute small, time-harmonic oscillations perpendicular to its plane, and this sets up a time-harmonic response in the rest of the plate. In Section 2 we determine the displacement field of this response by expanding it as a series of the (symmetrical) Rayleigh-Lamb modes of the plate; in Section 3 we show how the coefficients in ths expansion may be determined by the use of a suitable biorthogonality relation obtained by Fraser [2], and more generally by Gregory [3].

At each frequency ω, we find that in general the undamped outgoing waves are a superposition of all the propagating modes that are available at that frequency. We compute the total rate of energy transmission down the plate, per unit length in the z-direction (Fig. 3); and also the proportion of this energy that is carried by each propagating mode (Figs. 4, 5). We also compute the amplitude of the resultant force exerted on the plate by the piston, per unit length in the z-direction (Fig. 2). All these results are presented in Section 4.

An interesting feature of the results is the appearance of resonances when the dimensionless compressional wave number[1] kh takes one of the "cut-off" values

$$kh = (m + ½)\pi, \quad m \geq 0. \tag{1.1}$$

This does *not* however occur at the other cut-offs

$$Kh = m\pi \quad m \geq 1. \tag{1.2}$$

For $kh < 2$, Fig. 4 shows that the proportions of outgoing energy in the available modes vary rapidly, but as kh increases further it is obvious that by far the greatest proportion of energy is carried by the mode whose dimensionless propagation number α is closest to the dimensionless *compressional* wave number kh. This is shown in Fig. 6.

The time-harmonic problem solved here is related to the "impact" problem solved by Miklowitz [4, (section 7.3)]; indeed this impact problem could be solved by performing a Fourier integral (over ω) of our solution. However although our series expansion method is undoubtedly better in the time-harmonic problem considered here, the Fourier/Laplace transform method used in [4] is better for obtaining asymptotics of the solution of the impact problem.

The series expansion method employed in this paper is capable of much wider application, in particular to the corresponding problem of antisymmetrical vibration of the plate, and to the generation of waves in semi-infinite rods.

2 The Problem

Figure 1 depicts the problem to be solved. A semi-infinite plate, which has thickness $2h$, consists of homogeneous, isotropic, linearly elastic material and occupies the region $x \geq 0$, $|y| \leq h$, $|z| < \infty$ as shown. The faces $y = \pm h, x \geq 0$, $|z| < \infty$ are free of tractions, and the end $x = 0$, $|y| \leq h$, $|z| < \infty$ is in permanent contact with a perfectly smooth plane rigid piston. The piston is made to oscillate perpendicular to its own plane with small amplitude u_0 and angular frequency ω.

[1] k, K are the wave numbers of compressional and shear waves, respectively, at angular frequency ω.

Contributed by the Applied Mechanics Division for publication in the JOURNAL OF APPLIED MECHANICS.

Discussion on this paper should be addressed to the Editorial Department, ASME, United Engineering Center, 345 East 47th Street, New York, N.Y. 10017 and will be accepted until two months after final publication of the paper itself in the JOURNAL OF APPLIED MECHANICS. Manuscript received by ASME Applied Mechanics Division, July, 1982.

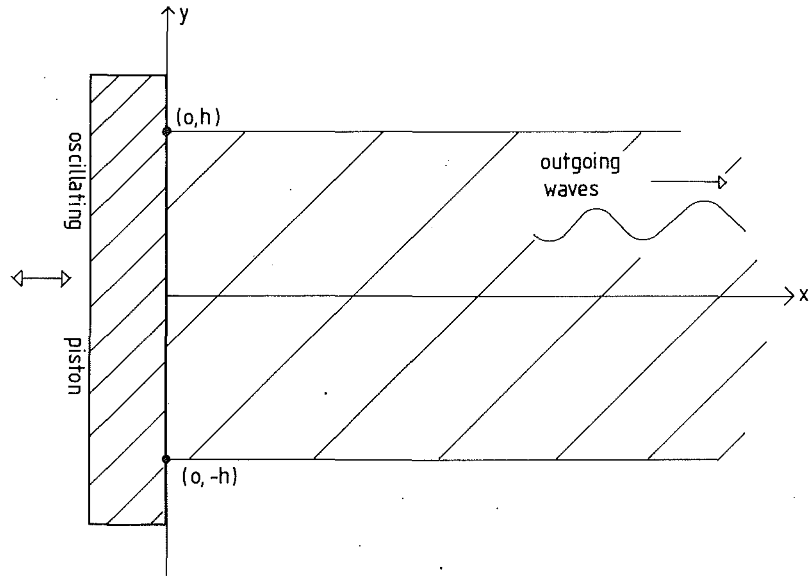

Fig. 1 The plate and the piston

The problem is to determine the resulting steady state response of the plate to this exitation, and in particular to determine

(*i*) the resultant force that must be applied to the piston to maintain the steady state motion,
(*ii*) the total flux of energy down the plate, and
(*iii*) the proportion of this energy carried by each of the propagating modes.

3 The Solution as a Series of Rayleigh-Lamb Modes

We will express $\mathbf{u}(x, y)$, the resulting time-harmonic, steady state displacement field in the plate[2], in the form[3]

$$\mathbf{u}(x,y) = u_0 \sum_{n=1}^{\infty} C_n \mathbf{U}^{(n)}(y) e^{i\alpha_n x/h}, \tag{3.1}$$

where

$$\mathbf{u}^{(n)} = h\mathbf{U}^{(n)}(y)e^{i\alpha_n x/h} \tag{3.2}$$

is the displacement field of the nth (symmetrical) Rayleigh-Lamb mode of the plate; the functions $\mathbf{U}^{(n)}(y)$ and the equation satisfied by the α_n are given in the Appendix. If α_n is real then the mode (3.2) is undamped as $x \to +\infty$ and may propagate energy down the plate; modes corresponding to complex α_n ($Im(\alpha_n) > 0$) propagate no energy, but these "evanescent" modes do contribute to the force exerted by the plate on the piston.

For any choice of the coefficients C_n, the expansion (3.1) defines a $\mathbf{u}(x, y)$ which satisfies the equation of time-harmonic elastic vibration, namely

$$k^2 \nabla^2 \mathbf{u} + (K^2 - k^2)\,\mathrm{grad}(\mathrm{div}\,\mathbf{u}) + k^2K^2\mathbf{u} = \mathbf{0}. \tag{3.3}$$

Also the expansion (3.1) satisfies the free surface conditions

$$\sigma_{xy}(x, \pm h) = \sigma_{yy}(x, \pm h) = 0, \tag{3.4}$$

since the individual modes (3.2) do so. Hence it only remains to satisfy the conditions at the piston $x = 0$, that is

$$u_x(0,y) = u_0, \tag{3.5}$$

$$\sigma_{xy}(0,y) = 0, \tag{3.6}$$

$|y| \le 1$. If we write the "stress vector" of the nth Rayleigh-Lamb mode as

$$\begin{pmatrix} \sigma_{xx}^{(n)} \\ \sigma_{xy}^{(n)} \end{pmatrix} \equiv \mu\, \mathbf{S}^{(n)}(y) e^{i\alpha_n x/h}, \tag{3.7}$$

where $\mathbf{S}^{(n)}(y)$ is given in the Appendix and μ is the shear modulus, then the coefficients C_n must be chosen to satisfy

$$\sum_{n=1}^{\infty} C_n U_x^{(n)}(y) = 1, \qquad |y| \le 1, \tag{3.8}$$

and

$$\sum_{n=1}^{\infty} C_n S_{xy}^{(n)}(y) = 0 \qquad |y| \le 1. \tag{3.9}$$

The C_n which satisfy (3.8) and (3.9) may be determined by employing the "biorthogonality relation[4]"

$$\int_{-h}^{h} \{ S_{xy}^{(m)} U_y^{(n)} - U_x^{(m)} S_{xx}^{(n)} \} dy = 0, \qquad (m \neq n) \tag{3.10}$$

which yields (compare with [2], Section 2)

$$C_n = -\frac{2}{J_n} \int_{-h}^{h} S_{xx}^{(n)} \frac{dy}{h}, \tag{3.11}$$

where

$$J_n = 2\int_{-h}^{h} \{ S_{xy}^{(n)} U_y^{(n)} - U_x^{(n)} S_{xx}^{(n)} \} \frac{dy}{h}. \tag{3.12}$$

On inserting the value of $S_{xx}^{(n)}$ given in the Appendix, (3.11) becomes

$$C_n = -\frac{4K^2h^2(K^2h^2 - 2k^2h^2)sh\gamma_n}{(2\alpha_n^2 - K^2h^2)\gamma_n J_n}. \tag{3.13}$$

The resultant force F in the x-direction exerted by the piston upon the plate (per unit length in the z-direction) is given by

[2] Clearly this displacement field is one of plane strain; also the time factor $e^{-i\omega t}$ is understood throughout.

[3] We do not prove here that the expansion (3.1) is possible. However there is little doubt that such a proof could be constructed along the lines given in Gregory [5], who proves a corresponding completeness theorem in the elastostatic case.

[4] Papkovich [6] seems to have been the first to employ such a biorthogonality relation (in an elastostatic plate bending problem). The relation (3.10), as used in the present context, was obtained by Fraser [2], and a very simple derivation of all such relations for anisotropic rods of general cross section has been given by Gregory [3].

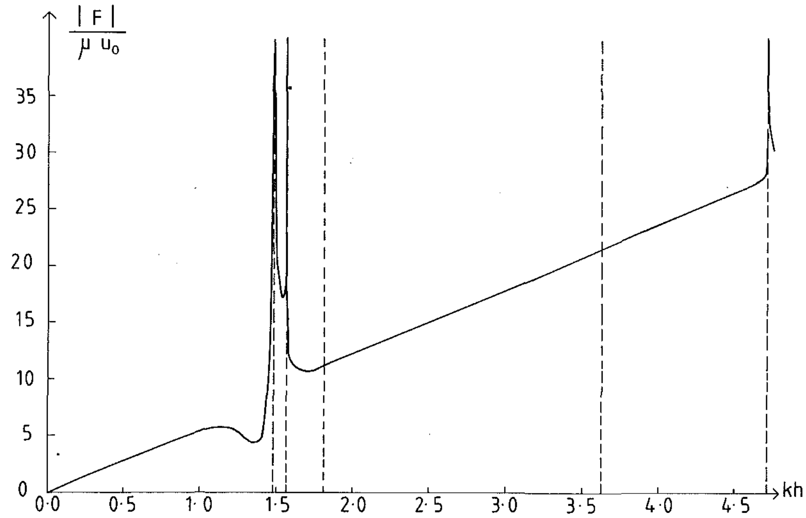

Fig. 2 $|F|/\mu u_0$ **for** $0 < kh < 4.75$ **and** $\nu = 1/4$

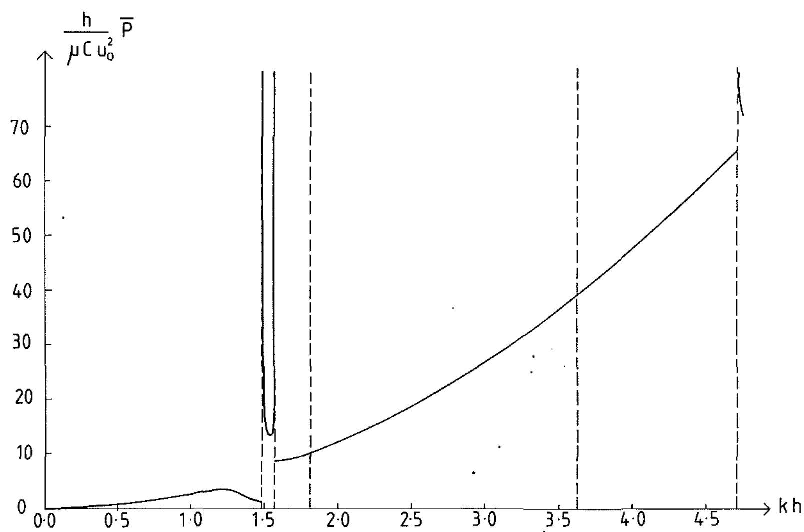

Fig. 3 $\bar{P}h/\mu C u_0^2$ **for** $0 < kh < 4.75$ **and** $\nu = 1/4$

$$F = -\int_{-h}^{h} \sigma_{xx}(0,y)\,dy$$
$$= -\mu u_0 \sum_{n=1}^{\infty} C_n \int_{-h}^{h} S_{xx}^{(n)} \frac{dy}{h}$$

which on using (3.11) becomes

$$F = \tfrac{1}{2}\mu u_0 \sum_{n=1}^{\infty} J_n C_n^2. \tag{3.14}$$

The mean total rate of working $\bar{P}$ of the piston (per unit length in the z-direction) is given by

$$\bar{P} = -\tfrac{1}{2}\, Re \int_{-h}^{h} \sigma_{xx}(0,y)\,[-i\omega u_x(0,y)]^* dy$$
$$= -\tfrac{1}{2}\omega u_0 Im(F). \tag{3.15}$$

In fact only the propagating modes (i.e., those whose α_n are real) contribute to $Im(F)$. The proportion E_n of the outgoing energy carried by the nth *propagating* mode is thus given by

$$E_n = \frac{Im(J_n)\,|C_n|^2}{\sum_{\alpha_m real} Im(J_m)\,|C_m|^2} \tag{3.16}$$

4 Results

The roots α_n of the (symmetrical) Rayleigh-Lamb equation ($A3$) were computed numerically for Poisson's ratio $\nu = 1/4$ ($K^2 = 3k^2$) and for kh in the range $0 < kh < 9.6$. The program to do this, which involves tracking the movement of each root as kh increases from zero, is fully explained in Gregory and Gladwell [1], Appendix 1; the nondimensional displacement and stress vector at $x = 0$, $\mathbf{U}^{(n)}(y)$, $\mathbf{S}^{(n)}(y)$ are then given by ($A2$) and ($A8$). The quantity J_n was calculated by evaluating the integral (3.12) explicitly, and this was checked by a direct numerical computation using a complex arithmetic version of a NAG library quadrature routine. The coefficients C_n are then given by (3.13); these values were checked by substituting them into the prescribed boundary conditions (3.8) and (3.9), and observing that satisfactory convergence to the prescribed data was obtained as the number of terms used was increased. The amplitude $|F|$ of the resultant force exerted by the piston, the mean total rate of working $\bar{P}$ of the piston, and the proportion E_n of outgoing energy carried by each propagating mode were then calculated from (3.14), (3.15), and (3.16).

Figure 2 shows $|F|/\mu u_0$ for $\nu = 1/4$ and kh in the range $0 < kh < 4.75$. The vertical dashed lines are the (dimensionless) cut-off wave numbers at which new propagating modes

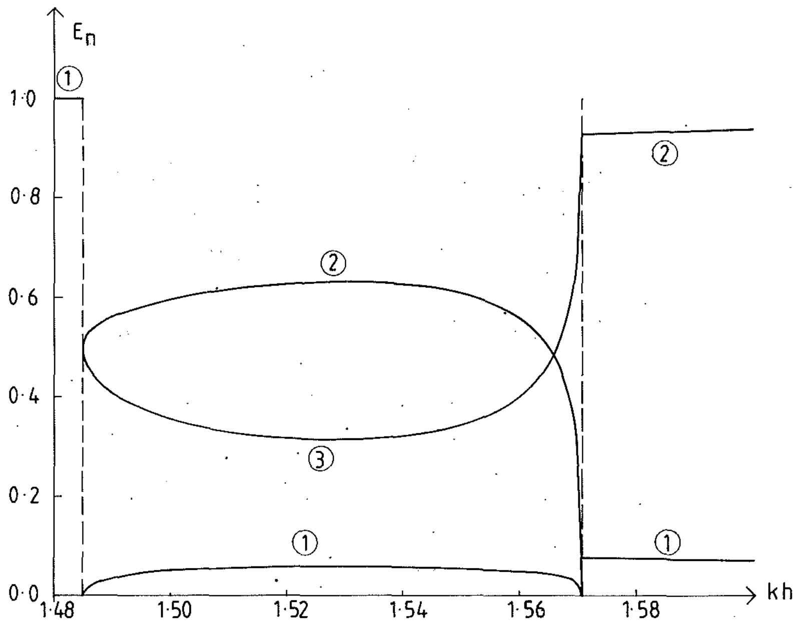

Fig. 4 The proportions of outgoing energy in the available propagating modes for 1.48 < kh < 1.6 and ν = ¼

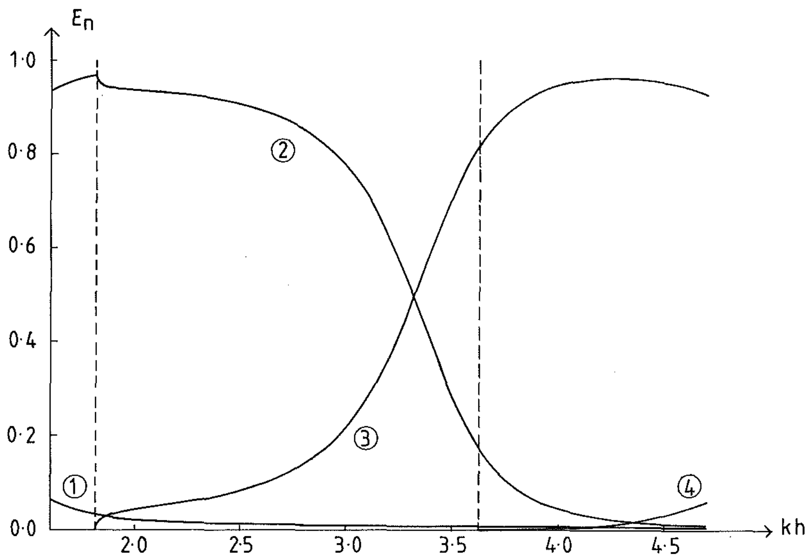

Fig. 5 The proportions of outgoing energy in the available propagating modes for 1.6 < kh < 4.75 and ν = ¼

appear (or exceptionally disappear). It will be noticed that as kh approaches the cut-offs 1.48, 1.57, and 4.71 from either side then $|F| \rightarrow \infty$, but this does not occur at the cut-offs 1.81 and 2.63. This may be explained by observing that (*i*) kh = 1.48 corresponds to the entry of a backward wave as the complex roots α_2, α_3 become real simultaneously; (*ii*) kh = 1.57, 4.71 belong to the sequence of "compressional" origin cut-offs $kh = (m + \frac{1}{2})\pi$; (*iii*) kh = 1.81, 3.63 belong to the sequence of "shear" origin cut-offs $Kh = m\pi$. At the cut-offs (*i*) and (*ii*) the propagating mode that is just appearing[5] (or disappearing) is in fact a standing mode of the semi-infinite plate satisfying the homogeneous boundary conditions $u_x(0, y) = \sigma_{xy}(0, y) = 0$; at the cut-offs (*iii*) this is not so. Thus resonances occur in cases (*i*) and (*ii*) but not in case (*iii*).

The same resonances are also evident in Fig. 3 which shows the mean total rate of working $\bar{P}$ of the piston, per unit length in the z-direction (C ($=\omega/k$) is the speed of compressional waves). It will be noticed that resonances occur at just the same cut-off frequencies as in Fig. 2, but $\bar{P} \rightarrow \infty$ only when kh approaches these cut-offs from *one* side. The reason is that only *propagating modes* (*i.e., modes with a real value of* α) can transport energy, and the modes in question correspond to real values of α only on one side of the cut-off.

The proportion of energy in each of the available propagating modes is shown in Figs. 4 and 5. Below kh = 1.48, only one propagating mode, α_1, is available and so this mode carries all the outgoing energy. For kh > 1.48, more than one propagating mode is available, and the outgoing energy is divided among these modes as shown; clearly these proportions vary rapidly with increasing kh. Figure 5 should be compared with the results of Torvik and McClatchey [7],

[5] In case (*i*) the standing mode is the *sum* of the second and third modes.

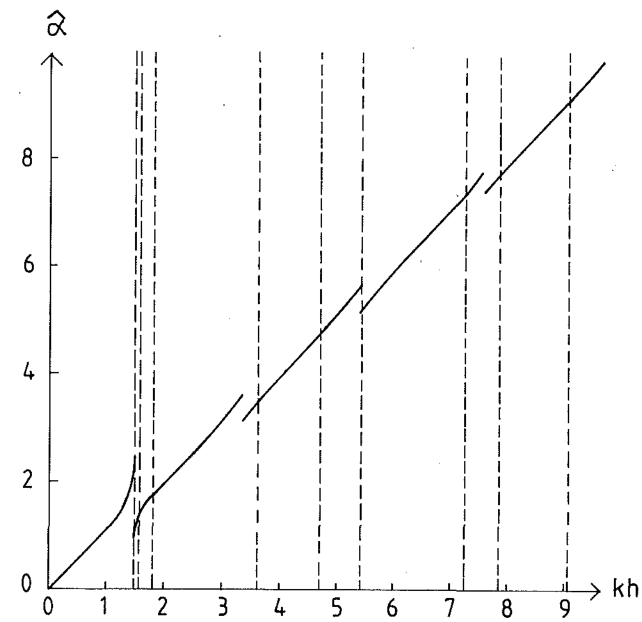

Fig. 6 $\hat{\alpha}$ **(the α-value of the Rayleigh-Lamb mode carrying the most energy) against** ***kh***

Fig. 3, who investigated a similar problem for which the edge-conditions were

$$\sigma_{xx}(0,y,z,t) = p_0 e^{-i\omega t}, \tag{4.1}$$

$$\sigma_{xy}(0,y,z,t) = 0. \tag{4.2}$$

Torvik's result is qualitatively (at least) very close to our own, which suggests that in other engineering applications it may be permissible to replace stress conditions such as (4.1) and (4.2) (for which there is no closed-form solution) by mixed conditions like (3.5) and (3.6), which can be solved in close form by the method of Section 3. For $kh > 2$ we observe that it is quite common for one mode alone to carry most of the outgoing energy (perhaps as much as 80 percent); this mode is the one with α-value closest to kh, the dimensionless *compressional* wave number. This effect is displayed in Fig. 6, where we show $\hat{\alpha}$ (the α-value of the Rayleigh-Lamb mode carrying the most energy) plotted against the dimensionless compressional wave number kh. It is quite striking that, over the full range shown, $\hat{\alpha} \doteqdot kh$.

References

1 Gregory, R. D., and Gladwell, I., "The Reflection of a Symmetric Rayleigh-Lamb Wave at the Fixed or Free Edge of a Plate," *Journal of Elasticity*, Vol. 13, 1983, pp. 185–206.

2 Fraser, W. B., "Orthogonality Relation for the Rayleigh-Lamb Modes of Vibration of a Plate," *Journal of the Acoustical Society of America*, Vol. 59, 1976, pp. 215–216.

3 Gregory, R. D., "A Note on Bi-orthogonality Relations for Elastic Cylinders of General Cross Section," *Journal of Elasticity*, Vol. 13, 1983, pp. 351–355.

4 Miklowitz, J., *The Theory of Elastic Waves and Waveguides*, North Holland, 1978.

5 Gregory, R. D., "The Semi-Infinite Strip $x \geq 0$, $-1, \leq y \leq 1$; Completeness of the Papkovich-Fadle Eigenfunctions When $\phi_{xx}(0, y)$, $\phi_{yy}(0, y)$ are Prescribed," *Journal of Elasticity*, Vol. 10, 1980, pp. 57–80.

6 Papkovich, P. F., "Two Questions of the Theory of Bending of Thin Elastic Plates," *P.M.M.*, Vol. 5, 1941.

7 Torvik, P. J., and McClatchey, J. J., "Response of an Elastic Plate to a Cyclic Longitudinal Force," *Journal of the Acoustical Society of America*, Vol. 44, 1968, pp. 59–64.

APPENDIX

The Symmetrical Rayleigh-Lamb Modes

The Rayleigh-Lamb modes of the plate $|y| \leq h$, which are symmetrical about the midplane $y = 0$, have displacement fields of the form

$$\mathbf{u}^{(n)} = h\mathbf{U}^{(n)}(y) e^{i\alpha_n x/h} e^{-i\omega t}, \tag{A1}$$

where

$$\mathbf{U}^{(n)}(y) = \begin{pmatrix} i\alpha_n ch(\gamma_n y/h) + \delta_n B_n ch(\delta_n y/h) \\ \gamma_n sh(\gamma_n y/h) - i\alpha_n B_n sh(\delta_n y/h) \end{pmatrix}, \tag{A2}$$

and α_n satisfies the symmetrical Rayleigh-Lamb equation

$$(2\alpha^2 - K^2h^2)^2 ch\ \gamma\ sh\ \delta - 4\alpha^2\gamma\delta\ sh\ \gamma\ ch\ \delta = 0. \tag{A3}$$

In the foregoing

$$\gamma = (\alpha^2 - k^2h^2)^{1/2}, \tag{A4}$$

$$\delta = (\alpha^2 - K^2h^2)^{1/2}, \tag{A5}$$

$$B = (2\alpha^2 - K^2h^2) ch\gamma / 2i\alpha\delta\ ch\ \delta. \tag{A6}$$

In the context of the *semi-infinite* plate $x \geq 0$, $|y| \leq h$, we are only interested in roots α_n of ($A3$) which are either complex with $Im(\alpha_n) > 0$, or are real and give a mode ($A1$) propagating energy to the right.[6] The method of numbering, and the numerical computation of the α_n as kh increases from zero are discussed carefully in [1], appendix 1.

We define the "stress vector" of the mode ($A2$) to be

$$\begin{pmatrix} \sigma_{xx}^{(n)} \\ \sigma_{xy}^{(n)} \end{pmatrix} = \mu \mathbf{S}^{(n)}(y) e^{i\alpha_n x/h} e^{-i\omega t}, \tag{A7}$$

where

$$\mathbf{S}^{(n)}(y) = \begin{pmatrix} -(2\gamma_n^2 + K^2h^2) ch(\gamma_n y/h) + 2i\alpha_n\delta_n B_n ch(\delta_n y/h) \\ 2i\alpha_n\gamma_n sh(\gamma_n y/h) + (2\alpha_n^2 - K^2h^2) B_n sh(\delta_n y/h) \end{pmatrix}, \tag{A8}$$

μ being the shear modulus.

[6]The α-values of these modes are not always positive; see Miklowitz [4, Chapter 4] for references and Gregory and Gladwell [1 (Appendix 1)] for further discussion of this point.

Three-Dimensional Analysis of Axisymmetric Transient Waves in Hollow Elastic Cylinders

P.-A. Svärdh[1]
Uttervägen 11,
S-72242 Västerås, Sweden

The axially symmetric problem of a semi-infinite, hollow, linear-elastic circular cylinder with traction-free lateral surfaces initially at rest and subjected to transient end loadings is solved using three-dimensional theory. Two cases are treated: an axial pressure applied to a radially clamped end and a prescribed axial velocity applied to an end that is free from shear stress. A double integral transform technique is used, and asymptotic solutions valid at large distances from the end are given for two types of time variation of the end loadings: step function and finite rise time function. A necessary condition for the validity of the asymptotic result is given.

Introduction

To fully understand wave propagation in a hollow elastic cylinder, results from the three-dimensional analysis are needed as a reference for results from approximate theories. The general case of a cylinder with inner radius a and outer radius b has been given very little attention in the literature, as to both exact and approximate analysis.

Three-dimensional wave propagation in elastic cylinders was first analysed by Pochhammer [1] and by Chree [2] (but not in Chree [3] which is often wrongly referred to). They studied the propagation of harmonic waves in an infinite, free, solid circular cylinder and obtained the frequency equation for longitudinal waves.

The treatment was extended to hollow cylinders in Chree [4]. A more thorough analysis was given by Ghosh [5]. Gazis [6, 7] investigated harmonic motion in a hollow rod and computed dispersion curves. Similar curves were given by Greenspon [8]. Further results of this kind are found in the works of Tournois, Vernet, and Bienvenu [9] and of Kumar [10]. In the papers by Mirsky and Herrmann [11] and McNiven, Shah, and Sackman [12] the exact theory serves as a reference for the respective approximate theories for thick-walled cylindrical shells proposed by the authors.

A solution to a transient problem for the solid cylinder, based on three-dimensional theory was given by Skalak [13]. He solved the problem of a sudden collinear impact of two semi-infinite solid rods using a Fourier-Laplace double transform technique. To invert the transforms, information about the exact dispersion spectrum is needed. This shows the importance of the early works in this field mentioned previously. Later Folk et al. [14] treated the problem of an axial pressure suddenly applied to a laterally clamped end of a semi-infinite rod using a method of analysis similar though not identical to that of Skalak. Both Skalak [13] and Folk et al. [14] presented an explicit long-time farfield solution valid at the head of the pulse, different from the simple step pulse expected from one-dimensional theory. In a companion paper, Fox and Curtis [15] presented results from a shock tube experiment which are in agreement with the theoretical solution at the pulse head. The analytical method developed by Folk et al. has been applied to other problems for the solid rod. DeVault and Curtis [16] considered a nonaxisymmetric end load giving a flexural pulse. Jones and Norwood [17] treated both the step pressure problem and the related problem of a constant axial velocity suddenly applied to the end which is free from shear stresses. Additional terms in the solution showing the warping of the cross sections were also given. Kennedy and Jones [18] studied the effect of a radially dependent axial end load which by means of a parameter could be varied from a uniform distribution to a point load concentrated at the center. Results from numerical finite difference calculations were also presented.

Numerical solutions to end load problems for cylinders based on the exact theory using finite difference technique were given by Bertholf [19], Alterman and Karal [20], and Nigul [21]. In [21] the pressure step problem for a hollow rod with a laterally clamped end was solved, and the results were given in a series of curves. The finite element method was used by Ramamurti and Ramanamurti [22] and recently by Bergman [23]. Experimental results, of interest in this context, are the study of pulses produced by longitudinal impact on a relatively thin-walled tube by Heimann and Kolsky [24] and the pulse dispersion measurements by Fitch [25].

As far as the present author knows, no exact analytical solution (like those in [13, 14]) to any transient end-load wave

[1] This research work was performed while the author was employed by the Department of Solid Mechanics, Uppsala University, Uppsala, Sweden.

Contributed by the Applied Mechanics Division for publication in the Journal of Applied Mechanics.

Discussion on this paper should be addressed to the Editorial Department, ASME, United Engineering Center, 345 East 47th Street, New York, N.Y. 10017, and will be accepted until two months after final publication of the paper itself in the Journal of Applied Mechanics. Manuscript received by ASME Applied Mechanics Division, June, 1983; final revision, December, 1983.

propagation problem for the hollow rod has been given. However, in a paper by Chong, Lee, and Cakmak [26], the double integral transform solution method developed in [14] was applied to the pressure step problem for the hollow rod. The authors used an approximate theory presented in [12]. It is a three-mode theory, taking extensional, radial, and axial shear motion into account.

In the present work (see also [27]) the method of Folk et al. [14] is applied to the problem of an axial pressure applied to a laterally clamped end of a semi-infinite hollow rod, and to the related problem of a prescribed velocity at the end that is free from shear stresses. Explicit solutions are given for two types of time dependence for the end conditions: step function and finite rise time function. These solutions are valid asymptotically at large distances from the end and at the head of the pulse. It should also be pointed out that the asymptotic solutions given here hold for a hollow cylinder with inner radius a and outer radius b with no restriction on the quotient a/b.

Statement of the Problem

The equations of motion of a linear elastic solid in the axisymmetric, nontorsional case expressed in cylindrical coordinates are

$$\rho\ddot{u}_r=(\lambda+2\mu)\frac{\partial\Delta}{\partial r}+2\mu\frac{\partial\Omega}{\partial z} \tag{1}$$

$$\rho\ddot{u}_z=(\lambda+2\mu)\frac{\partial\Delta}{\partial z}-\frac{2\mu}{r}\frac{\partial(r\Omega)}{\partial r} \tag{2}$$

Δ is the dilatation and Ω is the only nonzero rotation component in this case.

Prior to the application of the end loadings, the cylinder is assumed to be at rest, i.e., the initial conditions at $t=0$ are

$$u_r=u_z=0,\quad \dot{u}_r=\dot{u}_z=0 \tag{3}$$

The lateral surfaces are free from loading, so the boundary conditions at $r=a$ and $r=b$ for all z are

$$\sigma_r=\tau_{rz}=0 \tag{4}$$

Two different types of end loading at $z=0$ are considered. In the following they will be called the end pressure problem and the end velocity problem, respectively. They are both of the mixed type.

The End Pressure Problem.

$$\sigma_z(0,r,t)=-p(t),\quad u_r(0,r,t)=0 \tag{5}$$

Since the end condition (5) also implies that $\partial u_r(0,r,t)/\partial r=0$, it may be shown that

$$\Delta(0,r,t)=\frac{-p(t)}{\lambda+2\mu} \tag{6}$$

The End Velocity Problem.

$$\tau_{rz}(0,r,t)=0,\quad u_z(0,r,t)=w(t) \tag{7}$$

Since the end condition (7) also implies that $\partial u_z(0,r,t)/\partial r=0$, it may be shown that

$$\Omega(0,r,t)=0 \tag{8}$$

The functions $p(t)$ and $w(t)$ will be specified later.

Integral Transforms

The double-transform method of solution developed by Folk et al. [14] implies a choice of transforms that will ask only for the initial and boundary information given in the foregoing. The following set is used: sine, cosine transforms f^S, f^C, and Laplace transform g^L:

$$f^S=\int_0^\infty f\sin\gamma z\,dz,\qquad f^C=\int_0^\infty f\cos\gamma z\,dz,\qquad g^L=\int_0^\infty g\,e^{i\omega t}dt \tag{9}$$

The double transforms f^{SL} and f^{CL} are obtained if $g=f^S$ or f^C. The sine and cosine transforms have the following properties:

$$\left(\frac{\partial f}{\partial z}\right)^C=-f(0,r,t)+\gamma f^S,\qquad \left(\frac{\partial f}{\partial z}\right)^S=-\gamma f^C \tag{10}$$

In the Laplace transform used here the usual transform variable is replaced by $-i\omega$. ω is complex and $Im\,\omega$ must be > some constant. For the end pressure problem, the sine transform is applied to equation (1) and the cosine transform to equation (2). For the end velocity problem the order is reversed.

The doubly transformed equations of motion for both problems can be written in a concentrated form if the following formalism is introduced:

The end pressure problem: $*=SL$, $0=CL$, $Q=\gamma p^L/(\lambda+2\mu)$, upper position and sign.

The end velocity problem: $*=CL, 0=SL, Q=-\rho\omega^2 w^L/(\lambda+2\mu)$, lower position and sign.

Elimination of u_r^* and u_z^0 from these equations gives:

$$\frac{1}{r}\frac{\partial}{\partial r}r\frac{\partial\Delta^*}{\partial r}+\alpha^2\Delta^*=Q,\qquad \alpha^2=\frac{\rho\omega^2}{\lambda+2\mu}-\gamma^2 \tag{11}$$

$$\frac{\partial}{\partial r}\left(\frac{1}{r}\frac{\partial}{\partial r}r\Omega^0\right)+\beta^2\Omega^0=0,\qquad \beta^2=\frac{\rho\omega^2}{\mu}-\gamma^2 \tag{12}$$

The solution is

$$\Delta^*=A\ J_0(\alpha r)+BF_0(\alpha r,r)+\frac{Q}{\alpha^2} \tag{13}$$

$$\Omega^0=C\frac{J_1(\beta r)}{\beta}+D\ \beta F_1(\beta r,r) \tag{14}$$

J_0 and J_1 are the zeroth and first-order Bessel functions of the first kind. The second solutions F_0 and F_1 are taken as

$$F_0(x;r)=lnr\ J_0(x)+S_0(x) \tag{15}$$

$$F_1(x;r)=lnr\ J_1(x)-\frac{J_0(x)}{x}-\frac{dS_0(x)}{dx} \tag{16}$$

$$S_0(x)=\frac{x^2}{2^2}-\frac{x^4}{2^24^2}\left(1+\frac{1}{2}\right)+\frac{x^6}{2^24^26^2}\left(1+\frac{1}{2}+\frac{1}{3}\right)-\cdots \tag{17}$$

x stands for αr or βr.

The conventional second solutions $Y_0(x)$ and $Y_1(x)$ contain a factor lnx (instead of lnr). Since this would lead to difficulties in the inversion process, they are not used here. J_1/β and βF_1 are used in the expressions for Ω^0, because they contain only even powers of β and are finite when $\beta=0$. It remains to satisfy the boundary conditions (4). When the expressions for σ_r^* and τ_{rz}^0 are put $=0$ at $r=a$ and $r=b$, the following system of equations in the unknowns A etc. is obtained:

$$\begin{pmatrix} U_J(a) & U_F(a) & V_J(a) & \beta^2V_F(a)\\ U_J(b) & U_F(b) & V_J(b) & \beta^2V_F(b)\\ X_J(a) & X_F(a) & Y_J(a) & \beta^2Y_F(a)\\ X_J(b) & X_F(b) & Y_J(b) & \beta^2Y_F(b)\end{pmatrix}\begin{pmatrix}A\\B\\C\\D\end{pmatrix}=\begin{pmatrix}\zeta\\ \zeta\\0\\0\end{pmatrix} \tag{18}$$

where

$$\kappa=\beta^2-\gamma^2, \quad \zeta=\lambda\rho\omega^2 Q/((\lambda+2\mu)2\mu\alpha^2)$$

$$U_J(a)=-\kappa J_0(\alpha a)/2+\alpha^2 J_1(\alpha a)/\alpha a$$

$$V_J(a)=\mp 2\gamma(J_0(\beta a)-J_1(\beta a)/\beta a)$$

$$X_J(a)=\mp\gamma\alpha J_1(\alpha a), \quad Y_J(a)=\kappa J_1(\beta a)/\beta$$

$U_F(a)$ etc. are obtained if the J-functions are replaced by the F-functions. The expressions $U_J(b)$ etc., are analogous.

The solution is $A = N_1/G$, $B = N_2/G$ etc., where G is the determinant of the system matrix and N_i is the determinant that is obtained when the ith column in the system matrix is replaced by the column on the right-hand side. $G = 0$ is the frequency equation for harmonic waves in a hollow circular cylinder with free lateral surfaces, if γ is interpreted as the wave number and ω as the frequency. See [4, 5]. With A etc., determined, expressions for the double transforms of displacements, stresses, and strains may be found.

Inversion of the Transforms

The Fourier sine and cosine transforms will be inverted first. From the transform definitions (9) it is seen that the sine transform is an odd function of γ and that the cosine transform is an even function of γ. Therefore, the inversion integrals may be written

$$-\frac{i}{\pi}\int_{-\infty}^{\infty} f^{SL}e^{i\gamma z}d\gamma \qquad \text{and} \qquad \frac{1}{\pi}\int_{-\infty}^{\infty} f^{CL}e^{i\gamma z}d\gamma \tag{19}$$

From an inspection of the system (18) it is seen that all the quantities A, B, C, and D are functions of even powers of α and β. Since this implies that both Δ^* and Ω^0 contain only even powers of α and β, this can be shown to be the case for any displacement, stress, or strain. Hence, there are no branch points of the integrand in the complex γ plane.

The inversion is to be taken along the real γ-axis. To evaluate the integral with the aid of Cauchy's residue theorem, the path of integration is closed in the upper half of the complex γ plane. For large $|\gamma|$, the asymptotic forms of the functions J_0, F_0, etc. may be used to show that if f is any transformed displacement, stress, or strain, then $|f| \to 0$ as $|\gamma| \to \infty$. Hence Jordan's lemma applies to the integral over the semicircle, which thus vanishes for any displacement, stress, or strain as $|\gamma| \to \infty$. Since there are no branch points, the result of the inversion is equal to $2\pi i$ times the sum of the residues evaluated at the poles in the upper half plane.

There appears to be poles at $\alpha^2 = 0$, since A, B, C, and D are all proportional to $1/\alpha^2$ and the double transform of Δ contains the term Q/α^2. However, when $\alpha = 0$, equation (11) has the solution

$$\Delta^*=A+B\ ln\ r+\frac{Qr^2}{4} \tag{20}$$

Thus, since any transformed quantity depends on $\alpha \to \Delta^*$ only, it is seen that there exist finite limiting values when $\alpha \to 0$, i.e., no poles, for any transformed displacement, stress, or strain.

The remaining poles are determined from $G = 0$. The position of such a pole depends on ω and is denoted $\gamma_n(\omega)$. The imaginary part of $\gamma_n(\omega)$ must be positive because of the choice of integration path. When ω is real, the γ_n are the branches of the frequency equation for harmonic waves. In the Laplace inversion, the integration over ω will be taken along a line parallel and limitingly close to the real axis ($\omega = \xi + i\epsilon$, $\epsilon > 0$) for all reasonable choices of $p(t)$ and $w(t)$. We may write

$$\gamma_n(\omega)=\gamma_n(\xi)+\delta_n \tag{21}$$

where δ_n vanishes as $\omega \to \xi$. The formal solution is then obtained by carrying out the Laplace inversion. Here g stands for any displacement, stress, or strain.

$$g(z,r,t)=\sum_n \frac{1}{2\pi}\int_{-\infty+i\epsilon}^{\infty+i\epsilon} M(\gamma_n(\omega),r,\omega)e\ \exp\{i(\gamma_n z-\omega t)\}_{d\beta} \tag{22}$$

The denominator of M is $\partial G/\partial\gamma\ |_{\gamma=\gamma_n(\omega)}$. M is proportional to Q, and thus proportional to p^L and w^L as well. These integrals can not be evaluated exactly by simple means. However, asymptotic solutions valid at large distances from the end may be found.

Evaluation for Large z

Near the end, the evaluation is very difficult, among other things because of the branches with complex $\gamma_n(\xi)$. At large distance from the end $z = 0$, only branches with real $\gamma_n(\xi)$ can be expected to give significant contributions. It is thus obvious that much information about the solutions for displacements etc. in this region is obtained from the real solutions to the frequency equation for harmonic waves, i.e., the dispersion curves.

The situation in the hollow rod case is much more complicated than in the solid rod case, since in addition to a dependence on the Poisson's ratio ν we have a dependence on a geometrical parameter such as a/b. It is not the purpose of this work to make a detailed investigation of the frequency spectrum. However, many arguments from the analysis of the solid rod as to asymptotic behavior can be expected to apply here as well. The time dependence of the prescribed quantities ($p(t)$ or $w(t)$) at $z = 0$ has great influence on the results of the analysis. In the subsequent treatment, the p^L and $v^L = -i\omega w^L$ (i.e., the Laplace transform of the end velocity $v(t) = \dot{w}(t)$) are chosen from the class of functions having a simple pole at $\omega = 0$ and no other poles.

According to the saddle point method of integration, e.g. [35], the main contribution at a distance z and at a time t comes from the part of any branch in the spectrum near the point where $d\gamma_n/d\omega = t/z$, the saddle point. In general the total result is a sum of contributions from several branches. The ordinary saddle point expressions are not valid approximations when there are poles or zeros of the integrand near the saddle point, or when the quantity $z\ d^2\gamma_n/d\omega^2$ is small in that region. These exceptions are, however, very important in this special application.

The condition $d^2\gamma_n/d\omega^2 = 0$ at some point in the spectrum means that the γ_n, ξ curve has zero curvature. This implies that the group velocity $c_g = d\omega/d\gamma = [d\gamma/d\omega]^{-1}$ has a maximum or a minimum value there. The onset (for maximum c_g) of the contribution from the second branch was verified experimentally for the *solid* rod by Curtis [28].

It is of interest to study the values of the maximum group velocities of different branches in relation to the rod velocity $c_0 = (E/\rho)^{1/2}$. For the *hollow* rod, Chong, Lee, and Cakmak [26] showed that the maximum group velocity of the second branch exceeds c_0 if b/a is less than about 1.7 (depending slightly on Poisson's ratio ν). A few years earlier Heimann and Kolsky [24] gave experimental results that seem to support this.

Asymptotic Contribution From the First Branch

When the integrand has a pole in a point where $d^2\gamma/d\omega^2 = 0$, the result is a nondecaying contribution valid at large z and near the time $t = z/c_g$. When p^L or w^L have a simple pole at $\omega = 0$, such a result is obtained from the coincidence of this pole with the group velocity maximum of the first branch at $\omega = 0$ where $c_g = c_0$. It was shown by Chree [4] that the first two terms in the series expansion about this point ($\omega = \gamma = 0$) are

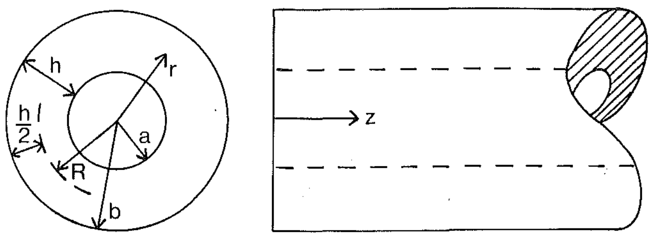

Fig. 1 Semi-infinite hollow rod with axisymmetric coordinates r and z

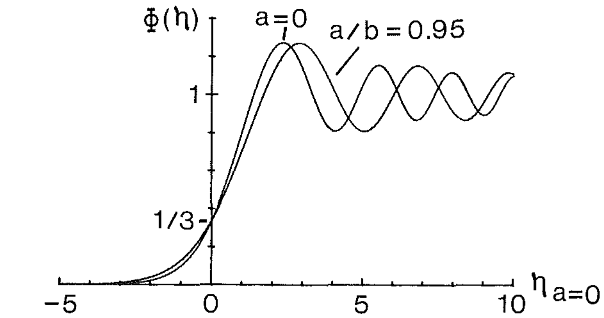

Fig. 2 The influence of a/b on the asymptotic result. Step end condition.

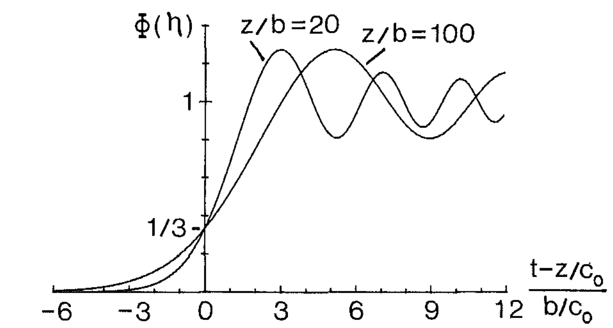

Fig. 3 The dispersive character of the asymptotic result. Step end condition. $\nu = 1/3, a/b = 1/2$.

$$\frac{\omega}{c_0} = \gamma - k\gamma^3 + \cdots, \qquad k = \nu^2 \frac{a^2+b^2}{4} \tag{23}$$

This may be inverted to give

$$\gamma = \frac{\omega}{c_0} + k\left(\frac{\omega}{c_0}\right)^3 + \cdots \tag{24}$$

When the system of equations (18) is solved in the limit $\omega \approx c_0\gamma \to 0$, the quantities B and D vanish. Thus in this case the contributions come from the low argument forms of the J-functions only. The asympotic form of the first branch part of (22) for the axial stress σ_z (all other stress components are vanishingly small) and for ϵ_z, ϵ_r, ϵ_θ and u_r then becomes

$$(\sigma_z, \epsilon_z, \epsilon_r, \epsilon_\theta, u_r) = \begin{Bmatrix} 1/E \\ 1/c_0 \end{Bmatrix} (-E, -1, \nu, \nu, \nu r) I \tag{25}$$

where

$$I = \frac{1}{2\pi}\int_{-\infty+i\epsilon}^{\infty+i\epsilon} \begin{Bmatrix} p^L \\ v^L \end{Bmatrix} \exp i\left[-\omega\left(t - \frac{z}{c_0}\right) + zk\left(\frac{\omega}{c_0}\right)^3\right] d\omega \tag{26}$$

Thus it is seen that for large distances, i.e., $z \gg b$, the solutions to the two problems have the same form, although the conditions at $z = 0$ are quite different.

Using the convolution theorem, the result (26) may be written

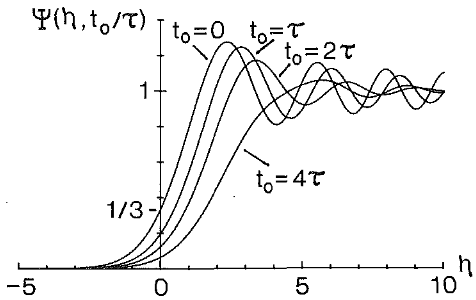

Fig. 4 The influence of different rise times on the asymptotic result at a certain distance z. Finite rise time end condition.

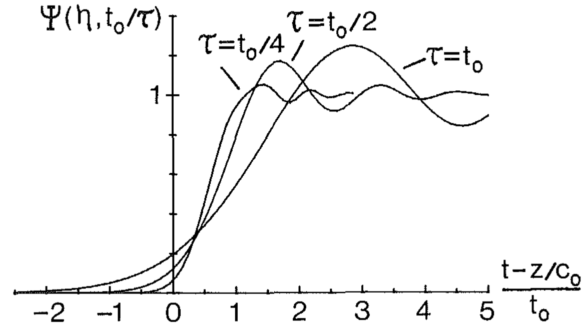

Fig. 5 The asymptotic result at different distances z for a certain rise time t_0. Finite rise time end condition.

$$I = \begin{Bmatrix} p \\ v \end{Bmatrix} * \frac{1}{\tau} Ai\left[-\frac{t - z/c_0}{\tau}\right] \tag{27}$$

where

$$\tau = \left[\frac{3\nu^2}{4} z(a^2+b^2)\right]^{1/3} \cdot \frac{1}{c_0} \tag{28}$$

The simplest example of a function whose Laplace transform has a simple pole in $\omega = 0$ is the Heaviside step function $H(t)$. With $p(t) = p_0H(t)$ or $v(t) = v_0H(t)$ (corresponding to $w(t) = v_0tH(t)$) we get

$$I = \begin{Bmatrix} p_0 \\ v_0 \end{Bmatrix} \int_{-\infty}^{\eta} Ai(-s)ds, \qquad \eta = \frac{t - z/c_0}{\tau} \tag{29}$$

Since $\int_{-\infty}^{0} Ai(-s)ds = 1/3$, this can be written in the equivalent form

$$I = \begin{Bmatrix} p_0 \\ v_0 \end{Bmatrix} \left[1/3 + \int_0^{\eta} Ai(-s)ds\right] \tag{30}$$

The expression within brackets is a function $\Phi(\eta)$. See Fig. 4 for $t_0 = 0$. It is the analogy of the result for the solid rod given in [13, 14, 17]. The maximum value is 1.274 occurring at $\eta = 2.338$ (the first zero of $Ai(-x)$). Note also that at the time $t = z/c_0$, i.e., when $\eta = 0$, it has the value 1/3. The dependence on a/b is shown in Fig. 2. The dispersive character is revealed in Fig. 3. The period of the oscillations increases as z increases, since the argument η is proportional to $z^{-1/3}$.

Any attempt to realize a step function in practice will imply a finite rise time. Therefore it is of interest to study the case when the end loadings start from zero and rise monotonously to a constant value in a finite time t_0. It may be shown (see [27]) that the Laplace transform of such a function has a pole in $\omega = 0$. To study the effect of a finite rise time quantitatively, the special case with a linear rising portion is chosen, i.e., $p(t) = p_0f(t)$ or $v(t) = v_0f(t)$, where

$$f(t) = \frac{1}{t_0}[tH(t) - (t - t_0)H(t - t_0)] \tag{31}$$

In this case the convolution integral can be reduced to

$$I = \left\{ \begin{matrix} p_0 \\ v_0 \end{matrix} \right\} \left[\frac{1}{3} + \frac{\tau}{t_0} \int_{\eta - t_0/\tau}^{\eta} G(s)\, ds \right] \tag{32}$$

where

$$G(s) = \int_0^s Ai(-u)\, du = \Phi(s) - 1/3 \tag{33}$$

The expression within brackets in (32) is a function $\Psi(\eta, t_0/\tau)$. It is plotted in Fig. 4 (τ constant, t_0 varied) and in Fig. 5 (t_0 constant, τ varied) with the aid of series expansions. It is seen from Fig. 4 that the main effect of the finite rise time is a reduction of the oscillation amplitude at a certain distance. The peak value = 1.274 when $t_0 = 0$ approaches 1 when $t_0/\tau \gg 1$. When $t_0/\tau < 0.5$ the result is essentially the curve for $t_0 = 0$ in Fig. 4 displaced $t_0/2\tau$ to the right. It is seen from Fig. 5 that the result is close to the nondispersive result when $\tau = t_0/4$. Note also the rise of the oscillation amplitude as τ, and thus z, increases.

The results given in this section are valid for large z, i.e., $z \gg b$ and for t close to z/c_0 according to the saddle point approximation. Since no assumption has been made about the relation between the inner radius a and the outer radius b, it is valid for a hollow rod with small inner radius as well as for a thin-walled cylindrical shell.

Validity of the Asymptotic Result: Step End Condition

The quantity τ can be written in dimensionless form:

$$\frac{c_0 \tau}{b} = \left[\frac{3}{4} \nu^2 (1 + (a/b)^2) \frac{z}{b} \right]^{1/3} \tag{34}$$

Thus it is seen that for fixed c_0 and b it depends on the parameters ν and a/b and on z/b.

The question arises whether or not it is possible to say how great z has to be to insure that the asymptotic result be valid. Since no wave in a linear elastic solid can travel faster than the dilatational velocity c_1, any valid result must be zero in the region $t < z/c_1$. If the asymptotic result is to be valid, it must at least be separated from the expected dilatational pulse at $t = z/c_1$, i.e., at $t = z/c_1$ the asymptotic result must be evanescent. The function $\Phi(\eta)$ decays rapidly when $\eta < 0$, and it is negligible when $\eta < -3$ ($\Phi(-3) = 0.0034$), so the separation condition could for example, be written,

$$\eta \Big|_{t = z/c_1} < -3, \qquad \text{or} \qquad \frac{z/c_0 - z/c_1}{\tau} > 3 \tag{35}$$

This inequality may be written as a conduction for z/b:

$$\frac{z}{b} > \frac{9}{2} \left[1 + (a/b)^2 \right]^{1/2} \frac{\nu}{(1 - c_0/c_1)^{3/2}} \tag{36}$$

The right-hand side of (36) is given in Table 1 for some combinations of ν and a/b. It exhibits a strong dependence on ν, whereas a/b has small influence. The condition (36) should be regarded as a necessary condition, suited for practical applications of this theory.

Discussion

The assumption that the asymptotic solution given here is the only nondecaying contribution for large z is based on the presupposition that all contributions from branches other than the first decay with z. Since the rise in amplitude near $t = z/c_0$ is a quasi-wave front, i.e., not a propagating discontinuity, the question arises whether there can exist some "signal" (or wave front) traveling with the dilatational velocity c_1, which is always greater than the rod velocity c_0. The numerical results of Bertholf [19] for the *solid* rod with the nonmixed end condition

Table 1 The necessary minimum value $(z/b)_{min}$

ν	$(z/b)_{min}$ for $a = 0$	$(z/b)_{min}$ for $a/b = 0.5$	$(z/b)_{min}$ for $a/b = 0.95$
0.1	381	426	526
0.2	77.4	86.6	107
0.3	26.3	29.4	36.3
0.4	10.1	11.3	13.9
0.5	2.25	2.52	3.10

$$\sigma_z = -p_0 H(t), \quad \tau_{rz} = 0 \tag{37}$$

show that the radial displacement and the axial strain both become nonzero at the time $t = z/c_1$ at distances up to a few diameters from the end. Nigul [21] gave numerical results for the *hollow* rod ($h/R = 0.2$) in the case when the end conditions are

$$\sigma_z = -p_0 H(t), \quad u_r = 0 \tag{38}$$

The curves given in [21] for the axial stress σ_z at different distances all have a narrow peak at $t = z/c_1$. There is also the expected rise of the amplitude near $t = z/c_0$. It remains to investigate whether the peak at $t = z/c_1$ is a consequence of the special end conditions or if such a phenomenon also can exist when the end conditions are otherwise. It is reasonable to assume that any type of dilatational front can be explained with the aid of the higher branches in the frequency spectrum. Hutchinson and Percival [29] showed that for the solid rod the maximum group velocity of the higher branches is the dilatational velocity c_1. If this is true for the hollow rod as well, a phenomenon like the peak could perhaps be explained as a sum of contributions from these maxima.

It is interesting to compare the results of this work with previously published solutions where approximate theories have been used. Berkowitz [30] solved an impact problem using the membrane theory, which is a thin shell theory, and Chong, Lee, and Cakmak [26] used a three-mode shell theory given in [12] to solve the end pressure problem (both mixed and nonmixed). The results of both [30] and [26] at $t \approx z/c_0$ are in agreement with equation (30). It should however be noted that in [30] the counterpart of (28) contains the mean radius R instead of $((a^2 + b^2)/2)^{1/2}$. However, the relative difference between these two quantities is less than 0.13 percent when $h/R < 0.1$. The wave front traveling with the plate velocity $c_p = (E/(\rho(1 - \nu^2)))^{1/2}$ given in [30] is a consequence of the assumption of plane stress within the shell wall implicit in the membrane theory and in many other thin shell theories. It seems to have no counterpart in the three-dimensional analysis. As to [26] it is found that to make their head of the pulse solution in agreement with the results of the present work, the adjustment factors k_1 and k_3 of the approximate thick shell theory should satisfy the condition $k_1 = k_3 = 1$.

Acknowledgments

The author wishes to thank Professor Hans Christian Fischer, Department of Solid Mechanics, Institute of Technology, Uppsala University, Uppsala, Sweden, for his encouraging support and guidance throughout this work, and Professor Bengt Lundberg, Department of Solid Mechanics, University of Luleå, Luleå, Sweden, for valuable suggestions.

References

1 Pochhammer, L., "Über die Fortpflanzungsgeschwindigkeiten Kleiner Schwingungen in einem Unbegrenzten Isotropen Kreiscylinder," *J. Reine Angew. Math.*, Vol. 81, 1876, pp. 324–336.

2 Chree, C., "Longitudinal Vibrations of a Circular Bar," *The Quarterly Journal of Pure and Applied Mathematics*, London, Vol. 21, 1886, pp. 287–298.

3 Chree, C., "The Equations of an Isotropic Elastic Solid in Polar and Cylindrical Coordinates, Their Solution and Application," *Trans. Camb. Phil. Soc.*, Vol. 14, 1889, pp. 250–369.

4 Chree, C., "Longitudinal Vibrations in Solid and Hollow Cylinders," *Proceedings of the Physical Society of London*, Vol. 16, 1899, pp. 304–322.

5 Ghosh, J., "Longitudinal Vibrations of a Hollow Cylinder," *Bulletin of the Calcutta Mathematical Society*, Vol. 14, 1923, pp. 31–40.

6 Gazis, D. C., "Exact Analysis of the Plane-Strain Vibrations of Thick-Walled Hollow Cylinders," *J. Acoust. Soc. Am.*, Vol. 30, 1958, pp. 786–794.

7 Gazis, D. C., "Three-Dimensional Investigation of the Propagation of Waves in Hollow Circular Cylinders I. Analytical Foundation," *J. Acoust. Soc. Am.*, Vol. 31, 1959, pp. 568–573; and "II. Numerical Results," *J. Acoust. Soc. Am.*, Vol. 31, 1959, pp. 573–578.

8 Greenspon, J. E., "Vibrations of a Thick-Walled Cylindrical Shell—Comparison of the Exact Theory With Approximate Theories," *J. Acoust. Soc. Am.*, Vol. 32, 1960, pp. 571–578.

9 Tournois, P., Vernet, J. L., and Bienvenu, G., "Ligne à Retard Dispersive Tubulaire pour la Compression des Impulsions Longues à Bande Etroite," *Revue Technique Thomsom—CSF*, Vol. 1, 1969, pp. 41–65.

10 Kumar, R., "Dispersion of Axially Symmetric Waves in Empty and Fluid-Filled Cylindrical Shells," *Acustica*, Vol. 27, 1972, pp. 317–329.

11 Mirsky, I., and Herrmann, G., "Axially Symmetric Motions of Thick Cylindrical Shells," ASME Journal of Applied Mechanics, Vol. 25, 1958, pp. 97–102.

12 McNiven, H. D., Shah, A. H., and Sackman, J. L., "Axially Symmetric Waves in Hollow, Elastic Cylinders, I," *J. Acoust. Soc. Am.*, Vol. 40, 1966, pp. 784–792; "II," *J. Acoust. Soc. Am.*, Vol. 40, 1966, pp. 1073–1076.

13 Skalak, R., "Longitudinal Impact of a Semi-Infinite Circular Elastic Bar," ASME Journal of Applied Mechanics, Vol. 24, 1957, pp. 59–64.

14 Folk, R., Fox, G., Shook, C. A., and Curtis, C. W., "Elastic Strain Produced by Sudden Application of Pressure to One End of a Cylindrical Bar, I. Theory," *J. Acoust. Soc. Am.*, Vol. 30, 1958, pp. 552–558.

15 Fox, G., and Curtis, C. W., "Elastic Strain Produced by Sudden Application of Pressure to One End of a Cylindrical Bar, II. Experimental Observations," *J. Acoust. Soc. Am.*, Vol. 30, 1958, pp. 559–563.

16 DeVault, G. P., and Curtis, C. W., "Elastic Cylinder With Free Lateral Surface and Mixed Time-Dependent End Conditions," *J. Acoust. Soc. Am.*, Vol. 34, 1962, pp. 421–432.

17 Jones. O. E., and Norwood, F. R., "Axially Symmetric Cross-Sectional Strain and Stress Distributions in Suddenly Loaded Cylindrical Elastic Bars," ASME Journal of Applied Mechanics, Vol. 34, 1967, pp. 718–724.

18 Kennedy, L. W., and Jones, O. E., "Longitudinal Wave Propagation in a Circular Bar Loaded Suddenly by a Radially Distributed End Stress," ASME Journal of Applied Mechanics, Vol. 36, 1969, pp. 470–478.

19 Bertholf, L. D., "Numerical Solution for Two-Dimensional Elastic Wave Propagation in Finite Bars," ASME Journal of Applied Mechanics, Vol. 34, 1967, pp. 725–734.

20 Alterman, Z., and Karal, F. C., Jr., "Propagation of Elastic Waves in a Semi-Infinite Cylindrical Rod Using Finite Difference Methods," *J. Sound Vib.*, Vol. 13, 1970, pp. 115–145.

21 Nigul, U., "Three-Dimensional Shell Theory of Axially Symmetric Transient Wave in a Semi-Infinite Cylindrical Shell," *Archiwum Mechaniki Stosowanej*, Vol. 19, 1967, pp. 839–856.

22 Ramamurti, V., and Ramanamurti, P. V., "Impact on Short Length Bars," *J. Sound Vib.*, Vol. 53, 1977, pp. 529–543.

23 Bergman, B. O., "Wave Propagation in Elastic Bodies" (in Swedish) Report 1982:051 E, Division of Structural Engineering, University of Luleå, Luleå, Sweden, 1982.

24 Heimann, J. H., and Kolsky, H., "The Propagation of Elastic Waves in Thin Cylindrical Shells," *J. Mech. Phys. Solids*, Vol. 14, 1966, pp. 121–130.

25 Fitch, A. H., "Observation of Elastic-Pulse Propagation in Axially Symmetric and Nonaxially Symmetric Longitudinal Modes of Hollow Cylinders," *J. Acoust. Soc. Am.*, Vol. 35, 1963, pp. 706–708.

26 Chong, K. P., Lee, P. C. Y., and Cakmak, A. S., "Propagation of Axially Symmetric Waves in Hollow Elastic Circular Cylinders Subjected to a Step-Function Loading," *J. Acoust. Soc. Am.*, Vol. 49, 1971, pp. 201–210.

27 Svärdh, P. A., "Analysis of Transient Stress Waves in Hollow Elastic Cylinders," UPTEC 82 23 R (Doctoral Thesis), Department of Solid Mechanics, Institute of Technology, Uppsala University, Uppsala, Sweden, 1982.

28 Curtis, C. W., "Second Mode Vibrations of the Pochhamer-Chree Frequency Equation," *J. Appl. Phys.*, Vol. 25, 1954, p. 928.

29 Hutchinson, J. R., and Percival, C. M., "Higher Modes of Longitudinal Wave Propagation in Thin Rods," *J. Acoust. Soc. Am.*, Vol. 44, 1968, pp. 1204–1210.

30 Berkowitz, H. M., "Longitudinal Impact of a Semi-Infinite Elastic Cylindrical Shell," ASME Journal of Applied Mechanics, Vol. 30, 1963, pp. 347–354.

S. K. Datta
Professor,
Department of Mechanical Engineering,
Fellow, Cooperative Institute for
Research in Environmental Sciences,
University of Colorado,
Boulder, Colo. 80309
Mem. ASME

K. C. Wong
Graduate Student.

A. H. Shah
Professor.

Department of Civil Engineering,
University of Manitoba,
Winnipeg, Canada

Dynamic Stresses and Displacements Around Cylindrical Cavities of Arbitrary Shape

Dynamic stresses and displacements around cylindrical cavities of various shapes, namely, circular, triangular, and square cavities are presented in this paper. Also presented are results for a pair of circular cavities of equal radii and a pair of circular and square cavities. These results are of interest in estimating the effects of corners and multiple scattering on the distribution of dynamic displacements and stresses around cylindrical holes or openings. Since exact analytical solutios are not available in these cases (except for a single circular hole) a numerical technique combining the finite element method (FEM) and the method of eigenfunction expansions is used here.

Introduction

Diffraction of elastic waves by circular cylindrical obstacles (cavities, rigid and elastic inclusions) has been studied by many authors. The quantities of engineering interest are the dynamic stresses and displacements around this inclusion or cavity boundary. Also of interest are the scattered displacement or stress amplitudes far away from this obstacle.

The near-field dynamic stresses and displacements have been studied in [1-5]. A comprehensive review of the subject of elastic wave diffraction by circular cylindrical discontinuities and dynamic stress concentration can be found in [6], where the diffraction of antiplane strain elastic waves by cylinders of elliptical and parabolic cross sections are also discussed. All these works rely on the representation of the displacement field in terms of eigenfunctions obtained by separation of variables.

In many practical applications the geometry is such that the eigenfunction expansion method is not applicable or is too cumbersome. A problem of the latter type involves elliptical or parabolic geometries. Diffraction by an elliptic cylinder has been studied in [7] using eigenfunction expansions.

Because of the limitation of the eigenfunction expansion method several numerical techniques have been employed to solve scattering by bodies of general shapes. Some of these are: the moment method, the T-matrix formulation, and the boundary element method. Recently we have used a combined finite element and eigenfunction expansion technique (FEEET) [8] to study diffraction by a single scatterer or a cluster of scatterers of general shapes. In [8] we presented the scattered far-field results. In the present paper we discuss the displacements and stresses around a single cylindrical opening or a pair of openings.

The method is outlined briefly in the following section, which is followed by a discussion of the numerical results for the cases when the incident wave is either a plane longitudinal wave or a plane SV-wave.

Formulation and Solution

For the case of plane-strain, a hybrid, combined analytical and numerical method was presented in our previous paper [8]. Hence, only a brief description of this method will be given here.

As shown in Fig. 1 interior region R_2, bounded by a circular boundary B of radius R_B contains all the scattering cavities, inhomogeneities and anisotropy. The exterior host region R_1 is assumed to be isotropic and homogeneous having Lamé constants λ and μ and mass density ρ. The displacement associated with the plane incident waves is denoted by $\mathbf{u}^{(i)}(x,y;t)$ and it will be assumed that their directions of propagation make an angle γ with the x-axis. Only harmonic time dependence of the form $e^{-i\omega t}$, where ω is the circular frequency, will be considered.

Subdividing R_2 into finite elements having $N_I + N_B$ number of modes, N_I being the number of interior nodes and N_B the number of boundary nodes, and minimizing the energy functional, the equations of motion can be written as [8]

Contributed by the Applied Mechanics Division and presented at the Winter Annual Meeting, New Orleans, La., December 9–14, 1984 of THE AMERICAN SOCIETY OF MECHANICAL ENGINEERS.

Discussion on this paper should be addressed to the editorial Department, ASME, United Engineering Center, 345 East 47th Street, New York, N.Y. 10017, and will be accepted until two months after final publication of the paper itself in the JOURNAL OF APPLIED MECHANICS. Manuscript received by ASME Applied Mechanics Division, September, 1983; final revision, February, 1984. Paper No. 84-WA/APM-33.

Copies will be available until August, 1980.

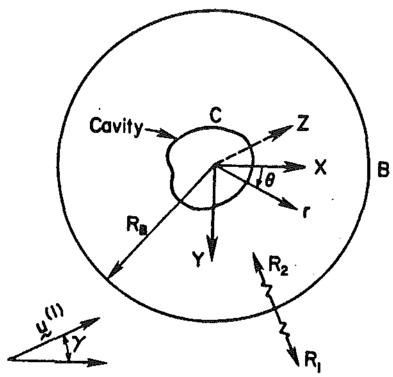

Fig. 1 Geometry of the problem

$$\begin{bmatrix} S_{II} & S_{IB} \\ S_{BI} & S_{BB} \end{bmatrix} \begin{Bmatrix} \mathbf{q}_I^{(2)} \\ \mathbf{q}_B^{(2)} \end{Bmatrix} = \begin{Bmatrix} 0 \\ \mathbf{p}_B^{(2)} \end{Bmatrix} \tag{1}$$

in which the vector $\mathbf{p}_B^{(2)}$ represents the interaction forces between the regions R_1 and R_2 at the boundary nodes. The elemental impedance matrices S_{ij} are defined as

$$[S^e] = \int_{R_e}\int([B^e]^T[D][B^e] - \rho_e\omega^2[L]^T[L])dx\, dy \tag{2}$$

where

$$[B^e] = \begin{bmatrix} \frac{\partial}{\partial x} & 0 \\ 0 & \frac{\partial}{\partial y} \\ \frac{\partial}{\partial y} & \frac{\partial}{\partial x} \end{bmatrix} \begin{bmatrix} L_1 & 0 & L_2 & \ldots \\ 0 & L_1 & 0 & \ldots \end{bmatrix} = [N][L]$$

Note that $[L]$ is a $2 \times 2N_e$ matrix representing the shape functions.

For isotropic material $[D]$ is a square 3×3 matrix given by

$$[D] = \begin{bmatrix} \lambda_e + 2\mu_e & \lambda_e & 0 \\ \lambda_e & \lambda_e + 2\mu_e & 0 \\ 0 & 0 & \mu_e \end{bmatrix}$$

It is seen from equation (1) that if boundary nodal displacements $\mathbf{q}_B^{(2)}$ are known, the interior nodal replacements $\mathbf{q}_I^{(2)}$ can be evaluated as

$$\{\mathbf{q}_I^{(2)}\} = -[S_{II}]^{-1}[S_{IB}]\{\mathbf{q}_B^{(2)}\} \tag{3}$$

The nodal interaction forces are then obtained from the equation

$$\{\mathbf{p}_B^{(2)}\} = [S_{BB} - S_{BI}S_{II}^{-1}S_{IB}]\{\mathbf{q}_B^{(2)}\} \tag{4}$$

Note that $S_{BI} = S_{IB}^T$.

Alternatively equation (4) can be used to calculate $\{\mathbf{q}_B^{(2)}\}$ in terms of the nodal forces $\{\mathbf{p}_B^{(2)}\}$. Equation (3) then is used to calculate the internal nodal displacements.

In the exterior region R_1 the scattered displacement components in polar coordinates can be written as [8]

$$\mathbf{u}_r^{(s)} = \sum_{n=1}^{N_B/2} [a_n g_{r_1}^{(n-1)} \cos(n-1)\vartheta + d_n g_{r_2}^{(n)} \cos n\,\vartheta + b_n g_{r_3}^{(n)} \sin n\,\vartheta + c_n g_{r_4}^{(n-1)} \sin(n-1)\vartheta], \tag{5}$$

$$\mathbf{u}_\vartheta^{(s)} = \sum_{n=1}^{N_B/2} [a_n g_{t_1}^{(n-1)} \sin(n-1)\vartheta + d_n g_{t_2}^{(n)} \sin n\,\vartheta + b_n g_{t_3}^{(n)} \cos n\,\vartheta + c_n g_{t_4}^{(n-1)} \cos(n-1)\vartheta], \tag{6}$$

where the functions $g_{r_i}^{(n)}$, $g_{t_i}^{(n)}$ have been defined in [8]. These are functions of r and satisfy the radiation conditions as $r \to \infty$.

Evaluating equations (5) and (6) at each of the N_B points on the circular boundary B the scattered displacement vector $\{\mathbf{q}_{r_B}^{(s)}\}$ can be written as

$$\{\mathbf{q}_{r_B}^{(s)}\} = [G]\{a\}, \tag{7}$$

where the components of $\mathbf{q}_{r_B}$ in polar coordinates are $u_{r_j}^{(S)}$ and $u_{\vartheta_j}^{(S)}$ $(j = 1, N_B)$. In writing equation (7) the constants a_n, b_n, c_n, d_n have been written as the vector $\{a\}$ with

$$a_n = a_n\ ,\ n = 1, \cdots, N_B/2,$$
$$d_n = a_{n+N_B/2}\ ,\ n = 1, \cdots, N_B/2$$
$$b_n = a_{n+N_B}\ ,\ n = 1, \cdots, N_B/2,$$
$$c_n = a_{n+3N_B/2}\ ,\ n = 1, \cdots, N_B/2,$$

Using the strain-displacement and stress-strain relations, the nodal stress vector can be written from equations (5)–(7) as

$$\{\sigma_{r_B}^{(s)}\} = [F]\{a\} = [F][G]^{-1}\{\mathbf{q}_{r_B}^{(s)}\}. \tag{8}$$

Now to compute the interaction force $\mathbf{p}_B^{(s)}$ it is assumed that the circular contour is divided into N_B equidistant points. Then $\mathbf{p}_B^{(s)}$ is calculated as

$$\{\mathbf{p}_B^{(s)}\} = [S_f]\{\mathbf{q}_B^{(s)}\}, \tag{9}$$

where $[S_f] = R_B(2\pi/N_B)[T]^T[F][G]^{-1}[T]$ and the component T_i of the transformation matrix is

$$[T_i] = \begin{bmatrix} \cos\vartheta_i & \sin\vartheta_i \\ -\sin\vartheta_i & \cos\vartheta_i \end{bmatrix}.$$

The unknown coefficient vector $\{a\}$, the boundary and interior nodal displacements $\{\mathbf{q}_B^{(2)}\}$ and $\{\mathbf{q}_I^{(2)}\}$ are now determined by imposing the continuity of displacements and traction force at the boundary nodes. Thus

$$\{\mathbf{q}_B^{(2)}\} = \{\mathbf{q}_B^{(s)}\} + \{\mathbf{q}_B^{(i)}\}, \tag{10}$$

$$\{\mathbf{p}_B^{(2)}\} = \{\mathbf{p}_B^{(s)}\} + \{\mathbf{p}_B^{(i)}\}. \tag{11}$$

The vectors $\{\mathbf{p}_B^{(i)}\}$ and $\{\mathbf{q}_B^{(i)}\}$ are the incident displacement and traction force vectors, respectively, on the boundary.

From equations (4), (10), and (11) the nodal displacements $\{\mathbf{q}_B^{(2)}\}$ are found from the equation

$$[S_{BB} - S_f - S_{BI}S_{II}^{-1}S_{IB}]\{\mathbf{q}_B^{(2)}\} = \{\mathbf{p}_B^{(i)}\} - [S_f]\{\mathbf{q}_B^{(i)}\}. \tag{12}$$

Knowing $\{\mathbf{q}_B^{(2)}\}$ the interior nodal displacements are found from equation (3) and the scattered displacement field $\{\mathbf{q}_B^{(s)}\}$ is obtained from equations (9), (6), (5), and (7).

The procedure outlined in the foregoing was used to solve first the case of single scattering by a circular cylindrical cavity. Numerical results obtained by the present method were found to agree very well with the exact solution. These and other results are discussed in the next section.

Numerical Results and Discussion

Diffraction of a plane P and a plane SV wave by a single cavity of circular triangular, and square shapes is studied by the method outlined in the foregoing. Also studied are scattering by a pair of circular cavities, and two cavities, one of which is circular and the other, square. For all the

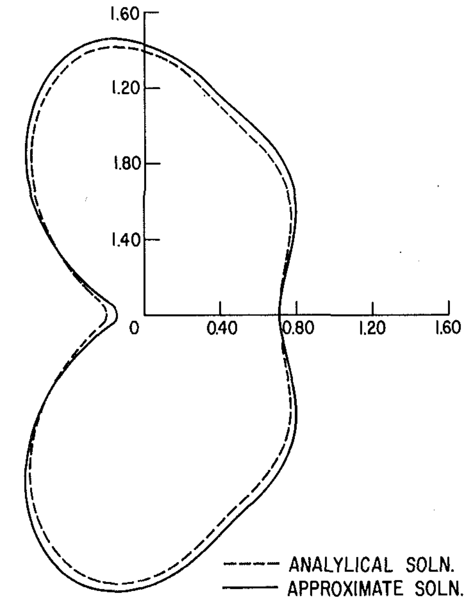

Fig. 2 Comparison of the exact and FEEET calculations for $|\sigma_{\vartheta\vartheta}/\sigma_0|$ at circular hole. *P* wave incident at γ = 0 deg, k_2a = 2.0.

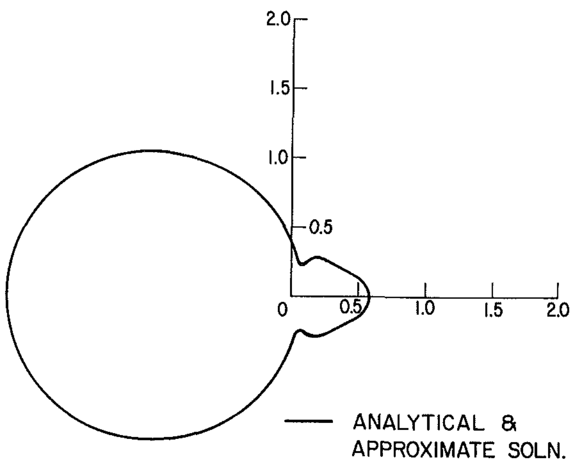

Fig. 3 Comparison of the exact and FEEET calculations for the normalized radial displacement of the circular cavity wall. *P* wave incident at γ = 0 deg, k_2a = 2.0.

numerical computations the Poisson's ratio of the host medium was assumed to be $\sigma = 0.3$. To test the accuracy of the present numerical method, results were first checked with the exact solutions for a single circular cavity. Figures 2 and 3 show the polar plots of the normalized absolute value of the hoop stress, $|\sigma^{\theta\theta}/\sigma_0|$, and the normalized radial displacement for different values of k_2a. Here a is the radius of the circular cavity and $k_2 = \omega/C_2$, C_2 being the shear wave speed in the medium. Note that the incident wave is a P wave represented by

$$\mathbf{u}^{(i)} = \nabla \phi^{(i)}$$

$$\phi^{(i)} = \sum_{n=0}^{\infty} \epsilon_n i^n J_n(k_1 r) \cos n(\vartheta - \gamma), \qquad (13)$$

Here $\epsilon_0 = 1$, $\epsilon_n = 2 (n > 0)$. For the purpose of applying the method outlined in the preceding section, the circular cavity C was enclosed by another circle B with $R_B = 1.3a$, a being the radius of C. The region in between B and C was divided up into finite elements. Various elements were used including constant strain triangles (CST). Total number of nodes on B

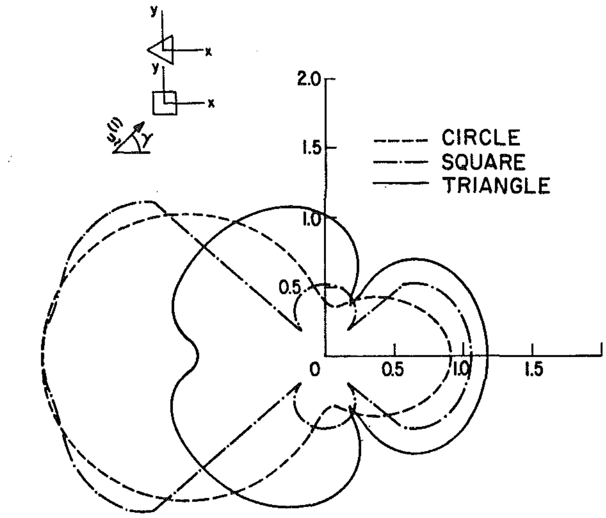

Fig. 4 Normal displacement of cavity walls. γ = 0 deg, k_2a = 1.0.

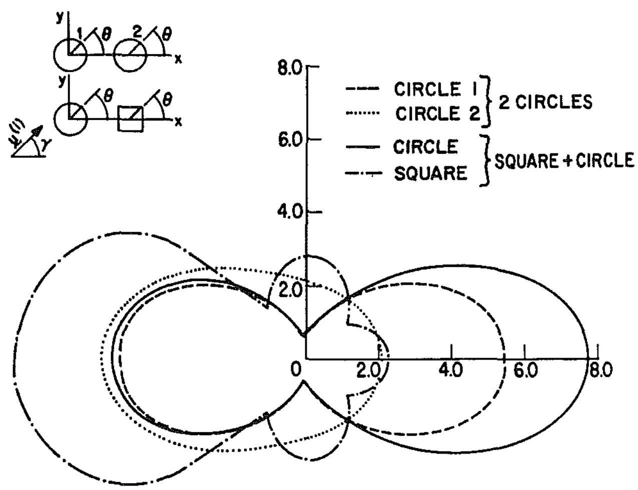

Fig. 5 Normal displacements of a pair of cavity walls. γ = 0 deg, k_2a = 1.0.

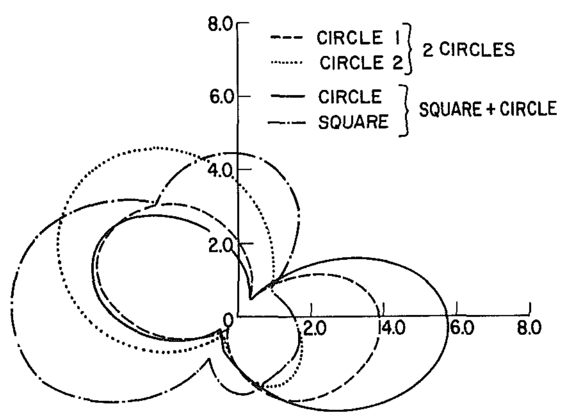

Fig. 6 Normal displacements of a pair of cavity walls. γ = −45 deg, k_2a = 1.0.

was taken to be 48 and three circular contours (including C) used. It was found that increasing the region R_2 by adding another circular contour did not cause any appreciable change. It was found that higher order elements gave better results. However, the improvement from four-node quadrilateral to eight-node quadrilateral was not very large.

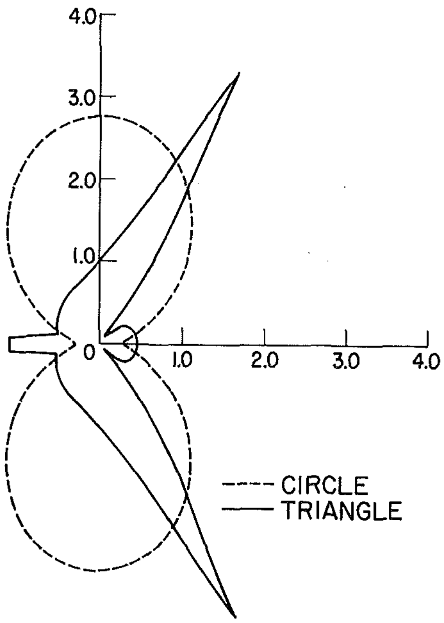

Fig. 7 Polar plot of the normalized hoop stress $|\sigma_{ss}/\sigma_0|$ $\gamma = 0$ deg, $k_2a = 0.15$.

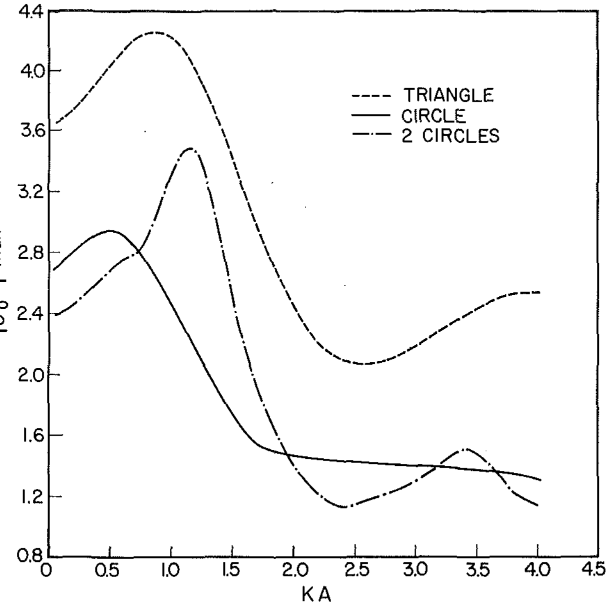

Fig. 9 Variation of $|\sigma_{ss}/\sigma_0|_{max}$ with k_2a. $\gamma = 0$ deg.

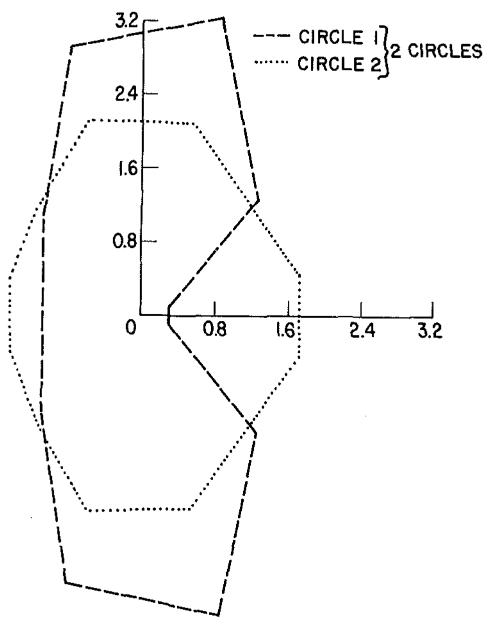

Fig. 8 Polar plots of $|\sigma_{ss}/\sigma_0|$. $\gamma = 0$ deg and $k_2a = 1.0$.

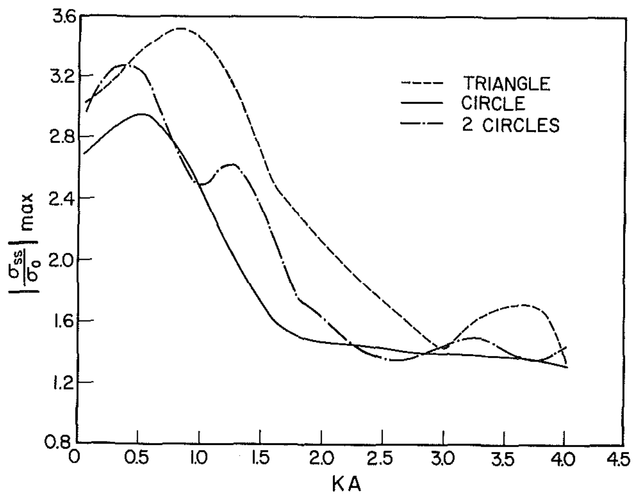

Fig. 10 Variation of $|\sigma_{ss}/\sigma_0|_{max}$ with k_2a. $\gamma = -45$ deg.

Even the constant strain triangle (CST) was found not to deviate much. In all the results presented in this paper mostly four-node elements in conjunction with some CST and five-node quadrilaterals were used. As can be seen from these figures the results obtained by the present method agree very well with the exact ones. Agreement was found to be well at lower k_2a also.

Figures 4–6 show the polar plots of the normalized amplitudes ($|u_N/u_0|$) of the normal displacements at the cavity walls. Note that $\sigma_0 = \mu k_2^2$ and $u_0 = k_1$. Here $k_1 = \omega/C_1$, C_1 is the P wave speed. The orientation of the triangle with respect to the incident wave direction is shown in the figure. It is seen that at long wavelengths the normal displacements of circular and square cavity walls are symmetric about x and y-axes, but for triangular hole larger displacements occur on the shadow side than on the illuminated side. It should be pointed out that normal displacements and the tangential stresses were computed at the midpoints between the nodes and that the corners were always nodes. It is noted that a segment of square boundary on the illuminated side moves by the same amount as the circle. This is seen to be true even when k_2a is quite large (Fig. 4). It was found that for the triangle maximum normal displacement occurs at around $k_2a = 1.5$, for the square at $k_2a = 0.75$. For all three shapes the maximum occurs on the illuminated side.

It was found that at long wavelengths the presence of the second circle nearly doubles the normal displacement on both of them from the value when there is only one and that the normal displacements are the same on both circles and that replacing the second circle by a square did not change the values on the first one. (For lack of space these results are not shown here.) As the frequency increases the interference effects change the displacements considerably (Fig. 14). It is found that the maximum normal displacements now occur on the square.

Polar plots of normalized hoop stresses around single circular and triangular holes are shown in Fig. 7 and the

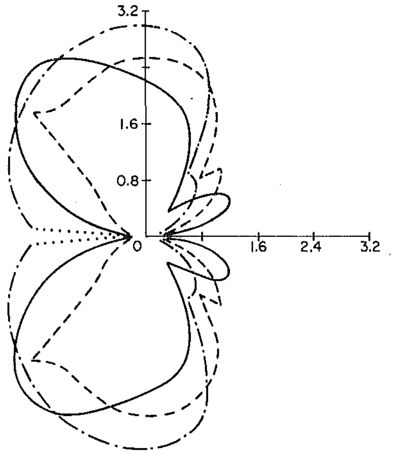

Fig. 11 Polar plots of normal displacement amplitudes. — — — square; — · — triangle; —— circle. $\gamma = 0$ deg, $k_2a = 2.0$.

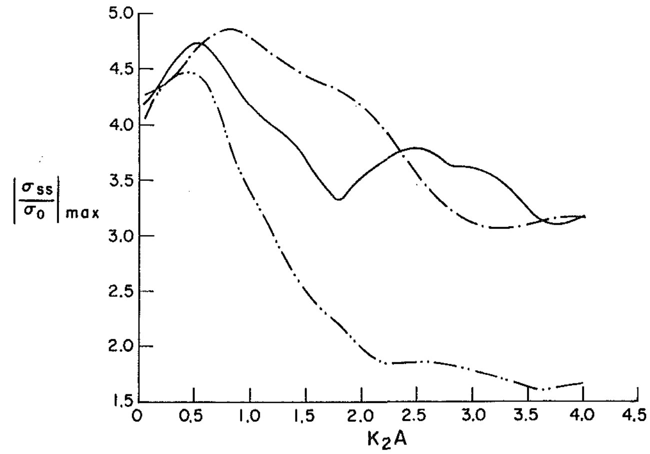

Fig. 13 Maximum hoop stress amplitudes versus frequency. $\gamma = 0$ deg. —— circle; — · — triangle; — · · · — two circles.

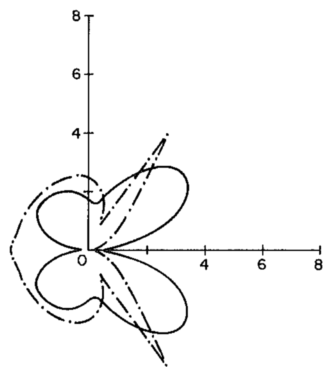

Fig. 12 Polar plots of hoop stress amplitudes. $\gamma = 0$ deg, $k_2a = 1.0$. Legends are as in Fig. 11.

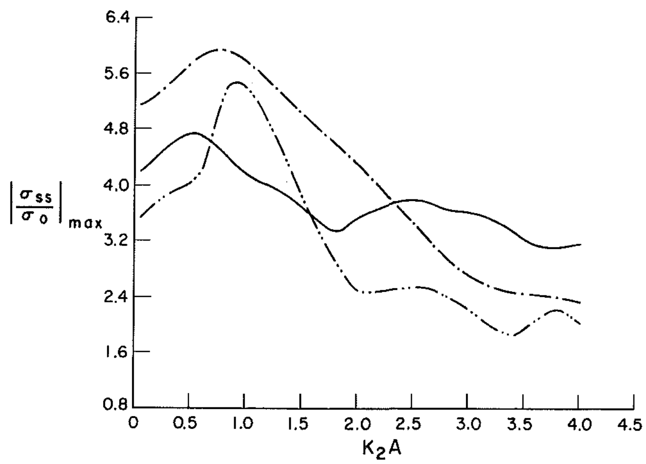

Fig. 14 Maximum hoop stress amplitudes versus frequency. $\gamma = -45$ deg. Legends are as in Fig. 13.

corresponding results for a pair of circles are shown in Fig. 8. Results for a square, and a circle in the presence of a square are omitted in order not to clutter up the figures. It is found that when $\gamma = 0$ deg, maximum hoop stress occurs (as expected) near the two corners of the triangular hole, whereas for the circle it is near $\vartheta = 90$ deg and 270 deg. Figure 8 shows the considerable changes that occur due to interference.

Finally, Figs. 9 and 10 show the variations of the maximum hoop stress as the frequency changes. It is seen that in all cases the maximum hoop stress increases first as the frequency increases from zero, but then decreases with increasing frequency. For a triangle it is seen that the maximum hoop stress oscillates at high frequencies. Also, interference effects between the two circles are clearly visible in the case of a pair of circles.

Figures 11–14 show some results for an incident plane *SV* wave. In this case

$$\mathbf{u}^{(i)} = \nabla \,\hat{}\, (\psi^{(i)} \mathbf{e}_z)$$

$$\psi^{(i)} = \sum_{n=0}^{\infty} \epsilon_n i^n J_n(k_2 r) \cos n(\vartheta - \gamma) \tag{14}$$

Figure 11 shows the polar plot of the magnitude of the normal displacements ($|U_N/u_0|$) around the cavity walls when $\gamma = 0$ deg. It would be expected from symmetry that this goes to zero at $\vartheta = 0$ deg and 180 deg. As can be seen the normal displacement for the circle goes smoothly to zero at these points. However, for a square it decreases abruptly as these points are approached showing the significant influence of the corners. But notice the significantly different behavior in the case of the triangle on the illuminated side near vertex. The displacement drops steeply to zero only as the vertex is approached.

The hoop stress distribution around single cavities are shown in Fig. 12. It was found that for the triangle at long wavelengths the same maximum occurs near all the corners and that the distribution is the same for $\gamma = 0$ deg and 180 deg. As Fig. 12 shows, at high frequencies the maximum occurs near the corners of the base when $\gamma = 0$ deg. It was found, however, that when $\gamma = 180$ deg the maximum occurred near the vertex. Maximum hoop stresses on a pair of scatterers are also quite different from those on single scatterers. It is found that when $\gamma = -45$ deg the maximum normal displacement reaches a very large value when the pair of scatterers is composed of a circle and square. Maximum hoop stress is shown in Figs. 13 and 14. These figures are to be contrasted with Figs. 9 and 10. It is seen that larger stresses are caused by shear waves than by longitudinal waves. Note that in the static limit when $\gamma = 0$ deg the maximum hoop stress on the triangle is larger than that on a circle, which is larger than that on a pair of circles. These are however quite close. For $\gamma = -45$ deg, on the other hand, the same relative ordering holds, but they are farther apart now. This is to be contrasted with the results for the longitudinal wave. There the same ordering is found to hold, but with larger spread when $\gamma = 0$ deg. For $\gamma = -45$ deg, however, the maximum hoop stress on a pair of circles is larger than that on one.

Acknowledgment

The work of SKD was supported in part by a grant (CEE-8120536) from the National Science Foundation, Earthquake Hazards Mitigation Program. Support was also provided by the Natural Science and Engineering Research Council of Canada through a grant (A-7988).

References

1 Pao, Y. H., "Dynamic Stress Concentration in an Elastic Plate," ASME Journal of Applied Mechanics, Vol. 29, 1961, pp. 199–305.

2 Baron, M. L., and Parmes, R., "Displacemet and Velocities Produced by the Diffraction of a Pressure Wave by a Cylindrical Cavity in an Elastic Medium," ASME Journal of Applied Mechanics, Vol. 19, 1962, pp. 385–395.

3 Baron, M. L., and Matthews, A. T., "Diffraction of a Pressure Wave by a Cylindrical Cavity in an Elastic Medium," ASME Journal of Applied Mechanics, Vol. 28, 1961, pp. 347–354.

4 Baron, M. L., and Matthews, A. T., "Diffraction of a Shear Wave by a Cylindrical Cavity in an Elastic Medium," ASME Journal of Applied Mechanics, Vol. 29, 1961, pp. 205–207.

5 Mow, C. C., and Mente, L. J., "Dynamic Stresses and Displacements around Cylindrical Discontinuities due to Plane Harmonic Shear Waves," ASME Journal of Applied Mechanics, Vol. 30, 1963, pp. 598–604.

6 Pao, Y. H., and Mow, C. C., *The Diffraction of Elastic Waves and Dynamic Stress Concentrations*, Crane and Russak, New York, 1973.

7 Schroll, K. R., and Cheng, S. L., "Dynamic Stresses Around Elliptical Discontinuities," ASME Journal of Applied Mechanics, V.ol. 39, 1972, pp. 133–138.

8 Shah, A. H., Wong, K. C., and Datta, S. K., "Single and Multiple Scattering of Elastic Waves in Two Dimensions," *Journal of the Acoustical Society of America*, Vol. 74, 1983, pp. 1033–1043.

T. D. Gerhardt,
Research Engineer,
U.S. Department of Agriculture,
Forest Service,
Forest Products Laboratory[1]
P.O. Box 5130,
Madison, Wis. 53705
Associate Mem. ASME

A Hybrid/Finite Element Approach for Stress Analysis of Notched Anisotropic Materials

A hybrid/finite element is proposed to calculate stresses or stress intensity factors at notches, fillets, cutouts, or other geometric discontinuities in plane-loaded anisotropic materials. Stress and displacement fields assumed in the element satisfy all governing elasticity equations. Furthermore, the shape and stress-free conditions of the discontinuity are modeled exactly using conformal mapping and analytic continuation. Continuity of analytic and finite element displacement fields on the remaining element boundary are enforced in an approximate manner with a variational principle. Numerical results are presented for both elliptical void and circular fillet hybrid elements. Comparisons are made to analytic solutions. Results indicate that structural models using a hybrid element with a coarse conventional element mesh yield efficient and accurate calculations of critical stresses.

Introduction

A hybrid/finite element (FE) approach is proposed to accurately calculate critical stresses or stress intensity factors associated with notches, fillets, or cutouts in plane-loaded anisotropic materials. Efficient structural design requires calculation of stress concentration factors (SCF) for many complex shapes. For example, SCF associated with wood beams containing rectangular, filleted edge notches are required for efficient design of wood pallets. Contemporary design handbooks, such as [1], are based predominately on photoelasticity studies. These results provide SCF for isotropic materials only. Recent experimental studies, however, do consider composite [2, 3] as well as isotropic [4–6] sheets.

Analytic approaches to calculate critical stresses are limited to problems involving voids of rather simple shape in infinite domains. Savin [7] extended the complex variable approach of Muskhelishvili [8] and derived a solution for an elliptical hole in a plane-loaded, infinite, anisotropic sheet. (A rather comprehensive review of research concerning bending of anisotropic plates with holes is available [9].) Recent analytic efforts have considered holes in both isotropic [10] and anisotropic [11] sheets. Significantly, the integral equation solution by Krenk [11] remains valid when the characteristic equation has multiple roots, i.e., for isotropic materials. Other related studies include circular holes in cylindrically orthotropic plates [12], rectangular [13] and V-shaped [14] voids in isotropic half planes. Also, Dhir [15] optimized hole shapes in infinite, isotropic sheets using an analytical/numerical procedure.

Numerical approaches can analyze problems involving finite domains. Various notches and cutouts in isotropic materials were modeled using the boundary integral equation technique [16–19]. Nikooyeh and Robinson [16] used this technique (in conjunction with expansions of improper Williams solutions for sharp corners [20]) to compute stresses at fillets of very small radii. Ogonowski [21] analyzed loaded holes in finite, orthotropic sheets using collocation. In other approaches, truncated power series expansions have been used to approximate the cutout shape [22, 23]. Rowlands et al. [2] compared such a solution with experimental results from a tensile-loaded composite plate containing a rectangular filleted cutout. The experimental and calculated SCF differed by 35 percent.

Stresses in composite [24, 25] and isotropic [26, 27] materials containing notches or fillets have been computed with conventional FE's. However, displacement-based elements have difficulty computing accurate SCF for several reasons. (a) Reliable calculation of stresses requires evaluation at interior (Gauss) points [28]. Thus, evaluation of edge stresses requires extrapolation, although alternative approaches have been proposed recently [29, 30]. (b) The displacement functions do not implicitly satisfy the free-surface boundary conditions [29]. (c) Approximating the shape of the notch or void by polynomial functions causes an error. Furthermore, using certain elements in curved shapes can cause an additional error [31, 32]. These cited difficulties dictate extremely small mesh sizes for stress analysis of the problems considered in this paper. (However, for certain problems, SCF were computed with a coarse FE mesh in conjunction with the J integral [33, 34].) In models of a gear root fillet [27] and a notched coupon specimen [25], 1356 and 998 elements were used, respectively.

[1] Maintained at Madison, Wis., in cooperation with the University of Wisconsin.

Contributed by the Applied Mechanics Division and presented at the Winter Annual Meeting, New Orleans, La., December 9–14, 1984 of THE AMERICAN SOCIETY OF MECHANICAL ENGINEERS.

Discussion on this paper should be addressed to the Editorial Department, ASME, United Engineering Center, 345-East 47th Street, New York, N.Y. 10017, and will be accepted until two months after final publication of the paper itself in the JOURNAL OF APPLIED MECHANICS. Manuscript received by ASME Applied Mechanics Division, October, 1983; final revision, March 1984. Paper No. 84-WA/APM-28.

Copies will be available until August, 1985.

In this paper, a hybrid/FE formulation is proposed that eliminates the difficulties cited in the preceding paragraph. A hybrid element is derived to structurally model the region of the notch or void. The assumed displacement and stress fields in the element's interior satisfy all governing differential equations of linear elasticity theory. Conformal mapping and reflection arguments, respectively, are used to model the shape and stress-free conditions of the notch exactly. A continuous representation of critical stresses is computed directly. This approach has some similarities to a combined modified mapping-collocation (MMC) and FE method used to model fillets [35] and elliptical cutouts [36] in isotropic materials. However, the method presented in this paper has several major advantages when compared to the combined MMC and FE technique. (*i*) The proposed method utilizes a variational principle to systematically connect the analytic and numerical representations of the structure. The combined MMC and FE method introduces a fictitious band of FE's for the connection. (*ii*) The proposed method computes the stiffness matrix for the hybrid element in terms of nodal displacements. Thus, insertion into existing FE programs is readily achieved. (*iii*) The combined MMC and FE method requires a large number of terms in the series expansions (with a least squares reduction) due to the sensitivity of the results to the location of boundary points. The method presented in this paper provides accurate results with very few terms. (*iv*) The proposed method is formulated in terms of an arbitrary conformal mapping function. This approach allows modeling diverse shapes of notches, fillets, cutouts, etc.

Analytic Representation

In this section, analytic representations for displacement and stress fields in the interior of the hybrid element are derived. Consider a region A in a plane-loaded anisotropic material with (x, y) physical coordinates. Define the complex variables z_j $(j = 1,2)$ by the affine transformation [37]

$$z_j = \gamma_j z + \delta_j \bar{z}; \quad j = 1,2 \tag{1}$$

where $z = x + iy$, $\gamma_j = (1 - is_j)/2$, and $\delta_j = (1 + is_j)/2$. The constant $i = \sqrt{-1}$, $\bar{z}$ is the complex conjugate of z, and s_j $(j = 1,2)$ are distinct roots of the characteristic equation

$$D_{11}s^4 - 2D_{13}s^3 + (2D_{12} + D_{33})s^2 - 2D_{23}s + D_{22} = 0 \tag{2}$$

with positive imaginary parts. (Real roots to equation (2) do not exist [7]. For multiple roots, an isotropic formulation is required.) The material constants D_{ij} are components of the elastic compliance matrix $[D]$.

Remarkably, all governing differential equations of linear elasticity theory are satisfied in region A by any pair of functions $\phi(z_1)$ and $\psi(z_2)$ which are analytic in the complex variables z_1 and z_2, respectively [7]. The stress $(\sigma_{xx}, \sigma_{yy}, \sigma_{xy})$ and displacement (u, v) components can be expressed in terms of $\phi(z_1)$ and $\psi(z_2)$ [7].

$$\{\sigma\} \equiv \left\{ \begin{matrix} \sigma_{yy} \\ \sigma_{xy} \\ \sigma_{xx} \end{matrix} \right\} = 2Re \left\{ \begin{bmatrix} 1 \\ -s_1 \\ s_1^2 \end{bmatrix} \phi'(z_1) + \begin{bmatrix} 1 \\ -s_2 \\ s_2^2 \end{bmatrix} \psi'(z_2) \right\} \tag{3}$$

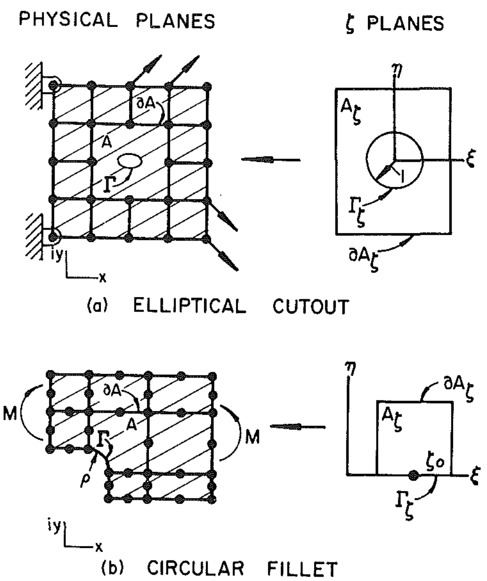

Fig. 1 Mapping examples

$$\{u\} \equiv \left\{ \begin{matrix} u \\ v \end{matrix} \right\} = 2Re \left\{ \begin{bmatrix} p_1 \\ q_1 \end{bmatrix} \phi(z_1) + \begin{bmatrix} p_2 \\ q_2 \end{bmatrix} \psi(z_2) \right\} + \left\{ \begin{matrix} -C_0 y + u_0 \\ C_0 x + v_0 \end{matrix} \right\} \tag{4}$$

The notation Re denotes the real part, the prime denotes a derivative with respect to the independent variable, the constants p_j, q_j $(j = 1,2)$ are defined in the Appendix, and the constants C_0, u_0, v_0 are associated with rigid body motion.

Now suppose a notch, fillet, cutout, or other geometric discontinuity, defined by a curve Γ, exists in the anisotropic material. Furthermore, assume an analytic function $\omega(\zeta)$ exists that maps either the unit circle or the real axis in a complex ζ plane onto Γ in the z plane. Define Γ_ζ as the shape of the discontinuity in the ζ plane. Elliptical void and circular fillet mappings are depicted in Fig. 1. Many different shapes of Γ can be modeled in this manner since numerous mapping functions are known. In fact, functions for mapping the unit circle onto $V-$, $U-$, and keyhole-shaped notches have been recently found [38]. For the anisotropic formulation presented here, induced functions $\omega_j(\zeta_j)$ (no sum on j) associated with mappings from complex ζ_j to z_j planes were constructed from equation (1).

$$z_j = \gamma_j \omega(\zeta) + \delta_j \overline{\omega(\bar{\zeta}^{\,l})} \equiv \omega_j(\zeta_j) \tag{5}$$

The constant $l = -1$ when Γ_ζ is the unit circle and $l = 1$ when Γ_ζ is the real axis. Equation (5) for $l = -1$ had been obtained by Milne-Thomson [37]. For both cases, $\bar{\zeta}^{\,l} = \zeta$ for all ζ on Γ_ζ.

Using equation (5), the stress and displacement components from equations (3) and (4) can be expressed in terms of ζ_j since $\phi'(z_1) = \phi'(\zeta_1)/\omega_1'(\zeta_1)$ and $\psi'(z_2) = \psi'(\zeta_2)/\omega_2'(\zeta_2)$. The analyticity of the induced mapping functions $\omega_j(\zeta_j)$ guarantees that the governing differential equations are satisfied by $\phi(\zeta_1)$ and $\psi(\zeta_2)$.

The rather simple shapes of Γ_ζ enable satisfaction of stress-free conditions on Γ using the principle of analytic continuation. The author satisfied these conditions exactly by taking $\phi(\zeta_1)$ and $\psi(\zeta_2)$ in the form:

$$\phi(\zeta_1) = F(\zeta_1)$$

and

$$\psi(\zeta_2) = B\overline{F(\bar{\zeta}_2)} + CF(\zeta_2) \quad (6)$$

The constants B and C are defined in the Appendix. F is an arbitrary function which is analytic on Γ_ζ. For unit circle mappings, Bowie and Freese [39] previously obtained equation (6). Note the ease and general applicability of satisfying stress-free conditions on Γ with a complex variable approach. Contrastingly, eigenvalue techniques are complicated for anisotropic problems and require separate analysis for each Γ.

Finite Element Formulation

Now specifically define A as a region with boundary ∂A and in the immediate vicinity of Γ. Two examples are depicted in Fig. 1. In this section, a hybrid FE is derived to structurally model the region A. Stress and displacement fields derived in the preceding section are cast into an FE formulation using a variational principle. This principle enforces continuity of analytic and polynomial displacement fields on ∂A in an aproximate manner. The order of the polynomial on ∂A is chosen to coincide with the order of the assumed fields in the conventional FE's that surround the hybrid element. Since these elements model the remainder of the structure, both finite domains and complex loading conditions can be considered.

The author assumed $F(\zeta)$ required in equation (6) as either a truncated Laurent expansion (unit circle mappings) or a truncated Taylor series expansion about ζ_0, a point on the real axis (real axis mappings). Substitution of these expansions into equation (6) yields:

$$\phi(\zeta_1) = \sum_{j=m}^{n} \{a_j(\zeta_1 - \zeta_0)^j\}$$

$$\psi(\zeta_2) = \sum_{j=m}^{n} \{\bar{a}_j B(\zeta_2 - \zeta_0)^h + a_j C(\zeta_2 - \zeta_0)^j\} \quad (7)$$

The constants $a_j = b_j + ic_j$, where b_j and c_j are real numbers, and n and m are integers. For unit circle mappings, $h \equiv -j$ and $\zeta_0 = 0$. For real axis mappings, $h \equiv j$ and $m = 0$.

Assumed fields for $\{u\}$ and $\{\sigma\}$ in A were obtained by substituting equations (7) and (5) into equations (3) and (4). Thus,

$$\{u\} = [U]\{\beta\} + \left\{ \begin{array}{c} -C_0 y + u_0 \\ C_0 x + v_0 \end{array} \right\} \quad (8)$$

$$\{\sigma\} = [S]\{\beta\} \quad (9)$$

where $\{\beta\}^T = [b_m, c_m, b_{m+1}, c_{m+1}, \ldots, b_n, c_n]$. In general, the $j = 0$ terms (b_0, c_0) can be excluded from the summations of equation (7). These terms contribute to rigid body motion only and can be included in u_0 and v_0. The author derived the following components for the real matrices $[U]$ and $[S]$.

$$\begin{aligned}
U(1,k) &= 2Re\{p_1\zeta_1^j + p_2(C\zeta_2^j + B\zeta_2^h)\} \\
U(1,k+1) &= 2Im\{-p_1\zeta_1^j + p_2(-C\zeta_2^j + B\zeta_2^h)\} \\
U(2,k) &= 2Re\{q_1\zeta_1^j + q_2(C\zeta_2^j + B\zeta_2^h)\} \quad (10) \\
U(2,k+1) &= 2Im\{-q_1\zeta_1^j + q_2(-C\zeta_2^j + B\zeta_2^h)\}
\end{aligned}$$

$$\begin{aligned}
S(r,k) &= (-1)^{r-1}(2j)\{Re[s_1^{r-1}\zeta_1^{j-1}/\omega_1'(\zeta_1) \\
&\quad + s_2^{r-1}(hB\zeta_2^{h-1}/j + C\zeta_2^{j-1})/\omega_2'(\zeta_2)]\} \quad (11) \\
S(r,k+1) &= (-1)^{r-1}(2j)\{Im[-s_1^{r-1}\zeta_1^{j-1}/\omega_1'(\zeta_1) \\
&\quad + s_2^{r-1}(hB\zeta_2^{h-1}/j - C\zeta_2^{j-1})/\omega_2'(\zeta_2)]\}
\end{aligned}$$

where Im denotes the imaginary part, $k \equiv 2(j-m) + 1$, $r = 1,2,3$, and $j \neq 0$. (If $m<0$ and $j>0$, $k \equiv 2(j-m)-1$.) The expansions chosen for $F(\zeta)$ are analytic on Γ_ζ and also generate analytic functions $\phi(\zeta_1)$ and $\psi(\zeta_2)$. Therefore, the stress and displacement fields of equations (8)-(11) satisfy both stress-free conditions on Γ and all governing elasticity equations in A.

The author formulated the stiffness matrix of the hybrid element using a variational principle, π, which allows incompatible boundary displacements [40-42].

$$\pi = \int_A \left(\{\sigma\}^T[L]\{u\} - \frac{1}{2}\{\sigma\}^T[D]\{\sigma\}\right)dA - \int_{\partial A}\{T\}^T(\{u\} - \{\tilde{u}\})ds - \int_{S_\sigma}\{\bar{T}\}^T\{\tilde{u}\}ds \quad (12)$$

The matrix $[L]$ is defined by the strain-displacement relations $\{\epsilon\} = [L]\{u\}$, where $\{\epsilon\}^T = [\epsilon_{yy}\ \epsilon_{xy}\ \epsilon_{xx}]$. The tractions $\{T\}^T = [T_x\ T_y]$ and S_σ is the portion of ∂A in which tractions $\{\bar{T}\}$ are prescribed. When $\{\bar{T}\} = \{0\}$, equation (12) reduces to a form of the Hellinger-Reissner principle [42]. The boundary displacements $\{\tilde{u}\}$ and tractions $\{T\}$ are defined only on ∂A and can be chosen independent of $\{u\}$ and $\{\sigma\}$ which are defined over A. The Euler equations for π are [40]:

in A: $\quad [L]\{u\} = [D]\{\sigma\} \quad (13)$

$\quad \sigma_{jk,k} = 0 \quad (14)$

on ∂A: $\quad T_j = \sigma_{jk}v_k \quad (15)$

$\quad \{u\} = \{\tilde{u}\} \quad (16)$

on S_σ: $\quad \{T\} = \{\bar{T}\} \quad (17)$

where v_j ($j=1,2$) are the direction cosines of the normal to ∂A. The assumed fields for $\{u\}$ and $\{\sigma\}$, i.e., equations (8) and (9), satisfy equations (13) and (14) identically. For this case, by Green's theorm:

$$\frac{1}{2}\int_A\{\sigma\}^T[D]\{\sigma\}dA = \frac{1}{2}\int_A\{\sigma\}^T[L]\{u\}dA = \frac{1}{2}\int_{\partial A}\{T\}^T\{u\}ds \quad (18)$$

Now π becomes

$$\pi = \int_{\partial A}\{T\}^T\left(\{\tilde{u}\} - \frac{1}{2}\{u\}\right)ds - \int_{S_\sigma}\{\bar{T}\}^T\{\tilde{u}\}ds \quad (19)$$

Hybrid elements for modeling circular fillets [43], V-notches [44], and general notch shapes [45] in *isotropic* materials have been formulated using equation (19). Schnack and Wolf [45] use stress functions with stress decay characteristic of notches in development of triangular hybrid elements. This approach allows arbitrarily shaped notches to be modeled and was applied in a stress optimization technique [46]. The approaches suggested in [43-45] (as well as an early approach by Rao et al. [47]) require eigenfunctions for expansions of stress and displacement. Calculation of eigenfunctions for anisotropic materials containing discontinuities is difficult. The complex variable approach of this paper, on the other hand, readily satisfies both governing differential equations and stress-free conditions on Γ through assumed friction analyticity and conformal mapping.

In modeling cracks, Tong et al. [40, 41] introduce conformal mapping as a technique to induce the proper crack tip singularity. However, as illustrated in both analytic [7, 8] and MMC [35, 36] approaches, this technique is substantially more powerful. Geometries, for which singularities do not exist or are unknown, can be modeled. Both rounded and sharp corners can be considered. Thus, an important contribution of the present paper is generalization of a complex variable, hybrid/FE technique to problems involving dicontinuities of diverse shapes. Clearly, the anisotropic crack element [41] is a special case of the present formulation.

To finish the FE formulation, fields must be assumed for $\{T\}$ and $\{\tilde{u}\}$ on ∂A. The tractions $\{T\}$ are assumed as to satisfy equation (15), i.e.,

$$\{T\} = [R]\{\beta\} \quad \text{where} \quad [R] = \begin{bmatrix} 0 & v_y & v_x \\ v_y & v_x & 0 \end{bmatrix} [S] \tag{20}$$

The boundary displacement field $\{\tilde{u}\}$ is interpolated from the nodal displacement on ∂A, $\{q\}$, i.e.,

$$\{\tilde{u}\} = [L]\{q\} \tag{21}$$

The polynomial form of $[L]$ depends on the type of displacement-based FE that surrounds region A.

Finally, consider the case when $\{\bar{T}\} = 0$. Self-equilibrated loadings were considered in [40]. Taking $C_0 = u_0 = v_0 = 0$ in equation (8) and then substituting equations (8), (9), (20), and (21) into equation (19) yields:

$$\pi = \{\beta\}^T[G]\{q\} - \frac{1}{2}\{\beta\}^T[H]\{\beta\} \tag{22}$$

where

$$[H] \equiv \int_{\partial A} [R]^T[U]ds \quad \text{and} \quad [G] \equiv \int_{\partial A} [R]^T[L]ds \tag{23}$$

Minimization of π in the usual manner determines the relation between $\{\beta\}$ and $\{q\}$, i.e.,

$$\{\beta\} = [H]^{-1}[G]\{q\} \tag{24}$$

The stiffness matrix for the hybrid element, $[k]$, is now computed by substitution of equation (24) into equation (22).

$$\pi = \frac{1}{2}\{q\}^T[k]\{q\} \quad \text{where} \quad [k] \equiv [G]^T[H]^{-1}[G] \tag{25}$$

Thus, calculation of $[k]$ involves evaluating two-line integrals along $\partial A - \Gamma$. (Neither integration nor definition of $\{\tilde{u}\}$ is required along Γ because $[R] = [0]$ on Γ.) Gauss quadrature was used for these integrations.

It is important to note that of the five Euler equations (equations (13)–(17)) associated with the variational principle of equation (12), only equation (16) has not been satisfied in the formulation. Thus, the coefficients $\{\beta\}$ are determined as to satisfy continuity of analytic and FE displacements in an approximate manner on $\partial A - \Gamma$. Numerical examples will show that accurate stresses can be calculated efficiently on Γ in spite of this approximation.

Numerical Examples

The stiffness matrix $[k]$ defined in equation (25) is formulated in terms of nodal displacements $\{q\}$ on the boundary $\partial A - \Gamma$. The hybrid element, therefore, can be readily inserted into existing FE programs. The author added the element to a program in the literature [48] he had previously modified [49]. A listing of the hybrid element subroutines is available upon request. All computing was done in double precision on a Sperry 1100/82 at the University of Wisconsin-Madison.

Three numerical examples are presented using an elliptical void mapping function. A circular fillet mapping function is used for a final example. The generality of the presented formulation is illustrated by the ease of modeling different discontinuities. *For a given* Γ, *only the derivative and inverse of* $\omega_j(\zeta_j)$ *must be defined.* Specification of Laurent or Taylor expansions is achieved directly by the value of m input. When specifying m and n, the number of terms must exceed the number of components in $\{q\}$ minus three. This is required to ensure $[k]$ has the correct rank [40].

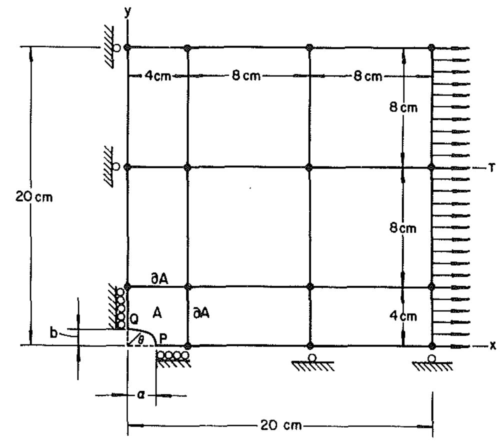

Fig. 2 Finite element mesh, linear elements

Table 1 Elliptical void; a = 0.25 cm, b = 0.125 cm; 7 GP/side; yellow poplar elastic properties

$\{\tilde{u}\}$	m	n	CPU (sec)	σ_Q/T	σ_P/T
Linear	−3	3	0.09	3.1955	−0.30301
Quadratic	−7	7	.18	3.1960	−.30326
Cubic	−11	11	.29	3.1953	−.30313
Elasticity [7]				3.1961	−.30332

Elastic properties typical for yellow-poplar at 11 percent moisture content were used in most of the examples. These properties are [50]: $E_x = 1.034 \times 10^7$ kPa (1.5×10^6 psi), $E_y = 0.092\ E_x$, $G_{xy} = 0.075\ E_x$, and $v_{xy} = 0.318$. Roots of equation (2) associated with these properties are $s_1 = 0.960818\ i$ and $s_2 = 3.431350\ i$. Orthotropic properties were chosen to facilitate comparison with published elasticity results and to enable use of symmetry in modeling. In other examples, the author found no difference in convergence characteristics of results using anisotropic rather than orthotropic properties.

Elliptical Mapping Function. The following conformal mapping function maps the unit circle in the ζ plane onto an ellipse in the z plane:

$$z = \omega(\zeta) = (a+b)\zeta/2 + (a-b)\zeta^{-1}/2 \tag{26}$$

where the constants a and b are the elliptical axes in the x and y directions, respectively. Transformations from the ζ_j to z_j planes (j = 1,2) were derived by substitution of equation (26) into equation (5):

$$z_j = \omega_j(\zeta_j) = (a - is_jb)\zeta_j/2 + (a + is_jb)\zeta_j^{-1}/2 \tag{27}$$

The inverses of equation (27) were found to be:

$$\zeta_j = \{z_j - \sqrt{z_j^2 - (a^2 + s_j^2b^2)}\}/(a - is_jb) \tag{28}$$

The branch of the square root is chosen so that $|\zeta_j| \geq 1$. Equations (27) and (28) agree with Savin's results [7].

The author analyzed a uniaxially loaded, orthotropic sheet (40 × 40 cm) with an elliptical void. Symmetry was enforced in the hybrid element by taking only real and odd values of a_j in the summations. Structural models were developed using a

Table 2 Elliptical void; $a = 0.25$ cm, $b = 0.125$ cm; linear elements; 7 GP/side; yellow-poplar elastic properties

m	n	σ_Q/T	σ_P/T
−3	3	3.196	−0.3030
−3	5	3.194	−.3028
−5	3	3.194	−.3028
−5	5	3.194	−.3029
−7	7	3.192	−.3024
−9	9	3.190	−.3023
−11	11	3.191	−.3022
−21	21	3.190	−.3021

Table 3 Elliptical void; $a = 0.05147$ cm, $b = 0.25$ cm; 7 GP/side; near isotropic elastic properties

$\{\tilde{u}\}$	m	n	CPU (sec)	σ_Q/T
Linear	−3	3	0.09	10.710
Quadratic	−7	7	.18	10.716
Cubic	−11	11	.28	10.716
Elasticity [7]				10.714

Table 4 Circular void; $r = 2$ cm; Cubic $\{\tilde{u}\}$l yellow-poplar elastic properties

Element	m	n	Gauss points per side	σ_Q/T	σ_P/T
Elliptical	−11	11	8	5.7836	−0.30573
Elliptical	−21	21	8	5.7839	−.31784
Elliptical	−31	31	8	5.7846	−.31897
Fillet	1	12	40	5.775	−.3434

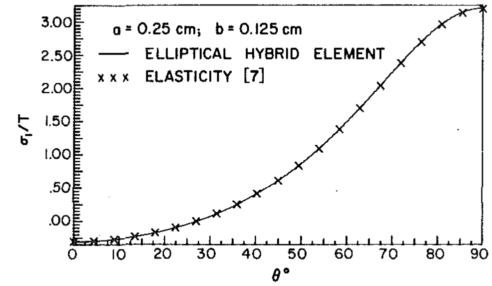

Fig. 3 Principal stress ratio on elliptical void

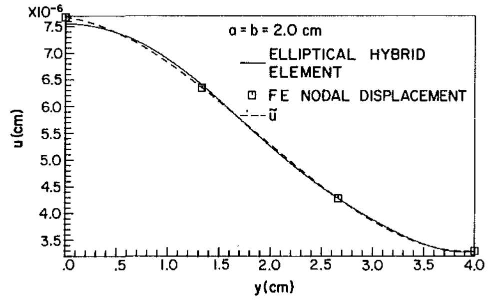

Fig. 4 Displacement u on line segment $x = 4.0$ cm and $0 \leq y \leq 4.0$ cm

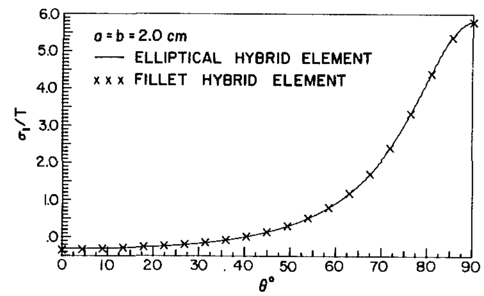

Fig. 5 Principal stress ratio on circular void.

hybrid element together with only eight displacement elements. Results using the linear, quadratic, and cubic isoparametric quadrilateral elements [51] follow. The model with linear elements is shown in Fig. 2.

$a = 0.25$ cm and $b = 0.125$ cm. A 40- × 40-cm sheet with a void $a = 0.25$ cm and $b = 0.125$ cm approximates an elliptical void in an infinite sheet. A closed form elasticity solution exists for the idealized problem [7]. In Table 1, numeric and analytic stresses are compared at points P ($\theta = 0$ deg) and Q ($\theta = 90$ deg) (see Fig. 2). Stress concentration factors calculated by the hybrid element differ from the elasticity results by less than 0.02, 0.007, and 0.03 percent for the three different $\{\tilde{u}\}$. Examples using smaller voids showed even closer agreement, indicating a small finite sheet effect. Remarkably, these results were obtained using close to the minimum number of terms required in the Laurent expansions (see Table 1). The author found hybrid stresses converged to five decimal places when seven Gauss points (GP) per side were used to integrate equation (23). Thus, integration ease combined with the small number of expansion terms provided efficient as well as accurate solutions. The efficiency is evidenced by the computer times (CPU) required to compute $[k]$ indicated in Table 1.

Analytic and numeric stresses computed on Γ are compared in Fig. 3. The hybrid element results use linear elements (Fig. 2) with $m = -3$ and $n = 3$. The agreement is excellent, especially since the Laurent expansion contained only four terms. For all points on Γ, the unequality $|\sigma_2|/T < 10^{-16}$ was satisfied indicating free-surface stress conditions were achieved.

Stresses computed for various values of m and n with a linear $\{\tilde{u}\}$ are compared in Table 2. The stability shown indicates again that accurate solutions can be obtained using few terms. From other numerical tests, the author found this type of stability was attained as long as the order of $\{\tilde{u}\}$ approximated the actual displacements on ∂A adequately.

$a = 0.05147$ cm and $b = 0.25$ cm. Schnack and Wolf [45] modeled a narrow elliptical cutout in a large, uniaxially-loaded, isotropic sheet. The authors chose a rather severe elliptical geometry, i.e., the ratio of major elliptical axis to minimum radius of curvature was taken as 23.592. This problem was used to compare various numerical techniques: integral equation method, conventional FE method, a combined integral equation and FE method, and the method previously discussed using triangular notch elements.

I modeled this problem with the mesh of Fig. 2 taking $a = 0.05147$ cm and $b = 0.25$ cm. Since the formulation presented in this paper is anisotropic, near isotropic properties ($E_x = 1.0$ kPa, $E_y = 1.00001\,E_x$, $G_{xy} = 0.40\,E_x$, and $\nu_{xy} = 0.25$) were used for this example. Results are presented in Table 3. The small radius of curvature at point Q (0.0106 cm) causes a large stress gradient, i.e., a SCF of 10.71. The results from the elliptical hybrid element differ from the elasticity result [7] by only 0.05, 0.02, and 0.02 percent for the three different $\{\tilde{u}\}$. The small radius of curvature at point Q caused no difficulty in stress calculations.

In the numerical comparison, Schnack and Wolf [45] reported the triangular notch elements yielded the most accurate and efficient solution. The computed SCF was 10.7, identical to results in Table 3 to three decimal places. The authors noted that this calculation took less than 60 sec CPU (LRZ München, TR440). Computing times for other numerical techniques ranged from 60–2400 sec with less accuracy for the most part. It is difficult to compare CPU times on different computers. The CPU times reported in reference [45], however, are two to four orders of magnitude greater than those in Table 3.

$a = b = 2.0$ cm. In this example, the void dimensions ($a = b = 2.0$ cm) were chosen to be the same order as the dimensions of the hybrid element. Yellow-poplar elastic properties were used. Computed stresses cannot be compared to Savin's solution [7] due to the finite domain. However, results will be compared to a circular fillet solution in the next section. A structural model was constructed using eight 12-node cubic elements (dimensions of Fig. 2) together with the hybrid element. Stress results for various values of m and n are shown in Table 4. Integration with eight GP/side provided convergence to five decimal places. Excellent stability in stress computation is evident, especially for the SCF. This degree of stability was not attained with either the linear or quadratic elements. The reason is apparent when $\{u\}$ and $\{\tilde{u}\}$ are compared on ∂A. For example, in Fig. 4, u and $\tilde{u}$ are compared on the segment $x = 4$ cm and $0 \le y \le 4$ cm. It is clear that neither the linear nor quadratic $\tilde{u}$ could adequately approximate u. In practice, however, the segment can easily be broken into two or more segments with satisfactory results (using more than eight FE's).

Circular Fillet Mapping Function. The following conformal mapping function maps the real axis in the ζ plane onto a circular fillet in the z plane [35]:

$$z = \omega(\zeta) = i\rho e^{-i\zeta} \tag{29}$$

where the constant ρ is the fillet radius. Substitution into equation (5) yields:

$$z_j = i\rho\{(1 - is_j)e^{-i\zeta_j} - (1 + is_j)e^{i\zeta_j}\}/2 \tag{30}$$

To the author's knowledge, these transformations have not appeared in the literature. The inverses of equation (30) are defined by:

$$e^{-i\zeta_j} = \{z_j - \sqrt{z_j^2 - \rho^2(1 + s_j^2)}\}/\{i\rho(1 - is_j)\} \tag{31}$$

The branch of the square root is chosen so that

$$Im\ \zeta_j \ge 0, \quad \text{i.e.,} \quad |e^{-i\zeta_j}| \ge 1$$

The numerical example chosen for the fillet coincides with the previous example, i.e., $\rho = 2.0$ cm and the FE mesh of Fig. 2. For the fillet model, $\{\tilde{u}\}$ must be defined and equation (23) integrated on four sides rather than two (see Fig. 1(*b*)). Cubic fields for $\{\tilde{u}\}$ were assumed on the four sides. Lower order polynomials could be used, but a new mesh with more displacement FE's would be required as mentioned previously. Symmetry in the fillet element was imposed by setting the appropriate FE nodes equal to zero. Since 13 nodes were used in ∂A, 23 terms were required in the Taylor expansion. For the following results, 24 terms were used ($m = 1$, $n = 12$).

Stresses at points P and Q computed by the two hybrid elements are compared in Table 4. Stresses along Γ are compared in Fig. 5. The agreement is remarkable, especially since the approximation on ∂A extends to Γ for the fillet. This fact necessitates greater computational effort to integrate equations (23) compared to the elliptical element. Results in Table 4 are for 40 GP/side. Clearly, a selective integration technique would improve efficiency.

For both the elliptical and fillet hybrid elements, the author found similar accuracy using three different sets of orthotropic properties. Also, structural models were constructed for stepped, flat tension bars with shoulder fillets.[2] Computed SCF (using near isotropic properties) were compared with published photoelasticity data (Fig. 65 in reference [1]) to examine the accuracy of the fillet element as the fillet radius was varied. Models were constructed with nine different ratios of fillet radius to minimum bar width ranging from 0.08125 to 0.25. Computed results differed from experimental results by 0.3 percent-4.5 percent.[2] Mean difference was only 2.2 percent.

Summary and Conclusions

A hybrid/FE method was presented to calculate stresses or stress intensity factors associated with geometric discontinuities in plane-loaded anisotropic materials. A hybrid element was formulated in terms of an arbitrary conformal mapping function. Thus, the element can structurally model members containing notches, fillets, or cutouts of diverse shapes.

Analysis of a small elliptical void in an orthotropic sheet indicated that accurate and efficient results were obtained with the hybrid element. Using only a few terms in the series expansions, excellent agreement was obtained with an elasticity solution. Moreover, computed stresses were insensitive to varying the number of terms chosen.

A narrow elliptical cutout in a large isotropic sheet was modeled using near isotropic material properties. Results from the hybrid element agreed well with both an elasticity solution and other numerical techniques compared in reference [45]. The small radius of curvature at the critical stress location caused no difficulty in stress calculations.

Structural models of an orthotropic sheet with a circular hole were developed with elliptical void and circular fillet hybrid elements. Computed stresses showed good agreement. Computed stresses were insensitive to the number of expansion terms chosen as long as the polynomial field on the element boundary was properly chosen. Results from both mapping functions indicated that accurate critical stresses can be obtained using a hybrid element with a coarse displacement element mesh. Using the proposed method, problems involving interaction of two or more holes or other discontinuities can be efficiently solved.

Acknowledgment

Research presented in this paper was motivated by a cooperative research program involving the National Wooden Pallet and Container Association (NWPCA), Virginia Polytechnic Institute and State University (VPI&SU), and the USDA Forest Service aimed at establishing design procedures for wood pallets. The method presented in this paper was used to compute deflections and SCF for wood beams containing rectangular, filleted edge notches.[2]

References

1 Peterson, R. E., *Stress Concentration Factors*, Wiley, New York, 1974.

2 Rowlands, R. E., Daniel, I. M., and Whiteside, J. B., "Geometric and Loading Effects on Strength of Composite Plates With Cutouts," *Composite Materials: Testing and Design* (Third Conf.), ASTM STP 546, American Society for Testing and Materials, 1974, pp. 361–375.

3 Daniel, I. M., "Biaxial Testing of $[0_2/\pm 45]_S$ Graphite/Epoxy Plates With Holes," *Exp. Mec*, Vol. 22, No. 5: May 1982, pp. 188–195.

4 Hanus, J. B., and Burger, C. P., "Stress Concentration Factors for Elliptical Holes Near An Edge," *Exp. Mech.*, Vol. 21, No. 9, Sept. 1981, pp. 336–340.

5 Wilson, I. H., and White, D. J., "Stress-Concentration Factors for Shoulder Fillets and Grooves in Plates," *J. Strain Anal.*, Vol. 8, No. 1, 1973, pp. 43–51.

6 Erickson, M., and Durelli, A. J., "Stress Distribution Around a Circular Hole in Square Plates, Loaded Uniformly in the Plane, on Two Opposite Sides of the Square," ASME Journal of Applied Mechanics, Vol. 48, 1981, pp. 203–204.

[2] Gerhardt, T. D., "Strength and Stiffness Analysis of Notched Oak Pallet Stringers, U.S. Department of Agriculture, Forest Service, Forest Products Laboratory, Madison, Wis., in preparation.

7 Savin, G. N., *Stress Concentration Around Holes*. Pergamon Press, New York, 1961.
8 Muskhelishvili, N. I., *Some Basic Problems of the Mathematical Theory of Elasticity*, 4th Ed., P. Noordhoff Ltd., Groningen, Netherlands, 1963.
9 Kosmodamianskii, A. S., "Flexure of Anisotropic Plates With Curvilinear Holes (Survey)," *Soviet Appl. Mech.*, Vol. 17 no. 2: Feb. 1981, pp. 103-109.
10 Theocaris, P. S., and Bardzokas, D., "Stresses and Displacements on the Boundary of a Hole in the Infinite Plate," *Acta Mechanica*, Vol. 39, 1981, pp. 183-194.
11 Krenk, S., "Stress Concentration Around Holes in Anisotropic Sheets," "*Appl. Math. Modelling*, Vol. 3, Apr. 1979, pp. 137-142.
12 Hoff, N. J., "Stress Concentrations in Cylindrically Orthotropic Composite Plates With a Circular Hole," ASME Journal of Applied Mechanics, Vol. 48, 1981, pp. 563-569.
13 Keer, L. M., and Chantaramungkorn, K., "An Elastic Half Plane Weakened by a Rectangular Trench," ASME Journal of Applied Mechanics, Vol. 42, 1975, pp. 683-687.
14 Theocaris, P. S., and Ioakimidis, N. I., "The *V*-Notched Elastic Half-Plane Problem," *Acta Mechanica*, Vol. 32, 1979, pp. 125-140.
15 Dhir, S. K., "Optimization in a Class of Hole Shapes in Plate Structures," ASME Journal of Applied Mechanics, Vol. 48, 1981, pp. 905-908.
16 Nikooyeh, H., and Robinson, A. R., "Approximate Determination of Stresses and Displacements Near a Rounded Notch," *Int. J. Solids and Struct.*, Vol. 17, No. 7, 1981, pp. 669-682.
17 Mukherjee, S., and Morjaria, M. "A Boundary Element Formulation for Planar Time-Dependent Inelastic Deformation of Plates With Cutouts," *Int. J. Solids and Struct.*, Vol. 17, No. 1, 1981, pp. 115-126.
18 Carroll, W. E., "Stress Analysis Using the Boundary Integral Analysis Technique," *Proc. 3rd Int. Conf. on Vehicle Structural Mechanics*, Detroit, Mich. Oct. 1979, pp. 3270-3274. Also, SAE Trans, Vol. 18, 1980.
19 Kishida, M., and Hanzawa, H., "On Interference Of Circular Notches and Loaded Ends (First Report, Plane Stress Problems)," *Bull. JSME*, Vol. 22, No. 173, Nov. 1979, pp. 1525-1531.
20 Williams, M. L., "Stress Singularities Resulting From Various Boundary, Conditions in Angular Corners of Plates in Extension," ASME Journal of Applied Mechanics, Vol. 19, 1952, pp. 526-528.
21 Ogonowski, J. M., "Analytical Study of Finite Geometry Plates With Stress Concentrations." McDonnell Aircraft Co. Report MCAIR 80-006, St. Louis, Mo. Presented at the 21st Structures, Structural Dynamics, and Materials Conf., Seattle, Wash., May 12-14, 1980.
22 De Jong, T., "Stresses Around Rectangular Holes in Orthotropic Plates," *J. Comp. Mater.*, Vol. 15, July 1981, pp. 311-328.
23 Kuliev, V. D., "The Singular Problem of the Theory of Elasticity for a Semi-Infinite Rectangular Cutout," *J. of Appl. Math. Mech.*, Vol. 44, No. 5, 1980, pp. 677-680.
24 Hong, C. S., and Crews, J. H., "Stress-Concentration Factors for Finite Orthotropic Laminates With a Circular Hole and Uniaxial Loading," NASA Tech. Pap. 1469. Langley Research Center, Hampton, Va., 1979.
25 Herakovich, C. T., and Bergner, H. W., "Finite Element Stress Analysis of a Notched Coupon Specimen for In-Plane Shear Behavior of Composites," *Composites*, Vol. 11, No. 3, July 1980, pp. 149-154.
26 Chen, P. C. T., and Cheng, Y. F., "Stress Analysis of an Overloaded Breech Ring," In: *Reliability, Stress Analysis, and Failure Prevention Methods in Mechanical Design*, Milestone, W. D., ed., American Society of Mechanical Engineers, New York, 1980, pp. 175-180.
27 Arai, N., Oeda, M., and Aida, T., "Study on the Stress at the Root Fillet and Safety for Slipping of Force-Fitted Helical Gears," *Bull. JSME*, Vol. 24, No. 198, Dec. 1981, pp. 2203-2209.
28 Barlow, J., "Optimal Stress Locations in Finite Element Models," *Int. J. Numer. Meth. Eng.*, Vol. 10, No. 2, 1976, pp. 243-251.
29 Allison, I. M., and Soh, A. K., "On the Determination of Boundary Stresses by the Finite Element Method," *Strain*, Vol. 17, No. 2, May 1981, pp. 55-59.
30 Cook, R. D., "Loubignac's Iterative Method in Finite Element Elastostatics," *Int. J. Numer. Meth. Eng.*, Vol. 18, No. 1, Jan. 1982, pp. 67-72.
31 Cook, R. D., and Zhao-Hua, F., "Control of Spurious Modes in the Nine-Node Quadrilateral Element," *Int. J. Numer Meth. Eng.*, Vol. 18, No. 10, Oct. 1982, pp. 1576-1580.
32 McNeill, N. J., and Hansen, J. S., "An Accuracy Study for a Class of Rectangular Isoparametric Finite Elements," *Computer Meth. in Appl. Mech. Eng.*, Vol. 25, No. 3, March 1981, pp. 335-341.
33 Parks, D. M., "Energy Variations in Notch Stress Analysis," ASME Journal of Applied Mechanics, Vol. 46, 1979, pp. 952-954.
34 Ranaweera, M. P., and Leckie, F. A., "*J* Integrals for Some Crack and Notch Geometries," *Int. J. Fracture*, Vol. 18, No. 1, Jan. 1982, pp. 3-18.
35 Freese, C. E., and Bowie, O. L., "Stress Analysis of Configurations Involving Small Fillets," *J. Strain Anal.*, Vol. 10, No. 1, 1975, pp. 53-58.
36 Freese, C. E., "Collocation and Finite Elements—a Combined Method," AMMRC TR 73-28, Army Mater. Mech. Res. Center, Watertown, Mass., June 1973, 12 p.
37 Milne-Thomson, L. M., *Plane Elastic Systems*, Springer-Verlag, Berlin, 1960.
38 Ling, Chih-Bing, "Conformal Transformations of Three Types of Edge Notches," *Quarterly Apply. Math.*, Vol. 37, No. 3, October 1979, pp. 303-311.
39 Bowie, O. L., Freese, C. E., "Central Crack in Plane Orthotropic Rectangular Sheet," *Int. J. Fract. Mech.*, Vol. 8, No. 1, Mar. 1972, pp. 49-57.
40 Tong, P., Pian, T. H. H., and Lasry, S. J., "A Hybrid-Element Approach to Crack Problems in Plane Elasticity," *Int. J. Numer. Meth. Eng.*, Vol. 7, No. 3, 1973, pp. 297-308.
41 Tong, P., "A Hybrid Crack Element for Rectilinear Anisotropic Material," *Int. J. Numer. Meth. Eng.*, Vol. 11, No. 2: 1977, pp. 377-382.
42 Pian, T. H. H., and Chen, Da-Peng, "Alternative Ways for Formulation of Hybrid Stress Elements," *Int. J. Numer. Meth. Eng.*, Vol. 18, No. 11: Nov. 1982, pp. 1679-1684.
43 Drumm, R., "An FEM (Finite Elements Method) Algorithm for Calculation of Stress Concentration." *Zeitschrift F•ur Angewandte Mathematik und Mechanik*, Vol. 61, No. 4: Apr. 1981, pp. T84-T86.
44 Lin, K. Y., and Tong, P., "Singular Finite Elements for the Fracture Analysis of *V*-Notched Plate," *Int. J. Numer. Meth. Eng.*, Vol. 15, 1980, pp. 1343-1354.
45 Schnack, E., and Wolf, M., "Application of Displacement and Hybrid Stress Methods to Plane Notch and Crack Problems," *Int. J. Numer. Meth. Eng.*, Vol. 12, 1978, pp. 963-975.
46 Schnack, E., "An Optimization Procedure for Stress Concentrations by the Finite Element Technique," *Int. J. Numer. Meth. Eng.*, Vol. 14, 1979, pp. 115-124.
47 Rao, A. K., Raju, I. S., and Krishna Murty, A. V., "A Powerful Hybrid Method in Finite Element Analysis," *Int. J. Numer. Meth. Eng.*, Vol. 3, 1971, pp. 389-403.
48 Taylor, R. L., "Computer Procedures for Finite Element Analysis," In: Zienkiewicz, O. C., *The Finite Element Method*, 3rd Ed., McGraw-Hill, London, 1977, Chapter 24, pp. 677-757.
49 Gerhardt, T. D., "Plane Stress Analysis of Wood Members Using Isoparametric Finite Elements: a Computer Program," Gen. Tech. Rep. FPL 35, U.S. Department of Agriculture, Forest Service, Forest Products Laboratory, Madison, Wis., Mar. 1983, p. 15.
50 Forest Products Laboratory, Forest Service, *Wood Handbook: Wood as an Engineering Material*. Agric. Handb. 72. U.S. Department of Agriculture Rev., ed. Aug. 1974.
51 Zienkiewicz, O. C., *The Finite Element Method*, 3rd ed., McGraw-Hill, London, 1977.

APPENDIX

Constants in equation (4):

$$p_k \equiv D_{11}s_k^2 - D_{13}s_k + D_{12} \quad (k=1,2)$$

$$q_k \equiv (D_{12}s_k^2 - D_{23}s_k + D_{22})/s_k \quad (k=1,2)$$

Constants in equation (6):

$$B \equiv (\bar{s}_2 - \bar{s}_1)/(s_2 - \bar{s}_2)$$

$$C \equiv (\bar{s}_2 - s_1)/(s_2 - \bar{s}_2)$$

Indentation of a Penny-Shaped Crack by an Oblate Spheroidal Rigid Inclusion in a Transversely Isotropic Medium

Y. M. Tsai
Professor,
Department of Engineering
Science and Mechanics,
and Engineering Research Institute,
Iowa State University,
Ames, Iowa 50011

The stress distribution produced by the identation of a penny-shaped crack by an oblate smooth spheroidal rigid inclusion in a transversely isotropic medium is investigated using the method of Hankel transforms. This three-part mixed boundary value problem is solved using the techniques of triple integral equations. The normal contact stress between the crack surface and the indenter is written as the product of the associated half-space contact stress and a nondimensional crack-effect correction function. An exact expression for the stress-intensity is obtained as the product of a dimensional quantity and a nondimensional function. The curves for these nondimensional functions are presented and used to determine the values of the normalized stress-intensity factor and the normalized maximum contact stress. The stress-intensity factor is shown to be dependent on the material constants and increasing with increasing indentation. The stress-intensity factor also increases if the radius of curvature of the indenter surface increases.

Introduction

Stress distributions for a penny-shaped crack in hexagonal aeolotropic crystals have been investigated in terms of two harmonic functions [1]. The approach of potential functions was used to solve the problem of spherical inclusions in a transversely isotropic material under pure shear [2]. The entire surface of the inclusion was in contact with the surrounding matrix material. Numerical results were given for a number of hexagonal crystals that were characterized as being transversely isotropic [2]. Many fiber-reinforced composite materials and platelet systems were also characterized as transversely isotropic media, which have five elastic constants [3].

The present work studies the indentation of a penny-shaped crack by a thin oblate spheroidal rigid inclusion in a transversely isotropic medium (Fig. 1). Only the inner part of the crack surface is subjected to the indentation of the inclusion, while the outer crack surface is free from stresses. The method of Hankel transforms is used to satisfy the equilibrium equations and the boundary conditions, which have three different parts. The solutions are obtained using the techniques of triple integral equations [4]. The normal contact stress between the indenter and the crack surface, as well as the stress-intensity factor, are obtained as the products of dimensional quantities and nondimensional functions. The values of the nondimensional functions are calculated and used to determine the values of the normalized stress-intensity factor and the maximum normal contact stress for various values of nondimensional parameters.

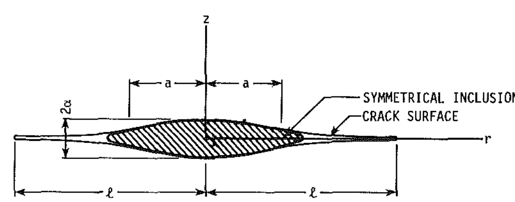

Fig. 1 Coordinates and configuration

Formal Solution

A penny-shaped crack with radius l is located inside a transversely isotropic medium. The surfaces of the crack are normal to the axis of symmetry of the material. The traction-free surfaces of the crack are indented by a smooth oblate spheroidal rigid inclusion (Fig. 1). The inner central portion of the crack surfaces is in contact with the inclusion body while the outer portion maintains the stress-free conditions. The problem has symmetrical properties with respect to the plane containing the penny-shaped crack. In cylindrical coordinates (r, θ, z) with z normal to the crack surfaces, the displacement has only two components u_r and u_z, and the mixed boundary conditions at $z=0$ can be written as:

Contributed by the Applied Mechanics Division and presented at the Winter Annual Meeting, New Orleans, La., December 9–14, 1984 of THE AMERICAN SOCIETY OF MECHANICAL ENGINEERS.

Discussion on this paper should be addressed to the Editorial Department, ASME, United Engineering Center, 345 East 47th Street, New York, N.Y. 10017, and will be accepted until two months after final publication of the paper itself in the JOURNAL OF APPLIED MECHANICS. Manuscript received by ASME Applied Mechanics Division, September, 1983. Paper No. 84-WA/APM-27.

Copies wil be available until August, 1985.

$$\sigma_{rz}=0, \quad r\geq 0 \tag{1}$$

$$u_z=\begin{cases} w(r), & 0\leq r\leq l \\ 0, & r>l \end{cases} \tag{2}$$

$$\sigma_{zz}=0, \quad a\leq r<l \tag{3}$$

The crack-shape function $w(r)$ in equation (2) is identical to the shape of the rigid indenter inside the contact area with radius equal to a, but is unknown outside the contact area. The unknown portion of the crack-shape function and the unknown contact radius a are to be determined later using the condition of vanishing normal stress in equation (3) and the finiteness of the contact stresses between the indenter and the crack surfaces.

The stress-strain relationships for a transversely isotropic medium can be written in cylindrical coordinates as follows [1, 5]:

$$\begin{aligned} \sigma_{rr} &= c_{11}e_{rr}+c_{12}e_{\theta\theta}+c_{13}e_{zz} \\ \sigma_{\theta\theta} &= c_{12}e_{rr}+c_{11}e_{\theta\theta}+c_{13}e_{zz} \\ \sigma_{zz} &= c_{13}e_{rr}+c_{13}e_{\theta\theta}+c_{33}e_{zz} \\ \sigma_{rz} &= c_{44}e_{rz}, \quad \sigma_{\theta z}=c_{44}e_{\theta z} \\ \sigma_{r\theta} &= 1/2(c_{11}-c_{12})e_{r\theta} \end{aligned} \tag{4}$$

The foregoing strains e_{ij} can be first written in terms of the displacements [1, 5] and then substituted into the preceding equations to obtain the stress-displacement relationships. The relationships are finally used in the equilibrium equations [1, 5] to form a system of partial differential equations for the displacements. The Hankel transforms are applied on the variable r of the partial differential equations, and the transformed equations in terms of the parameters are obtained as follows:

$$c_{44}\frac{\partial^2\hat{u}_r^1}{\partial z^2}-c_{11}s^2\hat{u}_r^1-(c_{13}+c_{44})s\frac{\partial\hat{u}_z^0}{\partial z}=0 \tag{5}$$

$$c_{33}\frac{\partial^2\hat{u}_z^0}{\partial z^2}-c_{44}s^2\hat{u}_z^0+(c_{13}+c_{44})s\frac{\partial\hat{u}_r^1}{\partial z}=0 \tag{6}$$

where $\hat{u}_r^1$ is the first-order Hankel transform of u_r, and $\hat{u}_z^0$ is the zeroth-order Hankel transform of u_z. To solve the foregoing two equations, the transformed displacements are chosen in the following forms:

$$\hat{u}_r^1=Ae^{-\lambda sz} \quad \text{and} \quad \hat{u}_z^0=Be^{-\lambda sz} \tag{7}$$

Equations (5) and (6) are satisfied if the parameter satisfies the following characteristic equation:

$$(c_{44}\lambda^2-c_{11})(c_{33}\lambda^2-c_{44})+(c_{13}+c_{44})^2\lambda^2=0 \tag{8}$$

The equation is a quadratic equation for λ^2 and has two roots λ_1^2 and λ_2^2. The roots are either both real or a pair of complex conjugates, depending on the values of the material constants. Both types of root give physically meaningful results [1]. For the first root λ_1, the constants in equation (7) are denoted as A_1 and B_1. Similarly, A_2 and B_2 are for the second root λ_2. For λ_1, equation (6) gives the following relationship:

$$\lambda_1A_1=(c_{33}\lambda_1^2-c_{44})B_1/(c_{13}+c_{44}) \tag{9}$$

Similar relationships hold for A_2, B_2, and λ_2.

To satisfy the stress boundary conditions in equations (1) and (3), the transformed forms of the stresses can be written from equation (1) as follows:

$$\hat{\sigma}_{rz}^1 = c_{44}(\partial\hat{u}_r^1/\partial z-s\hat{u}_z^0) \tag{10}$$

$$\hat{\sigma}_{zz}^0 = c_{13}(s\hat{u}_r^1)+c_{33}\partial\hat{u}_z^0/\partial z \tag{11}$$

In terms of the transformed displacements in equation (7), the relationship in equation (9) and its counterpart equation for λ_2, the stress boundary condition in equation (1) gives the following relationship:

$$B_1=-(c_{33}\lambda_2^2+c_{13})B_2/(c_{33}\lambda_1^2+c_{13}) \tag{12}$$

In terms of equations (7) and (12), the displacement boundary in equation (2) gives

$$B_2 = (c_{33}\lambda_1^2+c_{13})\hat{w}^0/(\lambda_1^2-\lambda_2^2)c_{33} \tag{13}$$

$$\hat{w}^0 = \int_0^l w(\lambda)\lambda J_0(\lambda s)d\lambda \tag{14}$$

If equations (7), (9), and (12)-(14) are substituted into equation (11), the transformed normal stress is obtained at $z=0$ as

$$\hat{\sigma}_{zz}^0=-Ks\hat{w}^0 \tag{15}$$

$$K=\frac{c_{44}(c_{13}+\lambda_1^2c_{33})(c_{13}+\lambda_2^2c_{33})}{c_{33}(c_{13}+c_{44})(\lambda_1+\lambda_2)\lambda_1\lambda_2} \tag{16}$$

The constant K is a real-valued function of the elastic constants and the characteristics roots. For an isotropic material, K reduces to $\mu/(1-\nu)$, where μ is the shear modulus and ν is Poisson's ratio.

Contact Stress

The indentation of the crack surfaces by the inclusion body produces normal contact stress inside the contact area between the indenter and the crack surfaces. To solve for the contact stress, a function of the transformed parameter s is introduced as follows:

$$\chi(s)=K\hat{w}^0s^2 \tag{17}$$

The transformed normal stress in equation (15) can be written in terms of χ, and the Hankel inversion of the resulting equation gives the expressions for the normal stress at $z=0$ as follows:

$$\sigma_{zz}=-\int_0^\infty\chi(s)J_0(sr)ds=\begin{cases}\sigma_1(r) & 0\leq r\leq a \\ 0, & a<r\leq l \\ \sigma_2(r), & l<r<\infty\end{cases} \tag{18}$$

The normal contact stress in the contact area is defined in the foregoing as $\sigma_1(r)$. The normal stress outside the crack surface is described as $\sigma_2(r)$. The three-part stress condition on the right-hand side of equation (18) leads to triple integral equations that are solved for the unknown functions $\sigma_1(r)$ and $\sigma_2(r)$, using the techniques similar to those presented in reference [4]. The Hankel inversion of equation (18) gives the following expression:

$$\chi(s)=-s\Big[\int_0^a\sigma_1(\lambda)\lambda J_0(\lambda s)+\int_l^\infty\sigma_2(\lambda)\lambda J_0(\lambda s)ds\Big] \tag{19}$$

To establish a system of integral equations for σ_1 and σ_2, the shape of the axisymmetrical indenter inside the contact area is described as $g(r)$. The normal displacements in equation (2) are calculated in terms of equations (7), (17), and (19). The portions of the displacement that have known values at this stage of calculations are written as

$$\int_0^a\sigma_1\lambda L(r,\lambda)d\lambda+\int_l^\infty\sigma_2\lambda L(r,\lambda)d\lambda=-g(r)K, \quad 0\leq r\leq a \tag{20}$$

$$\int_0^a\sigma_1\lambda L(r,\lambda)d\lambda+\int_l^\infty\sigma_2\lambda L(r,\lambda)d\lambda=0, \quad l<r<\infty \tag{21}$$

The function $L(r,\lambda)$ is defined in the Appendix. If equation (A-2) for $L(r,\lambda)$ in the Appendix is substituted into the first integral on the left-hand side of equation (20), the integral is integrated once by changing the order of integrations into the following form:

$$\int_0^r(r^2-x^2)^{-1/2}N(x)dx=-\pi/2\Big[Kg(r)+\int_l^\infty\sigma_2\lambda Ld\lambda\Big] \tag{22}$$

$$N(x)=\int_x^a(\lambda^2-x^2)^{-1/2}\lambda\sigma_1 d\lambda \tag{23}$$

If equation (22) is recognized as the Abel transform of $N(x)$, the inverse Abel transfrom of equation (22) [4] is integrated using equation (A-2) into the following expression:

$$N(x)=-K\frac{\partial}{\partial x}\int_0^x(x^2-t^2)^{-1/2}tgdt-\int_l^\infty\sigma_2\lambda(\lambda^2-x^2)^{-1/2}d\lambda \tag{24}$$

Equation (23) is now recognized as the Abel transform of $\lambda\sigma_1$. The inverse Abel transform is calculated in terms of equation (24). In the process of calculations, the first term on the right-hand side of equation (24) is first integrated by parts and then differentiated with respect to x. Furthermore, the identity in equation (A-4) [4] is used in the calculations of the second term on the right-hand side of equation (24). The results of the inversion calculations give the expression for the contact stress as follows:

$$\sigma_1(r)=\sigma_H-(a^2-r^2)^{-1/2}\pi K/2\Big\{g(0)+a\int_0^a(a^2-t^2)^{-1/2}g'dt$$

$$+1/K\int_l^\infty\sigma_2\eta(\eta^2-a^2)^{1/2}(\eta^2-r^2)^{-1}d\eta\Big\} \tag{25}$$

$$\sigma_H=\pi K/2\int_r^a(x^2-r^2)^{-1/2}dx\frac{\partial}{\partial x}\int_0^x xg'(x^2-t^2)^{-1/2}dt \tag{26}$$

The last term in equation (25) vanishes if the radius of the crack l approaches infinity. Under this condition, equation (26) can be split into an equation for determining the contact stress plus an auxiliary equation for the contact problem of an elastic half space [6]. The last term in the foregoing equation represents the effects of the crack on the distribution of the contact stress σ_1. The effects are incorporated in the next section in the form of an integral equation.

Stress-Intensity Factor

The normal stress outside the crack surface σ_2 is determined by bringing it out from the integral in equation (21). If the operations defined in equation (A-5) are operated over the variable r in equation (21), the equation can then be integrated over sine functions [7]. After the calculations, equation (21) becomes

$$\int_l^r\sigma_2\lambda(r^2-\lambda^2)^{-1/2}d\lambda=-\int_0^a\sigma_1\lambda(r^2-\lambda^2)^{-1/2}d\lambda \tag{27}$$

If equation (27) is recognized as the Abel transform of $\sigma_2\lambda$, the inverse Abel transform of equation (27) yields

$$\sigma_2(r)=-(r^2-l^2)^{-1/2}2/\pi\int_0^a\sigma_1 t(l^2-t^2)^{1/2}(r^2-t^2)^{-1}dt \tag{28}$$

The identity defined in equation (A-6) is used in obtaining the foregoing result. The stress σ_2 has square-root singularity at the crack tip $r=l$. If σ_2 in equation (28) is substituted into equation (25), the resulting equation may become an integral equation for determining the contact stress σ_1. However, there is an apparent singularity at $r=a$. This phenomenon is similar to that occurring in a half-space contact problem [6]. From a physical consideration, the contact stress should be finite for a smooth indenter whose contact surface does not have any abrupt change in slope [6]. If the value of r is set equal to a in equation (25), the requirement for the vanishing of the singular term yields the following auxiliary equation [6]:

$$g(0)+\int_0^a\frac{ag'(t)dt}{\sqrt{a^2-t^2}}=\frac{2}{\pi}\frac{1}{K}\int_l^\infty\frac{\eta d\eta}{\sqrt{\eta^2-a^2}\sqrt{\eta^2-l^2}}$$

$$\int_0^a\frac{\sigma_1 t(l^2-t^2)^{1/2}}{\eta^2-t^2}dt \tag{29}$$

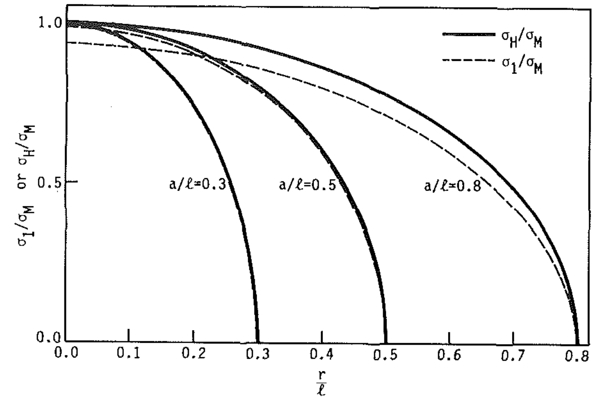

Fig. 2 Normalized normal contact stress

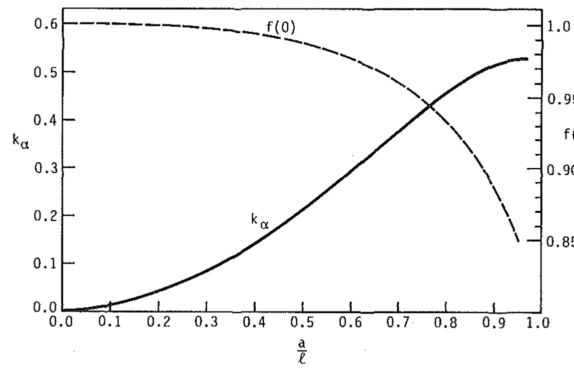

Fig. 3 Nondimensional function $k_\alpha(a/l)$ and the correction factor for the normal contact stress at the contact center $f(0)$

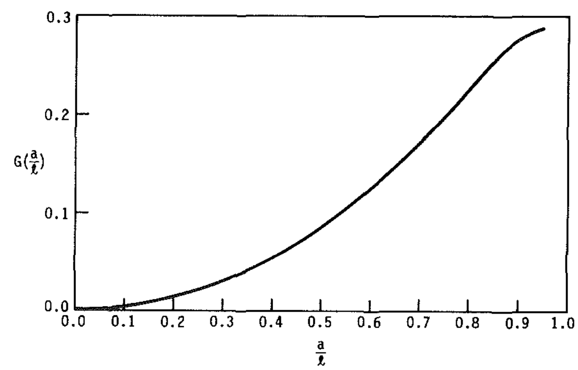

Fig. 4 Nondimensional function for the stress-intensity factor $G(a/l)$

In terms of equations (28) and (29), an integral equation is obtained from equation (25) as follows:

$$\sigma_1=\sigma_H-\frac{2^2}{\pi^2}\sqrt{a^2-r^2}\int_l^\infty\frac{(\eta^2-a^2)^{-1/2}\eta d\eta}{(\eta^2-l^2)^{1/2}(\eta^2-r^2)}$$

$$\int_0^a\frac{\sigma_1 t(l^2-t^2)^{1/2}}{\eta^2-t^2}dt \tag{30}$$

The associated half-space contact stress σ_H is known if the indenter shape $g(r)$ is specified [6]. Equation (30) is a Fredholm integral equation of the second kind, whose solution determines the contact stress σ_1.

If the contact surface of the rigid inclusion is spherical in shape with radius R, the shape of the indentation can be written as it was in reference [6]

$$g(r)=\alpha-r^2/2R \tag{31}$$

The condition required for equation (31) is that the radius of the contact area is small compared to the radius of the contact surface of the indenter. The condition is indeed satisfied in usual stress ranges [8, 9]. This equation also applies for an

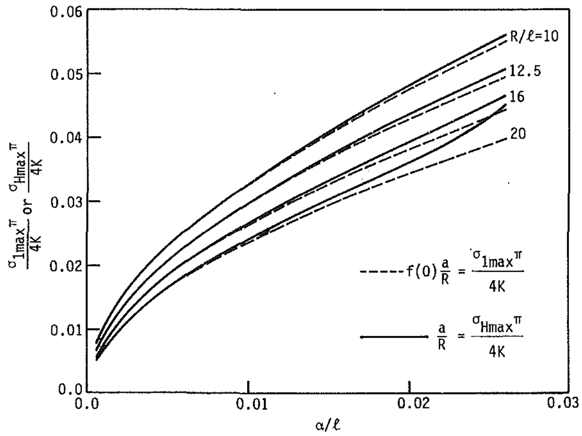

Fig. 5 Normalized minimum half-space contact stress and maximum normal contact stress

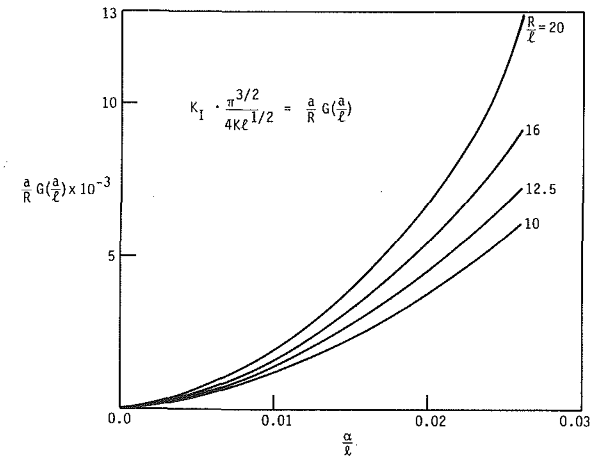

Fig. 6 Normalized stress-intensity factor

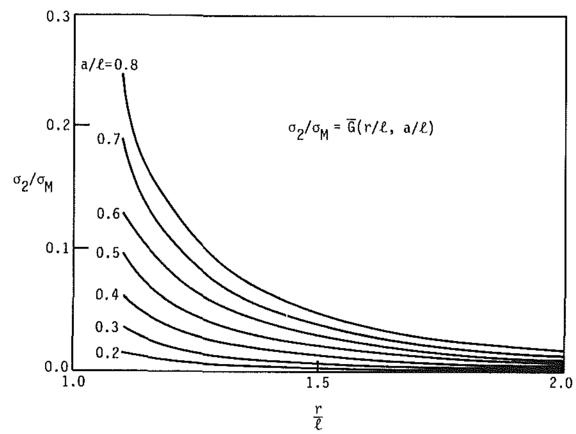

Fig. 7 Normalized normal stress outside the crack tip

oblate spheroid with semiaxes α and β. In this case, the radius of curvature of the spheroid at the center of the contact area is $R=\beta^2/\alpha$, α being the minor semiaxis along the z-axis. If equation (31) is substituted into equation (26), the associated half-space contact stress is found after integrations as

$$\sigma_H = -\sigma_M(1-r^2/a^2)^{1/2}; \quad \sigma_M = 4Ka/\pi R \tag{32}$$

The maximum value of σ_H is equal to σ_M which occurs at $r=0$. If the contact stress is written as $\sigma_1 = \sigma_H f(r)$ and then substituted into equation (30), a factor can be factored out and the resulting equation becomes an integral equation for the nondimensional contact stress correction function $f(r)$, due to the effects of the crack. The use of the transformations, $r=a\rho$, $t=a\lambda$, $\eta^2=(l^2-a^2)\cosh^2\theta+a^2$, further transforms equation (30) into the following nondimensional form:

$$f(a\rho) = 1 - \int_0^1 f(a\lambda)M(\rho,\lambda)d\lambda \tag{33}$$

$$M = \frac{2^2}{\pi^2}\int_0^\infty \frac{\lambda(1-\lambda^2)^{1/2}(l^2/a^2-\lambda^2)^{1/2}d\theta}{[(l^2/a^2-1)\cosh^2\theta+(1-\rho^2)][(l^2/a^2-1)\cosh^2\theta+1-\lambda^2]} \tag{34}$$

The correction function $f(r)$ is solved numerically from the Fredholm integral equation of the second kind in equation (33) by the method of successive approximations as was used in the earlier work [6]. Some typical normalized normal contact stresses are shown in Fig. 2 as a function of the nondimensional ratio a/l. The maximum value of the normal contact stress $\sigma_{1\max}$ occurs at the contact center $r=0$.

If equations (30) and (31) are substituted into equation (29), the maximum indentation α can be calculated, using the transformations similar to those for equation (33). The result is written as

$$\alpha/l = (l/R)k_\alpha(a/l) \tag{35}$$

$$k_\alpha = a^2/l^2\left\{1 - 8/\pi^2\int_0^\infty d\theta\int_0^1 F(\lambda,a/l)\left[(l^2/a^2-1)\cosh^2\theta + 1-\lambda^2\right]^{-1} d\lambda\right\} \tag{36}$$

$$F = (1-\lambda^2)^{1/2} f(a\lambda)\lambda(l^2/a^2-\lambda^2)^{1/2} \tag{37}$$

The nondimensional function k_α is calculated numerically and shown in Fig. 3 as a function of a/l.

The stress intensity factor is calculated from equation (28) in terms of the solution for σ_1 as follows:

$$K_I = \lim_{r\to l}\,[2\pi(r-l)]^{1/2}\sigma_2 = 2\sigma_M G(a/l)(l/\pi)^{1/2} \tag{38}$$

$$G(a/l) = a/l\int_0^1 F(\lambda,a/l)[l^2/a^2-\lambda^2]^{-1}d\lambda \tag{39}$$

Numerical results for the nondimensional function G are shown graphically in Fig. 4.

The behaviors of the stress-intensity factor and the maximum normal stresses σ_M and $\sigma_{1\max}$ can be studied using the nondimensional curves in Figs. 3 and 4. The value σ_M in equation (32) is proportional to a/R. Consequently, K_I in equation (38) and $\sigma_{1\max}$ are, respectively, proportional to aG/R and $af(0)/R$. For given values of the nondimensional ratios α/l and l/R, the value k_α is determined from equation (35), which in turn determines a/l from Fig. 3. The determined value of a/l multiplied by the given value of l/R gives the value a/R. If a/R is multiplied by the values of $f(0)$ in Fig. 3 and G in Fig. 4 at the determined value of a/l, the products $af(0)/R$ and aG/R are obtained and shown in Figs. 5 and 6, respectively. Using the data involved in earlier works [8, 9] as guidelines, the values of a/l and l/R in Figs. 5 and 6 are chosen in such a way that the maximum normal stresses are in usual stress ranges.

The normal stress outside the crack tip is calculated from equation (28) and written as:

$$\sigma_2 = \sigma_M \bar{G}(r/l,\, a/l) \tag{40}$$

$$\bar{G} = 2(r^2/l^2 - 1)^{-1/2} a/l\pi \int_0^1 F(\lambda, a/l)[r^2/a^2 - \lambda^2]^{-1} d\lambda \tag{41}$$

The nondimensional function $\bar{G}$ is calculated numerically and shown graphically for various values of a/l in Fig. 7.

Discussion and Conclusions

The indentation of a penny-shaped crack by an oblate smooth spheroidal rigid inclusion in a transversely isotropic medium is investigated using the method of Hankel transforms. The problem has the character of a three-part mixed boundary value problem and is solved using the techniques of a triple integral equation [4].

The normal contact stress between the crack surface and the indenter is written as the product of the associated half-space contact stress and a nondimensional crack-effect correction function. The nondimensional correction function is solved numerically from an integral equation by the method of successive approximations. The magnitude of the normal contact stress in the contact area is shown to be lower than the corresponding value of the associated half-space contact stress in Fig. 2.

The ratio of the maximum indentation to the crack radius l is written as the product of the ratio of l to the radius of the curvature of the indenter surface R and a nondimensional function k_α in equation (35). The calculated values of k_α are shown graphically in Fig. 3 as a function of the ratio of the contact radius a to the crack radius l. The curve for k_α can be used to determine the value of a for given values of l, R, and α. Once the value of a has been determined, the maximum normal contact stress $\sigma_{1\max}$ can be calculated using the curve for $f(0)$ in Fig. 3. The values for a/R and the normalized $\sigma_{1\max}$ are shown in Fig. 5 as functions of α/l and R/l. It can be seen there that both the contact radius and the maximum contact stress increase with increasing α if R and l are constant.

An exact expression for the stress-intensity factor is obtained in equation (38) and can be seen to be proportional to the constant K in equation (16), which is a real-valued function of the elastic constants and the characteristic roots. The constant K reduces to $\mu/(1-\nu)$ for an isotropic material, where μ is the shear modulus and ν the Poisson ratio. The value of the stress-intensity factor can be calculated using the nondimensional curve in Fig. 4. The curves for the calculated values of the normalized stress-intensity factor are shown in Fig. 6 as functions of the ratios R/l and α/l. The value of the stress-intensity factor increases if the indentation α or the radius of the indenter-surface curvature R increases. The normal stress outside the crack tip σ_2 is also obtained as the product of the maximum associated half-space contact stress and a nondimensional function. The distributions of the normalized normal stress σ_2 are shown in Fig. 7 as functions of a/l and the normalized distance r/l.

Acknowledgment

The present research was supported by the Engineering Research Institute of Iowa State University.

References

1 Elliott, H. A., "Three-Dimensional Stress Distributions in Hexagonal Aeolotropic Crystals," *Proceedings of the Cambridge Philosophical Society*, Vol. 44, 1948, pp. 522–533.

2 Chen, W. T., "Stress Concentration Around Spheroidal Inclusions and Cavities in a Transversely Isotropic Material Under Pure Shear," ASME Journal of Applied Mechanics, Vol. 37, 1970, pp. 85–92.

3 Christensen, R. M., *Mechanics of Composite Materials*, Wiley, New York, 1979.

4 Cooke, J. C., "Triple Integral Equations," *Quarterly Journal of Mechanics and Applied Mathematics*, Vol. 16, 1963, pp. 193–203.

5 Green, A. E., and Zerna, W., *Theoretical Elasticity*, Oxford University Press, London, 1954.

6 Tsai, Y. M., "Stress Distributions in Elastic and Viscoelastic Plates Subjected to Symmetrical Rigid Indentations," *Quarterly of Applied Mathematics*, Vol. 27, No. 3, 1969, pp. 371–380.

7 Watson, G. N., *Theory of Bessel Functions*, 2nd Ed., Cambridge University Press, London, 1966.

8 Tsai, Y. M., and Kolsky, H., "A Theoretical and Experimental Investigation of the Flaw Distribution on Glass Surfaces," *Journal of the Mechanics and Physics of Solids*, Vol. 15, 1967, pp. 29–46.

9 Tsai, Y. M., "Thickness Dependence of the Indentation Hardness of Glass Plates," *International Journal of Fracture Mechanics*, Vol. 15, No. 3, 1969, pp. 157–165.

APPENDIX

$$L(r,\lambda) = \int_0^\infty J_0(sr) J_0(\lambda s)\, ds \tag{A-1}$$

The preceding integral can be expressed in the following two different forms [4]:

$$L(r,\lambda) = \frac{2}{\pi} \int_0^{\min(\lambda,r)} (\lambda^2 - s^2)^{-1/2} (r^2 - s^2)^{-1/2} ds \tag{A-2}$$

$$L(r,\lambda) = \frac{2}{\pi} \int_{\max(\lambda,r)}^\infty (s^2 - \lambda^2)^{-1/2} (s^2 - r^2)^{-1/2} ds \tag{A-3}$$

$$\frac{\partial}{\partial\lambda} \int_\lambda^a x(x^2 - \lambda^2)^{-1/2} (t^2 - x^2)^{-1/2} dx$$

$$= -\lambda(t^2 - a^2)^{1/2} (t^2 - \lambda^2)^{-1} (a^2 - \lambda^2)^{-1/2} \tag{A-4}$$

$$\frac{\partial}{\partial r} \int_r^\infty x(x^2 - r^2)^{-1/2} J_0(\xi x)\, dx = -\sin(\xi r) \tag{A-5}$$

$$\frac{\partial}{\partial\lambda} \int_l^\lambda x(\lambda^2 - x^2)^{-1/2} (x^2 - t^2)^{-1/2} dx$$

$$= \lambda(l^2 - t^2)^{1/2} (\lambda^2 - l^2)^{-1/2} (\lambda^2 - t^2)^{-1} \tag{A-6}$$

Creep and Creep Recovery of 2618-T61 Aluminum Under Variable Temperature

U. W. Cho
Assistant Professor of Mechanical and Aerospace Engineering,
University of Missouri-Columbia,
Columbia, Mo, 65211
Assoc. Mem. ASME

W. N. Findley
Professor of Engineering,
Division of Engineering,
Brown University,
Providence, R.I. 02912
Fellow ASME

Creep and creep recovery data are reported for pure tension of 2618-T61 aluminum alloy under variable temperature between 200°C and 230°C. Varying temperature experiments involved an abrupt temperature increase and a linearly increasing and decreasing temperature at a constant stress of 137.9 MPa (20 ksi). A temperature-compensated time by Sherby and Dorn was employed to represent the effect of temperature. A temperature-history-dependent theory using data from constant stress creep and creep recovery together with the apparent activation energy was used to predict the creep under variable temperature. The predictions agreed quite well with the observed data. The apparent activation energy of this alloy was found to be 49,000 cal/mole°K.

Introduction

Most creep experiments of metals have been conducted at constant stresses and temperatures. But actual creep problems of structural members involve much more complex conditions such as varying stress and temperature, and gradients in both. As the creep behavior of metals is very sensitive to temperature as well as stress, and creep-controlling mechanisms change with stress and temperature, the proper constitutive relations should account for the effects of stress and temperature together. Since all the creep parameters are possibly affected by temperature, it will not be possible to construct one general relation covering the whole range of stress and temperature. It is desirable to find the simplest equation describing the temperature dependency of creep over a fairly narrow temperature range of practical interest.

In an earlier work by Blass and Findley [1], the creep behavior of 2618 aluminum alloy was reported for abrupt changes in temperature and combined stress states. In a series of works by Findley and Lai [2–4] creep of the same material were reported for variable stresses of combined tension and torsion at 200°C. A viscous-viscoelastic model was developed and extended for variable stresses employing a strain-hardening theory (SH) for nonrecoverable viscous creep components and a modified superposition principle (MSP) for recoverable viscoelastic creep components.

In the present paper, additional experiments on the same lot of material are reported for varying temperature. The temperature effect was incorporated into the original constitutive relation [2, 3] by replacing the actual time with an integral form of temperature-compensated time which was first introduced by Sherby and Dorn [5]. Then the behavior under variable temperature was predicted from the theory using data from tests at constant stress and temperature only.

Somewhat similar experiments on creep under variable temperature were performed by Mark and Findley [6] on a plastic for which an integral form of reduced time defined by Morland and Lee [7] was employed in the predictions. Creep experiments on 0.15 percent carbon steel under step changes in temperature during creep at a stress near the yield point were reported by Taira, Ohnami, and Sakato [8]. These experiments showed a marked difference in behavior between a step increase versus a step decrease in temperature. On a temperature decrease an "incubation period" of near zero creep was reported.

Materials and Specimens

An aluminum forging alloy 2618-T61 was employed in these experiments. Specimens were taken from the same lot of 63.5 mm (2.5 in.) diameter forged rod as used in [2–4] and the same as specimens *D-H* in [1]. Specimens were thin-walled tubes having outside diameter, wall thickness, and gage length of 25.4, 1.52, and 101.6 mm (1.0, 0.060, and 4 in.), respectively. A more complete description of material and specimens is given in [2].

Experimental Apparatus and Procedure

The combined tension and torsion creep machine used for these experiments was described in [9] and briefly in [2]. The temperature control and measurement employed was described in [1, 2]. The abrupt temperature increase was made manually by increasing the set point of a Thermac temperature controller. For continuously varying temperature, a clock motor and gear train were used to drive the set point of

Contributed by the Applied Mechanics Division and presented at the Winter Annual Meeting, New Orleans, La., December 9–14, 1984 of THE AMERICAN SOCIETY OF MECHANICAL ENGINEERS.

Discussion on this paper should be addressed to the Editorial Department, ASME, United Engineering Center, 345 East 47th Street, New York, N.Y. 10017, and will be accepted until two months after final publication of the paper itself in the JOURNAL OF APPLIED MECHANICS. Manuscript received by ASME Applied Mechanics Division, October, 1983; final revision, February, 1984. Paper No. 84-WA/APM-20.

Copies will be available until August, 1985.

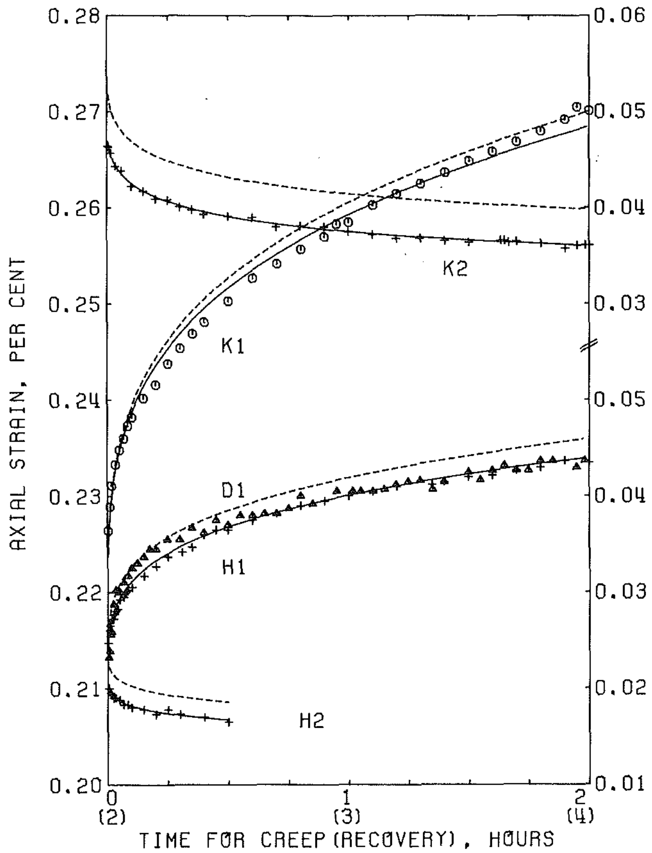

Fig. 1 Creep and creep recovery of 2618-T61 Al under pure tension of 137.9 MPa (20 ksi) and at 200°C (*D*1, *H*1, and *H*2), and at 230°C (K_1 and *K*2). Use ordinate scale on the left for creep and on the right for creep recovery.

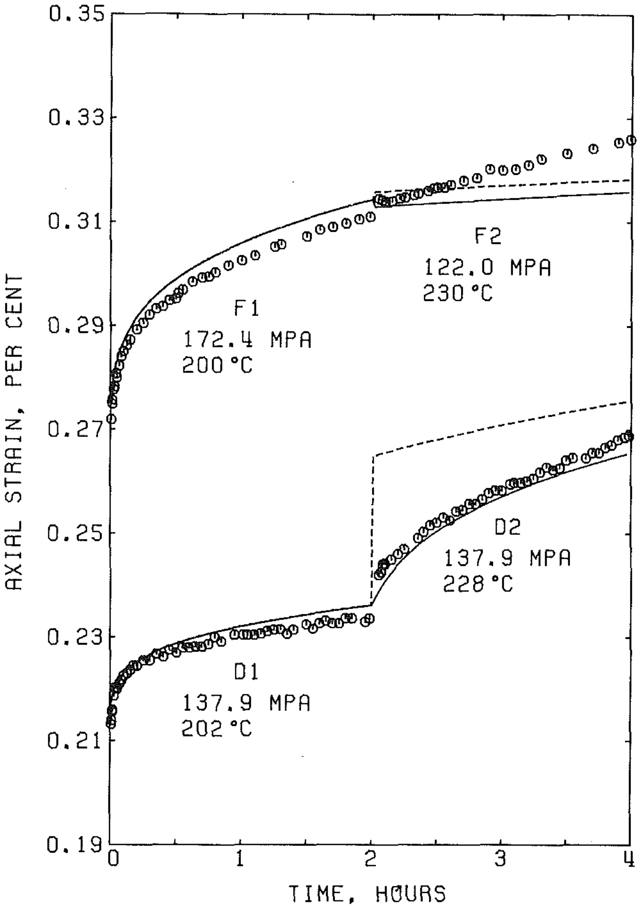

Fig. 2 Creep of 2618-T61 Al under an abrupt temperature increase with a simultaneous decrease of stress (*F*1-*F*2), and without a stress change (*D*1-*D*2)

two Thermac temperature controllers at constant rate. One of these Thermacs controlled the power to the heating lamp inside the specimen, and the other controlled the power to both top and bottom end heaters. The function of the heating lamp and end heaters were described previously [2]. Chromel-alumel thermocouples were used for control and chromel-constantan thermocouples were used for measuring. Stress was produced by applying dead weight at the end of a lever. The weights were applied by manual control of a jack in less than 10 sec. but without shock. For simultaneous temperature increase and loading, the temperature was first increased to the test temperature just before the load was applied. Similarly for continously increasing temperature, the clock motor was first started and then the load was applied. The time of the start of the test was taken to be the instant at which the load was fully applied. The gage length employed was measured at room temperature and no correction of gage length was made for thermal expansion.

Experimental Results

The results of tests *D*, *F*, *H*, *K* and *L* are shown in Figs. 1–4. The test data *D*, *F*, and *H* were taken from [1], and tests *K* and *L* are new.

Figure 1 shows results of creep and creep recovery tests at two different constant temperatures, 200°C (Tests *D* and *H*) and 230°C (Test *K*) under one constant tension stress of 137.9 MPa (20 ksi).

Figure 2 shows results of creep at an abrupt temperautre increase from 200°C to 230°C at constant tension stress (Test *D*), and simultaneous abrupt temperature increase and stress decrease (Test *F*). The increase in temperature was accomplished in about 20 sec [1].

Figures 3 and 4 show creep and creep recovery tests (Test *L*) during which the temperature increased and decreased at a contstant rate between 200°C and 230°C, as shown in the temperature curves in Figs. 3 and 4.

Analysis of Data

Viscous-Viscoelastic Model. Previous analysis [2] showed that the short time creep of 2618-T61 aluminum alloy at 200°C was well represented by a power function of time such as

$$\epsilon = \epsilon^0 + \epsilon^+ t^n, \qquad (1)$$

where ϵ^0 is the time-independent response, ϵ^+ is the coefficient of the time-dependent component, and $n = 0.270$ was a constant. By using the creep recovery tests, the time-dependent component was separated into recoverable and nonrecoverable components, and ϵ^0 was found to be elastic strain with negligible plastic strain.

Equation (1) may be rewritten as

$$\epsilon = \epsilon^E + \epsilon^{+VE} t^n + \epsilon^{+V} t^n, \qquad (2)$$

where ϵ^E is elastic strain and ϵ^{+VE} and ϵ^{+V} are the recoverable viscoelastic strain coefficient and the nonrecoverable viscous strain coefficient, respectively.

The ratio $r = \epsilon^{+VE}/\epsilon^{+V} = 0.55$ was a constant over the stress range considered. Then, $\epsilon^{+VE} = \epsilon^+ r/(1+r)$, and $\epsilon^{+V} = \epsilon^+/(1+r)$. The stress dependence of ϵ^+ was represented by a third-order multiple integral representation [10] as

$$\epsilon^+ = F(\sigma - \sigma^*) = F_1(\sigma - \sigma^*) + F_2(\sigma - \sigma^*)^2 + F_3(\sigma - \sigma^*)^3, \qquad (3)$$

where σ^* is the apparent creep limit below which negligible

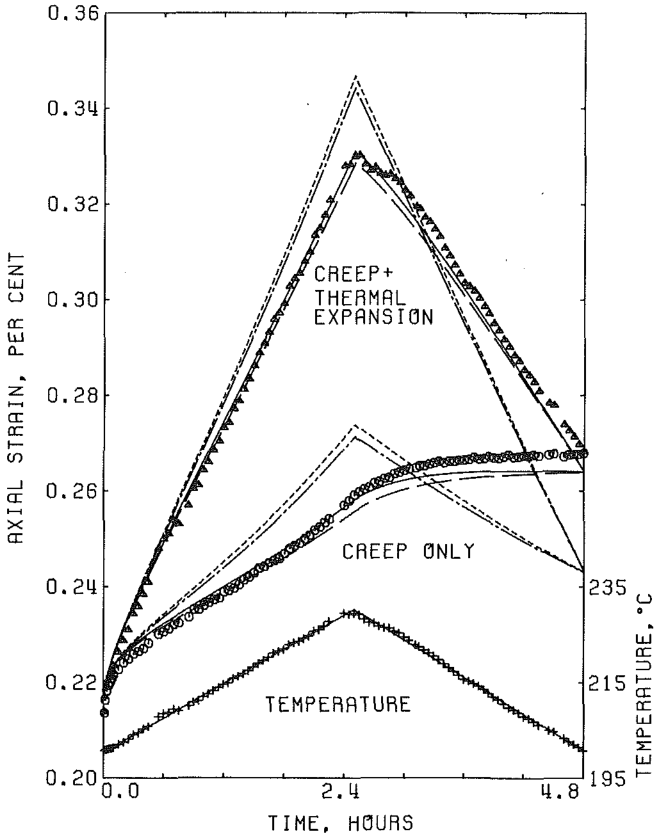

Fig. 3 Creep of 2618-T61 Al under linearly increasing and decreasing temperature between 200°C and 230°C at a constant tension of 137.9 MPa (20 ksi)

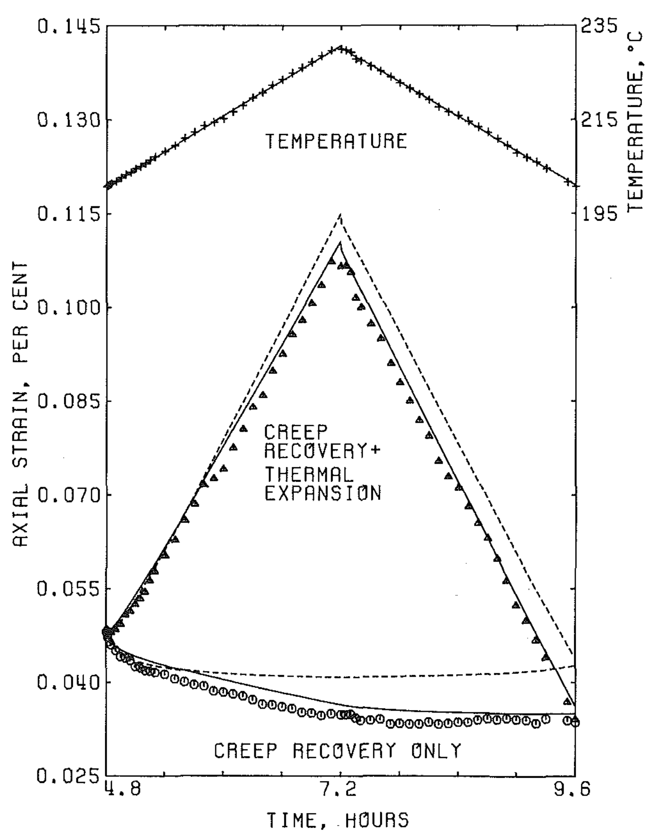

Fig. 4 Creep recovery of 2618-T61 Al under linearly increasing and decreasing temperature between 200°C and 230°C following the creep period shown in Fig. 3 at a constant tension of 137.9 MPa (20 ksi).

creep was assumed. Subsequent work [11] has shown that creep does occur at stresses below the apparent creep limit. The values of F_i and σ^* were determined in [2], and are a function of temperature.

Effect of Temperature. The temperature effect was incorporated in this paper by employing the temperature-compensated time, introduced by Sherby and Dorn [5] as

$$\theta=\int_0^t [e^{-Q/RT(s)}]ds, \tag{4}$$

where Q is the apparent activation energy, R is the gas constant (= 1.986 cal/mole). T is absolute temperature (°K), and s and t are previous and current time, respectively. Then creep under variable temperature can be described by replacing t with θ in equations (1)–(3). In [12] Dorn and Jaffe showed equation (4) to be applicable to small abrupt temperature changes over a wide temperature range. At a constant temperature, equation (1) may be rewritten as

$$\epsilon=\sigma/E(T)+C[e^{-Q/RT}t]^n, \tag{5}$$

where E is Young's modulus as a function of temperature. Comparing equation (1) and (5) $\epsilon^+ = Ce^{-nQ/RT}$, where C is now a function of stress only as

$$C=F'(\sigma-\sigma^*)=F_1'(\sigma-\sigma^*)+F_2'(\sigma-\sigma^*)^2+F_3'(\sigma-\sigma^*)^3, \tag{6}$$

where the creep limit, σ^* was assumed to be constant. Then the values of F_i' may be computed from F_i by dividing by $e^{-nQ/RT}$.

Determination of Activation Energy, Q. Assuming that Q is constant between 200°C and 230°C the values of Q may be determined from creep tests at the same stress but under two different temperatures as follows. From equations (1) and (5),

$$ln(\epsilon_1^+/\epsilon_2^+)=-\frac{nQ}{R}\left[\frac{1}{T_1}-\frac{1}{T_2}\right]. \tag{7}$$

Test data of $D1$, $H1$, and $K1$ shown in Fig. 1 were fitted to equation (1) by least squares with $n = 0.270$. For 200°C, the average of $D1$ and $H1$ was used, as $\epsilon^\circ = 0.2109$ percent, $\epsilon^+ = 0.019217$ percent/h^n. For 230°C, $K1$ yielded $\epsilon^\circ = 0.2147$ percent, $\epsilon^+ = 0.044604$ percent/h^n.

Using these values, the creep curves were computed and are shown as solid lines in Fig. 1. The apparent activation energy was calculated from equation (7) as $Q = 49{,}000$ cal/mole°K. From this value the F_i' in equation (6) were recalculated by separating the temperature effect as $F_1' = 795.6$ percent per MPa$-h^n$, $F_2' = -9.718$ percent per MPa$^2-h^n$, and $F_3' = 0.0993$ percent per MPa$^3-h^n$.

The activation energy was also calculated from two experiments in [1] in which the temperature was changed abruptly in about 20 sec during a creep test. Using the Dorn-Jaffe method [12] for test $D1$-$D2$, an increase in temperature from 202°C to 228°C at a tensile stress of 137.9 MPa (20 ksi), yielded $Q = 45{,}000$ cal/mole°K. Test $D3$-$D4$ involved a decrease in temperature from 228°C to 203°C at a constant combined stress of 137.9 MPa (20 ksi) tension and 79.3 MPa (11.5 ksi) torsion. A value of $Q = 50{,}000$ cal/mole°K was found from these data. These results compare well with the present determination from creep at two different temperatures.

Change of Young's Modulus, E. The Young's modulus was determined in [2] as $E = 65.02 \times 10^3$ MPa (9.43×10^6 psi)) at 200°C. The result of test $K1$ at 230°C showed that the elastic strain increased and thus E decreased as temperature increased. With assumptions of no plastic strain and a linear variation of E with temperature between 200°C and 230°C, the following relation was obtained.

$$E(T)=(76.98-0.02528\ T)\times 10^3 \text{ MPa}, \tag{8}$$

where T is absolute temperature (°K).

The creep curves as recalculated by equations (5), (6), and (8), are shown as dotted lines in Fig. 1.

Creep Recovery. Creep recovery was described by using the superposition principle (see [10]) as

$$\epsilon = \epsilon^{+V} t_1^n + \epsilon^{+VE} \left\{ t^n - (t-t_1)^n \right\}, \tag{9}$$

where t_1 is the time at which the stress was removed. Employing θ as in creep, equation (9) may be rewritten as

$$\epsilon = A\ \theta_1^n + B\{\theta^n - (\theta - \theta_1)^n\}, \tag{10}$$

where $\theta_1 = \int_0^{t_1} e^{-Q/RT(s)}\, ds$.

At constant temperature, equation (10) becomes for pure tension

$$\epsilon = \frac{1}{1+r} C\ e^{-nQ/RT} \{ t_1^n + r[t^n - (t-t_1)^n] \}, \tag{11}$$

where C is a function of stress as in equation (6), $A = C/(1+r)$, and $B = Cr/(1+r)$.

To check the applicability of equations (9)–(11) at different temperatures, equation (9) was fitted to the creep recovery data of $H2$ and $K2$; and $\epsilon^{+V} t_1^n$ and ϵ^{+VE} were determined by least squares using $n = 0.270$ as follows:

$H2$: $\epsilon^{+V} t_1^n = 0.0139$ percent, $\epsilon^{+VE} = 0.006219$ percent$/h^n$,

$K2$: $\epsilon^{+V} t_1^n = 0.0324$ percent, $\epsilon^{+VE} = 0.014783$ percent$/h^n$.

These values and equation (9) resulted in the recovery curves shown as solid lines as in Fig. 1. Also from the previous results of ϵ^{+}, the values of ϵ^{+V} were calculated by $\epsilon^{+V} = \epsilon^{+} - \epsilon^{+VE}$. The ratio r was calculated as $r = 0.50$ at 200°C and $r = 0.48$ at 230°C, which was close to $r = 0.55$, previously determined from several different stress levels at 200°C. Thus $r = 0.55$ may be suitable for the temperature range between 200°C and 230°C. In the following calculations $r = 0.55$ was adopted as before. Recovery curves recalculated by equation (11) are shown as dotted lines in Fig. 1.

Creep Under Variable Temperature. The temperature-compensated time, θ, as a form of equation (4), includes the effect of previous temperature history up to the current time, t. Thus the temperature-history-dependent theory (THD) for creep under variable temperature may be formulated as

$$\epsilon = \sigma/E(T) + \alpha_l (T - T_1) + C\left[\int_0^t e^{-Q/RT(s)}\, ds\right]^n, \tag{12}$$

where α_l is a linear thermal expansion coefficient, T_1 is a reference temperature, and the other parameters have the same meaning as in the previous section. For comparison, a temperature-history-independent theory (THI) was formulated as

$$\epsilon = \sigma/E(T) + \alpha_l (T - T_1) + C[e^{-Q/RT} t]^n, \tag{13}$$

which states that the total creep strain or creep rate is a function of the current temperature only.

Prediction of a Step Increase or Decrease in Temperature. By a step increase or decrease in temperature without change of stress following creep at another temperature, there may occur an instantaneous increase or decrease in axial strain from two different sources, as indicated by equation (12) or (13). One is the thermal expansion and the other is change of elastic strain by change of Young's modulus with temperature. Then, the net change of strain may be calculated as

$$\Delta\epsilon = \Delta\epsilon^E + \Delta\epsilon^T = \sigma_2/E(T_2) - \sigma_1/E(T_1) + \alpha_l (T_2 - T_1), \tag{14}$$

where $\sigma_2 = \sigma_1$ for test D Fig. 2, and the linear thermal expansion coefficient was determined from a small incremental temperature test after the creep recovery period in Tests K and L as $\alpha_l = 2.457 \times 10^{-3}$ percent/°C between 200°C and 230°C.

As the time-independent strain change was too large to be properly included in one plot, the strain change, $\Delta\epsilon = 0.0662$ percent was subtracted from data of test $D2$ and from the predictions by equation (12) or (13) for test $D2$. The (THD) curve by equation (12) was shown as solid lines and the (THI) curve by equation (13) was shown as dotted lines in Fig. 2.

Prediction of Simultaneous Increase in Temperature and Decrease in Stress. Test F involved a simultaneous increase in temperature (200°C → 230°C) and decrease in stress (172.4 MPa (25 ksi) → 122.0 MPa (17.7 ksi)). The calculation of period $F1$ for (THD) and (THI) are the same either by equation (12) or (13). The prediction of creep during period $F2$ was calculated by the modified viscous-viscoelastic (MVV) theory [3, 4] as

$$\epsilon^V = \{[F^V(\sigma_1)]^{1/n}\theta_1 + [F^V(\sigma_2)]^{1/n}(\theta - \theta_1)\}^n, \tag{15}$$

and ϵ^{VE} was frozen since the amount of stress decrease was less than the creep limit, $\sigma^* = 91.43$ MPa (13.26 ksi). See [3] for details. Also the net instantaneous strain change was calculated by equation (14) as $\Delta\epsilon = -0.0015$ percent. The (THD) curves determined by equation (12) and (15) are shown as solid lines and the (THI) curves by equation (13) and (15) are shown as dotted lines in Fig. 2.

Prediction of Linearly Increasing and Decreasing Temperature. Test L involved a linearly increasing and decreasing temperature during creep and during creep recovery periods as shown in Figs. 3 and 4. The temperature data in °C were fitted to the following four piecewise linear equations

$$\begin{aligned} T_1(t) &= 200.3 + 11.976\ \ t, && 0 < t \le 2.5 \\ T_2(t) &= 262.2 - 12.826\ \ t, && 2.5 < t \le 4.8 \\ T_3(t) &= 140.7 + 12.518\ \ t, && 4.8 < t \le 7.2 \\ T_4(t) &= 317.6 - 12.143\ \ t. && 7.2 < t \le 9.6 \end{aligned} \tag{16}$$

These equations are drawn as solid lines in Fig. 3 and 4. For the creep period (test $L1$), the (THD), or (THI) curve was calculated by equation (12) or (13), and shown as solid lines or dotted lines, respectively. Another plot of the data and predictions showing creep only was made by subtracting the thermal expansion from both data and theory. Also for comparison the predictions without change of elastic strain are shown as dash lines for (THD) curves and dash-dot lines for (THI) curves. In all the foregoing calculations the reference temperature was taken as the starting test temperature just before loading.

For creep recovery (test $L2$), the (THD) curves were calculated by equation (10) with and without thermal expansion and are shown as solid lines in Fig. 4. The (THI) curve was calculated by equation (11) with and without thermal expansion and shown as dotted lines in Fig. 4. In this plot, the disagreement between the (THI) curve and data was too large to be included in the same plot. So all the data and theory curves were drawn to be matched at the time of the first data point. Also the reference temperature was taken as the same one as in the creep period ($T_1 = 200$°C).

Discussion of Results

In Fig. 1, creep curves at 200°C ($D1$ and $H1$) were well represented by using $n = 0.270$ in equation (1). But at 230°C ($K1$) using $n = 0.270$ caused a slight deviation from the data, and the deviation would become bigger as time increased. The best fit curve to ($K1$) resulted in $n = 0.398$, which suggested that the power n might be a function of temperature.

The creep recovery curves are well represented by using $n =$

0.270 in equation (9) for both at 200°C and 230°C, which suggests that the recoverable viscoelastic strain has a constant power n independent of temperature.

In Fig. 2, creep at an abrupt temperature increase with no change of stress, as in test $D1$-$D2$, was quite well predicted by the (THD) equation. But the (THI) equation caused a jump in creep strain upon a step change in temperature, which is clearly an unreasonable prediction. For creep with a simultaneous stress drop and temperature increase, as in Test $F1$-$F2$, both the (THD) and (THI) equation predicted a much lower creep rate than the test data. This prediction might be improved by including the creep below the creep limit as found in [11], or by considering a change of the creep limit in equation (6) similar to the change of yield limit with temperature [13].

In Fig. 3, creep under linearly increasing and decreasing temperature was reasonably well described by the (THD) equation. Consideration of a change in the elastic strain with increasing temperature improved the prediction, but for decreasing temperature the curves without change of elastic strain (dash lines) gave a better prediction of creep rate than considering the change.

The prediction of recovery curves in Fig. 4 shows similar trends for the creep in Fig. 3. The predicted recovery rate was less than the test data. Obviously the results indicated that the (THI) equations are not applicable for creep under variable temperature.

No "incubation period" or near zero creep upon reduction of temperature, such as reported in [8], was observed in experiments on the present material reported in [1] in periods $D3$-$D4$ of Fig. 7 and 8 of [1]. The creep under combined tension and torsion continued after the drop in temperature as though there had been only a change in scale in plotting the results. Since the stress employed in $D3$-$D4$ of [1] at the higher temperature (228°C) was high enough to start third-stage creep in 0.3 h, the data were not well represented by equation (1) with $n = 0.270$. Hence the (THD) theory would not properly describe the data in $D3$-$D4$. However, the character of the results of $D3$-$D4$ is as described by the (THD) theory, equation (12). That is there no "incubation period" but a simple scale change.

Conclusions

1 A viscous-viscoelastic model with a replacement of a temperature-compensated time for the actual time described creep and creep recovery under variable temperature quite well.

2 The apparent activtion energy of 2618-T61 aluminum alloy was determined to be 49,000 cal/mole°K between 200°C and 230°C.

3 Creep under an abrupt change in temperature or a linearly increasing and decreasing temperature at constant stress was reasonably well described by a temperature-history dependent theory.

4 Creep under changes in both stress and temperature requires more detailed informations about temperature dependence on creep parameters.

Acknowledgment

This work was supported by the Army Research Office, Research Grant No. DAAG29-81-K-0138. The material was contributed by the Aluminum Company of America. The authors are grateful to Cathy Gavin for typing the manuscript.

References

1 Blass, J. J., and Findley, W. N., "Short-Time Biaxial Creep of an Aluminum Alloy With Abrupt Changes of Temperature and State of Stresses," ASME Journal of Applied Mechanics, Vol. 38, 1971, pp. 489–501.

2 Findley, W. N., and Lai, J. S., "Creep and Recovery of 2618 Aluminum Alloy Under Combined Stress With a Representation by a Viscous-Viscoelastic Model," ASME Journal of Applied Mechanics, Vol. 45, 1978, pp. 507–514.

3 Lai, J. S., and Findley, W. N., "Creep of 2618 Aluminum Under Step Stress Changes Predicted by a Viscous-Viscoelastic Model," ASME Journal of Applied Mechanics, Vol. 47, 1980, pp. 21–26.

4 Findley, W. N., and Lai, J. S., "Creep of 2618 Aluminum Under Side Steps of Tension and Torsion and Stress Reversal Predicted by a Viscous-Viscoelastic Model," ASME Journal of Applied Mechanics, Vol. 48, 1981, pp. 47–54.

5 Sherby, O. D., and Dorn, J. E., "Correlation of High Temperature Creep Data," Forty-First Technical Report, Institute of Engineering Research, University of California, Berkeley, June 1, 1955.

6 Mark, R., and Findley, W. N., "Nonlinear Variable Temperature Creep of Low Density Polyethylene," *Journal of Rheology*, Vol. 22, No. 5, 1978, pp. 471–492.

7 Morland, L. W., and Lee, E. H., "Stress Analysis for Linear Viscoelastic Materials With Temperature Variation," *Trans. Soc. Rheology*, Vol. 4, 1960, pp. 233–263.

8 Taira, S., Ohnami, M., and Sakato, M., "Influence of Temperature History on Creep," *Bulletin of JSME*, Vol. 5, No. 17, 1962, pp. 1–5.

9 Findley, W. N., and Gjelsvik, A., "A Biaxial Testing Machine for Plasticity, Creep or Relaxation Under Variable Principal-Stress Ratios," *Proceedings, ASTM*, Vol. 62, 1962, pp. 1103–1118.

10 Findley, W. N., Lai, J. S., and Onaran, K., *Creep and Relaxation of Nonlinear Viscoelastic Materials*, North-Holland, Amsterdam, 1976.

11 Ding, J. L., and Findley, W. N., "48 Hour Multiaxial Creep and Creep Recovery of 2618 Aluminum Alloy at 200°C," ASME Journal of Applied Mechanics, Vol. 51, 1984, pp. 125–132.

12 Dorn, J. E., and Jaffe, N., "Effect of Temperature on the Creep of Polycrystalline Aluminum by the Cross-Slip Mechanism," *Trans. Met. Soc. AIME*, Vol. 221, 1961, pp. 229–233.

13 Phillips, A., and Kasper, R., "On the Foundations of Thermoplasticity—An Experimental Investigation," ASME Journal of Applied Mechanics, Vol. 40, 1973, pp. 891–896.

The Exact Solution to an Ablation Problem With Arbitrary Initial and Boundary Conditions

L. N. Tao
Professor of Mechanics and Mathematics,
Department of Mechanical Engineering,
Illinois Institute of Technology,
Chicago, Ill. 60616
Fellow ASME

The problem of ablation by frictional heating in a semi-infinite solid with arbitrarily prescribed initial and boundary conditions is investigated. The study includes all convective motions caused by the density differences of various phases of the materials. It is found that there are two cases: (i) ablation appears immediately and (ii) there is a waiting period of redistribution prior to ablation. The exact solutions of velocities and temperatures of both cases are derived. The solutions of the interfacial positions are also established. Existence and uniqueness of the solutions are examined and proved. The conditions for the occurrence of these two cases are expressed by an inequality. Physical interpretation of the inequality is explored. Its implication coincides with one's expectation. Ablation appears only when the surface temperature is at or above the melting temperature.

1 Introduction

Problems of ablation have been studied for many years. An essential feature is the occurrence of phase changes. Surfaces that separate different phases are not at any fixed locations. They are unknown a priori and depend on the states of materials adjacent to them. These problems fall into the general classification of moving boundary problems or Stefan problems.

Moving boundary problems have been investigated since the 19th century by the early works of Neumann, Stefan, and others. The classical moving boundary problem is concerned with melting or freezing of a semi-infinite material initially at a constant temperature and being in contact with a different temperature at its surface where a change of phase takes place immediately. The exact solution to this moving boundary problem was established by Neumann (see [1]) in the 1860s and by Stefan [2] in 1889. The solution is elegant and simple. Temperatures of both phases are expressed in terms of a similarity variable $x/t^{1/2}$ and the position of the interfacial boundary is proportional to $t^{1/2}$. Thus the problem is solvable by a similarity transform, i.e., the partial differential equations of the problem are reducible to ordinary differential equations. Reduction to ordinary differential equations is possible only in some special situations. To seek mathematical solutions to problems with more comprehensive boundary and initial conditions has been the objective of many investigations. Since similarity solutions to more general problems are usually not possible, many different mathematical techniques and approximate methods have been devised and applied to find the solutions to these moving boundary problems. Specific references may be found in many books [3–8] and survey papers [9–12].

There have been numerous studies intended to find exact solutions to problems with more general initial and boundary conditions or to problems with more complicated differential equations. Only recently, some exact solutions of the classical Stefan problems with arbitrarily prescribed initial and boundary conditions in a semi-infinite region have been found [13–18]. The solutions to temperatures are expressed in series of functions and polynomials in the error integral family and time t, and the position of the interfacial boundary is an infinite series of $t^{1/2}$.

The problem of ablation by frictional heating is more involved than the classical Stefan problem. There are more unknowns. In addition to temperatures, velocity components also need to be considered. Another difficulty is those terms of energy dissipation, which are proportional to the squares of velocity gradients. Also, because different phases have different densities, there are convective motions induced by these density changes.

Ablation problems have been studied by many investigators. References to many of these can be found in the previously cited books and survey papers. Most of these solutions are approximate ones. There is, however, an exact similarity solution [19]. It adopts a commonly used assumption in moving boundary problems that the densities of all phases are equal. A consequence of this assumption is the absence of nonlinear terms in the momentum and energy equations. A recent paper [20] has removed this restriction of equal densities. By some appropriate changes of the variables, the materials behave as if all densities were equal. The

Contributed by the Applied Mechanics Division and presented at the Winter Annual Meeting, New Orleans, La., December 9–14, 1984 of THE AMERICAN SOCIETY OF MECHANICAL ENGINEERS.

Discussion on this paper should be addressed to the Editorial Department, ASME, United Engineering Center, 345 East 47th Street, New York, N.Y. 10017, and will be accepted until two months after final publication of the paper itself in the JOURNAL OF APPLIED MECHANICS. Manuscript received by ASME Applied Mechanics Division, December, 1983; final revision, February, 1984. Paper No. 84-WA/APM-26.

Copies will be available until August, 1985.

solution is again obtained by a similarity transformation. It is thus limited to problems with constant initial conditions. No exact solutions to problems with arbitrarily prescribed initial and boundary conditions have yet been found.

The purpose of this paper is to establish some exact solutions to ablation problems. We study the ablation problem of a semi-infinite solid, moving in a direction parallel to its surface, which is adjacent to a viscous incompressible fluid, subject to arbitrary initial and boundary conditions. The convective terms are first removed, as in [20], by some appropriate changes of the independent variables. This reduced problem in which all phases behave as if they had the same density is then solved for arbitrarily prescribed initial and boundary conditions.

In the next section we first formulate the problem and introduce the necessary transformations so that the equations are reduced to a set of equations without the convection terms. These equation are then solved exactly. The interfacial boundary, as in many moving boundary problems, is an infinite series of $t^{1/2}$. All solutions to the problem are shown to be uniquely determined if an inequality is satisfied. Physical interpretation of the inequality is explored. The result coincides with one's expectation. When ablation appears, the surface temperature must be at or above the melting point. Moreover, when this inequality is not satisfied initially, there is a delay of the occurrence of ablation prior to which the temperatures and velocities of the materials are redistributed and ablation will occur only after the surface temperature reaches the melting point. The complete solution to this case is also established.

2 Mathematical Solutions

Consider a solid body occupying the half space $x<0$ and a viscous incompressible fluid occupying the half space $x>0$. The solid is moving in a direction parallel to the surface of contact and its surface, due to the effect of frictional heating, reaches the melting temperature at $t=0$. Subsequently, there coexist three different phases: a solid in the domain of $-\infty<x<s$, a newly formed melt in $s<x<X$, and a liquid in $X<x<\infty$ where $s(t)$ is the position of the interface between the solid and the melt and $X(t)$ is the position of the interface between the melt and the liquid. For convenience, we convert the problem and let the solid be stationary. The melt and liquid are in motion. Also, we assume that the material properties of these three phases are different but constant. Let us denote these three phases: solid, melt, and liquid by subscripts 0, I, and II, respectively. Then, in the one-dimensional case the temperatures and the velocity components (parallel to the surface) of these three phases satisfy

(*i*) Differential Equations:

Solid:

$$\partial T_0/\partial t=\alpha_0(\partial^2 T_0/\partial x^2) \qquad -\infty<x<s(t)$$

Melt:

$$\partial v_I/\partial t+u_I(\partial v_I/\partial x)=\nu_I(\partial^2 v_I/\partial x^2) \qquad s(t)<x<X$$

$$\partial T_I/\partial t+u_I(\partial T_I/\partial x)=\alpha_I(\partial^2 T_I/\partial x^2)+(\nu_I/C_I)(\partial v_I/\partial x)^2 \tag{2.1}$$

Liquid:

$$\partial v_{II}/\partial t+u_{II}(\partial v_{II}/\partial x)=\nu_{II}(\partial^2 v_{II}/\partial x^2) \qquad X<x<\infty$$

$$\partial T_{II}/\partial t+u_{II}(\partial T_{II}/\partial x)=\alpha_{II}(\partial^2 T_{II}/\partial x^2)+(\nu_{II}/C_{II})(\partial v_{II}/\partial x)^2$$

(*ii*) Initial Conditions:

$$v_{II}(x,0)=\Phi(x)$$
$$T_0(x,0)=\Psi(x), \qquad T_{II}(x,0)=\Omega(x) \tag{2.2}$$

(*iii*) Boundary Conditions:

$$T_0(x,t) \qquad \text{regular as } x\rightarrow-\infty$$

$$v_{II}(x,t) \quad \text{and} \quad T_{II}(x,t) \qquad \text{regular as } x\rightarrow\infty \tag{2.3}$$

(*iv*) Interface Conditions at $x=s$:

$$v_I(s,t)=0, \qquad T_I(s,t)=T_0(s,t)=T_m=0$$
$$k_0(\partial T_0/\partial x)_{x=s}-k_I(\partial T_I/\partial x)_{x=s}=\rho_I L(ds/dt), \qquad s(0)=0$$

Here we have taken the melting temperature T_m of the solid to be the reference temperature

(*v*) Interface Conditions at $x=X$:

$$v_I(X,t)=v_{II}(X,t), \qquad T_I(X,t)=T_{II}(X,t)$$
$$\mu_I(\partial v_I/\partial x)_{x=X}=\mu_{II}(\partial v_{II}/\partial x)_{x=X}$$
$$k_I(\partial T_I/\partial x)_{x=X}=k_{II}(\partial T_{II}/\partial x)_{x=X}, \qquad X(0)=0 \tag{2.5}$$

The symbols in these equations have their usual meanings: k = conductivity, α = diffusivity, μ = viscosity, ν = kinematic viscosity, ρ = density, C = specific heat, and L = latent heat.

In addition to the preceding equations and conditions, we also need the continuity equations

$$\partial u_I/\partial x=0, \qquad \partial u_{II}/\partial x=0$$

These two equations show that the components of the velocity perpendicular to the surface are functions of t only. Therefore, applying the law of conservation of mass to the elements of interfaces at $x=s$ and $x=X$, we obtain

$$\rho_0(ds/dt)=\rho_I[(ds/dt)-u_I],$$
$$\rho_I[(dX/dt)-u_I]=\rho_{II}[(dX/dt)-u_{II}]$$

Also, we have

$$\rho_I(s-X)=\rho_0(s-0) \tag{2.6}$$

Therefore

$$X=-\epsilon r_I s$$

and

$$u_I=-\epsilon r_I(ds/dt), \qquad u_{II}=dX/dt=-\epsilon r_I(ds/dt) \tag{2.7}$$ [1]

where

$$r_i=\rho_{i-1}/\rho_i, \qquad \epsilon=1-(\rho_I/\rho_0)$$

The preceding system is a set of nonlinear equations for the unknowns T_i, v_i, and s. Fortunately, these nonlinear equations can be transformed to a system of linear ones. Introducing

$$\xi_0=x, \qquad \xi_I=\frac{x}{r_I}+\epsilon s, \qquad \xi_{II}=(x+\epsilon r_I s)/r_{II} \quad . \tag{2.8}$$

and

$$\beta_0{}^2=1/\alpha_0, \qquad \beta_i{}^2=r_i{}^2/\alpha_i, \qquad \gamma_i{}^2=r_i{}^2/\nu_i$$
$$\sigma_i=\nu_i/\alpha_i=\beta_i{}^2/\gamma_i{}^2=\text{Prandtl Number} \qquad (i=I,II)$$

we obtain

$$\gamma_i{}^2(\partial v_i/\partial t)=\partial^2 v_i/\partial \xi_i{}^2$$

[1] An error in [20] has been detected. The mass conservation law has been inappropriately applied to one of the interfaces. However, the result in [20] remains valid, if we set $\epsilon=0$ and with proper interpretations.

$$\beta_0{}^2(\partial T_0/\partial t) = \partial^2 T_0/\partial \xi_0{}^2$$
$$\beta_i{}^2(\partial T_i/\partial t) = (\partial^2 T_i/\partial \xi_i{}^2) + (\sigma_i/C_i)(\partial v_i/\partial \xi_i)^2 \qquad (2.9)$$

This set of transformations essentially changes the description in Eulerian coordinates to Lagrangian coordinates [17, 21]. The new domains of the three phases are $(-\infty,s)$, $(s,0)$ and $(0,\infty)$, respectively. The initial and boundary conditions remain unchanged, but the interface conditions are now

(*i*) at $x=s$ or $\xi_0=\xi_I=s$

$$v_I=0, \quad T_0=T_I=0$$
$$k_0(\partial T_0/\partial \xi_0) - (k_I/r_I)(\partial T_I/\partial \xi_I) = \rho_I L(ds/dt) \quad (2.10)$$

(*ii*) at $x=X$ or $\xi_I=\xi_{II}=0$

$$v_I=v_{II}, \qquad T_I=T_{II}$$
$$(\mu_I/r_I)(\partial v_I/\partial \xi_I) = (\mu_{II}/r_{II})(\partial v_{II}/\partial \xi_{II})$$
$$(k_I/r_I)(\partial T_i/\partial \xi_I) = (k_{II}/r_{II})(\partial T_{II}/\partial \xi_{II}) \qquad (2.11)$$

To complete the description of the problem, we need to specify the initial conditions $\Phi(x)$, $\Psi(x)$, and $\Omega(x)$. We assume that these arbitrary functions are regular at infinity and are expressible by power series,

$$\Phi(x) = \sum_0 \phi_n(\gamma_{II}x/r_{II})^n/n!,$$
$$\phi_n = \nu_{II}{}^{n/2}(d^n\Phi/dx^n)_0$$
$$\Psi(x) = \sum_0 \psi_n(-\beta_0 x)^n/n!,$$
$$\psi_n = (-\sqrt{\alpha_0})^n(d^n\Psi/dx^n)_0 \qquad (2.12)$$
$$\Omega(x) = \sum_0 \omega_n(\beta_{II}x/r_{II})^n/n!,$$
$$\omega_n = \alpha_{II}{}^{n/2}(d^n\Omega/dx^n)_0$$

Before we discuss the solutions to the problem, we recall that solutions of the diffusion equation may be expressed in products of the repeated error integrals and time t. Following [13–15], we introduce

$$E_n(\zeta) = [i^n\mathrm{erfc}(-\zeta) + i^n\mathrm{erfc}\zeta]/2$$
$$F_n(\zeta) = [i^n\mathrm{erfc}(-\zeta) - i^n\mathrm{erfc}\zeta]/2$$
$$G_n(\zeta) = [i^n\mathrm{erfc}(-\zeta) + (-1)^n i^n\mathrm{erfc}\zeta]/2 \qquad (2.13)$$

where $\zeta=\xi/(4t)^{1/2}$. The function $G_n(\zeta)$ is a polynomial of order n, and is closely related to Widder's heat polynomials [22]. Properties of these three functions follow directly from those of the repeated error integrals. With these functions, we now introduce the solutions of v_I, v_{II}, and T_0:

$$v_I(\xi,t) = \sum_0 a_n(2\tau)^n E_n(\gamma_I\zeta_I)$$
$$+ \sum_0 b_n(2\tau)^n F_n(\gamma_I\zeta_I)$$
$$v_{II}(\xi,t) = \sum_0 \phi_n(2\tau)^n G_n(\gamma_{II}\zeta_{II})$$
$$+ \sum_0 c_n(2\tau)^n i^n\mathrm{erfc}(\gamma_{II}\zeta_{II})$$
$$T_0(\xi,t) = \sum_0 \psi_n(2\tau)^n G_n(\beta_0\zeta_0)$$
$$+ \sum_0 d_n(2\tau)^n i^n\mathrm{erfc}(-\beta_0\zeta_0) \qquad (2.14)$$

where

$$\zeta_i = \xi_i/2\tau, \qquad \tau = t^{1/2}$$

Using (2.14), we see that v_{II} and T_0 satisfy their respective initial conditions. The boundary conditions are also satisfied since the prescribed functions are regular at infinity. To establish the other two temperature solutions, let us first evaluate the squares of velocity gradients,

$$(\sigma_i/C_i)(\partial v_i/\partial \xi_i)^2$$
$$= (1/4t)\sum_0 (2\tau)^n Q_{i,n}(\gamma_i\zeta_i) \qquad (2.15)$$

where

$$Q_{I,n}(\zeta) = (\beta_I{}^2/C_I)\sum_{m=0}^{n}[a_m F_{m-1}(\zeta) + b_m E_{m-1}(\zeta)]$$
$$\times [a_{n-m}F_{n-m-1}(\zeta) + b_{n-m}E_{n-m-1}(\zeta)]$$
$$Q_{II,n}(\zeta) = (\beta_{II}{}^2/C_{II})\sum_{m=0}^{n}[\phi_m G_{m-1}(\zeta)$$
$$-c_m i^{m-1}\mathrm{erfc}\zeta] \times [\phi_{n-m}G_{n-m-1}(\zeta) - c_{n-m}i^{n-m-1}\mathrm{erfc}\zeta] \quad (2.15)$$

It is noted that $G_{-1}(z) = F_{-1}(z) = 0$ and we have also used

$$i^{-m}\mathrm{erfc}(z) = (-1)^m\Phi_m(z) \qquad m \geq 1 \qquad (2.16)$$

where $\Phi_m(z)$ is the mth derivative of the error function erf(z).

We may now introduce the temperature solutions T_I and T_{II} as

$$T_I(\xi,t) = \sum_0 e_n(2\tau)^n E_n(\beta_I\zeta_I)$$
$$+ \sum_0 f_n(2\tau)^n F_n(\beta_I\zeta_I) + \sum_0 (2\tau)^n R_{I,n}(\beta_I\zeta_I)$$
$$T_{II}(\xi,t) = \sum_0 g_n(2\tau)^n G_n(\beta_{II}\zeta_{II})$$
$$+ \sum_0 h_n(2\tau)^n i^n\mathrm{erfc}(\beta_{II}\zeta_{II})$$
$$+ \sum_0 (2\tau)^n R_{II,n}(\beta_{II}\zeta_{II}) \qquad (2.17)$$

The particular integrals $R_{i,n}(\gamma)$ can be found by the use of variation of parameters,

$$R_{i,n}(\beta\zeta) = \int_{\delta_i}^{\zeta} P_{i,n}(\beta\zeta,y)Q_{i,n}(\gamma_i y)\,dy$$
$$P_{i,n}(\beta\zeta,y)$$
$$= 2^{n-2}n!\,\pi^{1/2}e^{\beta}i^2 y^2[i^n\mathrm{erfc}(\beta_i\zeta)i^n\mathrm{erfc}(-\beta_i y)$$
$$- i^n\mathrm{erfc}(\beta_i y)\,i^n\mathrm{erfc}(-\beta_i\zeta)] \qquad (2.18)$$

The solution to the position of the interfacial boundary $s(t)$ between the solid and the melt must be expressed, as in many other moving boundary problems, by a power series of $t^{1/2}$, not t. Accordingly, we express

$$s(t) = 2\tau\Lambda(\tau), \qquad \Lambda(\tau) = \sum_0 \lambda_n\tau^n \qquad (2.19)$$

Since ζ_I and ζ_{II} are defined in $(s,0)$ and $(0,\infty)$, we choose the integration constants of $R_{i,n}$ by

$$\delta_I = \lambda_0, \qquad \delta_{II} = 0 \qquad (2.20)$$

An alternate choice of δ_{II} could be ∞, which would simplify the evaluation of some not yet determined coefficients. However, for some materials it might lead to a divergent integral, particularly when $\beta_{II}{}^2 - 2\gamma_{II}^2 > 0$ since $Q_{II,n}(\zeta)$ is of the order of $0[\exp(-2\gamma_{II}{}^2\zeta^2)]$.

From the initial condition of $T_{II} = \Omega(x)$, we find that

$$g_n = \omega_n + 2^{n-2}n!\,\pi^{1/2}\int_0^\infty$$
$$\exp(\beta_{II}^2 y^2)i^n\mathrm{erfc}(\beta_{II}y)\,Q_{II,n}(\gamma_{II}y)\,dy \qquad (2.21)$$

The integrals in these coefficients are bounded, since $Q_{i,n}$ is of the exponential decay type and

$$\exp(\beta_{II} y^2) i^n \operatorname{erfc}(\beta_{II} y)$$

is bounded [16] between 0 and 1.

To complete the solutions, we must find the eight sets of coefficients, $a_n, b_n, c_n, d_n, e_n, f_n, h_n$, and λ_n. They will be found from the interface conditions at $\xi = s$ and $\xi = 0$. Inserting the solutions to the problem in these equations and setting them at $t=0$, we obtain

$$\begin{aligned}
&a_0 = -b_0 \operatorname{erf}(\gamma_I \lambda_0), \qquad d_0 = -\psi_0/\operatorname{erfc}(-\beta_0\lambda_0)\\
&b_0 = -\phi_0/[r_I(\gamma_{II}/\gamma_I) + \operatorname{erf}(\gamma_I\lambda_0)]\\
&c_0 = b_0 r_I(\gamma_{II}/\gamma_I), \qquad e_0 = -f_0 \operatorname{erf}(\beta_I \lambda_0)\\
&h_0 = -(k_I\beta_I r_{II}/k_{II}\beta_{II} r_I)\Big[f_0\\
&\qquad -(\pi^{1/2}/2)\int_{\lambda_0}^{0} e^{-\beta_I^2 y^2} Q_{I,0}(\gamma_I y)\,dy\Big]\\
&f_0 = \Big[g_0 - R_{I,0}(0) + (\pi^{1/2}/2)\\
&(k_I\beta_I r_{II}/k_{II}\beta_{II} r_I)\int_{\lambda_0}^{0} e^{\beta_I^2 y^2} Q_{I,0}(\gamma_I y)\,dy\Big]\\
&\qquad \times[(k_I\beta_I r_{II}/k_{II}\beta_{II} r_I) - \operatorname{erf}(\gamma_I\lambda_o)]^{-1}
\end{aligned} \tag{2.22}$$

And λ_o satisfies

$$\begin{aligned}
&k_0\beta_0 d_0[\exp(-\beta_0^2\lambda_0^2)\\
&\qquad -(k_I\beta_I/r_I) f_0 \exp(-\beta_I^2\lambda_0^2)] = \rho_I L \pi^{1/2}\lambda_0
\end{aligned} \tag{2.23}$$

where

$$R_{I,0}(0) = (\pi^{1/2}/2)\int_{\lambda_0}^{0} e^{-\beta_I^2 y^2} \operatorname{erf}(\beta_I y)\, Q_{I,0}(\gamma_I y)\,dy$$

The remaining coefficients can be determined from the eight interface equations by matching equal powers of τ, after all functions have been expanded in powers of τ. The process, if manageable, is very cumbersome. We prefer to differentiate these interfacial equations successively and evaluate them at $t=0$. Also, to circumvent negative powers of τ in the force-balance and heat-balance equations, we multiply the equations by $t^{1/2}$ before differentiations. Differentiations of these equations can be accomplished by a recent formula for the material time derivative of arbitrary order [23]. In the one-dimensional case where $f=f(x,t)$ and $x=x(t)$, we have

$$\begin{aligned}
D_t^N f(x,t) &= \sum_{n=0}^{N}\sum_{m=0}^{N-n} (N!/n!) Z_m^{N-n}(x)\,\partial_t^n \partial_x^m f\\
Z_m^n(x) &= \sum_{k_r}\prod_{r=1}^{n} [(D^r x/r!)^{k_r}/k_r!]
\end{aligned} \tag{2.24}$$

The sum in the last formula is extended to the whole set of multinomial coefficients, i.e., all non-negative integers k_r such that

$$\sum_{l}^{n} k_r = m, \qquad \sum_{l}^{n} r k_r = n \tag{2.25}$$

These multinomial coefficients are known [24]. Also, to find the derivatives of $R_{i,n}(\beta\Lambda)$, we use the extended Leibniz formula

$$\begin{aligned}
D_z^N\int^z f(z,y)\,dy &= \int^z \partial_z^N f(z,y)\,dy\\
&\quad + \sum_{p=0}^{N-1} D_z^{N-p-1}[\partial_z^p f(z,y)_{y=z}]
\end{aligned} \tag{2.26}$$

and the identity [25]

$$D_z^N[e^{z^2} i^n \operatorname{erfc} z] = (-2)^N[(N+n)!/n!] e^{z^2} i^{N+n}\operatorname{erfc} z \tag{2.27}$$

Performing differentiations of the eight interface equations, we obtain the recurrence formulas for $N \geq 1$,

$$\begin{aligned}
&\sum_{1}^{N} a_n[B_n^N(-\gamma_I) + B_n^N(\gamma_I)] + \sum_{0}^{N} b_n[B_n^N(-\gamma_I)\\
&\qquad\qquad - B_n^N(\gamma_I)] = 0\\
&\sum_{1}^{N}\psi_n A_n^N(\beta_0) + \sum_{0}^{N} d_n B_n^N(-\beta_0) = 0\\
&\sum_{1}^{N} e_n[B_n^N(-\beta_I) + B_n^N(\beta_I)] + \sum_{0}^{N} f_n[B_n^N(-\beta_I)\\
&\qquad\qquad - B_n^N(\beta_I)] = 0\\
&2\beta_0 k_0\Big[\sum_{0}^{N}\psi_n A_{n-1}^{N-1}(\beta_0) + \sum_{0}^{N} d_n B_{n-1}^{N-1}(-\beta_0)\Big]\\
&\quad -(\beta_I k_I/r_I)\Big\{\sum_{1}^{N} e_n[B_{n-1}^{N-1}(-\beta_I) - B_{n-1}^{N-1}(\beta_I)]\\
&\qquad + \sum_{1}^{N} f_n[B_{n-1}^{N-1}(-\beta_I) + B_{n-1}^{N-1}(\beta_I)]\\
&\qquad + \sum_{0}^{N} V_{n,I}^N(\beta_I)\Big\} = 2(N+1)\rho_I L\lambda_N\\
&a_N E_N(0) + b_N F_N(0) = \phi_N G_N(0) + c_N F_N(0)\\
&e_N E_N(0) + f_N F_N(0) + R_{I,N}(0) = g_N G_N(0) + h_N i^N \operatorname{erfc}(0)\\
&a_N F_{N-1}(0) + b_N E_{N-1}(0)\\
&= (\gamma_{II}\mu_{II} r_I/\gamma_I\mu_I r_{II})[\phi_N G_{N-1}(0) - c_N i^N\operatorname{erfc}(0)]\\
&e_N F_{N-1}(0) + f_N E_{N-1}(0)\\
&\qquad -(2^{N-1}/N)\pi^{1/2} i^N \operatorname{erfc}(0) F_{N-1}(0)\\
&= (k_{II}\beta_{II} r_I/k_I\beta_I r_{II})[g_N G_{N-1}(0) + h_N i^{N-1}\operatorname{erfc}(0)]
\end{aligned} \tag{2.28}$$

where

$$\begin{aligned}
A_n^N(\beta) &= 2^n \sum_{m=0}^{N^*} \beta^m Z_m^{N-n}(\lambda)\, G_{n-m}(\beta\lambda_0)\\
N^* &= \min(N-n, n)\\
B_n^N(\beta) &= 2^n \sum_{m=0}^{N-n} (-\beta)^m Z_m^{N-n}(\lambda)\, i^{n-m}\operatorname{erfc}(\beta\lambda_0)\\
V_{n,i}^N(\beta_i) &= 2^{n-1}\sum_{m=0}^{N-m} Z_m^{N-n}(\lambda)\,\partial_\Lambda^{m+1} R_{i,n}(\beta_i\Lambda)\,|_0\\
Z_m^n(\lambda) &= \sum_{k_r}\prod_{r=1}^{n}[(\lambda_r)^{k_r}/k_r!]
\end{aligned}$$

subject to

$$\sum_{1}^{n} k_r = m, \qquad \sum_{1}^{n} r k_r = n$$

and

$$\begin{aligned}
&\partial_\Lambda^N R_{i,n}(\beta_i\Lambda)\Big|_0 = \partial_\Lambda^m \int_{\delta_i}^{\Lambda} P_{i,n}(\Lambda,y) Q_{i,n}(\gamma_i y)\,dy\Big|_{\Lambda=\lambda_0}\\
&= 2^{n-2}\pi^{1/2}\Big\{\int_{\delta_i}^{\lambda_0} n!\,\beta_i{}^m e^{\beta_i^2 y^2}[(-1)^m i^{n-m}\operatorname{erfc}\\
&\qquad (\beta_i\lambda_0) i^n \operatorname{erfc}(-\beta_i y)\\
&\quad - i^n\operatorname{erfc}(\beta_i y)\, i^{n-m}\operatorname{erfc}(-\beta_i\lambda_0)] Q_{i,n}(\gamma_i y)\,dy\\
&\quad + \sum_{p=0}^{m-1}\sum_{q=0}^{p}\sum_{r=0}^{q} (-2)^{p+q}\binom{p}{q}\binom{q}{r}(n+q-r)!\, e^{\beta_i^2\lambda_0^2}\\
&\quad \times[(-1)^{p-q} i^{n-m-p-r}\operatorname{erfc}(\beta_i\lambda_0) i^{m-r-1}\operatorname{erfc}(-\beta_i\lambda_0)\\
&\quad - i^{n+q-r}\operatorname{erfc}(\beta_i\lambda_0) i^{n-m-p-r}\operatorname{erfc}(-\beta_i\lambda_0)]
\end{aligned}$$

$$\partial_y^{m-p-q-1} Q_{i,n}(\gamma_i y)\Big|_{y=\lambda_0}\Big\}$$

$$\partial_y^N Q_{I,n}(\gamma_I y)\Big|_{\lambda_0} = (\beta_I^2 \gamma_I^N / C_I) \sum_{m=0}^{N} \sum_{r=0}^{N}$$

$$\binom{N}{r} [(a_m + b_m) i^{m-r-1} \mathrm{erfc}(-\gamma_I \lambda_0) + (-1)^r (b_m - a_m) i^{m-r+1} \mathrm{erfc}(\gamma_I \lambda_0)][(a_{n-m} + b_{n-m}) i^{n-m+N-r-1} \mathrm{erfc}(-\gamma_I \lambda_0) + (-1)^{N-r} (b_{n-m} - a_{n-m}) i^{n-m+N-r-1} \mathrm{erfc}(\gamma_I \lambda_0)]$$

$$\partial_y^N Q_{II,n}(\gamma_{II} y)\Big|_{\lambda_0} = (\beta_{II}^2 \gamma_{II}^N / C_{II}) \sum_{m=0}^{N} \sum_{r=0}^{N}$$

$$\binom{N}{r} [\phi_m G_{m-r-1}(\gamma_{II}\lambda_0) - (-1)^r c_m i^{m-r-1} \mathrm{erfc}(\gamma_{II}\lambda_0)] [\phi_{n-m} G_{n-m+N-r-1}(\gamma_{II}\lambda_0) - (-1)^{N-r} c_{n-m} i^{n-m+N-r-1} \mathrm{erfc}(\gamma_{II}\lambda_0)] \tag{2.30}$$

From these equations, starting from $N=1$ sequentially, we may find all coefficients.

It is noted that the preceding solution includes the previous known similarity solutions [19, 20] as special cases. When $\Phi(x)$, $\Psi(x)$, and $\Omega(x)$ are constant, we have $\phi_n = \psi_n = \omega_n = 0$ $(n \geq 1)$. Then the recurrence formulas (2.28) become a set of homogeneous equations for the undetermined coefficients. Thus all coefficients are zero except those of the zeroth order. The complete solution of the problem is reduced to

$$\begin{aligned} v_I &= a_0 + b_0 \mathrm{erf}(\gamma_I \zeta_I) \\ v_{II} &= \phi_0 + c_0 \mathrm{erfc}(\gamma_{II} \zeta_{II}) \\ T_0 &= \psi_0 + d_0 \mathrm{erfc}(-\beta_0 \zeta_0) \\ T_I &= e_0 + f_0 \mathrm{erf}(\beta_I \zeta_I) + R_{I,0}(\beta_I \zeta_I) \\ T_{II} &= g_0 + h_0 \mathrm{erfc}(\beta_{II} \zeta_{II}) + R_{II,0}(\beta_{II} \zeta_{II}) \\ s &= 2\lambda_0 \tau \end{aligned} \tag{2.31}$$

It is in complete agreement with those in [19, 20].

3 Existence, Uniqueness, and Convergence

In the preceding section we have established the formal solution to the problem. The solution is meaningful only when all coefficients exist and are uniquely determined and when the series converge. It is the purpose of this section to show that all coefficients exist and are unique when an inequality is satisfied. This inequality is definitely required from the physics of the problem.

Let us first examine those coefficients of zeroth order. All coefficients of zeroth order are unique if λ_0 exists. The value of λ_0 satisfies

$$k_0 \beta_0 d_0 \exp(-\beta_0^2 \lambda_0^2) - (k_I / r_I) \beta_I f_0 \exp(-\beta_I^2 \lambda_0^2) = \rho_I L \pi^{1/2} \lambda_0 \tag{3.1}$$

This transcendental equation has both positive and negative roots. However a positive root is physically inadmissible, since it corresponds to an unrealistic cases where an increase of solid material would appear by ablation. We thus ignore the positive roots of this equation.

For negative λ_0, let us introduce $\lambda_0 = -\eta$ and rewrite the equation,

$$K_1 e^{(\beta_0{}^2 - \beta_I{}^2)\eta^2} \mathrm{erfc}(\beta_0 \eta) = 1 + K_2 \pi^{1/2} \beta_0 \eta e^{\beta_0{}^2 \eta^2} \mathrm{erfc}(\beta_0 \eta)$$

where

$$K_1 = -(k_I \beta_I / k_0 \beta_0 r_I)(f_0 / \psi_0), \quad K_2 = -\rho_I L / k_0 \beta_0{}^2 \psi_0 \tag{3.2}$$

We assume that all material constants are positive and $\psi_0 < 0$. To examine the existence of λ_0, we first note that for positive z, $\exp(z^2)\mathrm{erfc}(z)$ is monotone decreasing bounded between 1 and 0 [20]. Also $\pi^{1/2} z e^{z^2} \mathrm{erfc}(z)$ is monotone increasing [16] bounded between 0 and 1. Thus for positive η the left-hand side of (3.2) is monotone decreasing from K_1 to 0 when $K_1 > 0$ and is monotone increasing from K_1 to 0 when $K_1 < 0$. The right-hand side is monotone increasing from 1 to $1 + K_2$. Thus a unique solution to positive η or a negative λ_0 exists if and only if $K_1 > 1$ or

$$-(k_I \beta_I / k_0 \beta_0 r_I)(f_0 / \psi_0) > 1 \tag{3.3}$$

It is seen from (2.22) that when λ_0 exists, all coefficients of zeroth order exist and are unique.

Proof of the existence of coefficients of higher order can be accomplished as in some previous papers on moving boundary problems [13-18]. However, the present problem is more involved. The proof, though straight-forward, is quite lengthy. We will not reproduce it. Basically, we first solve for λ_N by eliminating all other coefficients or order N. It can then be shown that λ_N exists and is uniquely determined. This, in turn, shows that all coefficients of order N are uniquely determined.

Let us now turn to the convergence of the series solution. Their convergence can be implied from the maximum principle of the parabolic equation or can be proved directly as in some previous papers on moving boundary problems [13-18]. The complete detail of the direct proof is also very lengthy. It will not be reproduced here. Essentially, the maximum principle guarantees that the maximum value of the function occurs at the boundary of the $x-t$ domain. Since the data on the boundary are bounded by specification, both the velocity and temperature in the interior are less than the corresponding functions at one of the interfaces. We can thus state that all series solutions are convergent.

4 Physical Interpretation

In the preceding section we have shown that a unique solution of ablation exists only when the inequality

$$(k_I \beta_I / k_0 \beta_0 r_I) f_0 + \psi_0 > 0 \tag{4.1}$$

is satisfied. In this study we exclude the possibilities that resolidification might occur. For proper ablation we assume that $\psi_0 < 0$ and $\omega_0 > 0$. Using $\epsilon < 1$, we find from (2.23) and (2.15) that $R_{I,0}(\zeta) < 0$ and $Q_{I,0}(\zeta) > 0$. Then from (2.21) and (2.22) we find that $g_0 > 0$ and $f_0 > 0$. This in turn shows that K_1 is positive. Thus the foregoing inequality is satisfied by large values of f_0 or small absolute values of ψ_0. A large value of f_0 can be achieved by a large ϕ_0 or a large ω_0. Physically, it means that a unique solution exists when (*i*) the relative motion between the solid and the fluid is large, (*ii*) the initial temperature of the solid is close to the melting temperature, or (*iii*) the initial temperature of the fluid is high above the melting temperature. From a physical point of view, these three effects are expected to be the dominant factors.

To further explore the physical meaning of this inequality, let us first consider $K_1 = 1$. It shows $\lambda_0 = 0$. Equation (3.3) becomes

$$(k_I \beta_I / k_0 \beta_0 r_I) f_0 + \psi_0 = 0 \quad \text{or} \quad (k_{II} \beta_{II} / k_0 \beta_0 r_{II}) g_0 + \psi_0 = 0 \tag{4.2}$$

The condition $K_1 = 1$ is equivalent to the condition that the surface temperature of the solid at contact is initially at the melting temperature. To prove this assertion, let us consider the case where no ablation occurs. There are only two materials, solid and liquid. The velocity and temperature solutions are found to be

$$v_{II}(x,t)=\sum_0 \phi_n(2\tau)^n G_n(\gamma_{II}\zeta_{II}) + \sum_0 c_n^*(2\tau)^n i^n \mathrm{erfc}(\gamma_{II}\zeta_{II})$$

$$T_0(x,t)=\sum_0 \psi_n(2\tau)^n G_n(\beta_0\zeta_0) + \sum_0 d_n^*(2\tau)^n i^n \mathrm{erfc}(-\beta_0\zeta_0)$$

$$T_{II}(x,t)=\sum_0 g_n^*(2\tau)^n G_n(\beta_{II}\zeta_{II}) + \sum_0 h_n^*(2\tau)^n i^n \mathrm{erfc}(\beta_{II}\zeta_{II}) + \sum_0 (2\tau)^n R_{II,n}^*(\beta_{II}\zeta_{II}) \tag{4.3}$$

where $R_{II,n}^*(\zeta)$ is the same as $R_{II,n}(\zeta)$ in (2.18) with the exception that c_n are replaced by c_n^*. The preceding equations satisfy the prescribed initial conditions. Using the continuity requirements at the common boundary, we find

$$c_n^*=-[1+(-1)^n]\phi_n/2$$

$$h_n^*=d_n^*-(g_n^*-\psi_n)$$

$$d_n^*=(g_n^*-\psi_n)\left[\frac{1+(-1)^n}{2} + \frac{k_0\beta_0 r_{II}}{k_{II}\beta_{II}}\frac{1}{n-2}(1-(-1)^n)\right]/\left[1+\frac{k_0\beta_0 r_{II}}{k_{II}\beta_{II}}\right] \tag{4.4}$$

The surface temperature T_s at $x=0$ is

$$T_s(t)=T_0(0,t)=T_{II}(0,t) = \sum_0 (2\tau)^n[\psi_n G_n(0)+d_n^* i^n \mathrm{erfc}(0)] \tag{4.5}$$

Ablation will occur only when the surface temperature of the solid is at or above the freezing point. At $t=0$ we have

$$T_s(0)=T_0(0,0)=\psi_0+d_0^*>0$$

or

$$(k_0\beta_0 r_{II}/k_{II}\beta_{II})\psi_0+g_0^*>0 \tag{4.6}$$

This is the same as (4.2). Thus the inequality $K_1>1$ is equivalent to the statement that the surface temperature of the solid must be at or above the melting point before ablation appears.

5 Preablation

It has been shown that ablation starts immediately only when the inequality (3.3) is satisfied. When $K_1<1$, it does not mean that there is no ablation. With proper initial conditions the surface temperature of the solid, at some later time, may reach the melting point and ablation will then appear. It is also possible that the surface temperature of the solid will never reach the melting point, then no ablation will ever occur. If the initial conditions of both velocity and temperature are so prescribed that the surface temperature will reach the melting point at a later time, it is then necessary to know the "waiting" time t_w of this preablation period.

The solution to this preablation period is the same as in (4.3). The surface temperature at $x=0$ is

$$T_s(t)=\sum_0 (2\tau)^n[\psi_n+d_n^*]=T_{int}-\sum_0 p_n\tau^{n+1} \tag{5.1}$$

Using Lagrange's inversion formula, we find

$$t^{1/2}=\tau=\sum_0 q_n(T_{int}-T_s)^{n+1}/(n+1)! \tag{5.2}$$

where

$$q_n=D_\tau^n\{[\tau/(T_s)]^{n+1}\}_0=D_\tau^n[(\Sigma p_n\tau^n)^{-n-1}]_0$$

$$=\sum_{m=0}^{n}(-1)^m(m+n)!Z_m^n(p)/(p_0)^{m+n+1}$$

Taking $T_s=T_f=0$, we obtain

$$\tau_w=\sum_0 q_n(T_{int})^{n+1}/(n+1)! \tag{5.3}$$

With known waiting time τ_w, we may proceed to solve the ablation problem. In this case the initial conditions are no longer prescribed by specifications. They are generally not in some special forms suitable for known similarity solutions. The solution can, however, be analogously derived as those given in the previous sections. As a matter of fact, after we introduce

$$t^+=t-t_w, \qquad \Phi^+(x)=v_{II}(x,t_w)$$
$$\Psi^+(x)=T_0(x,t_w), \qquad \Omega^+(x)=T_{II}(x,t_w) \tag{5.4}$$

the velocity and temperature solutions are those derived in the previous sections.

Acknowledgment

This research was based on work supported by the National Science Foundation under Grant MEA 79-21350.

References

1 Riemann, G. F. B., and Weber, H., "Die Partiellen Differentialgleichungen der Mathematischen Physik," Bd. 2, 5-fl.Aufl., Braunschweig, 1912.

2 Stefan, J., "Über einige Probleme der Theorie der Wärmeleitung," *S.-B. Wien. Akad. Mat. Natur.*, Vol. 98, 1889, pp. 473–484.

3 Rubinstien, L. I., "The Stefan Problem," *Translations of Mathematical Monographs*, Vol. 27, American Mathematical Society, Providence, 1971.

4 Carslaw, H. S., and Jaeger, J. C., *Conduction of Heat in Solids*, 2nd Ed., Clarendon Press, Oxford, 1959.

5 Crank, J., *The Mathematics of Diffusion*, 2nd Ed., Clarendon Press, Oxford, 1975.

6 Ockendon, J. R., and Hodgkins, W. R., eds., *Moving Boundary Problems in Heat Flow and Diffusion*, Clarendon Press, Oxford, 1975.

7 Wilson, D. G., Solomon, A. D., and Boggs, P. T., eds., *Moving Boundary Problems*, Academic Press, New York, 1978.

8 Ozisik, M. N., *Heat Conduction*, Wiley, New York, 1980.

9 Fasano, A., and Primicerio, M., eds., *Free Boundary Problems: Theory and Applications*, 2 vols., Pitman, Boston, 1983.

10 Bankoff, S. G., "Heat Conduction or Diffusion With Change of Phase," *Advance in Chemical Engineering*, Vol. 5, 1964, pp. 75–150.

11 Muehlbauer, J. C., and Sunderland, J. E., "Heat Conduction With Freezing or Melting," ASME *Applied Mechanics Review*, Vol. 18, 1965, pp. 951–959.

12 Boley, B. A., "Survey of Recent Developments in the Fields of Heat Conduction in Solids and Thermo-Elasticity," *Nuclear Engineering and Design*, Vol. 18, 1972, pp. 377–399.

13 Tao, L. N., "The Stefan Problem With Arbitrary Initial and Boundary Conditions," *Quart. Appl. Math.*, Vol. 36, 1978, pp. 223–233.

14 Tao, L. N., "On Free Boundary Problems With Arbitrary Initial and Flux Conductions," *ZAMP*, Vol. 30, 1979, pp. 416–426.

15 Tao, L. N., "Free Boundary Problems With Radiation Boundary Conditions," *Quart. Appl. Math.*, Vol. 37, 1979, pp. 1–10.

16 Tao, L. N., "The Analyticity of Solutions of the Stefan Problem," *Arch. Rational Mech. Anal.*, Vol. 72, 1980, pp. 285–301.

17 Tao, L. N., "On Solidification Problems Including the Density Jump at the Moving Boundary," *Quart. J. Mech. Appl. Math.*, Vol. 32, 1979, pp. 175–185.

18 Tao, L. N., "The Stefan Problem of Polymorphous Material," ASME Journal of Applied Mechanics, Vol. 46, 1979, pp. 789–794.

19 Grigorian, S. S., "On Heating and Melting of a Solid Body Owing to Friction," *Prikl. Mat. Meh.*, Vol. 22, 1958, pp. 577–585; also English translation, *J. Appl. Math. Mech.*, Vol. 22, 1958, pp. 815–825.

20 Tao, L. N., "Ablation by Frictional Heating," ASME Journal of Applied Mechanics, Vol. 50, 1983, pp. 712–716.

21 Wilson, D. G., "Lagrangian Coordinates for Moving Boundary Problems," *SIAM J. Appl. Math.*, Vol. 42, 1982, pp. 1195–1201.

22 Widder, D. V., *The Heat Equation*, Academic Press, New York, 1975.

23 Tao, L. N., "On the Material Time Derivative of Arbitrary Order," *Quart. Appl. Math.*, Vol. 36, 1978, pp. 323–324.

24 Abramowitz, M., and Stegun, I. A., eds., *Handbook of Mathematical Functions*, Dover, New York, 1965.

25 Tao, L. N., "Heat Conduction With Nonlinear Boundary Conditions," *ZAMP*, Vol. 32, 1981, pp. 144–155.

E. N. Kuznetsov
Professor,
Department of General Engineering,
University of Illinois,
Urbana, Ill. 61801
Mem. ASME

Statics and Geometry of Underconstrained Axisymmetric 3-Nets

A 3-net is a system formed by three intersecting arrays of linear flexible members such that every intersection involves one member of each array. The subject of this study is an axisymmetric 3-net where the first array is meridional and the other two are inclined to a meridian at equal but opposite angles. If the net intersections are not fixed the system is underconstrained and, generally, does not possess a unique configuration. However, such systems allow exceptional configurations in which they lack kinematic mobility and admit prestress. Pertinent equations governing the intricately interrelated statics and geometry of axisymmetric 3-nets are developed and some closed-form solutions are obtained. On this basis, two particular classes of immobile (static) 3-nets are synthesized and two corresponding sets of feasible geometric shapes are investigated.

Introduction and Problem Statement

A 3-net is formed by three intersecting arrays of linear flexible members (Fig. 1) with every intersection involving one member from each of the arrays. If intersections are fixed the system is a discrete membrane: it can be given an arbitrary shape; its intrinsic geometry is invariant; under given loads and boundary conditions it behaves (and can be analyzed) as a conventional thin membrane. However, if the members of just one array are allowed to slide at the intersections, an underconstrained system results. The same is the case when the intersections are not fixed at all so that the members of all three arrays can mutually slide.

An underconstrained system has a positive number of degrees of freedom and generally admits a variety of geometric configurations. In any given configuration such a system can balance only special, so-called equilibrium loads; to support any other load, the system must change its configuration at the expense of kinematic and, possibly, elastic deformations. This intricate interrelation between the equilibrium loads and configurations of underconstrained systems underlies the concept of statically controlled geometry: system geometry is attained and, if desired, can be actively controlled by monitoring the external loads.

Varying the geometric parameters of an underconstrained system does not affect its number of degrees of freedom, and gives rise to a series of different geometric configurations. Among these there exist certain exceptional ones where the system, in spite of the positive number of degrees of freedom, lacks kinematic mobility [1]. Such exceptional configurations can be considered as natural configurations of an underconstrained system and can be identified or synthesized using the following statical criterion [2]: an underconstrained system allowing a stable state of self-stress is immobile (static). Note that only the statical *possibility* (not the actual presence) of a stable self-stress is the characteristic sign of the static configuration, although prestressing enhances the system performance in resisting a general load.

The geometry of an underconstrained system allowing self-stress is not arbitrary, which raises the problem of establishing the set of feasible shapes along with the corresponding statical-geometric interrelations. The present study addresses this problem as applied to an underconstrained axisymmetric 3-net. The system involves a net formed by two symmetrically inclined arrays of cables with either free or fixed intersections and an array of meridional members that are fixed only at their ends. Since meridians of a surface of revolution have zero geodesic curvature these members can be made of partially overlapping thin narrow strips enveloping the net surface. It is assumed that the cables resist only tension whereas the meridional members can support both tension and compression. In the latter case, the

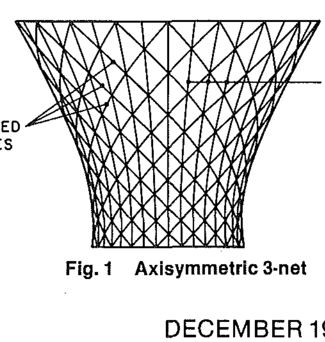

Fig. 1 Axisymmetric 3-net

Contributed by the Applied Mechanics Division and presented at the Winter Annual Meeting, New Orleans, La., December 9-14, 1984 of THE AMERICAN SOCIETY OF MECHANICAL ENGINEERS.

Discussion on this paper should be addressed to the Editorial Department, ASME, United Engineering Center, 345 East 47th Street, New York, N.Y. 10017, and will be accepted until two months after final publication of the paper itself in the JOURNAL OF APPLIED MECHANICS. Manuscript received by ASME Applied Mechanics Division, January, 1984. Paper No. 84-WA/APM-39. Copies will be available until August, 1985.

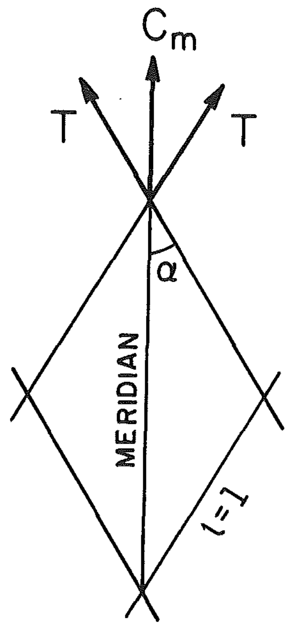

Fig. 2 Generic element of net

net is assumed sufficiently fine to prevent local buckling of the meridional members between two adjacent intersections (overall buckling is precluded by the tension arrays acting as a continuous lateral constraint).

It is readily seen that an entirely tensile 3-net must be of negative Gaussian curvature and the axial resultant of its prestressing forces is tension. It is not obvious in advance what these characteristics can be for a system involving compressed meridians. In particular, it is interesting whether a self-contained (statically self-balanced) system is feasible, i.e., whether the axial resultants of the compression and tension prestressing forces can cancel each other.

The solution to the stated problem in its entirety first calls for establishing the number and the nature of arbitrary elements governing the interdependent statics and geometry of an immobile underconstrained 3-net.

Pertinent Statical-Geometric Relations

In an underconstrained 3-net subjected to a normal surface load, the force in the meridional members per unit polar angle does not vary along the member length. Generally, this is not the case with the inclined cables where the force pattern is closely related to the intrinsic geometry of the net. If the tension, T, in a given cable, is referred to the unit length of its counterpart cable (Fig. 2), the resulting meridional and hoop forces are, respectively,

$$T_1 = T \operatorname{ctn} \alpha, \qquad T_2 = T \tan \alpha \tag{1}$$

where α is half the net angle. Introducing (1) into the equilibrium condition of an axisymmetric membrane in the meridional direction gives

$$r(T \operatorname{ctn} \alpha)' + r' T(\operatorname{ctn} \alpha - \tan \alpha) = 0 \tag{2}$$

Here r is the radius of revolution and a prime denotes differentiation with respect to the axial coordinate, z. Equation (2) admits a quadrature

$$Tr \operatorname{ctn}\alpha = C_n f(r) \tag{3}$$

where

$$f(r) = \exp\int_{r_0}^{r} \tan^2\alpha dr/r \tag{4}$$

with the subscript 0 designating (here and in the following) a reference axial location $z = z_0$. According to (1), expression (3) represents the meridional force in the net per unit polar angle and the integration constant C_n is the magnitude of this force

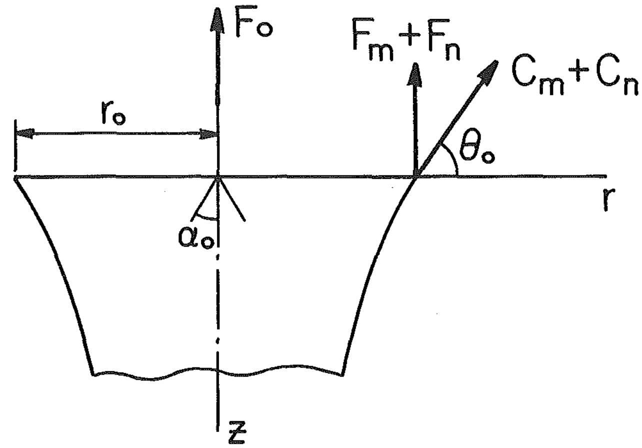

Fig. 3 Geometric parameters and forces of 3-net

at z_0. Note that solution (3) is valid for any normal surface pressure since normal load is irrelevant for equation (2).

Adding force (3) to the constant force C_m in the meridional members and projecting the sum on the z-axis (Fig. 3) allows the internal axial force in the 3-net, F, to be evaluated. Setting it equal to the axial force due to the surface pressure P results in

$$F = 2\pi[C_m + C_n f(r)]\sin \theta = F_0 + 2\pi\int_{r_0}^{r} Prdr \tag{5}$$

where

$$F_0 = 2\pi(C_m + C_n)\sin \theta_0 = F_m + F_n \tag{6}$$

and θ is the meridian slope. Equation (5) interrelates the equilibrium loads and configurations of an axisymmetric 3-net and can be used in two ways. First, for a given load, the corresponding equilibrium configuration of the 3-net can be determined. This is done by using the substitution:

$$\sin \theta = (1 + r'^2)^{1/2} \tag{7}$$

which reduces (5) to a first-order equation between r and z. Second, for a given 3-net (with a known geometry), the equilibrium loads can be evaluated. To this end, equation (5) is differentiated and, taking advantage of

$$\sigma_1 = d \sin \theta/dr, \qquad \sigma_2 = \sin \theta/r \tag{8}$$

where σ_1 and σ_2 are the principal curvatures of the surface, transformed to the following form

$$C_m\sigma_1/r + C_n(\sigma_1 + \sigma_2\tan^2\alpha)f(r)/r = P \tag{9}$$

From here, it is obvious that any equilibrium normal load is a linear combination of the two known axisymmetric functions – those accompanying the parameters C_m and C_n in (9). However, there exists a fundamental difference in this regard between an ordinary 3-net and a static one. For the latter, the possibility of a self-stress stipulated by the general criterion of a static system requires the existence of a nontrivial solution to the homogeneous equilibrium equation (hence the term "natural configuration"). In this case the two functions in (9) must be affine; as a result, the equilibrium load for a static 3-net is determined modulo one parameter.

Feasible shapes of static 3-nets are obtainable from the slightly modified equation (5) with $P = 0$:

$$[C + f(r)]\sin \theta = (C+1)\sin\theta_0 \qquad (C = C_m/C_n = F_m/F_n) \tag{10}$$

Note that F_m and F_n were introduced in (6) as the respective contributions of the meridional members and of the net to the total axial force at the reference parallel. In a prestressed 3-net, the two components of the axial force vary along the z-axis while their sum preserves.

Like the preceding pertinent equations, equation (10) contains function $f(r)$ which is defined by (4) and can be evaluated only upon specifying the relation betweeen r and α.

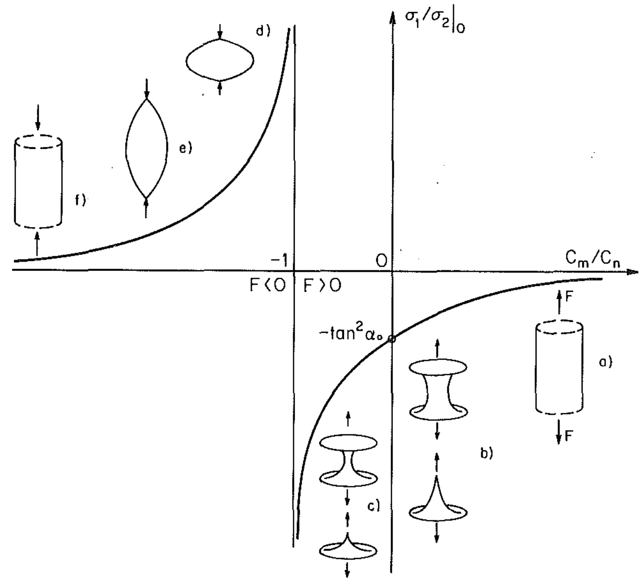

Fig. 4 Feasible shapes of Chebyshev 3-nets

This, in turn, requires knowing the intrinsic geometric properties of the net. In what follows, the two most important types of nets are investigated—a Chebyshev net and a geodesic net.

A Chebyshev net is most common: it has rhombic cells and fixed intersections. It was proved by Chebyshev that due to the variability of the net angle the net is applicable to any smooth surface. In the axisymmetric case,

$$r = c \sin \alpha \tag{11}$$

where c is the maximum radius kinematically attainable for the given net. Thus, for a Chebyshev net, equation (4) yields

$$f(r) = [(c^2 - r^2)/(c^2 - r_0^2)]^{1/2} = \cos \alpha_0 / \cos \alpha \tag{12}$$

A geodesic net is one formed by geodesic arrays. The significance of this net lies in the following fact: if, under a normal surface load and/or prestress, a net meets *one* of the three conditions: (*a*) it is geodesic; (*b*) its intersections do not transfer tangential forces; (*c*) member forces do not vary along the length; then *all* of the three conditions are met. An axisymmetric geodesic net obeys the Clairaut formula

$$r \sin \alpha = c \tag{13}$$

where c is the radius of the smallest parallel circle (if it is not the equator) of the net. As a result,

$$f(r) = (r_0/r)[(r^2 - c^2)/(r_0^2 - c^2)]^{1/2} = \cos \alpha / \cos \alpha_0 \tag{14}$$

and solution (3) becomes a relation similar to those well known in literature since pioneering works [3, 4]:

$$Tr/\sin \alpha = C_n / \cos \alpha_0 \tag{15}$$

Now particular configurations of static 3-nets are obtainable explicitly: after replacing $f(r)$ by either (12) or (14) and specifying parameters C, α_0, and θ_0, equation (10) can be integrated numerically upon the assignment of the initial radius r_0. However, r_0 is but a scale factor which only establishes the physical size of the system and does not contribute to the variety of feasible shapes. Therefore a systematic and comprehensive qualitative survey of these shapes is conveniently carried out on the basis of the foregoing closed-form solutions without numerical integration.

Chebyshev 3-Nets

This name is retained for a 3-net where the first array is diagonal to the Chebyshev net formed by the two remaining arrays. The set of equilibrium shapes is explored by studying the interrelations between parameters representing the state of self-stress and those describing the geometric configuration of a 3-net. The most convenient statical parameter is the ratio $C = C_m/C_n$ of the prestressing forces at the reference cross section $z = z_0$. The principal curvature ratio at the same location is chosen as the most suitable parameter characterizing the overall geometric shape of a 3-net. The sought relation is found from (9) and (12) at $P = 0$ and $r = r_0$:

$$\sigma_1/\sigma_2|_0 = -\tan^2\alpha_0/(C+1) \tag{16}$$

Combining (10) and (12) yields another useful relation:

$$(C + \cos \alpha_0/\cos \alpha)\sin \theta = (C+1)\sin \theta_0 \tag{17}$$

In Fig. 4, the graph of equation (16) is used as a reference for the set of equilibrium shapes evolving as a function of $C = C_m/C_n$. The limiting case of $C \rightarrow \infty$ results in a cylindrical 3-net (*a*) with inclined arrays force-free and the meridional members supporting the entire axial load F. As C decreases, a succession of entirely tensile, hourglass-shaped forms evolve, with a noteworthy case (*b*) where $C = 0$. In this configuration the meridional members are idle ($C_m = 0$, in transition from tension to compression) while the inclined array net carries the entire axial load. Equation (17) simplifies to

$$\sin \theta / \cos \alpha = \sin \theta_0 / \cos \alpha_0 \tag{18}$$

which allows the Gaussian curvature of the net surface to be evaluated from (8), (9), and (11) as follows:

$$K = \sigma_1 \sigma_2 = -\tan^2 \alpha \sin^2 \theta / r^2 = -\sin^2 \theta_0 / c^2 \cos^2 \alpha_0 = \text{const.} \tag{19}$$

As in known [5] the only surface of revolution with a constant negative Gaussian curvature is a pseudosphere. Therefore, a segment of a Chebyshev net (like a basketball net) stretched between two parallel rings has the form of a pseudosphere. This interesting result, apparently unknown in differential geometry, has been recently obtained in a different way in [6]. It is not difficult to demonstrate that, depending on the sum $\theta_0 + \alpha_0$ being greater than, equal to, or smaller than $\pi/2$, the net acquires, respectively, the form of a hyperbolic, parabolic, or elliptic pseudosphere.

To the left from the point $C = 0$ (Fig. 4) lies the domain of static 3-nets with the meridional array in compression. However, the total axial force F remains tensile until another station, $C = -1$, is reached. Here $F = 0$ and the 3-net should have become self-equilibrated; instead, as is seen from equations (16) and (17), with $C \rightarrow -1$, the system flattens (*c*) and degenerates.

All the 3-nets within the investigated range (except for the two limiting cases) have negative Gaussian curvature but do not necessarily contain an equator. An equator exists when the minimum radius and, by virtue of (11), the minimum net angle occur at $\theta = \pi/2$ and are positive. According to (17) and (6), this condition is satisfied when

$$\sin \theta_0 > C_a \equiv (C + \cos \alpha_0)/(C+1) = (F_m + F_n \cos \alpha_0)/F \tag{20}$$

If this condition is not satisfied the 3-net has an apex where $\alpha = 0$ and the meridian slope, θ_a, is given by

$$\sin \theta_a = \sin \theta_0 / C_a \tag{21}$$

The maximum radius of the net equals c [cf. (11)] and is the radius of regression circle. Here $\theta = 0$ and, as is seen from (10), a prestressed 3-net cannot contain its regression circle.

After disappearing at $C = -1$, the equilibrium shape emerges in a completely different form as a compression system (*d*). From here on, the system always contains an equator and two apexes where the meridian slope is determined by (21). With decreasing value of C, the equilibrium

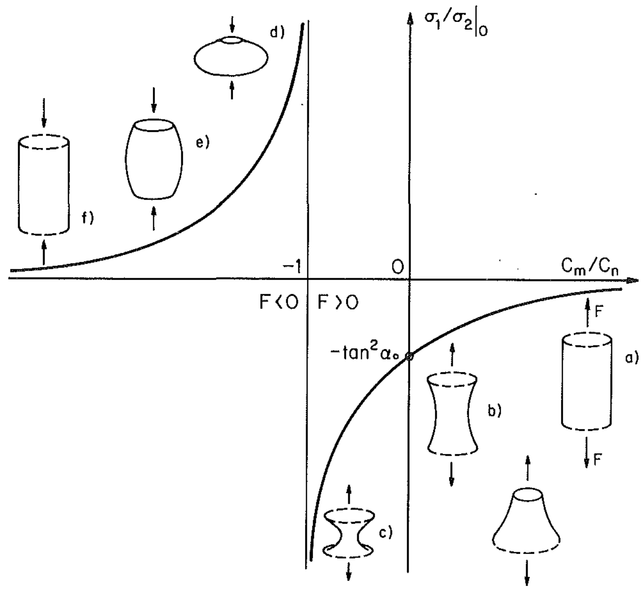

Fig. 5 Feasible shapes of geodesic 3-nets

shapes tend to become more and more oblong (*e*) and finally the limiting case of $C \rightarrow -\infty$ produces a cylinder (*f*) with compressed generators, thus completing the set of feasible shapes of static Chebyshev 3-nets.

Geodesic 3-Nets

The striking similarity between formula (12) for a Chebyshev net and its counterpart (14) for a geodesic net is somewhat surprising for the nets of such different geometric origins. This similarity is both the starting point and the basis of a far reaching parallelism in the analysis of the two nets. For a static geodesic 3-net, equation (16) preserves and its graph is used once again as a reference for the set of equilibrium shapes (Fig. 5). The key relation between the angle α and the meridian slope θ is obtained from (10) and (14):

$$(C+\cos\alpha/\cos\alpha_0)\sin\theta=(C+1)\sin\theta_0 \tag{22}$$

The cylindrical geodesic 3-net (*a*) corresponding to $C \rightarrow \infty$ is identical with its Chebyshev counterpart: in both cases the inclined arrays are two counterwound helices forming a net that is simultaneously Chebyshev and geodesic. With decreasing C, the originally force-free geodesic net takes on a gradually increasing portion of the axial load and at $C = 0$ it supports the entire load F. In this configuration the meridional members are force-free and do not exert any normal pressure on the net. As a result, the inclined cables have zero normal curvature in addition to being geodesic. This means that they are straight and the surface is ruled. Since the only axisymmetric ruled surface is a one-sheet hyperboloid of revolution, this is the shape of a static geodesic 3-net at $C = 0$ [(*b*) in Fig. 5].

The series of hourglass shapes between (*a*) and (*b*) do not always contain the equator. This is verified by evaluating cos α at the equator ($\theta = \pi/2$) from equation (22); cos α being positive requires that

$$\sin\theta_0 > C_t \equiv C/(C+1) = F_m/F \tag{23}$$

When (23) is not satisfied the 3-net surface truncates at the axial location with $\alpha = \pi/2$ where the meridian slope θ_t and the radius r_t are determined, respectively, by

$$\sin\theta_t=\sin\theta_0/C_t, \qquad r_t=c=r_0\sin\alpha_0 \tag{24}$$

Unlike Chebyshev 3-nets, static geodesic 3-nets of negative Gaussian curvature do not have a maximum radius and expand indefinitely in the axial direction with increasing radius. The corresponding parallel circles in Fig. 5 are shown by broken lines as opposed to the solid lines designating the terminal (truncation) parallels.

As is seen from (23), tensile systems with compressed meridional members ($0 > C > -1$) never truncate. When approaching the lower limits of this range the system flattens (*c*) and degenerates to emerge in a pill shape (*d*) as a compressed system. Its further evolution with decreasing C leads to a barrel shape (*e*) and at $C \rightarrow -\infty$ ends with the limiting cylindrical shape (*f*).

Note that at $C < -1$ condition (23) cannot be satisfied and the corresponding feasible shapes are always truncated. Indeed, since each of these shapes contains the equator, its plane can be taken as the reference plane, $z = z_0$; then $\sin\theta_0 = 1$ and, in accordance with (23) and (24)

$$\sin\theta_t=(C+1)/C=F/F_m<1 \tag{25}$$

Truncation of geodesic nets is well known [3, 4] in wound shell design where the shell shapes can be nearly arbitrary and both r_t and θ_t for a given shape depend on the chosen initial angle of winding, α_0. The situation is quite different for prestressed geodesic 3-nets. Here the feasible shapes are governed by statics, and the slope θ_t which is determined by the parameter C does not depend on the initial angle α_0.

Summary and Conclusions

1. The natural (static) configuration of an underconstrained axisymmetric 3-net is determined by three arbitrary parameters—the force ratio C, the meridian slope θ_0 and the angle α_0 at the initial parallel. The resulting set of feasible shapes provides a diverse variety of geometric features. A suitable segment of the feasible surface of revolution can be used for applications where the axial symmetry is of no relevance.

2. The established relations between the equilibrium loads and configurations of axisymmetric 3-nets are useful for system selection for a given load and the general assessment of the system's deformability (purely elastic deformation under equilibrium loads versus a combination of kinematic and elastic deformations under a general load).

3. In the context of statically controlled geometry, the found closed-form statical-geometric interrelations can be instrumental in obtaining a required geometric form with a high degree of precision. Subsequently this form can be either made permanent (by introducing additional constraints at the intersections or by fixing the surface with a matrix) or actively controlled (by adjusting the prestressing force or the surface load using some kind of feedback).

Acknowledgment

This material is based on work supported by the National Science Foundation under Grant No. CEE82-012099. The comments of Dr. W. B. Hall are greatly appreciated.

References

1 Levi-Civita, T., and Amaldi, U., *Lecioni di Meccanica Racionale*, Vol. 1, Bologna, 1930 (in Italian).

2 Kuznetsov, E. N., "Theory of Instantaneously Rigid Nets," Translation of the Soviet *Applied Mathematics and Mechanics*, Pergamon Press, Vol. 29, No. 3, 1965, pp. 654–660.

3 Read, W. S., "Equilibrium Shapes for Pressurized Fiberglass Domes," *Journal of Engineering for Industry*, Vol. 85, 1963, pp. 115–118.

4 Pipkin, A. C., and Rivlin, R. S., "Minimum-Weight Design for Pressure Vessels Reinforced with Inextensible Fibers," ASME Journal of Applied Mechanics, Vol. 30, 1963, pp. 103–108.

5 Kreyszig, E., *Introduction to Differential Geometry*, University of Toronto Press, 1968.

6 Kuznetsov, E. N., "Axisymmetric Static Nets," *International Journal of Solids and Structures*, Vol. 18, 1982, pp. 1103–1112.

P. J. Torvik
Professor and Head,
Department of Aeronautics and Astronautics,
Air Force Institute of Technology,
Wright-Patterson Air Force Base, Ohio 45433

A Variational Approach to the Dynamics of Structures Having Mixed or Discontinuous Boundary Conditions

A procedure is developed whereby the steady-state forced response and the modes of free vibration for elastic systems having mixed or discontinuous boundary conditions can be determined. Approximate solutions are obtained as a superposition of a set of functions, each of which satisfies the field equations but not the boundary conditions. The coefficients of this expansion are obtained through applying a variational principle developed from Hamilton's principle which for simple harmonic motion, is equivalent to Reissner's principle. The reduction from the general elastic solid to the elastic plate is given, as are some results obtained for the first several natural frequencies of an elastic circular plate, free on a portion of the boundary and clamped on the remainder.

1 Introduction

The natural frequencies of elastic plates have been determined by many methods. For thin plates of uniform thickness, simple shapes, and simple boundary conditions, the eigenfunctions may be determined through separation of variables, and the natural frequencies determined. Many such solutions have been tabulated [1].

For plates that are not of uniform thickness or properties, such approximate techniques as the Rayleigh-Ritz and Galerkin methods may be applied. These methods are best suited to estimating natural frequencies for systems having simple boundary conditions, i.e., bounding curves coincident with coordinate lines, and with continuous boundary conditions along segments of the bounding curves. In other cases, numerical methods such as finite difference and finite element techniques must be applied. A survey of progress in these more complicated problems has recently been prepared [2].

There are, however, problems for which the need for approximation arises not because of complications in the field equations, but through difficulty in satisfying the boundary conditions. Such examples are plates of complex shape and plates with discontinuous edge conditions. In such cases, appropriate trial functions can be constructed through superposition of functions that satisfy the field equations only, with the coefficients being determined by a process such as boundary integral techniques, collocation, minimization of squared error on the boundary, or the method of weighted boundary residuals. These same methods have been used with some success to determine natural frequencies of plates of various shapes [1, 3].

Discontinuous, or mixed boundary conditions may be divided into two classes, depending on whether one or more boundary specification changes. In the case of plates, the first class includes the transition from simply supported to clamped, from clamped to guided, from simply supported to free, or from guided to free. The second includes the transition from clamped to free and from simply supported to guided. Problems from this class have received some attention [4–7].

A variational principle developed from Hamilton's principle will be used to develop a procedure for determining the general response of elastic structures having mixed boundary conditions and then applied to find the natural frequencies of a circular plate, partly clamped and partly free.

2 The Variational Principle

In the application of Hamilton's principle, it is necessary to seek an extremal value of the Lagrangian function over a class of admissible virtual displacements that vanish, for all time, over the portion of the boundary where the displacements are to be prescribed [8]. For the class of problems considered in this work, finding such functions is not readily done; therefore it is of interest to investigate the possibility of extending the class of admissible functions to include functions that do not satisfy the boundary conditions on those segments of the boundary where tractions are presecribed, nor on those portions whre displacements are given.

This relaxation of requirements on the trial functions is

Contributed by the Applied Mechanics Division and presented at the Winter Annual Meeting, New Orleans, La., December 9–14, 1984 of The American Society of Mechanical Engineers.

Discussion of this paper should be addressed to the Editorial Department, ASME, United Engineering Center, 345 East 47th Street, New York, N.Y. 10017, and will be accepted until two months after final publication of the paper itself in the Journal of Applied Mechanics. Manuscript received by ASME Applied Mechanics Division, November, 1982; final revision, February, 1984. Paper No. 84-WA/APM-21.

Copies will be available until August, 1985.

precisely that permitted in the use of Reissner's principle [9], which is applicable to both the static response and the simple harmonic motion [10, 11] of elastic systems. Although the example problem considered in the present work is of this latter category and Reissner's principle is applicable, it is of interest to begin with Hamilton's principle and to derive a somewhat more general result.

We begin by writing a Lagrangian function, where the strain energy of an elastic material is written in terms of a strain energy density, W; the kinetic energy, K; and the potential energy of conservative external forces, A. Thus

$$L=\int_V W(e_{ij})\,dV-\int_V \frac{\rho}{2}\,\dot{u}_i\dot{u}_i dV - \int_{S_\sigma} T_i{}^* u_i dS - \int_V F_i u_i dV \tag{1}$$

The volume of interest, V, is enclosed by the surface $S = S_u + S_\sigma$, where S_u is the portion of the boundary on which displacements are to be prescribed and S_σ is the portion on which tractions, $T_i{}^*$, are given. The body force, F_i is presumed to be prescribed. The customary requirement that the displacements satisfy a boundary condition is replaced by a constraint,

$$C_1=\int_{S_u} \Gamma_i\,(u_i-u_i{}^*)dS \tag{2}$$

where the Γ_i are Lagrange multipliers. We assume, as in the further generalization of Reissner's principle due to Washizu, [12] that the strains and displacements may be varied independently. Thus, the requirement of satisfaction of the strain-displacement equations is replaced by constraints of the form

$$C_2=\int_V \lambda_{ij}\left[e_{ij}-\frac{1}{2}\,(u_{i,j}+u_{j,i})\right]dV \tag{3}$$

where the comma denotes partial differentiation. The strains are assumed to be symmetric, thus the λ_{ij} are also.

The new functional is

$$L^*(u_i,\dot{u}_i,\lambda_{ij},\Gamma_i)=U-K+A-C_1-C_2 \tag{4}$$

and may be recognized as a time-dependent version of the functional used in Washizu's generalization. We now seek to determine conditions under which the time integral of the modified Lagrangian function assumes a stationary value with all 21 arguments of the integrand varied independently. If the trial functions, u_i, and the λ_{ij} have sufficient continuity as to permit the necessary application of the divergence theorem, and if

$$\delta u_i\,(t_1)=\delta u_i\,(t_2)=0 \tag{5}$$

we find the vanishing of the first variation necessitates that

$$\begin{aligned}\int_{t_1}^{t_2}\int_V \left\{\frac{\partial W}{\partial e_{ij}}-\lambda_{ij}\right\}\delta e_{ij}dvdt &+\int_{t_1}^{t_2}\int_V \{-\lambda_{ij,i}+\rho\ddot{u}_i-F_i\}\,\delta u_i dvdt \\ &-\int_{t_1}^{t_2}\int_V \left\{e_{ij}-\frac{1}{2}\,(u_{i,j}+u_{j,i})\right\}\delta\lambda_{ij}dvdt \\ &+\int_{t_1}^{t_2}\int_{S_u} (\nu_j\lambda_{ij}-\Gamma_i)\,\delta u_i dSdt \\ &+\int_{t_1}^{t_2}\int_{S_\sigma} \{\nu_j\lambda_{ij}-T_i{}^*\}\,\delta u_i dSdt \\ &-\int_{t_1}^{t_2}\int_{S_u} \{u_i-u_i^*\}\,\delta T_i dSdt=0\end{aligned} \tag{6}$$

We recognize from the first integral that the Lagrange multipliers λ_{ij} have the physical interpretation of the components of stress in an elastic body, σ_{ij}, and from the fourth that the Γ_i have the physical interpretation of the components of traction, T_i, since the ν_j are the components of the normal vector at a point on the surface. Thus, three sets of Euler equations result

$$\frac{\partial W}{\partial e_{ij}}=\sigma_{ij}\quad \text{in}\quad V \tag{7}$$

$$\sigma_{ij,\,j}+F_i=\rho\ddot{u}_i\quad \text{in}\quad V \tag{8}$$

$$e_{ij}=\frac{1}{2}\,(u_{i,\,j}+u_{j,i})\quad \text{in}\quad V \tag{9}$$

and the necesary boundary conditions are seen to be

$$T_i=\nu_j\sigma_{ij}\quad \text{on}\quad S=S_u+S_\sigma \tag{10}$$

$$T_i=T_i{}^*\quad \text{on}\quad S_\sigma \tag{11}$$

$$u_i=u_i{}^*\quad \text{on}\quad S_u \tag{12}$$

Since these are the field equations and boundary conditions of elastodynamics, we conclude that the proposed extension is appropriate, whether it be viewed as a relaxation of the class of functions to be used with Hamilton's principle, or as an extension of Reissner's principle to other than simple harmonic motions. Equation (6), it should be noted, is included in the further generalization due to Yu [13]. This dynamic variational principle differs from that of Dean and Plass [14] in that δu_i need not vanish on S_u.

3 An Appropriate Method

Our interest here, of course, is not in deriving once again the equations of elastodynamics, but rather in developing a procedure whereby approximate solutions can be obtained for otherwise intractable problems. To do this, we return to equation (6) and make use of the identification that the Lagrange multipliers are, in fact, stresses and tractions.

We are interested in the class of problems for which a number of solutions to the field equations are readily obtained, but for which difficulties arise in obtaining solutions because of mixed boundary conditions. We assume that a large number, N, of systems of stresses, σ_{ij}^n, and displacements, u_i^n, can be found, and that each system satisfies equation (7)–(9). We then take as trial functions the superpositions of such solutions, or

$$\sigma_{ij}\,(x,t)=\sum_{n=1}^{N} a_n\sigma_{ij}{}^n\,(x,t) \tag{13}$$

and

$$u_i\,(x,t)=\sum_{n=1}^{N} a_n u_i{}^n\,(x,t) \tag{14}$$

Every such trial function will also satisfy the field equations. Tractions, T_i, may be constructed from these stresses so as to satisfy equation (10) on each point of S.

For such trial functions, the variational principle leads to the requirement that

$$\int_{t_1}^{t_2}\int_{S_\sigma} (T_i-T_i{}^*)\delta u_i dSdt-\int_{t_1}^{t_2}\int_{S_u} (u_i-u_i{}^*)\delta T_i dSdt=0 \tag{15}$$

We propose to construct an algorithm for determining the set of coefficients a_n which, for any N selected, leads to the best approximate solution in the form of equations (13) and (14). The most general arbitrary variation within the space spanned by these N solutions may also be written as an expansion of these same N solutions, or

$$\delta\sigma_{ij} = \sum_{m=1}^{N} \delta a_m \sigma_{ij}^m (x,t) \tag{16}$$

$$\delta u_i = \sum_{m=1}^{N} \delta a_m u_i^m (x,t) \tag{17}$$

Substituting these equations and (13) and (14) into equation (15) leads to a single equation. Since the variation must be arbitrary, however, any convenient choice of coefficients, δa_m, may be made. It is particularly convenient to make the selection:

$$\delta a_m = 0 \quad \text{for} \quad m \neq p, \quad m = 1,N \tag{18}$$

$$\delta a_m = 1 \quad \text{for} \quad m = p, \quad p = 1,N \tag{19}$$

so as to obtain a system of N equations for the N coefficients a_n, or

$$\sum_{n=1}^{N} a_n \int_{t_1}^{t_2} \left\{ \int_{S_\sigma} \nu_j \sigma_{ji}^n u_i^p \, dS - \int_{S_u} u_i^n \nu_j \sigma_{ji}^p \, dS \right\} dt$$

$$= \int_{t_1}^{t_2} \left\{ \int_{S_\sigma} T_i^* u_i^p \, dS - \int_{S_u} u_i^* \nu_j \sigma_{ji}^p \, dS \right\} dt \tag{20}$$

For any given boundary conditions, T_i^* and u_i^*, and for any selected set of solutions to the field equations, the a_n may be found and the approximate solution determined. It has been previously found [15] that static problems with mixed boundary conditions may be successfully treated in a similar manner.

The procedure may be applied to construct an approximate steady-state response to a prescribed boundary excitation

$$T_i^* = \theta_i^* (s) \cos \Omega t \quad \text{on} \quad S_\sigma \tag{21}$$

$$u_i^* = U_i^* (s) \cos \Omega t \quad \text{on} \quad S_u \tag{22}$$

We require N solutions to the field equations, of the form

$$\sigma_{ij}^n = S_{ij}^n (\Omega,\mathbf{x}) \cos \Omega t \tag{23}$$

$$u_i^n = U_i^n (\Omega,\mathbf{x}) \cos \Omega t \tag{24}$$

Substituting these into equation (24) yields a system of linear algebraic equations of the form

$$\sum_{n=1}^{N} a_n C_{np} (\Omega) = P_p \tag{25}$$

where

$$C_{np} = \int_{S_\sigma} \nu_j S_{ji}^n U_i^p \, dS - \int_{S_u} U_i^n \nu_j S_{ji}^p \, dS \tag{26}$$

and

$$P_p = \int_{S_\sigma} \theta_i^* U_i^p \, dS - \int_{S_u} U_i^* \nu_j S_{ji}^p \, dS \tag{27}$$

The time integrals have been eliminated from equation (20) since the equations must be satisfied at every instant. For $S_u = 0$, this procedure reduces to one previously used to determine the response of an elastic strip to a time-harmonic end loading [16].

An approximate solution for the free vibration of an elastic solid with homogeneous boundary conditions may be found by setting to zero the starred quantities. A set of homogeneous algebraic equations results and estimates of natural frequencies arise from finding values of Ω that cause

$$\det(C_{np}) = 0 \tag{28}$$

Corresponding mode shapes may be determined by returning the resulting value of Ω to equation (25) and computing ratios of coefficients.

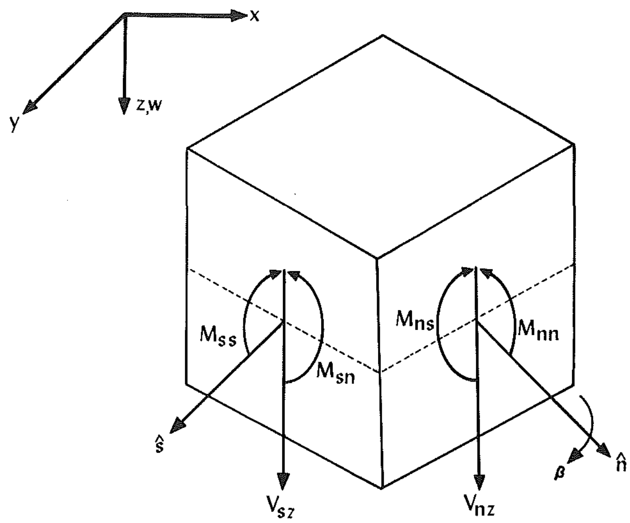

Fig. 1 Sign convention for boundary element

We have now completed the development of a procedure whereby approximations to the forced response of elastic solids to time-harmonic boundary excitations may be obtained. Approximations to the natural frequencies and the corresponding mode shapes may also be developed, even for objects of complex geometry. If the available set of solutions can be shown to be complete, convergence to an exact answer is to be expected in both cases. If the available set of solutions is merely "large," only an approximation can be anticipated.

4 Application to the Vibration of Plates

For the thin, elastic plate the tractions and displacements of equation (15) must be replaced by the moments, forces, displacement, and rotation at the boundary. Recognizing the presence of virtual work and complementary virtual work in equation (15), we write

$$\int_{t_1}^{t_2} \int_{C_\sigma} \{ -(M_{nn} - M_{nn}^*)\,\delta\beta + (Q_{nz} - Q_{nz}^*)\,\delta w \} \, ds \, dt$$

$$- \int_{t_1}^{t_2} \int_{C_\mu} \{ -(\beta - \beta^*)\delta M_{nn} + (w - w^*)\delta Q_{nz} \} \, ds \, dt = 0 \tag{29}$$

The integration path is the line formed by the intersection of the plate edge and midplane. Sign conventions are as given in Fig. 1. The resultant moment and force per unit length are

$$\mathbf{M}_n = \int_{-h/2}^{h/2} \mathbf{T} \, z dz \tag{30}$$

$$V_{nz} = \int_{-h/2}^{h/2} T_z dz \tag{31}$$

$$M_{nn} = \hat{n} \cdot \mathbf{M}_n \tag{32}$$

$$Q_{nz} = V_{nz} + \frac{\partial}{\partial s} (\hat{S} \cdot \mathbf{M}_n) \tag{33}$$

The transverse displacement is w, and the rotation,

$$\beta = \frac{\partial w}{\partial n} \tag{34}$$

Here $\hat{S}$ and $\hat{n}$ are the unit tangent and normal vectors at the boundary. The displacement, w, must satisfy the equation for a vibrating plate with distributed load, q,

$$D\nabla^4 w + \rho\, \ddot{w} = q \tag{35}$$

where ρ is the areal density, h is the thickness, E the modulus, and ν the Poisson's ratio for the plate.

$$D = \frac{Eh^3}{12(1-\nu^2)} \tag{36}$$

and

$$M_{xx} = \int_{-h/2}^{h/2} z\sigma_{xx} dz = -D(w_{xx} + \nu w_{yy}) \tag{37}$$

$$M_{yy} = \int_{-h/2}^{h/2} z\sigma_{yy} dz = -D(w_{yy} + \nu w_{xx}) \tag{38}$$

$$M_{xy} = \int_{-h/2}^{h/2} z\sigma_{xy} dz = -D(1+\nu)\, w_{xy} \tag{39}$$

If a number of solutions to equation (35) may be found, we let

$$w(x,y,t) = a_p W^p(x,y) \cos \omega t \tag{40}$$

and compute M_{nn}, β, and Q_{nz}. The variations are then written in terms of these same solutions and coefficients chosen in the manner of the preceding section.

Equation (26) becomes

$$C_{pq} = \int_{C_\sigma} \{ -M_{nn}^p \beta^q + Q_{nz}^p W^q \} ds - \int_{C_\mu} \{ -\beta^p M_{nn}^q + W^p Q_{nz}^q \} ds \tag{41}$$

As ω appears as a parameter in each displacement, rotation, moment, and force, the vanishing of det (C) provides a transcendental relationship for natural frequencies.

5 Example

As a demonstration of the procedure, we consider the free vibration of a complete circular plate of radius a, having a portion $(-\alpha/2 \le \theta \le \alpha/2)$ of the boundary free, and the remainder clamped, as in Fig. 2. The method we have developed requires the prior knowledge of a set of solutions to be field equation(s). Such a set is easily obtained for the free vibration of a thin plate, in the form

$$w(r,\theta,t) = \sum_{p=1}^{N} W(r,\theta) \cos \Omega t \tag{42}$$

where Ω is one of the natural frequencies (to be determined), and

$$W(r,\theta) = \sum_{p=1}^{N} W_p \cos p\theta = \sum_{p=1}^{N} [A_p J_p(Kr) + B_p I_p(Kr)] \cos p\theta \tag{43}$$

Such functions are appropriate for modes symmetric about a diameter bisecting the free portion of the boundary. For the antisymmetric modes, which will not be considered here, the replacement of $\cos p\theta$ by $\sin p\theta$ is required. Here J_P and I_P are the Bessel functions and modified Bessel functions of the first kind and order p, respectively. The parameter K, which is to be determined, is related to the natural frequency, plate density, and thickness, through

$$K^4 = \rho\Omega^2 / D \tag{44}$$

For a completely clamped plate, the boundary conditions can be satisfied by any one term of the series given by equation (43), leading to the well-known equation for the natural frequencies of the completely clamped circular plate [1]. For a plate with a free edge, the boundary conditions may also be satisfied by a single term. The first several eigenvalues have been tabulated [1].

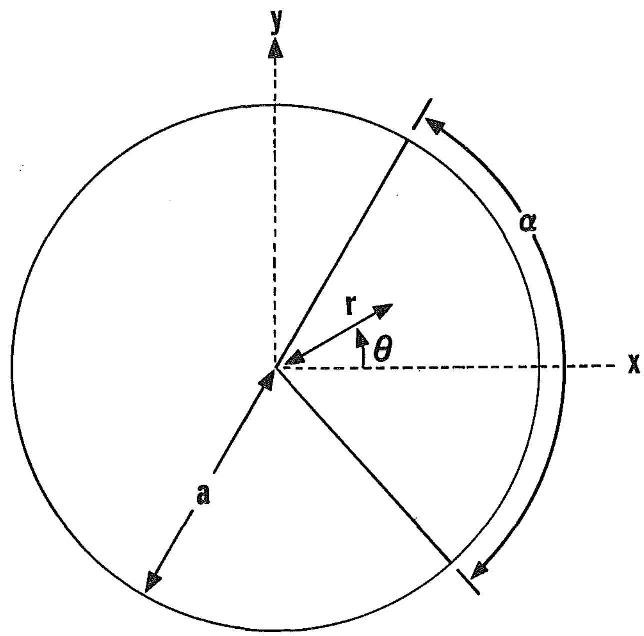

Fig. 2 Circular plate with mixed boundary conditions

For the problem at hand, however, no single term of equation (43) can satisfy the mixed boundary conditions. We may, however, apply the algorithm developed so as to determine the coefficients A_p and B_p which are required for the satisfaction of equation (29). Since this condition is necessary for the satisfaction of the modified form of Hamilton's Principle, we may argue that the resulting sets of coefficients, and the corresponding eigenvalues, are the best, in some sense, which can be obtained by approximating the desired boundary conditions with N functions of the form chosen.

At the boundary of a circular plate,

$$\hat{n} \cdot \mathbf{M}_n = M_{rr} = -D\left\{ \frac{\partial^2 w}{\partial r^2} + \nu\left(\frac{1}{r}\frac{\partial w}{\partial r} + \frac{1}{r^2}\frac{\partial^2 w}{\partial \theta^2} \right) \right\} \tag{45}$$

$$V_{nz} = -D\frac{\partial}{\partial r} \nabla^2 w \tag{46}$$

$$\hat{s} \cdot \mathbf{M}_n = M_{r\theta} = -D(1-\nu)\frac{\partial}{\partial r}\left(\frac{1}{r}\frac{\partial w}{\partial \theta} \right) \tag{47}$$

Substituting into equation (29), setting to zero the prescribed stress resultants and displacements, and eliminating the temporal dependence through integration, yields

$$\begin{aligned}
&\int_0^{\alpha/2} \left\{ \frac{\partial^2 W}{\partial r^2} + \frac{\nu}{r}\frac{\partial W}{\partial r} + \frac{\nu}{r^2}\frac{\partial^2 W}{\partial \theta^2} \right\}_{r=a} \delta\left\{ \frac{\partial W}{\partial r} \right\}_{r=a} d\theta \\
&- \int_0^{\alpha/2} \left\{ \frac{\partial}{\partial r}\nabla^2 W + \frac{(1-\nu)}{r}\frac{\partial^2}{\partial\theta\partial r}\left(\frac{1}{r}\frac{\partial W}{\partial \theta} \right) \right\}_{r=a} \delta\{W\}_{r=a} d\theta \\
&- \int_{\alpha/2}^{\pi} \delta\left\{ \frac{\partial^2 W}{\partial r^2} \left[+ \frac{\nu}{r}\frac{\partial W}{\partial r} + \frac{\nu}{r^2}\frac{\partial^2 W}{\partial \theta^2} \right\}_{r=a} \left\{ \frac{\partial W}{\partial r} \right\}_{r=a} d\theta \\
&+ \int_{\alpha/2}^{\pi} \delta\left\{ \frac{\partial}{\partial r}\nabla^2 W + \frac{(1-\nu)}{r}\frac{\partial^2}{\partial\theta\partial r}\left(\frac{1}{r}\frac{\partial W}{\partial \theta} \right) \right\}_{r=a} \{W\}_{r=a} d\theta = 0
\end{aligned} \tag{48}$$

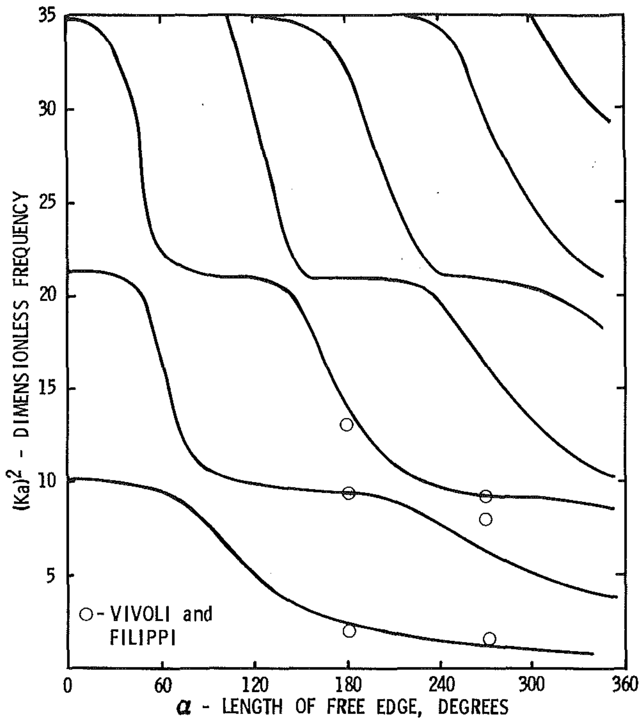

Fig. 3 Natural frequencies of circular plates having partially free, and partially clamped boundaries

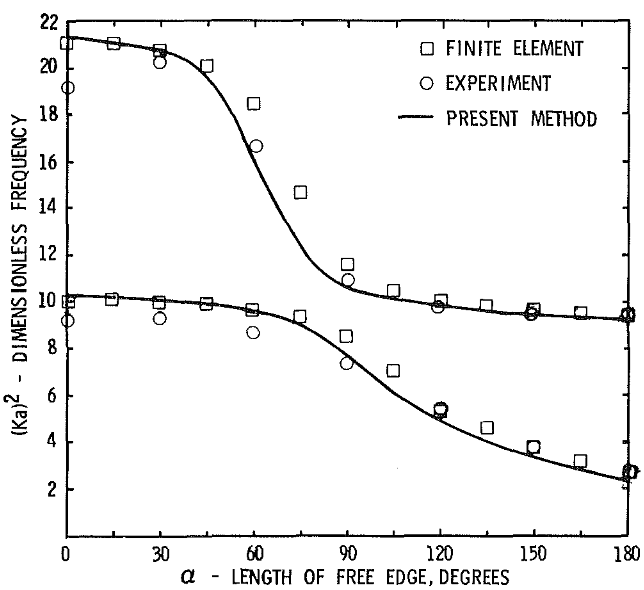

Fig. 4 Comparison of experimental and theoretical determinations of the natural frequencies of plates with mixed boundary conditions

Substituting the expansion for the displacement and for the variation leads to a system of $2N$ equations for N values of A_p and N values of B_p. We choose $\delta B_p = 0$ and $\delta A_p = 0$ for $p \neq q$, $\delta A_q = 1$ for $p = q$ to produce N equations of the form

$$\sum_{p=1}^{N} (A_p C_{pq} + B_p D_{pq}) = 0, \quad q = 1, N \tag{49}$$

and $\delta A_p = 0$, $\delta B_p = 0$ for $p \neq q$, $\delta B_p = 1$ for $p = q$ to produce a second set of N equations.

$$\sum_{p=1}^{N} (A_p E_{pq} + B_p F_{pq}) = 0, \quad q = 1, N. \tag{50}$$

Writing these as a single matrix equation leads to a $2N$ square array of coefficients, the determinant of which must vanish. For each value of K (defined through equation (44)) that causes the determinant to vanish, we may find a natural frequency of the plate.

Although tedious, the implementation of this process is straightforward. A computer program was written which evaluates the elements and determinants of the array for a trial value of frequency. The value of frequency was then incremented until the determinant changed sign. The search direction was then reversed, a smaller increment used, and the process repeated until the desired accuracy was obtained. Once an acceptable estimate of the natural frequency had been formed, the coefficients were evaluated, and the displacements and force resultants evaluated on the boundary so that the approximation to the boundary condition could be verified.

Results obtained with $N = 24$ are presented in Fig. 3. In the course of obtaining solutions for a plate free on $-\alpha/2 \leq \theta \leq \alpha/2$ and clamped on the remainder, one also finds the frequencies of the plate clamped on $-\alpha/2 \leq \theta \leq \alpha/2$ and free on the remainder. At any α, then, two sets of frequencies are found: those for a free edge angle $\alpha' = \alpha$, and those for a free edge angle $\alpha'' = 2\pi - \alpha$. The mode shape must be evaluated to determine which type of mode has been identified.

The circular plate with these mixed boundary conditions has been considered in four other investigations. Hemmig [17] conducted a series of experiments on steel plates with edges partially free and partially clamped. Some of his experimental results are given in Fig. 4. Eastep [18] used a finite element method (NASTRAN) to determine natural frequencies for this same problem, with results as shown on the Figure. One hundred forty-four trapezoidal and 24 triangular elements with a total of 1944 degrees of freedom were used to model the plate. Results of the present study were computed at 15 deg increments of the edge angle but are shown as solid lines. Expansions of up to 48 terms ($N = 24$) were employed.

Comparison of these three sets of results suggests that the usual difficulty in experimentally achieving a rigid clamping may have been encountered. For many values of α, the agreement between results obtained with the present method and those obtained with NASTRAN is quite good, but some discrepancy is noted for those values of α where the frequency is particularly sensitive to the clamping length. The results suggest, but certainly cannot be taken to demonstrate, that the present method leads to lower bounds. A similar trend has been noted [19] in results obtained for membranes with mixed edge conditions.

In an earlier work, Chen and Pickett [4] used a superposition of functions satisfying the differential equation with the coefficients being determined so as to minimize boundary error through least squares. These results differ significantly from all results published since that time.

The results obtained by Hirano and Okazaki [5] for the first mode, and confirmed by experiment, appear to lie slightly above the present results. Vivoli and Filippi [6] obtained experimental and theoretical results for the first four modes at two values of free-edge angles. With the exception of their value for the second symmetric mode of the quarter clamped plate, which was significantly higher than that obtained here, the agreement is satisfactory, as shown in Fig. 3. Finally, Narita and Leissa [7] have compared the present results with some results obtained by a Fourier series technique and found agreement between the two methods to be within a few percent, with the present results being slightly lower.

Summary

A procedure for determining the dynamic response of elastic structures by superposing functions that satisfy the differential equation of motion but not the boundary conditions has been developed. An algorithm for determining the necessary coefficients is developed from a modified form of Hamilton's principle. The application to an elastic system with a discontinuous boundary condition was demonstrated by considering the elastic plate, partially free and partially clamped. Numerical results for the first several modes were compared with available experiment, and results obtained by other methods with satisfactory agreement.

Acknowledgment

The author is indebted to Captain J. R. Van Sickel, Jr., USAF, who contributed some preliminary work to this problem while a graduate student at the Air Force Institute of Technology and successfully demonstrated the application of this method to the vibrating membrane [19]. Appreciation is also due to the Aeronautical Systems Division Computer Center, Wright-Patterson AFB for providing the necessary computational facilities, and to the Department of Engineering Mechanics, Ohio State University, for providing the congenial atmosphere in which this work was completed.

References

1 Leissa, A. W., "Vibration of Plates," NASA SP-160, National Aeronautics and Space Administration, Washington, D.C., 1969.

2 Leissa, A. W., "Recent Research in Plate Vibration, 1973-1976: Complicating Effects," *Shock and Vibration Digest*, Vol. 10, No. 12, Dec. 1978, pp. 21-35.

3 Leissa, A. W., "Recent Research in Plate Vibrations: Classical Theory," *Shock and Vibration Digest*, Vol. 9, No. 10, Oct. 1977, pp. 13-24.

4 Chen, S. S. H., and Pickett, G., "Bending of Uniform Plates of Arbitrary Shapes and With Mixed Boundary Conditions," *Developments in Mechanics*, Vol. 4, Proc. 10th Midwestern Mechanics Conference, 1967, pp. 411-427.

5 Hirano, Y., and Okazaki, K., "Vibrations With Circular Plates Having Partly Clamped and Partly Simply Supported Boundary," *Bull JSME*, Vol. 19, No. 132, 1976, pp. 610-618.

6 Vivoli, J., and Fillippi, P., "Eigenfrequencies of Thin Plates and Layer Potentials," *Journal of the Acoustical Society of America*, Vol. 55, No. 3, March 1974, pp. 562-567.

7 Narita, Y., and Leissa, A. W., "Flexural Vibrations of Free Circular Plates Elastically Constrained Along Parts of the Edge," *Int. J. Solids Structures*, Vol. 17, No. 1, 1981, pp. 83-92.

8 Fung, Y. C., *Foundations of Solid Mechanics*, Prentice-Hall, Englewood Cliffs, N.J., 1965, p. 399.

9 Reissner, E., "On a Variational Theorem in Elasticity," *Journal of Math. and Phys.*, Vol. XXIX, 1950, pp. 90-95.

10 Reissner, E., "On Variational Principles in Elasticity," *Calculus of Variations and Its Applications*, Proc. Sym. on Calculus of Variations, Vol. VIII, American Math. Soc., McGraw-Hill, 1958, pp. 1-6.

11 Plass, H. J., Jr., Gaines, J. H., and Newsom, C. D., "Application of Reissner's Variational Principle to Cantilever Plate Deflection and Vibration Problems," ASME JOURNAL OF APPLIED MECHANICS, Vol. 29, 1962, pp. 127-135.

12 Washizu, K., *Variational Methods in Elasticity and Plasticity*, Pergamon Press, Oxford, 1968, pp. 31-34.

13 Yu, Y. Y., "Generalized Hamilton's Principle and Variational Equation of Motion in Nonlinear Elasticity with Application to Plate Theory," *J. of Acoustical Society of America*, Vol. 36, No. 1, Jan. 1964.

14 Dean, T. S., and Plass, H. J., "A Dynamic Variational Principle for Elastic Bodies and Its Application to Approximation in Vibration Problems," *Development in Mechanics*, Vol. 3, No. 2, Proc. 19th Midwest Mechanics Conf., 1965, pp. 107-118.

15 Torvik, P. J., "On the Determination of Stresses, Displacements, and Stress Intensity Factors in Edge Cracked Sheets with Mixed Boundary Conditions," ASME JOURNAL OF APPLIED MECHANICS, Vol. 46, 1979, pp. 611-617.

16 Torvik, P. J., and McClatchey, J. J., "Response of an Elastic Plate to a Cyclic Longitudinal Force," *Journal of the Acoustical Society of America*, Vol. 44, No. 1, July 1968, pp. 59-66.

17 Hemmig, F. G., "Investigation of Natural Frequencies of Circular Plates With Mixed Boundary Conditions," M. S. Thesis, Air Force Institute of Technology, Wright-Patterson AFB, Ohio, Dec. 1975.

18 Eastep, F. E., and Hemmig, F. G., "Natural Frequency of Circular Plates With Partially Free, Partially Clamped Edges," *Journal of Sound and Vibration*, Vol. 84, No. 2, 1982.

19 Van Sickel, J. R., Jr., "Vibrations of Membranes and Plates With Mixed Boundary Condition, M.S. Thesis, Air Force Institute of Technology, Wright-Patterson AFB Ohio, Dec. 1978.

Nonlinear Vibration of Thin Elastic Plates

Part 1: Generalized Incremental Hamilton's Principle and Element Formulation

S. L. Lau[1]
Lecturer,
Department of Civil and
Structural Engineering,
Hong Kong Polytechnic,
Hong Kong
Mem. ASME

Y. K. Cheung
Professor and Head.

S. Y. Wu
Assistant Computer Officer.

Department of Civil Engineering,
University of Hong Kong,
Hong Kong

The finite element method has been widely used for analyzing nonlinear problems, but it is surprising that so far only a few papers have been devoted to nonlinear periodic structural vibrations. In Part 1 of this paper, a generalized incremental Hamilton's principle for nonlinear periodic vibrations of thin elastic plates is presented. This principle is particularly suitable for the formulation of finite elements and finite strips in geometrically nonlinear plate problems due to the fact that the nonlinear parts of inplane stress resultants are functions subject to variation and that the Kirchhoff assumption is included as part of its Euler equations. Following a general formulation method given in this paper, a simple triangular incremental modified Discrete Kirchhoff Theory (DKT) plate element with 15 stretching and bending nodal displacements is derived. The accuracy of this element is demonstrated via some typical examples of nonlinear bending and frequency response of free vibrations. Comparisons with previous results are also made. In Part 2 of this paper, this incremental element is applied to the computation of complicated frequency responses of plates with existence of internal resonance and very interesting seminumerical results are obtained.

Introduction

A systematic computer method for nonlinear structural vibrations was developed by the authors in a series of recent papers. This new approach is essentially the incremental harmonic balance method associated with finite element or Rayleigh-Ritz procedures in the time-space domain [1]. So far, some beam problems have been treated successfully in [2], and efforts were made to investigate the large-amplitude vibrations of plates in [3], where some simple examples were computed.

The most significant features of this new approach are that (*i*) it is not subjected to the limitation of weak nonlinearity and (*ii*) it can give the periodic solutions directly with any desired accuracy. In fact, for an undamped system, the periodic solutions cannot be obtained by direct integration because the initial conditions are not known beforehand; whereas for a damped system, the integration must be carried out over a sufficient number of periods so that the transient process due to the assumed initial conditions can be damped out and a steady-state periodic solution is reached.

[1] Honorary Research Associate, Department of Civil Engineering, University of Hong Kong, Hong Kong.

Contributed by the Applied Mechanics Division for publication in the JOURNAL OF APPLIED MECHANICS.

Discussion on this paper should be addressed to the Editorial Department, ASME, United Engineering Center, 345 East 47th Street, New York, N.Y. 10017, and will be accepted until two months after final publication of the paper itself in the JOURNAL OF APPLIED MECHANICS. Manuscript received by ASME Applied Mechanics Division, April, 1983; final revision, February, 1984.

The finite element method has been widely used to analyze nonlinear problems, but it is surprising that so far only a few papers have been devoted to nonlinear periodic vibrations. The first attempt to apply finite element method in large amplitude vibration is due to Chuh Mei [4, 5]. Later, Rao and Raju [6, 7] presented a simple finite element formulation in which the inplane displacements are assumed to be zero over the whole plate. Based on the same assumptions, Narayanaswanai and Rao [8] used a higher-order triangular element and treated free vibration of plates of arbitrary shape. Reddy [9] developed a mixed element and a penalty element, with which he calculated some nonlinear free vibration problems of plate using similar simplifications. Unfortunately, the scope of applicability of the foregoing finite elements are restricted to a certain extent because of the use of such assumptions and the dropping of higher harmonic terms.

The harmonic terms other than the fundamental one are necessary for fully revealing the behavior of nonlinear vibrations, such as the super/subharmonic and internal resonances, etc. However, it is indeed extremely difficult to include these terms without using an incremental formulation proposed in the present paper.

In this paper, a special variational principle for large deflection theory of thin plates is given, which is a generalization of its linear counterpart first published in [10], and which can be found in a text by Hu [11]. Based on this variational principle, a generalized incremental Hamilton's principle is developed. Since the Kirchhoff's assumption forms part of its Euler equations, the principle can be taken as a firm basis for formulating the DKT-type incremental element. A second special feature of this principle is that the nonlinear part of the inplane stress resultants are independent functions subject to variation; hence they can be properly chosen in line with the order of approximation of the inplane displacement interpolation and, as a result, the formulation of nonlinear terms in finite element/strip or Rayleigh-Ritz procedure can be greatly simplified. This fact is of great significance in reducing computation effort, as the nonlinear terms have to be formed repeatedly in nonlinear numerical analysis.

Based on the incremental Hamilton's principle, an incremental triangular element of thin plate is derived. This element is simple and effective, and all the matrices have been worked out in explicit and compact forms. The accuracy of this element is demonstrated via typical examples of bending and free vibrations with large deflections.

In Part 2 of this paper, the amplitude incremental plate element is applied to complicated nonlinear frequency responses of free and forced vibrations characterized with existence of internal resonance. Some very interesting results obtained here are believed to have appeared for the first time in literature, to the best knowledge of the authors.

Generalized Incremental Hamilton's Principle

Consider firstly a special variational principle for large deflection theory of thin elastic plates in the form

$$\delta\Big\{\iint_A [\tfrac{1}{2}\{\epsilon\}^T[D_p]\{\epsilon\}+\tfrac{1}{2}\{\epsilon\}^T[D_p][A]\{\theta\}+\tfrac{1}{2}\{S_n\}^T[A]\{\theta\}$$
$$-\tfrac{1}{2}[S_n]^T[D_p]^{-1}\{S_n\}+\tfrac{1}{2}\{\chi\}^T[D_b]\{\chi\}$$
$$+\{\gamma\}^T\{Q\}-\{d\}^T\{\bar q\}]dA$$
$$-\int_C \gamma_s M_{ns}ds-\int_{C_R}\bar R_n w ds+\int_{C_M}\bar M_n\psi_n ds$$
$$-\int_{C_p}(\bar p_x u+\bar p_y v)ds\Big\}=0 \qquad (1)$$

where (see Fig. 1)

$\{d\}$ $=[u,v,w]^T$ = displacement vector

ψ_x,ψ_y = rotation components of the normal-to-the-middle plane in x,y coordinate system

ψ_n,ψ_s = rotation components of the normal-to-the-middle plane in n,s coordinate system

$$\begin{Bmatrix}\psi_n\\ \psi_s\end{Bmatrix}=\begin{bmatrix} l & m\\ -m & l\end{bmatrix}\begin{Bmatrix}\psi_x\\ \psi_y\end{Bmatrix} \qquad (2)$$

l,m = directional cosine of the normal to the boundary in the middle plane

$\{\gamma\}$ = transverse shear strain vector

$$\{\gamma\}=\left[\frac{\partial w}{\partial x}-\psi_x,\frac{\partial w}{\partial y}-\psi_y\right]^T \qquad (3)$$

$\gamma_s=\dfrac{\partial w}{\partial s}-\psi_s$ = transverse shear strain along the boundary

$\{\chi\}$ = curvature strain vector

$$\{\chi\}=\left[-\frac{\partial\psi_x}{\partial x},-\frac{\partial\psi_y}{\partial y},-\left(\frac{\partial\psi_y}{\partial x}+\frac{\partial\psi_x}{\partial y}\right)\right]^T \qquad (4)$$

$\{\epsilon\}$ = linear part of the inplane strain vector

$$\{\epsilon\}=\left[\frac{\partial u}{\partial x},\frac{\partial v}{\partial y},\frac{\partial v}{\partial x}+\frac{\partial u}{\partial y}\right]^T \qquad (5)$$

$$\{\theta\}=\left[\frac{\partial w}{\partial x},\frac{\partial w}{\partial y}\right]^T \qquad (6)$$

$$[A]=\begin{bmatrix}\dfrac{\partial w}{\partial x} & 0 & \dfrac{\partial w}{\partial y}\\ 0 & \dfrac{\partial w}{\partial y} & \dfrac{\partial w}{\partial x}\end{bmatrix}^T \qquad (7)$$

M_{ns} = twisting moment along the boundary

$\{Q\}$ $=[Q_x,Q_y]^T$ = transverse shear force vector

$\{\bar q\}$ $=[\bar q_x,\bar q_y,\bar q_z]^T$ = load intensity vector

$\{S_n\}$ $=[S_{nx},S_{ny},S_{nxy}]^T$ = the nonlinear part of the inplane stress resultant vector due to deflection.

$$[D_p]=\frac{Eh}{1-\nu^2}\begin{bmatrix}1 & \nu & 0\\ \nu & 1 & 0\\ 0 & 0 & \dfrac{1-\nu}{2}\end{bmatrix} \qquad (8)$$

$$[D_b]=\frac{Eh^3}{12(1-\nu^2)}\begin{bmatrix}1 & \nu & 0\\ \nu & 1 & 0\\ 0 & 0 & \dfrac{1-\nu}{2}\end{bmatrix} \qquad (9)$$

E = Young's modulus; ν = Poisson's ratio; h = thickness of plate; $\bar M_n$ = bending moment prescribed along the boundary C_M; $\bar R_n$ = the equivalent shear force prescribed along the boundary C_R; $\bar p_x$, $\bar p_y$ = the inplane resultants prescribed along the boundary C_p; A = the middle plane of the plate; and C = the boundary of the plate.

In this variational equation, u, v, w, ψ_x, ψ_y are independent kinematically permissible functions; S_{nx}, S_{ny}, S_{nxy}, Q_x, Q_y, and M_{ns} are also independent functions, and their variations are free of any restriction. Carrying out the variation and integrating by parts, it is easy to transform equation (1) to the following form

$$\iint_A\Big\{-\left(\frac{\partial S_x'}{\partial x}+\frac{\partial S_{xy}'}{\partial y}+\bar q_x\right)\delta u-\left(\frac{\partial S_{xy}'}{\partial x}+\frac{\partial S_y'}{\partial y}+\bar q_y\right)\delta v$$
$$+\delta\{S_n\}^T(\tfrac{1}{2}[A]\{\theta\}-[D_p]^{-1}\{S_n\})$$
$$+\left(\frac{\partial M_x}{\partial x}+\frac{\partial M_{xy}}{\partial y}-Q_x\right)\delta\psi_x$$
$$+\left(\frac{\partial M_{xy}}{\partial x}+\frac{\partial M_y}{\partial y}-Q_y\right)\delta\psi_y-\Big[\frac{\partial}{\partial x}\Big(Q_x$$
$$+S_x\frac{\partial w}{\partial x}+S_{xy}\frac{\partial w}{\partial y}\Big)$$
$$+\frac{\partial}{\partial y}\left(Q_y+S_{xy}\frac{\partial w}{\partial x}+S_y\frac{\partial w}{\partial y}\right)+q_z\Big]\delta w$$
$$+\left(\frac{\partial w}{\partial y}-\psi_y\right)\delta Q_y+\left(\frac{\partial w}{\partial y}-\psi_y\right)\delta Q_y\Big\}dA$$
$$-\int_C\Big\{\left(\frac{\partial w}{\partial s}-\psi_s\right)\delta M_{ns}+[M_{ns}-(M_y-M_x)lm$$

$$-M_{xy}(l^2-m^2)]\delta\psi_s\Big\}ds$$

$$+\int_{C_R}\Big[\Big(Q_x+S_x\frac{\partial w}{\partial x}+S_{xy}\frac{\partial w}{\partial y}\Big)l+\Big(Q_y+S_{xy}\frac{\partial w}{\partial x}$$

$$+S_y\frac{\partial w}{\partial y}\Big)m+\frac{\partial M_{ns}}{\partial s}-\bar{R}_n\Big]\delta w\,ds$$

$$-\int_{C_M}(M_n-\bar{M}_n)\delta\psi_n ds+\int_{C_p}[(S_x'l+S_{xy}'m-\bar{p}_x)\delta u$$

$$+(S_{xy}'l+S_y'm-\bar{p}_y)\delta v]\,ds=0 \tag{10}$$

where

$$[S_x',S_y',S_{xy}']^T=[D_p](\{\epsilon\}+½[A]\{\theta\}) \tag{11}$$

$$[S_x,S_y,S_{xy}]^T=[D_p]\{\epsilon\}+\{S_n\} \tag{12}$$

$$[M_x,M_y,M_{xy}]^T=[D_b]\{\chi\} \tag{13}$$

Here S_x', S_y', and S_{xy}' are also the total inplane stress resultants but expressed in terms of displacements. They will coincide with the inplane stress resultants S_x, S_y, and S_{xy}, respectively, if the relation $\{S_n\} = 1/2\,[A]\,\{\theta\}$ is satisfied (see equation (14)).

It can be seen from equation (10) that owing to the arbitrariness of the variations, equation (1) is equivalent to the following conditions:

(*a*) All equilibrium equations in terms of independent functions listed in the foregoing.

(*b*) The relationship between $\{S_n\}$ and deflection:

$$\{S_n\}=[D_p]½[A]\{\theta\} \tag{14}$$

(*c*) Kirchhoff assumption of

$$\psi_x=\frac{\partial w}{\partial x},\quad \psi_y=\frac{\partial w}{\partial y}$$

together with

$$\psi_s=\frac{\partial w}{\partial s}\quad\text{and}\quad M_{ns}=(M_y-M_x)lm-M_{xy}(l^2-m^2)\quad\text{on}$$

boundary. (15)

(*d*) All force boundary conditions on the corresponding boundaries C_R, C_M, and C_p.

This special variational principle is particularly suitable for the formulation of geometrically nonlinear plate element. The main advantages are twofold:

(*i*) Since the Kirchhoff assumption forms part of its Euler equation, this variational principle will be helpful for overcoming the well-known difficulty in thin-plate element formulation.

(*ii*) The nonlinear part of the inplane stress resultants $\{S_n\}$ appears in equation (1) as independent functions subject to variation, so it is possible to interpolate $\{S_n\}$ in the same form as $[D_p]\{\epsilon\}$ so as to be consistent in the order of approximation between the two terms in the expression of inplane stress resultants given by equation (12). As a result of this, it can be seen that the second and third terms in the area integral of equation (1), which produce the nonlinear parts of stiffness matrix, will be reduced to a similar form.

Referring to equation (1), a corresponding Hamilton's principle for periodic vibration can be written as

$$\delta\int_0^{2\pi}\Big\{\iint[½\{\epsilon\}^T[D_p]\{\epsilon\}+½\{\epsilon\}^T[D_p][A]\{\theta\}$$

$$+½\{S_n\}^T[A]\{\theta\}$$

$$-½\{S_n\}^T[D_p]^{-1}\{S_n\}+½\{\chi\}^T[D_b]\{\chi\}+\{\gamma\}^T\{Q\}$$

$$-\{d\}^T\{\bar{q}\}-½\rho h\omega^2\frac{\partial\{d\}^T}{\partial\tau}\frac{\partial\{d\}}{\partial\tau}\Big]dA$$

$$-\int_C\gamma_s M_{ns}ds\Big\}\,d\tau=0 \tag{16}$$

where $\tau = \omega t$ = dimensionless time, ω = frequency of vibration, t = time, ρ = density. In equation (16), some boundary integrals have been dropped because they are not essential for element formulation and, moreover, can be regarded as having been combined into the terms $\{d\}^T\{\bar{q}\}$ by using generalized functions. The inplane inertia is taken into account but rotary inertia are neglected.

Assuming that a state of vibration denoted by $\{d^{(0)}\}$, . . . , ω_0 is given, the neighboring state can then be expressed by adding the corresponding increments onto them as follows

$$\left.\begin{aligned}\{d\}&=\{d^{(0)}\}+\{\Delta d\}\\ &\;\;\cdots\cdots\\ \omega&=\omega_0+\Delta\omega\end{aligned}\right\} \tag{17}$$

where $\Delta(\ \ )$ denotes the increment of corresponding quantity.

Applying the same procedure as used in [1], a generalized incremental Hamilton's principle for periodic vibration of thin elastic plates is obtained in the form

$$\int_0^{2\pi}\Big\{\iint_A\delta\{\Delta\epsilon\}^T[D_p]\{\Delta\epsilon\}dA+\iint_A[\delta\{\Delta\chi\}^T[D_b]\{\Delta\chi\}$$

$$+\delta(\{\Delta\gamma\}^T\{\Delta Q\})]dA-\int_C\delta(\Delta\gamma_s\Delta M_{ns})ds$$

$$+\iint_A[\delta(\{\Delta\epsilon\}^T[D_p][A^{(0)}]\{\Delta\theta\})$$

$$+\delta\{\Delta\theta\}^T([\Delta A]^T\{S^{(0)}\}+[A^{(0)}]^T\{\Delta S_n\})]dA$$

$$-\iint_A\rho\omega_0^2h\delta\{\Delta d\}^T\{\Delta d\}dA$$

$$-\iint_A 2\Delta\omega\omega_0\rho h\delta\{\Delta\dot{d}\}^T\{\dot{d}^{(0)}\}dA$$

$$-\iint_A\delta\{\Delta d\}^T\{\Delta\bar{q}\}dA+\iint_A[\delta\{\Delta\epsilon\}^T[D_p](\{\epsilon^{(0)}\}$$

$$+½[A^{(0)}]\{\theta^{(0)}\})+\delta\{\Delta\theta\}^T[A^{(0)}]\{S^{(0)}\}$$

$$+\delta\{\Delta\chi\}^T[D_b]\{\chi^{(0)}\}+\delta\{\Delta\gamma\}^T\{Q^{(0)}\}+\delta\{\Delta Q\}^T\{\gamma^{(0)}\}$$

$$-\rho\omega_0^2h\delta\{\Delta\dot{d}\}^T\{\dot{d}^{(0)}\}-\delta\{\Delta d\}^T\{\bar{q}^{(0)}\}]dA$$

$$-\int_C(\delta\Delta\gamma_s M_{ns}^{(0)}+\delta\Delta M_{ns}\gamma_s^{(0)})ds\Big\}d\tau=0 \tag{18a}$$

$$\int_0^{2\pi}\iint_A\delta\{\Delta S_n\}^T(½[A^{(0)}]\{\theta^{(0)}\}-[D_p]^{-1}\{S_n^{(0)}\})dA\,d\tau=0 \tag{18b}$$

$$\int_0^{2\pi}\iint_A\delta\{\Delta S_n\}^T([A^{(0)}]\{\Delta\theta\}-[D_p]^{-1}\{\Delta S_n\})dA\,d\tau=0 \tag{18c}$$

where

$$\{S^{(0)}\}=[D_p]\{\epsilon^{(0)}\}+\{S_n^{(0)}\} \tag{19}$$

and $\{S_n^{(0)}\}$ as well as $\{\Delta S_n\}$ can be expressed in terms of displacement parameters by equations (18b, c). The last two integrals in equation (18a) are retained to give corrective terms for preventing the solution from drifting away during incrementation. Since it has the same form as equation (1), the corrective term will vanish if the preceding solution is exact.

General Formulation of Incremental Thin Plate Element

In this section, based on the generalized incremental Hamilton's principle, a fairly general formulation of incremental element for large deflection of thin plates is presented.

For modified DKT element, the displacement functions can be generally assumed to be written in the form

$$\begin{Bmatrix} u \\ v \end{Bmatrix} = \underset{2\times m}{[N_p]} \quad \underset{m\times 1}{\{p\}} \tag{20}$$

$$w = \underset{1\times n}{[N_b]} \quad \underset{n\times 1}{\{b\}} \tag{21a}$$

$$\begin{Bmatrix} \psi_x \\ \psi_y \end{Bmatrix} = \underset{2\times l}{[N_\psi]} \ \underset{l\times n}{[T]} \quad \underset{n\times 1}{\{b\}} \tag{21b}$$

where $\{p\}$ and $\{b\}$ are stretching and bending nodal displacement vectors with m and n components, respectively, $[N_p]$, $[N_b]$, and $[N_\psi]$ are corresponding shape function matrices, $\underset{l\times n}{[T]}$ is a transformation matrix derived from the condition $\gamma_s = 0$ along the element boundary, and some other necessary restrictions imposed on the rotations ψ_x, ψ_y. The integer l is greater than n by a number of restraint conditions connecting ψ_x, ψ_y with the vector $\{b\}$.

From equations (19)–(21), the following formulas can be derived by equations (3)–(6):

$$\{\gamma\} = [B_\gamma]\{b\} \tag{22}$$

$$\{\chi\} = [B_b][T]\{b\} \tag{23}$$

$$\{\epsilon\} = [B_p]\{p\} \tag{24}$$

$$\{\theta\} = [[N_{bx}]^T[N_{by}]^T]^T\{b\} \tag{25}$$

where

$$[N_{bx}] = \partial[N_b]/\partial x,\ [N_{by}] = \partial[N_b]/\partial y,$$

$$[A] = \begin{bmatrix} \{b\}^T[N_{bx}]^T & 0 \\ 0 & \{b\}^T[N_{by}]^T \\ \{b\}^T[N_{by}]^T & \{b\}^T[N_{bx}]^T \end{bmatrix} \tag{26}$$

$$[A^{(0)}]\{\Delta\theta\} = \begin{bmatrix} \{b^{(0)}\}^T[G_x] \\ \{b^{(0)}\}^T[G_y] \\ \{b^{(0)}\}^T[G_{xy}] \end{bmatrix} \{\Delta b\} \tag{27}$$

in which $[G_x]$, $[G_y]$, and $[G_{xy}]$ are symmetric matrices

$$\underset{n\times n}{[G_x]} = [N_{bx}]^T[N_{bx}], \qquad \underset{n\times n}{[G_y]} = [N_{by}]^T[N_{by}]$$
$$\underset{n\times n}{[G_{xy}]} = [N_{bx}]^T[N_{by}] + [N_{by}]^T[N_{bx}] \tag{28}$$

Using the following equilibrium (Euler equations of the principle)

$$Q_x = \frac{\partial M_x}{\partial x} + \frac{\partial M_{xy}}{\partial y}, \qquad Q_y = \frac{\partial M_{xy}}{\partial x} + \frac{\partial M_y}{\partial y} \tag{29}$$

and equation (13), the transverse shear force can be expressed in terms of vector $\{b\}$ in the form

$$\underset{2\times l}{\{Q\}} = \underset{2\times l}{[C_Q]} \ \underset{l\times n}{[T]} \ \underset{n\times 1}{\{b\}} \tag{30}$$

The linear part of the inplane stress resultant is denoted by $\{S_l\}$,

$$\{S_l\} = [S_{lx}, S_{ly}, S_{lxy}]^T = [D_p][B_p]\{p\} \tag{31}$$

In finite element formulation, the nonlinear part $\{S_n\}$ expressed by equation (14) usually has significantly higher-order interpolation than that of $\{S_l\}$. It obviously serves no purpose. Using the present variational principle, it is possible and expedient to interpolate $\{S_n\}$ in the same form as that for $\{S_l\}$, i.e.,

$$\{S_n\} = [D_p][B_p]\{f\} \tag{32}$$

The vectors $\{f^{(0)}\}$ and its increment vector, being internal parameters, can be determined by using equations (18b,c) (25)–(28), and (33) as follows

$$\underset{m\times 1}{\{f^{(0)}\}} = \underset{m\times m}{[K_p]^{-1}} \tfrac{1}{2} \underset{m\times n}{[K_{pd}^d]} \quad \underset{n\times 1}{\{b^{(0)}\}} \tag{33}$$

$$\underset{m\times 1}{\{\Delta f\}} = \underset{m\times m}{[K_p]^{-1}} \quad \underset{m\times n}{[K_{pd}^d]} \quad \underset{n\times 1}{\{\Delta b\}} \tag{34}$$

$$\underset{m\times m}{[K_p]} = \iint_{A_e} [B_p]^T[D_p][B_p]dA \tag{35}$$

$$[K_{pd}^d] = \iint_{A_e} [B_p]^T[D_p]^T \begin{bmatrix} \{b^{(0)}\}^T & [G_x] \\ \{b^{(0)}\}^T & [G_y] \\ \{b^{(0)}\}^T & [G_{xy}] \end{bmatrix} dA \tag{36}$$

and A_e denotes the area of the element.

Now, inserting all the related expressions into equation (18a), the element contributions are obtained:

(A) Matrix Contributions

$$\int_0^{2\pi} \delta \begin{Bmatrix} \{\Delta p\} \\ \{\Delta b\} \end{Bmatrix}^T \left[\begin{array}{c|c} [K_p] & [K_{pd}^d] \\ \hline [K_{pb}^d]^T & [K_b] + [K_b^s] + [K_b^d] \end{array}\right] \begin{Bmatrix} \{\Delta p\} \\ \{\Delta b\} \end{Bmatrix} d\tau$$

$$+ \omega_0^2 \int_0^{2\pi} \delta \begin{Bmatrix} \{\Delta p\} \\ \{\Delta b\} \end{Bmatrix}^T \begin{bmatrix} [M_p] & [0] \\ [0] & [M_b] \end{bmatrix} \begin{Bmatrix} \{\Delta p\} \\ \{\Delta b\} \end{Bmatrix} d\tau \tag{37}$$

where $[K_p]$ and $[K_{pd}^d]$ have been given in equations (35) and (36),

$$\underset{m\times m}{[M_p]} = \iint_{A_e} \rho h [N_p]^T[N_p]dA \tag{38}$$

$$\underset{n\times n}{[K_b]} = [T]^T[E][T] + [K_c]^T + [K_c] \tag{39}$$

in which

$$[K_c] = [T]^T \iint_{A_e} [Q]^T[B_\gamma]dA,$$

$$[E] = \iint_{A_e} [E] = \iint_{A_e} [B_b]^T[D_b][B_b]dA$$

$$\underset{n\times n}{[M_b]} = \iint_{A_e} \rho h [N_b]^T[N_b]dA \tag{40}$$

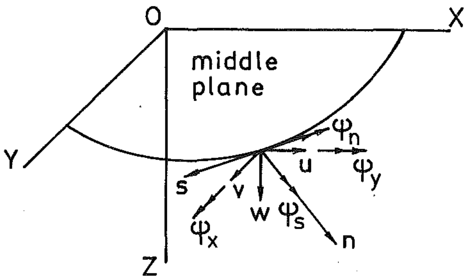

Fig. 1 Notations for plate displacements

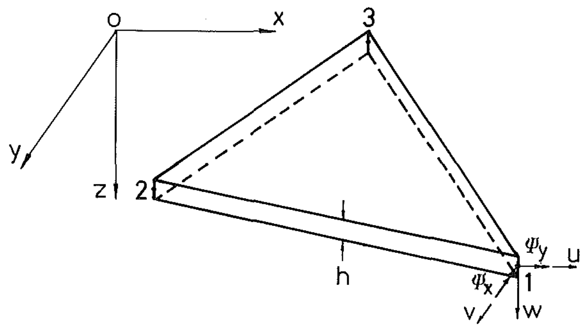

Fig. 2 Fifteen DOF incremental plate element, $\psi_x = \dfrac{\partial w}{\partial x}$, $\psi_y = \dfrac{\partial w}{\partial y}$

$$\overset{n\times n}{[K_b^d]} = [K_{pd}^d]^T[K_p]^{-1}[K_{pd}^k] \tag{41}$$

$$\overset{n\times n}{[K_b^s]} = \iint_{A_e} (S_x^{(0)}[G_x] + S_y^{(0)}[G_y] + S_{xy}^{(0)}[G_{xy}])dA \tag{42}$$

in which, by equations (19), (31) and (32),

$$[S_x^{(0)}, S_y^{(0)}, S_{xy}^{(0)}]^T = [D_p][B_p](\{p^{(0)}\} + \{f^{(0)}\})$$

(*B*) Right-Hand Vector Contributions:

$$\int_0^{2\pi} \delta \begin{Bmatrix} \{\Delta p\} \\ \{\Delta b\} \end{Bmatrix}^T \left(\begin{Bmatrix} \{R_p\} \\ \{R_b\} \end{Bmatrix} + \Delta\omega \begin{Bmatrix} \{F_p\} \\ \{F_b\} \end{Bmatrix} + \begin{Bmatrix} \{0\} \\ \{\Delta Z\} \end{Bmatrix} \right) d\tau \tag{43}$$

where

$$\overset{m\times 1}{\{R_p\}} = -[K_p]\{p^{(0)}\} - \tfrac{1}{2}[K_{pd}^d]\{b^{(0)}\} - \omega_0^2[M_p]\{\ddot{p}^{(0)}\} \tag{44}$$

$$\overset{n\times 1}{\{R_b\}} = \{Z^{(0)}\} - ([K_b] + [K_b^s])\{b^{(0)}\} - \omega_0^2[M_b]\{\ddot{b}^{(0)}\} \tag{45}$$

$$\overset{n\times 1}{\{Z^{(0)}\}} = \iint_{A_e} [N_b]^T \bar{q}_z^{(0)} dA \tag{46}$$

$$\overset{m\times 1}{\{F_p\}} = -2\omega_0[M_p]\{\ddot{p}^{(0)}\} \tag{47}$$

$$\overset{n\times 1}{\{F_b\}} = -2\omega_0[M_p]\{\ddot{b}^{(0)}\} \tag{48}$$

$$\overset{n\times 1}{\{\Delta Z\}} = \iint_{A_e} [N_b]^T \Delta q_z dA \tag{49}$$

It can be seen that, in this formulation, all the matrices arising from the nonlinear terms as well as the nonlinear inplane stress resultants $\{S_n\}$ etc. are expressed in terms of the elements of matrix $[K_{pd}^d]$. This fact greatly reduces the computing work in the evaluation of element matrices, because the nonlinear matrices have to be reformed in each incremental step or even for each iteration.

In periodic vibration, the nodal parameters are all periodic functions of time and they are expanded into Fourier series

$$\left.\begin{aligned} \{b\} &= \sum_{i=0} \{b_i\}\cos i\tau + \sum_{j=1} \{b_j\}\sin j\tau \\ \{p\} &= \sum_{i=0} \{p_i\}\cos i\tau + \sum_{j=1} \{p_j\}\sin j\tau \end{aligned}\right\} \tag{50}$$

Consequently, the final nodal parameters of the element are composed of the Fourier coefficients of the displacement increments, i.e., the amplitude increments Δb_i, Δp_i, etc. Thus, this element is in fact a finite prism in the time-space domain.

A Simple Incremental Triangular Thin Plate Element

In this section, a simple incremental element for geometrically nonlinear problem of thin plate will be deduced. This element is a modified DKT triangular element with only five degrees of freedom of stretching and bending displacement increments at each of the three corner nodes (Fig. 2). The successful application of this element to some simple nonlinear plate vibration problems was presented recently in an international conference [3], but the element formulation was not based on a complete variational principle. Here, the element is rededuced from the present general formulation, and is thus now established on a firm theoretical basis.

For this simple element, the nodal displacement vectors are

$$\{b\} = \left[w_1, \left(\frac{\partial w}{\partial x}\right)_1, \left(\frac{\partial w}{\partial y}\right)_1, w_2, \left(\frac{\partial w}{\partial x}\right)_2, \left(\frac{\partial w}{\partial y}\right)_2, w_3, \left(\frac{\partial w}{\partial x}\right)_3, \left(\frac{\partial w}{\partial y}\right)_3\right]^T \tag{51}$$

$$\{p\} = [u_1, v_1, u_2, v_2, u_3, v_3]^T \tag{52}$$

$\overset{2\times 6}{[N_p]}$ is the same as that for the constant plane stress element, $\overset{1\times 9}{[N_b]}$, $\overset{2\times 12}{[N_\psi]}$ are the same as those for the DKT element [12, 13] and with the same restrictions of

(*a*) $\gamma_s = 0$ on the element boundary, (*b*) ψ_n varies linearly along each edge, and the transformation matrix $[T]$ is derived from these restrictions. In contrast with the DKT element [12], the transverse shear strains are calculated by equation (22) and Q_x, Q_y by equation (30). However, it should be noted that the Kirchhoff assumption will be satisfied on average within the element by the variational principle itself automatically, so it is actually a thin plate element.

The element contributions are still expressed by equations (37)-(49), but the component matrices are greatly simplified as described in the following:

(*A*) With these shape functions, $[B_p]$ is a constant matrix and thus, instead of equation (35), the linear stretching stiffness matrix is simply expressed as

$$[K_p] = A_e[B_p]^T[D_p][B_p] \tag{53}$$

(*B*) Equation (36) is simplified to

$$[K_{pd}^d] = A_e[B_p]^T[D_p][\bar{G}_b] \tag{54}$$

where

$$[\bar{G}_b] = \begin{Bmatrix} \{b^{(0)}\}^T[\bar{G}_x] \\ \{b^{(0)}\}^T[\bar{G}_y] \\ \{b^{(0)}\}^T[\bar{G}_{xy}] \end{Bmatrix} \tag{55}$$

and

Table 1 Center deflection (w/h) of a simply supported square plate with immovable edges under uniform distributed load (Poisson's ratio = 0.3)

$\frac{qa^4}{Eh^4}$	Present				Reddy [9]		
	2×2	4×4	6×6	8×8	2×2	4×4	6×6
1	0.04506	0.04458	0.04440	0.04433	—	—	—
25	0.6670	0.6726	0.6714	0.6708	0.663	0.641	0.635
50	0.9366	0.9487	0.9464	0.9455	0.955	0.912	0.902
100	1.2515	1.2705	1.2667	1.2653	1.319	1.248	1.230
150	1.4623	1.4848	1.4797	1.4780	1.577	1.484	1.459
200	1.6249	1.6510	1.6453	1.6432	1.785	1.672	1.642
250	1.7615	1.7892	1.7828	1.7804	1.964	1.833	—

Table 2 Center deflection (w/h) of a clamped square plate with immovable edges under uniform distributed load (Poisson's ratio = 0.3)

$\frac{qa^4}{Eh^4}$	Present				Reddy [9]
	2×2	4×4	6×6	8×8	6×6
1	0.01498	0.01370	0.01377	0.01379	—
25	0.3498	0.3242	0.3257	0.3262	0.324
50	0.6148	0.5798	0.5825	0.5834	0.569
100	0.9676	0.9299	0.9339	0.9354	0.900
150	1.2066	1.1692	1.1742	1.1761	1.132
200	1.3840	1.3530	1.3587	1.3610	1.316
250	1.5409	1.5039	1.5102	1.5127	1.470

$$[\bar{G}_x] = \frac{1}{A_e}\iint_{A_e}[G_x]dA, [\bar{G}_y] = \frac{1}{A_e}\iint_{A_e}[G_y]dA,$$

$$[\bar{G}_{xy}] = \frac{1}{A_e}\iint_{A_e}[G_{xy}]dA \tag{56}$$

which can easily be integrated exactly.

(*C*) In this case, $\{S_l\}$ as well as $\{S_n\}$ are both reduced to constant over the element. According to equation (12), equations (33) and (34) together with equations (53) and (54), the inplane stress vector is expressed in the form

$$\{S^{(0)}\} = \{S_l^{(0)}\} + \{S_n^{(0)}\} = [D_p](\{\epsilon^{(0)}\} + \tfrac{1}{2}[\bar{G}_b]\{b^{(0)}\}) \tag{57}$$

(*D*) By using these formulas (53)–(57), the other two matrices (equations (41), (42)) arising from the nonlinear terms can also be expressed in terms of $[\bar{G}_x]$, $[\bar{G}_y]$ and $[\bar{G}_{xy}]$, i.e.,

$$[K_b^d] = [\bar{G}_b]^T[D_p][\bar{G}_b] \tag{58}$$

$$[K_b^s] = S_x^{(0)}[\bar{G}_x] + S_y^{(0)}[\bar{G}_y] + S_{xy}^{(0)}[\bar{G}_{xy}] \tag{59}$$

where $[K_b^s]$ is in fact the geometrical stiffness matrix in the current state.

(*E*) The linear part of the bending stiffness $[K_b]$, equation (39), is now reduced to that of the linear plate element of reference [10] and the explicit formulas are available in the Appendix of reference [3] in English. In paper [10], a factor c is introduced and thus the matrix $[K_b]$ is written as

$$[K_b] = [T]^T[E][T] + c([K_c]^T + [K_c]) \tag{60}$$

The stiffness $[K_b]$ can then be adjusted by the factor c continuously within a certain range and it is possible to improve the element performance further by choosing a proper value of c to balance the discrete Kirchhoff assumption error and discretization error. This point is similar to that of the Fried's C deg element, but it should be noted that the shear corrective term $([K_c]^T + [K_c])$ is different. When $c = 0$, $[K_b]$ is reduced to that of QQ3 or DKT element [12, 13]. When $c = 1$, equation (60) returns to equation (39) which is derived strictly in adherence to the variational principle proposed, or in other words, there is a theoretical value, i.e., $c = 1$. In paper [10], $c = 0.4$ is recommended according to a series of typical numerical experiments.

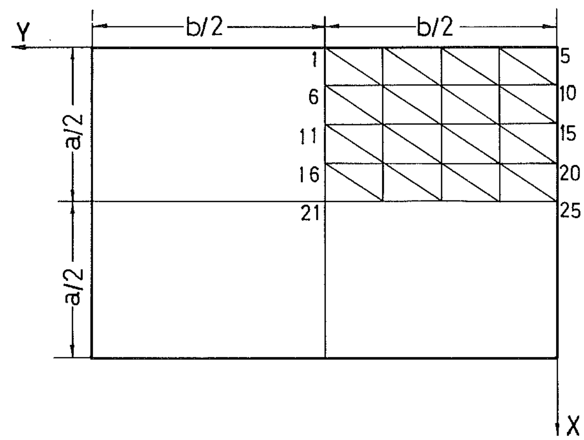

Fig. 3 Finite element mesh scheme

(*F*) The mass matrix $[M_p]$ and $[M_b]$, equations (38) and (40) can easily be integrated exactly in the present case.

Consequently, it can be seen that this incremental plate element is simple and in particular all the matrices arising from nonlinear terms as well as the inplane stresses etc. are expressed in terms of $[\bar{G}_x]$, $[\bar{G}_y]$, and $[\bar{G}_{xy}]$ which are just the geometrical stiffness matrices at the current state and can easily be integrated in explicit form.

Numerical Examples

To show the performance of the simple incremental triangular plate element, some test problems are investigated.

Static Problems. The simply supported and clamped square plates subject to uniformly distributed load are taken as test examples. The convergence is demonstrated in Tables 1 and 2. The center deflection w/h, computed with various element meshes, are listed in terms of the load factor qa^4/Eh^4, where a = length of plate edge, h = thickness of plate, and q = load intensity. The mesh scheme of a quarter plate is similar to that shown in Fig. 3. The available published numerical results obtained by Reddy [9] with penalty finite element (linear) are also given in these tables for comparison.

Table 3 Frequency ratio ω/ω_{11} for simply supported square plate with immovable edges

Center dimensionless amplitude	Present (FEM 4×4)	Rao et al. [6] (FEM 4×4)	Reddy [9] (FEM 4×4)	Chu-Herrmann [15] (perturbation)
0.2	1.0196	1.0185	1.0177	1.0195
0.4	1.0763	1.0717	1.0685	1.0757
0.6	1.1645	1.1534	1.1471	1.1625
0.8	1.2779	1.2565	1.2466	1.2734
1.0	1.4109	1.3753	1.3615	1.4024

Table 4 Frequency ratio ω/ω_{11} for clamped square plate with immovable edges

Center dimensionless amplitude	Present (FEM 4×4)	Rao et al. [6] (FEM 4×4)	Reddy [9] (FEM 4×4)
0.2	1.0073	1.0071	1.0062
0.4	1.0291	1.0278	1.0245
0.6	1.0648	1.0611	1.0540
0.8	1.1138	1.1053	1.0934
1.0	1.1762	1.1588	1.1411

It is worth pointing out that when the load is small, the center deflections approach the linear solution very accurately, for example, when $qa^4/Eh^4 = 1$. The analytical linear solutions are 0.04434 and 0.0138 for simply supported and clamped square plates, respectively. Usually, the solution does not converge monotonically, because the element is in fact a partially hybrid type.

Free Vibration Problems. The fundamental frequency-amplitude relationship of simply supported and clamped square plates with immovable edges were computed using a 4 × 4 mesh. A procedure with a four-eigenvector-basis and a two-harmonic-approximation (cos ωt, cos $3\omega t$ for deflection and cos $0\omega t$, cos $2\omega t$ for inplane displacements) for speeding up the numerical process as described in Part 2 [15] is applied. It means that the nodal deflections are expressed by equation (19) of Part 2. The results obtained together with the previously published ones are listed in Table 3. It can be seen that the present results are very close to the Chu-Herrmann's results, which are calculated by the perturbation method incorporated with elliptic integrals. The frequency ratios obtained by Rao et al. [6] and Reddy [9] with their own FEM however show similar differences. It may be because both use the same simplifications of assuming the inplane displacements to be zero over the whole middle plane of the plate and also only one harmonic term is retained in the formulation. Table 4 gives similar results for a clamped square plate.

It is interesting to note that a weak interaction developed between the fundamental mode (corresponding to ω_{11}) and the higher modes (corresponding to the frequencies ω_{13} and ω_{31}, see Part 2 for the meaning of these notations). This phenomenon can be revealed by carefully examining the third harmonic vibration shape of the plate. Figure 4 gives the third harmonic dimensionless amplitude variation (denoted by $A_3(x,y)$), in which curve 1 is for $\omega/\omega_{11} = 1.3850$, $A_{c1} = 0.9467$; curve 2 $\omega/\omega_{11} = 2.0399$, $A_{c1} = 1.734$, curve 3 $\omega/\omega_{11} = 2.3690$, $A_{c1} = 2.095$, where A_{c1} is the first harmonic dimensionless amplitude at plate center (refer to equation (20) of Part 2). When the total amplitude is small, the third harmonic term is very small in comparison with the first harmonic term (i.e. $A_{c3} << A_{c1}$) and, at the same time, the fundamental mode shape constitutes dominantly in both harmonic terms. But with the increase in amplitude, the ω_{13} and ω_{31}-mode shapes grow gradually and become the dominant components in the third harmonic terms as clearly shown in this figure. This fact tells us that the ω_{13} and ω_{31}-mode shapes are excited by the first harmonic term to some extent but not yet to a state of strong internal resonance.

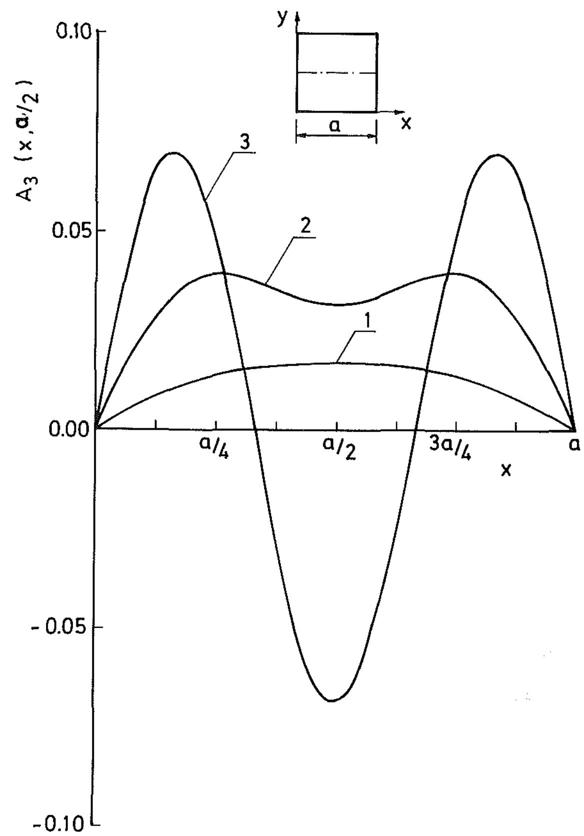

Fig. 4 Third harmonic dimensionless amplitude variation A_3 along the center line $y = a/2$ for simply supported square plate with immovable edges

In Part 2 of this paper, the phenomenon of strong internal resonance of plate will be investigated.

Concluding Remarks

In nonlinear finite element analysis, the reduction in the formulation work is of crucial importance, and the development of simple and reliable elements with strong convergent characteristics have attracted research workers' attention again in recent years. The generalized incremental Hamilton's principle presented in this paper enables the authors to interpolate the stretching stresses of linear and nonlinear parts in the same pattern, which leads to a significant simplification of the formulation of nonlinear terms, but with little loss of precision. This fact is of great significance in reducing the amount of computing work, because the nonlinear terms are required to be renewed at each step during incrementation or iteration. Moreover, this simplification procedure can be extended to general structural systems.

The finite element presented here does not require the introduction of any additional assumption to violate the original theory, therefore the numerical results obtained can be expected to approach the exact solution with the increasing number of elements and harmonic terms.

It is worth emphasizing that the present variational principles, equations (1) and (18*a–c*), are of the mixed type because of the inclusion of shear forces Q_x, Q_y, and twist M_{ns} as functions subjected to variation. Thus, the element proposed in this paper can be regarded as a partially hybrid type due to the elimination of force parameters such as Q_x and Q_y by equilibrium equations (equation (29)) in the formulation.

References

1 Lau, S. L., and Cheung, Y. K., "Amplitude Incremental Variational Principle for Nonlinear Vibration of Elastic Systems," ASME JOURNAL OF APPLIED MECHANICS, Vol. 48, 1981, pp. 959–964.

2 Cheung, Y. K., and Lau, S. L., "Incremental Time-space Finite Strip Method for Nonlinear Structural Vibrations," *Earthquake Engineering and Structural Dynamics*, Vol. 10, 1982, pp. 239–253.

3 Lau, S. L., Cheung, Y. K., and Wu, S. Y., "Amplitude Incremental Finite Element for Nonlinear Vibration of Thin Plates," *Proceeding of the International Conference on Finite Element Methods*, Shanghai, China, Aug. 2–6, 1982, pp. 184–190.

4 Chuh, Mei, "Nonlinear Vibrations of Beams by Matrix Displacement Method," *AIAA J.*, Vol. 10, 1972, pp. 355–357.

5 Chuh, Mei, "Finite Element Displacement Method for Large Amplitude Free Flexural Vibrations of Beam and Plates," *Computers and Structures*, Vol. 3, 1973, pp. 163–174.

6 Rao, G. V., Raju, K. K., and Raju, I. S., "Finite Element Formulation for the Large Amplitude Free Vibrations of Beam and Orthotropic Circular Plates," *Computers and Structures*, Vol. 6, 1976, pp. 169–172.

7 Rao, G. V., Raju, I. S., and Raju, K. K., "A Finite Element Formulation for Large Amplitude Flexural Vibrations of Thin Rectangular Plates," *Computers and Structures*, Vol. 6, 1976, pp. 163–167.

8 Chuh, Mei, Narayanaswana, R., and Rao, G. V., "Large Amplitude Free Flexural Vibration of Thin Plates of Arbitrary Shape," *Computers and Structures*, Vol. 10, 1979, pp. 675–681.

9 Reddy, J. N., "Simple Finite Elements With Relaxed Continuity for Nonlinear Analysis of Plates," *Proc. of the 3rd International Conference in Australia on F.E.M.*, July 1979, The University of New South Wales.

10 Lau, S. L., and Chen, S. C., "A Nine-Degree-of-Freedom Rapidly Converging Triangular Plate Element," *Acta Scientiarum Noturatium Universtatics SUNYATSENTI* (in Chinese), No. 4, 1974, pp. 46–66.

11 Hu, H. C., *Variational Principle of Elasticity and its Applications*, Science Press, Beijing, 1981.

12 Stricklin, J. A., Haisler, W. E., Tisdale, P. R., and Gunderson, R., "A Rapidly Converging Triangular Plate Element," *AIAA J.*, Vol. 7, 1969, pp. 180–181.

13 Batoz, J. L., Bathe, K. J., and Ho, L. W., "A Study of Three-Node Triangular Plate Bending Elements," *Int. J. Num. Meth. Eng.*, Vol. 5, 1980, pp. 1771–1812.

14 Fried, I., and Yang, S. K., "Triangular, Nine-Degree-of-Freedom, C°, Plate Bending Element of Quadratic Accuracy," *Quarterly of Applied Mathematics*, Vol. 31, 1973, pp. 303–312.

15 Lau, S. L., Cheung, Y. K., and Wu, S. Y., "Nonlinear Vibration of Thin Elastic Plates, Part 2: Internal Resonance by Amplitude Incremental Finite Element," ASME JOURNAL OF APPLIED MECHANICS, Vol. 51, 1984, pp. 845–851.

16 Chu, H. N., and Herrmann, G., "Influence of Large Amplitudes on Free Flexural Vibrations of Rectangular Elastic Plates," ASME JOURNAL OF APPLIED MECHANICS, Vol. 23, 1956, pp. 532–540.

S. L. Lau
Lecturer,
Department of Civil and Structural Engineering,
Hong Kong Polytechnic,
Hong Kong
Mem. ASME

Y. K. Cheung
Professor and Head.

S. Y. Wu
Assistant Computer Officer.

Department of Civil Engineering,
University of Hong Kong,
Hong Kong

Nonlinear Vibration of Thin Elastic Plates

Part 2: Internal Resonance by Amplitude-Incremental Finite Element

The simple amplitude-incremental triangular plate element derived in Part 1 of this paper is applied to treat the large-amplitude periodic vibrations of thin elastic plates with existence of internal resonance. A simply supported rectangular plate with immovable edges ($b/a = 1.5$) and having linear frequencies $\omega_{13} = 3.45\ \omega_{11}$ is selected as a typical example. The frequency response of free vibration as well as forced vibration under harmonic excitation are computed. To the best knowledge of the authors, these very interesting results for such plate problems have not appeared in literature previously. Some special considerations to simplify and to speed up the numerical process are also discussed.

1 Introduction

In Part 2 of this paper, the amplitude-incremental triangular plate element developed in Part 1 [1] (see Fig. 2 of Part 1) is applied to study the periodic vibrations of thin elastic plates with existence of internal resonance. The frequency response of free vibration as well as forced vibration under harmonic excitation are considered. Under the influence of internal resonance, the frequency response becomes very intricate. Up to the present, only a few papers are devoted to nonlinear plate vibrations in which internal resonance have been taken into account. Sridhar, Mook, and Nayfeh [2, 3] treated circular plates and Lobitz, Nayfeh, and Mook [4] dealt with elliptic plates by multiple time scales perturbation method. As is well known, the perturbation method is only capable of treating problems with weak nonlinearity and becomes very cumbersome when used to calculate higher-order approximations. The present amplitude-incremental method is the most suitable numerical approach capable of tracing very complicated frequency response curves. Moreover, it can give a solution with any desired accuracy, albeit at the cost of increased computer time. Strictly speaking, the present method is a seminumerical approach, because it is analytical in time (by expanding in Fourier series) and numerical in space (by using finite element method). Therefore, it should be an economic tool for periodic vibration problem in the same way as the finite strip method is good for many stress analysis problems.

However, to cope with such a complicated problem, some special considerations to simplify and to speed up the numerical process are needed. Some remarks on this problem are given in Section 2 of this paper.

A simply supported rectangular plate with aspect ratio $b/a = 1.5$ is chosen as a typical example, of which the linear frequency ω_{13} is slightly larger than three times the fundamental frequency ω_{11} and therefore, internal resonance may occur with increasing amplitude. A number of interesting results including the forced vibrations under the influence of internal resonance are obtained. Finally, some discussions concerning the internal resonance phenomena and the features of this new approach are discussed.

2 Remarks on Numerical Procedure

In Section 2 and Part 1 of this paper [1], some techniques for simplifying the formulation have been introduced. However, for a very complicated problem such as nonlinear plate vibration with internal resonance, it is obvious that other techniques for speeding up and simplifying the numerical procedure should also be incorporated, and some remarks on the computation procedure used in this paper are given in the following:

1. To achieve high efficiency, a reduced basis consisting of linear eigenvectors for the same problem is used in place of the nodal parameters for bending, although the inplane nodal displacements are left unchanged in view of the flexibility in satisfying various inplane boundary constraints more accurately. The eigenvectors can easily be computed by using the subspace iteration method with the corresponding linear modified DKT plate element, and with the same element mesh. The necessary matrix and vector transformations are carried out at the element level. Thus the displacement vector for an element is written as

[1] Honorary Research Associate, Department of Civil Engineering, University of Hong Kong, Hong Kong.

Contributed by the Applied Mechanics Division for publication in the JOURNAL OF APPLIED MECHANICS.

Discussion on this paper should be addressed to the Editorial Department, ASME, United Engineering Center, 345 East 47th Street, New York, N.Y. 10017, and will be accepted until two months after final publication of the paper itself in the JOURNAL OF APPLIED MECHANICS. Manuscript received by ASME Applied Mechanics Division, February, 1984.

$$\{d\} = [\{p\}^T, \{c\}^T]^T \tag{1}$$

where $\{p\}$ denotes the inplane nodal displacement vector

$$\{p\} = [u_1, v_1, u_2, v_2, u_3, v_3]^T \tag{2}$$

and

$$\{c\} = [c_1, c_2, \ldots\ldots, c_n]^T \tag{3}$$

in which c_1, c_2, ... are the normal coordinates corresponding to the reduced basis composed of n selected eigenvectors.

2. In the present paper, only periodic vibrations of an undamped system are considered and therefore the vectors $\{p^{(0)}\}$ and $\{c^{(0)}\}$ and their increments $\{\Delta p\}$ and $\{\Delta c\}$ can be expanded into Fourier series of the form

$$\{p^{(0)}\} = \sum_{i=1}^{H} \{p_{2i-2}^{(0)}\} \cos(2i-2)\tau,$$

$$\{c^{(0)}\} = \sum_{i=1}^{H} \{c_{2i-1}^{(0)}\} \cos(2i-1)\tau \tag{4}$$

$$\{\Delta p\} = \sum_{i=1}^{H} \{\Delta p_{2i-2}\} \cos(2i-2)\tau,$$

$$\{\Delta c\} = \sum_{i=1}^{H} \{\Delta c_{2i-1}\} \cos(2i-1)\tau \tag{5}$$

where H = number of harmonic terms and $\{p_{2i-2}^{(0)}\}$, $\{c_{2i-1}^{(0)}\}$, $\{\Delta p_{2i-2}\}$, and $\{\Delta c_{2i-1}\}$ are the corresponding Fourier coefficients.

3. When the element contributions are assembled, the linearized incremental matrix equation is written in the form

$$([K] - \omega_0^2[M]) \begin{Bmatrix} \{\Delta \bar{p}\} \\ \{\Delta \bar{c}\} \end{Bmatrix} = \{\bar{R}\} + \Delta\omega\{\bar{F}\} + \begin{Bmatrix} \{0\} \\ \{\Delta \bar{q}\} \end{Bmatrix} \tag{6}$$

where

$$\{\Delta \bar{p}\} = [\ldots\, \overbrace{[\Delta u_{i0}, \Delta v_{i0}][\Delta u_{i2}, \Delta v_{i2}] \ldots [\Delta u_{i,2H-2}, \Delta v_{i,2H-2}]}^{H \text{ Fourier terms}} \ldots]^T \tag{7}$$

$$\{\Delta \bar{c}\} = [\ldots \overbrace{\Delta c_{i1}, \Delta c_{i3}, \ldots, \Delta c_{i,2H-1}}^{H \text{ Fourier terms}} \ldots\ldots]^T \tag{8}$$

in which

- $[\Delta u_{ij}, \Delta v_{ij}]$ = the jth harmonic stretching amplitude increments of the ith node of the plate;
- Δc_{ij} = the jth harmonic bending amplitude increment of the ith normal coordinate;
- $[K]$ = the corresponding tangent stiffness matrix;
- $[M]$ = the corresponding mass matrix;
- $\{\bar{R}\}$ = the correction vector assembled from element contributions $\{R_p\}$ and $\{R_b\}$ (see equations (44) and (45) of Part 1);
- $\{\bar{F}\}$ = the unbalanced inertia force vector due to unit frequency increment that is assembled from element contributions $\{F_p\}$ and $\{F_b\}$ (see equations (47) and (48) of Part 1); and
- $\{\Delta \bar{q}\}$ = the corresponding transverse load increment vector.

All matrices and vectors are formed automatically by computer.

The solution process usually starts from a corresponding known linear solution with sufficiently small amplitude. For the fundamental frequency response, the initial solution can be taken as

$$\omega_0 = \omega_1, \quad \{\bar{c}^{(0)}\} = [\delta, 0, 0, \ldots\ldots]^T, \quad \{\bar{p}^{(0)}\} = \{0\} \tag{9}$$

where ω_1 = the fundamental linear frequency, $\{\bar{c}^{(0)}\}$ = initial bending amplitude vector with the first normal coordinate equal to an arbitrary small value δ while all the others are set at zero, and $\{\bar{p}^{(0)}\}$ = initial stretching amplitude vector.

4. The frequency response of nonlinear periodic vibration of a multiple degree-of-freedom system with existence of internal resonance is represented by complicated curves in the frequency-amplitude hyperspace. For tracing the curves of a nonlinear frequency response with a given forcing term incrementally, one increment, called active increment, has to be prescribed a priori in each step. To ensure that the numerical problem is well conditioned, the current active increment is selected among the increments Δc_{ij}, and $\Delta\omega$ as the fastest varying one. When an increment other than $\Delta\omega$ is selected, an algorithm similar to the one given in [5] for static problem will be used. The algorithm is summarized in the following.

First, equation (6) is written in the form

$$\begin{bmatrix} A_{11} & [A_{12}] \\ [A_{21}] & [A_{22}] \end{bmatrix} \begin{Bmatrix} \Delta a_1 \\ \{\Delta a_2\} \end{Bmatrix} = \begin{Bmatrix} \bar{R}_1 \\ \{\bar{R}_2\} \end{Bmatrix} + \Delta\omega \begin{Bmatrix} \bar{F}_1 \\ \{\bar{F}_2\} \end{Bmatrix} \tag{10}$$

where the first matrix $[A]$ denotes $([K] - \omega_0^2[M])$ of equation (6), Δa_1 denotes the active increment that is prescribed a value of $\Delta\bar{a}_1$, while $\{\Delta a_2\}$ is the remaining increments of the vector $[\{\Delta\bar{p}\}^T\{\Delta\bar{c}\}^T]^T$, and $\{\bar{R}_1\{\bar{R}_2\}^T\}^T = \{\bar{R}\}$, $\{\bar{F}_1\{\bar{F}_2\}^T\}^T = \{\bar{F}\}$, while $\{\Delta\bar{q}\}$ is dropped for simplicity. Equation (10) can be expanded as

$$A_{11}\Delta\bar{a}_1 + [A_{12}]\{\Delta a_2\} = R_1 + \Delta\omega F_1 \tag{10a}$$

$$[A_{22}]\{\Delta a_2\} = \{R_2\} - \{A_{21}\}\Delta\bar{a}_1 + \Delta\omega\{F_2\} \tag{10b}$$

Let $\{\Delta a_2\}$ be divided into two parts

$$\{\Delta a_2\} = \{\Delta a_2\}^{(1)} + \Delta\omega\{a_2\}^{(2)} \tag{11}$$

By inserting equation (11) into equation (10b), one obtains the equations for $\{\Delta a_2\}^{(1)}$ and $\{\Delta a_2\}^{(2)}$ which can be written in a form without relocating the storages for the coefficient matrix,

$$\begin{bmatrix} 1 & [0] \\ \{0\} & [A_{22}] \end{bmatrix} \left[\begin{array}{c|c} \Delta a_1^{(1)} & \Delta a_1^{(2)} \\ \{\Delta a_2\}^{(1)} & \{\Delta a_2\}^{(2)} \end{array}\right] = \left[\begin{array}{c|c} \Delta\bar{a}_1 & 0 \\ \{R_2\} - \{A_{21}\}\Delta\bar{a}_1 & \{F_2\} \end{array}\right] \tag{12}$$

Substituting equation (1) into equation (10a) and solving for $\Delta\omega$, we obtain

$$\Delta\omega = \frac{A_{11}\Delta\bar{a}_1 + [A_{12}]\{\Delta a_2\}^{(1)} - R_1}{F_1 - [A_{12}]\{\Delta a_2\}^{(2)}} \tag{13}$$

If $\{\Delta a_2\}^{(1)}$ and $\{\Delta a_2\}^{(2)}$ are solved from equation (12), then $\Delta\omega$ can be calculated from equation (13) and consequently $\{\Delta a_2\}$ is obtained from equation (11).

5. The preceding algorithm is in fact equivalent to the incremental method with one-step Newton-Raphson correction. However, to achieve a satisfactory accuracy, a (modified) Newton-Raphson iteration can be applied with an updated correction vector $\{\bar{R}\}$ each time.

Let

$$\{\bar{R}_n\} = [(\bar{R}_1)_n, \quad \{\bar{R}_2\}_n^T]^T$$

denote the nth updated correction vector then the nth correction for the vector $\{\Delta a\}$, i.e.,

$$\{\Delta a\}_n = [(\Delta a_1)_n, \{\Delta a_2\}_n^T]^T \qquad (\text{in fact } (\Delta a_1)_n = 0, \text{ as } \Delta a_1 \text{ is prescribed})$$

will be solved from the following equation (refer to equation (12))

$$\begin{bmatrix} 1 & 0 \\ 0 & [A_{22}] \end{bmatrix} \begin{bmatrix} (\Delta a_1)_n \\ \{\Delta a_2\}_n \end{bmatrix} = \begin{Bmatrix} 0 \\ \{\bar{R}_2\} \end{Bmatrix} \tag{14}$$

and the nth frequency correction $\Delta\omega_n$ will be calculated from (refer to equation (13))

$$\Delta\omega_n = \frac{[A_{12}]\{\Delta a_2\}_n - (\bar{R}_1)_n}{F_1 - [A_{12}]\{\Delta a_2\}_n^{(2)}} \tag{15}$$

Thus, the $(n+1)$th updated results are

$$\{a\}_{n+1} = \{a\}_n + \begin{Bmatrix} 0 \\ \{\Delta a_2\}_n \end{Bmatrix}, \omega_{n+1} = \omega_n + \Delta\omega_n \tag{16}$$

The iteration can be repeated until a criterion, similar to that given in [6], $\max |(\Delta a_i)_n / a_{i\ \mathrm{ref.}}| <$ permissible error, is satisfied. $(\Delta a_i)_n$ is the ith component of the most recently computed corrective increment and $a_{i\,\mathrm{ref.}}$ stands for the largest total amplitude of the same type.

6. As the system (equation (6)) is described by N + 1 generalized coordinates (the total number of components in $\{\Delta\bar{p}\}$ and $\{\Delta\bar{c}\}$ plus $\Delta\omega$), it traces a set of hyperspace curves in a $(N + 1)$-dimensional Euclidean space. A quadratic extrapolation technique is used to predict the next point after sufficient previous points have been obtained. Such a scheme can usually reduce the number of iterations required for the solution to converge. The magnitude of extrapolation is restrained in a way such that the measure of the errors in each step remains the same, but an upper limit of arc length increment can be imposed to ensure sufficient number of solution points are obtained to trace the space curve.

3 Internal Resonance Behavior of Plate

A simply supported rectangular plate with aspect ratio $b/a = 1.5$ (Fig. 3 of Part 1 [1]) is characterized by the fact that the linear frequency ω_{13} (its corresponding mode shape has one half wave in the x-direction and three half waves in the y-direction) is slightly larger than three times the fundamental frequency, ω_{11}, i.e.,

$$\omega_{13} = 3.45\omega_{11} \tag{18}$$

Under this circumstance, internal resonance between the two corresponding mode shapes may take place in the range of large amplitudes. The following analyses reveal that internal resonance does occur for the case of plate with immovable edges. However, it is interesting to note that in the case of the same plate with movable edges, the phenomenon of internal resonance fails to appear even though the nonlinear frequency has shifted to 2.5 ω_{11} as the center amplitude increases to a rather large value of four times the thickness. It is logical to conclude that the inplane restraints have a definite influence on the behavior of the nonlinear vibration of plates.

Table 1 Linear frequencies for simply supported rectangular plate with $b/a = 1.5$ ($\omega_{ij} = \lambda_{ij}\sqrt{D/\rho h}/a^2$

λ_{ij}	λ_{11}	λ_{13}	λ_{31}	λ_{15}
Present FEM	14.22	49.02	93.23	121.59
Analytical	14.26	49.35	93.21	119.53

In the following analysis, a finite element grid of 4 × 4 for a quarter of the plate is used (see Fig. 3 of Part 1 [1]) and the first four symmetric modes are considered to be satisfactory for making up the reduced basis. The corresponding linear frequencies computed by the present element are listed in Table 1 for reference. For simplicity only two harmonic terms will be taken in equations (4) and (5), this being the minimum number of harmonic terms that must be retained to reveal the phenomenon of internal resonance.

With these approximations, the nodal deflections of the plate are then expressed by the following formula

$$w(x_n, y_n, t) = h \sum_{i=1}^{4} \sum_{j=1}^{2} c_{i,2j-1}\,\phi_i(x_n, y_n)\cos(2j-1)\omega t \tag{19}$$

where x_n, y_n = coordinates of node n, $\phi_i(x_n, y_n)$ = the ith symmetric mode shape, $c_{i,2j-1}$ = the $(2j-1)$th harmonic amplitudes of the ith normal coordinate. For convenience in presenting the results graphically, the center point deflection is selected to represent the response of the plate, i.e.,

$$w_c(t)/h = A_{c1}\cos\omega t + A_{c3}\cos 3\omega t \tag{20}$$

where

$$A_{c1} = \sum_{i=1}^{4} c_{i,1}\phi_i\left(\frac{a}{2}, \frac{b}{2}\right) \tag{20a}$$

$$A_{c3} = \sum_{i=1}^{4} c_{i,3}\phi_i\left(\frac{a}{2}, \frac{b}{2}\right) \tag{20b}$$

Free Vibrations. The problem of free vibration will be considered first, as the backbone curves will given important information about the behavior of nonlinear plate vibrations.

The following two cases have been computed:

1. Plate With Movable Edges. The in plane boundary conditions are $v = 0$, $S_x = 0$ at $x = 0, a$; $u = 0$, $S_y = 0$ at $y = 0, b$. The computed results represented by the center point amplitude are plotted in Fig. 1. It shows that the internal excitation is very weak, and implies that the fundamental frequency cannot catch up with one-third of the second frequency with increasing amplitude under such inplane boundary conditions.

2. Plate With Immovable Edges. The inplane boundary conditions are $u = v = 0$ at $x = 0, a$ and $y = 0, b$. In this case the expected internal resonance does occur. The frequency responses of the center point amplitude (equation (20)) are shown in Fig. 2, and the nonlinear mode shapes at different amplitude levels are plotted in Figs. 3(a,b). The response curve starting at the linear fundamental frequency ω_{11} with zero amplitude shows a hardening type at the beginning. However when the frequency ratio is increased to the vicinity of $\omega/\omega_1 \doteq 1.18$, the third harmonic amplitude A_{c3} begins to grow apparently as its ω_{13} -mode component (viz. ϕ_2 in

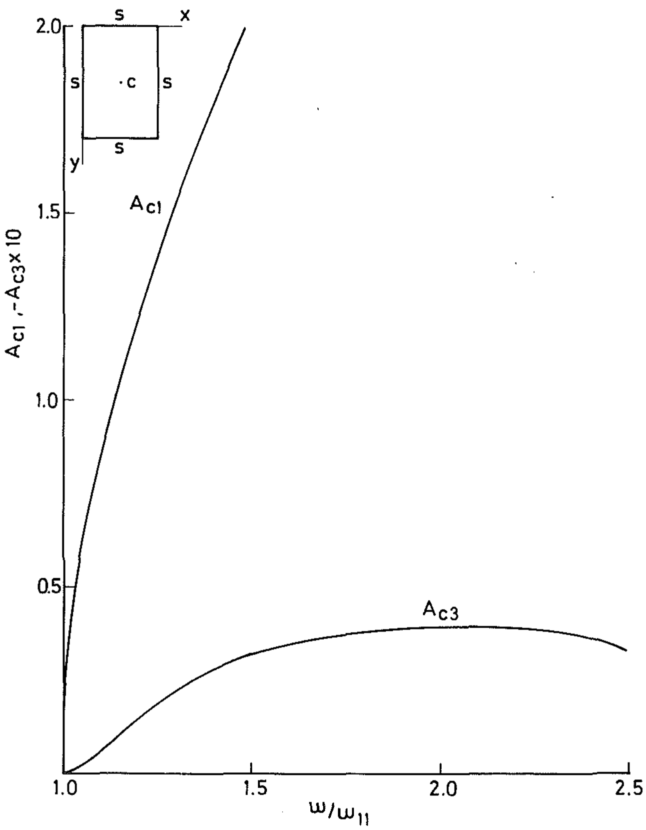

Fig. 1 Center amplitude versus frequency relation of simply supported rectangular plate with movable edges

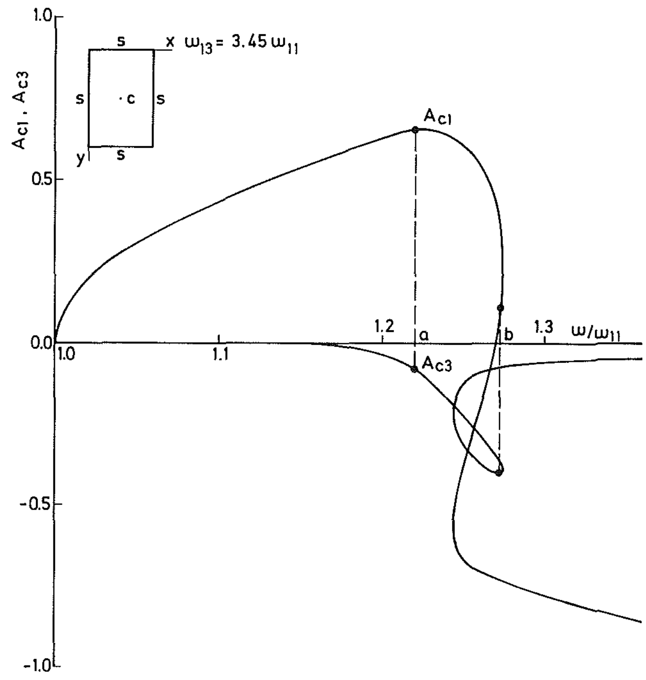

Fig. 2 Free internal resonance response of simply supported rectangular plate with immovable edges

equation (20*b*)) is being excited to a state of internal superharmonic resonance as shown in Fig. 2, and at the same time, the first harmonic amplitude A_{c1} which is mainly composed of the fundamental mode shape, (ϕ_1 in equation (20*a*)), begins a U-turn and drops sharply due to the transfer of energy to the third harmonic term. Continuing to trace this solution, the curve A_{c1} eventually crosses the axis and grows

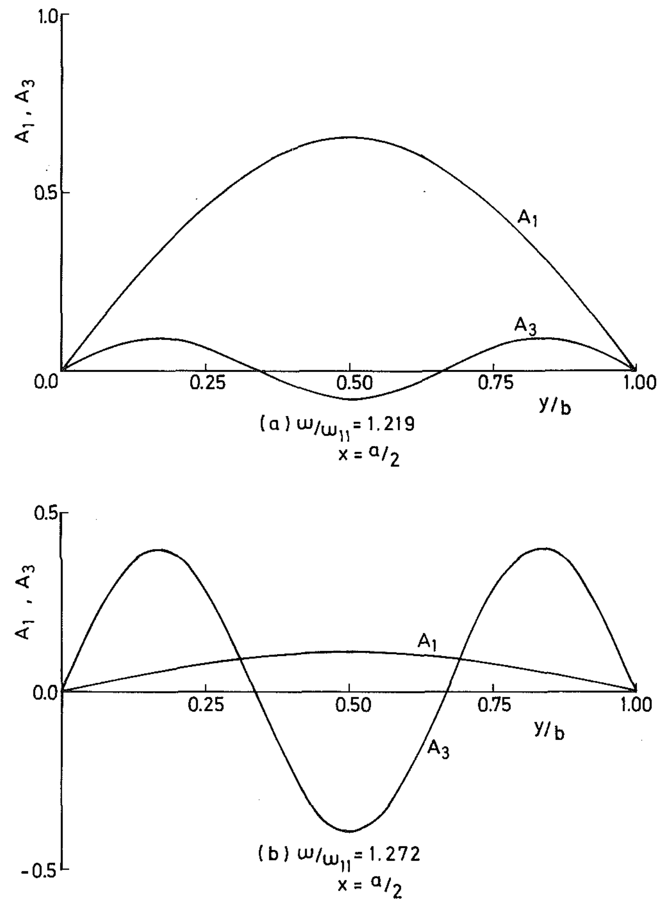

Fig. 3 Nonlinear mode shape of simply supported rectangular plate corresponding to points *a* and *b* on the frequency axis of Fig. 4

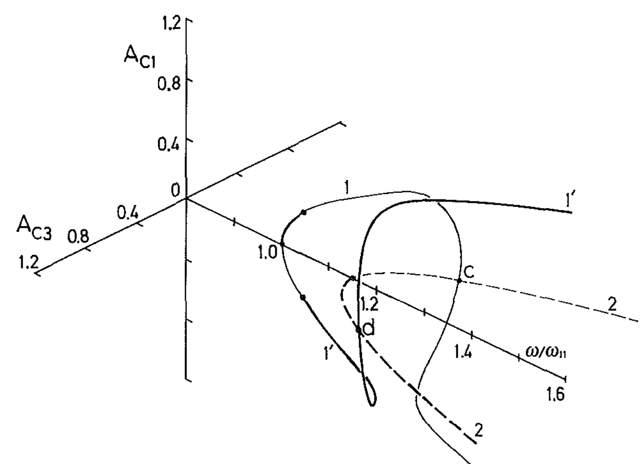

Fig. 4 Three-dimensional plotting of backbone curves by computer, —— ω_{11}-backbone, ---- ω_{13}-backbone

again in the negative direction (out of phase with the previous one) while the curve A_{c3} forms a loop and decreases again due to getting out of the internal resonance as shown in Fig. 2.

To obtain a complete amplitude-frequency response in the neighborhood of $\omega = \omega_{11}$ within the range of the present approximation (four eigenvectors and two harmonic terms), let us note the following facts: (*a*) The response curve (Fig. 2) would still represent a solution even if the sign of the coordinates is reversed. (*b*) There is another solution starting at 3ω

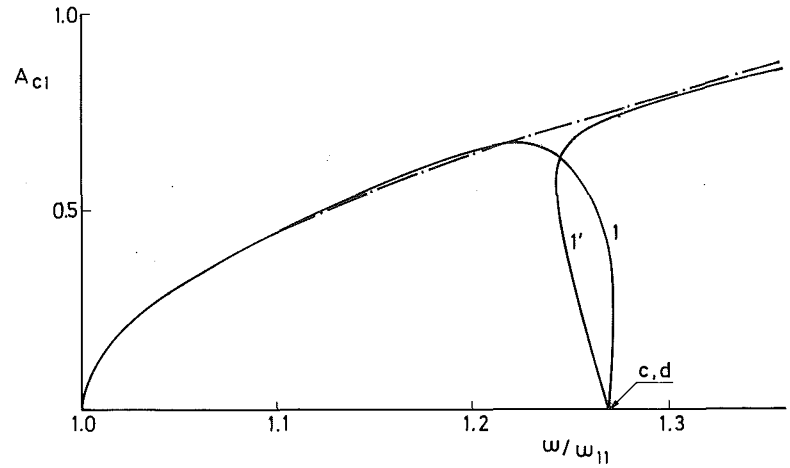

Fig. 5 Comparison of frequency response of free vibration, — • — • — • — one harmonic term solution, ____ two harmonic term solution

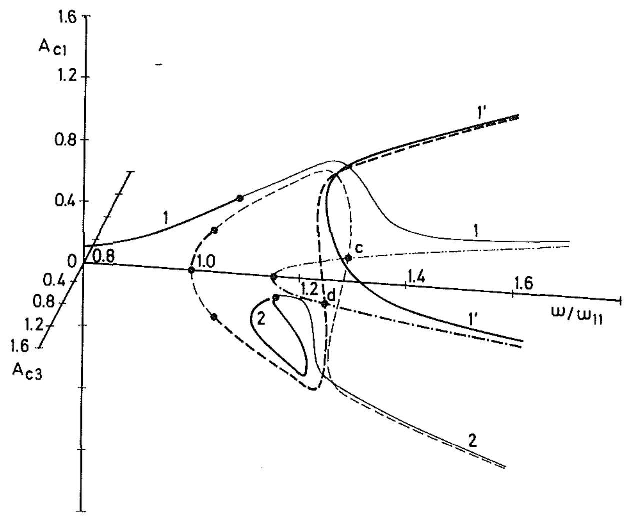

Fig. 6 Three-dimensional plotting of forced frequency response excited by uniformly distributed force $q = 4.8(Dh/a^3)\cos\omega t$, ____ forced vibration response, ------ ω_{11}-backbone, — • — • — • — ω_{13}-backbone

$= \omega_{13}$ with the first harmonic term equal to zero. In fact, this solution is nothing but the nonlinear free vibration corresponding to the linear frequency ω_{13}. With these facts in mind, the frequency responses can be drawn in the ω-A_{c1}-A_{c3} space as shown in Fig. 4. The curves that have positive A_{c3} are denoted by bold lines, otherwise by thin lines, and the intersecting points between the curves and the coordinate planes are marked with solid circles. Curve 1 actually represents the solution shown in Fig. 2, since the A_{c1} and A_{c3} curves are just the two projections of curve 1 on the ω-A_{c1} and ω-A_{c3} planes, respectively. Curve 1′ is obtained by reversing the signs of A_{c1} and A_{c3} from curve 1, so they are symmetrical with respect to the ω-axis. The screwlike character of the response curve can be seen clearly from the diagram. The dotted line 2 is the solution curve represented by

$$w_c = A_{c3}\cos 3\omega t$$

with 3ω stemming from the linear frequency ω_{13}. Points c and d denote the two bifurcation points.

Thus, the curves shown in Fig. 4 are the backbone curves of the plate taking into account the effects of internal resonance between the first two frequencies of symmetric modes.

It is obvious that if the third harmonic term was dropped, the internal resonance phenomenon would be phased out from the solution. For comparison, a solution obtained by retaining only one harmonic term, viz $\cos\tau$ for w (but still having two harmonic terms, viz 1 and $\cos 2\tau$ for u and v) is plotted with dash-dotted line and the previous two-term solution is plotted with a solid line in Fig. 5. From this figure, an interesting conclusion can be drawn such that except for the internal resonance phenomenon, the single term solution still provides a fairly good approximation for the remaining part of the projection curve on ω-A_{c1} plane. This fact is of great significance in practical nonlinear vibration analysis.

Forced Vibration. With such a complicated backbone curve, it would be interesting to trace the forced vibration behavior of the plate. In this section, the periodic vibration excited by an uniformly distributed load with an intensity of

$$q = \alpha(Dh/a^4)\cos\omega t$$

will be considered. In the preceding equation, α is a dimensionless force amplitude which is taken to be 4.8, and ω is the exciting frequency close to ω_{11}.

For forced vibration, the computation procedure has to be carried out in two steps. Firstly, a certain frequency is fixed, and the response is calculated by increasing the exciting force incrementally until a prescribed value is reached. After that, the amplitude-frequency response is then computed with the forcing term remaining constant using the same method outlined for the case of free vibration.

For undamped forced vibration there must be several separate branches of solution, i.e., the inphase and the out-of-phase resonance.

The computed frequency responses represented by the center amplitude (equation (20)) are plotted by computer as a space curve in Fig. 6. The backbone curves are also plotted in this figure with dotted line and dash-dotted line to facilitate the understanding of the relation between them (note that the angle of view is different from that of Fig. 4). Again as in Fig. 4, the bold and thin lines indicate their being in front of and behind the ω-A_{c1} planes, respectively.

(i) *Inphase Response.* The inphase response is shown by curve 1 and 1′. It is apparent that two separate branches exist due to the occurrence of superharmonic resonance caused by internal resonance.

The first branch (curve 1 in Fig. 6) starts at a frequency of ω

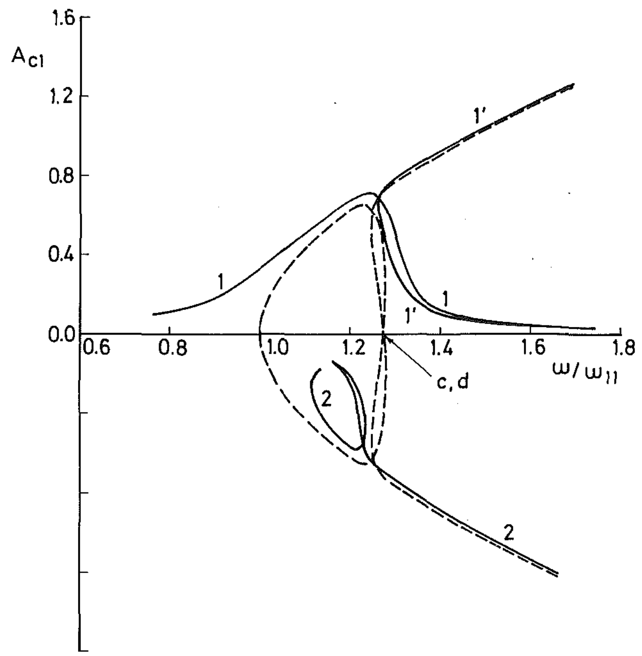

Fig. 7 The projection of forced frequency response on ω-A_{c1} plane, ____ forced frequency response, ---- ω_{11}-backbone

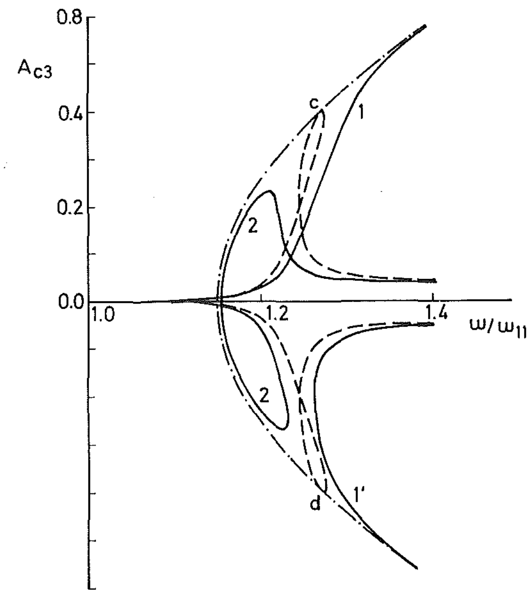

Fig. 8 The projection of forced frequency response on ω-A_{c3} plane, ____ forced vibration response, ---- ω_{11}-backbone — • — • — ω_{13}-*backbone*

$< \omega_{11}$, goes intitally along the backbone curve stemming from ω_{11} (dotted line, which will be simply called ω_{11}-backbone) and subsequently, near the bifurcation point c, turns to be the superharmonic resonance of the second symmetric mode-shape frequency with the amplitude A_{c3} growing toward infinity along the backbone curve stemming from ω_{13} (thin dash-dotted line, which will be simply called ω_{13}-backbone).

The second branch of this solution represented by curve 1′ follows another branch of the ω_{13}-backbone (bold dash-dotted line), and after passing the neighborhood of point d returns to the inphase fundamental resonance along side the ω_{11}-backbone (bold dotted line). It is interesting to note that the third harmonic term of this branch has a phase difference of π with that of the first branch just as the case about ordinary superharmonic resonance.

For clarity, the two projections of these curves on the ω-A_{c1} and ω-A_{c3} planes are plotted in Figs. 7 and 8 curve 1 and 1′).

(*ii*) *Out-of-Phase-Resonance.* This solution (curve 2 in Figs. 6–8), which starts at a frequency $\omega > \omega_{11}$, follows the ω_{11}-backbone (bold dotted line) at first and then turns to go along side the ω_{13}-backbone (dash-dotted line) and then penetrates the ω-A_{c1} plane as shown in Fig. 8. Finally, this curve also returns to the out-of-phase resonance of the fundamental frequency along another branch of the ω_{11}-backbone (thin dotted line). The two projections of this solution on the ω-A_{c1} and ω-A_{c3} planes are also plotted in Figs. 7 and 8 (curve 2). The out-of-phase resonance behaves differently in comparison with inphase resonance, as the former does not have any infinite branch.

It is worth pointing out that if the portions of the curve affected by internal resonance is ignored, the forced vibration response ω-A_{cl} shown in Fig. 7 will exhibit the same characater as that of the usual forced vibration without internal resonance.

4 Conclusions

1. The proposed computer method is an effective tool capable of tracing the complicated response of nonlinear structural vibrations

2. The frequency response obtained by retaining only one harmonic term for deflection still gives a good approximation except for the phenomenon of internal resonance. This fact is of practical significance and implies that an increase in the number of normal coordinates and harmonic terms should produce correspondingly a more complicated response. However, as shown by the example, the solution obtained by neglecting some higher harmonic terms could still be a good approximation if the internal resonances associated with these neglected terms are outside the interested frequency range or are somehow polished off by damping. Just under this understanding, it can be regarded that the approximate solution obtained by the present method will approach the actual solution of the original problem with increasing number of degrees of freedom and harmonic terms.

3. In connection with Point 2, it is expected that damping effects may play an important role in nonlinear vibration of real structures. Especially, since the damping factor usually has greater effects on higher harmonics, and it follows that those harmonics whose frequencies are far away from the frequency range under consideration may be neglected in practical analysis. Modal viscous damping can be introduced into the formulation without difficulty; however, the resulting coefficient matrix for the amplitude increments will no longer be symmetrical.

4. In this paper, only periodic response have been considered. In fact a wide variety of aperiodic responses also exist. Reference [6] represents an effort made toward this more complicated problem.

5. Stability analysis of periodic response has not been included here, in fact some parts of solutions presented are well known to be unstable. A parameter incremental method for computing the instability boundaries of nonlinear vibrations has been presented recently [7], however further general studies in instability including the parametrical combination resonance is required.

6. The super/subharmonic resonance may well appear in conjunction with internal resonances just as pointed out in paragraph (*i*), but they are not explored in full at present, because only those cases where the exciting frequency range is near $\omega = \omega_{11}$ have been treated.

References

1 Lau, S. L., Cheung, Y. K., and Wu, S. Y., "Nonlinear Vibration of Thin Elastic Plates, Part 1: Generalized Incremental Hamilton's Principle and Element Formulation," ASME JOURNAL OF APPLIED MECHANICS, Vol. 51, 1984, pp. 837–844.

2 Sridhar, S., Mook, D. T., and Nayfeh, A. H., "Nonlinear Resonances in The Forced Response of Plates. Part 1: Symmetric Responses of Circular Plates," *J. of Sound and Vibration*, Vol. 41, 1975, pp. 359–373.

3 Sridhar, S., Mook, D. T., and Nayfeh, A. H., "Nonlinear Resonances in the Forced Responses of Plates. Part 2:Asymmetric Responses of Circular Plates," *J. of Sound and Vibration*, Vol. 59, 1978, pp. 159–170.

4 Lobitz, D. W., Nayfeh, A. H., and Mook, D. T., "Nonlinear Analysis of Vibrations of Irregular Plates," *J. of Sound and Vibration*, Vol. 49, 1977, pp. 203–217.

5 Haisler, W. E., Stricklin, J. A., and Key, J. Y., "Displacement Incrementation in Nonlinear Structural Analysis of the Self-correcting Method," *Int. J. Num. Meth. Eng.*, Vol. 11, 1977, pp. 3–10.

6 Bergan, P. G., and Clough, R. W., "Convergence Criteria for Iterative Process," *AIAA Journal*, Vol. 10, 1972, pp. 1107–1108.

7 Lau, S. L., Cheung, Y. K., and Wu, S. Y., "Incremental Harmonic Balance Method With Multiple Time Scales for Aperiodic Vibration of Nonlinear Systems," ASME JOURNAL OF APPLIED MECHANICS, Vol. 50, 1983, pp. 871–876.

8 Lau, S. L., Cheung, Y. K., and Wu, S. Y., "Variable Parameter Incrementation Method for Dynamic Instability of Linear and Nonlinear Elastic Systems," ASME JOURNAL OF APPLIED MECHANICS, Vol. 49, 1982, pp. 849–853.

Dynamic Stability of a Nonlinear Cylindrical Shell

A. Tylikowski
Institute of Machine Design Fundamentals, Warsaw Technical University, Warszawa, Poland 02-524

The stability of the undeflected middle surface of a uniform elastic cylindrical shell governed by Kármán's equations is studied. The shell is being subjected to a time-varying axial compression as well as a uniformly distributed time-varying radial loading. Using the direct Liapunov method sufficient conditions for deterministic asymptotic as well as stochastic stability are obtained. A relation between stability conditions of a linearized problem and that of Kármán's equations is found. Contrary to the stability theory of nonlinear plates it is established that the linearized problem should be modified to ensure the stability of the nonlinear shell. The case when the shell is governed by the Itô stochastic nonlinear equations is also discussed.

Introduction

The static stability (buckling) of elastic plates and shells under a deterministic constant loading acting on the middle surfaces has been considered in literature during the past 40 years. The reformulation of buckling problems as a single nonlinear operator equation in some appropriate Hilbert space due to Berger and Fife [1] and Berger [2] has proved to be especially useful and was adopted for branching and stability problems of plates and shells, e.g., [3-5]. Such an approach was used to study the applicability of the linearization of the nonlinear equations for plates and shells in the buckling analysis. For example, Vorovitch [6] proved that, in contradistinction to the buckling of nonlinear plates, the stability of cylindrical shells cannot be analyzed by means of the linearized equations.

The investigation of the dynamic stability of cylindrical shells under time-varying axial loading and external pressure has been initiated by Bolotin [7] and numerous papers have been written on the problem during the past 20 years. Most papers were concerned with deterministic loadings while a few dealt with simultaneous stochastically interdependent axial and radial excitations, e.g., Lepore and Stoltz [8]. All these papers have applied finite dimensional or modal approximations in the stability analysis. Using the direct Liapunov method the present author established [9] that stability conditions for the linearized plates imply the stability of nonlinear plates described by symmetric Kármán equations.

The intent of the present paper is the investigation of the similar linearization of the problem for cylindrical shells obeying nonsymmetric Kármán equations. Using the Liapunov method, sufficient stability conditions for asymptotic stability, almost sure asymptotic stability as well as uniform stochastic stability are derived. The stability domains obtained by applying the linearized equations of motion are compared with those employing the dynamic Kármán shell theory.

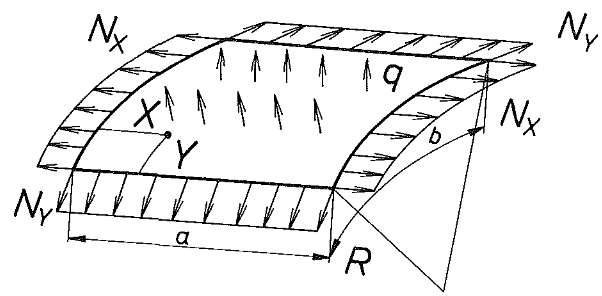

Fig. 1 Shell geometry

Problem Formulation

Let us consider a thin elastic cylindrical shell of constant thickness h and radius R, Fig. 1. If the material of the shell is of uniform density ρ and transverse displacement w of the shell is of an order comparable with thickness but relatively small as compared with other dimensions a, b of the shell, the differential equations that describe the transverse vibrations can be written in the form

$$D\Delta^2 w+\rho h\frac{\partial^2 w}{\partial T^2}+2\delta h\frac{\partial w}{\partial T}=N_X w_{,XX}+N_Y w_{,YY}+h[w,\Phi]+\frac{h}{R}\Phi_{,XX},\Delta^2\Phi=-\frac{E}{2}[w,w]-\frac{E}{R}w_{,XX},$$

$$(X,Y)\epsilon(0,a)\times(0,b) \tag{1}$$

where

$\Phi=$ the stress function

$E=$ Young modulus

Contributed by the Applied Mechanics Division for publication in the JOURNAL OF APPLIED MECHANICS.

Discussion on this paper should be addressed to the Editorial Department, ASME, United Engineering Center, 345 East 47th Street, New York, N.Y. 10017, and will be accepted until two months after final publication of the paper itself in the JOURNAL OF APPLIED MECHANICS. Manuscript received by ASME Applied Mechanics Division, February, 1983; final revision, December, 1983.

ν = Poisson ratio

$D = Eh^3/12(1-\nu^2)$ = flexural rigidity

δ = damping coefficient

T = real time

$$(\ .\ )_{,X} = \frac{\partial}{\partial X}$$

$$[f,g] = f_{,XX}g_{,YY} + f_{,YY}g_{,XX} - 2f_{,XY}g_{,XY}$$

with boundary conditions (simply supported shell)

$$\begin{aligned} w=0 &\quad \text{and} \quad w_{,XX}=0 \quad \text{at} \quad X=0,a \\ w=0 &\quad \text{and} \quad w_{,YY}=0 \quad \text{at} \quad Y=0,b \\ \Phi_{,YY}=0 &\quad \text{and} \quad \Phi_{,XY}=0 \quad \text{at} \quad X=0,a \\ \Phi_{,XX}=0 &\quad \text{and} \quad \Phi_{,XY}=0 \quad \text{at} \quad Y=0,b. \end{aligned}$$

For the shell subjected to a concentrated axial load $P(T)$ and a uniformly distributed radial loading $q(T)$, the initial membrane loads can be determined by assuming the shell remains circular and undergoes a uniform compression circumferentially. Consequently

$$N_X = P(T)/2\pi R,$$
$$N_Y = Rq(T).$$

Introducing dimensionless time $t = T(D/\rho h R^4)^{1/2}$ and coordinates $x = X/R$, $y = Y/R$, velocity $v = \partial w/\partial t$, reduced damping coefficient as well as reduced membrane loads

$$\beta = \delta R^2 (h/\rho D)^{1/2}, \quad \xi_x = N_X(T)R^2/D,$$
$$\xi_y = N_Y(T)R^2/D$$

equations (1) become

$$\Delta^2 w + \frac{\partial^2 w}{\partial t^2} + 2\beta\frac{\partial w}{\partial t} = \xi_x w_{,xx} + \xi_y w_{,yy} + \frac{h}{D}[w,\Phi] + \frac{Rh}{D}\Phi_{,xx},$$

$$\Delta^2\Phi = -\frac{E}{2}[w,w] - RE\ w_{,xx},$$

$$(x,y)\epsilon\Omega \equiv (0,a/R)\times(0,b/R). \tag{3}$$

Applying the operator Δ^{-2} (Green's operator of the biharmonic equation) to equation (3_2) and substituting the stress function Φ into equation (3_1) we obtain a nonlinear equation

$$\begin{aligned} \Delta^2 w + \frac{\partial^2 w}{\partial t^2} + 2\beta\frac{\partial w}{\partial t} &= \xi_x w_{,xx} + \xi_y w_{,yy} - \gamma_1[w,\Delta^{-2}[w,w]] \\ &- \gamma_2[w,\Delta^{-2}w_{,xx}] - \frac{\gamma_2}{2}(\Delta^{-2}[w,w])_{,xx} \\ &- \kappa(\Delta^{-2}w_{,xx})_{,xx},\ (x,y)\epsilon\Omega \end{aligned} \tag{4}$$

where

$$\gamma_1 = Eh/2D, \quad \gamma_2 = ERh/D, \quad \kappa = R^2Eh/D,$$

for functions $w\epsilon\dot{W}_{2,2}(\Omega)$.

$W_{2,2}(\Omega)$ denotes a Hilbert space with respect to the inner product

$$(u,v)_{2,2} = \int_\Omega (u_{,xx}v_{,xx} + 2u_{,xy}v_{,xy} + u_{,yy}v_{,yy})d\Omega.$$

$\dot{W}_{2,2}(\Omega)$ is the closure of $C_0^\infty(\Omega)$ in $W_{2,2}(\Omega)$ and thus can be itself regarded as a Hilbert space with the norm

$$\|w\|_{2,2} = (w,w)_{2,2}{}^{1/2}.$$

The conditions imposed on the stress function and the displacement (the boundary conditions (2)) can be written down as [10]

$$\begin{aligned} w=0 &\quad \text{and} \quad w_{,xx}=0 \quad \text{at} \quad x=0,a/R \\ w=0 &\quad \text{and} \quad w_{,yy}=0 \quad \text{at} \quad y=0,b/R \\ \Phi=0 &\quad \text{and} \quad \Phi_{,x}=0 \quad \text{at} \quad x=0,a/R \\ \Phi=0 &\quad \text{and} \quad \Phi_{,y}=0 \quad \text{at} \quad y=0,b/R. \end{aligned} \tag{5}$$

Let us assume that the solution to the equation (4) exists and belongs to the space $\dot{W}_{2,2}(\Omega)$. To estimate a deflected shell surface we introduce formal stability definitions by using a scalar measure $\|\ .\ \|$ (distance) of the solution of equation (4) with nontrivial initial conditions from the trivial solution. Our study of stability of the undeflected shell middle surface $w=0$ splits into three branches.

First, under the assumption that forces ξ_x, ξ_y acting in the shell middle surface are deterministic functions of time, conditions of asymptotic stability of the trivial solution, i.e., conditions that imply

$$\lim_{t\to\infty} \|w\| = 0$$

are derived.

Our second purpose is to discuss almost sure asympototic stability of the trivial solution, i.e.,

$$P\left\{\lim_{t\to\infty} \|w\| = 0\right\} = 1,$$

if the forces ξ_x, ξ_y are stochastic "nonwhite" processes.

In the third case, if the forces are broad-band normal stochastic processes we investigate the uniform stochastic stability of the trivial solution of equation (4), i.e., we formulate conditions implying the logic sentence

$$\bigwedge_{\epsilon>0}\bigwedge_{\delta>0}\bigvee_{r>0} \|w(\ .\ ,0)\| < r \Rightarrow P\left\{\sup_{t\ge 0} \|w(\ .\ ,t)\| > \delta\right\} < \epsilon.$$

We will study the foregoing kinds of stability via Liapunov functional approach.

Asymptotic Stability

We can give a unified treatment of stability analysis for both deterministic forces and stochastic "nonwhite" processes. We start from a linearized problem, i.e., omitting the nonlinear terms in equation (4) we obtain

$$\Delta^2 w + \frac{\partial v}{\partial t} + 2\beta v = \xi_x w_{,xx} + \xi_y w_{,yy} - \kappa(\Delta^{-2}w_{,xx})_{,xx}. \tag{6}$$

Using the Kozin's method derived for linear problems in [11], we construct the functional as follows

$$V_L = V_{Lp} + \kappa\int_\Omega (\Delta^{-1}w_{,xx})^2 d\Omega, \tag{7}$$

where the functional V_{Lp} is the same as in the stability analysis of a linear plate

$$V_{Lp} = \int_\Omega [(\Delta w)^2 + v^2 + 2\beta v w + 2\beta^2 w^2]d\Omega. \tag{8}$$

The functional V_L is positive-definite and its time derivative along equation (6) is equal to

$$\begin{aligned} \frac{dV_L}{dt} = 2\int_\Omega \{&(v+\beta w)(-2\beta v - \Delta^2 w + \xi_x w_{,xx} + \xi_y w_{,yy} \\ &- \kappa(\Delta^{-2}w_{,xx})_{,xx} + \beta v^2 + 2\beta^2 v w + \Delta w \Delta v \\ &+ \kappa\Delta^{-1}v_{,xx}\Delta^{-1}w_{,xx}\}d\Omega. \end{aligned} \tag{9}$$

Because of the smoothness of functions belonging to the space $\dot{W}_{2,2}$ it is permissible to integrate by parts the expressions in equation (9). Doing the foregoing operations and using the boundary conditions (5) we obtain

$$\frac{dV_L}{dt} = -2\beta V_L + 2U_L, \tag{10}$$

where

$$U_L=\int_\Omega \{ v+\beta w)(\xi_x w_{,xx}+\xi_y w_{,yy})$$
$$+2\beta^2 vw+2\beta^3 w^2 \} d\Omega. \tag{11}$$

Thus, the stability analysis is reduced to construction of a bound

$$U_L \leq \lambda(t) V_L, \tag{12}$$

where the positive function λ will be determined using the variational calculus [11]. The basic inequality (12) can be rewritten explicitly as

$$\lambda\int_\Omega \{ (\Delta w)^2+v^2+2\beta vw+2\beta^2 w^2+\kappa(\Delta^{-1} w_{,xx})^2 \} d\Omega$$

$$\geq \int_\Omega \{ (v+\beta w)(\xi_x w_{,xx}+\xi_y w_{,yy})+2\beta^2 vw+2\beta^3 w^2 \} d\Omega. \tag{13}$$

The associated Euler's equations of the variational problem $\delta(U_L-\lambda V_L)=0$ are given by

$$\xi_x w_{,xx}+\xi_y w_{,yy}+2\beta^2 w-\lambda(v+\beta w)=0,$$
$$[\xi_x w_{,xx}+\xi_y w_{,yy}+\beta(\beta-\lambda)](v+2\beta w)$$
$$-\lambda[\Delta^2 w+\kappa(\Delta^{-2} w_{,xx})_{,xx}]=0. \tag{14}$$

Solving equations (14) with respect to the function w and using the boundary conditions (5) we find the appropriate function λ as follows

$$\lambda=\max_{m,n=1,2,\ldots} (\alpha_m^2+\alpha_n^2)\,|2\beta^2-\alpha_m^2\xi_x-\alpha_n^2\xi_y|$$
$$/\{(\alpha_m^2+\alpha_n^2)^2[\beta^2+(\alpha_m^2+\alpha_n^2)^2]+\kappa\alpha_m^4\}^{1/2}, \tag{15}$$

where $\alpha_m=m\pi R/a, \qquad \alpha_n=n\pi R/b.$

From equation (10) and inequality (12) we have

$$V_L(t)\leq V_L(0)\exp\left[-2\left(\beta t-\int_0^t \lambda(s)\,ds\right)\right]. \tag{16}$$

Thus, it immediately follows that the sufficient condition for asymptotic stability with respect to measure $\|w\|=V_L^{1/2}$ is

$$\lim_{t\to\infty} \frac{1}{t}\int_0^t \lambda(s)\,ds \leq \beta, \tag{17}$$

or for almost sure asymptotic stability, if the processes ξ_x, ξ_y are ergodic and stationary, is

$$\mathrm{E}\lambda\leq\beta, \tag{18}$$

where E denotes the operator of the mathematical expectation.

The auxiliary linearized problem being solved we can now direct our attention to the nonlinear operator equation (4) governing the radial vibrations of the shell. We derive the functional adding a positive-definite operator term to the functional V_{Lp}

$$V=\int_\Omega [v^2+2\beta vw+2\beta^2 w^2+(\Delta w)^2]d\Omega$$
$$+\frac{\gamma_1}{2}\int_\Omega \left\{\Delta^{-1}[w,w]+\frac{\gamma_2}{\gamma_1}\Delta^{-1}w_{,xx}\right\}^2 d\Omega. \tag{19}$$

Upon differentiating (19), applying the bilinearity of operator [. , .], and evaluating the second derivative of displacements from equation (4) we obtain

$$\frac{dV}{dt}=2\int_\Omega \{ (v+\beta w)[-2\beta v-\Delta^2 w+\xi_x w_{,xx}+\xi_y w_{,yy}$$
$$-\gamma_1[w,\Delta^{-2}[w,w]]-\gamma_2[w,\Delta^{-2}w_{,xx}]$$
$$-\frac{\gamma_2}{2}(\Delta^{-2}[w,w])_{,xx}-\kappa(\Delta^{-2}w_{,xx})_{,xx}]+\beta v^2$$
$$+2\beta^2 vw+\Delta w\Delta v+2\gamma_1\Delta^{-1}[w,w]\Delta^{-1}[w,v]$$
$$+\gamma_2\Delta^{-1}[w,w]\Delta^{-1}v_{,xx}+2\gamma_2\Delta^{-1}w_{,xx}\Delta^{-1}[w,v]$$
$$+\left.\frac{\gamma_2^2}{\gamma_1}\Delta^{-1}w_{,xx}\Delta^{-1}v_{,xx}\right\} d\Omega. \tag{20}$$

We make an effort to transform equation (20) into the form (10). For this purpose we apply the symmetry property [2]

$$\int_\Omega [f,g]h\,d\Omega=\int_\Omega [g,h]f\,d\Omega=\int_\Omega [h,f]g\,d\Omega, \tag{21}$$

and prepare the following equalities using the Green's formula as well as the boundary conditions (5)

$$\int_\Omega v[w,\Delta^{-2}[w,w]]d\Omega=\int_\Omega \Delta^{-1}[w,w]\Delta^{-1}[w,v]d\Omega,$$

$$\int_\Omega v[w,\Delta^{-2}w_{,xx}]d\Omega=\int_\Omega \Delta^{-1}w_{,xx}\Delta^{-1}[w,v]d\Omega,$$

$$\int_\Omega v(\Delta^{-2}[w,w])_{,xx}d\Omega=\int_\Omega \Delta^{-1}v_{,xx}\Delta^{-1}[w,w]d\Omega,$$

$$\int_\Omega v(\Delta^{-2}w_{,xx})_{,xx}d\Omega=\int_\Omega \Delta^{-1}v_{,xx}\Delta^{-1}w_{,xx}d\Omega. \tag{22}$$

Upon substituting (21) and (22) into (20) we obtain equality (10), where

$$U=U_L-\frac{\beta\gamma_1}{2}\int_\Omega (\Delta^{-1}[w,w]+\frac{\gamma_2}{2\gamma_1}\Delta^{-1}w_{,xx})^2 d\Omega$$
$$-\frac{\gamma_2^2}{4\gamma_1^2}\int_\Omega (\Delta^{-1}w_{,xx})^2 d\Omega. \tag{23}$$

Therefore, the stability analysis depends on the construction of the bound, similar to the inequality (12) in the linearized problem

$$U\leq\lambda^* V,$$

or

$$\int_\Omega \{2\beta^2 vw+2\beta^3 w^2+(v+\beta w)(\xi_x w_{,xx}+\xi_y w_{,yy})\}d\Omega+$$
$$-\frac{\beta\gamma_1}{2}\int_\Omega \left(\Delta^{-1}[w,w]+\frac{\gamma_2}{2\gamma_1}\Delta^{-1}w_{,xx}\right)^2 d\Omega$$
$$+\frac{\beta\gamma_1 R^2}{2}\int_\Omega (\Delta^{-1}w_{,xx})^2 d\Omega\leq\frac{\lambda^*\gamma_1}{2}\int_\Omega \left(\Delta^{-1}[w,w]\right.$$
$$\left.+\frac{\gamma_2}{\gamma_1}\Delta^{-1}w_{,xx}\right)^2 d\Omega+\lambda^*\int_\Omega \{v^2+2\beta vw+2\beta^2 w^2$$
$$+(\Delta w)^2\}d\Omega. \tag{24}$$

Taking into account that the second term on the left-hand side is nonpositive and the first term on the right-hand side is nonnegative, inequality (24) will hold, if the function λ^* satisfies the modified condition involving the second-order functionals only

$$\int_\Omega \{2\beta^2 vw+2\beta^3 w^2+(v+\beta w)(\xi_x w_{,xx}+\xi_y w_{,yy})\}d\Omega$$
$$+\frac{\beta\gamma_1 R^2}{2}\int_\Omega (\Delta^{-1}w_{,xx})^2 d\Omega\leq\lambda^*\int_\Omega \{v^2+2\beta vw+2\beta^2 w^2$$
$$+(\Delta w)^2\}d\Omega. \tag{25}$$

We mention that inequality (25) differs significantly from inequality (13) relating to the linearized case. In contradistinction to the stability of a nonlinear plate [9], it is

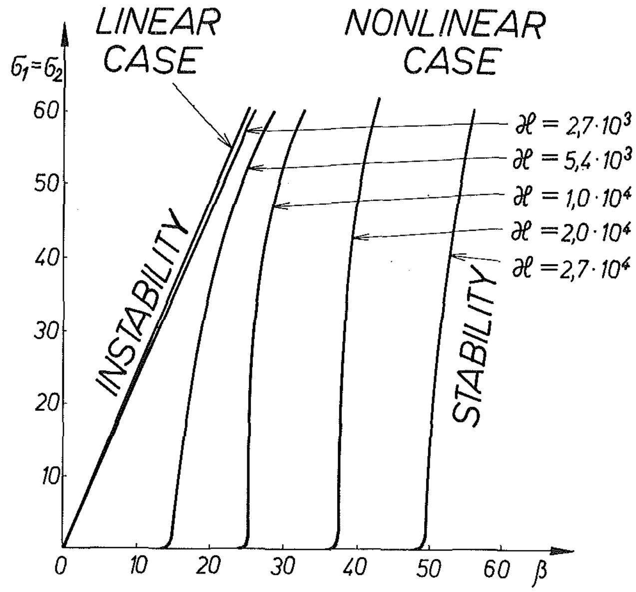

Fig. 2 Stability regions under deterministic periodic (sinusoidal) processes

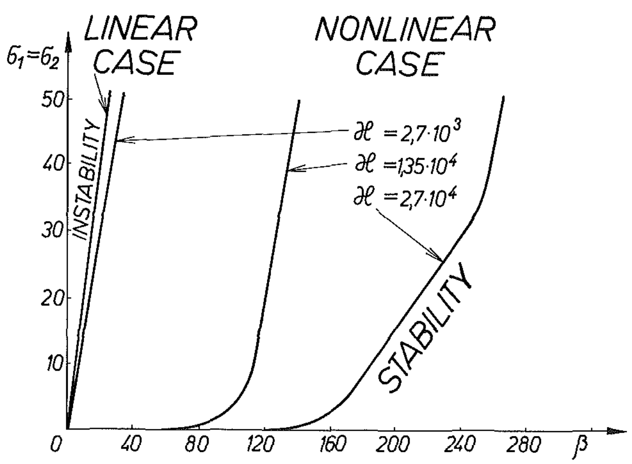

Fig. 3 Stability regions under uncorrelated Gaussian processes

found that the sufficient stability conditions (17) or (18) with a function λ^* satisfying inequality (12) can be not sufficient to ensure the stability of trivial solutions of Kármán's equations. The analogous difference relating to a static buckling of nonlinear plates and shells was reported by Vorovitch [6].

Similarly as in the linearized case we apply the calculus of variation to calculate the appropriate function λ^*

$$\lambda^* = \max_{m,n=1,2,\ldots} (\alpha_m^2+\alpha_n^2)^2(2\beta^2-\xi_x\alpha_m^2-\xi_y\alpha_n^2)^2 \Big/ \Big\{ \Big[(\alpha_m^2+\alpha_n^2)^4(\beta^2+(\alpha_m^2+\alpha_n^2)^2)(2\beta^2-\xi_x\alpha_m^2-\xi_y\alpha_n^2)^2 + \frac{\beta^2\kappa^2}{4}\alpha_m^8 \Big]^{1/2} - \frac{\beta\kappa}{2}\alpha_m^4 \Big\}. \tag{26}$$

The asymptotic stability regions as functions of β, σ, and κ evaluated numerically in the case when the loads are deterministic periodic (sinusoidal) processes with equal variances $\sigma_x = \sigma_y = \sigma$ and means equal to zero are shown in Fig. 2. As the second numerical example we take the shell loaded by uncorrelated Gaussian processes with means equal to zero. The dependence of stability regions on damping coefficient β, variance σ, and parameter κ is shown in Fig. 3. From the figures it is seen that the stability regions evaluated by means of the linearized theory depend slightly on the parameter $\kappa = 12(1-\nu^2)(R/h)^2$. On the contrary, when the nonlinear theory is assumed, the critical value β increases rapidly with increasing κ. The results confirm that the linearized theory is not sufficient to ensure the stability of shells governed by the nonlinear equations.

Uniform Stability of Stochastic Itô Equations

If the forces acting on the shell middle surface are broadband normal stochastic processes the dynamic equations (4) can be rewritten in Itô differential form due to Kushner [12]

$$dw = v\,dt,$$
$$dv = \Big\{ -2\beta v - \Delta^2 w - \gamma_1[w,\Delta^{-2}[w,w]] - \gamma_2[w,\Delta^{-2}w_{,xx}] - \frac{\gamma_2}{2}(\Delta^{-2}[w,w])_{,xx} - \kappa(\Delta^{-2}w_{,xx})_{,xx} \Big\} dt + \sigma_1 w_{,xx}d\xi_1(t) + \sigma_2 w_{,yy}d\xi_2(t), \tag{27}$$

where ξ_1, ξ_2 are the standard uncorrelated Wiener processes. Taking the functional in the same form as in (19) we apply Itô calculus to obtain its differential dV

$$dV = 2\int_\Omega \{\Delta w\Delta dw + (v+\beta w)dv + 2\beta^2 w dw + \beta v dw\} d\Omega + \gamma_1\int_\Omega \Big\{\Delta^{-1}[w,w] + \frac{\gamma_2}{\gamma_1}\Delta^{-1}w_{,xx}\Big\}\Big\{2\Delta^{-1}[w,dw] + \frac{\gamma_2}{\gamma_1}\Delta^{-1}dw_{,xx}\Big\}d\Omega + \int_\Omega \{\sigma_1^2(w_{,xx})^2 + \sigma_2^2(w_{,yy})^2\} d\Omega dt.$$

Substituting equations (27), using symmetry property (21) and equalities (22) the differential dV becomes

$$dV = 2\int_\Omega \Big\{-\beta v^2 - \beta(\Delta w)^2 + \frac{\beta\kappa}{8}(\Delta^{-1}w_{,xx})^2 + \frac{\sigma_1^2}{2}(w_{,xx})^2 + \frac{\sigma_2^2}{2}(w_{,yy})^2\Big\} d\Omega dt - 2\beta\gamma_1\int_\Omega \Big\{\Delta^{-1}[w,w] + \frac{3}{2R}\Delta^{-1}w_{,xx}\Big\}^2 d\Omega dt + 2\int_\Omega (v+\beta w)(\sigma_1 w_{,xx}d\xi_1(t) + \sigma_2 w_{,yy}d\xi_2(t))d\Omega.$$

On integrating with respect to t from s to $\tau_\delta(t)$, where $\tau_\delta(t) = \min\{\tau_\delta, t\}$, $\tau_\delta = \inf\{t: \|w\| > \delta > 0\}$, averaging and taking into consideration that $E\xi_i = 0$, $i = 1, 2$, it follows that

$$EV(\tau_\delta(t)) = V(s) + 2\int_0^{\tau_\delta(t)}\int_\Omega \Big\{-\beta v^2 - \beta(\Delta w)^2 + \frac{\beta\kappa}{8}(\Delta^{-1}w_{,xx})^2 + \frac{\sigma_1^2}{2}(w_{,xx})^2 + \frac{\sigma_2^2}{2}(w_{,yy})^2 - \beta\gamma_1(\Delta^{-1}[w,w] + \frac{3}{2R}\Delta^{-1}w_{,xx})^2\Big\} d\Omega dt.$$

We estimate the average of functional V assuming that

$$\int_\Omega \Big\{\beta v^2 + (\Delta w)^2 - \frac{\beta\kappa}{8}(\Delta^{-1}w_{,xx})^2 - \frac{\sigma_1^2}{2}(w_{,xx})^2 - \frac{\sigma_2^2}{2}(w_{,yy})^2\Big\} d\Omega \geq 0. \tag{28}$$

Thus, taking into account inequality (28) and neglecting the negative term

$$-\beta\gamma_1(\Delta^{-1}[w,w] + \frac{3}{2R}\Delta^{-1}w_{,xx})^2,$$

we find that the functional V is a supermartingale, i.e., $EV(\tau_\delta(t)) \leq V(s)$. Neglecting the first positive term βv^2 in the integrand of (28) and using Chebyshev's inequality it immediately follows that the sufficient condition for uniform stochastic stability of the trivial solution of equations (27) with respect to measure $\|w\| = V^{1/2}$ takes the form

$$\beta \geq \frac{1}{2}\max\{\sigma_1^2, \sigma_2^2\} \max_{m,n=1,2,\ldots} (\alpha_m^4 + \alpha_n^4) \Big/ \left\{(\alpha_m^2 + \alpha_n^2)^2 - \frac{\kappa}{8}\alpha_m^4 \Big/ (\alpha_m^2 + \alpha_n^2)^2\right\}. \quad (29)$$

It should be mentioned that for certain geometrical dimensions and mechanical properties of the shell, the ratio in equality (29) can be nonpositive, thus in this case condition (29) is useless.

For example, in the case $a \sim b \sim R$, $h = 0.1R$ inequality (29) becomes

$$\beta \geq \max\{\sigma_1^2, \sigma_2^2\}/2. \quad (30)$$

The condition (29) or (30) generates the sufficient stability regions as functions κ, σ_1, σ_2, or σ_1, σ_2. The result (30) is the same as a condition of uniform stability of nonlinear plates [9].

Conclusions

A method has been presented for analyzing the stability of nonlinear cylindrical shells subjected to a time-varying axial compression as well as a uniformly distributed time-varying radial loading. Two different dynamical models have been used, the first when the excitations are deterministic periodic or stochastic nonwhite processes, the second one is applicable to describing broad-band Gaussian excitations. Using the appropriate Liapunov functional, sufficient conditions have been developed to ensure both the asymptotic or almost sure asymptotic stability for the first model and the uniform stochastic stability for the second one. The major conclusion is that, contrary to the stability theory of nonlinear plates, the linearized problem should be modified to ensure the stability of nonlinear shells. The criteria developed in the paper define stability regions in terms of variances or intensities of the excitation processes, and the physical characteristics of the shell. A comparison of the results shows that the stability regions of nonlinear shells strongly depend on the system parameters. The result for the uniform stochastic stability indicates however that in some cases the sufficient conditions can be quite conservative.

References

1 Berger, M. S., and Fife, P. C., "On von Kármán Equations and the Buckling of a Thin Elastic Plate," *Bull. Amer. Math. Soc.*, Vol. 72, 1966, pp. 1006–1011.

2 Berger, M. S., "On von Kármán's Equations and the Buckling of a Thin Elastic Plate, I, The Clamped Plate," *Comm. on Pure and Applied Math.*, Vol. 20, 1967, pp. 687–719.

3 Berger, M. S., "Bifurcation Theory for Nonlinear Elliptic Partial Differential Equations," in: *Bifurcation Theory and Nonlinear Eigenvalue Problems*, Keller, J. S., and Antman, S., eds., Benjamin Inc., New York, Amsterdam, 1969.

4 Berger, M. S., "Global Analysis of Specific Nonlinear Eigenvalue Problems," *Rocky Mountains Journal of Mathematics*, Vol. 3, 1973, pp. 319–354.

5 Sather, D., "Branching of Solutions of Nonlinear Equations," *Rocky Mountains Journal of Mathematics*, Vol. 3, 1973, pp. 203–250.

6 Vorovitch, I. I., "Certain Estimations of Number of Solutions of Kármán's Equations in Connection with Stability Problems of Plates and Shells" (in Russian), in: L.I. Sedov 60th Anniversary Volume, Nauka, Moskva, 1969, pp. 111–118.

7 Bolotin, V. V., *The Dynamic Stability of Elastic Systems*, Holden-Day, San Francisco, 1964.

8 Lepore, J. A., and Stoltz, R. A., "Stability of Linear Cylindrical Shells Subjected to Stochastic Excitations," *Lect. Notes in Math.*, Vol. 294, 1972, pp. 239–251.

9 Tylikowski, A., "Stability of a Nonlinear Rectangular Plate," ASME Journal of Applied Mechanics, Vol. 45, 1978, pp. 583–585.

10 Volmir, A. S., *Nonlinear Dynamics of Plates and Shells*, in Russian, Nauka, Moskva, 1972.

11 Kozin, F., "Stability of the Linear Stochastic System," *Lect. Notes in Math.*, Vol. 294, 1972, pp. 186–229.

12 Kushner, H. J., "On the Optimal Control of a System Governed by a Linear Parabolic Equation with White Noise Inputs," *SIAM Journal on Control*, Vol. 6, 1968, pp. 596–614.

G. Garner[1]
The Charles Stark Draper Laboratory,
555 Technology Square,
MS 60,
Cambridge, Mass. 02139

S. Chandra[2]
Northeast Utilities,
P.O. Box 270,
Hartford, Conn. 06101
Mem. ASME

Fluid-Structure Coupling Between a Finite Cylinder and a Confined Fluid

The dynamic behavior of a finite length cylindrical rod in a fluid filled annulus is considered. The fluid and structure equations are solved simultaneously, with fluid-structure coupling accounted for. Coupled mode shapes and natural frequencies are obtained for various cases. It is found that for short lengths and/or higher modes, the effect of the fluid on the cylinder motion diminishes compared to the infinite cylinder case. In addition, coupled and in-vacuum mode shapes can differ in certain cases.

Introduction

When an elastic cylindrical rod vibrates in an external fluid, the effect of the fluid inertia may be accounted for by use of an effective fluid "added mass" in the equation of motion of the rod. The added mass is expressed as an added mass coefficient multiplied by the mass of the fluid displaced by the rod [1-4]. The added mass has been calculated by solving the equations of motion for the fluid using two-dimensional theory [5-9], or using three-dimensional theory and assuming the cylinder deforms as it would in a vacuum [10]. The various references considered a potential fluid [5-7, 10], a viscous incompressible fluid [8], and an inviscid compressible fluid [2].

In all cases the fluid equation was solved independently of the actual motion of the structure. When the two-dimensional fluid theory was used, the effect of the structure did not enter into the fluid equation. When the three-dimensional theory was used, the in-vacuum mode shapes were used rather than the actual mode shapes.

The fluid and structure equations for a rod vibrating in an annulus were solved simultaneously in [11] using a Fourier transform technique. There the fluid was assumed inviscid and compressible, and was flowing axially. The cylinder was pinned at both ends. The technique required fluid boundary conditions at infinity. The annulus was assumed to be infinite in length, with each end of the flexible rod attached to a rigid, semi-infinite cylinder.

The fluid and structure equations are solved simultaneously here using a different analytical technique from that in [11]. The fluid is assumed inviscid and incompressible, and there is no bulk fluid motion. In contrast to [11], the annulus is assumed finite in length. Various fluid and structure boundary conditions are considered.

Derivation of the Equations of Motion

Consider a finite length cylinder submerged in a confined potential fluid (Fig. 1). The equation of motion for the fluid is:

$$\nabla^2 V = \left[\frac{\partial^2}{\partial r^2} + \frac{1}{r}\frac{\partial}{\partial r} + \frac{1}{r^2}\frac{\partial^2}{\partial \phi^2} + \frac{\partial^2}{\partial x^2} \right] V(r,\phi,x,t) = 0 \qquad (1)$$

where $V(r,\phi,x,t)$ is the velocity potential. The fluid velocity $\mathbf{v}$ and pressure p are given by $\mathbf{v} = -\nabla V$ and $p = \rho(\partial V/\partial t)$, respectively, where ρ is the fluid density. Only small deformations of the cylinder are considered, so the pressure is given by a linearized Bernoulli equation.

The equation of motion for the cylinder is

$$EI\frac{\partial^4 y}{\partial x^4} + m\frac{\partial^2 y}{\partial t^2} = P(x,t) + F(x,t) \qquad (2)$$

where y = cylinder displacement, EI = cylinder flexural rigidity, m = cylinder mass per unit length, $P(x,t)$ = force per unit length acting on the cylinder due to fluid pressure, and $F(x,t)$ = force per unit length due to effects other than fluid pressure.

The fluid boundary conditions are $\partial V/\partial r = -\dot{y}\cos\phi$ at $r=a$ (where the dot denotes partial derivative with respect to time), $\partial V/\partial r = 0$ at $r=b$, and $V=0$ or $\partial V/\partial x = 0$ at $x=0$ and $x=L$. $V=0$ corresponds to an open end (zero fluctuating pressure), and $\partial V/\partial x = 0$ corresponds to a closed end (zero fluid velocity).

Using separation of variables, the solution to (1) may be written:

$$V = \sum_{n=1}^{\infty} R_n(r,t) X_n(x) \cos\phi \qquad (3)$$

where $R_n(r,t)$ and $X_n(x)$ are solutions to

[1] Also, Graduate Student, Department of Mechanical Engineering, Massachusetts Institute of Technology, Cambridge, Mass. 02139. Formerly with American Electric Power, 2 Broadway, New York, N.Y. 10004.

[2] Formerly with Combustion Engineering, Power Systems, 1000 Prospect Hill Road, Windsor, Conn. 06095.

Contributed by the Applied Mechanics Division for publication in the JOURNAL OF APPLIED MECHANICS.

Discussion on this paper should be addressed to the Editorial Department, ASME, United Engineering Center, 345 East 47th Street, New York, N.Y., 10017, and will be accepted until two months after final publication of the paper itself in the JOURNAL OF APPLIED MECHANICS. Manuscript received by ASME Mechanics Division, January, 1982; final revision, April, 1984.

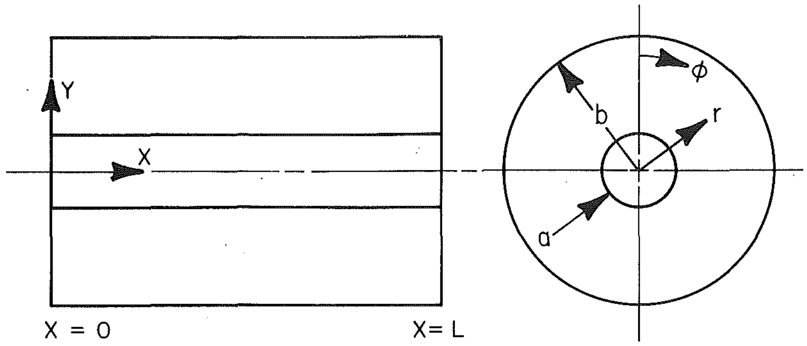

Fig. 1 Geometry of a finite length cylinder in a confined potential fluid

$$\left[\frac{\partial^2}{\partial r^2}+\frac{1}{r}\frac{\partial}{\partial r}-\left(\frac{1}{r^2}+\lambda_n^2\right)\right]R_n(r,t)=0 \tag{4}$$

$$\frac{d^2X_n}{dx^2}+\lambda_n^2X_n=0 \tag{5}$$

The solution to (5) is

$$X_n(x)=C_n\sin\lambda_n x+D_n\cos\lambda_n x \tag{6}$$

where C_n, D_n, and λ_n are determined by the boundary conditions at $x=0$ and $x=L$.

Substituting (3) into the boundary condition at $r=a$, multiplying by $X_n(x)$, and integrating over x from 0 to L produces

$$\left.\frac{\partial R_n(r,t)}{\partial r}\right|_{r=a}=-\frac{\int_0^L \ddot{y}(x,t)X_n(x)dx}{\int_0^L X_n^2(x)dx} \tag{7}$$

Substituting equation (3) into the boundary condition at $r=b$ produces

$$\left.\frac{\partial R_n(r,t)}{\partial r}\right|_{r=b}=0 \tag{8}$$

The solution to (4) with boundary conditions (7) and (8) is

$$R_n(r,t)=H_n(r)\ddot{Y}_n(t) \tag{9}$$

where

$$H_n(r)=\frac{1}{\lambda_n\Delta_n f_n}\left[I_1'(\lambda_n b)K_1(\lambda_n r)-K_1'(\lambda_n b)I_1(\lambda_n r)\right] \tag{10}$$

$$\Delta_n=I_1'(\lambda_n a)K_1'(\lambda_n b)-I_1'(\lambda_n b)K_1'(\lambda_n a) \tag{11}$$

$$Y_n(t)=\int_0^L y(x,t)X_n(x)dx \tag{12}$$

$$f_n=\int_0^L X_n^2dx \tag{13}$$

and prime denotes differentiation with respect to x.

Substituting (9) into (3) gives for the pressure distribution

$$p(r,\phi,x,t)=\sum_{n=1}^{\infty}\rho H_n(r)\ddot{Y}_n(t)X_n(x)\cos\phi \tag{14}$$

The force per unit length acting on the cylinder due to fluid pressure is

$$\begin{aligned}P(x,t)&=-\int_0^{2\pi}p(a,\phi,x,t)a\cos\phi\, d\phi\\&=-\rho\pi a\sum_{n=1}^{\infty}H_n(a)X_n(x)\ddot{Y}_n(t)\end{aligned} \tag{15}$$

Substituting (15) into (2) produces the following Fredholm integro-differential equation for the cylinder motion

$$EI\frac{\partial^4 y}{\partial x^4}+m\frac{\partial^2 y}{\partial t^2}=-\rho\pi a\sum_{n=1}^{\infty}H_n(a)\,X_n(x)\cdot\int_0^L\frac{\partial^2 y(x',t)}{\partial t^2}X_n(x')dx'+F(x,t) \tag{16}$$

Equation (16) is solved subject to the classical cylinder boundary conditions, with the $X_n(x)$ determined by equation (6) and fluid boundary conditions.

The equation of motion may be put in dimensionless form by defining $\eta=y/L$, $\xi=x/L$, $\tau=(EI/m)^{1/2}t/L^2$, $\Gamma=FL^3/EI$, and $G_n=\pi\rho a L\,H_n(a)/m$. Then (16) becomes

$$\frac{\partial^4\eta}{\partial\xi^4}+\frac{\partial^2\eta}{\partial\tau^2}=-\sum_{n=1}^{\infty}G_nX_n(\xi)\int_0^1\frac{\partial^2\eta(\xi',\tau)}{\partial\tau^2}\cdot X_n(\xi')d\xi'+\Gamma(\xi,\tau) \tag{17}$$

Free Vibration

***(a)* Eigenvalue Problem** Assume a solution for the ith normal mode of the form

$$\eta(\xi,\tau)=\psi_i(\xi)e^{i\Omega_i\tau} \tag{18}$$

where Ω_i is the dimensionless frequency and $\psi_i(\xi)$ is the mode shape. Substituting into (17) produces

$$\frac{d^4\psi_i}{d\xi^4}-\beta_i^4\psi_i=\beta_i^4\sum_{n=1}^{\infty}G_nX_n(\xi)\int_0^1\psi_i(\xi')X_n(\xi')d\xi' \tag{19}$$

where $\beta_i=\Omega_i^{1/2}$, and Ω_i is related to the circular frequency ω_i by

$$\Omega_i=L^2(m/EI)^{1/2}\omega_i \tag{20}$$

Equation (19) is a Fredholm integro-differential equation for the mode shapes $\psi_i(\xi)$ and natural frequencies Ω_i, and is subject to cylinder boundary conditions on $\psi_i(\xi)$.

Define the operator $\mathbf{P}$ by

$$\mathbf{P}[\psi(\xi)]=\sum_{n=1}^{\infty}G_nX_n(\xi)\int_0^1X_n(\xi')\psi(\xi')d\xi' \tag{21}$$

Then $\mathbf{P}$ has eigenvalues G_nf_n/L and corresponding eigenvectors $X_n(\xi)$. Equation (19) may be written

$$\frac{d^4\psi_i}{d\xi^4}=\beta_i^4[\mathbf{I}+\mathbf{P}]\psi_i \tag{22}$$

where $\mathbf{I}$ is the identity operator. The operator $\mathbf{I}+\mathbf{P}$ has eigenvalues $1+G_nf_n/L$ and corresponding eigenvectors $X_n(\xi)$. The inverse $\mathbf{Q}=(\mathbf{I}+\mathbf{P})^{-1}$ exists if $1+G_nf_n/L\neq 0$ for all n. This inequality holds because the quantity $G_nf_n/L>0$ for all n. Then $\mathbf{Q}$ is given by

$$\mathbf{Q}[\psi(\xi)]=\sum_{n=1}^{\infty}\frac{L/f_n}{1+\frac{G_nf_n}{L}}X_n(\xi)\int_0^1X_n(\xi')\psi(\xi')d\xi' \tag{23}$$

Table 1 Summary of cases considered

		Case 1	Case 2	Case 3
Boundary conditions		Pinned-pinned Closed-closed	Cantilevered Open-open	Cantilevered Open-open
Cylinder length L	(m)	1.0	3.854	8.268
Cylinder density ρ_c	(kg/m^3)	7.83×10^3	7.83×10^3	7.83×10^3
Cylinder outer radius a	(m)	1.0×10^{-2}	4.801×10^{-3}	1.935
Cylinder inner radius a_1	(m)	0.0	4.331×10^{-3}	1.88
Elastic modulus E	(Pa)	2.069×10^{11}	2.069×10^{11}	2.069×10^{11}
Fluid density ρ	(kg/m^3)	1.0×10^3	1.0×10^3	1.0×10^3
Annulus radius b	(m)	1.1×10^{-2}	5.042×10^{-3}	2.198
Density of material inside cylinder ρ_1	(kg/m^3)	0.0	1.016×10^4	1.0×10^3

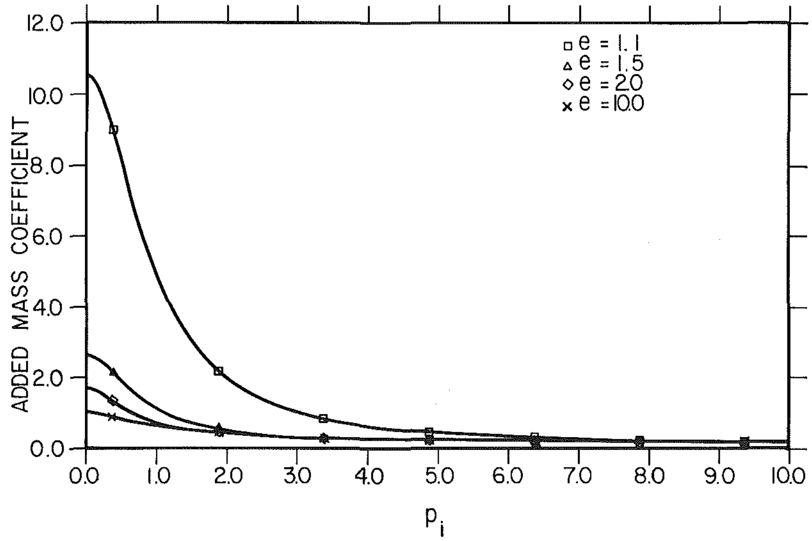

Fig. 2 Added mass coefficient for PP, open-open boundary conditions

Multiplying (22) by $\mathbf{Q}$ produces

$$\left(\mathbf{Q}\frac{d^4}{d\xi^4}\right)\psi_i(\xi)=\beta_i^4\psi_i(\xi) \tag{24}$$

Determining the mode shapes and natural frequencies is reduced to determining the eigenvalues and eigenvectors of the operator $\mathbf{Q}d^4/d\xi^4$.

***(b)* Solution of Eigenvalue Problem.** To solve (24), let the $\psi_i(\xi)$ be expressed as linear combinations of the in-vacuum mode shapes $\phi_m(\xi)$ of a cylinder with the same boundary conditions. The $\phi_m(\xi)$ satisfy

$$\frac{d^4\phi_m}{d\xi^4}=\beta_{m0}^4\phi_m \tag{25a}$$

$$\int_0^1 \phi_m\phi_n d\xi = F_m\delta_{mn} \tag{25b}$$

where $\Omega_{m0}=\beta_{m0}^2$ is the dimensionless frequency for the cylinder in vacuum, and F_m is a normalization constant. Henceforth, equation (25) will be referred to as the uncoupled problem (i.e., no fluid-structure coupling), and (24) will be referred to as the coupled problem.

$\psi_i(\xi)$ may be written

$$\psi_i(\xi)=\sum_{m=1}^{\infty}A_{mi}\phi_m(\xi) \tag{26}$$

Substituting (23), (25), and (26) into (24), multiplying both sides by $\phi_p(\xi)$, and integrating over ξ produces

$$\sum_{m=1}^{\infty}\sum_{n=1}^{\infty}\frac{\beta_{mo}^4 L/f_n}{1+\dfrac{G_n f_n}{L}}\left(\int_0^1 X_n\phi_p d\xi\right)\left(\int_0^1 X_n\phi_m d\xi\right)A_{mi}=\beta_i^4 F_p A_{pi} \tag{27}$$

Let the X_n and ϕ_p be normalized such that $f_n=L$ and $F_p=1$ respectively. Define the infinite column vector $\mathbf{A}_i=[A_{1i}A_{2i}\ldots]^T$, and the infinite matrices $\mathbf{B}=[J_{nm}]$, $\mathbf{R}=[\delta_{mn}/(1+G_n)]$, $\mathbf{S}=[\beta_{m0}^4\delta_{mn}]$, and $\mathbf{T}=\mathbf{B}^T\mathbf{R}\ \mathbf{B}\ \mathbf{S}$, where $J_{nm}=\int_0^1 X_n\phi_m d\xi$. Then (27) becomes

$$\mathbf{T}\mathbf{A}_i=\beta_i^4\mathbf{A}_i \tag{28}$$

The infinite system (28) is truncated and solved as a standard eigenvalue problem. The sums over m and n in (27) are truncated to M and N terms, respectively. Physically, this truncation involves deciding how many uncoupled cylinder modes M and fluid modes N contribute to the coupled mode in question. Note that the truncated matrices $\mathbf{B}$, $\mathbf{R}$, and $\mathbf{S}$ are $N\times M$, $N\times N$, and $M\times M$, respectively, and that $\mathbf{R}$ and $\mathbf{S}$ are diagonal.

The primary difference between the treatment here and in [11 Section V] is in the type of superposition used and the corresponding boundary conditions. Here the fluid force is expressed as a linear combination over a discrete basis $X_n(\xi)$, where the $X_n(\xi)$ satisfy fluid boundary conditions at $\xi=0$ and $\xi=1$. In [11], the fluid force is expressed as a linear combination over a continuous basis $e^{-i\bar{\alpha}\xi}$, where $\bar{\alpha}$ is a Fourier transform variable. In expressing this superposition as a

Table 2 Natural frequencies for Cases 1–3

Case	L/a	Mode number	In-vacuum natural frequency (Hz)	Coupled natural frequency (fluid-structure coupling) (Hz)	Natural frequency using two-dimensional fluid theory (Hz)
		1	40.37	36.04	26.37
		2	161.5	105.6	105.5
1	100	3	363.4	250.5	237.3
		4	646.0	423.9	421.9
		5	1009.0	677.5	659.3
		1	0.2424	0.1380	0.1377
		2	1.519	0.8646	0.8630
2	803	3	4.254	2.421	2.417
		4	8.336	4.744	4.735
		5	13.78	7.842	7.828
		1	32.16	18.22	12.43
		2	201.6	123.2	77.87
3	4.27	3	564.4	393.4	218.0
		4	1106.0	856.6	427.2
		5	1828.0	1518.0	706.3

Fourier integral, it is necessary to assume boundary conditions on the fluid at $\xi = \pm\infty$ (see [11], just under equation (35)). Equation (3) here corresponds to (33) in [11].

(c) Solutions for Various Boundary Conditions. The simplest case is where the cylinder is pinned at both ends, and the annulus is open at both ends. In this case $X_n(\xi) = \phi_n(\xi) = \sqrt{2}\sin n\pi\xi$, $\beta_{n0} = n\pi$, $f_n = L$, and $F_n = 1$. Then $J_{nm} = \delta_{nm}$, $\mathbf{B}$ is the identity matrix, and $\mathbf{T} = [\beta_{m0}^4 \delta_{mn}/(1+G_n)]$. The solution to (28) is

$$\beta_i^4 = i^4\pi^4/(1+G_i) \tag{29a}$$

$$\mathbf{A}_i = [0,0,\ldots,0,1,0,\ldots,0]^T \tag{29b}$$

(i.e., the ith entry is 1).

The natural frequencies are

$$\omega_i = (i^2\pi^2/L^2)[EI/m(1+G_i)]^{1/2} \tag{30}$$

From (30), the fluid added mass (per unit cylinder length) is mG_i. The added mass coefficient $C_{m,i}$ is the ratio of the added mass to the fluid mass displaced by the cylinder. Then

$$C_{m,i} = \frac{I_1'(ep_i)K_1(p_i) - K_1'(ep_i)I_1(p_i)}{p_i[I_1'(p_i)K_1'(ep_i) - I_1'(ep_i)K_1'(p_i)]} \tag{31}$$

where $p_i = i\pi a/L$ and $e = b/a$. $C_{m,i}$ is plotted in Fig. 2 as a function of p_i for various e. Note that as $L \to \infty$ and $p_i \to 0$, $C_{m,i} \to (e^2+1)/(e^2-1)$, which is the result obtained for a two-dimensional potential fluid [9]. In addition, the fluid has less of an effect on short length cylinders.

Additional cases with boundary conditions other than pinned-pinned, open-open are summarized in Table 1. Results for these cases were obtained by truncating the system (28). Adequate convergence for the lowest coupled modes was obtained using 30 uncoupled cylinder modes ($M = 30$) and 600 uncoupled fluid modes ($N = 600$).

Cases 2 and 3 are applicable to nuclear technology, i.e., a control rod inserted in a guide tube and a core support barrel in a reactor vessel, respectively. Data for these cases is obtained from [12]. For Case 3, L/a is sufficiently small that rotary inertia and shear deformation cannot be ignored. This case is included here to illustrate the relative importance of fluid-structure coupling for small L/a. For Cases 2 and 3, the cylinder is allowed to be hollow with inner radius a_1 and filled with material of density ρ_1.

Natural frequencies for Cases 1–3 are shown in Table 2. For modes 1–5, the uncoupled (i.e., no fluid present) natural frequency, coupled natural frequency accounting for fluid-structure coupling (i.e., solving the fluid and structure equations simultaneously), and natural frequency using two-dimensional fluid theory are given. The latter is based on an added mass coefficient $C_m = (e^2+1)/(e^2-1)$. In all cases, the frequency reduction due to the fluid is less when fluid-structure coupling is accounted for than when the two-dimensional fluid theory is used.

The effect of the fluid-structure coupling is largest when the parameter L/a is small. For Case 2, with $L/a = 803$, the coupled natural frequencies for the fluid-structure coupling and two-dimensional fluid theory cases are almost the same. For Case 1 ($L/a = 100$), the difference between the two cases is larger, while for Case 3 ($L/a = 4.27$), it is still larger. For higher modes, the effect of the fluid becomes less pronounced, and the coupled natural frequencies for the fluid-structure coupling case approach the uncoupled natural frequencies. This effect may be seen in the Case 3 results. This effect is not seen in Case 1 and 2 results because of the larger L/a; there the effect becomes significant in higher modes. These results are consistent with the results for the pinned-pinned, open-open case (Fig. 2). The effect of the fluid is largest when the parameter $i\pi a/L$ is small. The two-dimensional fluid theory case is approached as $i\pi a/L \to 0$. As $i\pi a/L \to \infty$ (either $i \to \infty$ or $L/a \to 0$), the effect of the fluid becomes negligible. The Case 3 results are quantitatively in error because rotary inertia and shear deformation have been neglected. However, the Case 3 results do indicate that fluid-structure coupling is important when L/a is small.

Coupled and uncoupled mode shapes are shown for Case 1, modes 3 and 5 (Fig. 3), and Case 3, modes 2 and 3 (Fig. 4). Mode shapes are not shown for Case 1, modes 1, 2, and 4; Case 3, mode 1; Case 2, modes 1–5 because there the difference between coupled and uncoupled mode shapes is negligible. Coupled and uncoupled mode shapes for Case 3, modes 4 and 5 exhibit similar but smaller differences than Case 3, modes 2 and 3. These results show that the coupled and uncoupled mode shapes can differ in certain cases. The use of uncoupled mode shapes for cylinder deformation [10] is not always justified.

In particular, Case 1, modes 3 and 5 exhibit substantial fluid coupling between in-vacuum modes 1 and 3, and 3 and 5, respectively. This occurs because the uncoupled fluid mode axial dependencies $X_n(\xi)$ differ from the in-vacuum structure modes $\phi_n(\xi)$ due to the pinned-pinned, closed-closed boundary conditions. The even cosine fluid modes have pressure maxima at the center of the cylinder and tend to excite corresponding next higher plus next lower odd in-vacuum structure modes. The odd cosine fluid modes have pressure nodes at the center and tend to excite only corresponding next higher even in-vacuum structure modes.

For Cases 2 and 3, the sine fluid modes are able to excite various centilevered, in-vacuum structure modes. However,

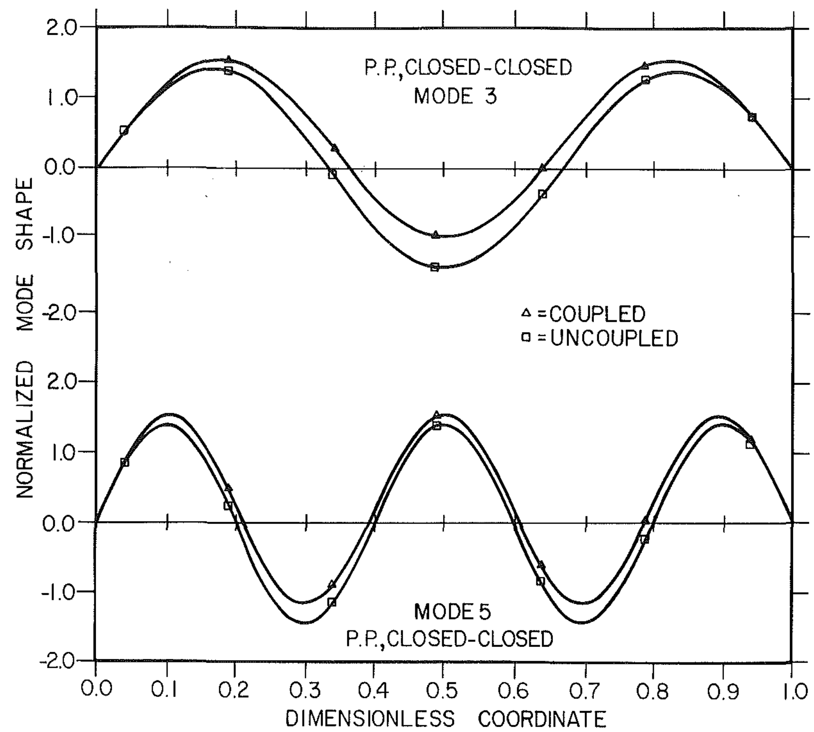

Fig. 3 Coupled and uncoupled mode shapes – Case 1, modes 3 and 5

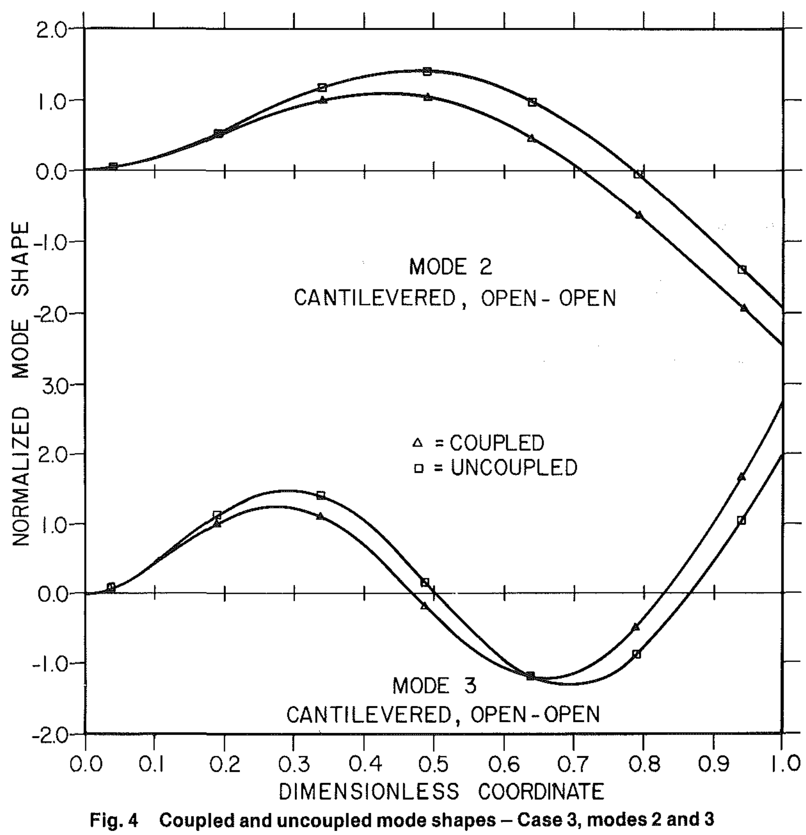

Fig. 4 Coupled and uncoupled mode shapes – Case 3, modes 2 and 3

for Case 2, a/L is small enough that, for the lower modes, the coefficients G_n are the same (see Fig. 2, equation (31), and note that $G_n = (\pi \rho a^2/m)C_{m,n}$). In equation (27), G_n is seen to affect the weighting of each fluid mode. This is to be expected, as G_n influences the added mass coefficient and therefore affects the amplitude of the pressure due to each fluid mode. When the G_n for a number of adjacent modes are the same, the **R** and **T** matrices become multiples of the identity matrix, and the different in-vacuum structure modes are uncoupled. For Case 3, a/L is large enough that the G_n for the lowest modes differ substantially. The in-vacuum structure modes 2–5 are coupled (see Fig. 4). Mode 1 is practically the same in-vacuum and with fluid present. Mode 1 is excited by the lowest sine fluid mode, and this fluid mode does not substantially excite higher in-vacuum structure modes. Note that for Case 3, as higher structure modes are considered, the G_n of adjacent modes are more nearly equal and the mode coupling becomes weaker. The results show that the in-vacuum and coupled modes are more nearly the same for Case 3, mode 5, than for Case 3, mode 2.

In general, two in-vacuum structure mode shapes will couple when fluid is present, and produce different in-fluid coupled mode shapes, if the following two conditions hold:

(*i*) The two in-vacuum structure mode shapes must be excitable by a common set of fluid mode shapes.

(*ii*) The weights of the fluid mode shapes, G_n, must differ.

These requirements guarantee that the off-diagonal terms in the **T** matrix will differ from zero sufficiently.

Conclusion

The dynamic coupling between a rod and fluid in an annulus has been considered. The fluid and structure equations, together with appropriate interface and boundary conditions, were solved simultaneously. It was found that the infinite cylinder added mass coefficient is valid for long cylinders and/or lower modes. For short cylinders and/or higher modes, the infinite cylinder solution will overpredict the added mass. As the parameter $i\pi a/L \rightarrow \infty$, the effect of the fluid becomes negligible, while as $i\pi a/L \rightarrow 0$, the infinite cylinder results are approached. The coupled and uncoupled mode shapes may differ in certain cases.

References

1 Lighthill, M. J., "Note on the Swimming of Slender Fish," *Journal of Fluid Mechanics*, Vol. 9, 1960, pp. 305–317.

2 Chen, S. S., and Wambsganss, M. W., "Parallel-Flow-Induced Vibration of Fuel Rods," *Nuclear Engineering and Design*, Vol. 18, 1972, pp. 253–278.

3 Paidoussis, M. P., "Dynamics of Cylindrical Structures Subjected to Axial Flow," *Journal of Sound and Vibration*, Vol. 29, 1973, pp. 365–385.

4 Blevins, R. D., *Flow-Induced Vibration*, Van Nostrand Reinhold, New York, 1977.

5 Chen, S. S., "Vibration of Nuclear Fuel Bundles," *Nuclear Engineering and Design*, Vol. 35, 1975, pp. 399–422.

6 Chung, Ho, and Chen, S. S., "Vibration of a Group of Circular Cylinders in a Confined Fluid," ANL-CT-76-25, Argonne National Laboratory, Feb. 1976.

7 Suss, S., Pustejovsky, M., and Paidoussis, M. P., "The Virtual Mass Matrix of a Cluster of Cylinders in Liquid Contained by a Rigid Outer Cylinder," McGill University, Department of Mechanical Engineering, Montreal, Quebec, MERL Report 76-1, July 1976.

8 Wambsganss, M. W., Chen, S. S., and Jendrzejczyk, J. A., "Added Mass and Damping of a Vibrating Rod in Confined Viscous Fluids," ANL-CT-75-08, Argonne National Laboratory, Sept. 1974.

9 Chen, S. S., and Chung, Ho, "Design Guide for Calculating Hydrodynamic Mass, Part I: Circular Cylindrical Structures," ANL-CT-76-45, Argonne National Laboratory, June 1976.

10 Weppelink, H., Van Campen, D. H., and Van Der Hoogt, P. J. M., "Three-Dimensional Calculation of the Coupled Vibrations of a Group of Circular Tubes in an Unconfined Liquid," *Transactions of the 5th Conference on Structural Mechanics in Reactor Technology*, Paper B 5/2, Berlin, Germany Aug. 1979.

11 Paidoussis, M. P., and Ostoja-Starzewski, M., "Dynamics of a Flexible Cylinder in Subsonic Axial Flow," *AIAA Journal*, Vol. 19, 1981, pp. 1467–1475.

12 "Donald C. Cook Nuclear Plant Units 1 and 2 Final Safety Analysis Report," Indiana and Michigan Electric Company, Ft. Wayne, Ind., Feb. 1971, DOCKET-50315-28.

S. L. Hendricks
Assistant Professor.

R. D. Klauber
Research Engineer.

Department of Engineering Science and Mechanics,
Virginia Polytechnic Institute and State University,
Blacksburg, Va. 24061

Optimal Control of a Rotor Partially Filled With an Inviscid Incompressible Fluid

Optimal control theory is used to stabilize a rotating cylinder partially filled with an inviscid, incompressible fluid. As an example, the theory is used to control a rotor consisting of two discrete masses connected by a flexible shaft. The fluid is inside one of the masses and the control force is applied to the other. The rotor-fluid system which is unstable without controls is shown to be stable when acted upon by a feedback force designed to minimize a suitable performance index.

Introduction

A hollow circular cylinder mounted on a flexible shaft and partially filled with liquid exhibits unstable behavior under certain operating conditions. This instability, first noticed by Kollmann [1], was explained analytically by Kuipers [2], Wolfe [3], and Hendricks and Morton [4–6]. The system is shown to be unstable when the rotor spin speed is such that the frequency of a surface wave in the liquid occurs near the vibrational frequency of the rotor. The resulting resonance causes exponential growth in the runout of the rotor and introduces a dangerous asynchronous whirling condition. The bounds of this unstable operating region depend on various system parameters such as mass ratio, damping coefficients, fluid viscosity, fill ratio, etc. [see 5, 6].

Recognizing the potential for destructive asynchronous whirl, the designer of rotating machinery (which handles fluid) is left with two options: to attempt to avoid the instability or to try to control it. This paper demonstrates that, if necessary, the instability can be controlled using a feedback control force which is the solution to an optimal control problem.

Previous efforts to use active control on an unstable rotor have been reported by Schweitzer [7] and Taylor [8]. Schweitzer [7] developed an active control scheme used to successfully control an empty viscoelastic rotor. The uncontrolled rotor is inherently unstable above a critical spin speed due to the internal damping of the viscoelastic material. Schweitzer used pole placement to determine gains in a linear feedback control scheme. He also reports some experimental results. Taylor [8] analyzed the motion of a cup on a flexible shaft containing a small loose ball. He found that the small ball produced an instability somewhat similar to that produced by an entrapped fluid. Taylor used linear regulator theory to control this unstable system. He demonstrated that a real-time active control was able to suppress whirl in his system by applying stabilizing forces to the cup.

This paper uses linear regulator theory to control a rotor-liquid system. The treatment is novel since the source of the instability is the entrapped fluid rather than a loose ball or a viscoelastic rotor material. Since many rotors now in use are flexible (and therefore multicritical) the theory is applied to a general two-critical rotor (the simplest multicritical rotor). The intent is to demonstrate the ability to control the entire system through the use of a single feedback force. The example rotor consists of two discrete masses connected by a flexible shaft. The first mass is a hollow cup that is partially filled with liquid. The control force will be applied to a second mass located at a different spot on the shaft. This system is designed to provide the control theory with a rigorous test since the source of the instability (first mass) is related to the control force (applied to the second mass) only by the dynamic coupling. A single critical rotor is not used because it would be an unrealistically easy task for the controller (since the control force would be applied directly at the source of the instability). Liquid-filled centrifuges, liquid-cooled gas turbines, and spinning rockets containing liquid fuel are examples for which this analysis may be applicable.

Problem Definition

The motion of the rotor-liquid system is governed by a set of ordinary differential equations for the rotor and a set of partial differential equations for the liquid. These equations are coupled: the liquid pressure on the cylinder wall is a distributed force that affects the motion of the rotor; the rotor is a noninertial reference frame that adds acceleration terms to the fluid equations. The system equations were developed in reference [5] for a single critical rotor. They are repeated here since a different rotor model (multicritical) is being used and the equations must be arranged in state space form to be used in the optimal control problem of this paper. Arranging the equations in state space form is a significant step in the solution process and has not been reported before.

Contributed by the Applied Mechanics Division and presented at the Winter Annual Meeting, New Orleans, La., December 9–14, 1984 of THE AMERICAN SOCIETY OF MECHANICAL ENGINEERS.

Discussion on this paper should be addressed to the Editorial Department, ASME, United Engineering Center, 345 East 47th Street, New York, N.Y. 10017, and will be accepted until two months after final publication of the paper itself in the JOURNAL OF APPLIED MECHANICS. Manuscript received by ASME Applied Mechanics Division, September, 1983; final revision, April, 1984. Paper No. 84-WA/APM-36.

Copies will be available until August, 1985.

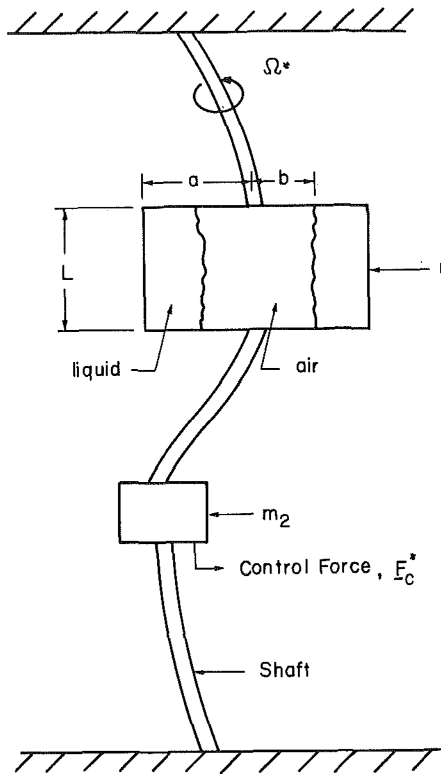

Fig. 1 Rotor system

The entire treatment is linear, the fluid is assumed to be inviscid and incompressible, and the rotor masses are not allowed to tilt. The rotor shown in Fig. 1 is meant to stand for any general two-mass rotor model. To keep the system general, the effect of the shaft is modeled as a series of springs and dashpots placed between the two masses and between each mass and ground (Fig. 2).

The dynamical equations of motion for the system are used as constraints on the minimization of a suitable cost function, resulting in a feedback control based on the solution to an algebraic matrix Riccati equation. The classical eigenvector solution approach (see Potter [9]) is used to solve the Riccati equation and determine the optimal control.

Theory

Rotor Equations. The equations of motion for the rotor are derived using the Lagrangian approach with the fluid pressure on the inner wall of the first mass and the control force acting on the second mass giving rise to appropriate generalized forces.

Consider the axially symmetric two-mass rotor of Fig. 1, modeled in Fig. 2 by linear springs, linear dampers, and discrete masses. The first mass (m_1) is a hollow circular cup containing fluid, the second mass (m_2) is a solid cylinder to which the control force $\mathbf{F}_c^*$ is applied.

Let ($\hat{\mathbf{I}}$, $\hat{\mathbf{J}}$, $\hat{\mathbf{K}}$) be a Cartesian coordinate system fixed in space, ($\hat{\mathbf{i}}$, $\hat{\mathbf{j}}$, $\hat{\mathbf{k}}$) a Cartesian coordinate system spinning with the cup at speed Ω^*, and ($\hat{\mathbf{r}}$, $\hat{\boldsymbol{\theta}}$, $\hat{\mathbf{z}}$) a cylindrical coordinate system also spinning with the cup (see Fig. 3). $\hat{\mathbf{K}}$, $\hat{\mathbf{k}}$, $\hat{\mathbf{z}}$ are all parallel to the neutral shaft.

The position, velocity, and acceleration of the first mass expressed in the cup fixed coordinate system are:

$$\mathbf{R}_1^* = x_1\hat{\mathbf{i}} + y_1\hat{\mathbf{j}} \qquad (1a)$$

$$\dot{\mathbf{R}}_1^* = (\dot{x}_1 - \Omega^* y_1)\hat{\mathbf{i}} + (\dot{y}_1 + \Omega^* x_1)\hat{\mathbf{j}} \qquad (1b)$$

$$\ddot{\mathbf{R}}_1^* = (\ddot{x}_1 - 2\Omega^*\dot{y}_1 - \Omega^{*2}x_1)\hat{\mathbf{i}} + (\ddot{y}_1 + 2\Omega^*\dot{x}_1 - \Omega^{*2}y_1)\hat{\mathbf{j}} \qquad (1c)$$

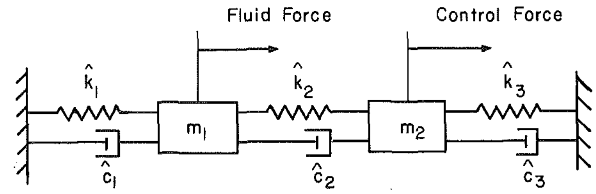

Fig. 2 Equivalent rotor model

The position and velocity of the second mass in the same coordinate system are:

$$\mathbf{R}_2^* = x_2\hat{\mathbf{i}} + y_2\hat{\mathbf{j}} \qquad (2a)$$

$$\dot{\mathbf{R}}_2^* = (\dot{x}_2 - \Omega^* y_2)\hat{\mathbf{i}} + (\dot{y}_2 + \Omega^* x_2)\hat{\mathbf{j}} \qquad (2b)$$

The kinetic energy T, the dissipation function D, and the potential energy V are:

$$T = \frac{1}{2} m_1 \dot{\mathbf{R}}_1^* \cdot \dot{\mathbf{R}}_1^* + \frac{1}{2} m_2 \dot{\mathbf{R}}_2^* \cdot \dot{\mathbf{R}}_2^* \qquad (3a)$$

$$D = \frac{1}{2}\hat{c}_1 \dot{\mathbf{R}}_1^* \cdot \dot{\mathbf{R}}_1^* + \frac{1}{2}\hat{C}_2(\dot{\mathbf{R}}_1^* - \dot{\mathbf{R}}_2^*)\cdot(\dot{\mathbf{R}}_1^* - \dot{\mathbf{R}}_2^*) + \frac{1}{2}\hat{c}_3 \dot{\mathbf{R}}_2^* \cdot \dot{\mathbf{R}}_2^* \qquad (3b)$$

$$V = \frac{1}{2}\hat{k}_1 \mathbf{R}_1^* \cdot \mathbf{R}_1^* + \frac{1}{2}\hat{k}_2(\mathbf{R}_1^* - \mathbf{R}_2^*)\cdot(\mathbf{R}_1^* - \mathbf{R}_2^*) + \frac{1}{2}\hat{k}_3 \mathbf{R}_2^* \cdot \mathbf{R}_2^* \qquad (3c)$$

The control force applied at $\mathbf{R}_2{}^*$is

$$\mathbf{F}_c^* = F_{xc}^*\hat{\mathbf{i}} + F_{yc}^*\hat{\mathbf{j}} \qquad (4)$$

The entrapped fluid pressure $\hat{P}(r^*, \theta, t)$ creates a distributed force

$$d\mathbf{F}_{fl} = \hat{P}(r^* = a, \theta, t)[\cos\theta\hat{\mathbf{i}} + \sin\theta\hat{\mathbf{j}}]a d\theta\, dz \qquad (5a)$$

applied at the cylinder wall located at

$$\mathbf{R}_{fl}^* = \mathbf{R}_1^* + a[\cos\theta\hat{\mathbf{i}} + \sin\theta\hat{\mathbf{j}}] + z\hat{\mathbf{k}}. \qquad (5b)$$

The generalized force in Lagrange's equation for x_1 is

$$\int_0^L \int_0^{2\pi} \frac{\partial \mathbf{R}_{fl}}{\partial \mathbf{x}_1} \cdot \hat{P}(r^* = a, \theta, r)[\cos\theta\hat{\mathbf{i}} + \sin\theta\,\hat{\mathbf{j}}]a d\theta\, dz \qquad (6)$$

The θ dependence of the pressure $\hat{P}(r^*, \theta, t)$ can be expanded in a complex Fourier series as

$$\hat{P}(r^*, \theta, t) = Re\left\{\sum_{n=0}^{\infty} \hat{P}_n(r^*, t)e^{in\theta}\right\} \qquad (7)$$

where $\hat{P}_n(r^*, t)$ is complex.

Use of equations (1) and (7) in (6) yields

$$Re\left\{aL\int_0^{2\pi}\left\{\cos\theta\left(\sum_{n=0}^{\infty}\hat{P}_n(a, t)[\cos(n\theta) + i\sin(n\theta)d\theta\right)\right\}\right\} \qquad (8)$$

All terms where n ≠ 1 vanish, leaving

$$Re\{\pi a L\hat{P}_1(a, t)\} = \pi a L\hat{P}_{1_{re}}(a, t). \qquad (9a)$$

The generalized force in the y_1 direction is similarly found to be

$$R_e\{i\pi a L\hat{P}_1(a, t)\} = -\pi a L\hat{P}_{1_{im}}(a, t). \qquad (9b)$$

To streamline notation $\hat{P}_1(r^*, t)$ will henceforth be written as simply $\hat{P}(r^*, t)$ since it represents the only part of the fluid pressure that affects the rotor motion.

Lagrange's equations of motion for the rotor are then derived in a straightforward manner. The system parameters are now nondimensionalized using m_1 = mass of the empty cup, a = radius of the cup inner surface, $\omega_0 = (\hat{k}_1/m_1)^{1/2}$ as the characteristic mass, length, and frequency. The following nondimensional terms are introduced:

$$
\begin{aligned}
&m = m_2/m_1 && \mathbf{R}_1 = \mathbf{R}_1^*/a \\
&c_1 = \hat{c}_1/2m_1\omega_0 && \mathbf{R}_2 = \mathbf{R}_2^*/a \\
&c_2 = \hat{c}_2/2m_1\omega_0 && f = b/a \\
&c_3 = \hat{c}_3/2m_1\omega_0 && \Omega = \Omega^*/\omega_0 \\
&k_1 = \hat{k}_1/m_1\omega_0^2 = 1 && \mu = \pi\rho a^2 L/m_1 \\
&k_2 = \hat{k}_2/m_1\omega_0^2 && \eta_1 = (x_1 - iy_1)/a \\
&k_3 = \hat{k}_3/m_1\omega_0^2 && \eta_2 = (x_2 - iy_2)/a \\
&r = r^*/a && \psi = (F_{xc}^* - iF_{yc}^*)/m_1 a\omega_0^2 \\
&z_0 = L/a && P(r, \theta, t) = \hat{P}(r^*, \theta, t)a/m_1\omega_0^2
\end{aligned}
\tag{10}
$$

where ρ is the fluid density, nondimensional cup mass is unity, and μ is the nondimensional fluid density. The two-dimensional displacements η_1 and η_2, the control force ψ, and the pressure P are expressed in complex notation for efficiency.

The nondimensionalized, complex Lagrange equations for the rotor motion are then:

$$
\begin{bmatrix} 1 & 0 \\ 0 & m \end{bmatrix} \begin{Bmatrix} \ddot{\eta}_1 \\ \ddot{\eta}_2 \end{Bmatrix} + \begin{bmatrix} 2(c_1 + c_2 - i\Omega) & -2c_2 \\ -2c_2 & 2(c_2 + c_3 - im\Omega) \end{bmatrix} \begin{Bmatrix} \dot{\eta}_1 \\ \dot{\eta}_2 \end{Bmatrix}
$$

$$
+ \begin{bmatrix} 1 + k_2 - \Omega^2 - 2i\Omega(c_1 + c_2) & -k_2 + 2i\Omega c_2 \\ -k_2 + 2i\Omega c_2 & k_2 + k_3 - m\Omega^2 - 2i\Omega(c_2 + c_3) \end{bmatrix} \begin{Bmatrix} \eta_1 \\ \eta_2 \end{Bmatrix} \tag{11}
$$

$$
= \begin{Bmatrix} \pi z_0 P(r = 1, t) \\ \psi \end{Bmatrix}
$$

Fluid Equations. The Euler and continuity equations for the fluid are

$$
\dot{\mathbf{q}} + (\nabla \cdot \mathbf{q})\mathbf{q} - \Omega^{*2}\mathbf{r}^* + 2\Omega^*\hat{\mathbf{k}} \times \mathbf{q} + \ddot{\mathbf{R}}_1^*
$$

$$
+ \frac{1}{\rho} \nabla \hat{P}(r^*, \theta, t) = 0 \tag{12a}
$$

$$
\nabla \cdot \mathbf{q} = 0 \tag{12b}
$$

where $\mathbf{q} = \mathbf{q}(r^*, \theta, t)$ is the fluid velocity relative to the cup and $\hat{P}(r^*, \theta, t)$ is the fluid pressure. The first five terms in equation (12a) represent the total inertial acceleration experienced by a fluid particle.

To nondimensionalize equations (12a,b), partially separate variables, and incorporate complex notation, the following representations are introduced:

$$
\hat{P}(r^*, \theta, t) = \frac{1}{2} \rho(\Omega^*)^2(r^{*2} - b^2)
$$

$$
+ Re\left\{ \sum_{n=0}^{\infty} P_n(r,t)e^{in\theta} \right\} \frac{m_1\omega_0^2}{a} \tag{13a}
$$

$$
\mathbf{q} = Re\left\{ \sum_{n=0}^{\infty} [(u_n(r, t)\hat{\mathbf{r}} + v_n(r, t)\hat{\theta})e^{in\theta}] \right\} a\omega_0 \tag{13b}
$$

where $u_n(r, t)$ and $v_n(r, t)$ are nondimensional complex scalar variables, and the first term on the right-hand side of equation (13a) represents the pressure due to the solid-body rotation of the fluid.

As before, only the $n = 1$ term in the pressure expansion affects rotor motion. Similarly, all terms in the velocity expansions where $n \neq 1$ decouple from the rotor motion and therefore can be dropped. Henceforth $u(r, t)$ and $v(r, t)$ will be used to represent $u_1(r, t)$ and $v_1(r, t)$, respectively.

Use of (13a, b) in (12a, b) yields the following linearized nondimensional complex fluid equations:

$$
\dot{u}(r, t) - 2\Omega v(r, t) + \frac{\pi z_0}{\mu} \frac{\partial P(r, t)}{\partial r} + (\ddot{\eta}_1 - 2i\Omega\dot{\eta}_1 - \Omega^2\eta_1) = 0 \tag{14a}
$$

$$
\dot{v}(r, t) + 2\Omega u(r, t) + \frac{i\pi z_0}{\mu r} P(r, t) + i(\ddot{\eta}_1 - 2i\Omega\dot{\eta}_1 - \Omega^2\eta_1) = 0 \tag{14b}
$$

$$
\frac{u(r, t) + iv(r, t)}{r} + \frac{\partial u(r, t)}{\partial r} = 0 \tag{14c}
$$

Equation (14c) can be solved for $v(r, t)$ and substituted into (14b) to yield

$$
P(r, t) = \frac{\mu}{\pi z_0} \left\{ \left[2i\Omega r - r^2 \frac{\partial^2}{\partial r \partial t} - r \frac{\partial}{\partial t} \right] u(r, t) \right.
$$

$$
\left. - r\left[\frac{\partial^2}{\partial t^2} - 2i\Omega \frac{\partial}{\partial t} - \Omega^2 \right] \eta_1 \right\}. \tag{15a}
$$

Use of this in (14a) results in the following simple equation:

$$
\frac{\partial}{\partial t} \left[3 \frac{\partial}{\partial r} + \frac{\partial^2}{\partial r^2} \right] u(r, t) = 0. \tag{15b}
$$

The solution is

$$
u(r, t) = f_1(t) + f_2(t)/r^2 \tag{16}
$$

where $f_1(t)$ and $f_2(t)$ are unknown functions of time.

Applying the no-penetration condition at the wall boundary $u(r = 1, t) = 0$, one finds that $f_1(t) = -f_2(t) \equiv \beta(t)$, thus

$$
u(r, t) = \beta(t)[1 - 1/r^2] \tag{17}
$$

At the free surface the radial position of the fluid can be expressed as

$$
r = f + \lambda(\theta, t) \tag{18}
$$

where f represents the unperturbed (wave free) surface position and λ, the perturbation (wave).

At the free surface the pressure must be zero and the radial velocity of the wave must match the radial velocity of the fluid. Applying these conditions to (13a), the linearized nondimensional boundary condition at the free surface is

$$
u(r = f, t) = -\frac{\pi z_0}{\mu\Omega^2 f} \dot{P}(r = f, t) \tag{19}
$$

The time derivative of (15a) at $r = f$ is then evaluated using (17). The result is substituted along with (17) into (19) producing:

$$
\left[1 + \frac{1}{f^2}\right]\ddot{\beta} - 2i\Omega\left[1 - \frac{1}{f^2}\right]\dot{\beta} - \Omega^2\left[1 - \frac{1}{f^2}\right]\beta
$$

$$
+ (\dddot{\eta}_1 - 2i\Omega\ddot{\eta}_1 \Omega^2 \dot{\eta}_1) = 0 \tag{20}
$$

Equation (20) is free of any dependence on r but it is third

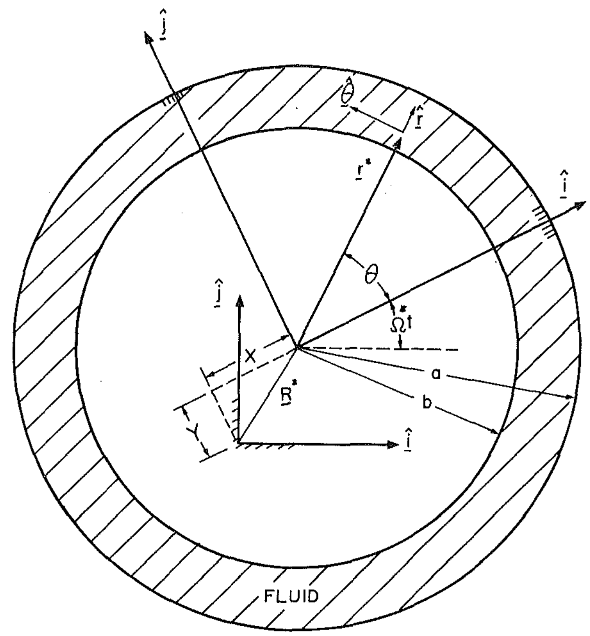

Fig. 3 Definition of coordinate systems (top view)

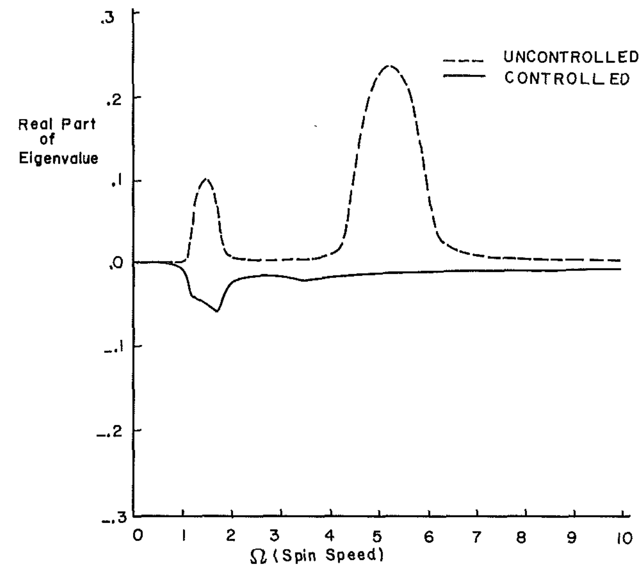

Fig. 4 System stability: real part of most unstable eigenvalue ($R = 100$)

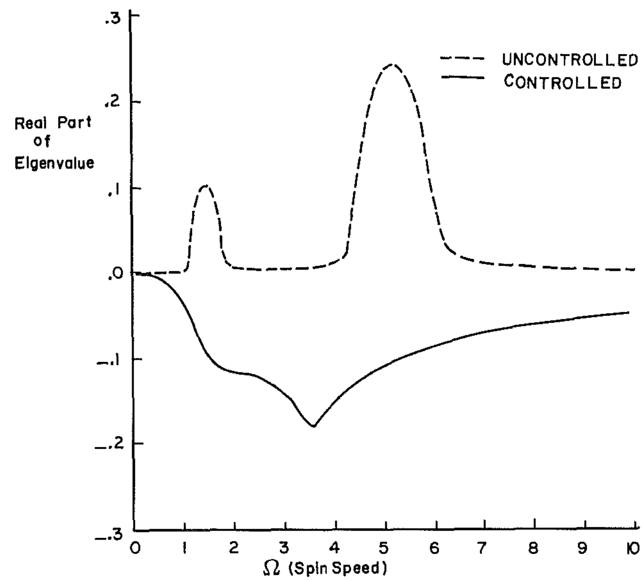

Fig. 5 System stability: real part of most unstable eigenvalue ($R = 1$)

order in time. Reduction to second order is accomplished by using equation (15a) at $r = 1$ in the first of equations (11), taking the time derivative of the result, solving for $\dddot{\eta}_1$, and using it in equation (20). All terms then become second or lower order in time and the original fluid system has been reduced to one ordinary differential equation in three complex variables (the cup displacement η_1, the second mass displacement η_2, and β, which measure the free surface wave velocity).

The equation is

$$-2(c_1+c_2)\ddot{\eta}_1+2c_2\ddot{\eta}_2+\left(1-\mu+\frac{1}{f^2}[1+\mu]\right)\ddot{\beta}$$

$$+(-1-k_2+2i\Omega[c_1+c_2])\dot{\eta}_1+(k_2-2i\Omega c_2)\dot{\eta}_2$$

$$-2i\Omega\left(1-\frac{1}{f^2}\right)(1+\mu)\dot{\beta}-\Omega^2\left(1-\frac{1}{f^2}\right)(1+\mu)\beta=0 \quad (21)$$

Combined Rotor Fluid Equations. Equations (11) and (21) can be combined into the single complex matrix equation

$$[M'']\{\ddot{Z}\}+[C'']\{\dot{Z}\}+[K'']\{Z\}=\psi\begin{Bmatrix}0\\1\\0\end{Bmatrix} \quad (22)$$

where

$$\{Z\}=\begin{Bmatrix}\eta_1\\ \eta_2\\ \beta\end{Bmatrix}$$

and $[M'']$, $[C'']$, and $[K'']$ are determined from (11) and (21).

State Space Formulation. By defining the state vector

$$\{Y\}=\begin{Bmatrix}Z\\ \dot{Z}\end{Bmatrix}$$

and premultiplying (22) by $[M'']^{-1}$, the three second-order equations (22) can be replaced by six first-order equations in the following form:

$$\{\dot{Y}\}=[A]\{Y\}+\{E\}\psi \quad (23)$$

Optimal Control Problem. The Control problem is to choose the force ψ so that the rotor-liquid system will be stable. There are may ways to choose the control force. We will choose ψ to be that particular force that minimizes the following performance index

$$J=\frac{1}{2}\int_0^\infty[\{Y^\dagger\}^T[Q]\{Y\}+\psi^\dagger R\psi]dt \quad (24)$$

where "†" denotes complex conjugation, $[Q]$ is a positive semidefinite hermitian weighting matrix, and R is a positive weighting scalar.

Applying the standard variational approach (see [10], Chapter 9), J is found to be minimized by the control force

$$\psi=-\{E^\dagger\}^T[K]\{Y(t)\}/R \quad (25)$$

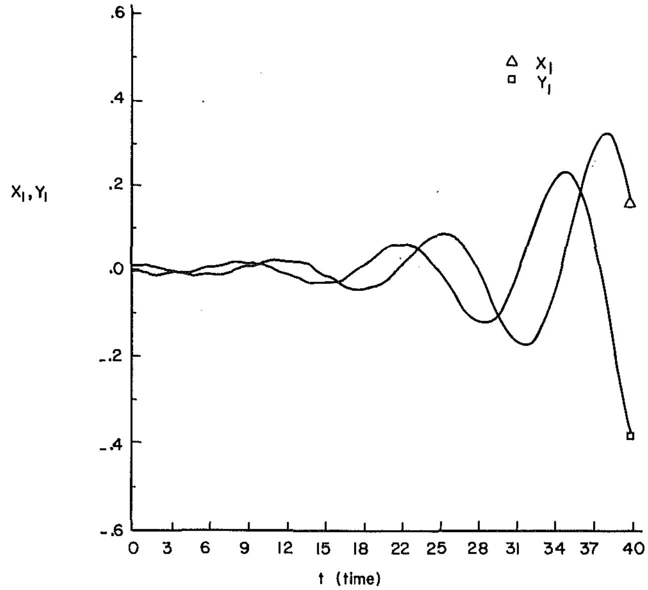

Fig. 6 Uncontrolled system: displacement of mass 1 (x_1 versus t, y_1 versus t)

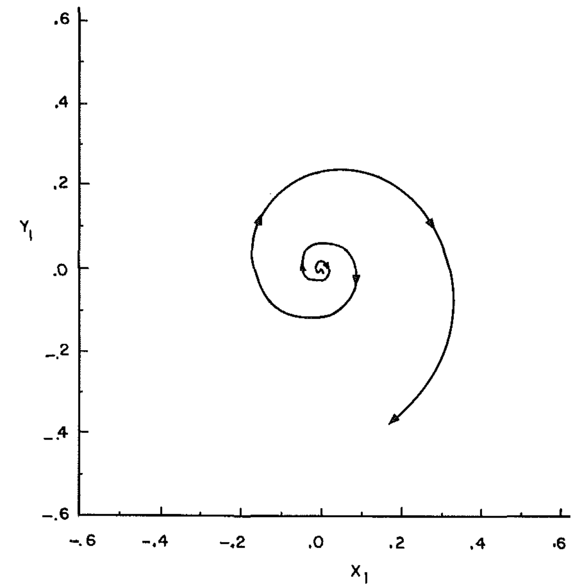

Fig. 8 Uncontrolled system (polar plot): displacement of mass 1 (x_1 versus y_1)

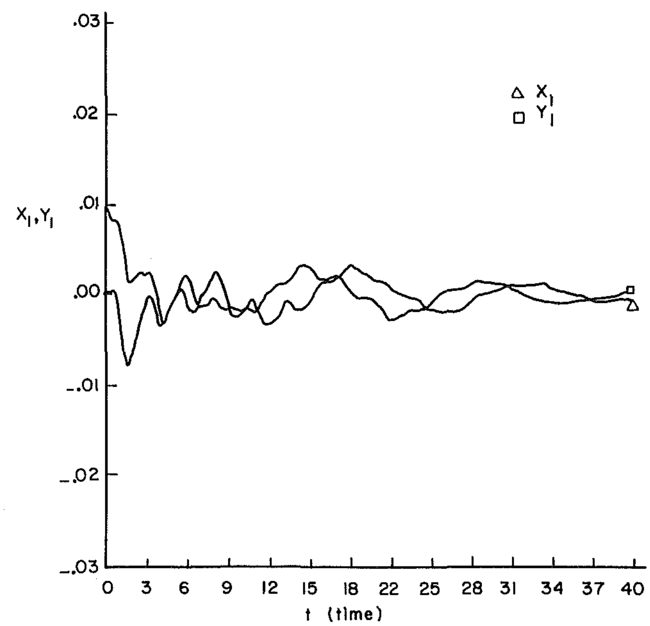

Fig. 7 Controlled system: displacement of mass 1 (x_1 versus t, y_1 versus t)

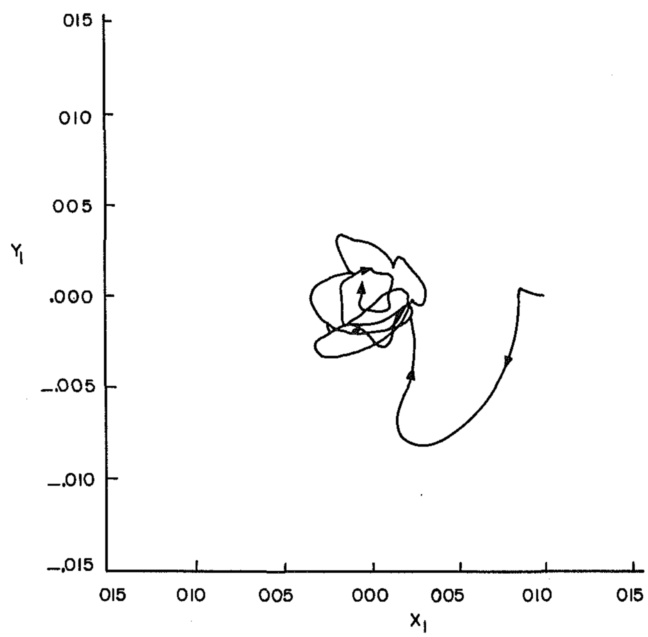

Fig. 9 Controlled system (polar plot): displacement of mass 1 (x_1 versus y_1) $R = 100$

where $[K]$ is a solution to the algebraic matrix Riccati equation

$$[K][A]+[A^{\dagger}]^T[K]+[Q]-[K]\{E\}\{E^{\dagger}\}^T[K]/R=0. \quad (26)$$

Equation (26) is solved using the eigenvector approach of reference [9].

To minimize J (equation (24)), the control must not let the rotor move very far from its nominal location, nor must it use much force. The operator can control the mixture of runout versus force that is acceptable by varying the elements in the weighting matrix $[Q]$ and the weighting scalar R.

For the control to be useful at all, it must stabilize the system. A quick check on the system eigenvalues will reveal the stability of the system.

Equation (23) with $\psi = 0$ represents the free (uncontrolled) system equations of motion. If one or more of the complex eigenvalues of $[A]$ has a positive real part, then the system is unstable. If the real parts of the eigenvalues are all negative, then the system is stable.

With (25) used in (23) the controlled system equations of motion can be expressed as

$$\{\dot{Y}\}=\left([A]-\frac{1}{R}\{E\}\{E^{\dagger}\}^T[K]\right)\{Y\}=[A_c]\{Y\}. \quad (27)$$

By finding the eigenvalues of $[A_c]$ and examining the real parts, stability of the controlled system can also be determined.

Results and Discussion

The theory was used to stabilize a sample rotor with the following nondimensional system parameters.

$$K_2=5.0 \qquad C_2=0.2 \qquad m=0.7$$
$$K_3=1.0 \qquad C_3=0.3 \qquad \mu=0.5$$
$$C_1=0.1 \qquad f=0.8 \qquad R=100$$

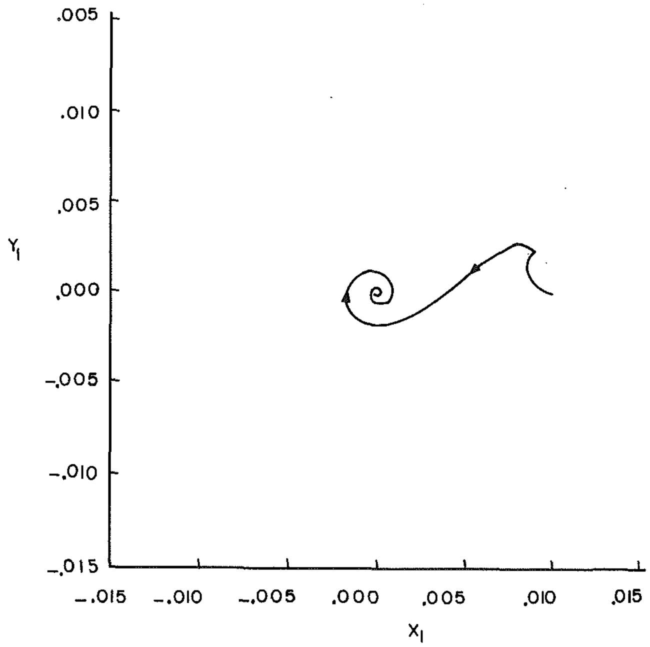

Fig. 10 Controlled system (polar plot): displacement of mass 1 (x_1 versus y_1) R = 100

These parameters were chosen to give two well-separated critical frequencies with light damping, but they have no other significance. All calculations presented here use $[Q] = [I]$ (the identity matrix).

Figure 4 is a plot of the real part of the most unstable eigenvalue as a function of spin speed. Results are shown for both the uncontrolled and the controlled case. The uncontrolled system is unstable to some degree over all operating speeds, though at system resonances the effect is greatly exacerbated (i.e., around $\Omega = 1.5$ and $\Omega = 5.0$). The controlled system eigenvalues are negative for all spin speeds, indicating that the control has made the system stable.

Figure 5 shows the same plot when the weighting scalar R has been reduced from $R = 100$ to $R = 1$. The control force does not now contribute as much to the penalty function (equation (24)) and the control force is able to make the system more stable. The price paid for this added stability is the use of more force. By choosing different values for the elements of the weighting matrix $[Q]$ and the weighting scalar R, the operator can control the stability to an acceptable level without using too much energy. He has the freedom to adapt the penalty function to his needs.

Figure 6 displays the free system (uncontrolled) response to an initial disturbance near the first critical speed ($\Omega = 1.5$). Only the motion of mass m_1 is shown. This is just the time history of the runout of the rotor. Note the exponential growth of the runout (revealing again the unstable nature of the uncontrolled system). Figure 7 shows the same system in the presence of a smart control force. This plot was made using a weighting factor of $R = 100$, placing a heavy penalty on the use of control force. As a result, the control force takes many oscillations to bring the system near the origin. Note that the system is now stable.

An instructive way to look at the motion of rotors is to make a polar plot. This is just a plot of the displacement in the x direction versus the displacement in the y direction with time as the parameter along the curve (remember that x and y are measured relative to a rotating set of axes). Figure 8 is polar plot of the uncontrolled system. This graphically illustrates the unstable nature of the uncontrolled system. The motion quickly spirals away from the origin. Figure 9 shows that the system can eventually be driven to the origin. This figure used the heavy penalty on the control force ($R = 100$: compare Fig. 7). Figure 10 (calculated using $R = 1$) shows that the control can accomplish the mission (drive the system to the origin) in a much cleaner manner if the operator is not so stingy with the use of force.

Conclusions

The rotor system modeled by two discrete masses, the first of which is a cylinder partially filled with ideal fluid, is inherently unstable over all operating speeds. The system equations have been massaged into state space form and used in an optimal control analysis to find a feedback force that not only controls the system but does so in an optimal manner. Even more important, the system has been shown to be controllable with a single force applied at a location that does not necessarily coincide with the source of the instability. This allows a rotor to be controlled from its most convenient location (taking care of course not to try to control it from a location that corresponds to one of the nodes of the system that you are trying to control). This should make the theory more attractive to implement on a real machine (where it may only be feasible to implement a control at one of the bearings for example). Obviously each rotor geometry would have to be investigated separately as to its controllability. It would be an easy matter to use a different rotor model in the theory.

The theory as applied in this paper assumes that all elements of the state vector (in this case runouts of both rotor masses and the motion of the fluid surface wave) can be measured and used for feedback. The displacements of the two masses can be easily measured using proximity probes. It is more difficult to measure the state of the entrapped fluid. A subsequent paper will explore the feasibility of controlling this system without actually measuring all of the state elements.

References

1 Kollmann, F. G., "Experimentelle und theoretische Untersuchungen uber die Kritischen Drehzahlen flussigkeitsgefulter Hohlkorper," *Forschund auf dem Gebiete des Ingenieurwessens*, Ausgabe B, Vol. 28, 1962, pp. 115–123 and 147–153.

2 Kuipers, M., "On the Stability of a Flexible Mounted Rotating Cylinder Partially Filled With Liquid," *Applied Scientific Research*, Section *A*, Vol. 13, 1964, pp. 121–137.

3 Wolfe, J. A., Jr., "Whirl Dynamics of a Rotor Partially Filled With Liquid," ASME Journal of Applied Mechanics, Vol. 35, 1968, pp. 676–682.

4 Hendricks, S. L., "Dynamics of Flexible Rotors Partially Filled With a Viscous Incompressible Fluid," Ph.D. Dissertation, University of Virginia, May 1979.

5 Hendricks, S. L., and Morton, J. B., "Stability of a Rotor Partially Filled With a Visocus Incompressible Fluid," ASME Journal of Applied Mechanics, Vol. 46, No. 4, 1979, pp. 913–918.

6 Hendricks, S. L., "Instability of a Damped Rotor Partially Filled With an Inviscid Liquid," ASME Journal of Applied Mechanics, Vol. 48, No. 3, 1981, p. 674.

7 Schweitzer, G., "Stabilization of Self-Excited Rotor Vibrations by an Active Damper," *Dynamics of Rotors*, Springer-Verlag, 1975, pp. 472–493.

8 Taylor, M., "Active Optimal Control for Suppression of Whirl of a Flexible Centrifuge," Ph.D. Dissertation, University of Virginia, Jan. 1979.

9 Potter, J. E., "Matrix Quadratic Solutions," *Siam Journal of Applied Mathematics*, Vol. 14, No. 3, May 1966, pp. 496–501.

10 Ogata, K., *State Space Analysis of Control Systems*, Prentice-Hall, Englewood Cliffs, N.J. 1967.

11 Luenberger, D. G., *Introduction of Dynamic Systems: Theory, Models, and Applications*, Wiley, New York, 1979.

A. San Andres
Graduate Research Assistant.

A. Z. Szeri
Professor.
Mem. ASME

Department of Mechanical Engineering,
The University of Pittsburgh,
Pittsburgh, Pa. 15261

Flow Between Eccentric Rotating Cylinders

In this numerical study of flow between eccentric cylinders, the size of the separation eddy and the position of the points of separation and reattachment are found to be Reynolds number dependent. The separation point moves in the direction of rotation upon increasing the Reynolds number, in contradiction to the first-order inertial perturbation theory of Ballal and Rivlin [1]. The numerical methods employed in this study include Galerkin's procedure with B-*spline test functions.*

Introduction

Flow between eccentric rotating cylinders is of considerable technical importance as it occurs in journal bearings. These bearings are in use in large rotating machinery, such as the turbines and generators of both conventional and nuclear power stations. Severe assumptions, viz., negligible curvature, fully developed flow in a channel of slowly varying cross section, and constant viscosity were made in the classical treatment of these bearings [2]. These assumptions lead to the formulation of what is now known as "Lubrication Theory." The theory served the designer well for decades, but the recent increase in size and speed of rotating machinery strained the theory [3]; there is now a serious need to update it. Temperature dependence of viscosity, and the fact that the viscosity of conventional lubricants decreases sharply with an increase in temperature, results in a considerable loss of load capacity relative to the predictions of classical theory. Fluid inertia has a seemingly smaller effect on pressure distribution under normal circumstances. It does, however, affect the ability of the bearing to respond to changes in load [4]. Sudden change in load may occur, e.g., if a turbine blade is lost through accident.

Flow between eccentric, rotating cylinders is also of interest to the fluid dynamicist; the flow is strongly Reynolds number dependent and occurs in a simple geometry. The full nonlinearities of two-dimensional curved flows are present, yet due to the geometric simplicity there is hope for a complete analysis of the problem. For this reason the basic flow between rotating cylinders and the stability of this flow occupied a prominent position in fluid mechanics, starting with the classical work of Taylor [5].

In one of the early publications on flow between eccentric rotating cylinders, Wannier [6] discussed the problem without restricting the geometry; he used complex variable techniques to solve the biharmonic equation, satisfied by the stream function in Stokes flow. Wannier showed that the Reynolds equation of classical lubrication theory constitutes the zero-order approximation to the Navier-Stokes equations, when the stream function is expanded in powers of the film thickness. Wood [7], using a modified bipolar coordinate system that reduces to polar coordinates as the eccentricity vanishes, analyzed the boundary layers that develop on the two cylinders at large Reynolds numbers. The eccentricity ratio is the small parameter of the perturbation analysis, and the solution is expressed in combinations of Bessel functions.

The effect of inertia is estimated from a perturbation of the Stokes flow in Kamal's analysis [8]. This work clearly indicates a change in position of separation and reattachment points when increasing the Reynolds number, and the considerable effect the clearance ratio has on the critical value of eccentricity for the appearance of flow reversal. Kamal's inertial correction is incorrect, however, as was pointed out first by Ashino [9] and later by Ballal and Rivlin [1]; even the solution to the Stokes problem shows disagreement with recent results. Another small perturbation analysis with the eccentricity ratio as the parameter was published by Kulinski and Ostrach [10]. Yamada [11] neglected curvature effects and solved the boundary layer equations for the case of a rotating outer cylinder. Assuming a perturbation series in the clearance ratio, Yamada showed that the results of the unperturbed flow agree with those of lubrication theory. The importance of the inertial correction is found in the pressure distribution: the largest negative pressure is greater in magnitude than the largest positive pressure.

DiPrima and Stuart [12] obtained linearized inertial corrections at small clearance ratios and at small values of the modified Reynolds number. Their zero-order approximation is identical to Lubrication Theory. Results presented by DiPrima et al. are in good agreement with those of Yamada.

The perturbation analysis of Ballal and Rivlin [1], the most complete analysis to date of the flow between eccentric rotating cylinders, assumes large kinematic viscosity and provides analytical solutions to the problem in two cases: (1)

Contributed by the Applied Mechanics Division and presented at the Winter Annual Meeting, New Orleans, La., December 9-14, 1984 of THE AMERICAN SOCIETY OF MECHANICAL ENGINEERS.

Discussion on this paper should be addressed to the Editorial Department, ASME, United Engineering Center, 345 East 47th Street, New York, N.Y. 10017, and will be accepted until two months after final publication of the paper itself in the JOURNAL OF APPLIED MECHANICS. Manuscript received by ASME Applied Mechanics Division, October, 1983; final revision, April, 1984. Paper No. 84-WA/APM-37.

Copies will be available until August, 1985.

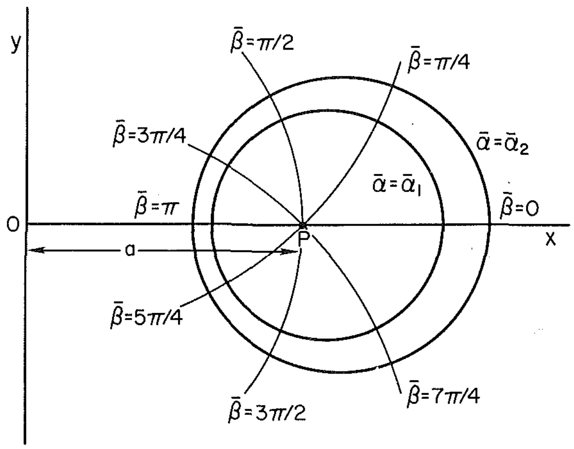

Fig. 1 Coordinate system and geometry

negligible inertial effects (the zero-order approximation) and, (2) first-order perturbation of noninertial flow. The solution is valid for arbitrary rotation of the cylinders and in arbitrary geometry. Pressure distributions along the cylinders are calculated and the streamline pattern is analyzed in considerable detail. Ballal and Rivlin also provide a number of conditions under which stagnation points, separation points, and eddys can exist, and discuss their location under various conditions.

It appears from this brief examination of previous work that solutions that treat the applicable form of the Navier-Stokes equations in their full nonlinearity and, at the same time, place no restriction on the geometry of the problem are not as yet available. Neither do we find significant attempts at analyzing the problem numerically.

The present research examines the isothermal flow of a Newtonian fluid between eccentric rotating cylinders, without making assumptions on the geometry of the problem. The treatment is numerical, it employs Galerkin's method with B-spline test functions, and retains the nonlinear terms of the Navier-Stokes equations. The stability of this flow and an extension to temperature-dependent viscosity will be the subject of subsequent papers.

Analytical

Relative to the bipolar coordinate system $\{\bar{\alpha}, \bar{\beta}\}$ of Fig. 1 the cylinders of radii R_1 and R_2, $R_1 < R_2$, have representation $\bar{\alpha} = \bar{\alpha}_1$ and $\bar{\alpha} = \bar{\alpha}_2$, $\bar{\alpha}_2 < \bar{\alpha}_1$, respectively. The Navier-Stokes and continuity equations are:

$$\frac{U}{\bar{h}}\frac{\partial U}{\partial\bar{\alpha}}+\frac{V}{\bar{h}}\frac{\partial U}{\partial\bar{\beta}}+V^2\frac{\sinh\bar{\alpha}}{a}-\frac{UV\sin\bar{\beta}}{a}$$
$$=-\frac{1}{\rho\bar{h}}\frac{\partial\bar{p}}{\partial\bar{\alpha}}+\nu\Big\{\frac{1}{\bar{h}^2}\Big(\frac{\partial^2U}{\partial\bar{\alpha}^2}+\frac{\partial^2U}{\partial\bar{\beta}^2}\Big)$$
$$-\frac{(\cosh\bar{\alpha}+\cos\bar{\beta})}{a\bar{h}}U+\frac{2\sinh\bar{\alpha}}{a\bar{h}}\frac{\partial V}{\partial\bar{\beta}}-\frac{2\sin\bar{\beta}}{a\bar{h}}\frac{\partial V}{\partial\bar{\alpha}}\Big\} \quad (1a)$$

$$\frac{U}{\bar{h}}\frac{\partial V}{\partial\bar{\alpha}}+\frac{V}{\bar{h}}\frac{\partial V}{\partial\bar{\beta}}+U^2\frac{\sin\bar{\beta}}{a}-\frac{UV\sinh\bar{\alpha}}{a}$$
$$=-\frac{1}{\rho\bar{h}}\frac{\partial\bar{p}}{\partial\bar{\beta}}+\nu\Big\{\frac{1}{\bar{h}^2}\Big(\frac{\partial^2V}{\partial\bar{\alpha}^2}+\frac{\partial^2V}{\partial\bar{\beta}^2}\Big)$$
$$-\frac{(\cosh\bar{\alpha}+\cos\bar{\beta})}{a\bar{h}}V-\frac{2\sinh\bar{\alpha}}{a\bar{h}}\frac{\partial U}{\partial\bar{\beta}}+\frac{2\sin\bar{\beta}}{a\bar{h}}\frac{\partial U}{\partial\bar{\alpha}}\Big\} \quad (1b)$$

$$\frac{\partial}{\partial\bar{\alpha}}(\bar{h}U)+\frac{\partial}{\partial\bar{\beta}}(\bar{h}V)=0 \quad (2)$$

Here $\bar{h} = a/(\cosh\bar{\alpha} - \cos\bar{\beta})$ is the Lamé coefficient and a is the distance between the pole and the origin of the Cartesian coordinate system.

If the inner and outer cylinders have constant angular velocities ω_1 and ω_2, respectively, the boundary conditions accompanying equations (1) and (2) are

$$V=R_1\omega_1;\quad U=0\quad \text{at}\quad \bar{\alpha}=\bar{\alpha}_1 \quad (3a)$$
$$V=R_2\omega_2;\quad U=0\quad \text{at}\quad \bar{\alpha}=\bar{\alpha}_2 \quad (3b)$$

In addition to (3) we require the velocity components U and V and the pressure $\bar{p}$ to be periodic and single-valued in $\bar{\beta}$. The equation of continuity is identically satisfied by writing

$$U=\frac{1}{\bar{h}}\frac{\partial\bar{\psi}}{\partial\bar{\beta}},\quad V=-\frac{1}{\bar{h}}\frac{\partial\bar{\psi}}{\partial\bar{\alpha}} \quad (4)$$

where $\bar{\psi}(\bar{\alpha},\bar{\beta})$ is the scalar stream function. $\bar{\psi}$ must be made to obey the global continuity condition:

$$\bar{\psi}(\bar{\alpha}_1,\bar{\beta})-\bar{\psi}(\bar{\alpha}_2,\bar{\beta})=Q \quad (5a)$$

There is no loss of generality in replacing (5a) by

$$\bar{\psi}(\bar{\alpha}_1,\bar{\beta})=Q,\quad \bar{\psi}(\bar{\alpha}_2,\bar{\beta})=0 \quad (5b)$$

Here Q is the flow rate across any simple curve joining the two cylinders.

The boundary conditions (3) when written in terms of the stream function $\bar{\psi}$ have the form:

$$-\frac{1}{\bar{h}}\frac{\partial\bar{\psi}}{\partial\bar{\alpha}}=R_1\omega_1,\quad \frac{\partial\bar{\psi}}{\partial\bar{\beta}}=0\quad \text{at}\quad \bar{\alpha}=\bar{\alpha}_1 \quad (6a)$$
$$-\frac{1}{\bar{h}}\frac{\partial\bar{\psi}}{\partial\bar{\alpha}}=R_2\omega_2,\quad \frac{\partial\bar{\psi}}{\partial\bar{\beta}}=0\quad \text{at}\quad \bar{\alpha}=\bar{\alpha}_2 \quad (6b)$$

Equations (1) and (2) are normalized next to facilitate numerical work. Define, for this purpose, nondimensional variables α, β, ψ, and the parameters δ, Δ, and ϵ

$$\alpha=\frac{\bar{\alpha}-\bar{\alpha}_1}{\Delta},\quad \beta=\bar{\beta}/2\pi,\quad \psi=\frac{\bar{\psi}}{R_1^2\omega};\quad 0<\alpha<1,\quad 0<\beta<1;$$
$$\delta=\frac{R_2-R_1}{R_1};\quad \Delta=\bar{\alpha}_2-\bar{\alpha}_1;\quad \epsilon=\frac{\sinh\Delta}{\sinh\alpha_2-\sinh\alpha_1} \quad (7)$$

where $\omega = \omega_1$, unless $\omega_1 = 0$ in which case $\omega = \omega_2$. We also use $\bar{h} = ah$. In lubrication literature δ is the radial clearance ratio and ϵ, $0 \le \epsilon \le 1$ is the eccentricity ratio.

Elimination of the pressure by cross-differentiation and substitution of (2) and (7) in equation (1) reduces the latter to

$$-2h\sin\beta\Big\{\Big(\frac{\Delta}{2\pi}\Big)^2\frac{\partial\psi}{\partial\alpha}\frac{\partial^2\psi}{\partial\beta^2}+\frac{\partial\psi}{\partial\alpha}\frac{\partial^2\psi}{\partial\alpha^2}\Big\}$$
$$+2h\sin\alpha\Big\{\Big(\frac{\Delta}{2\pi}\Big)^3\frac{\partial\psi}{\partial\beta}\frac{\partial^2\psi}{\partial\beta^2}+\Big(\frac{\Delta}{2\pi}\Big)\frac{\partial\psi}{\partial\beta}\frac{\partial^2\psi}{\partial\alpha^2}\Big\}$$
$$+\frac{1}{2\pi}\frac{\partial\psi}{\partial\beta}\frac{\partial^3\psi}{\partial\alpha^3}-\frac{1}{2\pi}\Big(\frac{\Delta}{2\pi}\Big)^2\frac{\partial\psi}{\partial\alpha}\frac{\partial^3\psi}{\partial\beta^3}$$
$$+\frac{1}{2\pi}\Big(\frac{\Delta}{2\pi}\Big)^2\frac{\partial\psi}{\partial\beta}\frac{\partial^3\psi}{\partial\alpha\partial\beta^2}-\frac{1}{2\pi}\frac{\partial\psi}{\partial\alpha}\frac{\partial^3\psi}{\partial\beta\partial\alpha^2}$$
$$=\frac{1}{\mathrm{Re}}\Big\{4(\cosh\alpha+\cos\beta)h\Big[\Delta\frac{\partial^2\psi}{\partial\alpha^2}+\Delta\Big(\frac{\Delta}{2\pi}\Big)^2\frac{\partial^2\psi}{\partial\beta^2}\Big]$$
$$+4h\sinh\alpha\Big[\Big(\frac{\Delta}{2\pi}\Big)^2\frac{\partial^3\psi}{\partial\alpha\partial\beta^2}$$
$$+\frac{\partial^3\psi}{\partial\alpha^3}\Big\}+4h\sin\beta\Big[\Big(\frac{\Delta}{2\pi}\Big)\frac{\partial^3\psi}{\partial\beta\partial\alpha^2}+\Big(\frac{\Delta}{2\pi}\Big)^3\frac{\partial^3\psi}{\partial\beta^3}\Big]$$
$$+\frac{1}{\pi}\Big(\frac{\Delta}{2\pi}\Big)\frac{\partial^4\psi}{\partial\alpha^2\partial\beta^2}+\frac{1}{\Delta}\frac{\partial^4\psi}{\partial\alpha^4}+\frac{1}{2\pi}\Big(\frac{\Delta}{2\pi}\Big)^3\frac{\partial^4\psi}{\partial\beta^4}\Big\} \quad (8)$$

over the unit square

$$R = \{(\alpha,\beta):\quad 0\le\alpha\le 1,\quad 0\le\beta\le 1\}$$

The Reynolds number is defined as $\mathrm{Re} = R_1^2\omega_n/\nu$, where $n = 1$, unless $\omega_1 = 0$ in which case $n = 2$.

The boundary conditions (6) have the nondimensional counterpart:

$$\frac{\partial\psi}{\partial\alpha} = -\Delta\left(\frac{\omega_1}{\omega}\right)\left(\frac{R_1}{R_1{}^2}\right)ah(0,\beta)\quad\text{at}\quad\alpha=0 \tag{9a}$$

$$\frac{\partial\psi}{\partial\alpha} = -\Delta\left(\frac{\omega_2}{\omega}\right)\left(\frac{R_2}{R_1{}^2}\right)ah(1,\beta)\quad\text{at}\quad\alpha=1 \tag{9b}$$

$$\psi(0,\beta) = Q/R_1{}^2\omega;\quad \psi(1,\beta)=0 \tag{9c}$$

and the periodicity conditions on the velocity reduce to:

$$\left.\frac{\partial^k\psi}{\partial\alpha^k}\right|_{\beta=0} = \left.\frac{\partial^k\psi}{\partial\alpha^k}\right|_{\beta=1};\quad 0\le k\le 2 \tag{10a}$$

$$\left.\frac{\partial^m\psi}{\partial\beta^m}\right|_{\beta=0} = \left.\frac{\partial^m\psi}{\partial\beta^m}\right|_{\beta=1};\quad 1\le m\le 2 \tag{10b}$$

The periodicity condition on pressure will be written in terms of the averaged pressure $P(\beta)$:

$$P(1)=P(0);\quad P=\int_0^1 p(\alpha,\beta)\quad d\alpha \tag{11}$$

so as to avoid the necessity of differentiating the solution. The β derivative of the nondimensional pressure p, where

$$p=\frac{\bar{p}(\alpha,\beta)}{2\pi\rho\nu\omega}\left(\frac{a}{R_1}\right)^2 \tag{12}$$

is obtained from (1b); it is given by

$$\begin{aligned}\frac{\partial p}{\partial\beta} = &-\frac{1}{\Delta h^2}\left\{\frac{1}{\Delta^2}\frac{\partial^3\psi}{\partial\alpha^3}+\frac{1}{(2\pi)^2}\frac{\partial^3\psi}{\partial\alpha\partial\beta^2}\right\}\\ &-\frac{2\sinh\alpha}{h}\left\{\frac{1}{\Delta^2}\frac{\partial^2\psi}{\partial\alpha^2}+\frac{1}{(2\pi)^2}\frac{\partial^2\psi}{\partial\beta^2}\right\}\\ &+\mathrm{Re}\left[\frac{1}{2\pi\Delta^2h^2}\left(\frac{\partial^2\psi}{\partial\alpha^2}\frac{\partial\psi}{\partial\beta}-\frac{\partial^2\psi}{\partial\alpha\partial\beta}\frac{\partial\psi}{\partial\alpha}\right)\right.\\ &\left.-\frac{\sin\beta}{h}\left\{\left(\frac{1}{\Delta}\frac{\partial\psi}{\partial\alpha}\right)^2+\left(\frac{1}{2\pi}\frac{\partial\psi}{\partial\beta}\right)^2\right\}\right]\end{aligned} \tag{13}$$

Numerical

In this formulation the system of equations (8)–(11) represent the basic flow between eccentric, rotating cylinders. We seek the weak form of solution

$$\begin{aligned}\psi(\alpha,\beta) &= \sum_{i=1}^{N_\alpha}\sum_{j=1}^{N_\beta}\psi_{ij}B_i(\alpha)B_j(\beta)\\ &= \sum_{i=3}^{N_\alpha-2}\sum_{j=2}^{N_\beta-2}\psi_{ij}B_i(\alpha)B_j(\beta)\\ &+\sum_{j=1}^{N_\beta}\left\{\sum_{i=1}^{2}\psi_{ij}B_i(\alpha)B_j(\beta)\right.\\ &\left.+\sum_{i=N_\alpha-1}^{N_\alpha}\psi_{ij}B_i(\alpha)B_j(\beta)\right\}\\ &+\sum_{i=3}^{N_\alpha-2}\left\{\sum_{j=1}^{2}\psi_{ij}B_i(\alpha)B_j(\beta)\right.\\ &\left.+\sum_{j=N_\beta-1}^{N_\beta}\psi_{ij}B_i(\alpha)B_j(\beta)\right\}\end{aligned} \tag{14}$$

Here $\{B_i(\alpha)\}_{i=1}^{N_\alpha}$ is a set of normalized B-splines in α of order k_α and smoothness index υ_α defined on the partition

$$\pi_\alpha:\quad 0=\alpha_1<\alpha_2<\ldots<\alpha_{l_\alpha+1}=1 \tag{15}$$

We assume smoothness $\upsilon_{\alpha_i}=\upsilon$, $2<i<l$, and a knot sequence $\{t_i\}_{i=1}^{N_\alpha+k_\alpha}$ given by

$$\begin{aligned}&\alpha_1=t_1=t_2=\ldots=t_{k_\alpha}\\ &\ldots\\ &\alpha_j=t_{k_\alpha+(j-2)d_\alpha+1}=\ldots=t_{k_\alpha+(j-1)d_\alpha}\\ &\ldots\\ &\alpha_{l_\alpha+1}=t_{N_\alpha+1}=\ldots=t_{N_\alpha+k_\alpha}\\ &2\le j\le l_\alpha;\quad d_\alpha=k_\alpha-\upsilon_{\alpha_i}\end{aligned} \tag{16}$$

The set of normalized B-splines in β, $\{B_j(\beta)\}_{j=1}^{N_\beta}$ is defined similarly. The dimension $N_\alpha\times N_\beta$ of the approximating subspace is given by [13]

$$N_\alpha=\sum_{i=2}^{l_\alpha}(k_\alpha-\upsilon_{\alpha_i});\quad N_\beta=\sum_{j=2}^{l_\alpha}(k_\alpha-\upsilon_{\beta_i})$$

The error in approximating by cubic splines is inversely proportional to $(N-1)^4$ [14].

In the second expression of (14) we have grouped the set τ_0 that is associated with the essential boundary conditions.

The set

$$\tau=\{B_i(\alpha)B_j(\beta):\quad 3\le i\le N_\alpha-2;\quad 2\le j\le N_\beta-2\} \tag{18a}$$

will provide the basis for functions defined on the region R which vanish on ∂R_0, viz., that part of the boundary ∂R for which the boundary conditions are essential.

The set

$$\begin{aligned}&\tau_0=\{B_i(\alpha)B_k(\beta),\quad B_m(\alpha)B_j(\beta)\}\\ &\quad 1\le i\le N_\alpha;\quad 2\le j\le N_\beta-2\\ &\quad k=1,N_\beta-1,N_\beta;\quad m=1,2,N_\alpha-1,N_\alpha\end{aligned} \tag{18b}$$

when restricted to ∂R_0 provides a basis for functions defined on ∂R_0.

In the application of Galerkin's method approximation (14) is substituted into equation (8), and the resultant equation is multiplied through by the test set τ. Integration over the unit square R yields the Galerkin coefficients:

$$\begin{aligned}\underline{\overline{X2}}_{ij}^{(p)} &= \int_0^1 B_i^{(c)}(x)B_j^{(d)}(x)\,dx\\ \underline{\overline{X3}}_{ijk}^{(p)} &= \int_0^1 B_i^{(b)}(x)B_j^{(c)}(x)B_k^{(d)}(x)\,dx\\ \underline{\overline{X4}}_{ijkl}^{(p)} &= \int_0^1 B_i^{(a)}(x)B_j^{(b)}(x)B_k^{(c)}(x)B_l^{(d)}(x)\,dx\end{aligned} \tag{19}$$

where

$a\le b\le c\le d$

$p = a+b+c+d+1$ (if $c>0$) $+\,2$ (if $b>0$) $+\,3$ (if $a>0$) and $X=A$ when $x=\alpha$ and $X=B$ when $x=\beta$, and the following set of nonlinear algebraic equations:

$$\begin{aligned}\sum_{m,p,r=1}^{N_\alpha}\sum_{n,q,s=1}^{N_\beta}\Big(\psi_{pq}\psi_{rs}\Big\{&\frac{\Delta^3}{2\pi}\,\underline{\overline{C1}}_{mn}\underline{\overline{A4}}_{imrp}^{(1)}\underline{\overline{B4}}_{jnqs}^{(2)}\\ &+2\pi\Delta\underline{\overline{C1}}_{mn}\underline{\overline{A4}}_{impr}^{(4)}\underline{\overline{B4}}_{jnqs}^{(0)}+\frac{\Delta^4}{(2\pi)^2}\underline{\overline{C2}}_{mn}\underline{\overline{A4}}_{impr}^{(0)}\underline{\overline{B4}}_{jnqs}^{(4)}\\ &+\Delta^2\underline{\overline{C2}}_{mn}\underline{\overline{A4}}_{impr}^{(2)}\underline{\overline{B4}}_{jnsq}^{(1)}-\Delta H_{mn}\underline{\overline{B4}}_{jnsq}^{(1)}(\underline{\overline{A4}}_{impr}^{(4)}+\underline{\overline{A4}}_{ipmr}^{(4)}+\underline{\overline{A4}}_{mpir}^{(4)})\\ &+\frac{\Delta^3}{(2\pi)^2}H_{mn}\underline{\overline{A4}}_{imrp}^{(1)}(\underline{\overline{B4}}_{jnqs}^{(4)}+\underline{\overline{B4}}_{jqns}^{(4)}+\underline{\overline{B4}}_{nqjs}^{(4)})\end{aligned}$$

$$+\frac{\Delta^3}{(2\pi)^2}H_{mn}\overline{A4}^{(1)}_{impr}\overline{B4}^{(4)}_{jnqs}$$

$$-\Delta H_{mn}\overline{A4}^{(4)}_{impr}\overline{B4}^{(1)}_{jnqs}\}\Big)$$

$$-\frac{1}{\mathrm{Re}}\sum_{m,p=1}^{N_\alpha}\sum_{n,q=1}^{N_\beta}\psi_{pq}\Big[2\pi\Delta^2\overline{C3}_{mn}\overline{A3}^{(2)}_{imp}\overline{B3}^{(0)}_{jnq}$$

$$+\frac{\Delta^4}{2\pi}\overline{C3}_{mn}\overline{A3}^{(0)}_{imp}\overline{B3}^{(2)}_{jnq}+\frac{\Delta^3}{\pi}\overline{C2}_{mn}\overline{A3}^{(1)}_{imp}\overline{B3}^{(2)}_{jnq} \tag{20}$$

$$-4\pi\Delta\overline{C2}_{mn}\overline{B3}^{(0)}_{jnq}(\overline{A3}^{(4)}_{imp}+\overline{A3}^{(4)}_{mip})-2\Delta^2\overline{C1}_{mn}\overline{A3}^{(2)}_{imp}\overline{B3}^{(1)}_{jnq}$$

$$+\frac{\Delta^4}{2\pi^2}\overline{C1}_{mn}\overline{A3}^{(0)}_{imp}(\overline{B3}^{(4)}_{jnq}+\overline{B3}^{(4)}_{njq})+\frac{\Delta^2}{\pi}H_{mn}\overline{A3}^{(2)}_{imp}\overline{B3}^{(2)}_{jnq}$$

$$+2\pi H_{mn}\overline{B3}^{(0)}_{jnq}(\overline{A3}^{(5)}_{mip}+\overline{A3}^{(5)}_{imp}+2\overline{A3}^{(7)}_{imp})+\frac{\Delta^4}{(2\pi)^3}H_{mn}\overline{A3}^{(0)}_{imp}(\overline{B3}^{(5)}_{njq}$$

$$+\overline{B3}^{(5)}_{jnq}+2\overline{B3}^{(7)}_{jnq}-\{B_n(\beta)B_j'(\beta)B_q''(\beta)\}^{\beta=1}_{\beta=0})\Big]=0$$

$$3\le i\le N_\alpha-2;\quad 2\le j\le N_\beta-2$$

In (20) the $\overline{C1}_{m,n}$, $1 \le m \le N_\alpha$, $1 \le n \le N_\beta$, represent the Fourier coefficients of $h^3 \sin\beta$ relative to the approximating subspace $B_i(\alpha)\,B_j(\beta)$, $1 \le i \le N_\alpha$, $1 \le j \le N_\beta$. This is indicated by the notation

$$2h^3\sin\beta=\{\overline{C1}_{m,n}\}^{N_\alpha,N_\beta}_{1,1} \tag{21a}$$

In a similar manner, we also have

$$2h^3\sinh\alpha=\{\overline{C2}_{m,n}\}^{N_\alpha,N_\beta}_{1,1}$$

$$4h^3(\cosh\alpha+\cos\beta)=\{\overline{C3}_{m,n}\}^{N_\alpha,N_\beta}_{1,1} \tag{21b}$$

$$h^2=\{H_{m,n}\}^{N_\alpha,N_\beta}_{1,1}$$

The boundary condition on the cylinders, equation (9), are satisfied in the weak form. They determine $4 \times N_\beta$ of the unknown coefficients:

$$\psi_{1,j}=\psi^*;\quad \psi_{2,j}=\psi^*+\frac{\kappa_1}{B_1'(0)}\bar{H}_j$$

$$\psi_{N_\alpha-1,j}=\frac{\kappa_2}{B_{N_\alpha}'(1)}\bar{\bar{H}}_j;\quad \psi_{N_\alpha j}=0;\quad 1\le j\le N_\beta \tag{22}$$

Here

$$\psi^*=\frac{Q}{R_1^2\omega};\quad \kappa_1=\Delta\Big(\frac{\omega_1}{\omega}\Big)\frac{a}{R_1};\quad \kappa_2=\Delta\Big(\frac{\omega_2}{\omega}\Big)\frac{aR_2}{R_1^2}$$

and

$$h(0,\beta)=\{\bar{H}_j\}^{N_\beta}_1;\quad h(1,\beta)=\{\bar{\bar{H}}_j\}^{N_\beta}_1 \tag{23}$$

The periodicity conditions (10) imposed on the stream function and its derivatives are satisfied by setting

$$\left.\begin{array}{l}\psi_{i,1}=\psi_{i,N_\beta}\\ \psi_{i,1}-\psi_{i,2}+\psi_{i,N_\beta}-\psi_{i,N_\beta-1}=0\end{array}\right\}3\le i\le N_\alpha-2$$

$$\sum_{i=3}^{N_\alpha-2}\Big\{\sum_{j=1}^{k_\beta}\psi_{ij}B_j''(0)-\sum_{j=N_\beta-k_\beta}^{N_\beta}\psi_{ij}B_j''(1)\Big\}=0;$$

The formulation is completed with the discretized form of the pressure constraint (11)

$$\sum_{p,i=1}^{N_\alpha}\sum_{q,j=1}^{N_\beta}\psi_{ij}\Big\{\frac{1}{\Delta^3}\overline{H2}_{pg}\overline{B2}^{(0)}_{qj}(\{B_p(\alpha)B_i''(\alpha)\}^{\alpha=1}_{\alpha=0}-\overline{A2}^{(4)}_{pi})$$

$$+\frac{1}{(2\pi)^2\Delta}\overline{H2}_{pq}\overline{A2}^{(1)}_{pi}\overline{B2}^{(2)}_{qj}+\frac{1}{\Delta^2}\overline{H3}_{pq}\overline{A2}^{(2)}_{pi}\overline{B2}^{(0)}_{qj}$$

$$+\frac{1}{(2\pi)^2}\overline{H3}_{pq}\overline{A2}^{(0)}_{pi}\overline{B2}^{(2)}_{qj}\Big\}$$

$$+\mathrm{Re}\sum_{p,i,m=1}^{N_\alpha}\sum_{q,j,n=1}^{N_\beta}\psi_{ij}\psi_{mn}\Big(-\frac{1}{2\pi\Delta^2}\overline{H2}_{pq}\overline{A3}^{(2)}_{pmi}\overline{B3}^{(1)}_{qjn}$$

$$+\frac{1}{2\pi\Delta^2}\overline{H2}_{pq}\overline{A3}^{(3)}_{pin}\overline{B3}^{(1)}_{qnj}+\frac{1}{\Delta^2}\overline{H4}_{pq}\overline{A3}^{(3)}_{pim}\overline{B3}^{(0)}_{qjn}$$

$$+\frac{1}{(2\pi)^2}\overline{H4}_{pq}\overline{A3}^{(0)}_{pim}\overline{B3}^{(3)}_{qjn}\Big)=0 \tag{25}$$

In (25) we have

$$\frac{1}{h^2}=\{\overline{H2}_{ij}\}^{N_\alpha,N_\beta}_{1,1};2\frac{\sinh\alpha}{h}=\{\overline{H3}_{ij}\}^{N_\alpha,N_\beta}_{1,1};$$

$$\frac{\sin\beta}{h}=\{\overline{H4}_{ij}\}^{N_\alpha,N_\beta}_{1,1} \tag{26}$$

Equations (20) and (25) represent $(N_\alpha-4)+(N_\beta-3)+1$ conditions for the unknown coefficients ψ_{ij}, $3 \le i \le N_a-2$, $2 \le j \le N_\beta-2$, and the yet unknown nondimensional flow rate ψ^*. Each of these conditions is in the form of a nonlinear algebraic equation.

The set of nonlinear equations were solved by an IMSL routine, using a Newton-like method [15] that is at least quadratically convergent. For Stokes flow calculations the process was initiated with zero starting values, it required 6–30 min CPU time on the PDP-10 for $N_\alpha = 8$, $N_\beta = 11$ and took 10–20 iterations to converge.

Computer times increase drastically and conditions become more demanding at Re > 0. The domain of starting values that yield convergent solutions shrinks with increasing Reynolds number and it was necessary to use continuation in Re. A typical sequence would be Re = 0, 0.5, 1, 5, 10, 20, 30, 35, 40, 50 (at $\delta = 1.0$ and $\epsilon = 0.5$).

Evaluation of equation (20) at each stage of the iterations requires multiple summations. Summations are performed only on nonzero coefficients of (19), and as there are $\sim N_\alpha w_\alpha^m$ nonzero coefficients in, say, α, multiple summations in α require $N_\alpha w_\alpha^m$ operations. Here m is the multiplicity of the summations, i.e., the number of indices of the coefficients, and $w_\alpha = 2k_\alpha - 1$ is the band width. For small N_α the number $N_\alpha w_\alpha^m$ is not a particularly tight upper bound on the number of nonzero coefficients and a number smaller than w_α could be used.

To evaluate the viscous contribution to the N_{EQ} equations of (20), $N_{EQ} = (N_\alpha-4) \times (N_\beta-3)$, we perform approximately $N_s \simeq 9 \times N_{EQ} \times w^4$ operations, as there are nine viscous terms in each equations. The corresponding number for inertial terms is $N_I \simeq 8 \times N_{EQ} \times w^6$. Thus the number of operations required for an inertial solution is approximately w^2 times the number of operations required for solution of Stokes flow.

The Newton-like method [15] employed for solution of the nonlinear algebraic system requires $(N_{EQ}^2 + 3N_{EQ})/2$ function evaluations per iterative step, as compared to $(N_{EQ}^2 + N_{EQ})$ for Newton's method. Thus N_T, the total number of operations per iteration step, is given by $N_T \sim (2wN_{EQ})^3$. For $N_\alpha = 8$, $N_\beta = 11$ and $k_\alpha = k_\beta = 4$ (cubic splines) in Stokes flow we have $N_T \sim 6 \times 10^7$ operations for each step in the iteration. Doubling the dimension of the appproximating subspace would necessitate performing $N_T \sim 6 \times 10^9$ operations per iterative step. On the PDP-10 computer of the University of Pittsburgh these numbers represent 5 min and 50 min, respectively, for a total of 10 iterations. To obtain corresponding figures for inertial flow, Re > 0, multiply by w^2. Thus $N_\alpha = 8$, $N_\beta = 11$ represents the practical upper bound on the size of the system, dictated by the time requirement on the computer available to us.

Discussion and Results

Results will be discussed under two headings. First we examine the accuracy of the numerical method relative to the work of Ballal and Rivlin [1]. Next we describe what appear to be new results concerning inertia effects in flow between eccentric rotating cylinders. In this latter section we also make comparison between our results and those of Ballal and Rivlin [1] and DiPrima and Stuart [12]. For small δ our results are, as expected, close to the results of classical lubrication theory.

Accuracy. Application of Galerkin's method makes solution of the steady state problem feasible. We have applied Galerkin's method on previous occasions. When the boundary conditions are homogeneous, we find that B-splines are attractive test functions. They have good approximating properties, and because they have local support, the storage requirement of a Galerkin coefficient is $N \times (2k-1)^m$, where m is the dimension of the coefficient.

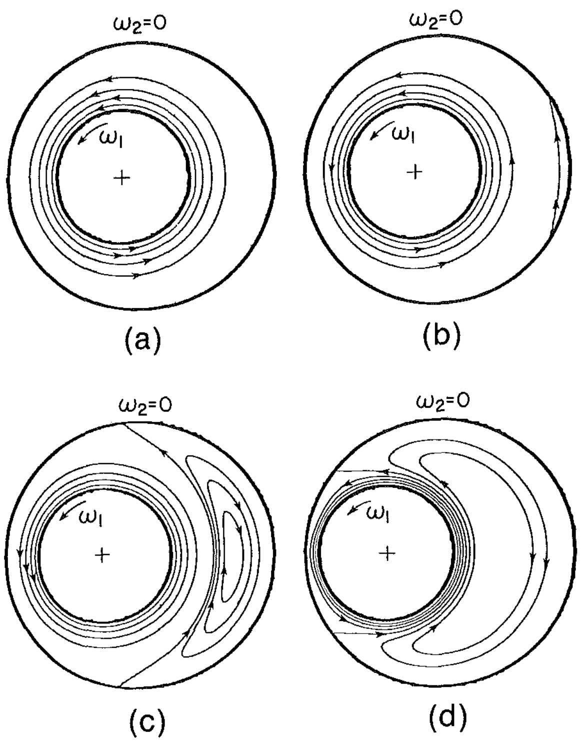

Fig. 2 Streamline pattern; Stokes flow ($\omega_2/\omega_1 = 1$, $\delta = 1.0$; (*a*) $\epsilon = 0.25$; (*b*) $\epsilon = 0.35$; (*c*) $\epsilon = 0.5$; (*d*) $\epsilon = 0.8$)

In comparison with the Chebyshev polynomial expansion scheme for the Orr-Sommerfeld equation representing Poiseuille flow between parallel plates, e.g., we find that at Re $= 20{,}000$ the Galerkin, B-spline formulation gives $C_1 = 0.237394 + i\,0.00373133$ for the first eigenvalue on a 36-bit machine in single precision [16]. The corresponding value by Chebyshev polynomials is $C_1 = 0.23752649 + i\,0.00373967$, obtained by Orszag [17] on a 48-bit machine in single precision. B-splines were also tested in a two-dimensional steady state problem, and performed well. For through flow between parallel rotating disks, results obtained with B-spline test functions [18] showed excellent agreement with experimental data from LDV measurements and also with calculations employing circular functions [19]. It is also noteworthy that implementation of the Galerkin, B-spline strategy is almost trivial, if only one makes use of the extensive subroutine package of de Boor [13].

Accuracy of the Galerkin, B-spline formulation in the present case is investigated for Stokes flow; several accurate solutions of this flow are available in the literature.

The effect of increasing the dimension of the approximating subspace is shown in Table 1. Here ψ^* is the nondimensional flow rate across any simple curve connecting the cylinders. The table also shows the corresponding value by Ballal and Rivlin [1]. Table 2 displays the azimuthal velocity component at various points (α, β) of the flow field, for various order approximations. It may be seen that the change in ψ^*, and also in V_β at most points, is in the fourth significant digit as the number of equations representing the flow is changed from 17 to 29.

Comparison of azimuthal and tangential velocity with that of Ballal and Rivlin shows excellent agreement for the various clearance ratios tested as does the distribution of average pressure. Figure 2 shows streamline pattern of our numerical

Table 1 Nondimensional flow rate (Stokes flow, $\epsilon = 0.5$, $(R_2 - R_1)/R_1 = 1.0$)

Ballal and Rivlin [1]	$N_\beta = 7$ $N_\alpha = 8$	$N_\beta = 9$ $N_\alpha = 8$	$N_\beta = 11$ $N_\alpha = 8$
0.2949077	0.2938225	0.294133	0.2943499

Table 2 Azimuthal velocity (Stokes flow, $\epsilon = 0.5$, $(R_2 - R_1)/R_1 = 1.0$)

a	Ballal and Rivlin [1]	$N_\beta = 7$ $N_\alpha = 8$	$N_\beta = 9$ $N_\alpha = 8$	$N_\beta = 11$ $N_\alpha = 8$
		$\beta = 0.0$		
0.0	29.0000	29.0000	29.0000	29.0000
0.2	17.4419	17.5889	17.4657	17.4939
0.4	8.4619	8.4712	8.4580	8.3585
0.6	2.2295	2.1623	2.2074	2.1582
0.8	−0.8420	−0.9753	−0.9243	−0.8406
1.0	0.0	0.0	0.0	0.0
		$\beta = 0.25$		
0.0	29.0000	29.0000	29.0000	29.0000
0.2	21.5330	21.4878	21.5175	21.5319
0.4	14.8975	14.8373	14.8419	14.8623
0.6	9.0828	9.0259	9.0107	9.0389
0.8	4.1036	4.0661	4.0474	4.0826
1.0	0.0	0.0	0.0	0.0
		$\beta = 0.50$		
0.0	29.0000	29.0000	29.0000	29.0000
0.2	26.3507	26.3859	26.3368	26.3568
0.4	22.2753	22.2534	22.2133	22.2223
0.6	16.6682	16.5546	16.5641	16.5947
0.8	9.3372	9.1785	9.2429	9.3084
1.0	0.0	0.0	0.0	0.0

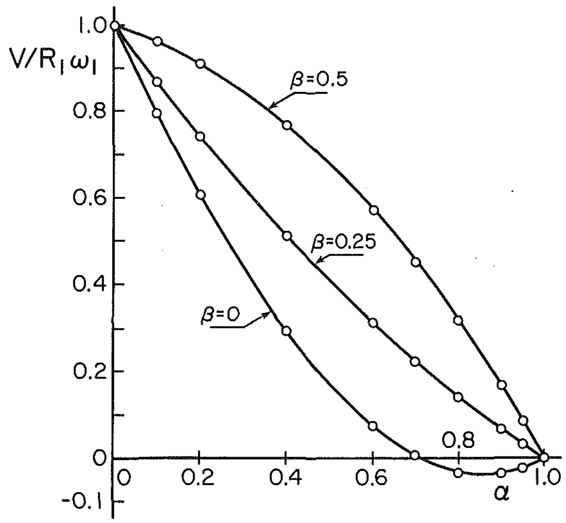

Fig. 3 Tangential velocity in Stokes flow (ω_2/ω_1 = 0, δ = 1.0, ϵ = 0.5. o, present solution; ——, Ballal and Rivlin [1]).

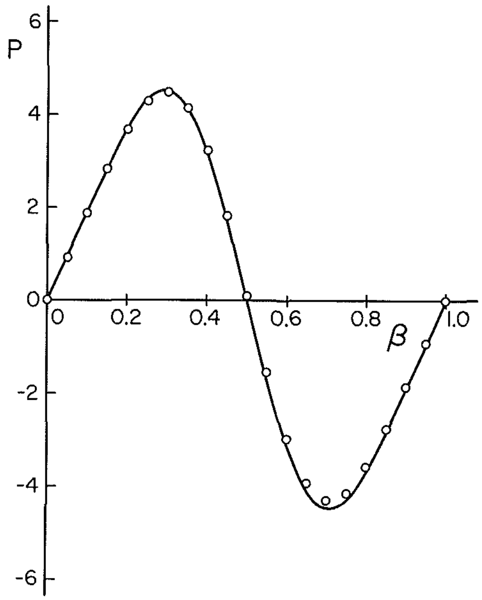

Fig. 4 Averaged pressure in Stokes flow (ω_2/ω_1 = 0, δ = 1.0, ϵ = 0.5. o, present solution; ——, Ballal and Rivlin [1]).

solution when the inner cylinder is rotating. Figure 3 displays the corresponding tangential velocity at $\epsilon = 0.5$ at three values of the β coordinate and the distribution of average pressure is shown in Fig. 4. Typical streamline pattern with the outer disk rotating and inner disk stationary are plotted in Fig. 5. For $\epsilon = 0.5$, Figs. 6 and 7 compare our results for azimuthal velocity and averaged pressure with those of Ballal and Rivlin [1]. Finally Fig. 8 displays the streamline pattern for counterrotating disks, $\omega_1/\omega_2 = -2$. The corresponding azimuthal velocity plot is shown in Fig. 9.

As may be concluded, the analysis of Ballal and Rivlin and the present numerical solution give near identical results for Stokes flow; that they also agree well with conclusions of classical lubrication theory will be discussed in connection with inertial solutions.

Inertial Effects. Figure 10 displays the streamline pattern for inertial solution at increasing values of the Reynolds number with the inner cylinder rotating and the outer cylinder stationary. Figure 11 shows corresponding pressure distributions. For Stokes flow, Re = 0, the pressure

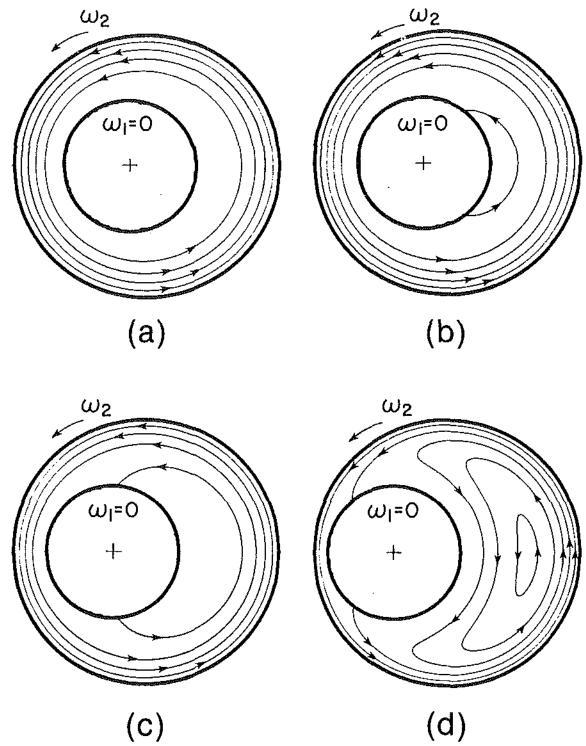

Fig. 5 Streamline pattern; Stokes flow (ω_1/ω_2 = 0, δ = 1.0; (*a*) ϵ = 0.25; (*b*) ϵ = 0.35; (*c*) ϵ = 0.5; (*d*) ϵ = 0.8)

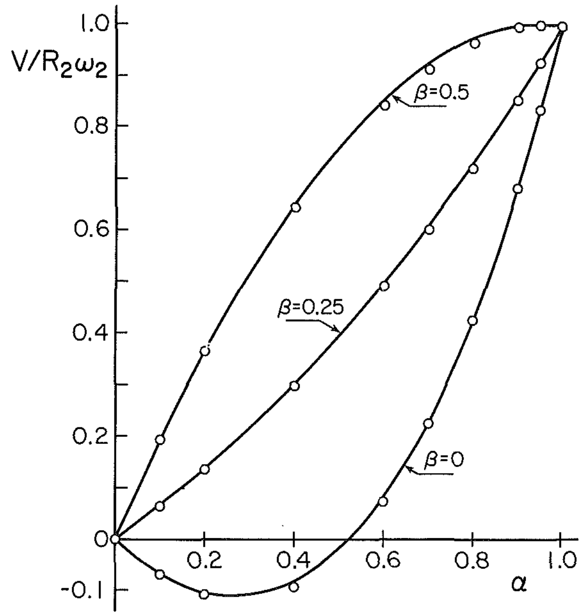

Fig. 6 Tangential velocity in Stokes flow (ω_1/ω_2 = 0, δ = 1.0, ϵ = 0.5. o, present solution; ——, Ballal and Rivlin [1]).

distribution is symmetric with respect to the line of centers, $\beta = 0.5$. The effect of fluid inertia is to decrease the value of the positive pressure and to increase the magnitude of the negative pressure relative to $P(0)$. This effect has already been predicted from approximate analyses in hydrodynamic lubrication (cf. [20]), although inertia effects seem to be less important there. Figure 12 shows the pressure distribution at $\delta = 0.046$, as calculated by the present method at Re = 100. This figure also contains results from the small perturbation solution of DiPrima and Stuart [12] at Re = 100, the noninertial solution of Ballal and Rivlin [1] and the classical noninertial lubrication approximation [3]. We may conclude

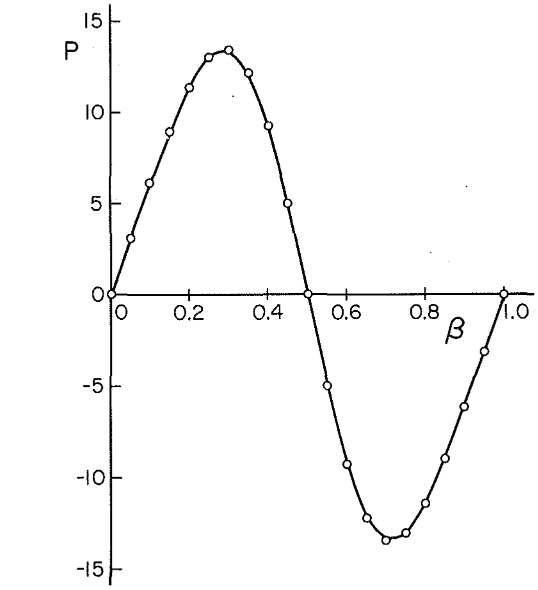

Fig. 7 Averaged pressure in Stokes flow (ω_1/ω_2 = 0, δ = 1.0, ϵ = 0.5. o, present solution; —, Ballal and Rivlin [1]).

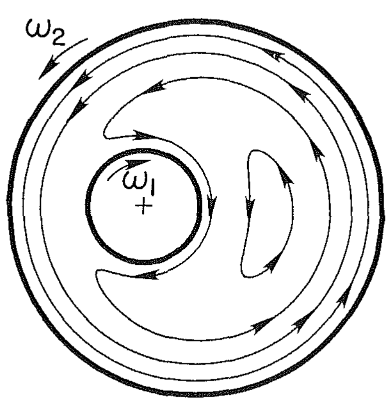

Fig. 8 Streamline pattern; Stokes flow (ω_1/ω_2 = −2, δ = 2.33, ϵ = 0.5)

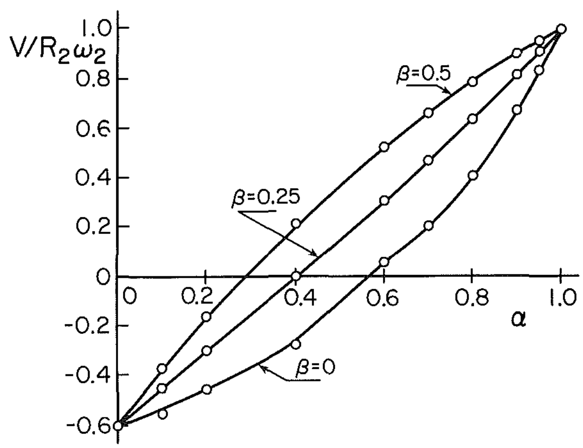

Fig. 9 Tangential velocity in Stokes flow (ω_1/ω_2 = −2, δ = 2.33, ϵ = 0.5). o, present solution; – – Ballal and Riolin [1].

that lubrication theory provides good pressure profiles at small values of the Reynolds number.[1]

There are three important conclusions to be drawn from

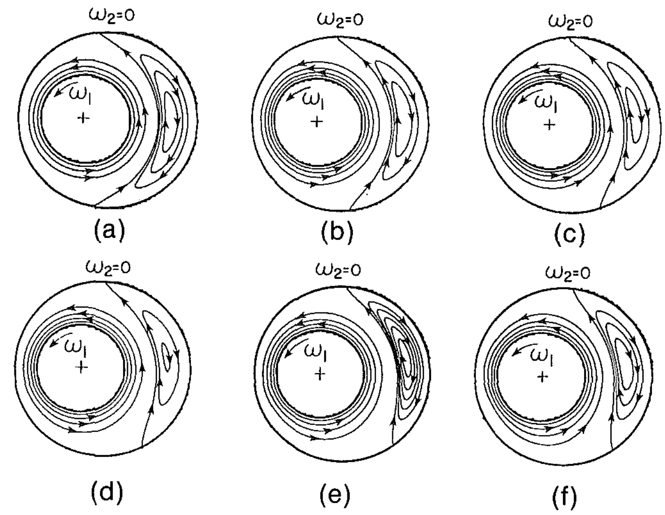

Fig. 10 Streamline pattern; flow with inertia (ω_2/ω_1 = 0; ϵ = 0.5, δ = 1.0; (*a*) Re = 0.0; (*b*) Re = 10; (*c*) Re = 20; (*d*) Re = 30; (*e*) Re = 40; (*f*) Re = 50)

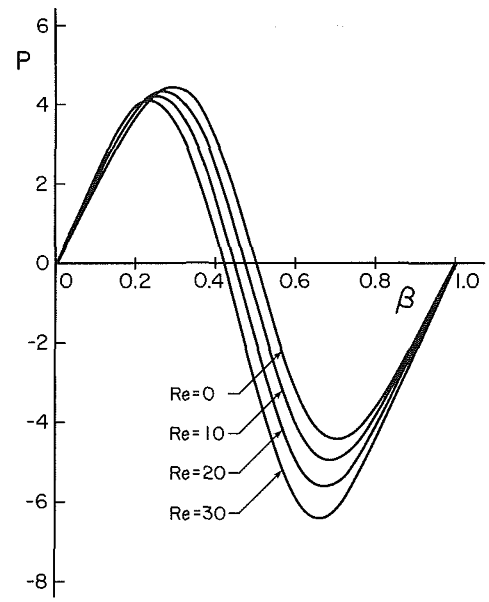

Fig. 11 Averaged pressure; flow with inertia (ω_2/ω_1 = 0, ϵ = 0.5, δ = 1.0)

Fig. 10: (*i*) the center of the separation eddy moves in the direction of rotation of the cylinder, (*ii*) the reattachment point moves in the direction opposite to rotation, and, (*iii*) the separation point moves in the direction of rotation when the inner cylinder is rotating and the outer cylinder is stationary.

Conclusions (*i*) and (*ii*), as stated in the foregoing, are in qualitative agreement with findings of Ballal and Rivlin [1]; however conclusion (*iii*) is in contradiction with results of their first-order perturbation theory. The dependence of the position of separation and reattachment points on Reynolds number is depicted in Fig. 13. The angle θ plotted here is the polar angle.

$$\theta = \tan^{-1}\left\{ \frac{\sinh\bar{\alpha}_1 \sin\bar{\beta}}{1-\cosh\bar{\alpha}_1\cos\bar{\beta}} \right\}$$

measured relative to the inner cylinder from the *x*-axis. Obrien, Jones, and Mobbs [21] have measured the position of the separation and reattachment points for some configurations of the rotating cylinders and, in qualitative

[1] This comment should not be interpreted to mean that fluid inertia has insignificant contribution in hydrodynamic lubrication. In lightly loaded journal bearings, e.g., fluid inertia effects result in an attitude angle in excess of $\pi/2$, leading to instability [4].

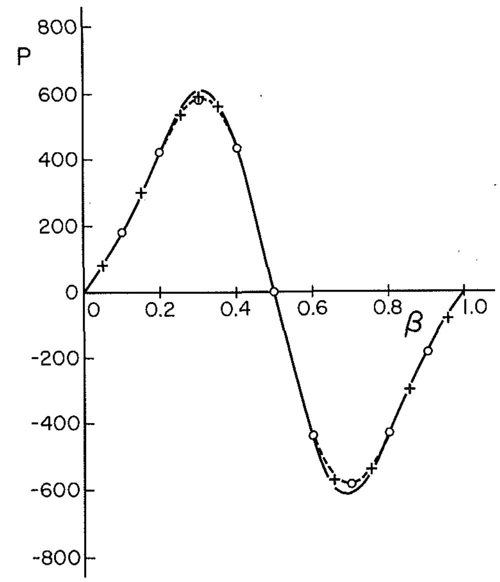

Fig. 12 Averaged pressure ($\omega_2/\omega_1 = 0$, $\delta = 0.064$, $\epsilon = 0.75$. Inertial solution, Re = 100: —, present method; o, DiPrima and Stuart [12]. Noninertial solution: +, Ballal and Rivlin [1]; ---, lubrication theory [3]).

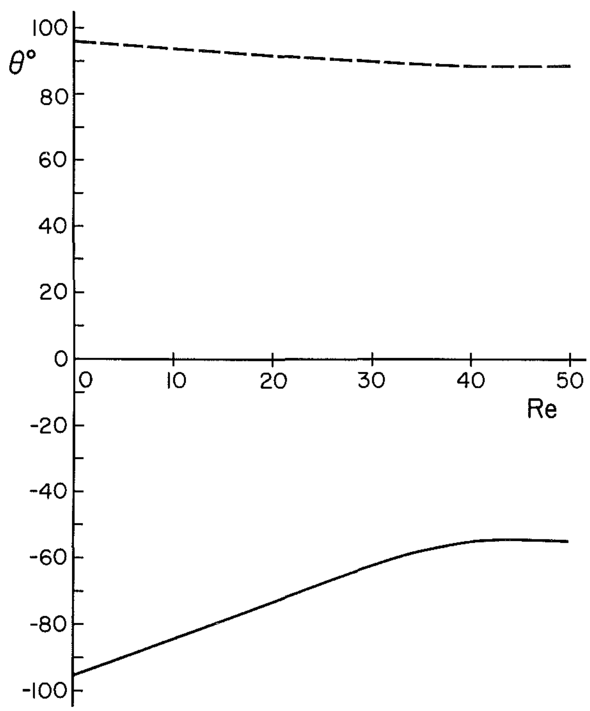

Fig. 13 Polar angle of separation and reattachment points; flow with inertia ($\omega_2/\omega_1 = 0$, $\epsilon = 0.5$, $\delta = 1.0$. —, separation point; ---, reattachment point).

agreement with us, found the separation point closer to the x-axis than the reattachment point.

Figure 14 displays streamlines obtained with the outer cylinder rotating and inner cylinder stationary. The inertial effect is quite noticeable. The center of the separation eddy and the separation point both move in the direction of rotation on increasing the Reynolds number. The reattachment point, on the other hand, moves in the direction opposite to rotation, at least at this value, $\epsilon = 0.5$, of the eccentricity ratio. Figure 15 depicts the polar angle of separation and reattachment points at $\epsilon = 0.5$ for various values of Re. The average pressure is plotted in Fig. 16 for

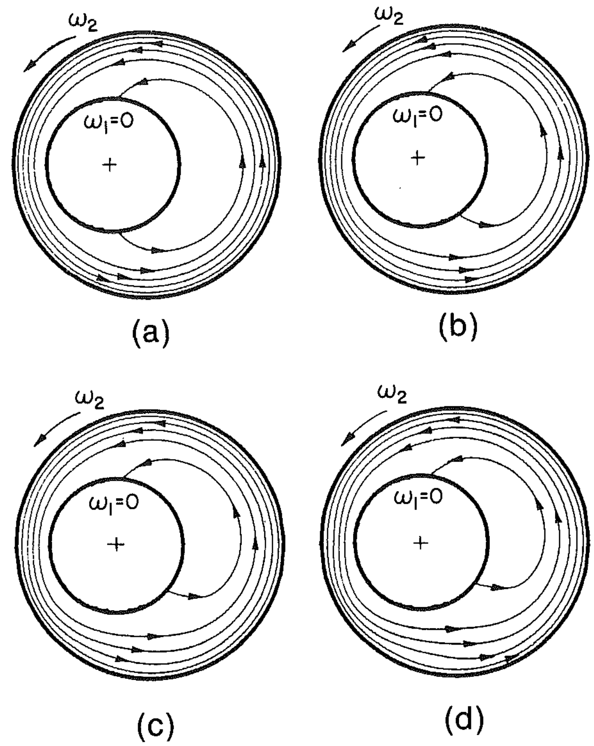

Fig. 14 Streamline pattern; flow with inertia ($\omega_1/\omega_2 = 0$, $\epsilon = 0.5$, $\delta = 1.0$, (*a*) Re = 0; (*b*) Re = 10; (*c*) Re = 20; (*d*) Re = 30)

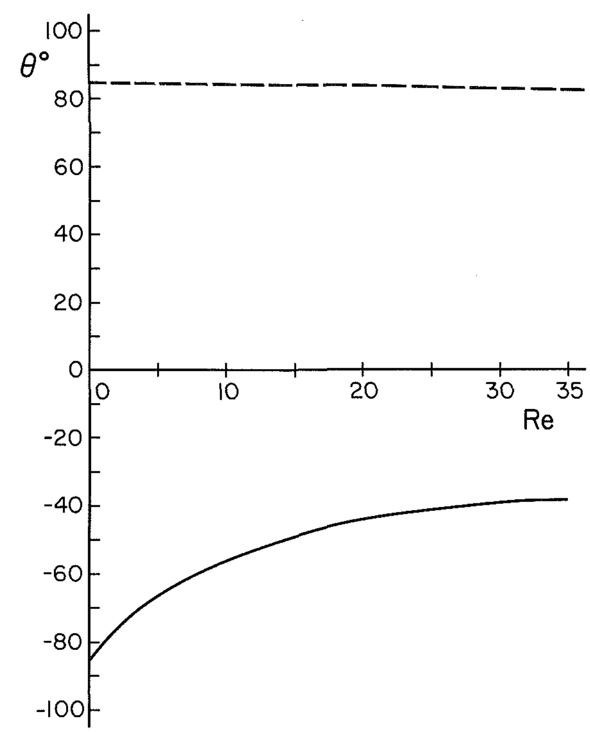

Fig. 15 Polar angle of separation and reattachment points; flow with inertia ($\omega_1/\omega_2 = 0$, $\delta = 1.0$, $\epsilon = 0.5$. —, separation point; ---, reattachment point).

stationary inner cylinder at various values of the Reynolds number.

The direction of movement of the separation points requires further study for rotating outer cylinder. For $0.2702 < \epsilon < 0.573$ "both separation points are displaced in the opposite sense to that of the rotation of the outer cylinder by the first-order inertial correction," according to Ballal and Rivlin [1]. They further state that "if $0.573 < \epsilon < 1$, the separation points are displaced in the same sense as that of the rotation of the outer cylinder." In Fig. 17 we plot the polar angle of the separation point against the eccentricity ratio ϵ for two values of the Reynolds number. It is concluded that the point of separation in Stokes flow is always upstream the point of separation in inertial flow of Re = 20.

The angular position of the reattachment point in both Stokes flow and inertial flow is shown in Fig. 18. According to our calculations, the reattachment point in Stokes flow is upstream from the reattachment point of the Re = 20 flow when in the eccentricity range $0.53 < \epsilon$; when in the range $0.31 < \epsilon < 0.53$ this situation is reversed.

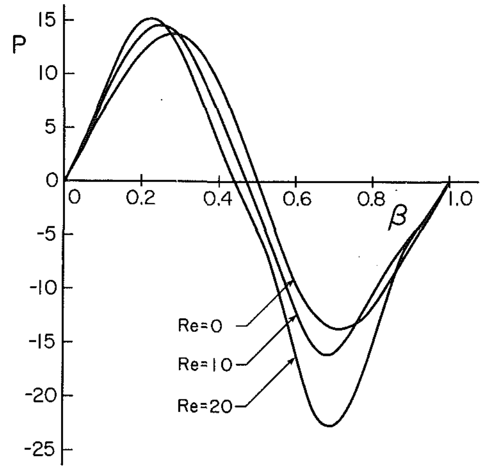

Fig. 16 Averaged pressure; flow with inertia ($\omega_1/\omega_2 = 0$, $\epsilon = 0.5$, $\delta = 1.0$)

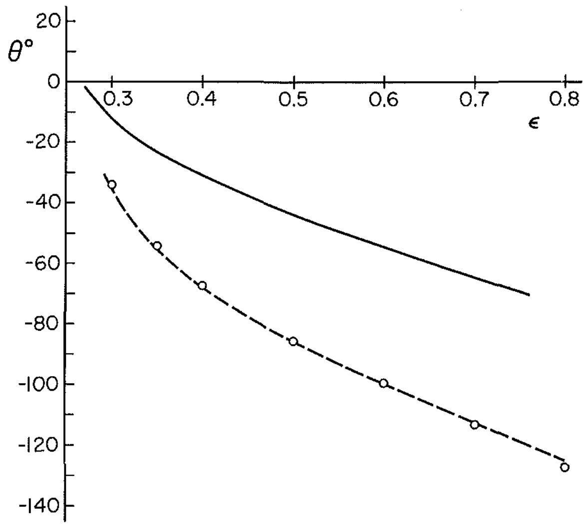

Fig. 17 Polar angle of separation point ($\omega_1/\omega_2 = 0$, $\delta = 1.0$. Present solution: ---, Re = 0; —, Re = 20. o, Re = 0; Ballal and Rivlin [1]).

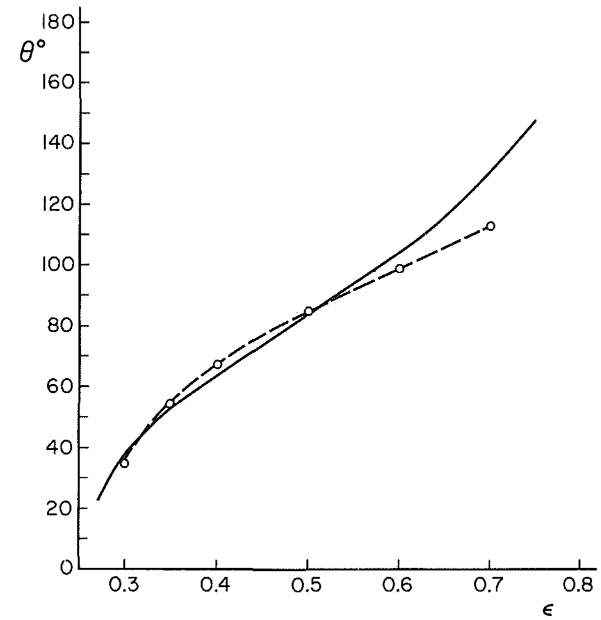

Fig. 18 Polar angle of reattachment point ($\omega_1/\omega_2 = 0$, $\delta = 1.0$. Present solution: ---, Re = 0; —, Re = 20. o, Re = 0; Ballal and Rivlin [1]).

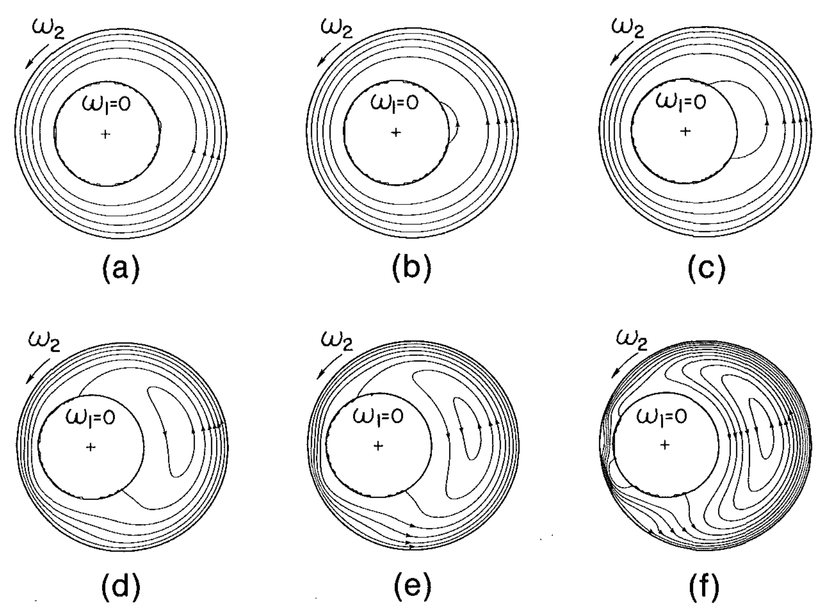

Fig. 19 Streamline pattern; inertial flow ($\omega_1/\omega_2 = 0$, $\delta = 1.0$, Re = 20; (*a*), $\epsilon = 0.27$; (*b*), $\epsilon = 0.3$; (*c*), $\epsilon = 0.4$; (*d*), $\epsilon = 0.6$; (*e*), $\epsilon = 0.65$; (*f*), $\epsilon = 0.75$)

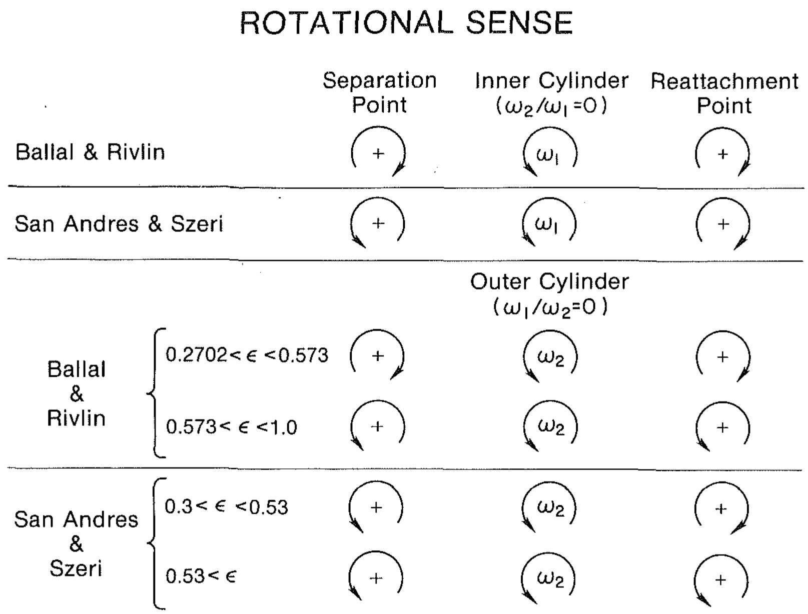

Fig. 20 Schematics of the movement of separation points

Figure 19 displays streamlines for rotating outer cylinder and various eccentricity ratios at Re = 20. It is indicated here that the resolution of our calculation breaks down at high eccentricity, due to machine limitations on the number of Galerkin terms we are able to carry. Finally, Fig. 20 offers a schematic comparison of the main results of Ballal and Rivlin with our calculations.

Three possible reasons for the discrepancy between our results and the first-order perturbation analysis of Ballal and Rivlin have been advanced. These are:

(1) Ballal and Rivlin's solution is a small Reynolds number perturbation of the Stokes flow (see footnote on p. 240 of paper by Ballal and Rivlin), and thus its validity is questionable for Re > 1. Their Fig. 29 has Re = 148.8.

(2) At high values of the Reynolds number, the first-order inertial correction, as supplied by Ballal and Rivlin, might completely be overshadowed by subsequent terms of the perturbation series, and the series diverges.

(3) Ballal and Rivlin calculate the flow rate from the Stokes problem and assume it to also apply to the first-order inertial correction. Thus their first-order correction does not satisfy the correct boundary conditions, and in consequence it does not insure continuity of pressure nor satisfaction of global flow continuity. We, on the other hand, by satisfying pressure continuity for the inertial flow, satisfy the boundary conditions at all values of the Reynolds number.

Our results that the separation point moves in the direction of rotation on increasing the Reynolds number is acceptable on physical grounds. There are instances, e.g., cylinder in cross flow, where it is well known that, at least in some region of the laminar Reynolds number, speeding up of the flow has the effect of delaying flow separation.

Acknowledgment

The authors are grateful to the reviewers for their constructive comments which resulted in Figs. 18 and 20 of the paper. They also wish to record their appreciation to Mr. M.-C. Jeng for his help with some of the contour plots.

References

1 Ballal, B., and Rivlin, P. S., "Flow of a Newtonian Fluid Between Eccentric Rotating Cylinders," *Arch. Rational Mech. Anal.*, Vol. 62, pp. 237–294.

2 Reynolds, O., "On the Theory of Lubrication and Its Application to Mr. Beuchamp Tower's Experiments," *Phil. Trans. Roy. Soc.*, Vol. 177, 1886, pp. 157–234.

3 Szeri, A. Z., *Tribology*, McGraw-Hill, New York, 1980.

4 Black, H. F., and Walton, M. H., "Theoretical and Experimental Investigations of a Short 360° Journal Bearing in the Transition Super-Laminar Regime," *J. Mech. Eng. Sci.*, Vol. 16, 1974, pp. 286–297.

5 Taylor, G. I., "Stability of a Viscous Liquid Contained Between Two Rotating Cylinders," *Phil. Trans. Roy. Soc.*, Series *A*, Vol. 223, 1923, pp. 289–343.

6 Wannier, G., "A Contribution to the Hydrodynamics of Lubrication," *Quart. Appl. Math.*, Vol. 8, 1950, pp. 1–32.

7 Wood, W., "The Asymptotic Expansions at Large Reynolds Numbers for Steady Motion Between Non-Coaxial Rotating Cylinders," *J. Fluid Mech.*, Vol. 3, 1957, pp. 159–175.

8 Kamal, M. M., "Separation in the Flow Between Eccentric Rotating Cylinders," ASME *Journal of Basic Engineering*, Vol. 88, 1966, pp. 717–724.

9 Ashino, I., "Slow Motion Between Eccentric Rotating Cylinders," *Bulletin, Japan Soc. Mech. Eng.*, Vol. 18, 1975, pp. 280–285.

10 Kulinski, E., and Ostrach, S., "Journal Bearing Velocity Profiles for Small Eccentricity and Moderate Modified Reynolds Number," ASME Journal of Applied Mechanics, Vol. 34, 1967, pp. 16–22.

11 Yamada, Y., "On the Flow Between Eccentric Cylinders When the Outer Cylinder Rotates," *Japan Soc. Mech. Eng.*, Vol. 45, 1968, pp. 455–462.

12 DiPrima, R. C., and Stuart, J. T., "Flow Between Eccentric Rotating Cylinders," ASME *Journal of Lubrication Technology*, Vol. 94, 1972, pp. 266–274.

13 de Boor, C., *A Practical Guide to Splines*, Springer-Verlag, New York, 1978.

14 Hall, C. A., "On Error Bounds for Spline Interpolation," *J. Approx. Theory*, Vol. 1, 1968, pp. 209–218.

15 Brown, K. M., "A Quadratically Convergent Newton-Like Method Based Upon Gaussian Elimination," *SIAM J. Num. An.*, Vol. 6, 1969, pp. 560–569.

16 Szeri, A. Z., and Giron, A., "Stability of Flow Over an Infinite Rotating Disk," *Num. Meth. Fluids*, in press.

17 Orszag, S. A., "Accurate Solution of the Orr-Sommerfeld Stability Equation," *J. Fluid Mech.*, Vol. 50, 1971, pp. 689–703.

18 Szeri, A. Z., Schneider, S. J., Labbe, F., and Kaufman, H. N., "Flow Between Rotating Disks. Part 1. Basic Flow," *J. Fluid Mech.*, Vol. 134, 1983, pp. 103–131.

19 Szeri, A. Z., and Adams, M. L., "Laminar Throughflow Between Closely Spaced Rotating Disks," *J. Fluid Mech.*, Vol. 86, 1978, pp. 1–14.

20 Constantinescu, V. N., and Galetuse, S., "On the Possibilities of Improving the Accuracy of the Evaluation of Inertia Forces in Laminar and Turbulent Films," ASME *Journal of Lubrication Technology*, Vol. 96, 1974, pp. 69–79.

21 Obrien, K. T., Jones, C. D., and Mobbs, F. R., "Separation and Cavitation in Superlaminar Flow Between Eccentric Rotating Cylinders," *Leeds-Lyon Symposium on Tribology*, Sept. 1974, pp. 69–72.

Asymmetric Flow of a Cylindrical Particle Through a Narrow Channel

M. Sugihara

H. Niimi

National Cardiovascular Center
Research Institute,
Osâka, Japan

The steady flow of a cylindrical particle with a circular or elliptic cross section through a narrow channel is investigated on the basis of the Stokes equation with emphasis on effects of its asymmetric location and orientation. Numerical analyses are carried out by use of the finite element method to determine the drag, lift, and torque acting on the particle as well as the velocity of the particle floating freely in the Poiseuille flow. The numerical results are applied to blood flow in capillaries.

1 Introduction

Since capillary blood flow should be understood under the interaction of individual red blood cells (RBC's) with the vessel wall, a number of theoretical studies have been made on the motion of particles through microvessels. Most studies are based on approximation theories; one is the lubrication theory and another is the expansion method in terms of small parameters such as the ratio of particle size to its distance from the vessel wall. The lubrication theory becomes inaccurate except in the narrow gap between the particle and the wall [1]. The expansion method is also inapplicable to the motion of particle in microvessels where the particle size becomes comparable to the vessel diameter. Thus, some numerical analyses have been made on the capillary blood flow, using the finite element method [1, 2]. Most analyses are restricted to steady and axisymmetric flows of particles with axisymmetric shape through circular tubes.

Quite recently, it has become clear in both in vivo and in vitro experiments that RBC's in capillary vessels are in asymmetric motion rather than in axisymmetric motion [3–5]. The flow patterns of RBC's are greatly influenced by their number density (hematocrit) in vessels; in narrow capillary vessels, RBC's travel in single file near the centerline at low hematocrit, while RBC's are drifted toward the wall floating in multifile at higher hematocrit [5, 6]. Thus, it is very important in microvascular flow dynamics to elucidate the asymmetric flow of a particle with asymmetric shape at a position in microvessels. There are few theoretical studies with respect to asymmetric flow of a particle except two cases: the steady flow of a spherical particle placed slightly off the axis of vessel by the expansion method [7, 8] and a tightly fitting particle based on the lubrication theory [9].

In this paper, we numerically investigate the steady motion of a particle in a narrow two-dimensional channel with special emphasis on effects of its asymmetric location and orientation in relation to capillary blood flow. According to experimental studies of RBC rheology, RBC's can be easily deformed by the external force, and moreover, their thin membrane, containing an internal viscous fluid, may be in a tank-treading motion in shear flow [10, 11]. These natures of RBC's may be of mechanical significance for their motion through a very narrow channel, but here we adopt the basic model of RBC: (*i*) RBC is rigid, and (*ii*) it is prescribed to be a circular or elliptic cylindrical particle. This is mainly for the reason that the RBC shape may be kept almost constant in steady and unidirectional flows considered here, and that the governing equation for the membrane motion is not yet well understood.

Concerning the equation of motion, we assume that the surrounding fluid is incompressible Newtonian. Then, the fluid motion is assumed to obey the Stokes equation since the Reynolds number characteristic of RBC motion is much less than unity. In the analyses, we use the finite element method in terms of the primitive variables, namely velocities and pressure [12].

2 Formulation of the Problem

Referring to the rectangular coordinates (x, y), the Stokes equations for the two-dimensional steady motion of an incompressible viscous fluid are

$$\frac{\partial p}{\partial x} = \mu \nabla^2 u, \quad \frac{\partial p}{\partial y} = \mu \nabla^2 v, \tag{1}$$

where $\nabla^2 = \partial^2/\partial x^2 + \partial^2/\partial y^2$, μ is the viscous coefficient, p is the pressure and $\mathbf{u} = (u, v)$ is the velocity vector. The equation of continuity is

$$\frac{\partial u}{\partial x} + \frac{\partial v}{\partial y} = 0. \tag{2}$$

The coordinate system may be so chosen that the walls of channel are at $y = \pm d$, and the center of a cross section of the particle is at the position $(0, \delta d)$ (Fig. 1). The boundary conditions to be satisfied are

$$\mathbf{u} = \mathbf{0} \qquad \text{at} \quad y = \pm d, \tag{3}$$

Contributed by the Applied Mechanics Division for publication in the JOURNAL OF APPLIED MECHANICS.

Discussion on this paper should be addressed to the Editorial Department, ASME United Engineering Center, 345 East 47th Street, New York, N.Y. 10017, and will be accepted until two months after final publication of the paper itself in the JOURNAL OF APPLIED MECHANICS. Manuscript received by ASME Applied Mechanics Division, January, 1983; final revision, December, 1983.

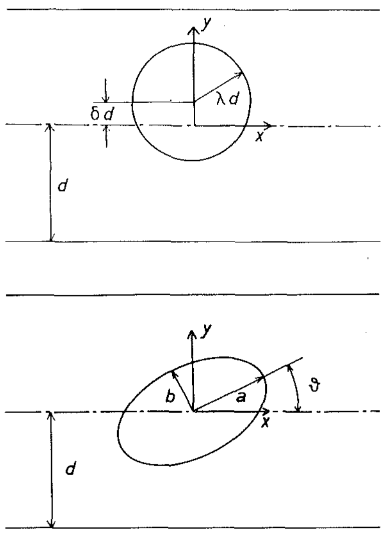

Fig. 1 Flow configurations

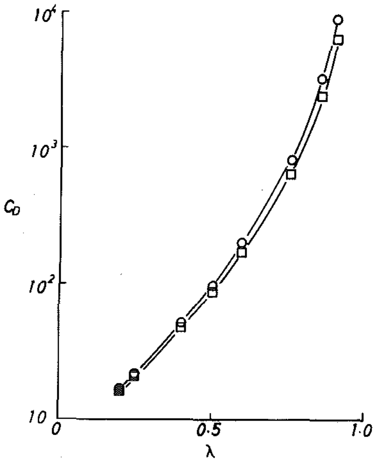

Fig. 2 Drag coefficient of a circular cylindrical particle at the centerline of the channel (○: case (*i*) in negative sense and □: case (*ii*) in positive sense) and Wakiya's result for $\lambda = 0.2$ (•: case (*i*) $C_D = -16.5$, and x: case (*ii*) $C_D = 16.1$)

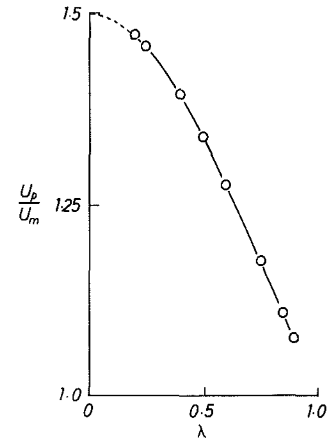

Fig. 3 Translating velocity ratio of a circular cylindrical particle floating freely at the centerline of the channel

$$\mathbf{u} = \mathbf{U}_c \qquad \text{on the surface of the particle,} \tag{4}$$

and

$$\mathbf{u} = \mathbf{U}_s \qquad \text{far from the particle,} \tag{5}$$

where $\mathbf{U}_c$ and $\mathbf{U}_s$ are to be prescribed. In numerical calculations, we apply the condition (5) at $x = \pm 1$, where 1 is taken sufficiently greater than the half width of the channel.

The equivalent variational functional for the preceding equations may be obtained as

$$J(\mathbf{u},p) = \iint_\Omega \left\{ \mu \left\{ \left(\frac{\partial u}{\partial x}\right)^2 + \left(\frac{\partial v}{\partial y}\right)^2 + \frac{1}{2}\left(\frac{\partial u}{\partial y} + \frac{\partial v}{\partial x}\right)^2 \right\} - p\left(\frac{\partial u}{\partial x} + \frac{\partial v}{\partial y}\right) \right\} ds \tag{6}$$

where Ω is the domain surrounded by the two walls, the particle and the planes at $x = \pm 1$. The property that J is stationary with respect to $(\mathbf{u}, p)$ under the subsidiary conditions (3)–(5) on the boundary of Ω provides equations (1) and (2) as the Euler equations [12].

In the present analysis, we use the finite element method. The application of variational principles to equation (6) yields simultaneous algebraic equations for the values of velocity components and pressure at the nodes. Using the values obtained, we can calculate the quantities of interest such as shear stresses and then the resultant force $\mathbf{F} = (F_x, F_y)$ acting on the particle per unit length together with the torque T about its center (for the finite element approximation, see the Appendix).

3 Results

The particle is assumed to have a circular cross section with radius λd or an elliptic cross section with semiaxes a and b $(a > b)$. For $\mathbf{U}_c$ and $\mathbf{U}_s$ in equations (4) and (5), the drag coefficient of the particle C_D, the lift coefficient C_L, and the torque coefficient C_T are defined as

$$C_D = F_x/\mu U, \qquad C_L = F_y/\mu U, \qquad C_T = T/\mu U d, \tag{7}$$

where U represents the magnitude of $\mathbf{U}_c$ or the maximum value of $\mathbf{U}_s$.

In numerical calculation, we take $1/d = 2.5$ considering the inlet length of low Reynolds number flow into a channel [13].

3.1 Circular Cylindrical Particle.

(*a*) *Lying at the Centerline of the Channel.* The two problems are considered: (*i*) the particle moving with a constant velocity U_p in an otherwise quiescent fluid, i.e., $\mathbf{U}_c = (U_p, 0)$ and $\mathbf{U}_s = (0, 0)$; and (*ii*) the stationary particle in the Poiseuille flow with the mean velocity U_m i.e., $\mathbf{U}_c = (0, 0)$ and $\mathbf{U}_s = (3/2 \bullet U_m (1 - y^2/d^2), 0)$. The drag coefficient C_D calculated in the two cases are shown in Fig. 2. The value in case (*i*) is plotted in the negative sense, while in case (*ii*) it is plotted in the positive sense. For comparison are also shown the theoretical points obtained by Wakiya for the special case of $\lambda = 0.2$ [14]. Our numerical results agree well with his theoretical result.

The superimposition of the two cases can provide the solution for a particle floating freely in Poiseuille flow. Assuming that the resultant force vanishes, we can determine the particle velocity. The ratio of the particle velocity U_p to the mean velocity U_m of the surrounding fluid is plotted in Fig. 3. It is interesting to note that U_p is always larger than U_m but approaches U_m as λ tends to unity.

(*b*) *Lying off-center of the Channel.* Three cases are considered: (*i*), (*ii*), in (*a*) and (*iii*) the particle rotating with the velocity U_r about the axis of cylindrical particle in a fluid at rest. In Fig. 4 are shown the drag coefficient C_D and the torque coefficient C_T against the deviation coefficient δ for $\lambda = 0.5$. It is seen that the particle experiences maximum drag at $\delta = 0$ for (*i*) and (*ii*). If we superimpose the three cases to achieve both the net drag and torque equal to zero, we can determine the translating velocity and the angular velocity of

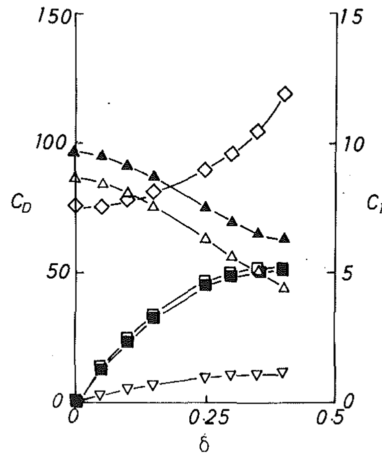

Fig. 4 Drag coefficient (▲: case (*i*) in negative sense, △: case (*ii*) in positive sense and ▽: case (*iii*) in negative sense) and torque coefficient (■: case (*i*) in negative sense, □: case (*ii*) in positive sense and ◇: case (*iii*) in negative sense) for a circular cylindrical particle

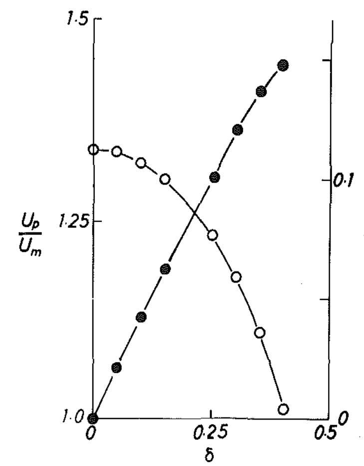

Fig. 5 Translating velocity ratio (○) and angular velocity ratio (●) of a circular cylindrical particle ($\lambda = 0.5$) floating freely

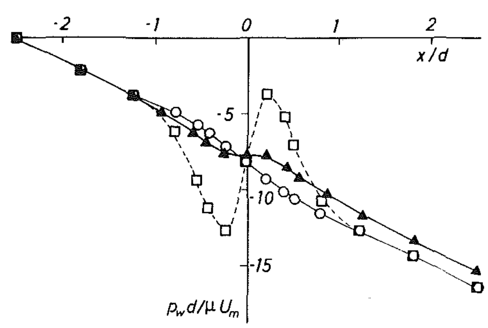

Fig. 6 Pressure distribution on walls for a circular cylindrical particle ($\lambda = 0.5$) floating freely (▲: pressure on either wall for $\delta = 0$, □: pressure on the wall nearer to the particle for $\delta = 0.25$ and ○: pressure on the other wall for $\delta = 0.25$). The pressure is taken to be zero at $x = -1$ ($1 = 2.5d$).

the particle floating freely. Figure 5 plots the ratios U_p/U_m and U_r/U_m. We note that increasing δ decreases the translating velocity but increases the angular velocity.

The pressure distribution on both walls, p_w, is shown in Fig. 6 for $\delta = 0$ and $\delta = 0.25$ in case of $\lambda = 0.5$. It is seen that the pressure changes markedly on the wall nearer to the particle. To see how the wall pressure changes with the particle position, let us define the additional loss of pressure head α due to the presence of the particle

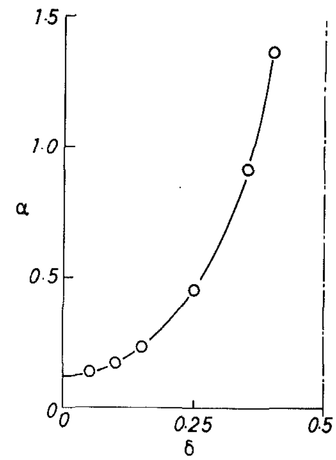

Fig. 7 Additional loss of pressure head due to the presence of a circular cylindrical particle ($\lambda = 0.5$) floating freely

$$\alpha = \frac{\Delta(p_w - p_0)}{dp_0/dx \cdot d}, \tag{8}$$

where p_0 is the pressure distribution on the wall without the particle, Δ means the difference between the up-stream (at $x = -1$), and down-stream values (at $x = +1$). Figure 7 is a plot of the additional loss of pressure head against δ for $\lambda = 0.5$. The figure indicates the rapid increase in the additional loss of pressure head as the particle position tends to the wall of channel.

3.2 Elliptic Cylindrical Particle. Let us confine ourselves to the case of a particle lying at the centerline of the channel. The angle of attack is taken as θ $(-\pi/2 < \theta < \pi/2)$ between the x-axis and the major axis of the cross section; its positive value means counterclockwise rotation about the center of the particle (see Fig. 1). As in Section 3.1, we derive the solution for the particle in motion (case (*i*)) and for the stationary particle in Poiseuille flow (case (*ii*)) and then superimpose the two solutions to determine the motion of the particle floating freely.

(*a*) *Aligned With the Flow Direction.* To determine the effects of the shape of particle, we change the length of axes keeping the cross-sectional area constant; $ab/d^2 = 0.25$. For convenience, we define the ratio of semiaxes length, η, of x-direction and y-direction. Figures 8 and 9 show the dependence of the drag coefficient C_D on η in cases (*i*) and (*ii*), and the ratio of the translating velocity U_p of the freely floating particle to the mean velocity U_m of the suspending fluid, respectively. As is evident from Fig. 9, the particle can move faster when its major axis is parallel to the flow direction and the ratio of major to minor axis increases.

(*b*) *Lying at Nonzero Angle of Attack.* The drag coefficient C_D and the lift coefficient C_L depend on the angle of attack θ. Figure 10 shows C_D and C_L versus θ $(0 \leq \theta \leq \pi/2)$ for the two cases (*i*) and (*ii*) when $a/d = 0.6$ and $b/d = 0.417$.

If the migration velocity of the particle toward the wall is negligibly small in comparison with the translating velocity, the motion may be considered to be quasi-steady. Then, the condition "freely floating" is obtained by superimposing the foregoing two cases (*i*) and (*ii*) and another case: (*iv*) the particle moving with a constant velocity U_q in the y-direction in the fluid at rest, i.e., $\mathbf{U}_c = (0, U_q)$ and $\mathbf{U}_s = (0, 0)$. Under this assumption, the motion of the particle floating freely is determined. Actually the migration velocity is under 1 percent of the translating velocity. In Fig. 11 is plotted the translating velocity of the particle. It is found that the particle with its major axis parallel to the flow direction travels fastest.

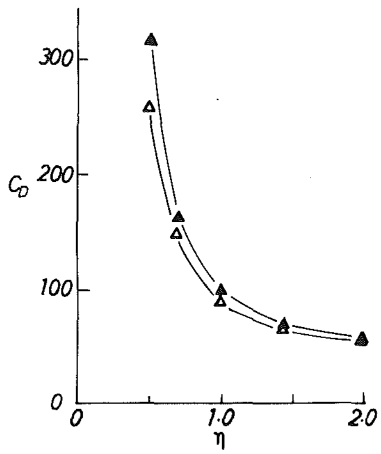

Fig. 8 Drag coefficient of an elliptic cylindrical particle (▲: case (*i*) in negative sense and △: case (*ii*) in positive sense)

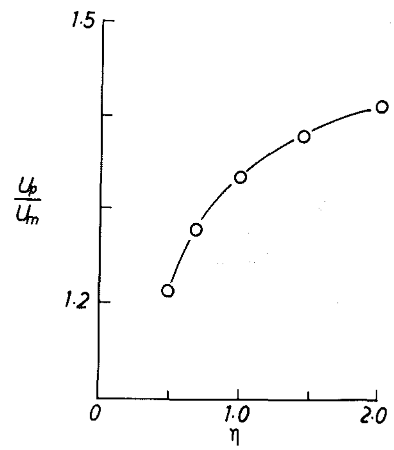

Fig. 9 Translating velocity ratio of an elliptic cylindrical particle

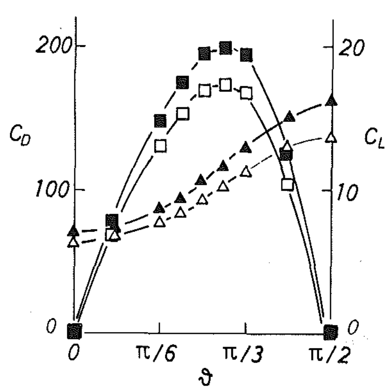

Fig. 10 Drag coefficient (▲: case (*i*) in negative sense and △: case (*ii*) in positive sense) and lift coefficient (■: case (*i*) in positive sense and □: case (*ii*) in negative sense) of an elliptic cylindrical particle

4 Discussion

The steady flow of a cylindrical particle in a channel has been calculated numerically using the finite element method. This method is very useful for treating complicated body shapes, though its application is almost confined to two-dimensional or axisymmetric finite domain problems. In our numerical formulation, the primitive variables have been used, because they are more physical and have lower-order equations than other variables such as the stream functions. Tong and Fung [2] used the stream function in studying a

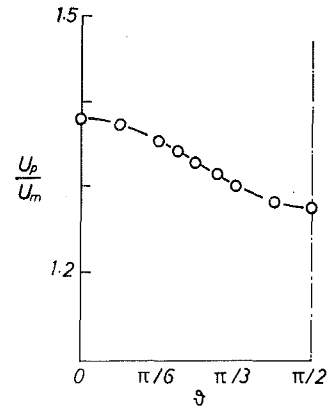

Fig. 11 Translating velocity ratio of an elliptic cylindrical particle floating freely

rectangular cylindrical particle in the Poiseuille flow. The present results in Fig. 3 have a tendency similar to their results.

The boundary condition (5) at the large distance from the particle has been applied at a finite distance $1 = 2.5d$. This is for the reason that a flow perturbation induced at a certain cross section of the channel reaches only a finite distance of the order of the channel half-width for low Reynolds number flow [13].

Our results obtained in the two-dimensional cases may contribute to a good understanding of capillary blood flow problems. First, let us apply our results to capillary hematocrit problem. It is known experimentally that when RBC's are made to flow through a small tube to a reservoir, their number density (H_t) in the tube is smaller than that (H_d) in the reservoir (Fahraeus effect). Especially, H_t/H_d depends strongly on the tube diameter; it decreases monotonically with decreasing tube diameter to about 10 μm and then increases with decreasing tube diameter to 2.7 μm (inverse-Fahraeus effect). Furthermore, H_t/H_d depends on the radial distribution of RBC in the capillary tube [6]. This effect may be closely related to the difference in traveling velocity between RBC's and suspending medium. If we consider the conservation law with respect to RBC's and medium, we have the ratio H_t/H_d as

$$H_t/H_d = 1/(H_d + (1-H_d)V_p/V_m), \qquad (9)$$

where V_p and V_m are the mean velocity of RBC's and the medium, respectively. The preceding equation indicates that the ratio H_t/H_d decreases with increasing velocity ratio V_p/V_m. Since our results are applicable to capillary blood flow at low hematocrit, it may be explained theoretically that the ratio H_t/H_d depends on the capillary diameter and the radial position of the RBC. In fact, Fig. 3 shows that H_t/H_d increases as the particle size parameter λ becomes larger, i.e., the channel width becomes smaller. This consequence corresponds to the inverse-Fahraeus effect. It is also predicted from Fig. 5 that H_t/H_d becomes larger as the particle flows nearer to the wall of channel.

Next, let us examine the capillary flow resistance. When RBC's flow through microvessels, the pressure may be changed by the shear flow in the lubrication layer between the RBC and the wall. Thus the relationship between pressure and flow must be understood under the interaction of RBC motion with the vessel wall. The pressure change due to the RBC motion can be demonstrated well by examining the wall pressure distribution. It is clear from Fig. 6 that the maximum change in pressure occurs just up and down-stream of the narrowest gap between the particle and the wall. Moreover, the pressure distribution depends strongly on the particle position; the change in wall pressure becomes larger as the particle approaches the wall. Figure 7 shows that the flow resistance increases as the distance between the particle and the wall decreases.

In the present analysis, we have considered the motion of an elliptic particle experiencing no torque at the centerline of the channel. If the particle is placed off-center, it will experience some torque as well as the drag and lift. Then, the elliptic particle floating freely will be either in a stationary motion with a definite angle of attack or in a flipping motion [15, 16]. The transition between the two modes of motion may be affected by the deformability of the particle besides its position and shape. The stationary motion and the flipping motion of a deformable body in tube or channel are left for further study.

Acknowledgments

The authors would like to express their hearty thanks to Professor T. Tatsumi for his continuous encouragement and to Dr. T. Yamakawa for his valuable discussion.

References

1 Skalak, R., Chen, P. H., and Chien, S., "Effect of Hematocrit and Rouleaux on Apparent Viscosity in Capillaries," *Biorheology*, Vol. 9, 1972, pp. 67-82.

2 Tong, P., and Fung, Y. C., "Slow Particulate Viscous Flow in Channels and Tubes—Application to Biomechanics," ASME JOURNAL OF APPLIED MECHANICS, Vol. 38, 1971, pp. 721-728.

3 Skalak, R., and Branemark, P.-I., "Deformation of Red Blood Cells in Capillaries," *Science*, Vol. 164, 1969, pp. 717-719.

4 Bagge, U., Branemark, P.-I., Karlsson, R., and Skalak, R., "Three-Dimensional Observation of Red Blood Cell Deformation in Capillaries," *Blood Cells*, Vol. 6, 1980, pp. 231-237.

5 Gaehtgens, P., "In Vitro Studies of Blood Rheology in Microscopic Tubes," in *The Rheology of Blood, Blood Vessels and Associated Tissues*, Gross, D. R., and Hwang, N. H. C., eds., Sijthoff and Noordhoff, 1981, pp. 257-275.

6 Albrecht, K. H., Gaehtgens, P., Pries, A., and Heuser, M., "The Fahraeus Effect in Narrow Capillaries (i.d. 3.3 to 11.0 μm)," *Microvasc. Res.*, Vol. 18, 1979, pp. 33-47.

7 Bungay, P. M., and Brenner, H., "The Motion of a Closely-Fitting Sphere in a Fluid-Filled Tube," *Int. J. Multiphase Flow*, Vol. 1, 1973, pp. 25-56.

8 Tözeren, H., "Torque on Eccentric Spheres Flowing in Tubes," ASME JOURNAL OF APPLIED MECHANICS, Vol. 49, 1982, pp. 279-283.

9 Secomb, T. W., and Skalak, R., "A Two-Dimensional Model for Capillary Flow of an Asymmetric Cell," *Microvasc. Res.*, 1982, Vol. 24, pp. 194-203.

10 Schmid-Schönbein, H., and Wells, R., "Fluid Drop-Like Transition of Erythrocytes Under Shear," *Science*, Vol. 165, 1969, pp. 288-291.

11 Schmid-Schönbein, H., and Gaehtgens, P., "What is Red Cell Deformability?," *Scand. J. Clin. Lab. Invest.*, Vol. 41, (Suppl. 156), 1981, pp. 13-26.

12 Olson, M. D., and Tuann, S. Y., "Primitive Variables versus Stream Function Finite Element Solutions of the Navier-Stokes Equations," *Finite Elements in Fluids*, Vol. 3, Gallagher, R. H., Zienkiewicz, O. C., et al. eds., Wiley, New York, 1978, pp. 73-87.

13 Lew, H. S., "My Approach to the Problem of Entry Flows," The University of Arizona Medical Center, Tucson, Ariz., 1972.

14 Wakiya, S., "Effect of a Submerged Object on a Slow Viscous Flow (Report VI) Elliptic Cylinder (Two Dimensional Case)," Research Reports of the Faculty of Engineering, Niigata University, 1959, pp. 31-41.

15 Kholeif, I. A., and Weymann, H. D., "Motion of a Single Red Blood Cell in Plane Shear Flow," *Biorheology*, Vol. 11, 1974, pp. 337-348.

16 Keller, S. R., and Skalak, R., "Motion of a Tank-Treading Ellipsoidal Particle in a Shear Flow," *J. Fluid Mech.* Vol. 120, 1982, pp. 27-47.

17 Chung, T. J., *Finite Element Analysis in Fluid Dynamics*, McGraw-Hill, New York, 1978.

18 Bercovier, M., and Pironneau, O., "Error Estimates for Finite Element Method Solution of the Stokes Problem in the Primitive Variables," *Numer. Math.*, Vol. 33, 1979, pp. 211-224.

APPENDIX

Finite Element Approximation

Let us mention briefly the finite element method used in the present analysis. The domain considered, Ω, is devided into 352 triangular elements with 780 nodes; each element has six nodal points (three corner nodes and three side nodes). A typical finite element grid used is shown in Fig. *A*. The shape of the particle is approximated by a polygon inscribed in its cross section.

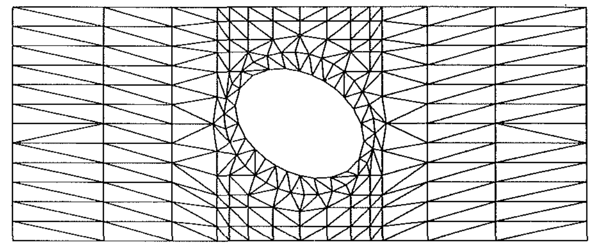

Fig. *A*. A typical finite element grid used for an elliptic cylindrical particle.

The velocity components are unknowns at the corner and the side nodes with quadratic interpolation functions ϕ_N $(N=1-6)$ in the local coordinates. The pressure is an unknown only at the corner nodes with linear interpolation functions ψ_N $(N=1-3)$. Then, the velocities and pressure within an element are represented by

$$u=\sum_{N=1}^{6}\phi_N u_N,\quad v=\sum_{N=1}^{6}\phi_N v_N,\quad p=\sum_{N=1}^{3}\psi_N p_N. \qquad (A\text{-}1)$$

where u_N, v_N, and p_N denote the nodal values of velocity components u, v, and pressure p, respectively.

Combining the nodal values and applying the variational principle to equation (6), we have a matrix equation:

$$[A]\{X\}=\{0\}. \qquad (A\text{-}2)$$

where the ith element of $\{X\}$ is the value of global node i in the form:

$$X_i=\begin{Bmatrix} u_i \\ v_i \\ p_i \end{Bmatrix}. \qquad (A\text{-}3)$$

The matrix A is the sum of all local element contributions; its submatrix a_{ij} may be written as follows:

$$a_{ij}=\Sigma\begin{bmatrix} a_1 & a_2 & a_3 \\ a_4 & a_5 & a_6 \\ a_7 & a_8 & 0 \end{bmatrix} \qquad (A\text{-}4)$$

and

$$a_1=\iint_S \mu\left\{2\frac{\partial\phi_N}{\partial x}\frac{\partial\phi_M}{\partial x}+\frac{\partial\phi_N}{\partial y}\frac{\partial\phi_M}{\partial y}\right\}dS,$$

$$a_2=\iint_S \mu\frac{\partial\phi_N}{\partial y}\frac{\partial\phi_M}{\partial x}dS,$$

$$a_3=-\iint_S \frac{\partial\phi_N}{\partial x}\psi_M dS,$$

$$a_4=\iint_S \mu\frac{\partial\phi_N}{\partial x}\frac{\partial\phi_M}{\partial y}dS,$$

$$a_5=\iint_S \mu\left\{\frac{\partial\phi_N}{\partial x}\frac{\partial\phi_M}{\partial x}+2\frac{\partial\phi_N}{\partial y}\frac{\partial\phi_M}{\partial y}\right\}dS,$$

$$a_6=-\iint_S \frac{\partial\phi_N}{\partial y}\psi_M dS,$$

$$a_7=-\iint_S \psi_N\frac{\partial\phi_M}{\partial x}dS,$$

$$a_8=-\iint_S \psi_N\frac{\partial\phi_M}{\partial y}dS,$$

where N and M represent the number of the local nodes in coincidence with the global node i and j, respectively, the summation is taken over the elements meeting at the global node i, and S is the area of the element. Equation (A-2) can be solved by Gaussian elimination method under boundary conditions (3)-(5).

The stress tensor may be expressed in terms of the nodal values of velocities and pressure:

$$\tau_{xx} = -p + 2\mu \frac{\partial u}{\partial x} = -\sum_{N=1}^{3} \psi_N p_N + 2\mu \sum_{N=1}^{6} \frac{\partial \phi_N}{\partial x} u_N,$$

$$\tau_{xy} = \tau_{yx} = \mu\left(\frac{\partial u}{\partial y} + \frac{\partial v}{\partial x}\right) = \mu \sum_{N=1}^{6} \left(\frac{\partial \phi_N}{\partial y} u_N + \frac{\partial \phi_N}{\partial x} v_N\right),$$

$$\tau_{yy} = -p + 2\mu \frac{\partial v}{\partial y} = -\sum_{N=1}^{3} \psi_N p_N + 2\mu \sum_{N=1}^{6} \frac{\partial \phi_N}{\partial y} v_N. \qquad (A\text{-}5)$$

If (n_x, n_y) is the unit vector outward normal to the surface of the particle and (x_0, y_0) is the center of the particle, the drag force $\mathbf{F}$ acting on the particle and torque T about its center are calculated by:

$$F_x = \int \tau_{nx} dl, \quad F_y = \int \tau_{ny} dl,$$
$$T = \int \{ (x - x_0)\tau_{ny} - (y - y_0)\tau_{nx} \} dl, \qquad (A\text{-}6)$$

and

$$\tau_{nx} = \tau_{xx} n_x + \tau_{xy} n_y, \tau_{ny} = \tau_{yx} n_x + \tau_{yy} n_y.$$

In the foregoing, integration is carried out along the circumference of the particle; a three-point Gauss rule is used in the numerical calculation.

Let us refer to the error estimate of our finite element approximation. The accuracy of the finite element solution is affected by the number of elements and nodes, and the shape of elements. According to the theory of error estimates, the error in L_2 norm of the first derivatives of $\mathbf{u}$ and p becomes $O(h^2)$, where h is the maximum dimension of the triangular elements [17, 18]. For the grid used in the present analysis, the dimension h is small near the particle but large away from it. It can be shown that in the region away from the particle, the flow field becomes almost quadratic and the pressure becomes almost linear. Consequently, the error will be small enough in the whole region considered.

Concerning the effect of the shape of element, any angle of the triangular elements is required not to be large for a good approximation. As seen in Fig. A, our grid includes several elements of obtuse-angled triangle in some cases. This factor will influence the accuracy of finite element solution.

Other factors of error lie in numerical integration of (A-6) and in the approximation of the particle shape. In fact, since integrands in (A-6) are not polynomials, integration can not be performed exactly. Moreover, we have approximated the particle shape by the polygon; this produces error in velocity components and pressure, especially near the particle, which affects the values of the drag, lift and torque acting on the particle.

Since the numerical errors are produced by various factors, it is difficult to estimate them exactly. The simple method of estimation is to compare a numerical result with the theoretical result. In the present analysis, the difference between our numerical result and the theoretical result is within 1 percent for the drag force experienced by a circular cylindrical particle ($\lambda = 0.2$, $\delta = 0$) (see Section 3.1). This suggests that our finite element approach may provide a satisfactory approximation for our study.

On the Role of a Compliant Surface in Long Squeeze Film Bearings

R. H. Buckholz
Department of Mechanical Engineering,
Columbia University,
New York, N.Y. 10027

The problem of compliant surface journal bearings with large slenderness ratio (length/diameter $\rightarrow \infty$) is analyzed for the case of small journal eccentricities. In this model an elastic circular cylinder has an axial length that is large compared to its diameter. The elastic cylinder is rubber, the inner rubber surface is wetted with a Newtonian lubricant, and the outer rubber surface is bound to a rigid surface. Immersed within the lubricant is a rigid circular journal. The journal is held fixed, and a translatory motion is assigned to the rigidly backed elastomer bearing. The resulting squeeze film is analyzed for near concentricity between the undeformed rubber surface and the rigid journal. The development of the model proceeds from the basic Navier displacement equations for a solid and the Stokes equations for the fluid. The special case of Poisson's ratio going to 1/2 is used for the solid. The field equations are linear; a nonlinearity is a consequence of the boundary conditions. Discrete distributions of singularities are used to represent the coupled fluid and elastic deformation. Surface stress traction vectors are matched at the liquid-solid interface. Explicit expressions for changes of the fluid film gap due to rubber deformation, together with the associated change in fluid film pressure, are presented.

I Introduction

Virtually all pieces of rotating machines utilize either a rolling element, or fluid film journal bearings to stabilize and confine the motion of rotating rigid shafts (journals). In the present technology, these journal bearings consist of a rigid shaft rotating within a rigid housing, separated by a film of lubricant, typically an oil or a grease. The reliability of these bearings is normally very high. However, all such bearings suffer from wear of the components with use, and the wear problems are greatly accelerated by the presence of fine solid particles in the lubricant, excessive heat caused by low lubricant levels, and stresses normal to the bearing axis caused by eccentric or translational external loads on the shaft. Excessive sliding contact that occurs between the bearing and journal surfaces, "wiping," caused by severe dynamic loading or misalignment, is a further threat to bearing reliability. Recent studies have shown that when the rotating member within the bearing is coated with an elastomeric material, such as a rubber or plastic, the sensitivity of the bearing to each of the aforementioned conditions is much reduced. This type of bearing, called a compliant surface bearing, is currently at the leading edge of lubrication science, and further study of their behavior is required to establish design criteria before full advantage can be taken of their potential. Because of the elastic nature of the bearing material, the performance of these bearings is substantially different from that of the now well-understood rigid wall bearing with incompressible lubricants. Compliant surface bearings have been treated theoretically by several authors, but these analyses were limited to numerical studies of rotating journals.

The first study to assess the effect of compliant surface bearings was Fogg's [6]; he investigated water lubricated rubber bearings. In a later study, Benjamin [1, 2] analyzed compliant surface (i.e., rubber) journal bearings; he included both the fluid dynamics and coupled linearly elastic field equations. Reynolds' equation was used to calculate fluid film pressures and the Navier equation was used to calculate elastomer deformation. Owing to the complexity of the full equations, a computational approach was taken to solve the coupled field equations. Benjamin discussed his solutions and the particular computational difficulties associated with the numerical approach where the Poisson ratio goes to one-half. Hori [7] studied rubber-surface squeeze film bearings; a finite length rubber pad was oscillated perpendicular to a rigid surface. A variational principle scheme was used in his calculations to avoid difficulties associated with the Poisson's ratio near one-half in the numerical calculation of rubber deformations. At high frequencies he found that viscoelastic effects in the rubber cannot be ignored. Several related ex-

Contributed by the Applied Mechanics Division and presented at the Winter Annual Meeting, New Orleans, La., December 9-14, 1984 of THE AMERICAN SOCIETY OF MECHANICAL ENGINEERS.

Discussion on this paper should be addressed to the Editorial Department, ASME, United Engineering Center, 345 East 47th Street, New York, N.Y. 10017, and will be accepted until two months after final publication of the paper itself in the JOURNAL OF APPLIED MECHANICS. Manuscript received by ASME Applied Mechanics Division, September, 1983; final revision, February, 1984. Paper No. 84-WA/APM-30.

Copies will be available until August, 1985.

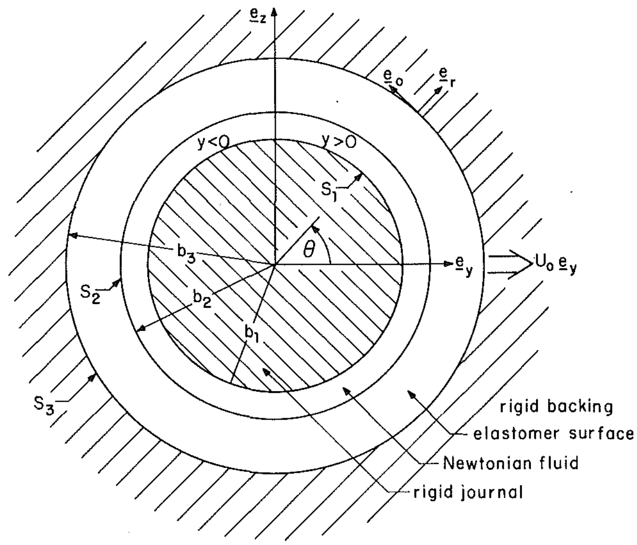

Fig. 1 Sketch to show notation, length scales are not mutually consistent; S_1 is the journal surface, S_2 is the liquid-rubber interface, and S_3 is the rigid-elastomer interface. Here the bearing is assigned a *uniform translational velocity in the* e_y *direction.*

perimental studies by Rightmire [11, 12] illustrate the usefulness of rubber-coated tilting and swing-pad bearings.

It is known from many experimental results that synthetic rubbers are nearly incompressible materials. In linear elasticity theory the Poisson's ratio, ν, is a measure of the compressibility for these elastomer materials. In attempting to carefully measure the compressibility of elastomers, Rightmire [10] devised an apparatus to determine Poisson's ratio. His study was confined to those rubber elastomer materials commonly used in bearings; and his results clearly demonstrated the nearly incompressible nature of various rubber compounds. For this reason I consider here an asymptotic theory for Poisson's ratio going to one-half, the incompressible limit. As might be expected the Navier elasticity equations have been investigated in this limit, Sokonikoff [13]. This incompressibility approximation has a rather distinctive feature; the Navier elasticity equations exhibit the same functional form as the low Reynolds number hydrodynamics equations, Stokes flow.

Here a primary motivation is the effect of compliant surfaces on squeeze films in lubrication. Viscous forces are dominant when compared to inertia forces. Mathematical models based on lubrication theory follow from a geometrical shape approximation to the Stokes flow hydrodynamical equations. For lubrication, the fluid motion in a thin gap of slowly changing thickness is synthesized from a linear combination of Couette and Poiseuille flows. The pressure gradient is then adjusted to satisfy conservation of mass; the resulting equation for the fluid film pressure is Reynolds' equation. Models based on Reynolds' equation provide the basis to our understanding of fluid film lubrication. The Reynolds' equation is the more familiar method for calculating lubrication film properties; because of the interest in this fluids-solids problem, a Stokes' equation approach has been taken to simplify the coupled fluids solids problem.

Current interest in low Reynolds number flows has led to a development of singularity superposition solution methods, Chwang [4]. A distinctive feature of these solution methods is the placement of singular solutions to Stokes' equation, and the adjustment of singularity strengths to satisfy boundary conditions. It is usually the case that singularity distributions are needed to satisfy the prescribed boundary conditions; such models usually result in integral equations for the strength of continuously distributed singular solutions. However, some exact solutions for simple geometries occasionally result from the distribution of a few discrete singularities. The latter approach is the one used here. The theory to be given is a mathematically simple one.

How can relatively deformable bearing surfaces change fluid film bearing performance? In attempting to answer this question several investigators have studied the coupled fluids-solid problem. While several theoretical models for various geometries have been proposed, little experimental data is available.

II Analysis

The development of this model proceeds in a manner aimed at understanding the effect of deformed bearing surfaces on fluid film pressure distribution as a function of prescribed dimensionless parameters. Here the asymptotic behavior for geometries of small eccentricities and for incompressible elastomers are studied. The geometry, governing equations, and boundary conditions are explicitly given in *II*-1. In *II*-2 the equations are solved subject to the given boundary conditions. In *II*-3 the amplitude functions for elastomer deformation are given. Limitations of these theoretically predicted elastomer deformation and fluid pressure field are discussed.

***II*.1. Governing Equations.** A Newtonian viscous fluid is contained in an annular gap that is bounded on the outside by a rubber layer of arbitrary uniform thickness, and this elastic rubber layer is bound to an inelastic solid at radius b_3. The notation and geometry used is shown in Fig. 1. The fluid motion and rubber deformation are given by an assigned translational velocity on the outer cylinder, $\mathbf{U} = U_0\,(t)\,\mathbf{e}_y$. The associated translational displacement for this rubber bearing is $\mathbf{D} = (\int_0^t U_0(t')dt')\mathbf{e}_y$. Accordingly, a fluid film pressure distribution is developed in the gap between the two surfaces S_1 and S_2. The mathematical situation we wish to investigate is the fluid flow between S_1 and S_2, the associated fluid film pressure, and the fluid-stress, traction-induced rubber deformation. Since the geometry is well suited to polar coordinates and the boundary condition is well suited to Cartesian, each will be used here as a matter of convenience. Fundamental equations describing the fluid velocity, $\mathbf{U}$, fluid pressure, $\tilde{P}$, rubber displacement, $\mathbf{W}^*$, and rubber pressure, P, are given.

(*a*) *Elastomer Field Equations.* The Navier equations for linear elasticity theory are applied to describe the rubber deformation, but the asymptotic form of the Navier equations for Poisson's ratio going to one-half are directly used. The strain tensor is defined as

$$e_{ij} = (W^*_{i,j} + W^*_{j,i})/2 \qquad (2.1)$$

and the associated stress tensor for Poisson's ratio equal to one-half is

$$\tau_{ij} = -P\delta_{ij} + 2\mu e_{ij} \qquad (2.2)$$

where μ is a material property related to the linear modulus of elasticity, E,

$$\mu = \tfrac{1}{3}E$$

The constraining effect of rubber incompressibility accounts for the pressure type term in the stress tensor, equation (2.2); this is an important difference caused by taking Poisson's ratio equal to one-half. Conservation equations for mass and linear momentum are

$$W^*_{i,i} = 0 \qquad (2.3)$$

and

$$0 = -P_{,i} + \mu W^*_{i,jj} \qquad (2.4)$$

(*b*) *Equations for Creeping Motion.* The Navier-Stokes equations are the governing equations for the fluid motion. They are simplified by virtue of the inertialess restriction; and the creeping flow equations, Stokes flow, for a Newtonian viscous fluid are directly used here. The rate-of-strain relationship is

$$\tilde{e}_{ij} = (U_{i,j} + U_{j,i})/2 \tag{2.5}$$

and the stress tensor is

$$\tilde{\tau}_{ij} = -\tilde{P}\delta_{ij} + 2\tilde{\mu}e_{ij} \tag{2.6}$$

Conservation of mass and conservation of linear momentum equations for the fluid are

$$U_{i,i} = 0 \tag{2.7}$$

and

$$0 = \tilde{P}_{,i} + U_{i,jj}\tilde{\mu} \tag{2.8}$$

Observe that equations describing the elastic deformation and the fluid motions are functionally the same; only the interpretation of the constants and dependent variables are different. In lubrication theory the analytical characterization for the pressure in the fluid film is usually given by Reynolds' equation. As mentioned, this coupled fluids-solid problem is mathematically simpler if the lubrication approximation is not used; Stokes equation is used directly to model the fluid motion.

(*c*) *Associated Boundary Conditions.* These fluid and solid field equations are subject to boundary conditions. For the fluid the no slip boundary condition is given as,

$$\mathbf{U} = U_y\mathbf{e}_y + U_z\mathbf{e}_z = 0 \quad \text{on} \quad S_1'$$
$$\mathbf{U} = \mathbf{U}_y\mathbf{e}_y + U_z\mathbf{e}_z = U_0\mathbf{e}_y \quad \text{on} \quad S_2'$$

where the location of the surface S_2 is unknown. It is necessary to match the fluid and solid surface tractions on the interface S_2. The surface stress traction vector $\tilde{t}_i$ on S_2 is defined as

$$\tilde{t}_i = \tilde{\tau}_{ij}n_j$$

where η_j is a unit normal to S_2.

The boundary conditions for the rubber layer bounded by S_2 and S_3 require zero deformation, **W**, on S_3, and the surface stress traction vectors for the fluid and solid must match at the interface S_2. Thus

$$\mathbf{W} = \mathbf{W}^* - \left(\int_0^t U_0(t')dt\right)\mathbf{e}_y = 0 \quad \text{on} \quad S_3'$$

where **W** is the rubber deformation, and **W*** is the displacement. The surface stress traction vector for the solid is defined as

$$t_i = \tau_{ij}n_j$$

where n_j is the unit normal to S_2. Matching surface stress traction vectors on S_2 requires that

$$t_i = \tilde{t}_i \quad \text{on} \quad S_2'$$

***II*.2 Solution Method.** Both the basic fluid and solid field equations to be solved are Stokes flow-type equations. While I am not concerned in this work with the development of the basic singularity solutions, these equations of motion are here solved by a singularity superposition method. An analysis of a similar kind was given by Chwang and Wu [4]; they formulated an integral equation approach for Stokeslet and doublet distributions to describe flows about bodies having a high degree of symmetry. Here, both the fluid flow and rubber deformation are investigated by a discrete distribution of singularity solutions to Stokes equation. To the lowest order this leads to an approximate solution for this coupled boundary value problem. The fundamental solution of Stokes equation for velocity, pressure, and vorticity is given below

$$\mathbf{U}_s = \alpha ln r^{-1} + (\alpha \cdot \mathbf{x})\mathbf{x}/r^2$$
$$P_s = 2\tilde{\mu}(\alpha \cdot \mathbf{x})r^{-2} \tag{2.9}$$
$$\omega = 2(\alpha \Lambda \mathbf{x})r^{-2}$$
$$\mathbf{x} = y\mathbf{e}_y + z\mathbf{e}_z \tag{2.9}$$

where $r^2 = y^2 + z^2$. This fluid motion corresponds to a point force located at the origin; the magnitude and direction of this force is

$$\mathbf{F} = 4\pi\mu\alpha$$

Here, α is a constant vector; and this singular solution is a Stokeslet. Three other useful solutions to Stokes equation are: the doublet

$$\mathbf{U}_2 = C_2\left(-\frac{1}{r^2}\mathbf{e}_y + \frac{2y}{r^3}\mathbf{e}_r\right)$$
$$P_2 = 0 \tag{2.10}$$

the Stokeson

$$\mathbf{U}_3 = C_3(3r^2\mathbf{e}_y - 2yr\mathbf{e}_r)$$
$$P_3 = C_3 8\mu y \tag{2.11}$$

and the uniform flow

$$\mathbf{U}_4 = C_4\mathbf{e}_y$$
$$P_4 = 0 \tag{2.12}$$

One of the difficulties in enforcing the no-slip boundary conditions at the location of the free surface S_2, the liquid-rubber interface is that its location is not known a priori. Its location is part of the solution.

To establish the starting point for the analysis, I refer to the one-dimensional solution to Reynolds' equation for squeeze film flow between eccentric cylinders, Cameron [3], and to the exact solution to Stokes equation for concentric cylinder squeeze film flows, Chwang [4]. When the location of S_2 is specified to be a circle with radius b_2, and origin coinciding with the center of S_1, then a simple exact solution to Stokes flow is known. The mathematical formulation here uses this exact solution, but b_2 is treated as an unknown, slowly changing function of the azimuthal coordinate.

This assumption that b_2 is a slowly changing function of the azimuthal coordinate is made possible by considering here only the cases of near concentricity between the journal and the deformed rubber surface (i.e., a first-order approximation to the small eccentricity case). Limitations to the extension of exact concentric Stokes flow solutions to describe the fluid dynamics of nonconcentric geometries by allowing b_2 to slowly change has been studied. The fluid pressure field predicted by Reynolds' lubrication equation is the same as the exact Stokes flow concentric solution when it is extended to the case of small journal eccentricities with rigid bearing surfaces.

The following theoretical analysis describes the case of near concentricity between the journal and the undeformed rubber surface. The approximate solution for the fluid motion follows from a standard approximating procedure for expressing the gap between surfaces S_2 and S_1 in an asymptotic power series using a "small constant parameter."

This parameter, τ, a deformation amplitude scaling, is introduced. The rubber deformation is assumed small relative to the undeformed gap thickness. A regular perturbation expansion for the deformed gap thickness is

$$\tilde{b}_2(\theta) - b_1 = b_2 - b_1 + \tau W_r(\theta) \tag{2.13a}$$

or

$$\tilde{b}_2(\theta) = b_2 + \tau W_r(\theta) \tag{2.13b}$$

where

$$|\tau W_r(\theta)| << (b_2 - b_1) \tag{2.13c}$$

The preceding expansion for $\tilde{b}_2$ is substituted into the exact solution for squeeze film lubricant flow in the annulus between two concentric circular cylinders. It should be emphasized that this approximation is correct provided the inequality, equation (2.13c), is valid. The fluid velocity field is now given by a superposition of a uniform flow, a Stokeson, a Stokeslet, and a doublet,

$$\mathbf{U}=\tilde{C}_4\mathbf{e}_y-\tilde{C}_1(ln^{b_1/r}\,\mathbf{e}_{y+y}r^{-1}\mathbf{e}_r)$$
$$+\tilde{C}_2(-\mathbf{e}_y r^{-2}+2yr^{-3}\mathbf{e}_r)-\tilde{C}_3(3r^2\mathbf{e}_y-2yr\mathbf{e}_r) \quad (2.14)$$

and

$$\tilde{C}_1=U_0\sigma(1+\tilde{\lambda}^2)=\sigma U_0\bar{C}_1 \quad (2.14a)$$

$$\tilde{C}_2=\frac{1}{2}U_0\sigma(b_1^2)=b_1^2U_0\sigma\bar{C}_2 \quad (2.14b)$$

$$\tilde{C}_3=\frac{1}{2}U_0\sigma b_1^{-2}\tilde{\lambda}^2=b_1^{-2}\bar{C}_3\sigma U_0 \quad (2.14c)$$

$$\tilde{C}_4=\frac{1}{2}U_0\sigma(1+3\tilde{\lambda}^2)=U_0\sigma\bar{C}_4 \quad (2.14d)$$

where

$$\sigma^{-1}=(1+\tilde{\lambda}^2)ln\frac{1}{\tilde{\lambda}}-(1-\tilde{\lambda}^2)$$

$$\tilde{\lambda}=b_1/\tilde{b}_2(\theta),\quad \lambda=b_1/b_2$$

The surface S_2 is no longer a circle, since $b_2(\theta)$ changes with the azimuthal coordinate. It is a feature of this singularity superposition method that the force applied to the inner cylinder by the fluid is simply expressed as

$$F=4\pi\mu\tilde{C}_1\mathbf{e}_y \quad (2.15)$$

The procedure used here allows $\tilde{C}_1$ to slowly vary with θ; for this reason the force on the inner cylinder is here calculated directly from integration of the pressure distribution. Alternatively, a distribution of Stokeslets can be determined to satisfy the no-slip boundary condition; the total force that the body must apply to the fluid is then found by the sum of the Stokeslet distribution alone.

In the limit of incompressibility the Navier equations for rubber deformation are identical in appearance to the Stokes flow equations. The rubber elastomer deformation is found using a discrete singularity superposition method. The solution technique employed uses four singularities: a uniform deformation, a Stokeson, a Stokeslet, and a doublet. The deformation is

$$\mathbf{W}=C_4\mathbf{e}_y-C_1(ln\frac{b_2}{r}\mathbf{e}_y+yr^{-1}\mathbf{e}_r)$$
$$+C_2(-\mathbf{e}_y r^{-2}+2yr^{-3}\mathbf{e}_r)-C_3(3r^2\mathbf{e}_y-2yr\mathbf{e}_r) \quad (2.16)$$

and the associated pressure is

$$P=-2\mu C_1 yr^2-8\mu C_3 y$$

The four constants are determined from the stress traction balance on S_2, and from the zero displacement boundary conditions on S_3. Balance of stress tractions on S_2 require that

$$[-\tilde{P}\delta_{ij}+\tilde{\mu}(U_{i,j}+U_{j,i})]n_i$$
$$=[-P\delta_{ij}+\mu(W_{i,j}+W_{j,i})]n_i \quad (2.17)$$

where n_i is the normal vector to S_2. The normal and shear components of $\mathbf{t}$ are

$$-\tilde{P}+2\tilde{\mu}\tilde{e}_{rr}=-P+2\mu e_{rr}\quad \text{at}\quad r=b_2 \quad (2.18)$$

$$2\tilde{\mu}\tilde{e}_{r\theta}=2\mu e_{r\theta}\quad \text{at}\quad r=b_2 \quad (2.19)$$

where

$$e_{rr}=\partial W_r/\partial r,\quad \tilde{e}_{rr}=\partial U_r/\partial r$$

and

$$e_{r\theta}=\frac{r}{2}\frac{\partial}{\partial r}\left(\frac{W_\theta}{r}\right)+\frac{1}{2r}\frac{\partial W_r}{\partial\theta},\quad \tilde{e}_{r\theta}=\frac{r}{2}\frac{\partial}{\partial r}\left(\frac{U_\theta}{r}\right)+\frac{1}{2r}\frac{\partial U_r}{\partial\theta}$$

The following four expressions for the constants C_1, C_2, C_3, and C_4 have been obtained from (2.18), equation (2.19), and the zero deformation condition on S_3.

$$\tilde{\mu}(\tilde{C}_1r^{-1}+\tilde{C}_3r-\tilde{C}_2r^{-3})=\mu(C_1r^{-1}+C_3r-C_2r^{-3}),$$
$$r=b_2 \quad (2.20)$$

$$\tilde{\mu}(\tilde{C}_3r-\tilde{C}_2r^{-3})=\mu(C_3r-C_2r^{-3}),\quad r=b_2 \quad (2.21)$$

$$0=C_4-C_1\left(ln\frac{b_2}{r}+1\right)+C_2r^{-2}-C_3r^2,\quad r=b_3 \quad (2.22)$$

and

$$0=C_4-C_1ln\frac{b_2}{r}-C_2r^{-2}-C_3 3\,r^2,\quad r=b_3 \quad (2.23)$$

The preceding boundary conditions for the rubber are applied at the location of the undeformed interface; this is typical for linear elasticity theory. Solutions to the fluid flow problem require applying the no-slip boundary condition at the location of the deformed surface S_2. Fluid pressure and flow are particularly sensitive to changes in gap size when S_1 and S_2 are nearly equal.

Solutions for these algebraic equations for C_i are determined. The local surface stress tractions for the fluid and the solid are balanced. Total force on the rubber layer is shown to be the same as the total force on inner rigid cylinder; this follows directly from the local stress balance at the interface. Recalling equation (2.15) the force on the inner cylinder is

$$\tilde{\mathbf{F}}=4\pi\tilde{\mu}\tilde{C}_1\mathbf{e}_y$$

and the force on the elastomer is

$$\mathbf{F}=4\pi\mu C_1\mathbf{e}_y$$

And from equations (2.19) and (2.20)

$$C_1=\frac{\tilde{\mu}}{\mu}\tilde{C}_1 \quad (2.24)$$

thus

$$\tilde{\mathbf{F}}=\mathbf{F}$$

Utilizing equations (2.21) to (2.23), the slowly changing coefficients for rubber displacement in terms of the coefficients C_i, $i=1,4$ are found. These results are

$$C_2=b_2^2U_0\sigma(1+\delta^4)^{-1}\left\{\lambda^{-2}\bar{C}_3-\bar{C}_2\lambda^2+\frac{1}{2}\bar{C}_1\delta^2\right\}\frac{\tilde{\mu}}{\mu} \quad (2.25)$$

$$C_3=b_3^{-2}U_0\sigma\left\{\frac{1}{2}\bar{C}_1-\delta^2(1+\delta^4)^{-1}\left[\lambda^{-2}\bar{C}_3-\bar{C}_2\lambda^2+\frac{1}{2}\bar{C}_1\delta^2\right]\right\}\frac{\tilde{\mu}}{\mu} \quad (2.26)$$

and

$$C_4=U_0\sigma\left\{\bar{C}_1\left(ln\delta+\frac{1}{2}\right)+2\left(\frac{1}{2}\bar{C}_1-\delta^2(1+\delta^4)^{-1}\left[\lambda^{-2}\bar{C}_3-\bar{C}_2\lambda^2+\frac{1}{2}\bar{C}_1\delta^2\right)\right]\right\}\frac{\tilde{\mu}}{\mu} \quad (2.27)$$

Hence, the fluid film-induced deformation of the rubber is determined using equation (2.16); the rubber deformations are given in polar coordinates

$$\mathbf{W}=W_r\mathbf{e}_r+W_\theta\mathbf{e}_\theta$$

Deformations expressed in polar coordinates are convenient for determining the change in fluid film gap size; the radial component of displacement, W_r, is

$$W_r=(C_4-C_1+C_2b_2^{-2}-C_3b_2^{-2})\cos\theta \quad (2.28)$$

Equations (2.24)-(2.27) are now substituted into the foregoing equation for W_r; the radial deformation W_r is then normalized by the radius b_2. This normalized radial deformation is given in terms of the slowly changing functions C_i, $i=1, 4$;

$$\hat{W}_r = \left(\frac{\bar{\mu}}{\mu}\frac{U_0}{b_2}\right)\sigma\left[\bar{C}_1\left(\frac{1}{2}-\frac{\delta^2}{2}+ln\delta+\frac{\delta^2}{2}\gamma\right)\right.$$

$$\left. -\bar{C}_2\lambda^2\gamma+\bar{C}_3\gamma\lambda^{-2}\right]\cos\theta \qquad (2.29)$$

where

$$\gamma=\frac{(\delta^2-1)^2}{1+\delta^4}$$

and the $\bar{C}_i$'s are defined in equations (2.14a)-(2.14c).

It is necessary to substitute the expansion for $\tilde{b}_2$, equation (2.13), into the C_i's in equation (2.29). The result is an implicit algebraic equation for W_r. Calculation of W_r is simplified by the inequality (2.13); if this inequality is granted then it is advantageous to use an iterative method to approximate W_r. To find a first approximation to W_r the C_i's in equation (2.29) are evaluated at b_2, thus

$$\hat{W}_{r0} = \left(\frac{\bar{\mu}U_0}{\mu b_2}\sigma\right)\left[C_{10}\left(\frac{1}{2}-\frac{\delta^2}{2}ln\delta+\frac{\delta^2}{2}\gamma\right)-C_{20}\lambda^2\gamma\right.$$

$$\left.+C_{30}\gamma\lambda^{-2}\right]\cos\theta \qquad (2.30)$$

where C_{10}, C_{20}, and C_{30} are given in the following

$$C_{10}=\bar{C}_1, \quad \tilde{\lambda}=b_1/b_2+0(\tau)$$
$$C_{20}=\bar{C}_2, \quad \tilde{\lambda}=b_1/b_2+0(\tau)$$
$$C_{30}=\bar{C}_3, \quad \tilde{\lambda}=b_1/b_2+0(\tau)$$

Equation (2.30) corresponds to the first-order, flow-induced deformation; this is the deformation expected when no interaction between deformation of S_2 and the fluid stress traction vector occurred. The slowly changing radius for S_2 is approximated as a combination of deformation and translation, thus

$$\tilde{b}_2(\theta)=b_2\left(1+\hat{W}_{r0}+\frac{1}{b_2}\int_0^t U_0(t')dt'\cos\theta\right) \qquad (2.31a)$$

$$\tilde{b}_2(\theta)=b_2(1+\tau\bar{W}(\delta_1\lambda)\cos\theta$$

$$+\frac{1}{b_2}\int_0^t U_0(t')dt'\cos\theta) \qquad (2.31b)$$

where

$$\bar{W}(\delta,\lambda)=\left[C_{10}\left(\frac{1}{2}-\frac{\delta^2}{2}ln\delta+\frac{\delta^2}{2}\gamma\right)-C_{20}\lambda^2\gamma+C_{30}\gamma\lambda^{-2}\right]$$

The small amplitude parameter, τ, defined earlier, is $\bar{\mu}\sigma U_o/\mu b_2$. The change in fluid film gap thickness is given by equation (2.31b), and the coefficients in $\bar{W}(\delta,\lambda)$ are given by equations (2.14a)-(2.14d). This result shows that to a first approximation the rubber deformation alters the fluid film gap shape such that an apparent eccentricity is present. The corresponding change in the fluid film pressure distribution is determined by substituting equation (2.31), the location of the deformed surface S_2, into the fluid pressure distribution

$$\tilde{P}=-2\bar{\mu}\tilde{C}_1yr^{-2}-8\bar{\mu}\tilde{C}_3y \qquad (2.32)$$

In light of the preceding result the journal load is calculated by integrating the pressure distribution on the journal surface. After substituting $\tilde{C}_1$ and $\tilde{C}_3$ into equation (2.32) the effect of gap change due to deformation is manifested in the following pressure distribution.

$$\tilde{P}=-12\bar{\mu}U_0b_2^2h^{-3}(\theta)\cos\theta \qquad (2.33)$$

The fluid film gap thickness, $h(\theta)$ is defined as

$$h(\theta)=\tilde{b}_2(\theta)-b_1$$

and

$$h(\theta)=\epsilon b_2\left\{1+\left(\frac{\tau\bar{W}(\delta,\lambda)}{\epsilon}+\frac{1}{b_2\epsilon}\int_0^t U(t')dt'\right)\cos\theta\right\}$$

The corresponding force **F** on the journal per unit axial length is

$$\mathbf{F}=\int_0^{2\pi}Pb_1\cos\theta d\theta \quad \mathbf{e}_y$$

and upon substitution of the pressure, then integration, the result is

$$\mathbf{F}=-\frac{6\bar{\mu}U_0(t)b_2^2b_1}{b_2^3\epsilon}\cdot\frac{\pi}{(1+\bar{\tau})(1-\bar{\tau}^2)^{1/2}}$$

$$\left\{\sum_{k=0}^{2}(-1)^K\frac{(3-2K)!!(2K-1)!!}{(2-K)!K!}\left(\frac{1+\bar{t}}{1-\bar{t}}\right)^K\right\}\mathbf{e}_y$$

for

$$\bar{t}=\left(\frac{\tau\bar{W}(\delta,\lambda)}{\epsilon}+\frac{1}{b_2\epsilon}\int_0^t U(t')dt'\right)$$

When comparing the preceding pressure distribution, equation (2.33), with the Reynolds' equation result for squeeze film pressures, one should keep in mind that (2.33) is only valid for small eccentricities. Representing the combined fluid-solid problem with a discrete singularity distribution limits this solution to small eccentricities. The principal advantage gained is the relative mathematical ease in incorporating the effect of rubber boundary deformation into fluid film pressures.

III Results

This theoretical model predicts changes in fluid film gap size subject to the restriction of small-amplitude displacements. To illustrate the results, three points are discussed. First, the nondimensional radial deformation amplitude function is plotted and discussed; second, some typical numbers for bearing applications are substituted into the radial displacement amplitude solution to show that small-amplitude deformations are realistic; and third, the rubber incompressible assumption is justified by estimating compressible displacement effects using actual Poisson ratios instead of the ideal incompressible value of one-half.

***III.*1 Nondimensional Radial Deformation Amplitude Function.** The theoretical result for radial deformation depends on the nondimensional parameters $\sigma\bar{\mu}U_0/\mu b_2$, λ and δ, thus an amplitude function for radial elastomer displacement is determined. To show this deformation as a function of rubber thickness, I consider the following rescaled form of equation (2.30),

$$\frac{\hat{W}}{\left(\frac{\bar{\mu}}{\mu}\frac{U_0}{b_2}\right)\sigma}=\bar{W}_r(\lambda_1\delta)\cos\theta \qquad (2.34)$$

In lubrication applications the parameter λ is relatively fixed near one in order to maintain journal load carrying capacity; however, the relative thickness of the elastomer can change through the parameter δ. Figures 2(a) and 2(b) show the amplitude function $\bar{W}_r(\delta,\lambda)$ for $\lambda=0.995$ and $\lambda=0.975$, respectively.

Figure (2a) is a plot of the radial displacement amplitude, for $\lambda=0.995$, as a function of the normalized rubber thickness. It is also a measure of the apparent eccentricity induced by the rubber deformation. In the limit as the rubber thickness goes to zero, $\delta \rightarrow 1$, the associated rubber deformation will vanish; this is shown in Fig. 2(*a*). Clearly the effect of rubber thickness on radial deformation is nearly flat for δ above 0.8, and elastomer deformation is best controlled using the parameter $\tilde{\mu}\sigma U_0/\mu b_2$. The second curve, Fig. (2*b*), for $\lambda = 0.975$, shows the radial displacement amplitude as a function of the normalized rubber thickness for a slightly different undeformed gap size. Note that $\lambda = 0.995$ and $\lambda = 0.975$ were chosen because of lubrication applications.

The fluid-induced deformation given by equation (2.34) is discussed using the coordinates shown in Fig. 1. For a positive velocity U_0 the fluid pressures in the gap where $y<0$ are larger than fluid pressures in the $y>0$ region; corresponding rubber deformation in the $y<0$ region causes an increased fluid gap thickness, and a decreased fluid gap thickness in the $y>0$ region. Rubber elastomer exposed to the higher fluid pressure fluid is pushed toward the lower fluid pressure region. With this deformed shape a corresponding change in fluid pressure is given by the slowly changing constants $\tilde{C}_i = 1,4$.

***III*.2 Typical Deformed Gap Geometry.** Using the foregoing radial deformation result, it is of interest to estimate actual gap size change due to fluid film surface tractions. The radial deformation is given in terms of the three parameters $\sigma\tilde{\mu}/\mu$ U_0/b_2, λ, and δ. As an example of radial deformation, the following physical constants were selected.

$$t = 0.000$$
$$\mu = 820 \text{ dynes/cm}^2$$
$$\nu = 0.49984$$
$$\tilde{\mu} = 50 \text{ cp}$$
$$b_2 = 2.54 \text{ cm}$$
$$U_0 = 10^{-2} \text{m/s}$$
$$b_2 - b_1 = 0.013 \text{ cm}$$
$$b_3 = 3.18 \text{ cm}$$

The deformed gap thickness is

$$h(\theta) = (0.013 - 0.0048\cos\theta)\text{cm}$$

A further fluid gap thickness change occurs when one applies the translational component of motion to $h(\theta)$; in the preceding example the fluid gap thickness does not change due to translation since $t = 0$.

The typical parameter values chosen indicate that small eccentricities can occur during deformations. It is noted that rubber deformation increases with increasing fluid viscosity, increasing translating speed, and decreasing gap thickness. Furthermore, the radical deformation is enhanced with decreasing elastomer shear modulus and increasing rubber thickness.

In this regard it is noted that more sophisticated singularity distributions are needed to generate the corresponding large amplitude journal eccentricities.

***III*.3 Relative Importance of Compressible Deformation.** Since the theoretical model developed predicts only incompressible deformations, a relative estimate of the compressible effects is made to verify this incompressible assumption. To estimate the importance of rubber compressibility, I will estimate the compressible displacements and compare them to the incompressible ones found herein. Recall that a change in the rubber volume can be estimated as

$$\frac{\Delta V}{V} = \frac{-3P_0}{2\mu}\left(\frac{1-2\nu}{1+\nu}\right)$$

where ΔV is the volume change and V is the original volume. For this two-dimensional problem the compressible deformation is estimated as

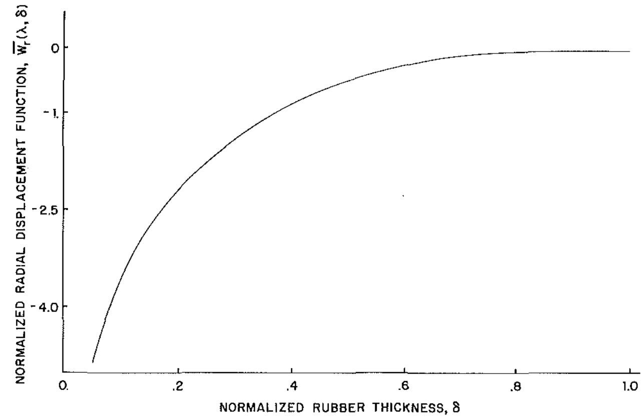

Fig. 2(*a*)

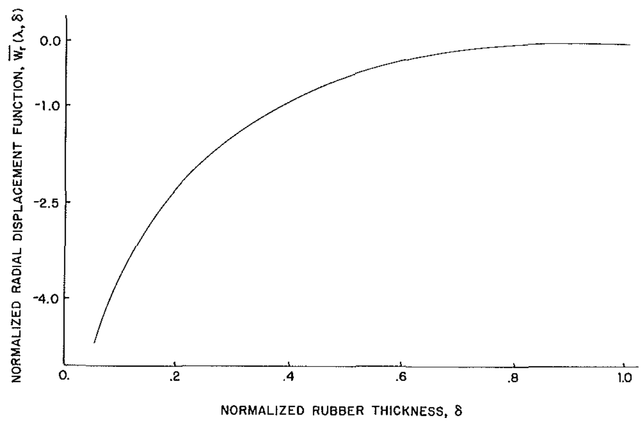

Fig. 2(*b*)

Fig. 2 Plot of displacement amplitude function for (*a*) $\lambda = 0.995$ and (*b*) $\lambda = 0.975$; $\bar{W}_r(\lambda, \delta)$ is shown as a function of the relative rubber thickness.

$$\frac{\Delta H}{H} = \frac{-3P_0}{2\mu}\left(\frac{1-2\nu}{1+\nu}\right) \tag{2.35}$$

where the fluid pressure P_0 is

$$P_0 = 8\tilde{\mu}U_0\sigma b_1^{-1}$$

From equation (2.34) the incompressible displacement is

$$\hat{W}_r = \frac{\tilde{\mu}}{\mu}\frac{U_0}{b_2}\sigma\bar{W}(\lambda,\delta)\cos\theta \tag{2.36}$$

Compressible deformation equation (2.36) is renormalized with the undeformed thickness of the rubber layer.

$$\hat{\hat{W}}_r = \hat{W}_r\left(\frac{b_2}{b_3 - b_2}\right) = \frac{P_0}{\mu}\frac{b_2}{b_3 - b_2}\bar{W}_r(\lambda,\delta)\cos\theta$$

Finally the deformation ratio is

$$R = \frac{\text{compressible displacement}}{\text{incompressible displacement}}$$

and

$$R = (1-2\nu)(1-\delta)/\delta\bar{W}_r(\lambda,\delta)$$

A typical value for Poisson's ratio, Rightmire [10], is $\nu = 0.499$. The incompressible assumption seems to be a good one since R is much less than one.

IV Concluding Remarks

Fluid flow and rubber deformation for compliant bearings are modeled using a singularity superposition method. The principal advantage of this approach is the relatively simple theoretical estimates for compliant bearing deformation. This approach also reduces the calculation of rubber deformation to determining three parameters, $\bar{\mu}\sigma U_0/\mu b_2$, δ, and λ. One limitation of this simple model is that eccentricities between the deformed elastomer and inner cylinder are asymptotically small. It is found that rubber deformation under fluid film pressures is equivalent to an apparent eccentricity between the inner cylinder and the bearing surface. Another feature predicted by the model is the occurrence of higher order harmonics in the rubber deformation, such deformation depends primarily on the change in pressure profiles induced by gap changes. Given typical values for oil lubricant viscosities and rubber sheet modules, it is found that rubber deformation consistent with the small departures from concentricity are possible. It is noted that estimates of rubber deformation due to Poisson's ratio near one-half show the incompressibility assumption for rubber to be successful.

I have examined here only the simplest of squeeze film bearing flows. That is steady, Newtonian fluid with uniform properties, and no cavitation. Thus, the conclusions on the validity are limited by these assumptions. However, the method presented here is suitable for treating more complex geometries using more elaborate singularity distributions.

It is hoped that the present work will lay the groundwork for further modeling improvements for compliant surface bearings. As a first step in this direction a generalization of this long bearing theory to arbitrary eccentricities might be considered. Here the singularity solution method can be used by considering distribution in place of discrete singularities. The further improvement would be of practical value.

Acknowledgments

This work was supported by National Science Foundation Grant No. MEA-81-06447.

References

1 Benjamin, M. K., and Castelli, V., "A Theoretical Investigation of Compliant Surface Journal Bearings," *J. of Lub. Tech.*, Vol. 93, 1971, pp. 191-202.

2 Benjamin, M. K., "Compliant Surface Bearings: An Analytic Investigation," Columbia University Thesis, 1969.

3 Cameron, A., *The Principles of Lubrication*, Wiley, New York, 1966, pp. 385-386.

4 Chwang, A. T., and Wu, T. Y., "Hydromechanics of Low-Reynolds-Number Flow. Part 2. The Singularity Method for Stokes Flows," *J. Fluid Mech.*, Vol. 67, 1975, pp. 787-815.

5 Elrod, H. C., "Exact and Approximate Theory for Linearly Compliant Layer with Inflexible Adhesive Backing," Columbia University Lub. Res. Lab., Report No. 2, 1965.

6 Fogg, A., and S. A. Hunwicks, "Some Experiments With Water Lubricated Rubber Bearings," *General Discussions on Lubrication and Lubricants*, Vol. 1, Institution of Mechanical Engineers, London, 1937, pp. 101-106.

7 Hori, Y., Kato, T., and Narumiya, H., "Rubber Surface Squeeze Films," *J. of Lub. Tech.*, Vol. 103, 1981, pp. 398-405.

8 Pirvics, J., and Castelli, V., "Elastomer Inertia Effects in Compliant Surface Bearings," Columbia University Lub. Res. Lab., Report No. 19, 1972.

9 Pirvics, J., and Castelli, V., "Elastomer Viscoelasticity Effects in Compliant Surface Bearings," Columbia University Lub. Res. Lab., Report No. 20, 1972.

10 Rightmire, G. K., "An Experimental Method for Determining Poisson's Ratio for Elastomers," *J. of Lub. Tech.*, Vol. 92, July, 1970, pp. 381-388.

11 Rightmire, G. K., Castelli, V., and Fuller, D., "An Experimental Investigation of a Tilting-Pad, Compliant Surface, Thrust Bearing," *J. of Lub. Tech.*, Vol. 98, Jan., 1976, pp. 95-110.

12 Rightmire, G. K., "The Swing-Pad Bearing: An Experimental Evaluation," Lubrication Research Laboratory, Dept. of Mechanical Engineering, Report No. 29, 1982.

13 Sokonikoff, I. S., *Mathematical Theory of Elasticity*, McGraw-Hill, New York, pp. 404-411, 1956.

S. A. Hall
Research Staff Member,
International Business Machines Corporation,
Yorktown Heights, N.Y. 10598
Mem. ASME

W. D. Iwan
Professor,
Department of Applied Mechanics,
California Institute of Technology,
Pasadena, Calif.
Mem. ASME

Oscillations of a Self-Excited, Nonlinear System

A system of self-excited, nonlinear differential equations exhibiting frequency entrainment is studied. Although similar equations describe electrical oscillators and machine-tool chattering, the results presented herein apply specifically to a model for the vortex-induced oscillation of linear structures. The equations are treated analytically by an approximate method, and two cases—partial nonlinear coupling and full nonlinear coupling—are identified. As applied to vortex-induced oscillations, the partially coupled case describes a structure having a single mode of oscillations, while the fully coupled case approximates continuous systems, such as undersea cables. Solutions for each case are examined for stability, and the results reveal several new types of behavior.

1 Introduction

A wide variety of physical systems may be classified as self-excited oscillators since they exhibit continuous, well-defined periodic oscillation without any "external" periodic excitation. Examples include many musical instruments, certain electrical circuits, machine-tool chattering, and the vortex-induced oscillations of structural components. Often, the self-excited oscillator is coupled to other oscillatory elements that possess their own distinct natural frequencies. In such a system, the frequency of the self-excited oscillator may be captured by the system resonance, a phenomenon called *entrainment*, or *lock-in*. The vortex-induced oscillation of elastic structural elements is an important example of this phenomenon.

There have been a number of experimental and analytical studies of self-excited systems, most relating to the problem of vortex-induced oscillation [1-8]. Analytically, it has become customary [4] to model the system by a single-mode, damped linear oscillator coupled to a self-excited oscillator of the van-der-Pol type [8]. By appropriate selection of model parameters, this approach has produced results that agree reasonably well with experimental observations, provided that the natural frequencies of the system are well separated. However, when the natural frequencies of the system are closely spaced, as in certain large marine systems, the customary, single-mode analysis is no longer valid. In such a case, distinct lock-in may or may not occur depending on the system parameters [3].

To gain further insight into the behavior of self-excited systems with closely spaced natural frequencies, a two-mode system is considered herein. It may be shown [3] that an important class of physical systems of this type may be modeled mathematically by a set of two damped linear oscillators coupled to two van-der-Pol oscillators. Such is the problem addressed in this paper. An approximate analysis reveals several new types of response behavior.

2 Formulation

Consider a linear two-mode system with natural frequencies Ω_1 and Ω_2 both close to unity. Let these two modes be coupled to two self-excited, van-der-Pol-type oscillators with unit frequency. Consistent with physical arguments for the vortex-shedding problem [1, 3], it will be assumed that the self-excited oscillators are coupled in a nonlinear fashion through the velocity-dependent terms. The coupling between the self-excited oscillators and the linear oscillators will be assumed to be linear in velocity and displacement terms. The coupling assumed is the simplest form possible that retains the basic physics of the problem.

Under the foregoing assumptions, the equations governing the response will be

$$\ddot{x}_1 + a_1\dot{x}_1 + \Omega_1^2 x_1 = \alpha\dot{x}_3 + \beta x_3 \qquad (1a)$$

$$\ddot{x}_2 + a_2\dot{x}_2 + \Omega_2^2 x_2 = \alpha\dot{x}_4 + \beta x_4 \qquad (1b)$$

$$\ddot{x}_3 + (p\dot{x}_3^2 + q\dot{x}_4^2 - b)\dot{x}_3 + x_3 = \gamma\dot{x}_1 + \delta x_1 \qquad (1c)$$

$$\ddot{x}_4 + (p\dot{x}_4^2 + q\dot{x}_3^2 - b)\dot{x}_4 + x_4 = \gamma\dot{x}_2 + \delta x_2, \qquad (1d)$$

where dots denote differentiation with respect to time t. Equations (1a) and (1b) describe the modal characteristics of the system, while equations (1c) and (1d) specify the self-excited components associated with these modes. For the problem of vortex-induced oscillation of a cable, equations (1a) and (1b) would represent the response of two adjacent modes of the cable, while equations (1c) and (1d) would represent the influence of the shed vortices coupled to the two modes. It will be assumed that all coefficients are of order ϵ ($\epsilon << 1$), with the exception of Ω_1 and Ω_2, which are assumed to differ from unity by quantities of order ϵ. The

Contributed by the Applied Mechanics Division and presented at the Winter Annual Meeting, New Orleans, La., December 9-14, 1984 of THE AMERICAN SOCIETY OF MECHANICAL ENGINEERS.

Discussion on this paper should be addressed to the Editorial Department, ASME, United Engineering Center, 345 East 47th Street, New York, N.Y. 10017, and will be accepted until two months after final publication of the paper itself in the JOURNAL OF APPLIED MECHANICS. Manuscript received by ASME Applied Mechanics Division, February, 1983; final revision, December, 1983. Paper No. 84-WA/APM-24.

Copies will be available until August, 1985.

nonlinearity, damping, and coupling are therefore assumed to be small.

Without loss of generality, equations (1) may be written in vector form as

$$\ddot{\mathbf{x}}+\mathbf{x}=\epsilon\mathbf{f}(\mathbf{x},\dot{\mathbf{x}}) \tag{2}$$

where $\mathbf{x} = (x_1, \ldots, x_4)$ and the definition of $\mathbf{f}(\mathbf{x}, \dot{\mathbf{x}})$ follows directly. An approximate analysis of this system of equations may be carried out using a variation of the method of multiple time scales [6]. To this end, let the solution $\mathbf{x}$ be expanded as a power series in ϵ,

$$\mathbf{x}=\mathbf{x}^{(0)}(t,T)+\epsilon\mathbf{x}^{(1)}(t,T), \tag{3}$$

truncated here to two terms, each of which depends on time t as well as the "slow time" ϵt, denoted hereafter as T. Then, defining D_0 and D_1 as the partial derivatives with respect to t and T, respectively, substituting equation (3) into equation (2), and equating coefficients of like powers of ϵ gives the following two equations for $\mathbf{x}^{(0)}$ and $\mathbf{x}^{(1)}$:

$$\begin{aligned}\epsilon^0:&\quad D_0^2\mathbf{x}^{(0)}+\mathbf{x}^{(0)} = 0\\ \epsilon^1:&\quad \epsilon(D_0\mathbf{x}^{(1)}+\mathbf{x}^{(1)}) = -2\epsilon D_0D_1\mathbf{x}^{(0)}+\epsilon\mathbf{f}(\mathbf{x}^{(0)},D_0\mathbf{x}^{(0)}).\end{aligned} \tag{4}$$

Denoting complex conjugation by overscoring, the ϵ^0 equation is satisfied by

$$x_m^{(0)}=H_m(T)e^{it}+\bar{H}_m(T)e^{-it}, m=1,\ldots,4 \tag{5}$$

where $H_m(T)$ is a slowly varying complex function. Consequently, the ϵ^1 equation becomes

$$\epsilon(D_0^2x_m^{(1)}+x_m^{(1)})=-2i\left(\epsilon\frac{dH_m}{dT}e^{it}-\epsilon\frac{d\bar{H}_m}{dT}e^{-it}\right)+\epsilon f_m(\mathbf{x}^{(0)},D_0\mathbf{x}^{(0)}). \tag{6}$$

To proceed further, the functions ϵf_m in the system (2) must be specified. First-order differential equations for the H_m are then generated by substituting equation (5) into equation (6), and requiring that the sum of the secular terms in equation (6) vanish.

Writing the functions ϵf_m appropriate to equations (1) yields

$$\begin{aligned}\epsilon(D_0^2x_m^{(1)}+x_m^{(1)}) &= \left(U_m-2i\epsilon\frac{dH_m}{dT}\right)e^{it}+\text{c.c.},\quad m=1,2\\ \epsilon(D_0^2x_m^{(1)}+x_m^{(1)}) &= W_me^{3it}+\left(V_m-2i\epsilon\frac{dH_m}{dT}\right)e^{it}+\text{c.c.},\quad m=3,4\end{aligned} \tag{7}$$

where "c.c." denotes the complex conjugate of all preceding terms, and

$$\begin{aligned}U_m &= (1-\Omega_m^2-ia_m)H_m+(i\alpha+\beta)H_{m+2},\quad m=1,2\\ V_m &= (i\gamma+\delta)H_{m-2}+ibH_m-3ipH_m^2\bar{H}_m-2iqH_mH_n\bar{H}_n\\ &\quad -iq\bar{H}_mH_n^2,\quad m=3,4\\ W_m &= iH_m(qH_n^2+pH_m^2),\quad m=3,4.\end{aligned} \tag{8}$$

In the latter equations, and henceforth, $n = 4$ when $m = 3$, and $n = 3$ when $m = 4$.

The requirement that secular terms vanish on the right side of equations (7) gives

$$-2i\epsilon\frac{dH_m}{dT}+(1-\Omega_m^2-ia_m)H_m+(ia+\beta)H_{m+2}=0,\quad m=1,2$$

$$-2i\epsilon\frac{dH_m}{dT}+ibH_m-3ipH_m^2\bar{H}_m-2iqH_mH_n\bar{H}_n-iq\bar{H}_mH_n^2+(i\gamma+\delta)H_{m-2}=0,\quad m=3,4. \tag{9}$$

These equations are satisfied by the following solution form for the complex amplitudes H_m

$$H_m(T)=\frac{1}{2}A_m(T)e^{i\theta_m(T)},\quad m=1,\ldots,4. \tag{10}$$

By substituting equation (10) into equation (5), the unknown real quantities $A_m(T)$ and $\theta_m(T)$ may be identified, respectively, as slowly varying amplitudes and phases:

$$x_m^{(0)}=A_m\cos(t+\theta_m),\quad m=1,\ldots,4. \tag{11}$$

Substituting equations (10) and (11) into equations (9), and separating real and imaginary parts gives, upon rearrangement, the following set of eight, first-order, nonlinear differential equations in the amplitudes and phases:

$$\begin{aligned}\dot{A}_m &= -\frac{1}{2}a_mA_m+\frac{1}{2}A_{m+2}(\alpha\cos\mu_m-\beta\sin\mu_m),\quad m=1,2\\ \dot{\theta}_m &= -\frac{1}{2}(1-\Omega_m^2)-\frac{A_{m+2}}{2A_m}(\beta\cos\mu_m+\alpha\sin\mu_m),\quad m=1,2\\ \dot{A}_m &= \frac{1}{2}bA_m-\frac{3}{8}pA_m^3-\frac{1}{8}qA_n^2A_m(2+\cos 2\phi)\\ &\quad +\frac{1}{2}A_{m-2}(\gamma\cos\mu_{m-2}+\delta\sin\mu_{m-2}),\quad m=3,4\\ \dot{\theta}_m &= \frac{(-1)^m}{8}qA_n^2\sin 2\phi-\frac{A_{m-2}}{2A_m}(\delta\cos\mu_{m-2}\\ &\quad -\gamma\sin\mu_{m-2}),\quad m=3,4\end{aligned} \tag{12}$$

where the phases differences μ_1, μ_2, and ϕ are defined as

$$\mu_1\equiv\theta_1-\theta_3,\quad \mu_2\equiv\theta_2-\theta_4,\quad \phi\equiv\theta_4-\theta_3. \tag{13}$$

3 Steady-State, Monofrequency Solutions

For steady-state, monofrequency oscillations at some unknown frequency ω, assumed to differ from unity by a quantity of order ϵ, the amplitudes A_m in equations (12) must be constant, while the phases θ_m must drift at the same, slow, constant rate $\omega-1$. Thus, approximate, steady-state, monofrequency oscillations of the system (1) are described by

$$\begin{aligned}&-a_mA_m+A_{m+2}(\alpha\cos\mu_m-\beta\sin\mu_m)=0,\quad m=1,2\\ &(2\omega-1-\Omega_m^2)A_m+A_{m+2}(\beta\cos\mu_m+\alpha\sin\mu_m)=0,\quad m=1,2\\ &bA_m-\frac{3}{4}pA_m^3-\frac{1}{4}qA_n^2A_m(2+\cos 2\phi)\\ &\quad +A_{m-2}(\gamma\cos\mu_{m-2}+\delta\sin\mu_{m-2})=0,\quad m=3,4\\ &2(\omega-1)A_m-\frac{(-1)^m}{4}qA_n^2A_m\sin 2\phi\\ &\quad +A_{m-2}(\delta\cos\mu_{m-2}-\gamma\sin\mu_{m-2})=0,\quad m=3,4\end{aligned} \tag{14}$$

This system comprises eight, nonlinear algebraic equations for the eight unknowns ($A_1, \ldots, A_4, \mu_1, \mu_2, \phi, \omega$). The method of solution depends strongly on whether the coupling parameter q is zero or nonzero.

3.1 Partially Coupled Oscillations ($q=0$). It is apparent from equations (1) that if $q=0$, the pair of oscillators (x_1, x_3) is uncoupled from the pair (x_2, x_4). Consequently the system of eight equations (14) resolves into two identical, uncoupled sets of four equations. For specificity, consider the set involving x_1 and x_3. The first pair of equations (14) may then be solved for $\cos\mu_1$ and $\sin\mu_1$. Squaring and adding gives an expression for A_1/A_3. Substituting these results into the second pair of equations (14) produces a frequency equation and an amplitude equation of the form

$$F_j(\omega) = 0, \qquad j = 1 \tag{15}$$

$$G_j(\omega) = A_{j+2}^2, \quad j = 1, \tag{16}$$

where the functions F_j and G_j are defined as

$$F_j(\omega) \equiv \frac{4}{3p}\left\{2(1-\omega) - \frac{k_b(2\omega-1-\Omega_j^2)+k_a a_j}{(2\omega-1-\Omega_j^2)^2+a_j^2}\right\} \tag{17}$$

$$G_j(\omega) \equiv \frac{4}{3p}\left\{b + \frac{-k_a(2\omega-1-\Omega_j^2)+k_b a_j}{(2\omega-1-\Omega_j^2)^2+a_j^2}\right\} \tag{18}$$

and

$$k_a \equiv \alpha\delta + \beta\gamma, \quad k_b \equiv \alpha\gamma - \beta\delta. \tag{19}$$

The form of the solution to equations (15) and (16) may be simplified by replacing the pair of frequency variables (ω, Ω_1) appearing in equations (17) and (18) with "frequency detuning" variables D and d, defined as

$$D \equiv \frac{1}{2}(2\omega-1-\Omega_1^2) \approx \omega - \Omega_1$$

$$d \equiv \frac{1}{2}(1-\Omega_1^2) \approx 1-\Omega_1, \tag{20}$$

where the indicated approximations hold to order ϵ. D is the detuning between the response frequency ω and the natural frequency of the oscillator x_1, while d is the detuning between the natural frequencies of the two oscillators x_3 and x_1. Substituting into equation (15) yields

$$d = D + \frac{1}{2}\left\{\frac{2k_b D + k_a a_1}{4D^2 + a_1^2}\right\}. \tag{21}$$

For each value of D, the amplitude A_3 is given by equation (16). The boundaries of real amplitude may be found by setting $G_1(\omega) = 0$.

To investigate stability of the preceding solutions, it is necessary to return to equations (12), prior to assumption of the steady state. Using these equations together with equations (13), expressions for $\dot{A}_1$, $\dot{A}_3$, and $\dot{\mu}_1$ may be written in the form

$$\dot{\mathbf{X}} = \mathbf{J}(\mathbf{X}), \tag{22}$$

where $\mathbf{X} \equiv (A_1, A_3, \mu_1)$. The steady-state solution $\mathbf{X}_0$ satisfies $\mathbf{J}(\mathbf{X}_0) = \mathbf{O}$, so if $\mathbf{X}$ is perturbed slightly away from $\mathbf{X}_0$, the perturbation $\hat{\mathbf{X}}$ satisfies, to first order,

$$\dot{\hat{\mathbf{X}}} = \left[\frac{\partial \mathbf{J}}{\partial \mathbf{X}}\right]_{\mathbf{X}=\mathbf{X}_0} \hat{\mathbf{X}}. \tag{23}$$

The eigenvalues of the Jacobian matrix are found to satisfy a cubic equation whose coefficients are polynomial functions of the independent variable D. The Routh conditions may then be applied to determine which solutions are stable.

3.2 Fully Coupled Oscillations ($q \neq 0$). When $q \neq 0$, all four oscillators x_m in equations (1) are coupled together. Upon inspection of these equations, it is clear that two entirely different brands of nontrivial solution are possible:

Case 1: Nondegenerate solutions, for which all four x_m are nonzero.

Case 2: Degenerate solutions, which are of two types:

$$x_1, x_3 \neq 0 \quad \text{and} \quad x_2 = x_4 = 0 \quad \text{(Type 1)}$$

$$x_2, x_4 \neq 0 \quad \text{and} \quad x_1 = x_3 = 0 \quad \text{(Type 2)} \tag{24}$$

For any given set of parameters (α, β, γ, δ, p, q, etc.) it is not clear a priori which type of steady-state solution (if any) will prevail.

Case 1: Nondegenerate solutions. Consider first the nondegenerate case. Initially, solution of the eight steady-state equations (14) in the eight unknowns ($A_1, \ldots, A_4, \mu_1, \mu_2, \phi, \omega$) proceeds in direct analogy to the solution of the partially coupled system, yielding the amplitude equation (16)

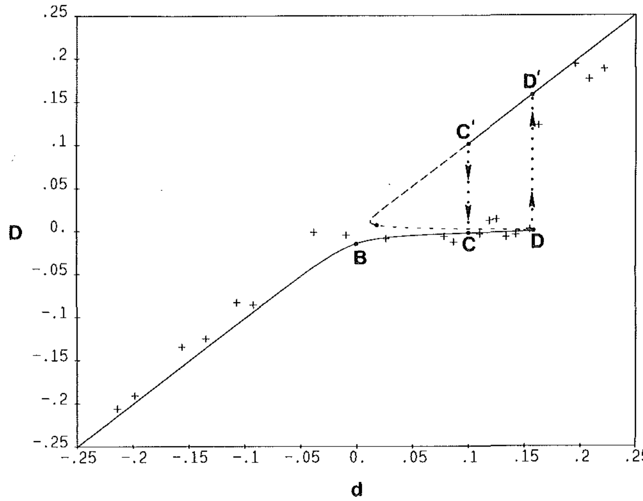

Fig. 1 Partially coupled oscillations: typical frequency response

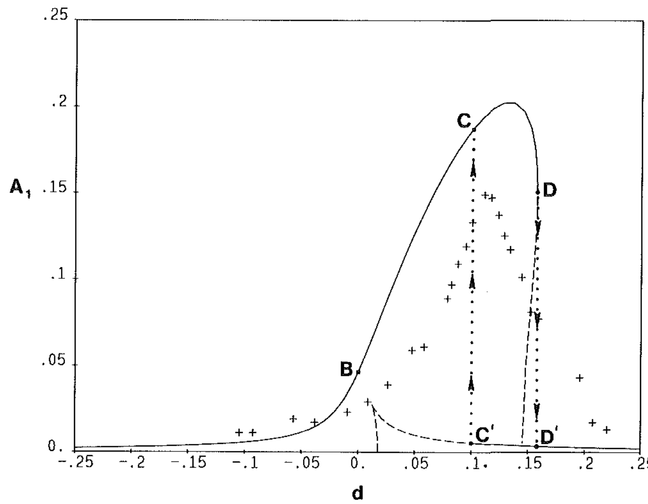

Fig. 2 Partially coupled oscillations: amplitude response corresponding to Fig. 1

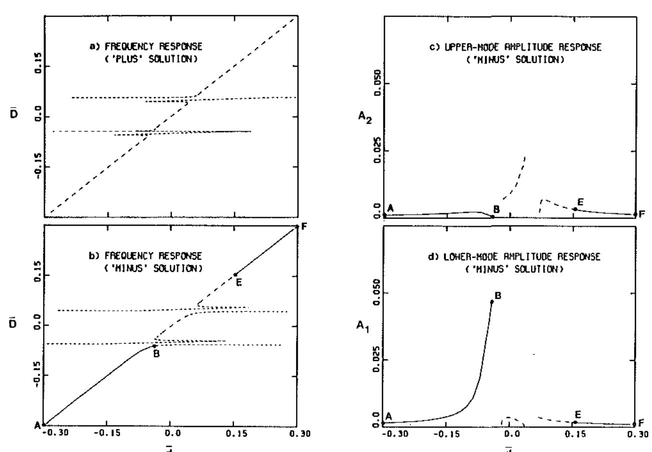

Fig. 3 Fully coupled oscillations: typical nondegenerate solutions ($\Delta = 0.1$)

for $j = 1, 2$. Further elimination gives, in place of equation (15),

$$(F_1^2 - F_2^2)^2 + \left[(F_1G_1 + F_2G_2) - \frac{2q}{3p}(F_1G_2 + F_2G_1)\right]^2$$

$$= \left(\frac{q}{3p}\right)^2 (F_1G_2 + F_2G_1)^2, \tag{25}$$

where F_j and G_j are defined for $j = 1, 2$ by equations (17) and (18).

As in the foregoing, detuning variables may be introduced here to recast the frequency equation in simpler form. Let

$$\bar{D} \equiv \frac{1}{2}\left\{2\omega - 1 - \frac{\Omega_2^2 + \Omega_1^2}{2}\right\} \approx \omega - \frac{\Omega_1 + \Omega_2}{2} \tag{26}$$

$$\bar{d} \equiv \frac{1}{2}\left\{1 - \frac{\Omega_2^2 + \Omega_1^2}{2}\right\} \approx 1 - \frac{\Omega_1 + \Omega_2}{2} \tag{27}$$

$$\Delta \equiv \frac{1}{2}(\Omega_2^2 - \Omega_1^2) \approx \Omega_2 - \Omega_1 \tag{28}$$

The quantities $\bar{D}$ and $\bar{d}$, based on the mean of Ω_1 and Ω_2, are directly analogous to D and d, introduced earlier for the partially coupled case. The additional variable Δ is necessary here to measure the difference between Ω_2 and Ω_1. Writing equation (25) in terms of the detuning variables gives

$$K_2\bar{d}^2 + K_1\bar{d} + K_0 = 0, \tag{29}$$

where K_2, K_1, and K_0 are algebraic functions of the system parameters and the independent variable $\bar{D}$. Hence, for each value of $\bar{D}$ there are two possible solutions $\bar{d}$, which are either both real or both nonreal, depending on the sign of the discriminant. For each real frequency solution $\bar{d}$, the amplitudes and phases ($A_1, \ldots, A_4, \mu_1, \mu_2, \phi$) may be recovered by back substitution. The amplitude solution is real if and only if both functions G_j are positive.

As for the case of partially coupled oscillations, if a solution is real, stability may then be investigated using equations (12), which yield a set of seven first-order differential equations in the four amplitudes and three phase differences. Unlike the previous case, the seven-by-seven Jacobian of the present case is too large to permit a convenient, analytical determination of stability conditions. The stability results given in Section 4 were obtained by analytical differentiation to obtain the Jacobian matrix, followed by numerical determination of the eigenvalues.

Case 2: Degenerate Solutions. As specified by equations (24), there are two types of degenerate solutions. However, since the two types are completely analogous to each other, only one of them need be considered explicitly. Considering Type-1 solutions, the steady-state equations reduce, for the nondegenerating degrees of freedom (x_1, x_3), to equations (14). The same equations reduce, for the degenerating degrees of freedom (x_2, x_4), to the identity $0=0$, since $A_2 = A_4 = 0$. Therefore, steady-state degenerate solutions are identical to those for the partially coupled case.

It remains to investigate the stability of these solutions. The stability analysis is quite different from the partially coupled case – even though the steady-state solutions are identical – because, in the fully coupled context, arbitrary perturbations about the steady-state may include nonzero perturbed values of the degenerating degrees of freedom. Thus the full system of eight equations (12), involving all four amplitudes ($A_1, \ldots, A_4$) and three phase differences (μ_1, μ_2, ϕ) must be considered.

However, a problem arises: since the steady-state amplitudes of the degenerating degrees of freedom are zero, it is meaningless to speak of the corresponding phases. Hence, for Type-1 solutions, the steady-state values of the phase differences μ_2 and ϕ are not well defined. Consequently, a stability analysis based on equations (12), which require well-defined A's, μ's, and ϕ, must be abandoned in the degenerate case.

An alternative stability method is to perturb the original differential equations (1) about the exact, degenerate steady-state. In such an approach, the concept of phases for the degenerating degrees of freedom is absent, so the problem discussed in the foregoing does not arise. Retaining terms to

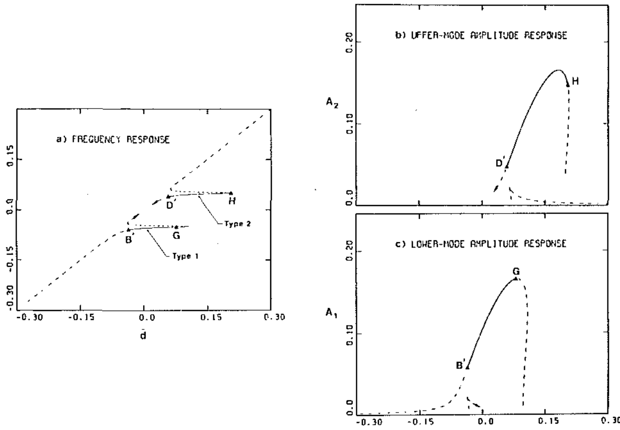

Fig. 4 Fully coupled oscillations: typical degenerate solutions (Δ = 0.1)

first order in ϵ yields two pairs of perturbational equations which are completely uncoupled from each other, one pair for the nondegenerating degrees of freedom, and another pair for the degenerating degrees of freedom. The degenerate, steady-state solution to equations (1) will be stable if and only if the solutions to both pairs of perturbational equations decay with time. For the nondegenerating degrees of freedom, the stability characteristics may be determined as for the partially coupled case. Thus, independent of the difference between Ω_1 and Ω_2, (as measured by the parameter Δ), solutions that are unstable in the partially coupled case are also unstable in the fully coupled case.

Additional stability bounds are imposed on the fully coupled solution by the degenerating degrees of freedom, the stability characteristics of which cannot be inferred from previous work. However, if the exact parametric excitation is replaced by the approximate value given by the asymptotic method, the stability characteristics may be deduced using Floquet theory. In the present investigation, a set of principle solutions, which depend on the parameter Δ, is determined by numerical integration. Next, the associated, one-period transfer matrix and its eigenvalues are found numerically. According to Floquet theory, the system will be stable if and only if all eigenvalues have complex moduli less than unity. As a result of these additional stability conditions, solutions that are stable in the partially coupled case are not necessarily stable in the fully coupled case. Moreover, these additional conditions cause the stability of degenerate solutions to depend on the difference between Ω_1 and Ω_2.

4 Numerical Example

The results presented in the following were obtained using the following values of the parameters in equations (1): $\alpha = 0.000988$, $\beta = 0.00104$, $\gamma = 0.740$, $\delta = 1.156$, $a_1 = a_2 = 0.00613$, $b = 0.126$. In addition, for the case of partially coupled oscillations, $p = 0.270$ and $q = 0$, while for the case of fully coupled oscillations, $p = 0.405$ and $q = 0.810$. These values, appropriate to the vortex-induced oscillation of spring-supported cylinders and elastic cables in air, were obtained by fitting a simplified mathematical model of vortex shedding [3] to experimental data on harmonically forced, rigid cylinders [5] as well as spring-supported cylinders [2]. According to this model, spring-supported cylinders are described by partially coupled oscillations of equations (1), while elastic cables are approximated by fully coupled oscillations. Although the parameter values stated in the foregoing are not all strictly in accordance with the order ϵ approximations implied by equation (2), it will be shown in the following that accurate results are nevertheless obtained.

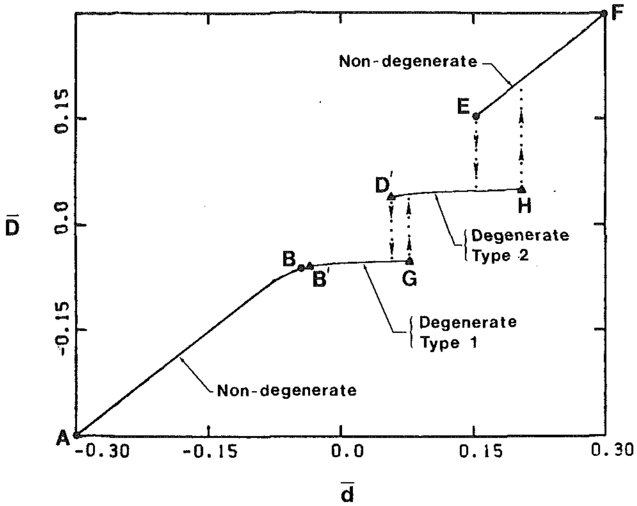

Fig. 5 Fully coupled oscillations: composite frequency solution (Δ = 0.1)

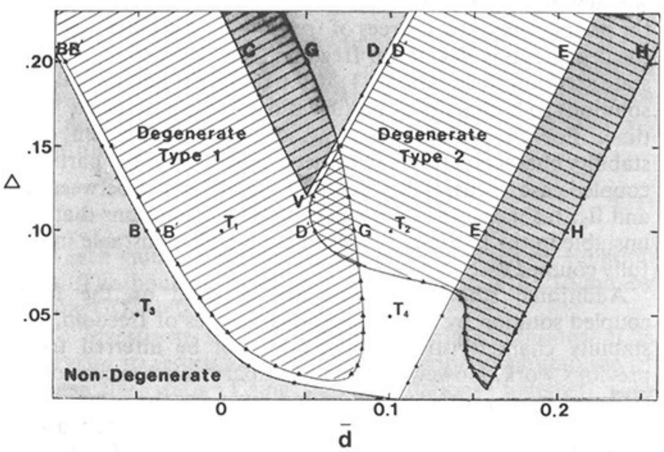

Fig. 6 Composite solution map

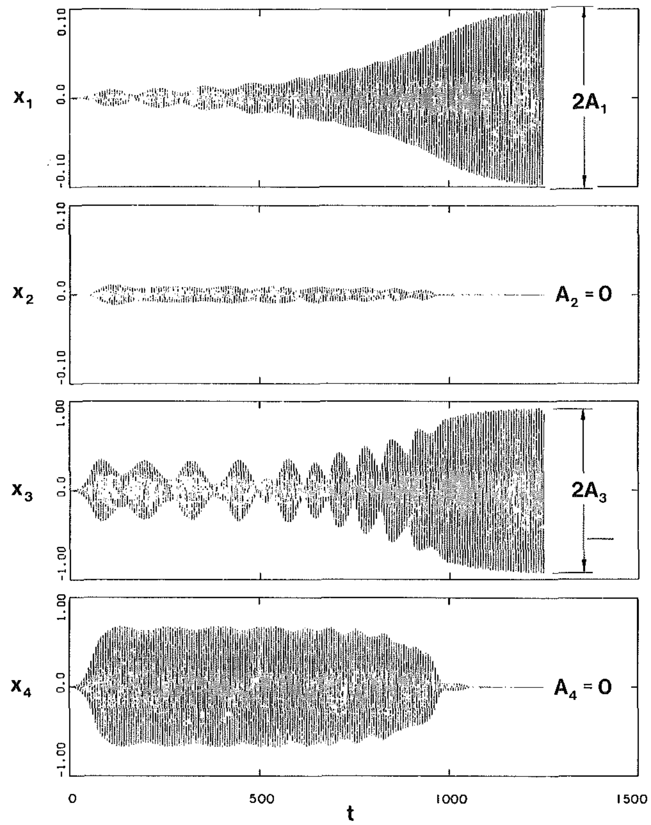

Fig. 7 Numerical solution versus analytic prediction for test point T_1 of Fig. 6

4.1 Partially Coupled Oscillations. The results for the partially coupled case are shown in Figs. 1 and 2. Portions of the frequency response curve $d(D)$ which generate imaginary amplitudes (A_3, A_1) are shown as short-dashed lines. Solutions that are real but unstable are shown as long-dashed lines, while solutions that are real and stable – the only ones of physical interest – are shown as solid lines.

Figure 1 illustrates that when the natural frequency (Ω_1) of the linear oscillator x_1 is sufficiently greater than the natural frequency (unity) of the self-excited oscillator x_3 ($d<0$), the response frequency ω closely approaches that of the self-excited oscillator ($D \approx d$). However, when Ω_1 is only slightly less than unity ($0<d<0.16$), the self-excited oscillator is entrained by the resonance of the linear oscillator, and the response frequency approaches Ω_1 ($D \approx 0$). This is "lock-in." For sufficiently small values of Ω_1 ($d>0.16$), the response again approaches the frequency of the self-excited oscillator ($D \approx d$). The transition from one type of response to the other occurs abruptly, and is characterized by hysteretic jumps ($CDD'C'$ in the figure). The precise point of transition depends on whether the detuning is being increased or decreased.

As indicated in Fig. 2, the amplitude response shows a definite peak for detuning d between 0 and 0.16, corresponding to the region of lock-in. Amplitude jumps are also present, corresponding to the frequency jumps of Fig. 1.

In the case of vortex-induced oscillation, the frequency of the self-excited oscillator – and hence d – is proportional to the fluid-flow velocity. The general trends of Figs. 1 and 2 agree with the observed, vortex-induced oscillations of single-mode structures. To illustrate this point, data from the aforementioned experimental study [2] of spring-supported cylinders in air have been plotted on the figures. Although the experimental results shown here do not display the hysteretic jumps predicted by the model, other runs from the same experiment (at lower values of the damping constant a_1) do display such hysteresis, a phenomenon that has not been simulated by previous nonlinear models of vortex-induced oscillation.

4.2 Fully Coupled Oscillations. The results for a coupled two-mode system with Δ = 0.1 are shown in Figs. 3 and 4. Figure 3 shows the nature of the nondegenerate solution and Fig. 4 that of the degenerate solution. Solid lines denote real, stable solutions, long-dashed lines denote real, unstable solutions, and short-dashed lines denote frequency solutions that generate nonreal amplitudes. In Figure 3, the "plus" and "minus" frequency solutions – which correspond to the two solutions of the quadratic equation (29) – are plotted separately for clarity. However, for the parameters under consideration, the "plus" solution is never real and stable, so the corresponding amplitude plots are omitted. For the set of parameters under consideration, nondegenerate solutions do not exhibit lock-in to any great degree. For other sets of parameters, nondegenerate, locked-in solutions have been found, which are real and stable, but such solutions do not appear to have physical meaning. At point B, the upper-mode amplitudes vanish, so this point must represent the boundary between nondegenerate solutions and degenerate solutions of Type 1.

From Fig. 4 it is observed that real, stable solutions for the degenerate case occur only in the locked-in segments $B'G$ and $D'H$. These lock-in bands are suppressed as the modal

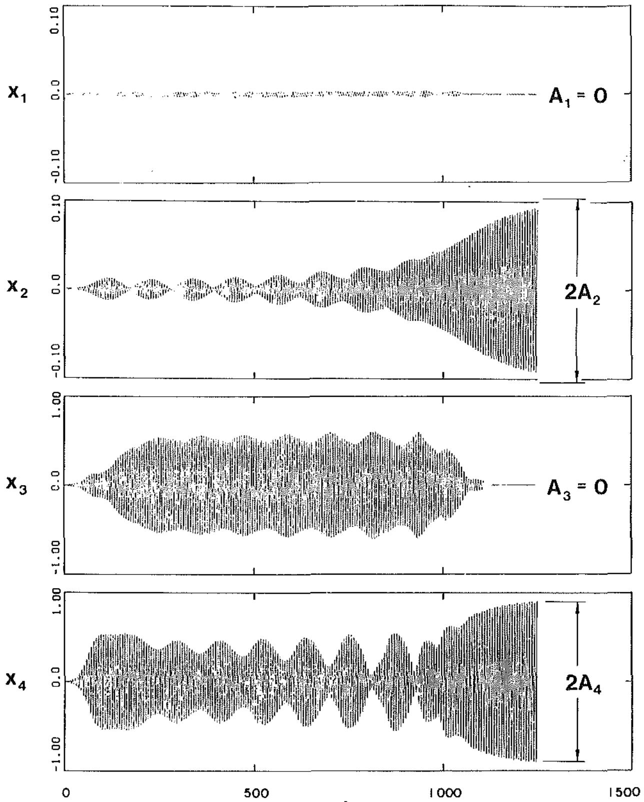

Fig. 8 Numerical solution versus analytic prediction for test point T_2 of Fig. 6

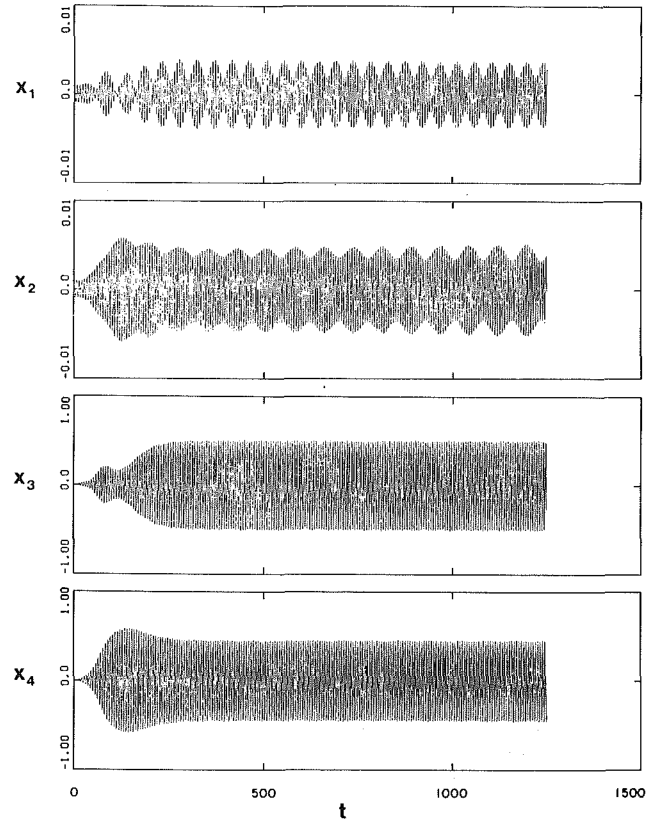

Fig. 10 Numerical solution for test point T_4 of Fig. 6

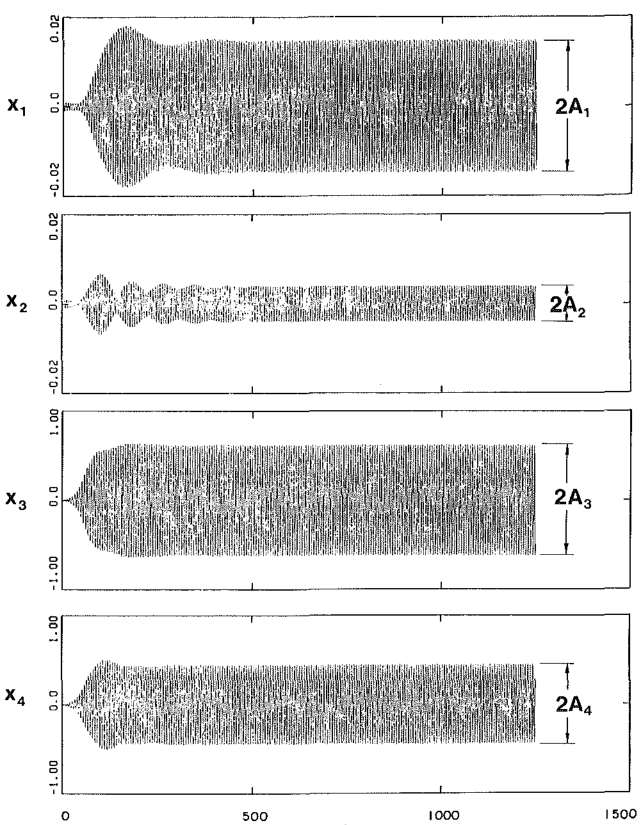

Fig. 9 Numerical solution versus analytic prediction for test point T_3 of Fig. 6

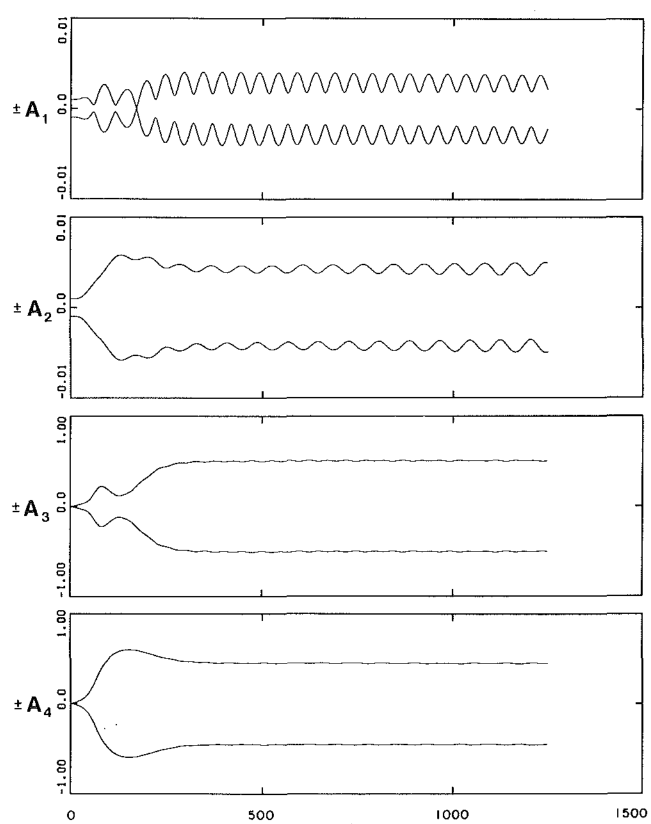

Fig. 11 Analytic prediction for test point T_4 of Fig. 6

frequency separation Δ decreases; the presence of the upper mode causes instability of the right end of the lower-mode lock-in band, while the presence of the lower mode causes instability of the left end of the upper-mode lock-in band.

By piecing together the real, stable solutions from Figs. 3 and 4, the composite frequency solution shown in Fig. 5 is obtained. A similar composite could be constructed for the response amplitude, if desired. Nondegenerate and degenerate solutions "fit together" at the points $B-B'$, and ideally, these two points should coincide. The slight mismatch is attributable to the fact that the stability analysis used to obtain point B is entirely different from that used to obtain point B', as discussed in Section 3.

The nature of the composite solution will depend greatly on the value of the intermodal coupling parameter Δ. Figure 6 is a map of the composite solutions obtained by computing the various solution boundaries for a number of values of Δ. Thus, the lettered points at $\Delta=0.10$ correspond to those of Fig. 5. Nondegenerate solutions exist in the three shaded regions while degenerate solutions exist in the hatched regions. The narrow white gaps between the $B-B'$ and $D-D'$ boundaries are artificial, as indicated in the preceding paragraph. On the other hand, the large white area is genuine. In this region, the differential equations fail to admit simple harmonic solutions of any sort, as discussed earlier. Overlapping regions indicate hysteretic behavior. In particular, lock-in overlap occurs in the region where Type-1 and Type-2 degenerate solutions coexist.

The phenomenon of lock-in suppression – the inhibition of degenerate solutions as $\Delta \rightarrow 0$ – is clearly displayed by the solution map, particularly for the upper mode. Lock-in suppression has two effects. First, it reduces the extent of lock-in overlap, and second, it gives rise to the region of complex solutions (the white region of the figure). Decomposition of the two-mode problem into two one-mode problems at large values of Δ is clearly indicated by the solution map. The shaded, triangular wedge of nondegenerate solutions near the center of the map represents the "dead" area between modes where both modal response amplitudes are relatively small. Thus, the two modes may be considered well separated if Δ is sufficiently large that this wedge separates the two types of degenerate solution.

The approximate analysis may be verified by numerical integration of the equations (1). Results for four combinations of Δ and $\bar{d}$ are shown in Figs. 7–10. These test points, denoted by T_1–T_4 on Fig. 6, are selected to represent the four types of solutions predicted analytically by the solution map. On Figs. 7–9, the steady-state amplitudes predicted by the asymptotic method are shown at the right of each plot. Clearly, the analytical predictions are quite good – qualitatively, each solution is of the type predicted, and quantitatively, the amplitude predictions are accurate. As predicted by the steady-state stability analysis, the solution shown in Fig. 10 for point T_4 is not simple harmonic. Although the steady-state equations yield no further information for such a case, the asymptotic method itself does yield such information. The equations for the amplitudes and phases, equations (12), may be integrated numerically with small initial conditions, yielding the results shown in Fig. 11. A comparison of Fig. 11 and Fig. 10 indicates that the asymptotic method does an acceptable job in predicting the envelope of the response, even when the solution is not steady state.

Acknowledgment

This research was sponsored in part by a grant from the National Science Foundation. Any opinions, findings, and conclusions presented are those of the authors, and do not necessarily reflect the views of the Foundation.

References

1 Blevins, R. D., *Flow-Induced Vibration*, Van Nostrand Reinhold Co., New York, 1977.

2 Parkinson, G. V., Feng, C. C., and Ferguson, N., "Mechanics of Vortex-Excited Oscillation of Bluff Cylinders," Proc. of Symposium on Wind Effects on Buildings and Structures, Loughborough University of Technology, 1968, pp. 27.1–27.18.

3 Hall, S. A., "Vortex-Induced Vibrations of Structures," Ph.D. Thesis, California Institute of Technology, Pasadena, Calif., 1981.

4 Hartlen, R. T., and Currie, I. G., "Lift Oscillation Model for Vortex-Induced Vibration," *J. Eng. Mech. Div., Am. Soc. Civil Eng.*, Vol. 96, 1970, pp. 577–591.

5 Koopman, G. H., "The Vortex Wakes of Vibrating Cylinders at Low Reynolds Numbers," *J. Fluid Mech.*, Vol. 28, Part 3, 1967, pp. 501–512.

6 Nayfeh, A. H., and Mook, D. T., *Nonlinear Oscillations*, Wiley, New York, 1979.

7 Skop, R. A., and Griffin, O. M., "On a Theory for the Vortex-Excited Oscillation of Flexible Cylindrical Structures," *J. Sound and Vibration*, Vol. 41, No. 3, 1975, pp. 263–274.

8 van der Pol, B., "Forced Oscillations in a Circuit with Non-linear Resonance," *Phil. Mag.*, S. 7. Vol. 3, No. 13, 1927, pp. 65–80.

J. W. Kamman
Assistant Professor,
Department of Aerospace and
Mechanical Engineering,
University of Notre Dame
Notre Dame, Ind. 46556

R. L. Huston
Professor of Mechanics,
Department of Mechanical and
Industrial Engineering,
Location 72,
University of Cincinnati,
Cincinnati, Ohio 45221
Mem. ASME

Dynamics of Constrained Multibody Systems

A new automated procedure for obtaining and solving the governing equations of motion of constrained multibody systems is presented. The procedure is applicable when the constraints are either (a) geometrical (for example, "closed-loops") or (b) kinematical (for example, specified motion). The procedure is based on a "zero eigenvalues theorem," which provides an "orthogonal complement" array which in turn is used to contract the dynamical equations. This contraction, together with the constraint equations, forms a consistent set of governing equations. An advantage of this formulation is that constraining forces are automatically eliminated from the analysis. The method is applied with Kane's equations—an especially convenient set of dynamical equations for multibody systems. Examples of a constrained hanging chain and a chain whose end has a prescribed motion are presented. Applications in robotics, cable dynamics, and biomechanics are suggested.

Introduction

During the past five years there has been increasing interest in formulations of the equations of motion of large multibody systems. Interest has arisen almost simultaneously in three areas: robotics, biomechanics, and space vehicle dynamics. In each area, analysts have been seeking efficient automated procedures for obtaining and solving the governing equations of motion.

This interest in multibody systems stems from two sources: first, many structural systems (for example, robots, chains, manipulators, and biodynamic models) can be modeled by multibody systems; and second, it has just recently been possible, with advances in computational methods, to obtain efficient numerical formulations and solutions of the governing dynamical equations.

Recently attention has focused on *constrained* multibody systems – that is – systems possessing closed loops or systems with specified motion. These systems are useful in modeling robot arms, closed mechanisms, docking manipulators of spacecraft, ship cranes, restrained human body models, and cables anchored at both ends. This paper presents a formulation of the governing equations of such systems.

Governing Equations. References [1–19] represent a partial list of recently reported research efforts on multibody systems. For open-chain and disjoint rigid systems, the governing equations of motion can be written in the form:

$$a_{ij}\ddot{x}_j = f_i \quad (i, j = 1, \ldots, n) \tag{1}$$

where the x_j represent the generalized coordinates of the system; the a_{ij} are functions of the x_j and the inertia properties of the system; the f_i are functions of the x_j, their time derivatives $\dot{x}_j$, and the applied forces on the system; n is the number of degrees of freedom of the system; and the repeated index j represents a sum over that index.

Constraint Equations. If there are constraints on the system (occurring, for example, with closed loops or with specified motion), there occur an additional set of equations of the form:

$$b_{ij}\dot{x}_j = g_i \quad (i = 1, \ldots, m; j = 1, \ldots, n) \tag{2}$$

where the b_{ij} are functions of the x_j, the g_i are functions of time, and where $m < n$. There are thus $m + n$ equations for the n x_j. However, since there are m constraint equations, the number of degrees of freedom is reduced from n to $n - m$. Moreover, for large systems the b_{ij} are, in general, transcendental functions of the x_j and they are thus difficult to solve for m of the x_j in terms of the remaining $n - m$ x_j. Hence, the question that arises is: What are the best methods for efficiently reducing equations (1) and (2) to a set of consistent equations that may be used to determine the motion of the system.

Objective. The objective of this paper is to address and answer this question. The intent is to find "algorithmic" procedures suitable for large systems with many bodies. The analysis is made for connected rigid systems. Extension to disjoint and flexible systems can be obtained by generalization of the developed procedures.

The balance of the paper itself is divided into four parts with the following part presenting the proposed reduction and solution procedure. Application with Kane's equations is presented in the next part. Examples and a brief discussion are presented in the final two parts.

Contributed by the Applied Mechanics Division and presented at the Winter Annual Meeting, New Orleans, La., December 9–14, of THE AMERICAN SOCIETY OF MECHANICAL ENGINEERS.

Discussion on this paper should be addressed to the Editorial Department, ASME, United Engineering Center, 345 East 47th Street, New York, N.Y. 10017, and will be accepted until two months after final publication of the paper itself in the JOURNAL OF APPLIED MECHANICS. Manuscript received by ASME Applied Mechanics Division, October, 1983; final revision, February, 1984. Paper No. 84-WA/APM-25.

Copies will be available until August, 1985.

Solution and Reduction Procedures

Available Methods. If there are m constraint equations of the form of equations (2), the constrained multibody system will have $n-m$ degrees of freedom. One approach is to reduce equations (1) and (2) to a consistent set of $n-m$ equations and solve equations (2) for m, say the last m, of the $\dot{x}_j$ in terms of the remaining $n-m$ $\dot{x}_j$ [20]. The velocities and angular velocities of the multibody system can then be expressed in terms of these $n-m$ $\dot{x}_j$. This in turn produces a reduced set of governing equations of the form:

$$\hat{a}_{ij}\ddot{x}_j=\hat{f}_i \quad (i,j=1,\ldots,n-m) \tag{3}$$

where the $\hat{a}_{ij}$ and the $\hat{f}_i$ are obtained from the a_{ij} and the f_i after the m $\dot{x}_j$ are replaced in equations (1).

This approach is particularly convenient for small systems. There are difficulties, however, in an automated formulation for large systems. Among these difficulties is the problem of obtaining a consistent solution of equations (2) for the m $\dot{x}_j$.

A variation of this approach is to consider equations (1) and (2) as a set of $m+n$ equations for the n x_j and m constraining force and torque components. However, this approach also has the difficulty of not being readily adapted to an automated formulation for large systems, in addition to having the disadvantage of increasing the number of equations to be solved.

A *second* approach to reducing equations (1) and (2) based on an ingenious matrix procedure discussed by Hemami and Weimer [21][1]: equations (1) and (2) are written in the matrix form:

$$A\ddot{x}=f \quad \text{and} \quad B\dot{x}=g \tag{4}$$

where A is an $n\times n$ symmetric matrix, B is an $m\times n$ matrix, and $\ddot{x}$, $\dot{x}$, and f are $n\times 1$ column arrays. The procedure is then to obtain the "orthogonal complement" C of B (an $n\times m$ matrix of rank $n-m$ such that $BC=0$), and to premultiply the dynamics equation by C^T, the transpose of C. The governing equations are then:

$$C^TA\ddot{x}=C^Tf \qquad \text{and} \qquad B\dot{x}=g \tag{5}$$

Compared with the other approaches, this method is better suited for an automated formulation for large systems. Also, since $BC=0$, it can be shown that the constraining force and torque components are eliminated from the ensuing equations. As noted in [21], however, the orthogonal complement matrix C is not unique. Also, in the absence of a formal construction procedure, C could be difficult to obtain – especially for large systems.

A *third* approach is to combine the foregoing two approaches. It is found that this can be done in such a way that the computational difficulties are avoided while the computational advantages are retained. The procedure, which is based on the zero-eigenvalues therorem as recorded by Walton and Steeves [23], is outlined in the following paragraphs.

Zero-Eigenvalues Theorem. Let E be the $n\times n$ matrix B^TB. Then the rank of E is less than or equal to m since from equation (2), the rank of B is less than or equal to m. Hence, the eigenvalue equation $Ey=\lambda y$ has at least $n-m$ zero-eigenvalues. Let y^r $(r=1,\ldots,s)$ be the independent eigenvectors associated with these zero-eigenvalues, where $s \geq n-m$. Let T be the $n\times s$ matrix whose columns are y^r. Then

$$ET=B^TBT=0 \tag{6}$$

By premultiplying by T^T, it is seen that

$$T^TB^TBT=0 \qquad \text{or} \qquad (BT)^T(BT)=0 \qquad \text{or} \qquad BT=0 \tag{7}$$

[1] A similar approach is also presented in [22].

Therefore, T is an orthogonal complement of B. Finally, let the $\dot{x}_j$ $(j=1,\ldots,n)$ be expressed in terms of s independent "generalized speeds" z_r $(r=1,\ldots,s)$ through the relation

$$\dot{x}=Tz \qquad \text{or} \qquad \dot{x}_j=t_{jr}z_r \tag{8}$$

where z is the column array whose elements are z_r and t_{jr} are the elements of T. Equations (8) may now be used to reduce equations (1) in a manner similar to that of equations (5).

Application: Kane's Equations

Kinematics. An ideal procedure for developing equations (1) is to use Kane's dynamical equations [14, 24–27]. In this procedure, the angular velocities of the bodies of the system and the velocities of their mass centers are written in the form:

$$\boldsymbol{\omega}_k=\omega_{kjs}\dot{x}_j\mathbf{n}_s \qquad \text{and} \qquad \mathbf{v}_k=v_{kjs}\dot{x}_j\mathbf{n}_s \tag{9}$$
$$(k=1,\ldots,N;\, j=1,\ldots,n;\, s=1,2,3)$$

where $\mathbf{n}_s$ are mutually perpendicular unit vectors fixed in a convenient reference frame – usually an inertial reference frame, and, as before, there is a sum over the range of the repeated indices. The coefficients ω_{kjs} and v_{kjks} are the scalar components of the "partial angular velocity" and "partial velocity" vectors: $\partial\boldsymbol{\omega}_k/\partial\dot{x}_j$ and $\partial\mathbf{v}_k/\partial\dot{x}_j$. They are functions of x_j and their functional form depends on the connection configuration of the bodies of the system [10].

By differentiation of equations (9), the angular accelerations of the bodies and the accelerations of their mass centers may be expressed as:

$$\boldsymbol{\alpha}_k=(\dot{\omega}_{kjs}\dot{x}_j+\omega_{kjs}\ddot{x}_j)\mathbf{n}_s \quad \text{and} \quad \mathbf{a}_k=(\dot{v}_{kjs}\dot{x}_j+v_{kjs}\ddot{x}_j)\mathbf{n}_s \tag{10}$$

Kinetics. If the system is subjected to known externally applied forces (for example, gravity or contact forces), they may be represented, on a typical body B_k, by a single force $\mathbf{F}_k$ passing through the mass center together with a couple with torque $\mathbf{M}_k$. Then the generalized active force F_j associated with $\dot{x}_j$ is [10, 25]:

$$F_j=v_{kjs}F_{ks}+\omega_{kjs}M_{ks} \tag{11}$$

where F_{ks} and M_{ks} are the $\mathbf{n}_s$ components of $\mathbf{F}_k$ and $\mathbf{M}_k$ and where there is a sum from 1 to N on k and from 1 to 3 on s.

Similarly, let the inertia force system on B_k be represented by the single force $\mathbf{F}_k{}^*$ passing through the mass center together with a couple with torque $\mathbf{M}_k{}^*$. Then $\mathbf{F}_k{}^*$ and $\mathbf{M}_k{}^*$ may be expressed as:

$$\mathbf{F}_k{}^*=-m_k\mathbf{a}_k \qquad \text{(no sum)} \tag{12}$$

and

$$\mathbf{M}_k{}^*=-\mathbf{I}_k\cdot\boldsymbol{\alpha}_k-\boldsymbol{\omega}_kX(\mathbf{I}_k\cdot\boldsymbol{\omega}_k) \qquad \text{(no sum)} \tag{13}$$

where m_k is the mass of B_k and $\mathbf{I}_k$ is the inertia dyadic of B_k relative to its mass center.

The generalized inertia force $F_j{}^*$ associated with $\dot{x}_j$ is [10, 25]:

$$F_j{}^*=v_{kjs}F_{ks}{}^*+\omega_{kjs}M_{ks}{}^* \tag{14}$$

where $F_{ks}{}^*$ and $M_{ks}{}^*$ are the n_s components of $\mathbf{F}_k{}^*$ and $\mathbf{M}_k{}^*$ and where there is a sum over the repeated indices.

Governing Equations. Kane's dynamical equations of motion (some-times called Lagrange's form of d'Alembert's principle) [25] are then:

$$F_j+F_j{}^*=0 \quad (j=1,\ldots,n) \tag{15}$$

By substituting from equations (9)–(14), equations (1) are obtained where a_{ij} and f_i are

$$a_{ij}=m_kv_{kis}v_{kjs}+I_{ksq}\omega_{kis}\omega_{kjq} \tag{16}$$

and

$$f_i=F_i-(m_kv_{kis}\dot{v}_{kus}\dot{x}_u+I_{ksh}\omega_{kis}\omega_{kuh}\dot{x}_u$$
$$+e_{wsh}I_{ksr}\omega_{kuw}\omega_{kvr}\omega_{kih}\dot{x}_u\dot{x}_v) \tag{17}$$

where I_{ksh} are the $\mathbf{n}_s$ and $\mathbf{n}_h$ components of $\mathbf{I}_k$, e_{wsh} is the permutation symbol, and there is a sum over repeated indices.

Constraint Equations. Equations (1) together with equations (16) and (17) represent the governing dynamical equations for *open*-chain systems. However, if the system has closed loops or specified motion of some of its members, equations (1) are no longer valid. Instead, there are constraint equations in the form of equations (2) which need to be satisfied to insure that the loops and specified motions are maintained during the motion of the system. For the loops, these constraint equations are *holonomic* [25] and they may be written in the form:

$$h_i(x_j)=0 \qquad (i=1,\ldots,p;j=1,\ldots,n) \tag{18}$$

where p is the number of constraint equations due to the loops, n is the number of degrees of freedom of the unconstrained system, and $p<n$. (These equations may be obtained by simply adding to zero the relative position vectors of the connecting joints around the respective loops.) By differentiating, equations (18) become linear relations in the $\dot{x}_j$ and they may be expressed as:

$$b_{ij}\dot{x}_j=0 \quad (i=1,\ldots,p;j=1,\ldots,n) \tag{19}$$

where the b_{ij} are, in general, functions of x_j and t.

For specified motion, the constraint equations take the form:

$$b_{ij}\dot{x}_j=g_i \quad (i=1,\ldots,q;j=1,\ldots,n) \tag{20}$$

where q is the number of constraint equations due to the specified motion, n is the number of degrees of freedom, and $q<n$. To illustrate these equations, suppose a point P of a typical body B_k has a prescribed velocity, say $\mathbf{v}(t)$. Then let $\mathbf{v}(t)$ be expressed in the form of equations (4). That is, let

$$\mathbf{v}(t)=v_s(t)\mathbf{n}_s=v_{Pjs}\dot{x}_j\mathbf{n}_s \tag{21}$$

where $v_s(t)$ ($s=1, 2, 3$) are the $\mathbf{n}_s$ projections of $\mathbf{v}$. The constraint equations are then simply:

$$v_{Pji}\dot{x}_i(t)=v_i(t) \qquad (i=1,2,3;j=1,\ldots,n) \tag{22}$$

Similarly, suppose the angular velocity of typical body B_k is prescribed as $\mathbf{\Omega}(t)$. Then, from equations (9), the constraint equations take the form:

$$\omega_{kji}\dot{x}_j=\Omega_i(t) \quad (i=1,2,3;j=1,\ldots,n) \tag{23}$$

where $\Omega_i(t)$ are the $\mathbf{n}_i$ projections of $\mathbf{\Omega}(t)$. Equations (22) and (23) are thus of the form of equations (20).

Although the loop constraints in equations (18) are holonomic, the specified motion constraints as in equations (22) and (23) are, in general, *nonholonomic*. However, this does not present any difficulty since in references [24] and [25] it is shown that equations (15) may be applied with both holonomic and nonholonomic systems.

For the loops, the constraint *forces* are "internal," and as such, they do not contribute to the generalized active forces of equations (11) (see [25]). However, the constraint forces required to give points or bodies of the system a prescribed motion, may indeed contribute to the generalized forces. For example, if the force system required to give typical body B_k an angular velocity $\mathbf{\Omega}(t)$ and point P a velocity $\mathbf{v}(t)$, is equivalent to a force $\mathbf{P}$ passing through P together with a couple with torque $\mathbf{T}$ applied to B_k, then from equations (11), (22), and (23), the contribution of $\mathbf{P}$ and $\mathbf{T}$ to the generalized active force F_j is:

$$\text{Contribution to } F_j\text{:} \quad v_{Pjs}P_s+\omega_{kjs}T_s \tag{24}$$

where P_s and T_s are the $\mathbf{n}_s$ components of $\mathbf{P}$ and $\mathbf{T}$.

Reduced Governing Equations. Using equations (8) the reduced governing equations are then obtained as follows: The velocity and angular velocity vectors of equations (9) may be written as:

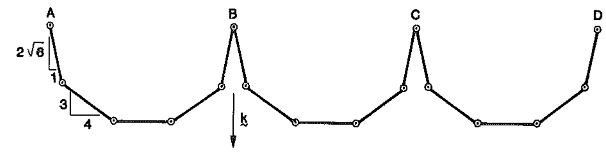

Fig. 1 Initial configuration of 15-link chain

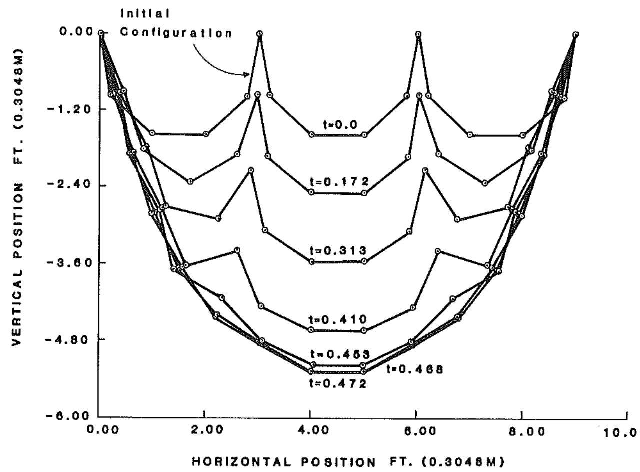

Fig. 2 Chain configuration after release

$$\omega_k=\omega_{kjp}t_{jr}z_r\mathbf{n}_p \qquad \text{and} \qquad \mathbf{v}_k=v_{kjp}t_{jr}z_r\mathbf{n}_p \tag{25}$$

$$(k=1,\ldots,N;j=1,\ldots,n;$$
$$p=1,2,3;r=1,\ldots,s\geq n-m)$$

The generalized active and inertia forces then take the reduced forms

$$\hat{F}_r=v_{kjp}t_{jr}F_{kp}+\omega_{kjp}t_{jr}M_{kp}=F_jt_{jr} \tag{26}$$

and

$$\hat{F}_r^*=v_{kjp}t_{jr}F_{kp}^*+\omega_{kjp}t_{jr}M_{kp}^*=F_j^*t_{jr} \tag{27}$$

Notice that in view of equations (22), (23), (24), and (7), the constraining force and torque components associated with the specified motion do not contribute to the $\hat{F}_r$.

Finally, the governing dynamical equations become

$$a_{ij}t_{ir}\ddot{x}_j=f_it_{ir} \quad (r=1,\ldots,s;i,j=1,\ldots,n)$$

or

$$T^TA\ddot{x}=T^Tf \tag{28}$$

where the a_{ij} and f_i are given by equations (16) and (17) and are the elements of the $n\times n$ matrix A and $n\times 1$ column vector f, respectively. These equations, together with the constraint equations (2), govern the motion of the multibody system.

Computer Methods. This approach, together with the procedures used to develop equations (16), (17), and (28), are ideally suited for the preparation of computer algorithms for their numerical computation and solution. Development of these algorithms might proceed as outlined in reference [10]: First, let the physical and geometrical parameters (masses, inertias, mass center locations, connection joint locations) of the bodies of the system be read into the computer. Next, let a "lower numbered body array" [10], defining the connection configuration of the system, be created. This array, together with initial values of the dependent variables x_j, can then be used to develop transformation matrices as well as the arrays v_{kjp}, $\dot{v}_{kjp}$, ω_{kjp}, $\dot{\omega}_{kjp}$ and b_{ij}. By using equations (16) and (17), together with information on the specified motion, the arrays a_{ij}, f_i, and g_i can then be evaluated. By knowing b_{ij}, a standard eigenvalue subroutine can be used to assemble the t_{ij}

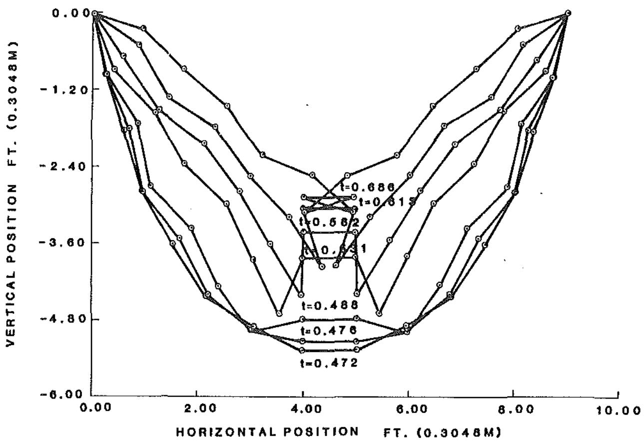

Fig. 3 Chain configuration after rebound

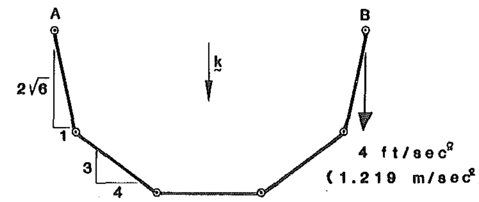

Fig. 4 Initial Configuration of five-link chain

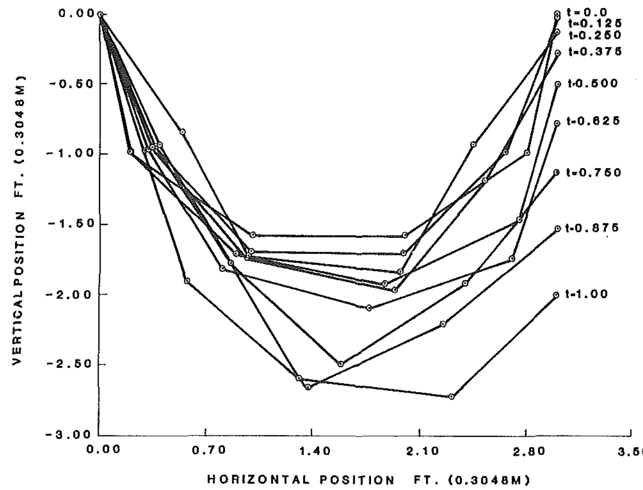

Fig. 5 Chain configuration with specified end motion

array. Finally, the governing differential equation coefficients can be computed from equations (28). These equations, together with the constraint equations, may then be numerically integrated to obtain incremental values in the dependent variables. The process may then be repeated until a history of the configuration and motion of the system is obtained.

Specific computer algorithms for generating and solving the governing equations have been written by using this general procedure. These algorithms have been assembled into a computer code applicable to a broad class of constrained multibody systems. Information about the code can be obtained from the authors.

Examples

To illustrate these procedures, a chain consisting of 15 pin-connected links was placed in the configuration shown in Fig. 1. The links were identical rods having a length of 1 ft (0.3048m). The system was then placed in a gravity field directed along a unit vector k, with support points A, B, C, and D as shown in Fig. 1. (The support points were spaced at 3 ft (0.914m) intervals[2].) Points B and C were then released while A and D were held fixed. Using the computer algorithms previously described, the ensuing motion of the system was numerically determined. Figures 2 and 3 show the system configuration at various times after release, as it drops and rebounds.

To validate these results, the governing equations were also solved using the first of the reduction methods described in the foregoing – that is, by manually solving the constraint equations for two of the dependent variable derivatives and then forming a reduced set of governing equations. The results for both methods were identical.

As a second example, and as an example illustrating prescribed motion, a system of five pin-connected links was placed in the configuration shown in Fig. 4. As before, the links were identical 1-ft rods. The system was then placed in a gravity field in the **k** direction and point B was given a constant acceleration of a 4 ft/sec^2 (1.219/sec^2) in the **k** direction, while end A remained fixed as depicted in Fig. 4. The ensuing motion of the system was then numerically determined using the computer algorithms described in the foregoing. Figure 5 shows the system configuration at various times. As before, the results checked identically with those obtained by the variable elimination method.

Discussion

A principal computational advantage of the developed procedure is that the orthogonal complement array is obtained automatically through using the eigenvectors of zero eigenvalues of the equation $Ey = \lambda y$. Moreover, these eigenvectors can be obtained efficiently through standard algorithms for determining eigenvalues and eigenvectors.

A beneficial consequence of the procedure is that the constraining forces are automatically eliminated from the governing equations. Also, the procedure automatically leads to a set of independent generalized speeds z_r ($r = 1, \ldots, n - m$). Interestingly, these generalized speeds do not appear in the final set of governing equations. Instead, they are eliminated in the formation of the reduced generalized forces of equations (26) and (27) through use of the reduced partial velocity and partial angular velocity vectors obtained from equations (25). Indeed, these reduced partial velocity and partial angular velocity vectors may be viewed as *base vectors* in the r-dimensional space characterized by the z array.

In this context, the columns of T are seen to be orthogonal to the rows of B, the constraint array. Hence, in the n-dimensional space characterized by the x array, let the rows of B be considered as "constraint vectors." Then through the t_{jr} in equations (28) the motion of the multibody system is constrained to directions orthogonal to these constraint vectors. Moreover, the final dynamical equations themselves may be obtained from the original dynamical equations (1) by simply taking the inner product with t_{jr} – a procedure which is valid when equations (1) are in the form obtained through use of Kane's equations.

Acknowledgment

Support for this research was partially provided by the Office of Naval Research under Contract N00014-76C-0139 and by the National Science Foundation under Grant MEA810-11110. The authors also acknowledge helpful comments of the reviewers of this and an earlier version of the paper. Finally, the authors appreciate the assistance of Mr. Timothy King in preparing the figures.

[2] *Note that the configuration shown in Fig. 1 is not a static equilibrium configuration.*

References

1 Bayazitoglu, Y. A., and Chace, M. A., "Methods of Automated Dynamic Analysis of Discrete Mechanical Systems," ASME JOURNAL OF APPLIED MECHANICS, Vol. 40, 1973, pp. 809–819.

2 Chace, M. A., "Analysis of the Time Dependence of Multifreedom Mechanical Systems in Relative Coordinates," ASME JOURNAL OF ENGINEERING FOR INDUSTRY, Vol. 89, 1967, pp. 119–125.

3 Chace, M. A., and Bayazitoglu, Y. O., "Development and Application of a Generalized d'Alembert Force for Multifreedom Mechanical Systems," ASME *Journal of Engineering for Industry*, Vol. 93, 1971, pp. 317–327.

4 Gupta, V. K., "Dynamic Analysis of Multigrid-Body Systems," ASME *Journal of Engineering for Industry*, Vol. 96, 1974, pp. 886–892.

5 Hollerback, J. M., "A Recursive Lagrangian Formulation of Manipulator Dynamics and a Comparative Study of Dynamics Formulation Complexity," *IEEE Transactions, Systems, Man, and Cybernetics*, Vol. SMC-10, 1980, pp. 730–736.

6 Hooker, W. W., and Margulies, G., "The Dynamical Attitude Equations for an *n*-Body Satellite," *Journal of the Astronautical Sciences*, Vol. 12, 1965, pp. 123–128.

7 Hooker, W. W., "A Set of *r* Dynamical Attitude Equations for an Arbitrary *n*-Body Satellite Having *r* Rotational Degrees of Freedom," *AIAA Journal*, Vol. 8, 1970, pp. 1205–1207.

8 Hooker, W. W., "Equations of Motion for Interconnected Rigid and Elastic Bodies," *Celestial Mechanics*, Vol. 11, 1975, pp. 337–359.

9 Huston, R. L., and Passerello, C. E., "On the Dynamics of Chain Systems," ASME Paper No. 74-WA/Aut 11, 1974.

10 Huston, R. L., Passerello, C. E., and Harlow, M. W., "Dynamics of Multi-Rigid-Body Systems," ASME JOURNAL OF APPLIED MECHANICS, Vol. 45, 1978, pp. 889–894.

11 Huston, R. L., and Passerello, C. E., "On Multi-Rigid-Body System Dynamics," *Computers and Structures*, Vol. 10, 1979, pp. 439–446.

12 Huston, R. L., and Passerello, C. E., "Multibody Structural Dynamics Including Translation Between the Bodies," *Computers and Structures*, Vol. 12, 1980, pp. 713–720.

13 Jerkovsky, W., "The Transformation Operator Approach to Multisystems Dynamics, Part I: The General Approach," *Matrix and Tensor Quarterly*, Vol. 27, 1976, pp. 48–59.

14 Kane, T. R., and Levinson, D. A., "Formulation of Equations of Motion for Complex Spacecraft," *Journal of Guidance and Control*, Vol. 3, 1980, pp. 99–112.

15 Orin, D. E., McGhee, R. B., Vukobratovic, M., and Hartoch, G., "Kinematic and Kinetic Analysis of Open-Chain Linkages Utilizing Newton-Euler Methods," *Mathematical Biosciences*, Vol. 43, 1979, pp. 107–130.

16 Stepanenko, Y., and Vukobratovic, M., "Dynamics of Articulated Open Chain Active Mechanisms," *Mathematical Biosciences*, Vol. 28, 1976, pp. 137–170.

17 Uicker, J. J., Jr., "Dynamical Behavior of Spatial Linkages," ASME *Journal of Engineering for Industry*, Vol. 91, 1969, pp. 251–265.

18 Vukobratovic, M., "Computer Method for Dynamic Model Construction of Active Articulated Mechanisms Using Kinetostatic Approach," *Mechanism and Machine Theory*, Vol. 13, 1978, pp. 19–39.

19 Wittenburg, J., *Dynamics of Systems of Rigid Bodies*, B. G. Teubner, Stuttgart, 1977.

20 Passerello, C. E., and Huston, R. L., "Another Look at Nonholonomic Systems," ASME JOURNAL OF APPLIED MECHANICS, Vol. 40, 1973, pp. 101–104.

21 Hemami, H., and Weimer, F. C., "Modeling of Nonholonomic Dynamic Systems With Applications," ASME JOURNAL OF APPLIED MECHANICS, Vol. 48, 1981, p. 177.

22 Huston, R. L., and Passerello, C. E., "On Constraint Equations—A New Approach," ASME JOURNAL OF APPLIED MECHANICS, Vol. 41, 1974, pp. 1130–1131.

23 Walton, W. C., Jr., and Steeves, E. C., "A New Matrix Theorem and Its Application for Establishing Independent Coordinates for Complex Dynamical Systems With Constraints," NASA Technical Report TR R-326, 1969.

24 Kane, T. R., "Dynamics of Nonholonomic Systems," ASME JOURNAL OF APPLIED MECHANICS, Vol. 28, 1961, pp. 574–578.

25 Kane, T. R., *Dynamics*, Holt, Rinehart, and Winston, New York, 1968.

26 Kane, T. R., Likins, P. W., and Levinson, D. A., *Spacecraft Dynamics*, McGraw-Hill, New York, 1982.

27 Huston, R. L., and Passerello, C. E., "On Lagrange's Form of d'Alembert's Principle," *Matrix and Tensor Quarterly*, Vol. 23, 1973, pp. 109–112.

J. A. Brandon[1]
Research Student,
Manufacturing and Machine Tools Division,
Department of Mechanical Engineering,
UMIST, Manchester,
Manchester, England
Assoc. Mem. ASME

A Discussion of Alternative Duncan Formulations of the Eigenproblem for the Solution of Nonclassically, Viscously Damped Linear Systems

An equivalent alternative formulation of the usual Duncan Method of solution of a system of general viscous damping is discussed. For the solution of systems this alternative statement of the problem is no better and is in fact potentially inferior to the standard method. A potentially important application however removes a significant limitation in the implementation of the local modification procedures of Weissenburger and Pomazal.

Introduction

The anaysis of damped linear systems was facilitated by Lord Rayleigh [1] by assuming that the distribution of damping within a structure takes the same form as either the distribution of mass or stiffness (or a linear combination of both). Proportional damping as used by Rayleigh was shown to be a special case of a move general "classical damping" by Caughey [2]. The classical damping assumption is applicable to a large range of structural applications where it provides significant computational attractions. There are however large classes of problems where such models are unacceptable and alternative methods of analysis are necessary.

The method due to Duncan (Frazer et al. [3]) involves the augmentation of an $n \times n$ quadratic eigenproblem with a trivial identity to give a simpler $2n \times 2n$ linear eigenproblem. Although it will be shown that there are two possible identities that may be adjoined, one has been almost totally predominant in the literature. The alternative augmentation is considered here, which in general is less useful, but has a potentially important application. This method has been used recently by Meirovitch [4] but without any comparison.

[1] Current affiliation: Lecturer in Manufacturing Systems, Department of Mechanical Engineering and Engineering Production, University of Wales Institute of Science and Technology, Cardiff, CF1 3XE Wales.

Contributed by the Applied Mechanics Division and presented at the Winter Annual Meeting, New Orleans, La., December 9–14, 1984 of THE AMERICAN SOCIETY OF MECHANICAL ENGINEERS.

Discussions on this paper should be addressed to the Editorial Department, ASME, United Engineering Center, 345 East 47th Street, New York, N.Y. 10017, and will be accepted until two months after final publication of the paper itself in the JOURNAL OF APPLIED MECHANICS. Manuscript received by ASME Applied Mechanics Division, November, 1982; final revision, January, 1984. Paper No. 84-WA/APM-23.

Copies will be available until August, 1985.

Classical Damping

The behavior of an n degree-of-freedom, viscously damped, linear system may be represented by the equation

$$\mathbf{M}\ddot{x} + \mathbf{C}\dot{x} + \mathbf{K}x = f(t) \tag{1}$$

where

$\mathbf{M}$ is $n \times n$ positive definite symmetric.
$\mathbf{K}$,$\mathbf{C}$, non-negative definite symmetric,
$\mathbf{x}$ displacement vector,
$f(t)$ vector of applied forces.

The modal method of analyzing (1) requires transformation of the homogeneous form of (1) to the frequency domain to give the eigenproblem

$$(\mathbf{M}\lambda^2 + \mathbf{C}\lambda + \mathbf{K})x = \mathbf{0} \tag{2}$$

The common assumption of Classical Damping allows the solution of (2) to be directly related to the solution of the corresponding conservative problem:

$$(\mu\mathbf{M} + \mathbf{K})x = \mathbf{0} \tag{3}$$

The eigenvalues of (3) are all negative unless $\mathbf{K}$ is singular when some may be zero. The eigenvectors are real and (even for equal eigenvalues (Bishop et al. [5])) give the orthogonality relation:

$$\phi_r^T\mathbf{K}\ \ \phi_s = \phi_r{}^T\mathbf{M}\ \ \phi_s = \mathbf{0} \tag{4}$$

If we now form the modal matrix

$$\Phi = \{\phi, \ldots\ldots \phi_n\} \tag{5}$$

Then this matrix may be used to give a coordinate transformation which uncouples (3) into n independent single-degree-of-freedom systems:

$$x = \Phi q \tag{6}$$

$$\mathbf{m} = \Phi^T\mathbf{M}\ \ \Phi = \text{diag}\ \{m_i\} \tag{7}$$

$$\kappa = \Phi^T \mathbf{K} \ \Phi = \text{diag}\{\kappa_i\} \tag{8}$$

This gives

$$(\mu\mathbf{m} + \kappa)q = \mathbf{0} \tag{9}$$

The damped system (3) is classical if

$$\Phi^T \mathbf{C} \ \Phi = \mathbf{c} = \text{diag}\{c_i\} \tag{10}$$

The necessary and sufficient condition was provided by Caughey and O'Kelly [6].

$$\mathbf{K} \ \mathbf{M}^{-1}\mathbf{C} = \mathbf{C} \ \mathbf{M}^{-1}\mathbf{K} \tag{11}$$

The most usual form of classical damping is proportional damping

$$\mathbf{C} = \alpha\mathbf{M} + \beta \ \mathbf{K} \tag{12}$$

It can be seen that analogous to (9) we are able to uncouple the system of equations (3) to give

$$\text{diag}\{\lambda^2 m_i + \lambda c_i + \kappa_i\}q = \mathbf{0} \tag{13}$$

which is again resolved into n independent single-degree-of-freedom systems. The eigenvectors are identical to the original problem (3) and eigenvalues occur in complex pairs.

Nonclassical Damping

If the $\mathbf{C}$ matrix fails to satisfy (11) then there is not in general a coordinate transformation of the initial eigenproblem (2) to the diagonal (uncoupled) eigenproblem (13). The widely used method generally attributed to Duncan adjoins the trivial identity:

$$\mathbf{M} \ \dot{x} - \mathbf{M}\dot{x} = \mathbf{0} \tag{14}$$

to the system in (1) giving

$$\begin{pmatrix} \mathbf{0} & \mathbf{M} \\ \mathbf{M} & \mathbf{C} \end{pmatrix} \begin{pmatrix} \ddot{x} \\ x \end{pmatrix} + \begin{pmatrix} -\mathbf{M} & \mathbf{0} \\ & \mathbf{0} \ \mathbf{K} \end{pmatrix} \begin{pmatrix} \ddot{x} \\ x \end{pmatrix} = \begin{pmatrix} \mathbf{0} \\ f(t) \end{pmatrix} \tag{15}$$

writing

$$\mathbf{A} = \begin{pmatrix} \mathbf{0} & \mathbf{M} \\ \mathbf{M} & \mathbf{C} \end{pmatrix}, \quad \mathbf{B} = \begin{pmatrix} -\mathbf{M} & \mathbf{0} \\ \mathbf{0} & \mathbf{K} \end{pmatrix} \quad \mathbf{y} = \begin{pmatrix} \dot{x} \\ x \end{pmatrix}$$

transforms the homogeneous form of (15) to the eigenproblem

$$\lambda\mathbf{A}y + \mathbf{B}y = 0 \tag{16}$$

Both the eigenvalues and eigenvectors of (16) will now be complex in conjugate pairs. Although the form of (16) duplicates that of (3) it has lost sign definiteness from both $\mathbf{B}$ and $\mathbf{A}$. In addition to having complex eigenvectors, it may be that the eigensystem is defective, i.e., there may not be a complete set of eigenvectors. (This can occur only when repeated eigenvalues are found.) The theoretical implications of such cases are however beyond the scope of this paper. They are however covered thoroughly in standard texts in linear algebra (e.g., Noble [7]).

As an alternative augmentation to the original eigenproblem (2) consider now a further trivial identity:

$$\mathbf{K}\dot{x} - \mathbf{K}\dot{x} = \mathbf{0} \tag{17}$$

Adjoining this to (1) gives

$$\begin{pmatrix} \mathbf{M} & \mathbf{0} \\ \mathbf{0} & -\mathbf{K} \end{pmatrix} \begin{pmatrix} \ddot{x} \\ \dot{x} \end{pmatrix} + \begin{pmatrix} \mathbf{C} & \mathbf{K} \\ \mathbf{K} & \mathbf{0} \end{pmatrix} \begin{pmatrix} \ddot{x} \\ x \end{pmatrix} = \begin{pmatrix} f(t) \\ \mathbf{0} \end{pmatrix} \tag{18}$$

Defining

$$\mathbf{P} = \begin{pmatrix} \mathbf{M} & \mathbf{0} \\ \mathbf{0} & -\mathbf{K} \end{pmatrix}, \quad \mathbf{Q} = \begin{pmatrix} \mathbf{C} & \mathbf{K} \\ \mathbf{K} & \mathbf{0} \end{pmatrix}$$

and using the homogeneous form of the eigenproblem:

$$(\lambda \ \mathbf{P} + \mathbf{Q})y = \mathbf{0} \tag{19}$$

Because equations (16) and (19) represent the same physical problem, the same eigenvectors and eigenvalues must be common to the two problems. Thus (19) apparently provides an equally good method of solving (1).

We may however perceive a reason for the choice of (16) rather than (19) that is something more than arbitrary. Considering the relatively comon case when $\mathbf{K}$ is singular then:

$$\mathbf{P}, \mathbf{Q}, \text{ and } \mathbf{B} \text{ are all singular,}$$

only $\mathbf{A}$ is nonsingular. Consequently only (16) may be converted to a standard eigenproblem (by Choleski factorization for example.)

If given the choice between an eigenproblem with at least one nonsingular matrix and one where neither is guaranteed the prudent analyst will choose the former. This will decrease (but not eliminate entirely) some of the computational problems associated with singular stiffness matrices. Thus in the absence of any demonstrable advantages of the alternative formulation the historical development is vindicated. It will however be shown that the alternative formulation has significant advantages in some local modification problems.

Local Modification Methods of Weissenburger and Pomazal

Consider the conservative eigenproblem (3). Let it be assumed that a full set of eigenvalues λ_i are known such that

$$\lambda_1 \leq \lambda_2 \leq . \ . \ . \ . \ .\lambda_n$$

and the corresponding eigenvectors ϕ_i. By suitable scaling of eigenvectors it is possible to perform the coordinate transformation (6), (7), and (8) to transform the $\mathbf{M}$ and $\mathbf{K}$ matrices to

$$\mathbf{m} = \text{diag}\left\{\frac{1}{\lambda_i}\right\} \tag{20}$$

$$\mathbf{k} = \quad \mathbf{I} \qquad \text{(identity)} \tag{21}$$

Consider now a mass modification Δm at the ith coordinate. Now the new mass matrix is given by

$$\mathbf{M}' = \mathbf{M} + \Delta m \ \ \mathbf{e}_i\mathbf{e}_i^T \quad (e_i \text{ unit vector}) \tag{22}$$

and the new mass matrix in transformed (normal) coordinates

$$\mathbf{m}' = \mathbf{m} + \Delta m \ \ r_i^T r_i = \mathbf{m} + \boldsymbol{\delta}\mathbf{m} \tag{23}$$

where r_i is the ith row of Φ defined in (5).

We may write the modified system as

$$(\mathbf{m}' + \nu \ \ \kappa)q = \mathbf{0} \tag{24}$$

where $\nu_i = -1/\omega_i^2$ where ω_i is a natural frequency of the modified system.

We may solve (24) as a straightforward eigenproblem, but the analysis of Weissenburger [8, 9] shows how to exploit the structure of the modification matrix $\boldsymbol{\delta}\mathbf{m}$. By his method the relationship between the eigenvalues and eigenvectors of the modified system and the original eigenproperties is derived explicitly. This is potentially valuable information in understanding the behavior of the system. (Weissenburger also applied similar analysis to stiffness modifications.)

Weissenburger transforms the eigenproblem (24) to an alternative problem:

$$\sum_{\kappa=1}^{n} \frac{r_{i,\alpha}}{(\nu - \mu_\kappa)} - \frac{1}{\delta m} = 0 \tag{25}$$

where $r_{i,\kappa}$ is the κth element of r_i. The n eigenvalues of (25) may now be found using a Newton-Raphson method, again exploiting the relation to the structure of the original problem.

The eigenvectors of (24) may be found using

$$q_{j,k} = \frac{\beta_j r_{i,\kappa}}{\nu_j - \mu_\kappa} \tag{26}$$

where $q_{j,\kappa}$ is the kth element of the jth eigenvector of (24); β may be any suitable eigenvector normalization coefficient. The terms of q_j are the coefficients of the eigenvectors of the original problem and hence we have the required relationship between the initial and final solution.

The work of Weissenburger on conservative systems was extended to systems with both classical and more general forms of viscous damping by Pomazal [10, 11]. Since a modification to a classically damped system is likely to result in a nonclassically damped system it is necessary to use a Duncan form of (23).

The Duncan form used by Pomazal is (15) the formulation that appears to be used almost exclusively in the literature. Bearing in mind the proviso concerning equal roots (a subject covered exhaustively in the text) the incorporation of stiffness of damping modifiations follows that of Weissenburger since a stiffness modification Δk at the ith coordinate may be incorporated into $\mathbf{B}$ in the form:

$$\delta\mathbf{B} = \Delta k \ \mathbf{e}_{n+i}\mathbf{e}_{n+1}{}^{T} \tag{27}$$

and a damping modification Δc at the ith coordinate may be incorporate into $\mathbf{A}$ in the form:

$$\delta\mathbf{A} = \Delta c \ \mathbf{e}_{n+i}\mathbf{e}^{T}{}_{n+1} \tag{28}$$

Thus a stiffness or damping modiciation results in a form that may be treated in the same way as the analysis provided by Weissenburger for the conservative case.

Consider now a mass modification Δm at the ith coordinate. This will modify $\mathbf{A}$ by

$$\delta\mathbf{A} = \Delta m\,(\mathbf{e}_{n+i}\mathbf{e}_i^T + \mathbf{e}_i\mathbf{e}_{n+i}{}^{T}) \tag{29}$$

and will also modify $\mathbf{B}$ by

$$\delta\mathbf{B} = \Delta m \ \mathbf{e}_i\mathbf{e}_i^T \tag{30}$$

It is now no longer possible to apply Weissenbuger's procedure although Pomazal suggests that it may be implemented in three stages. In doing this he observes however that the computational advantage of applying Weissenburger's procedure will be lost.

From a practical viewpoint the variation of mass in a structure is usually more straigtforward to implement than either stiffness or damping changes. Thus the increases computational effort for mass changes was acknowledged by Pomazal to be a serious limitation of the method.

Consider now the effect of a mass change on the alternative formulation of the Duncan form (19):

$$(\lambda P + \mathbf{Q})Y = \mathbf{0} \tag{31}$$

since the mass matrix $\mathbf{M}$ now occurs only once in the partitioned form of $\mathbf{P}$ the effect of a mass change Δm at the ith coordinate gives rise to $\delta\mathbf{P}$:

$$\delta\mathbf{P} = \Delta m \ \mathbf{e}_i\mathbf{e}_i^T \tag{32}$$

we may therefore reduce a mass modification to this formulation of the Duncan form to a standard Weissenburger problem. The mass modification now needs only one computational step for its incorporation, thus eliminating the limitation identified by Pomazal.

Conclusion

The alternative formulation of the Duncan transformation has some disadvantages over the standard formulation for solution of nonclassically viscously damped systems. If the solutions of such a system are known however use of the alternative form will overcome the (significant) limitations encountered by Pomazal in the analysis of mass modifications.

Acknowledgments

The author wishes to express his appreciation for the support and encouragement of his Supervisor Dr. A. Cowley. He is also grateful for the interest and assistance of Dr. I. Gladwell of the Mathematics Department of the University of Manchester. This work is part of a study program supported by the United Kingdom Science and Engineering Research Council.

References

1 Rayleigh, *The Theory of Sound*, Volume II, Dover, New York, 1945.

2 Caughey, T. K., "Classical Normal Modes in Damped Linear Systems," ASME JOURNAL OF APPLIED MECHANICS, Vol. 27, 1960, pp. 269–271.

3 Frazer, R. A., Duncan, W. J., and Collar, A. R., *Elementary Matrices*, C.U.P., 1946.

4 Meirovitch, L., *Computational Methods in Structural Dynamics*, Sijthoff and Nordhoff, 1980.

5 Bishop, R. E. D., Gladwell, G. M. L., and Michaelson, S., *The Matrix Analysis of Vibration*, C.U.P., 1965.

6 Caughey, T. K., and O'Kelly, M. E. J., "Classical Normal Modes in Damped Linear Dynamic Systems," ASME JOURNAL OF APPLIED MECHANICS, Vol. 32, 1965, pp. 583–588.

7 Noble, B., *Applied Linear Algebra*, Prentice-Hall, Englewood Cliffs, N.J., 1969.

8 Weissenburger, J. T., "The Effect of Local Modifications on the Eigenvalues and Eigenvectors of Linear Systems," Sc.D. Dissertation, Sever Institute, Washington University, St. Louis, Mo., 1966.

9 Weissenburger, J. T., "The Effect of Local Modifications on the Vibration Characteristics of Linear Systems," ASME JOURNAL OF APPLIED MECHANICS, Vol. 35, 1968, pp. 327–332.

10 Pomazal, R. J., "The Effect of Local Modifications on the Eigenvalues and Eigenvectors of Damped Linear Systems," Ph.D. Dissertation, Michigan Tech. University, 1969.

11 Pomazal, R. J., and Snyder, V. W., "Local Modifications of Damped Linear Systems," *A.I.A.A. J.*, Vol. 9, 1971, pp. 2216–2221.

G. P. Solomos
Structural Consultant,
Athens, Greece

P-T. D. Spanos
Professor,
Department of Civil Engineering and
Mechanical Engineering,
Rice University,
P.O. Box 1892
Houston, Texas 77251
Mem. ASME

Oscillator Response to Nonstationary Excitation

Analytical solutions are presented regarding probability density distributions of various response parameters of a lightly damped oscillator. The oscillator is subjected to a broad-band stochastic excitation which possesses a time-variant power spectrum. The analytical solutions are derived by utilizing appropriate Fokker-Planck equations which govern Markovian approximations of the response parameters considered. The reliability of the approximate analytical solution is tested by using pertinent data generated by a digital Monte Carlo study.

Introduction

In dealing with problems of linear random vibration, basically two approaches can be followed. In the first, the system response is expressed in terms of the system excitation by using a convolution integral. This representation leads to determinations of the statistical moments of the response but not to a *direct* determination of its probability density function. For this purpose appropriate theorems of the theory of probability must be considered. For example, the response of a linear system to Gaussian excitation, will be Gaussian, as well. This approach has been successfully applied to determine response statistics for both stationary and nonstationary excitations [1-6]. The second approach is applicable only if the response parameter considered is exactly or approximately, a Markovian process. In this case the backward and forward Kolmogorov equations can be used to deal with the problem of determining the probability density of the response parameter. However, the class of the Kolmogorov equations that is amenable to a general, nonstationary, exact solution is limited. Pertinent expressions have been obtained for linear single and multidegree-of-freedom systems excited by stationary white noise [7], and shot noise [8]. The method of separation of variables and eigenfunction expansion for the resulting eigenvalue problem is often used [9, 10]. For more realistic excitation models of several physical phenomena provided by nonstationary processes, the derivation of the exact solutions of Kolmogorov equation becomes a quite difficult task.

In this paper, it is shown that it is possible to derive reliable approximate analytical expressions for the time-dependent probability distributions of several response parameters of a randomly excited and lightly damped linear oscillator. The excitation is not necessarily Gaussian and possesses an arbitrary broad-band, time-variant power spectrum. This is accomplished by solving appropriate Fokker-Planck or backward Kolmogorov equations. Numerical simulations data are used to test the reliability of the developed analytical solutions.

Contributed by the Applied Mechanics Division and presented at the Winter Annual Meeting, New Orleans, La., December 9-10, 1984 of THE AMERICAN SOCIETY OF MECHANICAL ENGINEERS.

Discussion on this paper should be addressed to the Editorial Department, ASME, United Engineering Center, 345 East 47th Street, New York, N.Y., 10017, and will be accepted until two months after final publication of the paper itself in the JOURNAL OF APPLIED MECHANICS. Manuscript received by ASME Applied Mechanics Division, October, 1983; final revision, April, 1984. Paper No. 84-WA/APM-38.

Copies will be available until August, 1985.

Mathematical Formulation

Consider the motion of a single-degree-of-freedom linear oscillator with damping ratio denoted by ζ, and natural frequency denoted by ω_n

$$\ddot{x} + 2\zeta\omega_n\dot{x} + \omega_n^2 x = w(t). \tag{1}$$

The excitation $w(t)$ is a nonstationary, zero-mean, random process possessing a time-variant power spectrum $S_w(\omega,t)$. It is assumed that $S_w(\omega,t)$ is broad-band over the entire duration of the motion. It is known that $w(t)$ admits a spectral representation of the form [11]

$$w(t) = \int_{-\infty}^{\infty} A(\omega,t)\exp(i\omega t)dZ(\omega), \tag{2}$$

where $A(\omega,t)$ is a function of time and frequency, slowly varying with time. The symbol $Z(\omega)$ represents a random process with orthogonal increments, that is,

$$E[dZ(\omega_i)dZ^*(\omega_j)] = \delta_{ij}E[|dZ(\omega_i)|^2] = \delta_{ij}\bar{S}(\omega_i)d\omega_i. \tag{3}$$

In this equation $E[\ ]$ represents the operator of mathematical expectation, δ_{ij} is the Kronecker delta, the asterisk denotes complex conjugate, and $\bar{S}(\omega)$ is an appropriate stationary power spectrum. The power spectrum of $w(t)$ is given by the equation

$$S_w(\omega,t) = |A(\omega,t)|^2\bar{S}(\omega). \tag{4}$$

Next, the amplitude $a(t)$ and phase $\phi(t)$ of the response are defined implicitly by the equations

$$x(t) = a(t)\cos[\omega_n t + \phi(t)], \tag{5}$$

$$\dot{x}(t) = -a(t)\omega_n\sin[\omega_n t + \phi(t)]. \tag{6}$$

Stochastic ordinary differential equations governing the evolution of $a(t)$ and $\phi(t)$ can be obtained by combining equations (1), (5), and (6). These equations can be partially decoupled using an approximate averaging technique. This technique is applicable for lightly damped oscillators subjected to compatibly "weak" excitations. That is

$$\zeta << 1, \tag{7}$$

$$S_w(\omega,t) = 0(\zeta) \quad \text{as} \quad \zeta \to 0 \quad \forall t \tag{8}$$

The averaging procedure consists of a deterministic and a stochastic part and is described extensively in references such as [9, 12, 13]. It leads to the following first-order stochastic differential equations for $a(t)$ and $\phi(t)$, respectively,

$$\dot{a} = -\zeta\omega_n a + \frac{\pi S_w(\omega_n,t)}{2\omega_n^2 a} + \frac{\sqrt{\pi S_w(\omega_n,t)}}{\omega_n}\eta_1(t), \tag{9}$$

$$\dot{\phi} = \frac{\sqrt{\pi S_w(\omega_n,t)}}{\omega_n a}\eta_2(t). \tag{10}$$

In these equations $\eta_1(t)$ and $\eta_2(t)$ are stationary, zero-mean uncorrelated white noise processes with unit intensity. Therefore, the response vector (a,ϕ) becomes approximately a two-dimensional Markov process.

Fokker-Planck Equations

The Fokker-Planck equation associated with equations (9) and (10) is

$$\frac{1}{\zeta\omega_n}\frac{\partial f}{\partial t} = \frac{\partial}{\partial a}\left[\left(a - \frac{s^2(t)}{a}\right)f\right] + s^2(t)\frac{\partial f^2}{\partial a^2} + \frac{s^2(t)}{a^2}\frac{\partial^2 f}{\partial \phi^2}. \tag{11}$$

The symbol $f \equiv f(a,\phi,t|a_1,\phi_1,t_1)$ denotes the joint transition probability density function of $a(t)$ and $\phi(t)$; it is defined as $f(a,\phi,t|a_1,\phi_1,t_1)dad\phi =$ Prob[the amplitude and phase are at time t at the differential element centered at point (a,ϕ) and with sides da, $d\phi$, given that at time t_1 they were at the differential element centered at point (a_1,ϕ_1) and with sides $da_1, d\phi_1$]. The function $s^2(t)$ is defined by the equation

$$s^2(t) = \frac{\pi S_w(\omega_n,t)}{2\zeta\omega_n^3}. \tag{12}$$

For notational convenience introduce the new variable

$$\Phi = \omega_n t + \phi. \tag{13}$$

This change of variables alters the form of equation (11) to

$$\frac{1}{\zeta\omega_n}\left(\frac{\partial f}{\partial t} + \omega_n\frac{\partial f}{\partial \Phi}\right) = \frac{\partial}{\partial a}\left[\left(a - \frac{s^2(t)}{a}\right)f\right] + s^2(t)\frac{\partial^2 f}{\partial a^2} + \frac{s^2(t)}{a^2}\frac{\partial^2 f}{\partial \Phi^2}. \tag{14}$$

It is clear that now f stands for the transition density function $f(a,\Phi,t|a_1,\Phi_1,t_1)$ of the Markov vector (a,Φ). The initial condition for f is

$$f(a,\Phi,t_1|a_1,\Phi_1,t_1) = \delta(a-a_1)\delta(\Phi-\Phi_1). \tag{15}$$

Clearly, this condition implies that there can be no change in the state of the system if the transition time is zero. It is noted that the domains of amplitude and phase are, respectively, the sets $[0, \infty)$ and $(-\infty,\infty)$. Compatibly with the physics of the problem, the boundary conditions for f must be

$$f(\infty,\Phi,t|a_1,\Phi_1,t_1) = 0, \tag{16}$$

$$f(0,\Phi,t|a_1,\Phi_1,t_1) = \text{finite}, \tag{17}$$

and

$$f(a,\Phi+2\pi,t|a_1,\Phi_1,t_1) = f(a,\Phi,t|a_1,\Phi_1,t_1). \tag{18}$$

Equation (14) does not appear to lend itself readily to exact solution by any of the standard methods that are applicable to partial differential equations. Therefore, the determination of the transition density function $f(.|.)$ is not pursued any further at this point. Instead, it is decided to concentrate on deriving statistics for the processes of response displacement and velocity. For brevity, the quantity $\dot{x}/\omega_n$ is set equal to a new variable y

$$y = \dot{x}/\omega_n. \tag{19}$$

From this point on, both y and $\dot{x}$ are called velocity, indiscriminately. Using this new notation, equations (5) and (6) can be written in the form

$$x = a\cos\Phi, \tag{20}$$

$$y = -a\sin\Phi. \tag{21}$$

Equations (20) and (21) are utilized in transforming equation (14) into an equation governing the transition probability density function $g \equiv g(x,y,t|x_1,y_1,t_1)$ of the displacement and velocity. Analogously to the previous definition, the function g is defined as $g(x,y,t|x_1,y_1,t_1)dxdy =$ Prob[the displacement and velocity are at time t at the differential element of the phase plane centered at point (x,y) and with sides dx,dy, given that at time t_1 they were at the differential element centered at point (x_1,y_1) and with sides dx_1,dy_1]. To derive an equation for g, the relationship between the probability density functions f and g is written as

$$f(a,\Phi,t|a_1,\Phi_1,t_1) = g(x,y,t|x_1,y_1,t_1)|J|. \tag{22}$$

The symbol $|J|$ signifies the absolute value of the Jacobian of the transformation expressed by equations (20) and (21), specifically $J = -a$. Substituting equation (22) into equation (14) and replacing the differential operators in terms of x and y, after some tedious mathematical manipulations, the following equation is obtained for g

$$\frac{1}{\zeta\omega_n}\frac{\partial g}{\partial t} = \frac{\partial}{\partial x}(xg) + \frac{\partial}{\partial y}(yg) + \frac{1}{\zeta}\left(-y\frac{\partial g}{\partial x} + x\frac{\partial g}{\partial y}\right) + s^2(t)\left(\frac{\partial^2 g}{\partial x^2} + \frac{\partial^2 g}{\partial y^2}\right) \tag{23}$$

In addition to satisfying equation (23), the function g must satisfy the initial condition

$$g(x,y,t_1|x_1,y_1,t_1) = \delta(x-x_1)\delta(y-y_1), \tag{24}$$

and the boundary conditions

$$g(\pm\infty,y,t|x_1,y_1,t_1) = 0, \tag{25}$$

$$g(x,\pm\infty,t|x_1,y_1,t_1) = 0. \tag{26}$$

Displacement-Velocity Statistics

Transition Probability Density. Equation (23) is a second-order partial differential equation involving the independent variables t,x,y. However, its order can be reduced to one by introducing the characteristic function

$$M(\theta_1,\theta_2,t) = \int_{-\infty}^{\infty}\int_{-\infty}^{\infty} g(x,y,t|x_1,y_1,t_1) \exp(i\theta_1 x + i\theta_2 y)dxdy. \tag{27}$$

In terms of M, equation (23) becomes

$$\frac{1}{\zeta\omega_n}\frac{\partial M}{\partial t} + \left(\theta_1 + \frac{\theta_2}{\zeta}\right)\frac{\partial M}{\partial \theta_1} + \left(\theta_2 - \frac{\theta_1}{\zeta}\right)\frac{\partial M}{\partial \theta_2} = -s^2(t)[\theta_1^2 + \theta_2^2]M. \tag{28}$$

Furthermore, equation (24) yields

$$M(\theta_1,\theta_2,t_1) = \exp(i\theta_1 x_1 + i\theta_2 y_1). \tag{29}$$

The general solution to equation (28) can be obtained by first solving the subsidiary equations

$$\frac{dt}{1/\zeta\omega_n} = \frac{d\theta_1}{\theta_1 + \dfrac{\theta_2}{\zeta}} = \frac{d\theta_2}{\theta_2 - \dfrac{\theta_1}{\zeta}} = \frac{dM}{s^2(t)[\theta_1^2 + \theta_2^2]M}. \tag{30}$$

Note that the first two of these equations constitute a system of two simultaneous linear differential equations in θ_1, θ_2, with solution

$$\theta_1 = \exp(\zeta\omega_n t)[c_1\cos(\omega_n t) + c_2\sin(\omega_n t)] \tag{31}$$

$$\theta_2 = \exp(\zeta\omega_n t)[c_2\cos(\omega_n t) - c_1\sin(\omega_n t)]. \tag{32}$$

Based on these results the solution to the third equation is found

$$M \exp\left[(\theta_1^2+\theta_2^2)\exp(-2\zeta\omega_n t)\frac{\pi}{2\omega_n^2}\int_{t_1}^{t}\exp(2\zeta\omega_n z)S_w(\omega_n,z)dz\right] = c_3. \tag{33}$$

Clearly, c_1, c_2, and c_3 are constants of integration. The general solution to equation (28) is next constructed in the form [14, 15]

$$M(\theta_1,\theta_2,t) = \Psi(c_1,c_2)\exp\left[-\frac{\theta_1^2+\theta_2^2}{2}\exp(-2\zeta\omega_n t)\frac{\pi}{\omega_n^2}\int_{t_1}^{t}\exp(2\zeta\omega_n z)S_w(\omega_n,z)dz\right], \tag{34}$$

where Ψ is an arbitrary function. Satisfaction of the initial condition specified by equation (29) requires that Ψ be of the form

$$\begin{aligned}\Psi = \exp\{ & ix_1\exp[-\zeta\delta_n(t-t_1)][\theta_1\cos\omega_n(t-t_1) \\ & -\theta_2\sin\theta\omega_n(t-t_1)] + iy_1\exp[-\zeta\omega_n(t-t_1)] \\ & [\theta_1\sin\omega_n(t-t_1)+\theta_2\cos\omega_n(t-t_1)]\}\end{aligned} \tag{35}$$

Thus, equation (34) becomes

$$\begin{aligned}M(\theta_1,\theta_2,t) = \exp\{ & i\theta_1\exp[-\zeta\omega_n(t-t_1)] \\ & [x_1\cos\omega_n(t-t_1)+y_1\sin\omega_n(t-t_1)] \\ & + i\theta_2\exp[-\zeta\omega_n(t-t_1)][-x_1\sin\omega_n(t-t_1)+y_1\cos\omega_n(t-t_1)] \\ & -\frac{\theta_1^2+\theta_2^2}{2}\exp(-2\zeta\omega_n t)\frac{\pi}{\omega_n^2}\int_{t_1}^{t}\exp(2\zeta\omega_n z)S_w(\omega_n,z)dz\}.\end{aligned} \tag{36}$$

The last equations is readily recognized as the characteristic function of a two-dimensional Gaussian distribution with means values

$$\bar{x} = \exp[-\zeta\omega_n(t-t_1)]\{x_1\cos\omega_n(t-t_1)+y_1\sin\omega_n(t-t_1)\} \tag{37}$$

$$\bar{y} = \exp[-\zeta\omega_n(t-t_1)]\{-x_1\sin\omega_n(t-t_1)+y_1\cos\omega_n(t-t_1)\} \tag{38}$$

and variances, for both x and y, equal to

$$c(t_1,t) = \frac{\pi}{\omega_n^2}\exp(-2\zeta\omega_n t)\int_{t_1}^{t}\exp(2\zeta\omega_n z)S_w(\omega_n,z)dz. \tag{39}$$

Therefore, the solution for the transition density function of x and y is

$$g(x,y,t\,|\,x_1,y_1,t_1) = \frac{1}{2\pi\ c(t_1,t)}\exp\left[-\frac{(x-\bar{x})^2+(y-\bar{y})^2}{2\ c(t_1,t)}\right] \tag{40}$$

Unconditional Probability Density. The Markovian property of a process is quite advantageous since the availability of the transition density function can lead to the determination of any order statistics. For the two-dimensional Markov vector (x,y), one can find the joint unconditional probability density function as follows. Suppose that the probability density function of x and y at time $t_1 \geq 0$, $p(x_1,y_1,t_1)$ is known. The the density function of x and y at time $t \geq t_1$ is given by the equation

$$p(x,y,t) = \int_{-\infty}^{\infty}\int_{-\infty}^{\infty} p(x_1,y_1,t_1)g(x,y,t\,|\,x_1,y_1,t_1)dx_1dy_1. \tag{41}$$

This general equation is next applied to the case, frequently encountered in engineering applications, of an oscillator having initially a known displacement x^* and velocity y^*. That is, $x_0 \equiv x(0) = x^*$ and $y_0 \equiv y(0) = y^*$, or equivalently

$$p(x_0,y_0,0) = \delta(x_0-x^*)\delta(y_0-y^*). \tag{42}$$

If equation (42) is substituted into equation (41), the probability density function of x and y is obtained in the form

$$p(x,y,t) = \frac{1}{\sqrt{2\pi c}}\exp\left\{-\frac{[x-e^{-\zeta\omega_n t}(x^*\cos\omega_n t+y^*\sin\omega_n t)]^2}{2c}\right\}$$

$$\frac{1}{\sqrt{2\pi c}}\exp\left\{-\frac{[y-e^{-\zeta\omega_n t}(-x^*\sin\omega_n t+y^*\cos\omega_n t)]^2}{2c}\right\}, \tag{43}$$

where $c = c(0,t)$.

It is a straightforward matter to calculate moments of any order for the displacement or velocity. In particular, the mean values are

$$E[x] = e^{-\zeta\omega_n t}(x^*\cos\omega_n t + y^*\sin\omega_n t) \tag{44}$$

$$E[y] = e^{-\zeta\omega_n t}(-x^*\sin\omega_n t + y^*\cos\omega_n t) \tag{45}$$

while the variances are given by the strikingly simple form

$$\sigma_x^2(t) = \sigma_y^2(t) = c(0,t). \tag{46}$$

It must be noted however at this point, that the exact solutions for $E[x]$ and $E[y]$ can be readily determined by solving the homogeneous part of equation (1) with initial conditions $x(0) = x^*$ and $\dot{x}(0) = \dot{x}^*$. Specifically it is found that

$$E[x] = \frac{e^{-\zeta\omega_n t}}{\omega_d}[x^*(\omega_d\cos\omega_d t + \zeta\omega_n\sin\omega_d t) + \dot{x}^*\sin\omega_d t] \tag{47}$$

and

$$E[y] = \frac{E[\dot{x}]}{\omega_n} = \frac{e^{-\zeta\omega_n t}}{\omega_d}[-x^*\omega_n\sin\omega_d t + \frac{\dot{x}^*}{\omega_n}(\omega_d\cos\omega_d t - \zeta\omega_n\sin\omega_d t], \tag{48}$$

where $\omega_d = \omega_n\sqrt{1-\zeta^2}$. These equations are exact irrespective of the magnitude of ζ. Therefore, as is readily seen equations (44) and (45) are accurate if $O(\zeta)$ terms are neglected.

Amplitude-Phase Statistics

Transition Probability Density. The availability of the statistics of x and y can have an immediate application toward the determination of the statistics of a and Φ. Specifically, by simply transforming variables via equations (20)–(22), equation (40) yields the joint transition probability density function of the amplitude and phase, $\tau = t - t_1 > 0$,

$$f(a,\Phi,t\,|\,a_1,\Phi_1,t_1) = \frac{a}{2\pi\ c(t_1,t)}\exp\left\{-\frac{[a\cos\Phi - a_1\cos(\Phi_1+\omega_n\tau)e^{-\zeta\omega_n\tau}]^2 + [a\sin\Phi - a_1\sin(\Phi_1+\omega_n\tau)e^{-\zeta\omega_n\tau}]^2}{2c(t_1,t)}\right\} \tag{49}$$

Actually, it can be shown, by direct substitution, that equation (49) satisfies equation (14). This verification is tedious and will not be presented here. Note that equation (49) satisfies, as well, the conditions expressed by equations (15)–(18).

Clearly, if the initial values of amplitude and phase are, respectively, a^* and Φ^*, given by

$$a^* = \sqrt{x^{*2}+y^{*2}}, \tag{50}$$

$$\Phi^* = -\tan^{-1}\left(\frac{y^*}{x^*}\right), \tag{51}$$

then, the joint unconditional density of a and Φ, after appropriate cancellation of terms, is

$$p(a,\Phi,t) = \frac{a}{2\pi c}\exp\left[-\frac{a^2-2aa^*\cos(\Phi-\Phi^*-\omega_n t)+a^{*2}e^{-2\zeta\omega_n t}}{2c}\right]. \tag{52}$$

It is noted that for nonzero initial oscillator conditions the response amplitude and phase are statistically dependent. On the contrary, when the oscillator is initially at rest, $a^*=0$, then

$$p(a,\Phi,t) = \frac{1}{2\pi}\,\frac{a}{c}\exp\left(-\frac{a^2}{2c}\right) = p(\Phi)p(a,t), \tag{53}$$

That is, a and Φ are statistically independent. In addition, the distribution of the phase is uniform in the interval $[-\pi,\pi)$, while the distribution of the amplitude is of a Rayleigh type.

Unconditional Probability Densities. If equation (52) is integrated over phase, it yields the probability density function for the amplitude. Specifically, it is found that

$$p(a,t) = \frac{a}{c}\exp\left[-\frac{a^2+a^{*2}e^{-2\zeta\omega_n t}}{2c}\right]I_0\left(\frac{aa^*e^{-\zeta\omega_n t}}{c}\right). \tag{54}$$

In equation (54) use has been made of the following relationship [16] regarding the Bessel function I_0

$$I_0(z) = \frac{1}{\pi}\int_0^\pi \exp(\pm z\cos\Psi)d\Psi. \tag{55}$$

The expression of equation (54) is identical to that reported in reference [17], where the statistics of the amplitude alone have been studied. This result supports the validity of the derived expressions and verifies the consistency of the procedures followed.

Equation (52) integrated over amplitude would yield the probability density function of the phase. This procedure is lengthy, and after several manipulations yields

$$p(\Phi,t) = \frac{1}{2\pi}\exp\left[-\frac{a^{*2}e^{-2\zeta\omega_n t}}{2c}\right] + \frac{a^*e^{-\zeta\omega_n t}\cos(\Phi-\Phi^*-\omega_n t)}{2\sqrt{2\pi c}}$$
$$\exp\left[-\frac{a^{*2}e^{-2\zeta\omega_n t}\sin^2(\Phi-\Phi^*-\omega_n t)}{2c}\right]$$
$$\left[1+\operatorname{erf}\left(\frac{a^*e^{-\zeta\omega_n t}\cos(\Phi-\Phi^*-\omega_n t)}{\sqrt{2c}}\right)\right] \tag{56}$$

Some of the properties of this distribution directly derivable from equation (56) deserve special attention.

(i) When $t\to 0$, then $c\to 0$, $\exp(-\zeta\omega_n t)\to 1$, $\operatorname{erf}(a^*/2c)\to 1)$, and the phase Φ (now denoted by Φ_0) will be close to Φ^* with the consequence that $\cos(\Phi_0-\Phi^*)\simeq 1$, and $\sin(\Phi_0-\Phi^*)\simeq\Phi_0-\Phi^*$. Under these conditions

$$\lim_{t\to 0} p(\Phi,t) = \lim_{c\to 0}\frac{1}{\sqrt{2\pi\ c/a^{*2}}}\exp\left[-\frac{(\Phi-\Phi^*)^2}{2c/a^{*2}}\right] = \delta(\Phi_0-\Phi^*), \tag{57}$$

which is the actual distribution of the phase at zero time.

(ii) If the structure is initially at rest ($a^*=0$), then

$$p(\Phi,t) = \frac{1}{2\pi} \tag{58}$$

that is, the distribution of phase is uniform in the interval $[-\pi,\pi)$. This type of distribution has been derived previously, equation (53).

(iii) The distribution that $p(\Phi,t)$ depends on the time function $\exp(-2\zeta\omega_n t)/c$. The behavior of this function can be readily studied by using equation (39). Specifically,

$$\exp(-2\zeta\omega_n t)/c = \frac{\omega_n^2}{\pi}\left[\int_0^t \exp(2\zeta\omega_n z)S_w(\omega_n,z)dz\right]^{-1}. \tag{59}$$

Clearly, if the spectrum $S_w(\omega,t)$ exhibits an exponential decay with time, such that $\exp(2\zeta\omega_n t)S_w(\omega,t)\to 0$ as $t\to\infty$, then the left-hand side of equation (59) becomes eventually constant. Consequently, as $t\to\infty$, the phase distribution becomes mathematically simpler. Furthermore, if $S_w(\omega,t)=s(\omega)$, equation (59) yields

$$\lim_{t\to 0} p(\Phi,t) = \frac{1}{2\pi}. \tag{60}$$

That is, for a step-modulated stationary excitation, regardless of the initial state, the distribution of the phase becomes eventually uniform

Energy Statistics

Another useful application of the statistics of the amplitude, as derived in the foregoing, is the determination of statistics for the total energy per unit mass of the oscillator

$$E(t) = \frac{1}{m}\left(\frac{1}{2}kx^2+\frac{1}{2}m\dot{x}^2\right)$$
$$= \frac{1}{2}\omega_n^2x^2+\frac{1}{2}\dot{x}^2 = \frac{1}{2}\omega_n^2a^2. \tag{61}$$

Combining equations (54) and (61) yields

$$p(E,t) = \frac{1}{\omega_n^2 c}\exp\left[-\frac{E+E^*e^{-2\zeta\omega_n t}}{\omega_n^2 c}\right]I_0\left(\frac{2\sqrt{EE^*}e^{-\zeta\omega_n t}}{\omega_n^2 c}\right). \tag{62}$$

where E^* is the energy of the oscillator at time $t=0$. Then, the moments of the energy can be determined by using the following equation [17]

$$\int_0^\infty E^m p(E,t)dE = \left(\frac{\omega_n^2}{2}\right)^n\int_{\alpha_0}^{\infty 2m} p(a,t)da = \left(\frac{\omega_n^2}{2}\right)^m E[a^{2m}]$$
$$= \left(\frac{\omega_n^2}{2}\right)^m (2c)^m\Gamma(1+m)\exp\left[-\frac{a^{*2}e^{-2\zeta\omega_n t}}{2c}\right]M$$
$$+m,1,\frac{a^{*2}e^{-2\zeta\omega_n t}}{2c}\Big), \tag{63}$$

In equation (63) $M(.\,,\,.\,,\,.)$, and $\Gamma(\bullet)$ denote the confluent hypergeometric function and the gamma function, respectively. Note that if the oscillator is initially at rest, equation (62) yields

$$p(E,t) = \frac{1}{\omega_n^2 c}\exp\left(-\frac{E}{\omega_n^2 c}\right) \tag{64}$$

which is the classical Maxwell-Boltzmann exponential distribution.

Numerical Simulations – Discussion

It has been deemed important to test the validity of the derived analytical expressions by comparing them with data generated by appropriate numerical simulations.

As excitation $w(t)$ has been selected, a modulated broadband process which can be expressed in the following form

$$w(t) = \psi(t)v(t). \tag{65}$$

In equation (65) $v(t)$ is a stationary random process with power spectrum $S_v(\omega)=S_0\,|\sin\omega\tau^*/\omega\tau^*|$ where S_0 and τ^* are

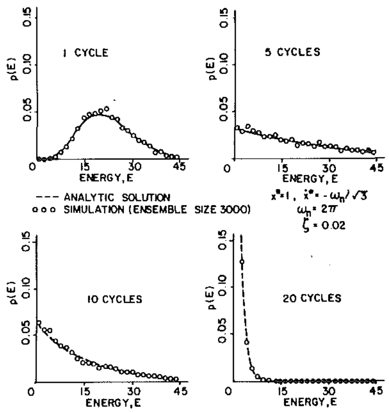

Fig. 1 Energy probability density at discrete times

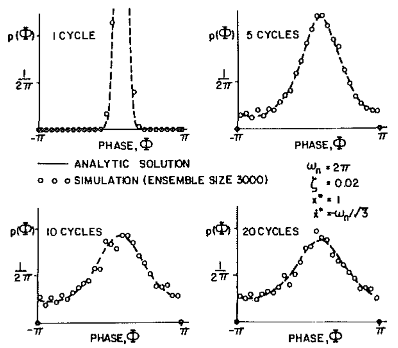

Fig. 2 Response phase probability density at discrete time

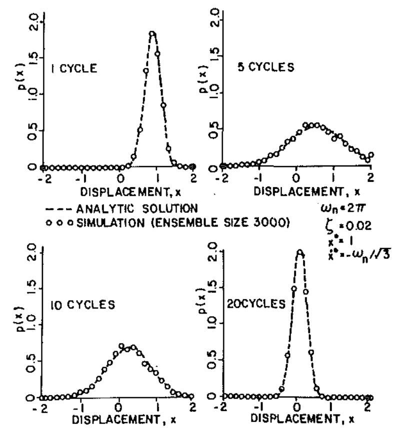

Fig. 3 Response displacement probability density at discrete times

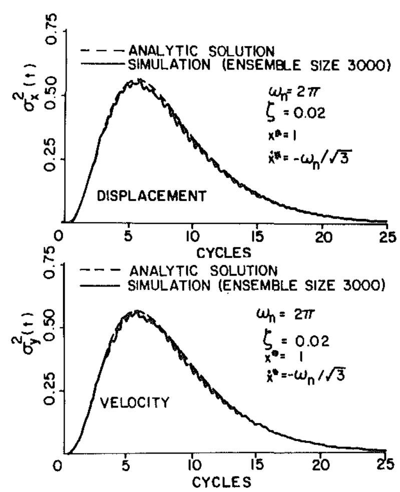

Fig. 4 Response displacement and velocity variances versus time

constants. Furthermore $\psi(t)$ is a deterministic slowly varying function of time. In this case the evolutionary power spectrum of $w(t)$ is given by the equation

$$S_w(\omega,t) = |\psi(t)|^2 S_0 \left| \frac{\sin\omega\tau^*}{\omega\tau^*} \right| \tag{66}$$

The modulating function $\psi(t)$ which has been chosen is given by the equation [5]

$$\psi(t) = k_1(e^{-\beta_1 t} - e^{-\beta_2 t}),\ t \geq 0,\ \beta_2 > \beta_1 > 0, \tag{67}$$

where $\beta_1 = 0.25\ \text{sec}^{-1}$, $\beta_2 = 0.50\ \text{sec}^{-1}$, and k_1 is a normalization constant such as $\psi_{max} = 1$. Furthermore, the constant spectral value S_0 has been selected to yield

$$\sqrt{\pi S_0 / 2\zeta\omega_n^3} = 1 \text{ (length unit)}. \tag{68}$$

The case of an oscillator with $\omega_n = 2\pi$ rad/sec, $\zeta = 0.02$, $x^* = 1$ (unit), and $\dot{x}^* = -\omega_n/\sqrt{3}$ (units) has been considered. An ensemble of 3000 oscillator response records has been digitally simulated for $\tau^* = \pi/10\omega_n$.

Figure 1 shows how the total energy of the oscillator is distributed at different times. Initially, the energy takes on values close to E^*; theoretically its probability distribution is a delta function at E^*. As time advances and the motion builds up, the energy can take on values appreciably different from E^*. Thus, its probability distribution spreads out over a broader range. Finally, as the oscillator comes to rest the energy assumes small values and its probability density function "shrinks" to become a delta function at zero. As is shown in Fig. 1 the analytical curves fit the simulated points quite well.

The evolution in time of the phase distribution is shown in Fig. 2. Initially, the values of the phase are clustered in the neighborhood of $\Phi^* = \pi/6$. However, as time increases the probability mass is distributed over a much broader range of values in the interval $[-\pi,\pi)$. Again, a quite close agreement between the theoretical and simulation results is seen.

In Fig. 3 the Gaussian distribution of the displacement is shown for the same oscillator. It is observed that this distribution starts as a delta function at $x^* = 1$, it broadens with time, and it becomes again a delta function at zero as the motion ceases to exist. The analytical curves and the simulation data match quite well. It must be noted that the quality of the agreement of the theoretical and the simulated data shown in Figs. 1-3 is slightly influenced by the fact that the calculations have been made for times which correspond to integer multiples of the undamped natural period of oscillation, that is $t = t_l = l2\pi/\omega_n$, $l = 1,2 \ldots$. Clearly, the oscillatory terms that have been neglected in deriving equations (9) and (10) vanish at $t = t_l$. Therefore, the reliability of these equations is enhanced at $t = t_l$. This comment can be further supported by observing that for $\zeta << 1$, thus $\omega_d \approx \omega_n$, equations (44) and (45) coincide with the exact equations (47) and (48) for $t = t_l$. In any case, since the exact solutions for the time-dependent mean displacement and mean velocity of the oscillator are readily available, the usefulness of the developed approximate solutions should be also assessed based on their reliability in predicting the variances of the displacement and the velocity of the oscillator response. In this regard, Fig. 4 shows an excellent agreement between the theoretical results and corresponding simulation data along the entire duration of the excitation.

Concluding Remarks

The statistics of several response parameters of a lightly damped oscillator excited by a broad-band random process have been examined. The amplitude and phase of the response have been approximately modeled by a two-dimensional Markov vector. The corresponding Fokker-Planck equation with proper initial and boundary conditions appended, has been considered. This equation has led to analytical expressions providing the transition probability densities of the amplitude-phase, and the displacement-velocity vectors. Furthermore, solutions have been derived for marginal probability densities of the displacement, velocity, amplitude, phase, and total energy of the oscillator response. The reliability of the analytical solution has been tested by considering the response of the oscillator to an excitation the power spectrum of which varies exponentially in time. The analytical results have been found to be in close agreement with data produced by a Monte Carlo study which involved 3000 digitally simulated response records. It is noted that some of the approximations involved in the derivation of the solutions which have been presented in this paper are similar to those commonly used in addressing a classical random vibration problem. Specifically, the stationary response statistics of a lightly damped linear oscillator to a broad-band stationary excitation can be approximately determined by replacing the original excitation by a white noise process; its constant spectrum is taken equal to the spectral value of the original excitation at the natural frequency of the oscillator [14]. The validity and the limitation of this approximation has been examined extensively. These examinations could be used to supplement the information provided by the presented Monte Carlo data in connection with the reliability of the method. Finally, it must be recognized that the developed solutions are based on treating the random excitation, in many respects, as a shot noise. Thus, expressions for various response statistics could be determined by using equation (1), and input-output relationships of linear systems which are valid irrespective of the amount of damping. However, this approach does not take advantage of the smallness of damping and does not appear to lead to a direct proof of the Gaussian property of the response, unless the excitation is Gaussian.

Acknowledgment

The financial support of this work by the grant NAG-3-210 from the NASA Lewis Research Center is gratefully acknowledged. The second author would like to express thanks to Professor S. Ariaratham for his constructive comments.

References

1 Rice, S. O., "Mathematical Analysis of Random Noise," in *Selected Papers on Noise and Stochastic Processes*, Wax, N., ed., Dover, New York, 1954.

2 Caughey, T. K., and Stumpf, H. J., "Transient Response of a Dynamic System Under Random Excitation," ASME Journal of Applied Mechanics, Vol. 28, 1961, pp. 563–566.

3 Hammond, S. K., "On the Response of Single and Multidegree of Freedom Systems to Non-stationary Random Excitations," *J. Sound Vib.*, Vol. 7, 1968, pp. 393–416.

4 Barnoski, R. L., and Maurer, J. R., "Mean-Square Response of Simple Mechanical Systems to Non-stationary Random Excitation," ASME Journal of Applied Mechanics, Vol. 36, No. 2, June 1969, pp. 221–227.

5 Shinozuka, M., and Sato, Y., "Simulation of Nonstationary Random Process," *J. Eng. Mech. Div.*, ASCE, Vol. 93, No. EM1, 1967, pp. 11–40.

6 Yang, J. N., "Non-stationary Envelope Process and First Excursion Probability," *J. Struct. Mech.*, Vol. 1, 1972, pp. 231–248.

7 Wang, M. C., and Uhlenbeck, G. E., "On the Theory of the Brownian Motion II," in *Selected Papers on Noise and Stochastic Processes*, Wax, N., ed., Dover, New York, 1954.

8 Lin, Y. K., "On Nonstationary Shot Noise," *J. Acoust. Soc. Am.*, Vol. 36, 1964, pp. 82–84.

9 Stratonovich, R. L., *Topics in the Theory of Random Noise,* Vol. I and II, Gordon and Breach, New York, 1963.

10 Caughey, T. K., "Derivation and Application of the Fokker-Planck Equation to Discrete Nonlinear Dynamical Systems Subjected to White Random Excitation," *J. Acoust. Soc. Am.*, Vol. 35, 1963, pp. 1683–1692.

11 Priestley, M. B., "Power Spectral Analysis of Non-Stationary Random Processes," *J. Sound Vib.*, Vol. 6, 1967, pp. 86–97.

12 Spanos, P-T. D., "Probabilistic Earthquake Energy Spectra Equations," *J. Eng. Mech. Div.*, ASCE, Vol. 106, No. EM1, 1980, pp. 147–159.

13 Spanos, P-T. D., and Lutes, L. D., "Probability of Response to Evolutionary Process," *J. Eng. Mech. Div.*, ASCE, Vol. 106, No. EM2, 1980, pp. 213–224.

14 Lin, Y. K., *Probabilistic Theory of Structural Dynamics*, R. E., Krieger, Huntington, New York, Reprint, 1976.

15 Dennemeyer, R., *Introduction to Partial Differential Equations and Boundary Value Problems*, McGraw-Hill, New York, 1968.

16 Abramowitz, M., and Stegun, I. A., eds., *Handbook of Mathematical Functions*, Dover, 9th printing, New York, 1970.

17 Spanos, P-T. D., and Solomos, G. P., "Markov Approximation to Transient Vibration," *J. Eng. Mech. Div.*, ASME, Vol. 109, No. EM4, 1983, pp. 1134–1116.

Effects of Warping and Pretwist on Torsional Vibration of Rotating Beams

K. R. V. Kaza
Research Scientist,
Structures Branch.

R. E. Kielb
Research Scientist.
Mem. ASME

National Aeronautics and Space Administration,
Lewis Research Center,
Cleveland, Ohio 44135

The effect of pretwist and warping on the torsional vibration of short-aspect-ratio rotating beams is examined for application to the modeling of turbofan, turboprop, and compressor blades. The equations of motion and the associated boundary conditions by using both Wagner's hypothesis and Washizu's theory are derived and a few minor limitations of the Wagner's hypothesis, as applied to thick blades, are pointed out and discussed. The equations for several special cases are solved in a closed form. Results are presented indicating the effect of warping, pretwist, and rotation on torsional vibration of beams as aspect ratio is varied. The results show that the structural warping and pretwist terms have a significant effect on torsional frequency and mode shapes of short-aspect-ratio blades whereas the inertial warping terms have negligible effect. Since the torsional frequencies and mode shapes are very important in aeroelastic analyses by using modal methods, the structural warping terms should be included in modeling turbofan, turboprop, compressor, and turbine blades.

Introduction

It is well-known that a *rotating beam* experiences a centrifugally induced tensile force that increases the effective torsional stiffness. The increase in stiffness under the action of a tensile force was intuitively explained by Wagner [1], Budiansky and Mayers [2], and Houbolt and Brooks [3]. This intuitive approach has become known as Wagner's hypothesis and will be described later. Biot [4] and Goodier [5] showed the same increase in stiffness by applying the theory of elasticity.

By extending Wagner's hypothesis to pretwisted beams without explicitly considering warping, Chu [6], Houbolt and Brooks [3], and Carnegie [7] showed that there is an increase in torsional stiffness due to pretwist. Washizu [8] and Shorr [9] showed a similar increase in stiffness by using the theory of elasticity and by explicitly including warping. Although not specifically stated, the other researchers [10–13] have implicitly used Wagner's hypothesis to derive the equations of motion that include rotation and pretwist and showed a similar increase in torsional stiffness.

Without using either Wagner's hypothesis (implicitly or explicitly) or warping of the cross sections of the beam, Rosen and Friedmann [14] concluded that there is no increase in torsional stiffness due to pretwist. Subsequently, Rosen [15], following a procedure similar to that of [8], considered warping explicitly and showed an increase in torsional stiffness due to pretwist, which is slightly different from that calculated by using Wagner's hypothesis. Thus, it is necessary to use Wagner's hypothesis or to consider warping explicitly to account properly for the increase in torsional stiffness due to pretwist.

An additional increase in torsional stiffness that is exclusively due to warping was considered in references [10, 12, 16]. This increase in stiffness was quantified in [16] but with an inconsistent set of boundary conditions. Hence, there is a need to further examine the increase in stiffness.

Warping also introduces several additional terms [12] in the torsional equation of motion and in the associated boundary conditions. One is an inertial term and the other is associated with rotation. These will be discussed further in later sections. The effects of these terms on torsional frequencies has apparently not been previously studied by researchers for low-aspect-ratio blades.

The effects of nonlinear twist and axial tension on torsional vibrations by retaining up to third-degree terms in the equations of motion were first addressed in [3, 17, 18] among several others. More recently, similar effects on steady state deflections were investigated in [19] for a special case of a large-aspect-ratio twisted beam, and the results reconfirmed the previously published findings that the nonlinear effects are important under certain conditions. These effects also were investigated in [20] by using more general forms for displacements.

It is evident from the published literature that the torsional vibration of twisted rotating blades has received considerable attention. However, there still remain some unanswered questions. These include: (1) What are the limiting values of

Contributed by the Applied Mechanics Division and presented at the Winter Annual Meeting, New Orleans, La., December 9–14, 1984 of THE AMERICAN SOCIETY OF MECHANICAL ENGINEERS.

Discussion on this paper should be addressed to the Editorial Department, ASME, United Engineering Center, 345 East 47th Street, New York, N.Y. 10017, and will be accepted until two months after final publication of the paper itself in the JOURNAL OF APPLIED MECHANICS. Manuscript received by ASME Applied Mechanics Division, August, 1983; final revision, April, 1984. Paper No. 84-WA/APM-41.

Copies will be available until August, 1985.

aspect ratio, thickness ratio, and pretwist angle for which Wagner's hypothesis is applicable? Specifically, is Wagner's hypothesis appropriate to derive the equations of motion for vibration of twisted rotating beams that are employed to model turbofan, turboprop, and compressor blades? (2) What are the values of aspect ratio and thickness ratio beyond which the warping of the cross sections should be considered? (3) What is the effect of inertial warping on torsional frequencies? (4) How do the torsional mode shapes change with the inclusion of the warping in both the differential equations and boundary conditions? (5) Is it possible to obtain closed-form solutions for the torsional frequencies and mode shapes, at least for special nonrotating cases with warping and pretwist included? To answer these questions, two sets of equations of motion and the required boundary conditions for vibration of a pretwisted beam are derived systematically by using both Wagner's hypothesis and Washizu's theory. The differences between the two sets are brought out and discussed. The equations for certain special cases are solved in a closed form to quantify the effects of warping and pretwist on nonrotating torsional frequencies. The general equations for the rotating beam are then solved by the Galerkin method.

Equations of Motion

Wagner's hypothesis assumes that the pretwisted beam consists of helical fibers in the undeformed state. When the beam is twisted, the spiral becomes longer if the elastic twist is in the same direction as the pretwist and shorter in the opposite case. Elongation of the fiber causes tension. This tension is mostly longitudinal but has a small component directed tangentially in the plane of a cross section. These tangential components produce a torque [3], which must be added to the Saint Venant's torque caused by shear force. Alternatively, this additional torque can also be obtained by considering the stress along the twisted fiber while deriving the equations of motion [10–13]. This latter approach will be considered first.

The equations of motion and the associated boundary conditions will be derived by using Hamilton's principle in the form

$$\int_{t_0}^{t_1} (\delta T_k - \delta U)\, dt = 0 \tag{1}$$

where the strain energy U and the kinetic energy T_k are

$$\left.\begin{aligned} U &= \frac{1}{2}\int_0^L \int_A \int \left[E\gamma_{yy}^2 + G\left(\gamma_{yz}^2 + \gamma_{yx}^2\right)\right] dx\, dy\, dz \\ T_k &= \frac{1}{2}\int_0^L \int_A \int \rho \frac{d\bar{r}_1}{dt} \cdot \frac{d\bar{r}_1}{dt}\, dx\, dy\, dz \end{aligned}\right\} \tag{2}$$

where E, G, ρ, and L are Young's modulus, shear modulus, material density, and blade length, respectively. The expressions for the strain components, γ_{yy}, γ_{yz}, and γ_{yx}, and for the position vector $\bar{r}_1$ will be defined later.

A schematic of the coordinate systems is shown in Fig. 1. The pretwist angle, $\xi(y)$, varies with y, the blade axial coordinate. Then, the curvatures of the undeformed and deformed elastic axes follow from [12, 13] and are

$$\bar{\omega}_{xyz} = \bar{e}_y \xi' \tag{3}$$

$$\bar{\omega}_{y_3 y_3 z_3} = \bar{e}_y (\xi' - \alpha') \tag{4}$$

where the prime represent derivatives with respect y. Also the relation between the unit vector triads of the xyz and $x_3y_3z_3$ systems follow from [12, 13] and are

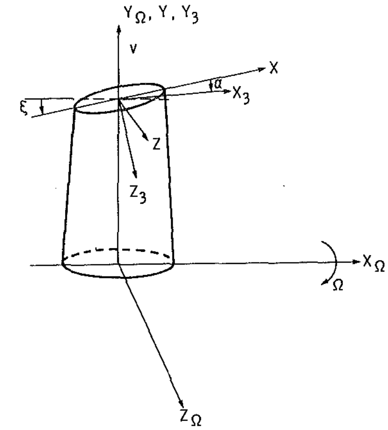

Fig. 1 Blade coordinate systems

$$\left.\begin{aligned} \bar{e}_{x_3} &= \bar{e}_x\left(1 - \frac{\alpha^2}{2}\right) + \bar{e}_z \alpha \\ \bar{e}_{y_3} &= \bar{e}_y \\ \bar{e}_{z_3} &= -\bar{e}_x \alpha + \bar{e}_z\left(1 - \frac{\alpha^2}{2}\right) \end{aligned}\right\} \tag{5}$$

where α is the elastic twist angle. The position vectors of an arbitrary point on the blade before and after deformation are

$$\bar{r}_0 = \bar{R}_0 + \bar{e}_x x + \bar{e}_z z \tag{6}$$

$$\bar{r}_1 = \bar{R}_1 + \bar{e}_{x_3} x + \bar{e}_{y_3} \lambda\alpha' + \bar{e}_{z_3} z \tag{7}$$

where $\bar{R}_0$ and $\bar{R}_1$ are the position vectors of a point on the elastic axis before and after deformation and the warping function λ is assumed to be an antisymmetric function of x and z only. The angular velocity vector is

$$\bar{\omega} = \Omega\left(\bar{e}_x \cos\xi + \bar{e}_z \sin\xi\right) \tag{8}$$

where Ω is the rotational speed. Then the Green's strain tensor, ϵ_{ij}, based on a Lagrangian description can be obtained from

$$d\bar{r}_1 \cdot d\bar{r}_1 - d\bar{r}_0 \cdot d\bar{r}_0 = 2[dx\ dy\ dz]\left[\epsilon_{ij}\right] \begin{Bmatrix} dx \\ dy \\ dz \end{Bmatrix} \tag{9}$$

Substituting equations (6) and (7) into equation (9), one obtains the required strain components

$$\epsilon_{yy} = v' + \lambda\alpha'' + \frac{z^2 + x^2}{2}(\alpha'^2 - 2\alpha'\xi') + \text{H.O.T.} \tag{10a}$$

$$2\epsilon_{yx} = -\left(z - \frac{\partial\lambda}{\partial x}\right)\alpha' + \text{H.O.T.} \tag{10b}$$

$$2\epsilon_{yz} = \left(x + \frac{\partial\lambda}{\partial z}\right)\alpha' + \text{H.O.T.} \tag{10c}$$

where v is axial deflection. The other components involve higher-order terms and are neglected.

It is convenient to eliminate the axial equation of motion. This is done by explicitly considering the foreshortening due to torsion. The expression for foreshortening is obtained by making use of the force equilibrium condition in the axial direction, i.e., the integral of the fiber stress over the cross section must be equal to the total tension. Thus,

$$T_c = E\int_A \int \epsilon_{yy}\, dx\, dz = EA\left[v' + \frac{k_A^2}{2}(\alpha'^2 - 2\alpha'\xi')\right] \tag{11}$$

where

$$\int_A \int \lambda \, dx \, dz = 0$$

$$A = \int_A \int dx \, dz; \quad Ak_A^2 = \int_A \int (x^2 + z^2) dx \, dz \qquad (12)$$

From equation (11), one can write

$$v' = \frac{T_c}{EA} - \frac{k_A^2}{2} (\alpha'^2 - 2\alpha'\xi') = v_e' - U_F' \qquad (13)$$

where the expression for shoreshortening is

$$U_F = \frac{1}{2} \int_0^y k_A^2 (\alpha'^2 - 2\alpha'\xi') dy \qquad (14)$$

By assuming that the beam is rigid ($EA \rightarrow \infty$) in the axial direction, the expressions for strain components, equation (10), simplify to

$$\epsilon_{yy} = \lambda\alpha'' + \frac{\left(z^2 + x^2 - k_A^2\right)}{2} (\alpha'^2 - 2\alpha'\xi') \qquad (15a)$$

$$2\epsilon_{yx} = -\left(z - \frac{\partial\lambda}{\partial x}\right)\alpha'; \quad 2\epsilon_{yz} = \left(x + \frac{\partial\lambda}{\partial z}\right)\alpha' \qquad (15b)$$

Notice that the component ϵ_{yy} is the strain along the twisted fiber. This strain will be used to account for the increase in torsional stiffness due to centrifugal loads and to pretwist. Then, the required engineering components of strain in equation (2) are

$$\gamma_{yy} = \epsilon_{yy}; \quad \gamma_{yx} = 2\epsilon_{yx}; \quad \gamma_{yz} = 2\epsilon_{yz} \qquad (16)$$

Also the expression for $\bar{R}_1$ is

$$\bar{R}_1 = (y + v)\bar{e}_y = (y - U_F)\bar{e}_y \qquad (17)$$

Substituting equations (5) and (17) into equation (7), yields

$$\bar{r}_1 = (y - U_F + \lambda\alpha')\bar{e}_y + \left[x\left(1 - \frac{\alpha^2}{2}\right) - z\alpha\right]\bar{e}_x + \left[z\left(1 - \frac{\alpha^2}{2}\right) + x\alpha\right]\bar{e}_z \qquad (18)$$

Substituting equations (8), (14), (16), and (18) into equation (2) and the result into equation (1), taking the indicated variations, integrating over the blade, and integrating over time, yields the following equation of motion after neglecting some higher-order and Coriolis terms

$$(GJ\alpha')' + \left(EB_1\xi'^2\alpha'\right)' + \left(T_ck_A^2\alpha'\right)' - (EC_1\alpha'')''$$
$$- mk_m^2\alpha + m\Omega^2\left(k_{m_2}^2 - k_{m_1}^2\right)\alpha \cos 2\,\xi + \left(mk_\lambda^4\dot{\alpha}'\right)^{\bullet\prime}$$
$$- \left(m\Omega^2k_\lambda^4\alpha'\right)' = -\left(T_ck_A^2\xi'\right)' \qquad (19)$$

and the following boundary conditions

$$\Big[m\Omega^2k_\lambda^4\alpha'\delta\alpha + T_ck_A^2(\alpha' - \xi')\delta\alpha - EC_1\alpha''\delta\alpha' + (EC_1\alpha'')'\delta\alpha - EB_1\xi'^2\alpha'\delta\alpha - GJ\alpha'\delta\alpha\Big]\Big|_0^L = 0 \qquad (20)$$

where the dot denotes derivative with respect to time and the other quantities are

$$\left.\begin{aligned}
J &= \int_A \int \left[\left(z - \frac{\partial\lambda}{\partial x}\right)^2 + \left(x + \frac{\partial\lambda}{\partial z}\right)^2\right] dx \, dz \\
C_1 &= \int_A \int \lambda^2 \, dx \, dz \\
B_1 &= \int_A \int \left(x^2 + z^2 - k_A^2\right)^2 \, dx \, dz \\
Ak_A^2 &= \int_A \int (x^2 + z^2) dx \, dz \\
k_m^2 &= k_{m_1}^2 + k_{m_2}^2 \\
mk_{m_1}^2 &= \int_A \int \rho z^2 \, dx \, dz \\
mk_{m_2}^2 &= \int_A \int \rho x^2 \, dx \, dz \\
mk_\lambda^4 &= \int_A \int \rho\lambda^2 \, dx \, dz \\
T_c &= \int_y^L m\Omega^2 y \, dy \\
m &= \int m \, \rho \, dx \, dz
\end{aligned}\right\} \qquad (21)$$

The boundary conditions relevant to a beam built-in at $y = 0$ and free at $y = L$ are: the twisting angle and warping displacement (proportional to α') must be zero at the root, and the torque and warping stress (proportional to α'') must be zero at the free end. See also the discussion on these boundary conditions by Barr in [16]. Then, equation (20) reduces to

$$\begin{aligned}
&\alpha(0) = \alpha'(0) = \alpha''(L) = 0 \\
&m\Omega^2k_\lambda^4\alpha'(L) + \left[EC_1\alpha''(L)\right]' - EB_1\xi'^2\alpha'(L) - GJ\alpha'(L) = 0
\end{aligned} \qquad (22)$$

As mentioned earlier, the equation of motion can also be derived by using the theory presented in [8]. This theory requires that the expressions for stresses and strains be written in the local Cartesian reference system, rather than in the curvilinear coordinate system. Let the Cartesian system be x_1, y_1, and z_1, and the corresponding strain components be $\epsilon_{y_1y_1}$, $\epsilon_{y_1x_1}$, $\epsilon_{y_1z_1}$. Washizu [8] derived the transformation between these Cartesian components and the Green strain components given in equation (10). By using those transformations, the expressions for the required Cartesian components are

$$\left.\begin{aligned}
\epsilon_{y_1y_1} &= v' + \lambda\alpha'' + \frac{z^2 + x^2}{2}\alpha'^2 - \left(z\frac{\partial\lambda}{\partial x} - x\frac{\partial\lambda}{\partial x}\right)\alpha'\xi' \\
2\epsilon_{y_1x_1} &= -\left(z - \frac{\partial\lambda}{\partial x}\right)\alpha' \\
2\epsilon_{y_1z_1} &= \left(x + \frac{\partial\lambda}{\partial z}\right)\alpha'
\end{aligned}\right\} \qquad (23)$$

By using the preceding expressions for strain components instead of those given by equations (10a)-(10c) and by using Hamilton's principle again for deriving the equation of motion, one obtains the following equation of motion:

$$(GJ\alpha')' + \left[E\underline{\left(B_{11} - k_{AA}^4 A\right)}\xi'^2\alpha'\right]' + \left(T_c k_A^2 \alpha'\right)' - (EC_1\alpha'')'' - mk_m^2\ddot{\alpha} + m\Omega^2\left(k_{m_2}^2 - k_{m_1}^2\right)\alpha\cos 2\xi + \left(mk_\lambda^4\dot{\alpha}'\right)^{\cdot\,\prime} - \left(m\Omega^2 k_\lambda^4\alpha'\right)' = -\left(T_c \underline{k_{AA}^2}\xi'\right)' \tag{24}$$

and the boundary conditions:

$$\left.\begin{aligned} &\alpha(0) = \alpha'(0) = \alpha''(L) = 0 \\ &m\Omega^2 k_\lambda^4\alpha'(L) + \left[EC_1\alpha''(L)\right]' - E\underline{\left(B_{11} - k_{AA}^4 A\right)}\xi'^2\alpha'(L) - GJ\alpha'(L) = 0 \end{aligned}\right\} \tag{25}$$

where

$$\left.\begin{aligned} Ak_{AA}^2 &= \int_A\int\left(z\frac{\partial\lambda}{\partial x} - x\frac{\partial\lambda}{\partial z}\right)dx\,dz \\ B_{11} &= \int_A\int\left(z\frac{\partial\lambda}{\partial x} - x\frac{\partial\lambda}{\partial z}\right)^2 dx\,dz \end{aligned}\right\} \tag{26}$$

The form of equations (24) and (25) is the same as that of equations (19) and (22) with the exception of the two underlined coefficients.

To examine the differences between the two sets of equations a thin rectangular beam is considered. The warping function for the sections can be approximated as

$$\lambda = -xz \tag{27}$$

Then,

$$\left.\begin{aligned} B_1 &= \int_A\int\left(x^2 + z^2\right)dx\,dz - k_A^2\int_A\int(x^2 + z^2)dx\,dz \\ B_{11} - Ak_{AA}^4 &= \int_A\int\left(x^2 - z^2\right)^2 dx\,dz - k_{AA}^2\int_A\int(x^2 - z^2)dx\,dz \\ Ak_A^2 &= \int_A\int(x^2 + z^2)dx\,dz \\ Ak_{AA}^2 &= \int_A\int(x^2 - z^2)dx\,dz \end{aligned}\right\} \tag{28}$$

If the cross section is thin, $(t/c)^2 \ll 1$, one can show that

$$\left.\begin{aligned} B_1 &\approx B_{11} - Ak_{AA}^4 \\ k_A^2 &\approx k_{AA}^2 \end{aligned}\right\} \tag{29}$$

and, hence, the equations of motion and boundary conditions obtained from these two methods are identical. This clearly validates the applicability of the Wagner's hypothesis for twisted, rotating, slender beams with *thin cross sections*. Furthermore, this hypothesis is independent of aspect ratio.

Special Cases of Equations

It is of interest to specialize equations (18) and (22) and compare the resulting equations with the corresponding ones in the published literature. Two such cases are considered:

Case *I*: $\Omega = k_\lambda = 0$ (rotation and inertial warping are zero)

$$(GJ\alpha')' + \left(EB_1\xi'^2\alpha'\right) - (EC_1\alpha'')'' - mk_m^2\ddot{\alpha} = 0 \tag{30}$$

$$\left.\begin{aligned} &\alpha(0) = \alpha'(0) = \alpha''(L) = 0 \\ &\left[EC_1\alpha''(L)\right]' - EB_1\xi'^2\alpha'(L) - GJ\alpha'(L) = 0 \end{aligned}\right\} \tag{31}$$

The differential equation (30) is the same as that derived in [16]. However, there are some differences in boundary conditions. For discussions of these differences, see the discussion at the end of [16].

Case *II*: $C_1 = k_\lambda = 0$ (warping constants are zero)

$$(GJ\alpha')' + \left[EB_1\xi'^2\alpha'\right]' + \left(T_c k_A^2\alpha'\right)' + mk_m^2\ddot{\alpha} + m\Omega^2\left(k_{m_2}^2 - k_{m_1}^2\right)\alpha\cos 2\xi = 0 \tag{32}$$

$$\alpha(0) = \alpha'(L) = 0 \tag{33}$$

Equations (32) and (33) are the same as the corresponding ones in [3, 9, 12, 13].

It is also of interest to specialize equations (24) and (25) and to compare the resulting equations with the corresponding ones in the published literature. The form of the second term on the left-hand side of equation (24) was examined in [15] by using the theory of [8]. This represents an increase in torsional stiffness due to pretwist. The present term is in agreement with that presented in [15].

The term on the right-hand side of equation (24) represents a torsion moment due to pretwist. This is similar to the second term on the left-hand side of equation (24), but is independent of elastic twist. Hence, it is not a stiffness term. The effect of the term is to cause a steady untwist of the pretwisted beam under centrifugal loading. The form of this term was examined in [21] by using the theory of [8]. The present term is in agreement with that given in [21].

Results and Discussions

To quantify the effects of the individual terms on vibration frequencies, uniform nonrotating and rotating beams are considered separately. Since the effects of some individual terms were studied in a piecewise manner in the published literature all these results are not entirely new. In the following section, an attempt is made to present the effects of these terms in a unified manner. The present results are compared with the previous results wherever possible.

Nonrotating Beam. The equation of motion and the boundary conditions for the nonrotating beam case follow from equations (19) and (22) and are:

$$GJ\alpha'' + EB_1\xi'^2\alpha'' - EC_1\alpha^{IV} - mk_m^2\ddot{\alpha} - mk_\lambda^4\ddot{\alpha}'' = 0 \tag{34}$$

$$\left.\begin{aligned} &\alpha(0) = \alpha'(0) = \alpha''(L) = 0 \\ &EC_1\alpha'''(L) - EB_1\xi'^2\alpha'(L) - GJ\alpha'(L) = 0 \end{aligned}\right\} \tag{35}$$

The special case of these equations without the inertial warping terms and pretwist terms were solved in [22].

The sectional properties for a rectangle of chord c and thickness t are

$$\left.\begin{aligned} \lambda &= -xz & GJ &= \frac{Gct^3}{3} \\ EB_1 &= \frac{Etc^5}{180} & EC_1 &= \frac{Ec^3t^3}{144} \\ m &= \rho tc & mk_m^2 &= \frac{\rho tc^3}{12} \\ k_\lambda^4 &= \frac{t^2c^2}{144} & k_A^2 &= \frac{c^2}{12} \end{aligned}\right\} \quad (36)$$

Defining

$$\bar{\eta} = \frac{\eta}{L} \quad (37)$$

and assuming simple harmonic motion in the form

$$\alpha = \varphi e^{i\omega_{NR}t} \quad (38)$$

equations (34) and (35) can be written as

$$\varphi^{IV} - A_2\varphi'' - B\varphi = 0 \quad (39)$$

$$\left.\begin{aligned} \varphi(0) = \varphi'(0) = \varphi''(1) \\ \varphi'''(1) = A_1\varphi'(1) \end{aligned}\right\} \quad (40)$$

where

$$\left.\begin{aligned} A_2 &= \frac{24}{1+\nu}\left(\frac{L}{c}\right)^2 + \frac{4}{5}\frac{c^2}{t^2}\xi'^2 - \frac{B}{12}\left(\frac{t}{L}\right)^2 \\ B &= 12\frac{\rho}{E}\frac{L^4}{t^2}\omega_{NR}^2 \\ A_1 &= \frac{24}{1+\nu}\left(\frac{L}{c}\right)^2 + \frac{4}{5}\frac{c^2}{t^2}\xi'^2 \end{aligned}\right\} \quad (41)$$

The solution to equation (39) subject to the boundary conditions, equation (40) is

$$\varphi(\bar{\eta}) = D_1\left[\left(\sinh k_1\bar{\eta} - \frac{k_1}{k_2}\sin k_2\bar{\eta}\right) - \frac{k_1^2\sinh k_1 + k_1k_2\sin k_2}{k_1^2\cosh k_1 + k_2^2\cos k_2}(\cosh k_1\bar{\eta} - \cos k_2\bar{\eta})\right] \quad (42)$$

Table 1 Nonrotating beam torsional frequencies
$[t/c = 0.05]$

L/c	Mode	Pretwist 0 deg	15 deg	30 deg	45 deg	60 deg
		ω_{NRn}/ω_{on}				
2	$n=1$	1.1443	1.2785	1.6099	2.0565	2.5325
	2	1.2436	1.3704	1.6869	2.1190	2.5841
	3	1.4281	1.5408	1.8309	2.2378	2.6838
4	$n=1$	1.0656	1.1014	1.2018	1.3586	1.5446
	2	1.0959	1.1307	1.2289	1.3828	1.5660
	3	1.1536	1.1868	1.2811	1.4296	1.6077
6	$n=1$	1.0421	1.0582	1.1050	1.1821	1.2788
	2	1.0562	1.0721	1.1184	1.1946	1.2903
	3	1.0838	1.0993	1.1444	1.2191	1.3131
8	$n=1$	1.0310	1.0401	1.0669	1.1121	1.1703
	2	1.0391	1.0481	1.0747	1.1195	1.1774
	3	1.0550	1.0639	1.0901	1.1344	1.1915
10	$n=1$	1.0245	1.0303	1.0476	1.0771	1.1158
	2	1.0297	1.0355	1.0527	1.0821	1.1205
	3	1.0400	1.0458	1.0628	1.0919	1.1301

Table 2 Nonrotating beam torsional frequencies
$[t/c = 0.20]$

L/c	Mode	Pretwist 0 deg	15 deg	30 deg	45 deg	60 deg
		ω_{NRn}/ω_{on}				
2	$n=1$	1.1443	1.1532	1.1795	1.2237	1.2810
	2	1.2436	1.2520	1.2767	1.3186	1.3727
	3	1.4281	1.4354	1.4573	1.4944	1.5429
4	$n=1$	1.0656	1.0679	1.0747	1.0864	1.1020
	2	1.0959	1.0981	1.1047	1.1161	1.1314
	3	1.1536	1.1557	1.1620	1.1729	1.1875
6	$n=1$	1.0421	1.0431	1.0462	1.0515	1.0585
	2	1.0562	1.0572	1.0602	1.0654	1.0724
	3	1.0838	1.0847	1.0876	1.0927	1.0995
8	$n=1$	1.0310	1.0315	1.0333	1.0362	1.0402
	2	1.0391	1.0396	1.0413	1.0443	1.0483
	3	1.0550	1.0555	1.0572	1.0601	1.0640
10	$n=1$	1.0245	1.0248	1.0259	1.0279	1.0304
	2	1.0297	1.0301	1.0312	1.0331	1.0356
	3	1.0400	1.0404	1.0415	1.0434	1.0459

Table 3 Rotating beam torsional frequency

$[L/c = 3; t/c = 0.05]$

Ω rad/sec	With TT^a term			With TR^b term			With $TT^a + TR^b$ terms		
	ω_{R1}/ω_{NR1}	ω_{R2}/ω_{NR2}	ω_{R3}/ω_{NR3}	ω_{R1}/ω_{NR1}	ω_{R2}/ω_{NR2}	ω_{R3}/ω_{NR3}	ω_{R1}/ω_{NR1}	ω_{R2}/ω_{NR2}	ω_{R3}/ω_{NR3}
0	1.0000	1.0000	1.0000	1.0000	1.0000	1.0000	1.0000	1.0000	1.0000
276.5	1.0035	1.0024	1.0019	0.9970	0.9996	0.9999	1.0003	1.0021	1.0018
552.9	1.0140	1.0095	1.0077	0.9873	0.9987	0.9996	1.0013	1.0082	1.0073
829.4	1.0311	1.0212	1.0173	0.9718	0.9971	0.9991	1.0029	1.0183	1.0164
1105.9	1.0545	1.0373	1.0305	0.9505	0.9950	0.9984	1.0050	1.0323	1.0289

[a] TT = Tension-torsion
[b] TR = Tennis-racket

Table 4 Rotating beam torsional frequency

$[L/c = 6; t/c = 0.2]$

Ω rad/sec	With TT^a term			With TR^b term			With $TT^a + TR^b$ terms		
	ω_{R1}/ω_{NR1}	ω_{R2}/ω_{NR2}	ω_{R3}/ω_{NR3}	ω_{R1}/ω_{NR1}	ω_{R2}/ω_{NR2}	ω_{R3}/ω_{NR3}	ω_{R1}/ω_{NR1}	ω_{R2}/ω_{NR2}	ω_{R3}/ω_{NR3}
0	1.0000	1.0000	1.0000	1.0000	1.0000	1.0000	1.0000	1.0000	1.0000
276.5	1.0010	1.0008	1.0007	0.9991	0.9999	0.9999	1.0001	1.0007	1.0006
552.9	1.0039	1.0030	1.0027	0.9967	0.9996	0.9999	1.0006	1.0026	1.0026
829.4	1.0088	1.0067	1.0061	0.9925	0.9991	0.9998	1.0013	1.0058	1.0059
1105.9	1.0157	1.0119	1.0109	0.9866	0.9985	0.9995	1.0023	1.0104	1.0104

[a] TT = Tension-torsion
[b] TR = Tennis-racket

where

$$\left.\begin{aligned} k_1 &= \left[\left(\frac{A_2^2}{4}+B\right)^{\frac{1}{2}} + \frac{A_2}{2}\right]^{1/2} \\ k_2 &= \left[\left(\frac{A_2^2}{4}+B\right)^{\frac{1}{2}} - \frac{A_2}{2}\right]^{1/2} \end{aligned}\right\} \qquad (43)$$

The frequencies are obtained by solving the following transcendental equation:

$$A_2^2 - A_1A_2 + 2B + (2B + A_1A_2)\cos k_2 \cosh k_1 + (2A_1 - A_2)\sqrt{B}\sin k_2 \sinh k_1 = 0 \qquad (44)$$

The nondimensional frequencies ω_{NR1}/ω_{01}, ω_{NR2}/ω_{02}, ω_{NR3}/ω_{03} for the first three torsional modes of several blade configurations are tabulated in Tables 1 and 2. The reference frequency ω_{on} for the nth mode is obtained from the Saint Venant's theory of torsion and is

$$\omega_{on} = \frac{n\pi}{L}\frac{t}{c}\sqrt{\frac{G}{\rho}} \qquad (n = 1,3,5, \ldots) \qquad (45)$$

Results in Table 1 are for low-thickness-ratio ($t/c = 0.05$) blades having aspect ratios (L/c) varying from 2–10, and pretwist angles varying from 0–60 deg. Results in Table 2 are for high-thickness-ratio ($t/c = 0.2$) blades. With the help of these results, the effects of individual terms can be assessed.

Inertial Warping. The last term in equation (34) is the inertial warping term. When this term is set to zero, the coefficients A_1 and A_2 in equations (40), (41), (43), and (44) will be equal. To assess the significance of this term, equation (44) was solved for $A_1 = A_2$ and for $A_1 \neq A_2$. Comparison of the results, although not shown, revealed that the inertial warping term has a negligible effect on frequency. Thus, this term can be neglected in the formulation and will not be discussed further.

Elastic Warping. This is reflected as the third term in the differential equation (34) and as the first term of the last boundary condition, equation (35). To illustrate the effect of the elastic warping, let us consider the results for zero pretwist angle in Tables 1 and 2. Since the inertial warping terms have negligible effect and since the pretwist angle is set to zero, the value listed is simply the ratio of the frequencies with and without these terms in equations (34) and (35). Obviously, these terms increase the frequency in all three modes. For $L/c = 2$ and for both $t/c = 0.05$ and 0.2, the increase is approximately 15, 25, and 45 percent for the first, second, and third modes, respectively. For large-aspect ratio, the effect is smaller.

Pretwist. This is reflected as the second term in the differential equation (34) and also as the second term of the last boundary condition, equation (35). These two terms increase the effective torsional stiffness and hence the frequencies for all the modes. For example, from Tables 1 and 2, for a pretwist angle of 30 deg and $L/c = 2$, the increase is 30–40 percent for $t/c = 0.05$ and is 2–3 percent for $t/c = 0.2$. This increase is with respect to the untwisted value that includes the $EC_1\alpha^{IV}$ term. Again for large-aspect ratios, the effect is smaller.

The preceding quantitative observations suggest that for low-aspect-ratio blades, which are used for turbofans and compressors, the elastic warping and pretwist terms should be included in the formulations. Since the torsional frequencies and mode shapes are very important in aeroelastic analysis by using the modal approach, the hyperbolic mode shapes given in equation (42) should be used rather than the usual sinusoidal mode shapes for representing torsional deflections.

The effects of one of the elastic warping terms on torsional frequency was studied for certain blade configurations in [23] by using the Raleigh-Ritz method. The same configurations were analyzed by using the present closed-form approach and very good agreement was found between the two sets of results.

Rotating Beam. The equations of motion and boundary conditions for a rotating beam are given by equations (19) and (22). For a free-vibration analysis, the term on the right-hand side of equation (19) is set to zero. These equations are solved by using Galerkin's method [3] in conjunction with the mode shapes given by equation (42). A total of five modes are used in this analysis.

To illustrate the effect of the tension-torsion coupling term $(T_c k_A^2 \alpha')'$ and the "tennis-racket" effect term, $m\Omega^2 (k_{m_2}^2 - k_{m_1}^2) \alpha \cos 2\xi$, the first three torsional frequencies are calculated with and without these terms at different rotational speeds. The variational of nondimensional frequencies ω_{R1}/ω_{NR1}, ω_{R2}/ω_{NR2}, ω_{R3}/ω_{NR3} with rotational speed for two blade configurations, ($L/c = 3$ and $t/c = 0.05$; $L/c = 6$ and $t/c = 0.2$) is shown in Tables 3 and 4.

The first configuration is a low-aspect-ratio thin blade, which approximately represents a compressor blade and the second one is a large-aspect-ratio thick blade, which approximately represents a propeller blade. The results show that the tension-torsion coupling term, which is a centrifugal stiffening term, causes an increase in torsional frequency with rotation of approximately 0–5 percent and that the tennis-racket term, which is a centrifugal softening term, causes a decrease in torsional frequency with rotation of approximately 0–5 percent for a low-aspect-ratio thin blade. The same is true for high-aspect-ratio thick blades but the percentage increase in torsional frequency is lower. The *net* effect of rotation is to very slightly increase the torsional frequency with rotation. This is in contrast to the strong stiffening effect of rotation observed on the out-of-plane bending frequencies. The presence of both the centrifugal softening and stiffening terms and their net effect on torsional frequencies are similar to the presence of corresponding terms and their effect on the bending frequencies in the plane of rotation of a rotating beam. The tension-torsion term is very important for blades that have low torsional stiffness. The tension-torsion term is independent of the blade twist angle but the tennis-racket term is a function of twist angle. These quantitative results further show that it is always safer to retain both terms in the torsion equation.

Conclusions

The governing equations of motion and the associated boundary conditions for torsional vibration of a beam including pretwist, warping, and rotation are derived by using both Wagner's hypothesis and Washizu's theory. These equations are solved for special cases. The results are presented in a unified manner to illustrate the effect of each term on torsional frequency. Based on the derivation and the results, the following conclusions are drawn.

1. The application of Wagner's hypothesis is valid in deriving the equations of motion for pretwisted, rotating, slender beams with *thin cross sections.*

2. The torsional vibration frequencies of a nonrotating uniform beam including pretwist and elastic and inertial warping terms are presented in a closed form for the first time in published literature.

3. The warping term $EC_1 \alpha^{IV}$ has a significant effect on torsional frequency, and its effect is more significant for low-aspect-ratio blades than for high-apsect-ratio blades. The presence of this term introduces hyperbolic functions in addition to trigonometric functions in the vibration mode shapes. Thus, this warping term should be included in calculating torsional frequencies and flutter of turbomachinery blades using beam models.

4. The inertial warping term has a negligible effect.

5. The pretwist term, $EB_1 \xi'^2 \alpha''$, also increases the torsional frequency, and this increase is more significant for low-aspect-ratio thin blades than for high-aspect ratio thick blades.

6. The tension-torsion coupling term $(T_c k_A^2 \alpha')'$ is a centrifugal stiffening term and increases the torsional frequency approximately 5 percent at a rotational speed of 1100 rad/sec. The effect of this term is more significant for blades that have low nonrotating torsional frequencies.

7. The "tennis-racket" term is a centrifugal softening term and decreases the torsional frequency approximately 5 percent at a rotational speed of 1100 rad/sec.

Acknowledgments

The authors wish to thank Mr. Oliver McGee, a graduate student working at NASA Lewis, for programming the equations and calculating the results.

References

1 Wagner, H., "Torsion and Buckling of Open Sections," NACA TM-807, Oct. 1936.

2 Budiansky, B., and Mayers, J., "Influence of Aerodynamic Heating on the Effective Torsional Stiffness of Thin Wings," *Journal of the Aeronautical Sciences*, Vol. 23, No. 12, Dec. 1956, pp. 1081–1093.

3 Houbolt, J. C., and Brooks, G. W., "Differential Equations of Motion for Combined Flapwise Bending, Chordwise Bending, and Torsion of Twisted Nonuniform Rotor Blades," NACA TR-1346, 1958.

4 Biot, M. A., "Increase of Torsional Stiffness of a Prismatical Bar Due to Axial Tension," *Journal of Applied Physics*, Vol. 10, No. 12, Dec. 1939, pp. 860–864.

5 Goodier, J. N., "Elastic Torsion in the Presence of Initial Axial Stress," ASME Journal of Applied Mechanics, Vol. 17, Dec. 1950, pp. 383–387.

6 Chu, C., "The Effect of Initial Twist on the Torsional Rigidity of Thin Prismatical Bars and Tubular Members," *Proceedings of the First U.S. National Congress of Applied Mechanics*, E. Sternberg, ed., ASME, New York, 1952, pp. 265–269.

7 Carnegie, W., "Vibrations of Pretwisted Cantilever Blading," *Proceedings of the Institution of Mechanical Engineers*, Vol. 173, No. 12, 1959, pp. 343–374.

8 Washizu, K., "Some Considerations on a Naturally Curved and Twisted Slender Beam," *Journal of Mathematics and Physics*, Vol. 43, June 1964, pp. 111–116.

9 Shorr, B. F., "Theory of Twisted Nonuniformly Heated Bars," NASA TM-75758, Feb. 1980.

10 Hodges, D. H., and Dowell, E. H., "Nonlinear Equations of Motion for the Elastic Bending and Torsion of Twisted Nonuniform Blades," NASA TN D-7818, Dec. 1974.

11 Friedmann, P., "Influence of Structural Damping, Preconing, Offsets and Large Deflections on the Flap-Lag-Torsional Stability of a Cantilevered Rotor Blade," AIAA Paper 75-780, 1975.

12 Kaza, K. R. V., and Kvaternik, R. G., "Nonlinear Aeroelastic Equations for Combined Flapwise Bending, Chordwise Bending, Torsion and Extension of Twisted Nonuniform Rotor Blades in Forward Flight," NASA TM-74059, Aug. 1977.

13 Kaza, K. R. V., and Kielb, R. E., "Coupled Bending-Bending-Torsion Flutter of a Mistuned Cascade With Nonuniform Blades," AIAA Paper 82-0726, 1982, to be published in *AIAA Journal*, Oct., 1984.

14 Rosen, A., and Friedmann, P., "Nonlinear Equations of Equilibrium of Elastic Helicopter or Wind Turbine Blades Undergoing Moderate Defor-

mations" (UCLA-ENG-7718, California Univ.; NASA Contract NSG-3082.) DOE/NASA/3082-78/1, NASA CR-159478, 1978.

15 Rosen, A., "The Effect of Initial Twist on Torsional Rigidity of Beams—Another Point of View," TAE Report No. 360, Technion Israel Institute of Technology, Apr. 1978; also ASME Journal of Applied Mechanics, Vol. 47, No. 2, June 1980, pp. 389–393.

16 Carnegie, W., "Vibrations of Pre-Twisted Cantilever Blading: An Additional Effect Due to Torsion," *Proceedings of the Institution of Mechanical Engineers*, Vol. 176, No. 13, 1962, pp. 315–322.

17 Niedenfuhr, F. W., "On the Possibility of Aeroelastic Reversal of Propeller Blades," *Journal of the Aeronautical Sciences*, Vol. 22, No. 6, June 1955, pp. 438–440.

18 White, W. F., Jr., and Malatino, R. E., "A Numerical Method for Determining the Natural Vibration Characteristics of Rotating Nonuniform Cantilever Blades," NASA TMX-72751, Oct. 1975.

19 Rosen, A., "Theoretical and Experimental Investigation of Nonlinear Torsion and Extension of Initially Twisted Bars," ASME Journal of Applied Mechanics, Vol. 50, June 1983, pp. 321–326.

20 Shield, R. T., "Extension and Torsion of Elastic Bars With Initial Twist," ASME Journal of Applied Mechanics, Vol. 49, Dec. 1982, pp. 779–786.

21 Hodges, D. H., "Torsion of Pretwisted Beams Due to Axial Loading," ASME Journal of Applied Mechanics, Vol. 47, 1980, pp. 393–397.

22 Duggan, A. P., and Slyper, H. A., "Torsional Vibration of Pretwisted Cantilever Beams," *International Journal of Mechanical Sciences*, Vol. 11, 1969, pp. 871–883.

23 Leissa, R. W., and Ewing, M. S., "Comparison of Beam and Shell Theories for the Vibrations of Thin, Turbomachinery Blades," ASME Paper 82-GT-223, Apr. 1982.

T. C. Huang
Professor,
Department of Engineering Mechanics,
University of Wisconsin,
Madison, Wisc. 53706
Mem. ASME

Y. Youm
Associate Professor,
Department of Mechanical Engineering,
Catholic University of America,
Washington, D.C.
Mem. ASME

Exact Displacement Analysis of Four-Link Spatial Mechanisms by the Direction Cosine Matrix Method

A method of displacement analysis of the four-link spatial mechanism is developed. The results through this analysis will be exact solutions that can be obtained without resorting to numerical or iteration schemes. In the analysis, the position of a link in a mechanism can be fully defined if its direction and length are known. Therefore, this analysis involves the calculation of the unknown direction cosines and length of each link for a given configuration of the mechanism. In finding the direction cosines of the unknown unit vectors involved for each link and rotating axis, two types of coordinates, the global and the local, are generally used. Then, a direction cosine matrix between each local coordinate system and the global coordinates is established. Thus, the unknown direction cosines of the local coordinates, the links, and the rotating axes are obtained in global coordinates. In this development, direction cosine matrices are used throughout the analysis. As an illustration, the application of this method to the study of four-link spatial mechanisms, RGGR, RGCR, RRGG, and RRGC will be presented.

Introduction

A recent survey of space mechanism research [1], which covers analytical methods developed mainly since the 1950s with numerous pertinent references, serves as an extensive and informative source of background material. However, several selective references of well-known methods for the displacement analysis of spatial linkage may be mentioned. Among them are the 4×4 matrix iterative method [2, 3], the dual number quarternion method [4, 5], the geometric transformation method [6, 7], the vector method [8–10], the screw method [11–15], the tensor method [16], the line geometric method [17], and the geometrical configuration method [18], etc. Most of these methods involve high level mathematics of complicated mathematical manipulation, and all require numerical or iterative schemes for solutions.

A method of displacement analysis using direction cosine matrices as transformation matrices for the four-link spatial mechanisms is developed and applied to various four-bar spatial linkages in this paper. The mathematics involved are elementary; the operations are simple without loss of geometric interpretation, and the solutions are exact. The analysis starts by choosing an appropriate local coordinate system and assigns direction cosines to the related unit vectors. These direction cosines in the local coordinates are obtained by applying the dot product of unit vectors and using given angle data. Then, a direction cosine matrix between the global and the local coordinates is obtained, by using known unit vectors, the direction cosines of the local coordinates, and a special property of the direction cosine matrix. Using this special property of the direction cosine matrix, that is, that each element of the matrix equals its own cofactor, we obtain exact analytical solutions without resorting to numerical or iterative schemes. When the direction cosine matrix is known, the unknown unit vectors in the global coordinates can be fully calculated.

Analytical solutions in closed-form, input-output relations for a few spatial four-bar linkages are obtained in [4, 6, 7]. In [6, 7], the rotation matrix is used, together with one or two constraints particular to the linkage concerned. However, the solutions for these closed-form, input-output relations will have to be obtained by numerically solving transcendental equations. In the present paper, the direction cosine matrices are used in successive steps of the analysis, from the input end to the output end of the linkage mechanism. In the process, the constraints of the mechanism, such as the constant length of a link or the constant angle between two links, are taken care of automatically. The solutions are obtained without resorting to numerical or iteration schemes. It should be mentioned that, for a simple case of the 2R-2G mechanism, the input-output relation, developed in [20], can be reduced to a closed-form solution.

Contributed by the Applied Mechanics Division and presented at the Winter Annual Meeting, New Orleans, La., December 9–14, 1984 of THE AMERICAN SOCIETY OF MECHANICAL ENGINEERS.

Discussion on this paper should be addressed to the Editorial Department, ASME, United Engineering Center, 345 East 47th Street, New York, N.Y. 10017, and will be accepted until two months after final publication of the paper itself in the JOURNAL OF APPLIED MECHANICS. Manuscript received by ASME Applied Mechanics Division, December, 1982; final revision, July, 1984. Paper No. 84-WA/APM-22.

Copies will be available until August, 1985.

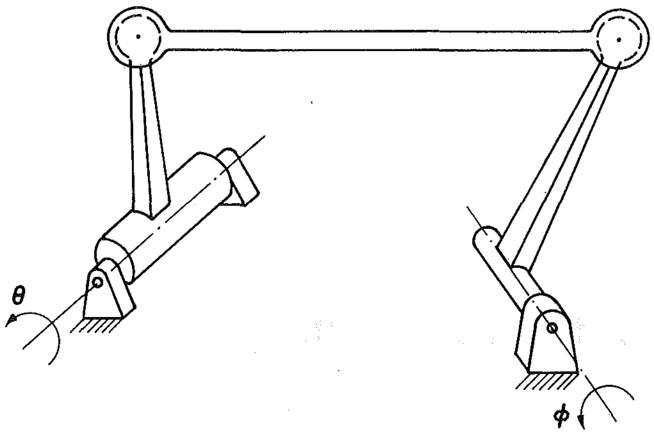

Fig. 1 A RGGR four-link spatial mechanism

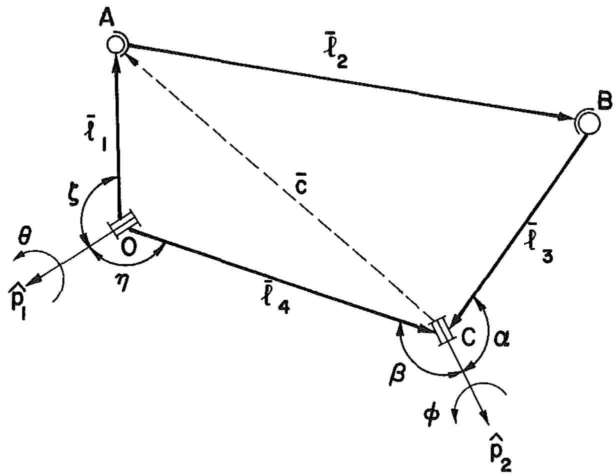

Fig. 2 The schematic diagram of a RGGR mechanism

In this paper, this direction cosine matrix method will be applied to obtain analytical solutions for the four-bar spatial linkages, an RGGR, an RGCR, an RRGG, and an RRGC, with numerical illustration.

1 Displacement Analysis of the RGGR Mechanism

The RGGR four-link spatial mechanism as shown in Fig. 1 is a generalization of the planar four-bar mechanism RRRR. It is one of the most versatile and practical configurations of three-dimensional mechanisms and will function as a single degree of freedom linkage with a passive degree of freedom in the connecting link. A schematic diagram of an RGGR mechanism is shown in Fig. 2.

The known quantities of the mechanism are the lengths, l_1, l_2, l_3, l_4, the vector $\bar{l}_4$, the directions of rotations, $\hat{p}_1$, $\hat{p}_2$, the angles ζ, η, α, β, from the construction of mechanism, and the input angle θ. The unknown quantities are $\hat{l}_1$, $\hat{l}_2$, and $\hat{l}_3$.

(*a*) Input Angle θ. The input angle θ for the rotation about the $\hat{p}_1$-axis can be measured with any arbitrary reference. As shown in Fig. 3, θ is chosen as the angle between the two planes formed by $\hat{p}_1$ and $\hat{l}_4$, and $\hat{p}_1$ and $\hat{l}_1$ in which the $\hat{p}_1\hat{l}_4$-plane chosen as a reference. Both the angle ζ between $\hat{p}_1$ and $\hat{l}_1$, and the angle η between $\hat{p}_1$ and $\hat{l}_4$ are chosen to be less than π.

Let the local coordinates x_1, y_1, z_1 associated with $\hat{p}_1$ with the origin at 0 be chosen as follows:

The x_1-axis is set along the known rotating axis $\hat{p}_1$ and has the same positive direction as $\hat{p}_1$.

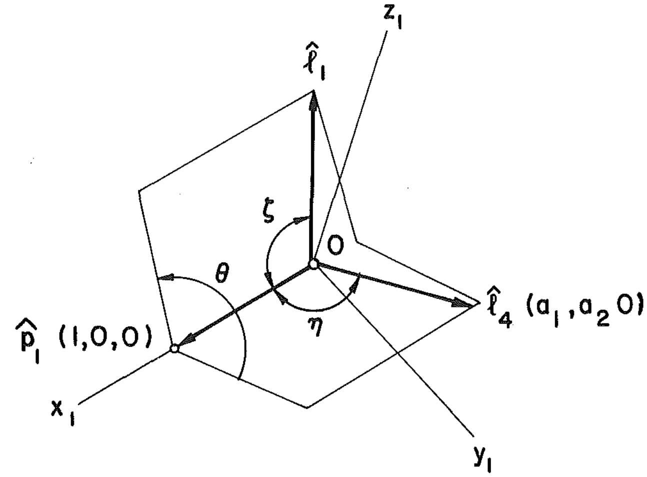

Fig. 3 A local coordinate system and input angle measurement

The y_1-axis is set in the plane of $\hat{p}_1$ and $\hat{l}_4$ and the angle between $\hat{l}_4$ and the y-axis is less than $\pi/2$.

The z_1-axis follows the right-hand rule.

With this local coordinate system the input angle θ can now be measured between the x_1y_1-plane and the x_1l_1-plane with the x_1y_1-plane as references.

(*b*) Analysis of $\hat{l}_1$. The direction cosines of the unit vectors $\hat{p}_1$, $\hat{l}_1$, and $\hat{l}_4$ in the local coordinates system associated with $\hat{p}_1$ are expressed in the parenthesis for each unit vector as $\hat{p}_1(1, 0, 0)$, $\hat{l}_1$ $(\cos\zeta,\ \sin\zeta\cos\theta,\ \sin\zeta\sin\theta)$, and $\hat{l}_4(a_1', a_2', 0)$, respectively.

To find $\hat{l}_1$ in global coordinates, the direction cosine transformation matrix $[T_{ij}]$ should be defined. With $\hat{p}_1$ and $\hat{l}_4$ known in global coordinates we have

$$\{\hat{p}_{1x},\hat{p}_{1y},\hat{p}_{1z}\}^T_{\text{global}} = \underset{L\rightarrow G}{[T_{ij}]_1}\ \{1,0,0\}^T_{\text{local}} \tag{1}$$

from which

$$(T_{11})_1 = \hat{p}_{1x}, \quad (T_{21})_1 = \hat{p}_{1y}, \quad (T_{31})_1 = \hat{p}_{1z} \tag{2}$$

$L \rightarrow G$ underneath $[T_{ij}]_1$ indicates transformation from local to global coordinates. From now on the subscripts global, local, and $L \rightarrow G$ will be omitted for simplicity. Similarly,

$$\{\hat{l}_{4x},\hat{l}_{4y},\hat{l}_{4z}\}^T = [T_{ij}]_1\{a_1',a_2',0\}^T \tag{3}$$

in which

$$a_1' = \hat{l}_4 \bullet \hat{p}_1 = \cos\eta \tag{4}$$

$$a_2' = \sqrt{1-(a_1')^2} = \sin\eta \tag{5}$$

where positive sign is taken for the square root as a result of construction of the local coordinate system. Thus

$$\{\hat{l}_{4x},\hat{l}_{4y},\hat{l}_{4z}\}^T = [T_{ij}]_1\{\cos\eta,\sin\eta,0\}^T \tag{6}$$

or

$$\begin{aligned}\hat{l}_{4x} &= (T_{11})_1\cos\eta + (T_{12})_1\sin\eta \\ \hat{l}_{4y} &= (T_{21})_1\cos\eta + (T_{22})_1\sin\eta \\ \hat{l}_{4z} &= (T_{31})_1\cos\eta + (T_{32})_1\sin\eta\end{aligned} \tag{7}$$

Solving $(T_{12})_1$, $(T_{22})_1$, and $(T_{32})_1$ gives

$$\begin{aligned}(T_{12})_1 &= (\hat{l}_{4x} - \hat{p}_{1x}\cos\eta)/\sin\eta \\ (T_{22})_1 &= (\hat{l}_{4y} - \hat{p}_{1y}\cos\eta)/\sin\eta \\ (T_{32})_1 &= (\hat{l}_{4z} - \hat{p}_{1z}\cos\eta)/\sin\eta\end{aligned} \tag{8}$$

Now $(T_{13})_1$, $(T_{23})_1$, and $(T_{33})_1$ can be found as their cofactors. Thus

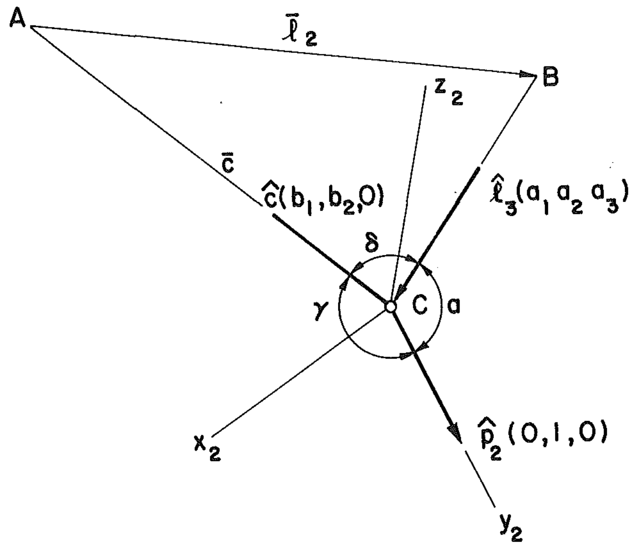

Fig. 4 A local coordinate system and links l_2 and l_3

$$(T_{13})_1 = (\hat{p}_{1y}\hat{l}_{4z} - \hat{p}_{1z}\hat{l}_{4y})/\sin\eta$$
$$(T_{23})_1 = -(\hat{p}_{1x}\hat{l}_{4z} - \hat{p}_{1z}\hat{l}_{4x})/\sin\eta$$
$$(T_{33})_1 = (\hat{p}_{1x}\hat{l}_{4y} - \hat{p}_{1y}\hat{l}_{4x})/\sin\eta \qquad (9)$$

Therefore

$$[T_{ij}]_1 = \frac{1}{\sin\eta}\begin{bmatrix} \hat{p}_{1x}\sin\eta & \hat{l}_{4x} - \hat{p}_{1x}\cos\eta & \hat{p}_{1y}\hat{l}_{4z} - \hat{p}_{1z}\hat{l}_{4y} \\ \hat{p}_{1y}\sin\eta & \hat{l}_{4y} - \hat{p}_{1y}\cos\eta & \hat{p}_{1z}\hat{l}_{4x} - \hat{p}_{1x}\hat{l}_{4z} \\ \hat{p}_{1z}\sin\eta & \hat{l}_{4z} - \hat{p}_{1z}\cos\eta & \hat{p}_{1x}\hat{l}_{4y} - \hat{p}_{1y}\hat{l}_{4x} \end{bmatrix} \qquad (10)$$

Now $\hat{l}_1$ in global coordinates can be found as

$$\{\hat{l}_{1x}, \hat{l}_{1y}, \hat{l}_{1z}\}^T = [T_{ij}]_1\{\cos\zeta, \sin\zeta\cos\theta, \sin\zeta\sin\theta\}^T \qquad (11)$$

(*c*) **Analysis of $\hat{l}_3$.** Let vector $\bar{c}$ be defined such that it forms a closed loop with vectors $\bar{l}_2$ and $\bar{l}_3$ as shown in Fig. 4. It also forms a closed loop with vectors $\bar{l}_1$ and $\bar{l}_4$. From the figure

$$\bar{c} = \bar{l}_1 - \bar{l}_4 \quad \text{and} \quad \hat{c} = \bar{c}/|\bar{c}| \qquad (12)$$

A local coordinate system with the origin at joint C is set such that the y_2-axis is along the known vector $\hat{p}_2$ as shown in Fig. 4. The x_2-axis is in the plane that consists of known vectors $\bar{c}$ and $\hat{p}_2$, perpendicular to the y_2-axis and the angle between $\hat{c}$ and x_2-axis is less than $\pi/2$. The z-axis will follow the right-hand rule. The direction cosines of the unit vectors $\hat{p}_2$, $\hat{c}$, and $\hat{l}_3$ in the local coordinate system are expressed in the parenthesis for each unit vector as $\hat{p}_2$ (0, 1, 0), $\hat{c}$ (b_1, b_2, 0), and $\hat{l}_3$ (a_1, a_2, a_3), respectively.

The unknown direction cosines in the local coordinate system will be found by applying the dot product of unit vectors and using the known angles from its design. The direction cosine b_2 can be obtained from unit vectors $\hat{p}_2$ and $\hat{c}$ and the known angle γ as follows.

$$\begin{aligned} \hat{p}_2 \cdot \hat{c} &= \hat{p}_{2x}\hat{c}_x + \hat{p}_{2y}\hat{c}_y + \hat{p}_{2z}\hat{c}_z \text{ in global coordinates} \\ &= \cos\gamma \\ &= b_2 \text{ in local coordinates} \end{aligned} \qquad (13)$$

from which

$$b_2 = \cos\gamma \qquad (14)$$

where the angle γ between $\hat{p}_2$ and $\hat{c}$ is taken to be less than π. Therefore

$$b_1 = \sqrt{1 - b_2^2} = \sin\gamma \qquad (15)$$

where the positive sign is taken for the square root as a result of construction of the local coordinate system.

The direction cosines a_1, a_2, and a_3 of unit vector $\hat{l}_3$ can be obtained as follows. From the dot product of $\hat{l}_3$ and $\hat{p}_2$, and $\hat{l}_3$ and $\hat{c}$ we have

$$-\hat{l}_3 \cdot \hat{p}_2 = -a_2 = \cos\alpha \qquad (16)$$
$$-\hat{l}_3 \cdot \hat{c} = -a_1 b_1 - a_2 b_2 = \cos\delta \qquad (17)$$

where the known angle α between $\hat{p}_2$ and $-\hat{l}_3$, and the unknown angle δ between $\hat{c}$ and $-\hat{l}_3$ are chosen to be less than π. By applying the cosine law to ΔABC

$$\cos\delta = (l_3^2 + c^2 - l_2^2)/2l_3 c \qquad (18)$$

Therefore

$$a_1 = -(\cos\delta + a_2 b_2)/b_1 \qquad (19)$$

in which b_1, b_2, a_2, and $\cos\delta$, have been just defined in equations (14)–(16), and (18). The direction cosine a_3 can now be calculated as

$$a_3 = \pm\sqrt{1 - a_1^2 - a_2^2} \qquad (20)$$

The positive and negative signs of a_3 correspond to two possible positions of joint B for the given problem. If $1 - a_1^2 - a_2^2 = 0$, then the mechanism is not working.

Summarizing, we have

$$b_1 = \sin\gamma \quad a_1 = -(\cos\delta - \cos\alpha\cos\gamma)/\sin\gamma$$
$$b_2 = \cos\gamma \quad a_2 = -\cos\alpha$$
$$a_3 = \pm\sqrt{1 - a_1^2 - a_2^2} \qquad (21)$$

The transformation matrix from local to global coordinates can now be determined as follows. As

$$\{\hat{p}_{2x}, \hat{p}_{2y}, \hat{p}_{2z}\}^T = [T_{ij}]_2 \quad \{0,1,0\}^T \qquad (22)$$

and

$$\{\hat{c}_x, \hat{c}_y, \hat{c}_z\}^T = [T_{ij}]_2 \quad \{b_1, b_2, 0\}^T \qquad (23)$$

from which

$$(T_{12})_2 = \hat{p}_{2x}, (T_{22})_2 = \hat{p}_{2y}, (T_{32})_2 = \hat{p}_{2z} \qquad (24)$$

and

$$(T_{11})_2 = [\hat{c}_x - (T_{12})_2 b_2]/b_1$$
$$(T_{21})_2 = [\hat{c}_y - (T_{22})_2 b_2]/b_1 \qquad (25)$$
$$(T_{31})_2 = [\hat{c}_z - (T_{32})_2 b_2]/b_1$$

Since each element in a direction cosine matrix is equal to its own cofactor, therefore

$$(T_{13})_2 = (T_{21})_2(T_{32})_2 - (T_{22})_2(T_{31})_2$$
$$(T_{23})_2 = (T_{12})_2(T_{31})_2 - (T_{11})_2(T_{32})_2 \qquad (26)$$
$$(T_{33})_2 = (T_{11})_2(T_{22})_2 - (T_{12})_2(T_{21})_2$$

The resulting transformation matrix is

$$[T_{ij}]_2 = \frac{1}{\sin\gamma}\begin{bmatrix} \hat{c}_x - \hat{p}_{2x}\cos\gamma & \hat{p}_{2x}\sin\gamma & \hat{p}_{2z}\hat{c}_y - \hat{p}_{2y}\hat{c}_z \\ \hat{c}_y - \hat{p}_{2y}\cos\gamma & \hat{p}_{2y}\sin\gamma & \hat{p}_{2x}\hat{c}_z - \hat{p}_{2z}\hat{c}_x \\ \hat{c}_z - \hat{p}_{2z}\cos\gamma & \hat{p}_{2z}\sin\gamma & \hat{p}_{2y}\hat{c}_x - \hat{p}_{2x}\hat{c}_y \end{bmatrix} \qquad (27)$$

Now the unit vector $\hat{l}_3$ in global coordinates can be obtained from

$$\{\hat{l}_{3x}, \hat{l}_{3y}, \hat{l}_{3z}\}^T = [T_{ij}]_2\{a_1, a_2, a_3\}^T \qquad (28)$$

and the vector $\bar{l}_3$ is

$$\bar{l}_3 = l_3\hat{l}_3 \qquad (29)$$

Note that

if $\alpha + \beta > \gamma$, l_3 has two positions

if $\alpha + \beta = \gamma$, l_3 has one position

if $\alpha + \beta < \gamma$, it is an impossible case

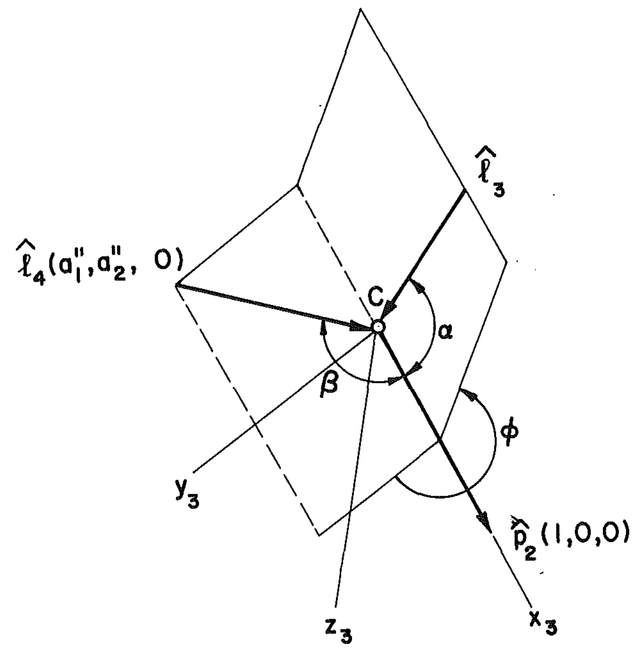

Fig. 5 A local coordinate system and output angle measurement

(*d*) **Analysis of $\hat{l}_2$.** Let us consider the equation

$$\bar{l}_2 + \bar{l}_3 + \bar{c} = 0 \tag{30}$$

or its scalar form

$$\begin{aligned} l_2\hat{l}_{2x} + l_3\hat{l}_{3x} + c\hat{c}_x &= 0 \\ l_2\hat{l}_{2y} + l_3\hat{l}_{3y} + c\hat{c}_y &= 0 \\ l_2\hat{l}_{2z} + l_3\hat{l}_{3z} + c\hat{c}_z &= 0 \end{aligned} \tag{31}$$

From these equations the components of unit vector $\hat{l}_2$ can be solved as

$$\begin{aligned} \hat{l}_{2x} &= -(l_3\hat{l}_{3x} + c\hat{c}_x)/l_2 \\ \hat{l}_{2y} &= -(l_3\hat{l}_{3y} + c\hat{c}_y)/l_2 \\ \hat{l}_{2z} &= -(l_3\hat{l}_{3z} + c\hat{c}_z)/l_2 \end{aligned} \tag{32}$$

Therefore

$$\bar{l}_2 = l_2\hat{l}_2 \tag{33}$$

(*e*) **Output Angle ϕ.** The output angle ϕ for the rotation about the $\hat{p}_2$-axis can be measured with any arbitrary reference. As shown in Fig. 5, ϕ is chosen as the angle between the two planes formed by $\hat{p}_2$ and $\hat{l}_4$, and $\hat{p}_2$ and $\hat{l}_3$, and $\hat{p}_2\hat{l}_4$ plane is chosen as a reference. Both the angle α between $\hat{p}_2$ and $-\hat{l}_3$ and the angle β between $\hat{p}_2$ and $-\hat{l}_4$ are chosen to be less than π and they are known angles from the mechanism.

Let the local coordinates x_3, y_3, and z_3 with the origin at C be chosen as follows:

x_3-axis is along the known rotating axis $\hat{p}_2$ and has the same positive direction as $\hat{p}_2$.

y_3-axis is in the plane of $\hat{p}_2$ and $\hat{l}_4$ and the angle between $-\hat{l}_4$ and the y-axis is less than $\pi/2$.

z_3-axis follows the right-hand rule.

It is seen that the angle ϕ can now be measured between x_3y_3-plane and x_3l_3-plane with x_3y_3-plane as reference.

The direction cosines of the unit vectors $\hat{p}_2$, $\hat{l}_3$, and $\hat{l}_4$ in the local coordinate system are expressed in the parenthesis for each unit vector as $\hat{p}_2$ (1, 0, 0), $\hat{l}_3$ ($-\cos\alpha$, $-\sin\alpha\cos\phi$, $-\sin\alpha\sin\phi$), and (a_1'', a_2'', 0), respectively.

To find ϕ, the same procedure used to find $\hat{l}_1$ will be followed. The transformation matrix $[T_{ij}]_3$ is obtained as

$$[T_{ij}]_3 = \frac{1}{\sin\beta}\begin{bmatrix} \hat{p}_{2x}\sin\beta & -\hat{l}_{4x} - \hat{p}_{2x}\cos\beta & -\hat{p}_{2y}\hat{l}_{4z} + \hat{p}_{2z}\hat{l}_{4y} \\ \hat{p}_{2y}\sin\beta & -\hat{l}_{4y} - \hat{p}_{2y}\cos\beta & -\hat{p}_{2z}\hat{l}_{4x} + \hat{p}_{2x}\hat{l}_{4z} \\ \hat{p}_{2z}\sin\beta & -\hat{l}_{4z} - \hat{p}_{2z}\cos\beta & -\hat{p}_{2x}\hat{l}_{4y} + \hat{p}_{2y}\hat{l}_{4x} \end{bmatrix} \tag{34}$$

Therefore

$$\{\hat{l}_{3x}, \hat{l}_{3y}, \hat{l}_{3z}\}^T = -[T_{ij}]_3\{\cos\alpha,\ \sin\alpha\cos\phi,\ \sin\alpha\sin\phi\}^T \tag{35}$$

This equation in $\hat{l}_3$ can be expanded into

$$\begin{aligned} \hat{l}_{3x} &= -[(T_{11})_3\cos\alpha + (T_{12})_3\sin\alpha\cos\phi + (T_{13})_3\sin\alpha\sin\phi] \\ \hat{l}_{3y} &= -[(T_{21})_3\cos\alpha + (T_{22})_3\sin\alpha\cos\phi + (T_{23})_3\sin\alpha\sin\phi] \\ \hat{l}_{3z} &= -[(T_{31})_3\cos\alpha + (T_{32})_3\sin\alpha\cos\phi + (T_{33})_3\sin\alpha\sin\phi] \end{aligned} \tag{36}$$

From any two of these three equations $\sin\phi$ and $\cos\phi$ can be solved. If the first two equations are chosen, we obtain

$$\sin\phi = \frac{[-(T_{22})_3\hat{l}_{3x} + (T_{12})_3\hat{l}_{3y}] - [(T_{11})_3(T_{22})_3 - (T_{12})_3(T_{21})_3]\cos\alpha}{[(T_{13})_3(T_{22})_3 - (T_{12})_3(T_{23})_3]\sin\alpha} \tag{37}$$

$$\cos\phi = \frac{[-(T_{23})_3\hat{l}_{3x} - (T_{13})_3\hat{l}_{3y}] - [(T_{11})_3(T_{23})_3 - (T_{13})_3(T_{21})_3]\cos\alpha}{[(T_{12})_3(T_{23})_3 - (T_{13})_3(T_{22})_3]\sin\alpha} \tag{38}$$

These two equations can be simplified as

$$\sin\phi = \frac{(T_{22})_3\hat{l}_{3x} - (T_{12})_3\hat{l}_{3y} + (T_{33})_3\cos\alpha}{(T_{31})_3\sin\alpha} \tag{39}$$

$$\cos\phi = \frac{-(T_{23})_3\hat{l}_{3x} + (T_{13})_3\hat{l}_{3y} + (T_{32})_3\cos\alpha}{(T_{31})_3\sin\alpha} \tag{40}$$

From these two equations the angle ϕ can be completely determined.

2 Displacement Analysis of the RGCR Mechanism

The RGCR four-link spatial mechanism whose schematic diagram is shown in Fig. 6 is similar to the RGGR mechanism except that one of the spherical joints is replaced by a cylindrical joint.

The known data of the mechanism for the analysis are the lengths l_1, l_2, the vector $\bar{l}_4$, the directions of rotation of $\hat{p}_1$, $\hat{p}_2$, the angles ζ, η, α, β, and the input angle θ. The unknown quantities are $\hat{l}_1$, $\hat{l}_2$, and $\hat{l}_3$. The angles, ζ between $\hat{p}_1$ and $\hat{l}_1$, η between $\hat{p}_1$ and $\hat{l}_4$, α between $\hat{p}_2$ and $\hat{l}_3$, and β between $\hat{p}_2$ and $\hat{l}_4$ are chosen to be less than π and they are known angles from the construction of the mechanism.

In the analysis, the only difference from the RGGR is the calculation of $\bar{l}_3$. The analysis of $\bar{l}_3$ is as follows. From Fig. 6,

$$\bar{c} = \bar{l}_1 - \bar{l}_4 \quad \text{and} \quad \hat{c} = \bar{c}/|\bar{c}| \tag{41}$$

By applying cosine law to ΔABC we obtain

$$c^2 = l_2^2 + l_3^2 - 2l_2l_3\cos\psi \tag{42}$$

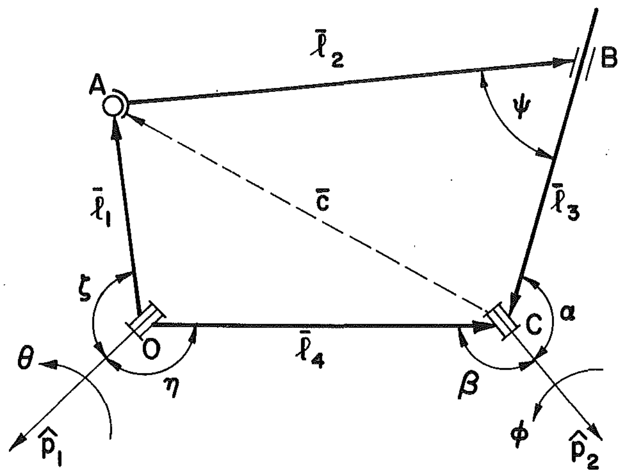

Fig. 6 The schematic diagram of a RGGR four-line spatial mechanism and its known data

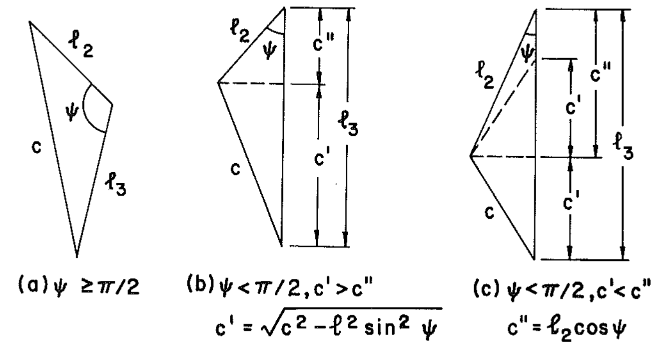

Fig. 7 Transmission angle and l_3

To solve l_3 the preceding equation is rewritten as

$$l_3^2 - (2l_2\cos\psi)\,l_3 + (l_2^2 - c^2) = 0 \tag{43}$$

This gives

$$l_3 = l_2\cos\psi \pm \sqrt{c^2 - l_2^2\sin^2\psi} \tag{44}$$

in which the rules of choice of positive and negative signs before the square root are as follows:

(*i*) For $\psi \geq \pi/2$ positive sign only and there is only one solution.

(*ii*) For $\psi < \pi/2$ and $\sqrt{c^2 - l^2\sin^2\psi} > l_2 \cos\psi$, positive sign only and there is only one solution.

(*iii*) For $\psi < \pi/2$ and $l_2\cos\psi > \sqrt{c^2 - l^2\sin\psi}$, positive and negative signs correspond to two positions for two solutions of l_3.

Figure 7 illustrates the choice of these rules. Also by applying the cosine law to ΔABC, we obtain

$$\cos\delta = (l_3^2 + c^2 - l_2^2)/2l_3c. \tag{45}$$

Now, the unknown unit vectors $\hat{l}_3$ can be obtained in the same manner as finding $\hat{l}_3$ in the RGGR mechanism by using the local coordinate system and their direction cosines of corresponding unit vectors.

3 Displacement Analysis of the RRGG Mechanism

The RRGG four-link spatial mechanism is a variation of the popular RGGR four-link spatial linkage. Each mechanism has a single degree of freedom, with a passive degree of freedom in the GG link. A schematic diagram of a RRGG mechanism is shown in Fig. 8.

The known quantities of the mechanism are the lengths l_1, l_2, and l_3, the vector $\bar{l}_4$, the direction of rotation $\hat{p}_1$, the angles ζ, η, α, and β from the linkage design, and the input angle θ. The angle ζ, between $\hat{p}_1$ and $\hat{l}_1$, and the angle η, between $\hat{p}_1$ and $\hat{l}_4$, are chosen to be less than π.

Both the angle α, between $\hat{p}_2$ and $\hat{l}_2$, and the angle β, between $\hat{p}_2$ and $-\hat{l}_1$, are also chosen to be less than π. The unknown quantities are $\hat{l}_1$, $\hat{l}_2$, and $\hat{l}_3$.

After calculating $\hat{l}_1$ by equation (11), $\hat{p}_2$ is determined by the direction cosine matrix method as illustrated earlier. $\hat{p}_2$ is calculated as

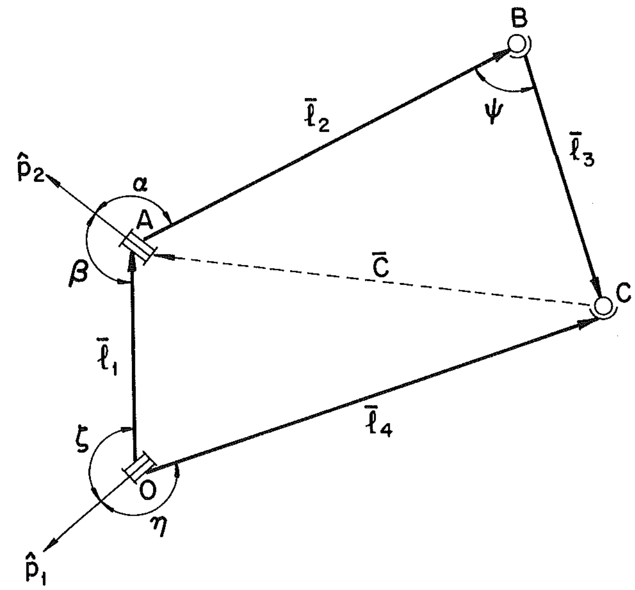

Fig. 8 The schematic diagram of the RRGG mechanism and its known data

$$\begin{Bmatrix} \hat{p}_{2x} \\ \hat{p}_{2y} \\ \hat{p}_{2z} \end{Bmatrix} = \frac{1}{\sin\zeta} \begin{bmatrix} \hat{p}_{1x} + \hat{l}_{1x}\cos\zeta & -\hat{l}_{1x}\sin\zeta & \hat{l}_{1y}\hat{p}_{1z} - \hat{l}_{1z}\hat{p}_{1y} \\ \hat{p}_{1y} + \hat{l}_{1y}\cos\zeta & -\hat{l}_{1y}\sin\zeta & \hat{l}_{1z}\hat{p}_{1x} - \hat{l}_{1x}\hat{p}_{1z} \\ \hat{p}_{1z} + \hat{l}_{1z}\cos\zeta & -\hat{l}_{1z}\sin\zeta & \hat{l}_{1x}\hat{p}_{1y} - \hat{l}_{1y}\hat{p}_{1x} \end{bmatrix} \begin{Bmatrix} b_1 \\ b_2 \\ b_3 \end{Bmatrix} \tag{46}$$

where

$$b_1 = (\cos\rho - \cos\zeta\cos\beta)/\sin\zeta$$
$$b_2 = \cos\beta$$
$$b_3 = \pm\sqrt{1 - b_1^2 - b_2^2}$$

The positive and negative signs of b_3 can be decided from the observation of the given mechanism construction in the local coordinate system.

Once $\hat{p}_2$ is determined, the analyses of $\hat{l}_2$ and $\hat{l}_3$ of the RRGG are similar procedure as the analysis of $\hat{l}_2$ and $\hat{l}_3$ of the RGGR by letting $\hat{l}_2$ and $\hat{l}_3$. Therefore, the transformation matrix equation (27) could be used with negative $\hat{c}$ components in calculation of $\hat{l}_2$.

The output angle ϕ for the rotation about the $\hat{p}_2$-axis can be measured with any arbitrary reference. The ouptut angle ϕ is chosen as the angle between the two planes formed by $\hat{p}_2$ and $\hat{l}_1$, and $\hat{p}_2$ and $\hat{l}_2$. The p_2l_2-plane is chosen as a reference. The output angle could be completely determined from the following two equations

$$\sin\phi = \frac{-(T_{22})_4\hat{l}_{2x} + (T_{12})_4\hat{l}_{2y} + (T_{33})_4\cos\alpha}{(T_{31})_4\sin\alpha} \tag{47}$$

and

$$\cos\phi = \frac{(T_{23})_4 \hat{l}_{2x} - (T_{13})_4 \hat{l}_{2y} + (T_{32})_4 \cos\alpha}{(T_{31})_4 \sin\alpha} \quad (48)$$

where the transformation matrix $[T_{ij}]_4$ is obtained as

$$[T_{ij}]_4 = \frac{1}{\sin\beta} \begin{bmatrix} \hat{p}_{2x}\sin\beta & -\hat{l}_{1x} - \hat{p}_{2x}\cos\beta & -\hat{p}_{2y}\hat{l}_{1z} + \hat{p}_{2z}\hat{l}_{1y} \\ \hat{p}_{2y}\sin\beta & -\hat{l}_{1y} - \hat{p}_{2y}\cos\beta & -\hat{p}_{2z}\hat{l}_{1x} + \hat{p}_{2x}\hat{l}_{1z} \\ \hat{p}_{2z}\sin\beta & -\hat{l}_{1z} - \hat{p}_{2z}\cos\beta & -\hat{p}_{2x}\hat{l}_{1y} + \hat{p}_{2y}\hat{l}_{1x} \end{bmatrix} \quad (49)$$

4 Displacement Analysis of the RRGC Mechanism

The displacement analysis of the RRGC four-link spatial mechanism shown in Fig. 9 can be performed by using part of the analysis scheme of the RRGG.

The known data of the RRGC mechanism shown in Fig. 9 are the lengths l_1 and l_2, the vectors $\bar{l}_4$, and $\hat{l}_3$, the direction of rotation $\hat{p}_1$, the angles ζ, η, α, β, ϵ, and the input angle θ. The definition of the angles is the same as the RRGG, except angle ϵ between $\hat{l}_3$ and $\hat{l}_4$, which is chosen to be less than π. The unknown quantities of this mechanism are $\hat{l}_1$, $\hat{l}_2$, and l_3.

The displacement analysis of the RRGC can be performed easily by using part of the analysis scheme of the RRGG for $\hat{p}_2$ and part of the similar analysis scheme of the RGCR for l_3 and the output angle.

5 Numerical Examples

For the numerical illustrations, the dimensions and other known data of the spatial four-bar linkages are given as follows.

Example 1

RGGR mechanism

l_1 = 101.6 mm
l_2 = 381.0 mm
l_3 = 254.0 mm
l_4 = 314.2 mm
$\bar{l}_4$ = (304.8, 0, 76.2)
$\hat{p}_1$ = (0, 0, 1)
$\hat{p}_2$ = (1, 0, 0)
ρ = 90 deg
α = 90 deg

Example 2

RGCR mechanism

l_1 = 203.2 mm
l_2 = 381.0 mm
l_4 = 314.2 mm
$\bar{l}_4$ = (304.8, 0, 76.2)
$\hat{p}_1$ = (0, 0, 1)
$\hat{p}_2$ = (0, 0, 1)
ρ = 90 deg
α = 90 deg
ψ = 74 deg

Example 3

RRGG mechanism

l_1 = 119.0 mm
l_2 = 248.6 mm
l_3 = 186.7 mm
l_4 = 225.6 mm
$\hat{l}_4$ = (1, 0, 0)
$\hat{p}_1$ = (0, 0, 1)
α = 90 deg
β = 92.27 deg
γ = 0 deg
ρ = 158.17 deg

Example 4

RRGC mechanism

l_1 = 119.0 mm
l_2 = 248.6 mm
l_4 = 228.6 mm
$\hat{l}_3$ = (0.4082, 0.8165, 04082)
$\hat{l}_4$ = (1, 0, 0)
$\hat{p}_1$ = (0, 0, 1)
ζ = 90 deg
α = 90 deg
ϵ = 108 deg

With input angle θ as a parameter, the vectors $\bar{l}_1$, $\bar{l}_2$, and $\bar{l}_3$, the output angle ϕ, and the transmission angle ψ are determined. The transmission angle is defined as an angle between $-\hat{l}_2$ and $\hat{l}_3$. The results of Example 1 are tabulated in Table 1 for two possible configurations of the RGGR mechanism, i.e., there are two output angles ϕ_1 and ϕ_2 for a given input angle θ. The transmission angles are the same in both configurations. Table 2 shows three components of each of the vector $\bar{l}_1$, $\bar{l}_2$, and $\bar{l}_3$ in the global coordinates corresponding to a particular input angle, in this case, θ = 60 deg for the RGGR mechanism. For Example 2, Table 3 shows output angle and the calculated length of link 3 corresponding to input angle θ in the RGGR mechanism.

For Examples 3 and 4, the results are tabulated in Table 4 for the RRGG mechanism and in Table 5 for the RRGC mechanism. Tables 4 and 5 show the results of the transmission angle and output angle for each input angle.

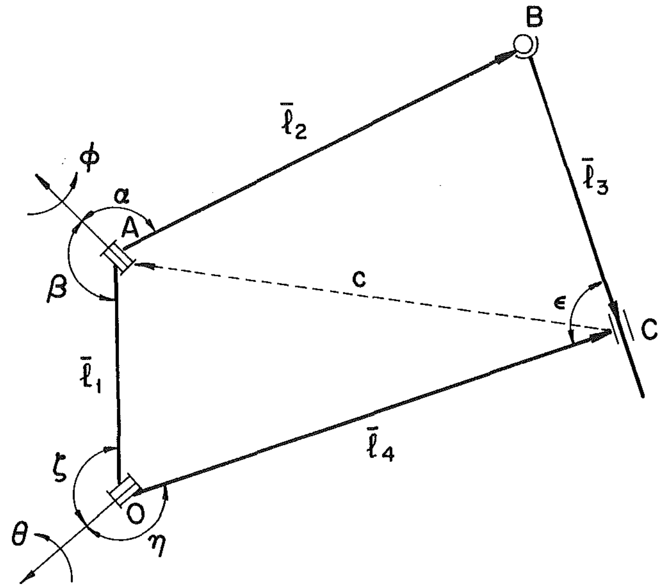

Fig. 9 The schematic diagram of RRGC four-link spatial mechanism and its known data

Table 1 Output angle ϕ and transmission angle ψ versus input angle θ of the RGGR mechanism, all angles in degree

θ	ϕ_1	ϕ_2	ψ
110	91.6	165.6	65.8
100	75.1	179.5	62.3
90	63.0	190.8	58.7
80	53.3	201.3	54.9
70	45.3	211.9	51.0
60	38.4	223.4	47.2
50	32.5	236.3	43.5
40	27.4	251.4	40.1
30	23.4	269.2	37.1
20	21.0	290.0	34.8
10	21.8	312.1	33.4
0	29.9	330.1	32.9
−10	47.9	338.2	33.4
−20	70.0	339.0	34.8
−30	90.8	336.6	37.1
−40	108.6	332.6	40.1
−50	123.7	327.5	43.5
−60	136.6	321.6	47.2
−70	148.1	314.7	51.0
−80	158.7	306.7	54.9
−90	169.2	297.0	58.7
−100	180.5	284.9	62.3
−110	194.4	268.4	65.8

Table 2 Positions of the RGGR mechanism in system coordinates at θ = 60 deg, all lengths in mm

	Configuration 1 $\hat{i}$	$\hat{j}$	$\hat{k}$	Configuration 2 $\hat{i}$	$\hat{j}$	$\hat{k}$	Resultant
$\bar{l}_1$	50.8	88.0	0.0	50.8	88.0	0.0	101.6
$\bar{l}_2$	254.0	69.8	275.3	254.0	−262.5	−108.4	381.0
$\bar{l}_3$	0.0	−157.2	−199.1	0.0	174.5	184.6	254.0
$\bar{l}_4$	304.8	0.0	76.2	304.8	0.0	76.2	314.2

Table 3 Output angle ϕ and the length of link 3 versus input angle θ of the RGCR mechanism, angles in degree and lengths in mm

θ	ϕ_1	l_3
90	248.4	181.6
100	264.3	270.5
110	274.5	324.6
120	282.6	365.4
130	289.5	397.4
140	295.7	422.5
150	301.3	441.4
160	306.3	454.7
170	311.0	462.6
180	315.2	465.2
190	318.9	462.6
200	322.3	454.7
210	325.1	441.4
220	327.4	422.5
230	328.9	397.4
240	329.4	365.4
250	328.5	324.6
260	325.1	270.5
270	315.8	181.6

In the numerical example of configuration 2 of the RRGC mechanism, the input angle is limited to the range of 80 to -160 deg due to the construction of the mechanism. Another limitation should be observed. The motion that joint B of the mechanism passes through the cylindrical joint C during an increment of the input angle from -100 to -110 deg is impossible in actual cases, although it is theoretically possible in the analysis. Therefore, the range of motion of configuration 2 is divided into two intervals -80 to -100 deg and -110 to -160 deg.

Conclusion

The direction cosine matrix method has been developed for a displacement analysis applicable to all types of four-link, spatial mechanisms. The analyses of the RGGR, RGCR, RRGG, and RRGC mechanisms have been illustrated to demonstrate this method. The advantage of this method is that the analysis yields exact solutions without loss of geometric interpretation and without the need for either numerical or iterative schemes.

The special property of the direction cosine matrix, that each element equals its own cofactor, is the focus of this analysis. Using this property, we avoid the inherent difficulties in the displacement analysis of four-link spatial mechanisms. For example, without using this property, equation (9) would be replaced by

$$T_{13} = \pm\sqrt{1-T_{11}^2-T_{12}^2}$$

$$T_{23} = \pm\sqrt{1-T_{21}^2-T_{22}^2}$$

$$T_{33} = \pm\sqrt{1-T_{31}^2-T_{32}^2}$$

and only one of the eight sets of possible combinations would be the solution. In another example, an algebraic equation of up to eighth-degree polynomial in reference [10] has to be solved numerically.

The extension of this method to a displacement analysis of mechanisms with more than four links and the continuation of kinematic analyses for determining velocities and accelerations of mechanisms with four or more links will be the topics of forthcoming papers.

Table 4 Output angle ϕ and transmission angle ψ versus input angle θ of the RRGG mechanism, all angles in degree

θ	ϕ_1	ϕ_2	ψ
0	137.5	225.8	24.2
10	156.0	245.4	25.4
20	172.9	263.6	28.8
30	188.3	279.5	33.6
40	202.3	293.1	39.2
50	215.1	304.6	45.4
60	227.1	314.3	51.8
70	238.3	322.8	58.3
80	248.7	330.3	64.7
90	258.6	337.1	71.0
100	268.0	343.4	77.1
110	276.8	349.3	82.8
120	285.1	355.0	33.2
130	293.0	0.6	93.0
140	300.5	6.1	97.1
150	307.6	11.6	100.5
160	374.3	17.3	103.0
170	320.8	23.1	104.6
180	326.9	29.1	105.1
190	332.9	35.4	104.6
200	338.6	41.9	103.0
210	344.2	48.8	100.5
220	349.8	56.0	97.1
230	355.3	63.6	93.0
240	0.9	71.7	88.2
250	6.8	80.1	82.8
260	12.9	89.1	77.1
270	19.4	98.6	71.0
280	26.6	108.6	64.7
290	34.7	119.4	58.3
300	43.9	130.9	51.8
310	54.6	143.3	45.4
320	67.2	156.8	39.2
330	82.1	171.7	33.6
340	99.3	188.1	28.8
350	118.1	206.4	25.4
360	137.5	225.8	24.2

Table 5 Output angle ϕ and transmission angle ψ versus input angle θ of the RRGC mechanism, all angles in degree

θ	ϕ_1	ψ_1	ϕ_2	ψ_2
Interval 1				
80	293.5	79.1	276.2	100.9
70	297.1	65.3	258.2	114.7
60	297.0	55.8	242.3	124.2
50	295.3	47.6	225.8	132.4
40	292.5	40.2	208.0	139.8
30	288.7	33.6	189.2	146.4
20	283.8	27.9	170.5	152.1
10	277.8	23.2	153.3	156.8
0	270.8	19.8	138.3	160.2
−10	262.5	17.8	125.4	162.2
−20	252.8	17.0	114.4	163.0
−30	241.3	17.3	104.9	162.7
−40	227.7	18.3	96.5	161.7
−50	212.0	20.0	89.0	160.0
−60	194.9	22.3	82.3	157.7
−70	177.3	25.1	76.1	155.0
−80	160.8	28.3	70.3	151.7
−90	145.9	32.0	64.8	148.0
−100	132.7	36.1	59.6	143.9
Interval 2				
−110	120.8	40.8	54.7	139.2
−120	109.7	45.9	49.9	134.1
−130	98.9	51.7	45.3	128.3
−140	87.8	58.2	41.2	121.8
−150	75.5	66.0	37.9	114.0
−160	59.7	76.7	37.2	103.3

References

1 Yang, A. T., "A Brief Survey of Space Mechanisms," *Design Technology Transfer*, ASME, 1974, pp. 315-321.

2 Uicker, J. J., Jr., "Displacement Analysis of Spatial Mechanisms by an Iterative Method Based on 4×4 Matrices," M.S. thesis, Northwestern University, Evanston, Ill., June, 1963.

3 Uicker, J. J., Jr., Denavit, J., and Hartenberg, R. S., "An Iterative Method for the Displacement Analysis of Spatial Mechanisms," ASME JOURNAL OF APPLIED MECHANICS, Vol. 31, 1964, pp. 309–314.

4 Yang, A. T., "Application of Quaternion Algebra and Dual Numbers to the Analysis of Spatial Mechanisms," Ph. D. Dissertation, Columbia University, New York, 1963.

5 Yang, A. T., and Freudenstein, F. F., "Application of Dual-Number Quaternion Algebra to the Analysis of Spatial Mechanism," ASME JOURNAL OF APPLIED MECHANICS, Vol. 31, 1964, pp. 300–308.

6 Gupta, V. K., "Kinematic Analysis of Plane and Spatial Mechanisms," ASME *Journal of Engineering for Industry*, Vol. 95, 1973, pp. 481–486.

7 Suh, Chung-Ha, and Radcliffe, C. W., *Kinematics and Mechanisms Design*, Wiley, New York, 1978, pp. 79–94.

8 Chace, M., "Vector Analysis of Linkages," ASME *Journal of Engineering for Industry*, Vol. 85, 1963, pp. 289–297.

9 Chace, M., "Development and Application of Vector Mathematics for Kinematic Analysis of Three-Dimensional Mechanisms," Ph.D. Dissertation, University of Michigan, Ann Arbor, Mich., 1964.

10 Chace, M., "Solutions to the Vector Tetrahedron Equations," ASME *Journal of Engineering for Industry*, Vol. 87, 1965, pp. 228–234.

11 Dimentberg, F. M., *The Determination of the Positions of Spatial Mechanism*, Akad Nauk., Moscow, USSR, 1950, p. 142.

12 Dimentberg, F. M., and Kislitsyn, S. G., "Application of Screw Calculus to the Analysis of Three-Dimensional Mechanisms," *Proceedings of the Second All-Union Conference on Basic Problems in the Theory of Machines and Mechanisms*, Moscow, USSR, 1960, pp. 55–56.

13 Soni, A. H., and Harrisberger, L., "Application of (3×3) Screw Matrix to Kinematic and Dynamic Analysis of Mechanisms," *VDI-Brichte*, 1968.

14 Bagci, C., "The RSRC Space Mechanism Analysis by 3×3 Screw Matrix, Synthesis for Screw Generation by Variational Methods," Dissertation, Oklahoma State University, Stillwater, Okla., 1969.

15 Duffy, J., "An Analysis of Five, Six and Seven-Link Spatial Mechanisms," *Proceedings of Third World Congress for the Theory of Machines and Mechanisms*, Kupari, Yugoslavia, 1971, Vol. C, pp. 83–98.

16 Ho, C. Y., "An Analysis of Spatial Four-Bar Linkage by Tensor Method," *IBM Journal of Research and Development*, Vol. 10, No. 3, May 1966, pp. 207–212.

17 Yuan, M. S. C., "Displacement Analysis of the RRCCR Five-Link Spatial Mechanism," ASME JOURNAL OF APPLIED MECHANICS, Vol. 37, 1970, pp. 689–696.

18 Wallace, D. M., and Freudenstein, F. F., "The Displacement Analysis of the Generalized Tracta Coupling," ASME JOURNAL OF APPLIED MECHANICS, Vol. 37, 1970, pp. 713–718.

19 Harrisberger, L., "A Number Synthesis Survey of Three-Dimensional Mechanisms," ASME *Journal of Engineering for Industry*, Vol. 87, 1965, pp. 213–220.

20 Hartenberg, R. S., and Denavit, J., *Kinematic Synthesis of Linkages*, McGraw-Hill, New York, 1964, pp. 344–347.

Journal of Applied Mechanics

Design Data and Methods

Engineering Formulas for Fractures Emanating From Cylindrical and Spherical Holes[1]

R. H. Nilson[2] **and W. J. Proffer**[2]

Generalized integral formulas based on the weight-function technique are used to calculate stress intensity and opening displacements for planar or axisymmetric fractures emanating from a cylindrical or spherical hole in an elastic medium. These approximate formulas reduce to known exact solutions in the limits of very short (notch) fractures or very long (penny-shaped or Griffith) fractures. In the intermediate range, where fracture length is comparable to hole size, the approximation is generally accurate within a few percent, as demonstrated by comparison with available numerical results for the planar problem of a circular hole with an arbitrary number of radial cracks as well as the axisymmetric problems of a cylindrical or spherical hole with a disk-shaped circumferential fracture. The generalized integral formulas provide a fast, simple, and reasonably accurate method for solving a broad class of engineering problems, including hydraulic and explosive fracturing applications, in which the following features are important: cavity pressurization, stress concentration around the cavity due to in situ compressive stresses, arbitrary pressure distribution along fracture, varying fracture length, and multiple fracturing.

1 Introduction

Fractures emanating from cylindrical and spherical cavities are of practical importance not only in the design of load-carrying structures [1], but also in a variety of geological applications such as hydrofracture of oil wells [2], rock blasting with explosives [3], well shooting with explosives or propellants [4], and containment of underground nuclear tests [5]. In all of these geological problems the fractured surfaces are pressurized by a flowing liquid or gas, so the pressure distribution is generally nonuniform and it not known beforehand. To analyze the coupled problem of fluid motion and rock deformation it is customary and expedient to rely on closed-form integral representations for the stress intensity at the fracture tip and the opening displacement along the fracture.

The well-known integral formulas for wedge-shaped [6] (planar) and penny-shaped [7] (axisymmetric) fractures do not, however, take into account the presence of the pressurized cavity that is the source of the fractures. Yet it is the local stress field around the cavity that controls the initiation of the fracture [8, 9], so this feature must be included in any unified treatment of fracture initiation and propagation. Moreover, in high-pressure blasting and well-shooting applications the hoop tension around the cavity is sufficient to drive the fractures for several cavity radii [3, 10], even without any pressurization of the fractured surfaces. In all instances the fracture is initially short compared to the cavity diameter, but usually grows very long compared to the cavity diameter, suggesting the need for an analytical model that spans the full range of fracture length. Also there is a desire for some degree of precision in the calculation of opening displacements, since the fluid flow rate along the fracture is very sensitive to the size of the aperture. Finally, there is a need for computational speed, since the opening displacements and stess intensity must generally be calculated at each discrete time step in a hydraulic fracturing analysis.

Previous investigators have used mapping and collocation methods or finite element methods to investigate the problem of fractures emanating from cylindrical [10–14] and spherical [15] holes. Such studies provide highly accurate numerical results for a number of very important special cases. However, these methods are somewhat costly and rather cumbersome to be directly implemented in an overall treatment of the hydraulic fracturing process, and the available tabular and graphical results do not include the effect of pressure variation along the fracture.

The present paper describes a pair of simple closed-form integral formulas that can be used to rapidly calculate stress intensity and opening displacements for planar or axisymmetric fractures emanating from cylindrical or spherical holes. All of the following features are taken into account:

1. arbitrary pressure distribution along fracture,
2. influence of cavity pressurization,
3. ratio of fracture length to cavity size,
4. compressive stress concentrations around cavity, and
5. multiple fractures.

Comparison with previous analytical and numerical work shows that accuracy is generally within a few percent for a broad range of test problems.

[1]This work was sponsored by the Defense Nuclear Agency under RDT&E RMSS Code C4000 83466J24AMXJA 00002 H2590D.

[2]S-Cubed, P.O. Box 1620, La Jolla, Calif. 92038. R. H. Nilson is an Assoc. Mem. ASME.

Manuscript received by ASME Applied Mechanics Division, November, 1983; final revision, May, 1984.

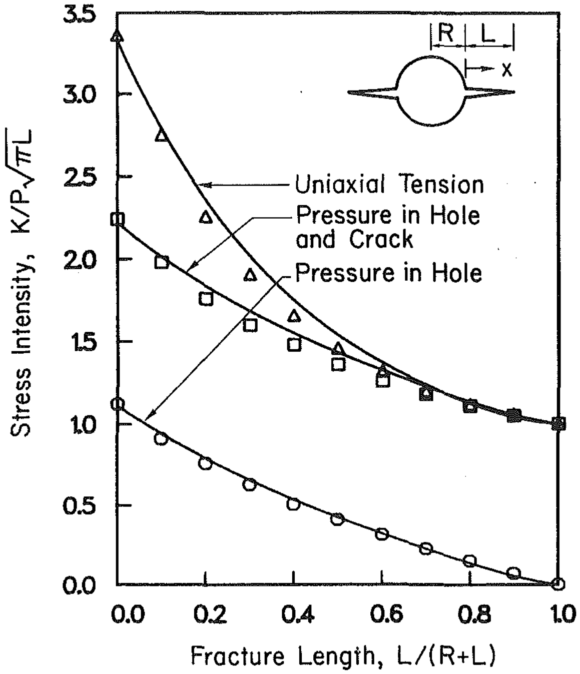

Fig. 1 Wedge-shaped fractures emanating from a cylindrical hole. Comparison of present formula (solid lines) with collocation results of Bowie [11] (symbols) for three different loading configurations.

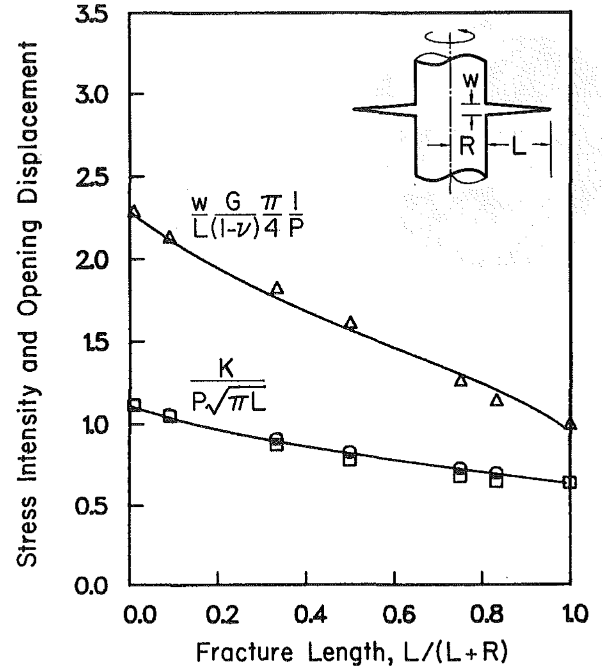

Fig. 2 Disk-shaped fracture emanating from a cylindrical hole. Comparison of present formula (solid lines) with collocation results (△, ○) of Keer, Luk, and Freedman [14] and finite element results (□) of Benzley [14].

2 Analysis

In accordance with the weight-function methodology of Bueckner [16] and Rice [17], the strength of the tensile stress singularity at the tip of a fracture emanating from a hole in an infinite elastic medium can be calculated from the following integral formula

$$K=\frac{2}{\sqrt{\pi}}\sqrt{L}\int_0^L (P-\sigma)f\left(\frac{x}{L},\frac{L}{R}\right)\frac{dx}{\sqrt{L^2-x^2}} \tag{1}$$

in which K is the (mode 1) stress intensity factor, L is the length of the fracture, R is the radius of the hole, x is the position variable along the fracture, $P(x)$ is the internal pressure within the fracture, and $\sigma(x)$ is external confining stress acting normal to the fracture plane. The configuration function, f, is closely related to the weight function, M, of Bueckner [16] and Rice [17] $M = 2(L/\pi(L^2 = x^2))^{1/2}f$; either depends only on the geometry. The simplified form of equation (1) assumes that any loading due to the pressurization of the hole or the application of confining stress has been included in $P(x)$ or $\sigma(x)$ as an equivalent crack-line loading, in accordance with the rules of superposition [18, 19].

The width of the fracture (twice the opening displacement) is derived directly from the stress intensity relationship (1) by application of Castigliano's theorem in the manner suggested by Paris [19, 20]

$$w(x)=\frac{4}{\pi}\frac{(1-\nu)}{G}\int_x^L\left(\int_0^a (P-\sigma)f\left(\frac{\xi}{a},\frac{a}{R}\right)\frac{d\xi}{\sqrt{a^2-\xi^2}}\right)$$

$$f\left(\frac{x}{a},\frac{a}{R}\right)\left(\frac{a+R}{x+R}\right)^n\frac{a\,da}{\sqrt{a^2-x^2}} \tag{2}$$

in which G and ν are the shear modulus and Poisson's ratio, and $n = 0$ or 1 for planar or axisymmetric cases, respectively.

To apply the formulas (1) and (2), it is only necessary to insert a general expression for the weighting function, f. Numerical methods [21] could be used to obtain tabular listings of $f(x/L)$ for specific geometries and particular

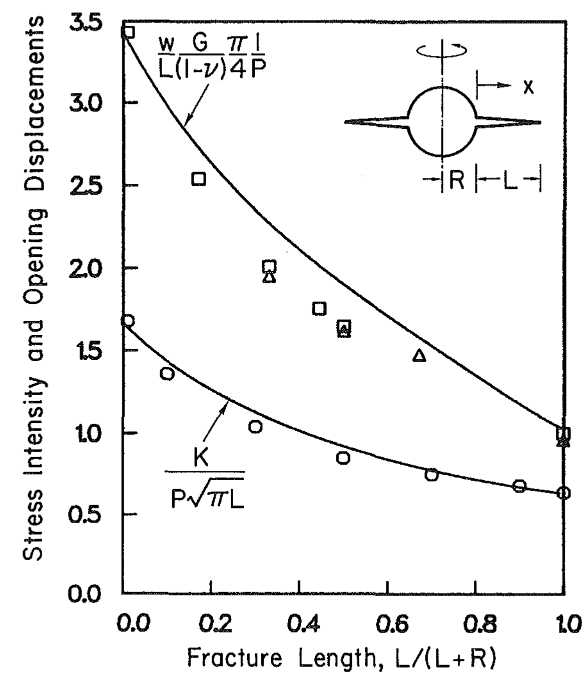

Fig. 3 Disk-shaped fracture emanating from a spherical cavity. Comparison of present formulas (solid lines) with collocation results (○,□) of Atsumi and Shindo [15] and present finite elements calculations (△) [24].

choices of L/R, but the computations are tedious, and the outcome must eventually be fitted with analytical formulas to avoid storage and interpolation of extensive tables. In the present instance, moreover, the limiting forms of f are available in closed form for small and large values of L/R, so it is a relatively simple matter to splice together these limits with smooth analytic functions. To this end, it is convenient to partition the weight function into a product of two functions ($f = f_{\mathrm{rad}} f_{\mathrm{notch}}$) which will each be chosen in an arbitrary, but reasonable, fashion.

Radial divergence effects will be represented by $f_{\rm rad}$

$$f_{\rm rad} = \left(\frac{x+R}{L+R}\right)^n = \left(\frac{x/L+R/L}{1+R/L}\right)^n \quad (3)$$

such that $f_{\rm rad} = 1$ in planar problems with $n = 0$, while in axisymmetric problems with $n = 1$

$$f_{\rm rad} \to 1 \qquad \text{when} \quad L/R << 1 \quad (4)$$

$$\to x/L \qquad \text{when} \quad L/R >> 1 \quad (5)$$

The effects of a stress-free (or uniformly pressurized) cavity surface are acounted for by $f_{\rm notch}$, which is based on the expectation that all short cracks should be equivalent to an external notch crack in the wall of a half space

$$f_{\rm notch} = 1 + 0.3\left(1-\frac{x}{L}\right)\left(\frac{1}{1+L/R}\right)^{2m} \quad (6)$$

so

$$f_{\rm notch} \to 1 + 0.3\left(1-\frac{x}{L}\right) \qquad \text{when} \qquad L/R << 1 \quad (7)$$

$$\to 1 \qquad \text{when} \qquad L/R >> 1 \quad (8)$$

In the short crack limit the correction function, $0.3(1 - x/L)$, is a good approximation to the "Green's function" which was numerically determined by Hartranft and Sih (see Fig. 4.5 in reference [22]) by application of the alternating method to a planar edge crack. These free-surface corrections should decay at least as fast as $(R/(R+L))^m$, owing to the radial divergence around a cylindrical ($m = 2$) or spherical ($m = 3$) cavity. A somewhat stronger decay is, however, expected because the free surface curves away from the fracture and is of very limited extent, compared to the wall of a half space.

The long fracture limit of the proposed formulas is in precise agreement with the well-known exact solutions [6, 7]

$$K = \frac{2}{\sqrt{\pi}}\sqrt{L}\int_x^L (P-\sigma)\left(\frac{x}{L}\right)^n \frac{dx}{\sqrt{L^2-x^2}} \quad (9)$$

$$w = \frac{4}{\pi}\,\frac{(1-\nu)}{G}\int_0^L \left(\int_0^a (P-\sigma)\left(\frac{\xi}{a}\right)^n \frac{d\xi}{\sqrt{a^2-\xi^2}}\right)\frac{a\,da}{\sqrt{a^2-x^2}} \quad (10)$$

for both the planar problem ($n = 0$) and the axisymmetric problem ($n = 1$). Thus, the formulas should be essentially exact for very long fractures as well as for short notch fractures, even for arbitrary distributions of pressure along the fracture.

Cavity pressure causes a hoop tension around the cavity, as given by the following expressions in which P_c is the cavity pressure, R is the cavity radius, and the cylindrical cavity is assumed to be very long [23].

$$\text{sphere:} \qquad \sigma_\theta = -P_c/2\,(R/(R+x))^3 \quad (11)$$

$$\text{cylinder:} \qquad \sigma_\theta = -P_c(R/(R+x))^2,\ \sigma_z = 0 \quad (12)$$

This loading is superposed as a negative contribution to the compressive stress, $\sigma(x)$, acting along the crack. For very short fractures ($R/L >> 1$) this treatment amounts to the superposition of a tensile stress that is uniform along the crack and is of magnitude P_c or $P_c/2$ for the cylindrical and spherical cases, respectively, in keeping with previous exact analyses [10–15]. For very long fractures ($R/L << 1$), this treatment is equivalent to the application of a splitting force (integral of σ_θ) of proper magnitude at the center of the cavity, in keeping with the asymptotic argument of Ouchterlony [10]. So, again, the analytical approach should be exact in the limiting cases of short or long fractures.

The intermediate range, with fracture length comparable to hole radius, can only be checked by comparison with the numerical results that are available for some special cases. In evaluating the present analytical formulas (1) and (2), all integrations are done by the trapezoidal rule using only 10 discrete intervals along the fracture. Singularities are removed by rewriting the differentials as follows:

$$\frac{a\,da}{\sqrt{a^2-x^2}} = d\sqrt{a^2-x^2}, \qquad \frac{d\xi}{\sqrt{a^2-\xi^2}} = d\sin^{-1}(\xi/a) \quad (13)$$

and then simply replacing the nonsingular differentials with their finite differences across the integration intervals. Although these measures slightly degrade the accuracy, they are in keeping with our goal of providing engineering accuracy with speed and simplicity.

3 Comparison With Numerical Results

The plane strain problem of two radial cracks emanating from a cylindrical hole is illustrated in Fig. 1. The normalized stress intensity factor predicted by equation (1) is in good agreement with the numerical results of Bowie [9, 11, 20] for three different loading configurations. When the pressure is restricted to the hole, the hoop tension of equation (12) is the only loading along the crack; $K^* = 1.12$ in the short-crack limit [16, 17] and $K^* \to 0$ in the long-crack limit. When pressure is applied to the fractured surfaces as well as the hole, $K^* = 2(1.12)$ in the short crack limit, and $K^* = 1$ in the long limit when this geometry becomes equivalent to a Griffith crack [6] in an infinite medium. In the third case the cracked hole is subjected to a uniaxial tensile stress, P. So, analogous with the treatment of cavity pressurization, it is appropriate to apply a tensile loading of

$$\sigma_\theta = \frac{P}{2}(2 + 1/(1+x/R)^2 + 3/(1+x/R)^4) \quad (14)$$

which is taken from the exact solution [23] for the stress concentration around an unfractured hole. Since all three configurations are well approximated, the integral formulas should perform well in the general hydrofracture problem where the hole is uniformly pressurized, the fracture is nonuniformly pressured, and the in situ compressive stress field is biaxial.

The axisymmetric problem of a disk-shaped fracture emanating from a long cylindrical hole is illustrated in Fig. 2. The normalized stress intensity and the normalized fracture width predicted by equations (1) and (2) are in good agreement with the numerical results reported by Keer, Luk, and Freedman [14] for the case of uniform pressure acting on the walls of the cylinder and the surface of the fracture. The crack pressure is the only loading applied in the present analysis, since no axial stresses are induced by the pressurization of a long cylindrical hole. In the short crack limit $K^* = 1.12$ and $w^* = 1.46(\pi/2)$, in agreement with notch crack solutions [16, 22]. In the long crack limit $K^* = 2/\pi$ and $w^* = 1$, in agreement with the exact solution (9, 10) for a penny-shaped crack in an infinite medium [7]. This example provides a test of the weighting function, $f_{\rm rad}$, which seems to give an adequate accounting of radial divergence effects.

The axisymmetric problem of a disk-shaped fracture emanating from a spherical cavity is illustrated in Fig. 3. The stress intensity and opening displacement from (1) and (2) are in reasonable agreement with the numerical results of Atsumi and Shindo [15] for the case of uniform pressure applied within the cavity and the fracture. Here, the cavity pressure contributes a hoop stress of $P/2$ at the cavity wall, in accordance with (11), so $K^* = (3/2)1.12$ and $w^* = (3/2)(\pi/2)1.46$ in the short fracture limit. As in the previous example, the problem becomes equivalent to the penny-shaped configuration as the fracture grows larger. The analytical approximation (1) and (2) is about 10 percent too large in the intermediate range, which suggests a somewhat

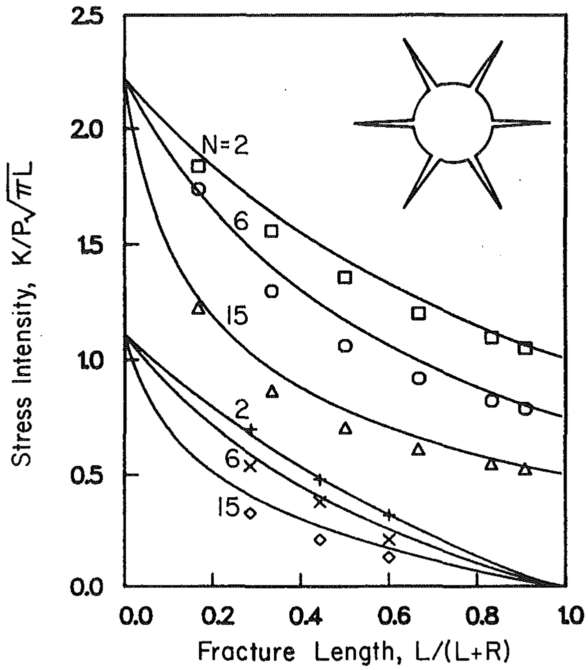

Fig. 4 Multiple-shaped fractures 2, 6, or 15 emanating from a cylindrical hole. Comparison of present formula (solid lines) with numerical results of Ouchterlony (symbols) [10] for pressure in hole and cracks (□, ○, △) and for pressure in hole only (+, ×, ◇).

larger error than in the previous examples. Also included in Fig. 3 are some finite element results [24] which the authors obtained as a check on the analytical formula, prior to our awareness of the work by Atsumi and Shindo.

4 Multiple Fractures

Mutiple fractures are expected to occur when the rise time of the driving pressure pulse is relatively short compared with the time required for stress waves to circle the cavity [4] as in blasting and tailored-pulse well shooting. The present formula (1) and (2) can be extended to planar multifracture configurations by including in the overall weighting function, f, an additional multiplier, f_N, of the following form

$$f_N = \frac{\left(f_\infty + f_\infty \dfrac{L}{\pi R/N}\right)}{\left(f_\infty + \dfrac{L}{\pi R/N}\right)} \tag{15}$$

in which

$$f_\infty = 2\,\frac{\sqrt{N-1}}{N} \tag{15}$$

and N is the number of fractures. Thus, the multiplier is unity ($f_N = 1$) when the fracture length, L, is small compared to the circumferential distance between fractures; while for long fractures the multiplier approaches an asymptotic value ($f = f_\infty$) which depends only on the number of fractures. The particular form of f_∞ given in the foregoing is recommended by Ouchterlony [10] as having "a high degree of accuracy" in calculating the stress intensity factor of fully pressurized star cracks (i.e., long fracture limit), and the proposed form of f_N recovers the desired notch crack behavior in the short fracture limit. The intermediate range of fracture length, shown in Fig. 4, is in good agreement with the numerical results of Ouchterlony for the planar problem of a pressurized hole, with and without pressure on the crack surfaces (as in Fig. 1).

Opening displacements of the multifractures can be calculated from equation (2) provided that f_N is included in both the weight functions that appear. The calculated displacement at the entrance, or mouth, of each fracture is then reduced by a factor of $f_\infty{}^2$, in the long fracture limit, which agrees with the star crack analysis of Williams [13] in the limit of large N. The calculated displacements near the tip of the fracture will also be reduced by $f_\infty{}^2$, in the long fracture limit, which is in conflict with the requirement that near-tip displacements must always be proportional to K, and hence proportional to f_∞. This deficiency can be corrected by the introduction of a slightly more complex weight function, such as

$$f_\infty = 1 + \frac{\pi}{2}\left(\frac{2\sqrt{N-1}}{N} - 1\right)\left(1 - \frac{x^2}{L^2}\right)^{1/2} \tag{17}$$

which properly recognizes that "near-tip" loadings always have the same effect on stress intensity, regardless of the presence of other fractures, which are relatively far away compared to the size of the "near-tip" region. The use of (17) instead of (16) ensures that displacements behave properly at both ends of the fracture; it does not affect the upper three curves in Fig. 4, and it causes a slight lowering of the bottom three curves, in better agreement with the data. In the execution of practical hydrofracture calculations, however, it seems that the simple formula (16) usually gives about the same overall result as (17). In closing, it is noted that the other weight functions, f_{notch} and f_{rad}, do preserve the correct behavior of opening displacements at both ends of the fracture.

5 Discussion and Summary

The generalized integral formulas (1) and (2) and the analytical weight functions (3), (6), and (15) proposed here provide a fast and simple approximation, with engineering accuracy, for a broad class of fracturing problems. The formulas are essentially exact when fractures are either very short or very long compared to the cavity radius, regardless of the pressure distribution along the fracture and whether or not the cavity is pressurized. The intermediate range of fracture lengths has been checked against numerical results for several different geometries and loading configurations.

Although the limiting forms of the equations are dictated by previous exact solutions, the transitional character was arbitrarily chosen to be as simple as possible while still consistent with physical expectations. Agreement could be improved by introducing more degrees of freedom in the weighting functions and adjusting the parameters to fit the available numerical results. Similarly, rigorous expansion techniques [25] could be used to generate additional constraints to be satisfied by the transitional functions. But it is difficult to maintain the desired degree of generality in making such refinements, and computational complexity is certain to increase. So, it seemed more useful to demonstrate that acceptable engineering accuracy is generally obtainable using a very simple, and yet broadly applicable, approximations.

References

1 Savin, G. N., *Stress Concentration Around Holes*, Pergamon Press, New York, 1961.

2 Howard, G. C., and Fast, C. R., *Hydraulic Fracturing*, Society of Petroleum Engineers of AIME, Dallas 1970.

3 Kutter, H. K., and Fairhurst, C., "On the Fracture Process in Blasting," *Intl. J. Rock Mech. Min. Sci.*, Vol. 8, 1971, pp. 181-202.

4 Warpinski, N. R., Schmidt, R. A., Copper, P. W., Walling, H. C., and Northrop. D. A., "High Energy Gas Frac: Multiple Fracturing in a Borehole," *Proc. 20th U. S. Symp. on Rock Mech.*, Austin, Texas, June 4-6, 1979, pp. 143-152.

5 Keller, C. E., Davis, A. H., and Stewart, J. N., "The Calculation of Steam Flow and Hydraulic Fracturing in a Porous Medium With the KRAK Code," Los Alamos Scientific Laboratories, LA-5602-MS, 1974.

6 England, A. H., and Green, A. E., "Some Two-Dimensional Crack and Punch Problems in Classical Elasticity," *Proc. Camb. Phil. Soc.*, Vol. 59, 1963, p. 489.

7 Sneddon, I. N., and Lowengrub, M., *Crack Problems in the Classical Theory of Elasticity*, Wiley, New York, 1969.

8 Haimson, B., and Fairhurst, C., "Initiation and Extension of Hydraulic Fractures in Rocks," *SPE Journal*, Vol. 7, No. 3, 1967, pp. 310–318.

9 Abou-Sayed, A. S., Brechtel, C. E., and Clifton, R. J., "In Situ Stress Determination by Hydrofracturing: A Fracture Mechanics Approach," *J. Geoph. Res.*, Vol. 83, No. B6. 1978. pp. 2851–2862.

10 Ouchterlony, F., "Fracture Mechanics Applied to Rock Blasting," *Third Congress, Int. Soc. Rock Mechanics*, Vol. II, B., 1974, pp. 1377–1382.

11 Bowie, O. L., "Analysis of an Infinite Plate Containing Radial Cracks Originating From the Boundary of an Internal Circular Hole," *J. Math. and Phys.*, Vol. 35, 1956, p. 60.

12 Kutter, H. K., "Stress Analysis of a Pressurized Circular Hole with Radial Cracks in an Infinite Elastic Plate," *Int. J. Fracture Mech.*, Vol. 6, No. 3, 1970, pp. 233–247.

13 Williams, W. E., "A Star-Shaped Crack Deformed by an Arbitrary Internal Pressure," *Int. J. Eng. Sci.*, Vol. 9, 1971, pp. 705–712.

14 Keer, L. M., Luk, V. K., and Freedman, J. M., "Circumferential Edge Crack in a Cylindrical Cavity," ASME JOURNAL OF APPLIED MECHANICS, Vol. 44, 1977, pp. 250–754.

15 Atsumi, A., and Shindo, Y., "Axisymmetric Singular Stresses in a Thick-Walled Spherical Shell With an Internal Edge Crack," ASME JOURNAL OF APPLIED MECHANICS, Vol. 50, March 1983, pp. 37–42.

16 Bueckner, H. F., "A Novel Principle for the Computation of Stress Intensity Factors," *ZAMM*, Vol. 50, 1970, pp. 529–546.

17 Rice, J. R., "Some Remarks on Elastic Crack-Tip Stress Fields," *Int. J. Solids Structures*, Vol. 8, 1972, pp. 751–758.

18 Aamodt, B., and Bergon, P. G., "On the Principle of Superposition for Stress Intensity Factors," *Eng. Fracture Mech.*, Vol. 8, 1976, pp. 437–440.

19 Parker, A. P., and Bowie, O. L., "The Weight Function for Various Boundary Condition Problems," *Eng. Fracture Mech.*, Vol. 18, No. 2, 1983, pp. 473–477.

20 Tada, H., Paris, P. C., and Irwin, G. R., *Stress Analysis of Cracks Handbook*, Del Research Corp., 226 Woodbourne Drive, St. Louis, Mo., June 1973.

21 Paris, P. C., McMeeking, R. M., and Tada, H., "The Weight Function Method for Determining Stress Intensity Factors," in *Cracks and Fractures*, Swedlow, J. L., and Williams, M. L., eds., ASTM Special Technical Publication 601, Philadelphia, Pa., 1976, pp. 471–489.

22 Hartranft, R. J., and Sih, G. C., "Solving the Edge and Surface Crack Problems by an Alternating Method," in *Method of Analysis and Solution of Crack Problems*, Sih, G. C., ed., Noordhoff, Leyden, 1973.

23 Muskhelishvili, N. I., *Some Basic Problems of the Theory of Elasticity*, Noordhoff, Holland, 1953.

24 Trangenstein, J. A., Proffer, W. J., and Read, H. E., "SASWIS, A General Purpose Three-Dimensional Ground Motion and Continuum Mechanics Code,"' S-CUBED Report No. SSS-R-81-4781, Nov. 1980.

25 Benthem, J. P., and Koiter, W. T., "Asymptotic Approximations to Crack Problems," in *Methods of Analysis and Solution of Crack Problems*, Sih, G. C., ed., Noordhoff, Leyden, 1973.

Journal of Applied Mechanics

Brief Notes

A Brief Note is a short paper that presents a specific solution of technical interest in mechanics but which does not necessarily contain new general methods or results. A Brief Note should not exceed 1500 words *or equivalent* (a typical one-column figure or table is equivalent to 250 words; a one line equation to 30 words). Brief Notes will be subject to the usual review procedures prior to publication. After approval such Notes will be published as soon as possible. The Notes should be submitted to the Technical Editor of the JOURNAL OF APPLIED MECHANICS. Discussions on the Brief Notes should be addressed to the Editorial Department, ASME, United Engineering Center, 345 East 47th Street, New York, N. Y. 10017, or to the Technical Editor of the JOURNAL OF APPLIED MECHANICS. Discussions on Brief Notes appearing in this issue will be accepted until two months after publication. Readers who need more time to prepare a Discussion should request an extension of the deadline from the Editorial Department.

Wave-Front Approximations in a Moving Coordinate System

J. G. Harris[1]

A wave-front approximation to the wave emitted when a propagating mode III crack abruptly slows it speed of advance is calculated. Of particular interest is the approximation of the Cagniard-deHoop inversion integral when it is expressed in terms of the variables of a moving coordinate system.

Introduction

To approximate the emission from a subsurface rupture, Harris and Achenbach [1] calculated a wave-front approximation to the wave radiated by a propagating mode *III* crack when it abruptly changed its speed of advance. In that paper most of the details of the calculation were suppressed. The purpose of this Note is to explain how this wave-front approximation was made using a moving coordinate system, the Cagniard-deHoop inversion technique, and Watson's lemma. The principal point to be made is that, because it is expressed in terms of the coordinates of the moving system, the Cagniard-deHoop inversion integral must be approximated with great care.

Problem Formulation

A mode *III* crack has been propagating at a constant speed v_1 along the x-axis in the direction of increasing x for $t<0$ and has induced an associated wave field. When the crack tip reaches $x=0$ at $t=0$ it suddenly slows its speed of advance to a new, constant speed v_2, emitting as it does so, an additional wave field. It is this second wave field that will be approximated here.

[1]Assitant Professor, Department of Theoretical and Applied Mechanics, University of Illinois, Urbana, Ill. 61801. Assoc. Mem. ASME

Manuscript received by ASME Applied Mechanics Division, January, 1983; final revision, January, 1984.

At $x=0$ and $t=0$ the crack is assumed to be semi-infinite and to lie in the (x,z)-plane. Suppose the crack continued to advance with speed v_1. Then the displacement, for $x>0$, on the positive side of the crack, $y=0^+$, would be

$$w(x,0^+,t)=H(t-x/v_1)f(x,t) \tag{1}$$

where, for small t and thus small x, $f(x,t)$ has the approximate form [2]

$$f(x,t)=f_0(t-x/v_1)^{\kappa/2},\ \ \kappa\geq 1. \tag{2}$$

The parameter $\kappa=1$ for brittle fracture, otherwise $\kappa>1$; f_0 is a constant. Because the crack tip does not propagate with speed v_1 but rather with speed v_2, the crack opening must be closed by subtracting (1) from the displacement at the crack's surface for $v_2 t<x\leq v_1 t$.

To put these ideas into a mathematical form, introduce the moving coordinate

$$q=x-v_2 t \tag{3}$$

and formulate an initial boundary-value problem, for the second wave-field, in the coordinate system (q,y). The formulation, and its subsequent solution parallels that given by Achenbach [3] for a mode *II* crack, so that the only details that need be given here are the boundary conditions. In the moving coordinate system the z-displacement $w(x,y,t)=W(q,y,t)$ and the boundary conditions at $y=0^+$ (the problem is antisymmetric) are

$$\partial W/\partial y=H(q)T^+,\ \ W=H(-q)W^- - H(q)H(t-s_{12}q)F(q,t) \tag{4a,b}$$

where, from (1) and (2), $f(x,t)=F(q,t)$ and

$$F(q,t)=F_0(t-s_{12}q)^{\kappa/2},\ \ F_0=f_0/(v_1 s_{12})^{\kappa/2} \tag{5a,b}$$

for small t and thus small q. The function $H(t)$ is the Heaviside step function, $s_{12}=(v_1-v_2)^{-1}$, and T^+ and W^- are unknowns. The Laplace transform over time (transform variable p) of the solution to this problem is

$$\bar{W}(q,y,p)=-\frac{p}{2\pi i}\int_{Br}\frac{\gamma^-(-s_{12})}{\gamma^-(\xi)}\bar{F}^*(\xi,p)\exp[p(\xi q-\gamma y)]d\xi \tag{6}$$

where Br is the Bromwich path. The functions γ^- and γ are given by

$$\gamma^-=[s-\xi(1+s\ v_2)]^{1/2},\ \ \gamma=[s^2(1-v_2\xi)^2-\xi^2]^{1/2} \tag{7a,b}$$

and $s=1/c$ where c is the shear-wave wave-speed. The term $\bar{F}^*(\xi,p)$ is the combined spatial (transform variable $p\xi$) and temporal Laplace transform of $F(q,t)$. For large p

$$\bar{F}^*(\xi,p)=\bar{F}(p)/[p(\xi+s_{12})] \tag{8a}$$

$$\bar{F}(p)=F_0\Gamma[(\kappa+2)/2]/p^{(\kappa+2)/2} \tag{8b}$$

where Γ is the gamma function. The integral (6) represents the additional wave field excited when the crack abruptly slows it speed of advance. The remainder of this Note outlines how to approximate $w(x,y,t)$ and $\partial w/\partial t$ near the wave front starting from (6).

Wave-Front Approximation

Introduce the polar coordinates (R,Θ) by setting $q=R\cos\Theta$ and $y=R\sin\Theta$. In (6) let

$$\tau=-\xi R\cos\Theta+\gamma R\sin\Theta \tag{9}$$

and distort the integration contour to a Cagniard-deHoop contour [4]. Then approximate the resulting integral for large p using Watson's lemma [5]. The result of these operations is the following:

$$\bar{W}(q,y,p)=-[\lim_{\tau\to\tau^+}A(\tau)]\frac{\bar{F}(p)}{\pi}\int_{\tau^+}^{\infty}\frac{e^{-p\tau}}{(\tau-\tau^+)^{1/2}}d\tau \tag{10a}$$

$$A(\tau)=Im\left\{\frac{\gamma^-(-s_{12})(d\xi^+/d\tau)(\tau-\tau^+)^{1/2}}{\gamma^-[\xi^+(\tau)][\xi^+(\tau)+s_{12}]}\right\} \tag{10b}$$

where

$$\tau^+=sR\{v_2s\cos\Theta+[1-(v_2s\ \sin\Theta)^2]^{1/2}\}/[1-(v_2s)^2] \tag{11}$$

and $\xi^+(\tau)$ is found by inverting (9) and taking that branch which makes $Im(\xi)\geq 0$. Therefore the displacement for τ near τ^+ is

$$W(q,y,\tau)=-(\pi)^{-1}A(\tau^+)F(\tau)^*(\tau-\tau^+)^{1/2} \tag{12}$$

where $A(\tau^+)$ is calculated by taking the limit indicated in (10a) and * means that the two functions are to be convolved with one another. From (10a) the variable τ is identified as the time t. But τ^+ is not as easy to identify. Clearly it is an arrival time; however, it is one that depends on time t through the moving coordinates (R,Θ). Looking back at (10a), it would seem, at first glance, that if τ is identified as time, then the lower limit of integration contains the variable of integration.

This quizzical result can be resolved by noting that it is the difference $(\tau-\tau^+)$ that is wanted. To calculate this return to the fixed coordinate system. Setting $x=r\cos\theta$ and $y=r\sin\theta$, and noting that $R\cos\Theta=(r\cos\theta-v_2t)$ and $R\sin\Theta=r\sin\theta$, (11) can be approximated to give

$$\tau^+=[-s(v_2t\cos\theta-r)]/(1-v_2s\cos\theta)+O[(t-sr)^2] \tag{13}$$

Therefore,

$$\tau-\tau^+=(t-sr)/(1-v_2s\cos\theta)+O[(t-sr)^2]. \tag{14}$$

Note that as $\tau\to\tau^+$, $t\to sr$ and $\tau^+\to sr$; and the amplitude term in (12) becomes $A(sr)$. One might at first be tempted into evaluating τ^+ at $t=sr$, and thus be led to the reasonable but erroneous result that $(\tau-\tau^+)=(t-sr)$. However, as shown in the foregoing, the time t in (13) must be retained if the doppler factor $(1-v_2s\cos\theta)^{-1}$ in (14) is not to be lost. Further, it is interesting to note that (14) can be interpreted as follows: The time difference $(\tau-\tau^+)$ is that between the successive emissions made as the original crack is closed, while $(t-sr)$ is that between the successive wave-front arrivals of these emissions [6].

The wave-front approximation to the displacement $w(r,\theta,t)$ thus becomes

$$w(r,\theta,t)=-(c/2\pi r)^{1/2}E(\theta,v_1,v_2)e(t-sr) \tag{15}$$

where

$$E(\theta,v_1,v_2)=\frac{[2s(1+v_1s)(v_1-v_2)]^{1/2}}{(1-v_2s\cos\theta)^{(\kappa+1)/2}}\frac{\sin(\theta/2)}{(1-v_1s\cos\theta)} \tag{16}$$

and

$$e(t)=F_0H(t)\Gamma[(\kappa+2)/2]t^{(\kappa+1)/2}/\Gamma[(\kappa+3)/2] \tag{17}$$

It is also of interest to examine the time derivatives in the two coordinate systems. They are related as follows:

$$\partial w/\partial t=DW/D\tau,\ \ DW/D\tau=\partial W/\partial\tau-v_2(\partial W/\partial q). \tag{18a,b}$$

It can be shown that for large p the Laplace transfrom over time of $DW/D\tau$ is

$$(\overline{DW/D\tau})=p[1-v_2\xi^+(\tau^+)]\bar{W}(q,y,p) \tag{19}$$

where $\bar{W}(q,y,p)$ is given by (10a). At this point (19) is treated exactly as was (10a). Note that the factor within the brackets equals the droppler factor $(1-v_2s\cos\theta)^{-1}$, but that the p causes the inverse transform of (19) to be multiplied by the compensating factor $(1-v_2s\cos\theta)$. Thus the wave-front approximation, in the fixed coordinate system, to the particle velocity is simply

$$\partial w/\partial t=-(c/2\pi r)^{1/2}E(\theta,v_1,v_2)(\partial e/\partial t). \tag{20}$$

Summary

The central point of the analysis is that, because a moving coordinate system us used τ^+ depends on t, as well as (x,y), and must be approximated as given in (13). Care in calculating the time derivative is also needed.

Acknowledgment

The author wishes to thank Mao-Kuen Kuo and John Pott for bringing this problem to his attention and the National Science Foundation for support through Grant MEA-8104738.

References

1 Harris, J. G., and Achenbach, J. D., "Love Waves Excited by Discontinuous Propagation of a Rupture Front," *Geophysical Journal of the Royal Astronomical Society*, Vol. 72, 1983, pp. 337–351.

2 Achenbach, J. D., "Dynamic Effects in Brittle Fracture," *Mechanics Today*, Vol. 1, Nemat-Nasser, S., ed., Pergamon, New York, 1972, pp. 13–19.

3 Ibid., pp. 19–30.

4 Achenbach, J. D., *Wave Motion in Elastic Solids*, North-Holland, New York, 1973, pp. 298–301.

5 Ibid, p. 272.

6 Levine, H., *Unidirectional Wave Motion*, North-Holland, New York, 1978, pp. 46–53 and pp. 105–110.

Large-Amplitude Vibrations of Rectangular Plates

B. B. Aalami[1]

1 Introduction

The natural frequency of vibration of a thin sheet depends on its geometry and material properties, as well as on the magnitude of the amplitude of vibration. Other conditions remaining unchanged, the larger the amplitude of vibration, the higher is the frequency. Thin plates develop membrane stresses under lateral deflection, which enhance their flexural stiffness. Deflections of the order of plate thickness for thin

[1]Professor of Engineering, San Francisco State University, 1600 Holloway Ave, San Francisco, Calif. 94132.

Manuscript received by ASME Applied Mechanics Division, February, 1982; final revision, March, 1984.

and $s=1/c$ where c is the shear-wave wave-speed. The term $\bar{F}^*(\xi,p)$ is the combined spatial (transform variable $p\xi$) and temporal Laplace transform of $F(q,t)$. For large p

$$\bar{F}^*(\xi,p)=\bar{F}(p)/[p(\xi+s_{12})] \tag{8a}$$

$$\bar{F}(p)=F_0\Gamma[(\kappa+2)/2]/p^{(\kappa+2)/2} \tag{8b}$$

where Γ is the gamma function. The integral (6) represents the additional wave field excited when the crack abruptly slows it speed of advance. The remainder of this Note outlines how to approximate $w(x,y,t)$ and $\partial w/\partial t$ near the wave front starting from (6).

Wave-Front Approximation

Introduce the polar coordinates (R,Θ) by setting $q=R\cos\Theta$ and $y=R\sin\Theta$. In (6) let

$$\tau=-\xi R\cos\Theta+\gamma R\sin\Theta \tag{9}$$

and distort the integration contour to a Cagniard-deHoop contour [4]. Then approximate the resulting integral for large p using Watson's lemma [5]. The result of these operations is the following:

$$\bar{W}(q,y,p)=-[\lim_{\tau\to\tau^+}A(\tau)]\frac{\bar{F}(p)}{\pi}\int_{\tau^+}^{\infty}\frac{e^{-p\tau}}{(\tau-\tau^+)^{1/2}}d\tau \tag{10a}$$

$$A(\tau)=Im\left\{\frac{\gamma^-(-s_{12})(d\xi^+/d\tau)(\tau-\tau^+)^{1/2}}{\gamma^-[\xi^+(\tau)][\xi^+(\tau)+s_{12}]}\right\} \tag{10b}$$

where

$$\tau^+=sR\{v_2s\cos\Theta+[1-(v_2s\ \sin\Theta)^2]^{1/2}\}/[1-(v_2s)^2] \tag{11}$$

and $\xi^+(\tau)$ is found by inverting (9) and taking that branch which makes $Im(\xi)\geq 0$. Therefore the displacement for τ near τ^+ is

$$W(q,y,\tau)=-(\pi)^{-1}A(\tau^+)F(\tau)^*(\tau-\tau^+)^{1/2} \tag{12}$$

where $A(\tau^+)$ is calculated by taking the limit indicated in (10a) and * means that the two functions are to be convolved with one another. From (10a) the variable τ is identified as the time t. But τ^+ is not as easy to identify. Clearly it is an arrival time; however, it is one that depends on time t through the moving coordinates (R,Θ). Looking back at (10a), it would seem, at first glance, that if τ is identified as time, then the lower limit of integration contains the variable of integration.

This quizzical result can be resolved by noting that it is the difference $(\tau-\tau^+)$ that is wanted. To calculate this return to the fixed coordinate system. Setting $x=r\cos\theta$ and $y=r\sin\theta$, and noting that $R\cos\Theta=(r\cos\theta-v_2t)$ and $R\sin\Theta=r\sin\theta$, (11) can be approximated to give

$$\tau^+=[-s(v_2t\cos\theta-r)]/(1-v_2s\cos\theta)+O[(t-sr)^2] \tag{13}$$

Therefore,

$$\tau-\tau^+=(t-sr)/(1-v_2s\cos\theta)+O[(t-sr)^2]. \tag{14}$$

Note that as $\tau\to\tau^+$, $t\to sr$ and $\tau^+\to sr$; and the amplitude term in (12) becomes $A(sr)$. One might at first be tempted into evaluating τ^+ at $t=sr$, and thus be led to the reasonable but erroneous result that $(\tau-\tau^+)=(t-sr)$. However, as shown in the foregoing, the time t in (13) must be retained if the doppler factor $(1-v_2s\cos\theta)^{-1}$ in (14) is not to be lost. Further, it is interesting to note that (14) can be interpreted as follows: The time difference $(\tau-\tau^+)$ is that between the successive emissions made as the original crack is closed, while $(t-sr)$ is that between the successive wave-front arrivals of these emissions [6].

The wave-front approximation to the displacement $w(r,\theta,t)$ thus becomes

$$w(r,\theta,t)=-(c/2\pi r)^{1/2}E(\theta,v_1,v_2)e(t-sr) \tag{15}$$

where

$$E(\theta,v_1,v_2)=\frac{[2s(1+v_1s)(v_1-v_2)]^{1/2}}{(1-v_2s\cos\theta)^{(\kappa+1)/2}}\frac{\sin(\theta/2)}{(1-v_1s\cos\theta)} \tag{16}$$

and

$$e(t)=F_0H(t)\Gamma[(\kappa+2)/2]t^{(\kappa+1)/2}/\Gamma[(\kappa+3)/2] \tag{17}$$

It is also of interest to examine the time derivatives in the two coordinate systems. They are related as follows:

$$\partial w/\partial t=DW/D\tau,\ \ DW/D\tau=\partial W/\partial\tau-v_2(\partial W/\partial q). \tag{18a,b}$$

It can be shown that for large p the Laplace transfrom over time of $DW/D\tau$ is

$$(\overline{DW/D\tau})=p[1-v_2\xi^+(\tau^+)]\bar{W}(q,y,p) \tag{19}$$

where $\bar{W}(q,y,p)$ is given by (10a). At this point (19) is treated exactly as was (10a). Note that the factor within the brackets equals the droppler factor $(1-v_2s\cos\theta)^{-1}$, but that the p causes the inverse transform of (19) to be multiplied by the compensating factor $(1-v_2s\cos\theta)$. Thus the wave-front approximation, in the fixed coordinate system, to the particle velocity is simply

$$\partial w/\partial t=-(c/2\pi r)^{1/2}E(\theta,v_1,v_2)(\partial e/\partial t). \tag{20}$$

Summary

The central point of the analysis is that, because a moving coordinate system us used τ^+ depends on t, as well as (x,y), and must be approximated as given in (13). Care in calculating the time derivative is also needed.

Acknowledgment

The author wishes to thank Mao-Kuen Kuo and John Pott for bringing this problem to his attention and the National Science Foundation for support through Grant MEA-8104738.

References

1 Harris, J. G., and Achenbach, J. D., "Love Waves Excited by Discontinuous Propagation of a Rupture Front," *Geophysical Journal of the Royal Astronomical Society*, Vol. 72, 1983, pp. 337–351.

2 Achenbach, J. D., "Dynamic Effects in Brittle Fracture," *Mechanics Today*, Vol. 1, Nemat-Nasser, S., ed., Pergamon, New York, 1972, pp. 13–19.

3 Ibid., pp. 19–30.

4 Achenbach, J. D., *Wave Motion in Elastic Solids*, North-Holland, New York, 1973, pp. 298–301.

5 Ibid, p. 272.

6 Levine, H., *Unidirectional Wave Motion*, North-Holland, New York, 1978, pp. 46–53 and pp. 105–110.

Large-Amplitude Vibrations of Rectangular Plates

B. B. Aalami[1]

1 Introduction

The natural frequency of vibration of a thin sheet depends on its geometry and material properties, as well as on the magnitude of the amplitude of vibration. Other conditions remaining unchanged, the larger the amplitude of vibration, the higher is the frequency. Thin plates develop membrane stresses under lateral deflection, which enhance their flexural stiffness. Deflections of the order of plate thickness for thin

[1] Professor of Engineering, San Francisco State University, 1600 Holloway Ave, San Francisco, Calif. 94132.

Manuscript received by ASME Applied Mechanics Division, February, 1982; final revision, March, 1984.

sheets such as load bearing skins or glass panels are not uncommon [1]. It is established that amplitudes of this magnitude significantly affect the vibration behavior and the resonance characteristics of thin plates [2–4].

Large-amplitude flexural vibrations of rectangular plates for small strains are described by two coupled fourth-order partial differential equations, which were first derived by Herrmann [4] as an extension of the static von Karman [5] equations. The exact solution to these equations is yet unknown. References to other earlier contributions on this subject may be found in [6, 7].

Herein, a general approximate approach is presented for the large-amplitude vibrations of plates having different boundary conditions. The large-amplitude deflection of plates is governed by the large deflection equations of plates [5, 8], which yield the deflected profile and the resulting membrane stresses. Herein, the membrane stresses evaluated are considered as constant throughout the vibration. Subsequently, the frequency is calculated using Herrmann's equations with the constant membrane stresses obtained from the large deflection analysis. An iteration procedure used in obtaining the frequencies allows the plate to take its preferred mode of vibration at the preselected large amplitude. The membrane stresses developed in vibration oscillate between zero (neutral position) and maximum (max deflection), when the plate attains its greatest stiffenss. In the present treatment, frequencies are evaluated with membrane stresses frozen at their greatest values, yielding a constant and maximum membrane stiffness during vibration. The solutions obtained are upper bounds to the true frequency.

The main features of the present analysis are: (*i*) a great reduction in computational effort: (*ii*) obtaining upper bounds to the large-amplitude vibrations of rectangular plates, which together with the lower bound solutions available through small deflection analyses, provide a comprehensive reference basis: (*iii*) using a general numerical method, all the boundary conditions can be dealt with. The method can be extended to cover orthotropic plates: (*iv*) the frequencies obtained are in close agreement with the limited available solutions: and (*v*) the analysis does not allow for shear deformation and the inplane inertia forces.

To demonstrate the potential of the treatment presented, solutions are obtained for simply supported and clamped rectangular plates having different boundary conditions. The results obtained are compared with the available solutions.

2 Theory

2.1 Governing Equations. Assume a large deflection rectangular plate in static equilibrium under the action of an applied transverse pressure q_{xy}. Let the static deflections be w_s. If the plate is now subjected to a sinusoidally varying exitation force of small magnitude relative to q_{xy}, it would vibrate about the equilibrium position with an amplitude w_d, which would not, by assumption, be large enough the affect the general state of membrane stresses in the plate. The analysis determines the natural frequencies of this plate, for which the membrane stresses remain constant at values relating to w_s. The static deflection, and the membrane forces are expressed by:

$$\left\{\begin{aligned} & w_{s,xxxx}+2w_{s,xxyy}+w_{s,yyyy}-\frac{1}{D}[f_{,yy}w_{s,xx}-2f_{,xy}w_{s,xy} \\ & \qquad +f_{,xx}w_{s,yy}]=q_{xy/D} \qquad (1) \\ & f_{,xxxx}+2f_{,xxyy}+f_{,yyyy}=Eh[(w_{s,xy})^2-w_{s,xx}w_{s,yy}] \end{aligned}\right.$$

where a comma followed by subscripts represents partial differentiation with respect to the subscripts. The membrane forces are derived from the following:

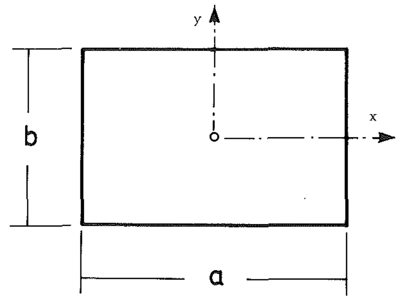

Fig. 1 Large-amplitude frequencies (Ω_l) of square plates with stress-free inplane boundary conditions (Yamaki [3]). Small-amplitude frequencies (Ω_s) are for rotationally free plates 19.68, and for rotationally fixed plates 35.86.

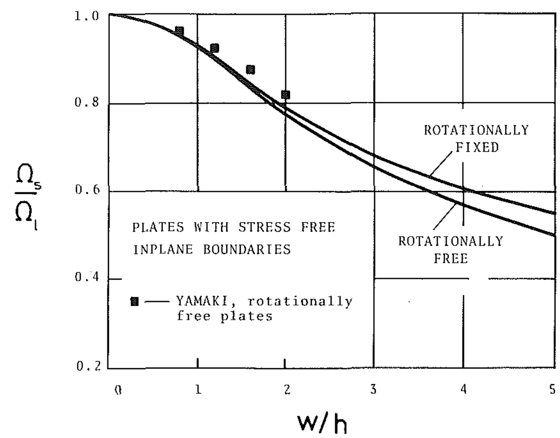

Fig. 2 Large-amplitude frequencies (Ω_l) of square plates with immovable boundaries (Yamaki [3]), Ramachandran [9], Wah [10], Mei [11]. Small amplitude frequencies (Ω_s) are for rotationally free plates 19.68, and for rotationally fixed plates 35.86.

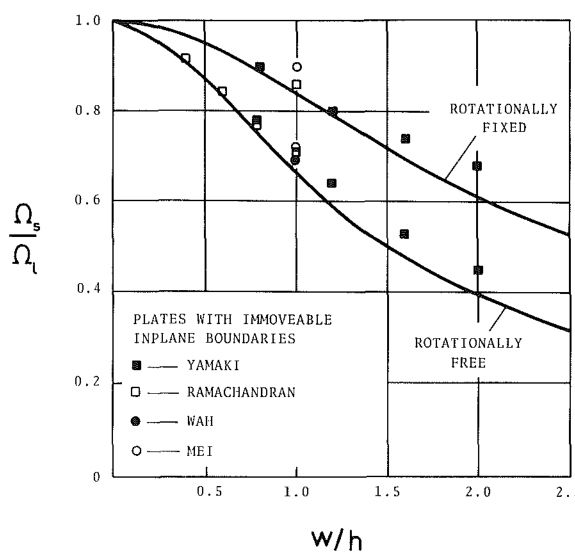

Fig. 3 Large-amplitude frequencies (Ω_l) of rectangular plates with different aspect ratios. Upper section for rotationally free plates with zero inplane normal and shearing stresses, with small-amplitude frequencies (Ω_s) equal to: for $b/a = 1$, 19.68; $b/a = 2$, 12.28; $b/a = 3$, 10.91. Lower section for rotationally fixed plates with immovable boundaries with Ω_s equal to: for $b/a = 1$, 35.86; $b/a = 2$, 24.42; $b/a = 3$, 23.05.

$$N_x=f_{,yy}; \quad N_y=f_{,xx}; \quad N_{xy}=-f_{,xy} \qquad (2)$$

The inertia force considered is due to transverse motion and has an intensity of $mw_{d,tt}$. The equation of motion of the plate can now be written by adding $(mw_{d,tt})$ to the flexural equation of the set of equations (1), and interpreting the total deflection w as the sum of $(w_s + w_d)$. The second equation, however, is based on the static deflections w_s for the evaluation of the governing membrane stresses.

$$\left\{\begin{aligned} & w_{,xxxx} + 2w_{,xxyy} + w_{,yyyy} - \frac{1}{D}[f_{,yy}w_{,xx} - 2f_{,xy}w_{,xy} \\ & \qquad + f_{,xx}w_{,yy}] = \frac{q_{xy}}{D} - \frac{m}{D}w_{d,tt} \\ & f_{,xxxx} + 2f_{,xxyy} + f_{,yyyy} = Eh[(w_{s,xy})^2 - w_{s,xx}w_{s,yy}] \end{aligned}\right. \tag{3}$$

Subtracting the static component of deflection associated with q_{xy} from the first equation gives:

$$w_{d,xxxx} + 2w_{d,xxyy} + w_{d,yyyy} - \frac{1}{D}[f_{,yy}w_{d,xx} - 2f_{,xy}w_{d,xy} + f_{,xx}w_{d,yy}] = -\frac{m}{D}w_{d,tt} \tag{4}$$

Assume a simple harmonic motion for the first mode.

$$w_d(x,y,t) = w_a(x,y)\sin(\omega t + \alpha) \tag{5}$$

Substituting equation (5) in equation (4) and cancelling the term $\sin(\omega t + \alpha)$ results in the governing frequency equation:

$$w_{a,xxxx} + 2w_{a,xxyy} + w_{a,yyyy} - \frac{1}{D}[f_{,yy}w_{a,xx} - 2f_{,xy}w_{a,xy} + f_{,xx}w_{a,yy}] = m\omega^2 w_a \tag{6}$$

Equation (6) represents the natural vibrations of the plate with large amplitudes in terms of w and f. For any preselected large amplitude w_a, values of f are first determined from the set of equations (1) relating to the stationary position of maximum deflection, for which $w_s = w_a$. Substitution in equation (6) for the calculated values of f, yields a standard eigenvalue problem.

2.2 Boundary Conditions. For edges parallel to y-axis, (*a*) flexural boundary conditions, (*i*) for rotationally free edges $w = 0$ and $w_{,xx} = 0$, (*ii*) for rotationally fixed edges $w = 0$ and $w_{,x} = 0$; (*b*) membrane boundary condition, (*i*) for all the cases treated $f_{,xy} = 0$, (*ii*) for the inplane condition perpendicular to the edges, two cases are considered, i.e., $f_{,yy} = 0$ to match the simply supported cases, or inplane displacement equated to zero to match the fixed condition.

2.3 Numerical Solutions. First equations (1) are solved. Subsequently, with known values of f, the eignevalue problem given by equation (6) is treated, using finite differences with a mesh having 300–400 nodes over the entire plate. The algebraic eigenvalue problem derived from equation (7) is given by:

$$[A]\{w_a\} = \Omega\{w_a\} \tag{7}$$

where $[A]$ is a square matrix depending on f and representing the left-hand side of equation (6) expressed in finite differences. $\{w_a\}$ is the unknown column eigenvector. Ω is nondimensionalized frequency. Stress function f is found from equations (1) and is used to form $[A]$. The smallest eigenvalue of $[A]$ is found using the power method with the following iteration:

$$\left\{\begin{aligned} & \{\bar{w}\}_{i+1} = [A]^{-1}\{w\}_i \\ & \{w\}_{i+1} = C_i\{\bar{w}\}_{i+1} \end{aligned}\right. \tag{8}$$

where the subscripts refer to the number of iteration. $\{\bar{w}\}_{i+1}$ is the assumed eigenvector for the $(i+1)$th iteration. The iteration is carried through for $i = 0,1, \ldots .$ until the evaluated eigenvector $\{w\}_{i+1}$ from $(i+1)$th iteration is sufficiently close to the eigenvector $\{w\}_i$ from the preceding iteration. $\{w\}_i$ is then the required eigenvector. C_i is the normalizing factor and can be shown to converge the smallest eigenvalue Ω_1 as $\{w\}$ converges.

3 Discussion of Results

The applicability of the method is demonstrated through treatment of two sets of plates with different flexural and membrane boundary conditions. The solutions presented extend the range of published amplitudes. A third set of solutions for rectangular plates serves to demonstrate the influence of aspect ratios on large-amplitude vibrations. Figures 1 and 2 show the large-amplitude frequencies of square plates with stress free and immovable boundary conditions, respectively. The results from the present analysis yield higher frequencies compared to the available solutions. However, the agreement is close for most practical purposes. Figure 3 represents large-amplitude natural frequencies of simply supported and rotationally fixed rectangular plates of different aspect ratios. The large-amplitude frequency for any given amplitude may be evaluated by simply dividing the given small-amplitude frequency (Ω_s) through the measured ordinate of the curve at the selected amplitude. Note that the solutions presented apply equally to the small vibrations of plates undergoing large deflections under a uniformly distributed loading to a static deflection equal to the large amplitude given herein.

Acknowledgment

The author wishes to thank Professor A. K. Basu, Chariman, Civil Engineering Department, Indian Institute of Technology, for his valuable discussions.

References

1 Aalami, B., and Williams, D. G., *Thin Plate Design for Transverse Loading*, Wiley, New York, 1977.

2 Chu, H. N., and Herrmann, G., "Influence of Large Amplitudes on Free Flexural Vibrations of Rectangular Plates," ASME Journal of Applied Mechanics, Vol. 23, Dec. 1956, pp. 532–540.

3 Yamaki, N., "Influence of Large Amplitude on Flexural Vibrations of Elastic Plates," *ZAMM*, Vol. 41, No. 12, 1961, pp. 501–510.

4 Herrmann, G., "Influence of Large Amplitudes on Flexural Motions of Elastic Plates," NACA TN 3578, 1955.

5 Von Karman, T., "Festigkeitsprobleme im Maschinenbau," *Encyklopaedie der Mathematischen Wissenschaften*, Vol. 4, 1910, p. 349.

6 Prabhakara, M. K., and Chai, C. Y., "Nonlinear Flexural Vibrations of Orthotropic Plates," *Journal of Sound and Vibration*, Vol. 52, No. 4, 1977, pp. 511–518.

7 Vendhan, C. P., "An Investigation into Nonlinear Vibrations of Thin Plates," *International Journal of Nonlinear Mechanics*, Vol. 12, 1977, pp. 209–221.

8 Aalami, B., "Large Deflection of Rectangular Plates Under Patch Loading," *Journal of Structural Division*, ASCE, Nov. 1972, pp. 261–269.

9 Ramachandran, J., "Large Amplitude Vibrations of Elastically Restrained Rectangular Plates," ASME Journal of Applied Mechanics, Vol. 40, Sept. 1973, pp. 881–813.

10 Wah, Y., "Large Amplitude Flexural Vibrations of Rectangular Plates," *Int. J. Mech. Sci.*, Vol. 5, 1963, pp. 425–438.

11 Mei, C., "Finite Element Displacement Method for Large Amplitude Free Flexural Vibrations of Beams and Plates," *Journal of Computers and Structures*, Vol. 3, 1973, pp. 163–174.

Inviscid Steady Flow Past Turbofan Mixer Nozzles

W. C. Chin[1]

Introduction

The thrust and noise benefits mixer nozzles offer are well known in aircraft engine design. Analytical viscous studies

[1] President, Applied AeroNalysis, 7703 Meadowbriar Lane, Houston, Texas 77063. Mem. ASME.

Manuscript received by ASME Applied Mechanics Division, December, 1983; final revision, February, 1984.

deflection w as the sum of $(w_s + w_d)$. The second equation, however, is based on the static deflections w_s for the evaluation of the governing membrane stresses.

$$\left\{\begin{aligned} & w_{,xxxx}+2w_{,xxyy}+w_{,yyyy}-\frac{1}{D}[f_{,yy}w_{,xx}-2f_{,xy}w_{,xy} \\ & \qquad +f_{,xx}w_{,yy}]=\frac{q_{xy}}{D}-\frac{m}{D}w_{d,tt} \\ & f_{,xxxx}+2f_{,xxyy}+f_{,yyyy}=Eh[(w_{s,xy})^2-w_{s,xx}w_{s,yy}] \end{aligned}\right. \tag{3}$$

Subtracting the static component of deflection associated with q_{xy} from the first equation gives:

$$w_{d,xxxx}+2w_{d,xxyy}+w_{d,yyyy}-\frac{1}{D}[f_{,yy}w_{d,xx}-2f_{,xy}w_{d,xy} +f_{,xx}w_{d,yy}]=-\frac{m}{D}w_{d,tt} \tag{4}$$

Assume a simple harmonic motion for the first mode.

$$w_d(x,y,t)=w_a(x,y)\sin(\omega t+\alpha) \tag{5}$$

Substituting equation (5) in equation (4) and cancelling the term $\sin(\omega t + \alpha)$ results in the governing frequency equation:

$$w_{a,xxxx}+2w_{a,xxyy}+w_{a,yyyy}-\frac{1}{D}[f_{,yy}w_{a,xx}-2f_{,xy}w_{a,xy}+f_{,xx}w_{a,yy}] =m\omega^2 w_a \tag{6}$$

Equation (6) represents the natural vibrations of the plate with large amplitudes in terms of w and f. For any preselected large amplitude w_a, values of f are first determined from the set of equations (1) relating to the stationary position of maximum deflection, for which $w_s = w_a$. Substitution in equation (6) for the calculated values of f, yields a standard eigenvalue problem.

2.2 Boundary Conditions. For edges parallel to y-axis, (a) flexural boundary conditions, (i) for rotationally free edges $w = 0$ and $w_{,xx} = 0$, (ii) for rotationally fixed edges $w = 0$ and $w_{,x} = 0$; (b) membrane boundary condition, (i) for all the cases treated $f_{,xy} = 0$, (ii) for the inplane condition perpendicular to the edges, two cases are considered, i.e., $f_{,yy} = 0$ to match the simply supported cases, or inplane displacement equated to zero to match the fixed condition.

2.3 Numerical Solutions. First equations (1) are solved. Subsequently, with known values of f, the eignevalue problem given by equation (6) is treated, using finite differences with a mesh having 300–400 nodes over the entire plate. The algebraic eigenvalue problem derived from equation (7) is given by:

$$[A]\{w_a\}=\Omega\{w_a\} \tag{7}$$

where $[A]$ is a square matrix depending on f and representing the left-hand side of equation (6) expressed in finite differences. $\{w_a\}$ is the unknown column eigenvector. Ω is nondimensionalized frequency. Stress function f is found from equations (1) and is used to form $[A]$. The smallest eigenvalue of $[A]$ is found using the power method with the following iteration:

$$\left\{\begin{aligned} & \{\bar{w}\}_{i+1}=[A]^{-1}\{w\}_i \\ & \{w\}_{i+1}=C_i\{\bar{w}\}_{i+1} \end{aligned}\right. \tag{8}$$

where the subscripts refer to the number of iteration. $\{\bar{w}\}_{i+1}$ is the assumed eigenvector for the $(i+1)$th iteration. The iteration is carried through for $i = 0,1, \ldots .$ until the evaluated eigenvector $\{w\}_{i+1}$ from $(i+1)$th iteration is sufficiently close to the eigenvector $\{w\}_i$ from the preceding iteration. $\{w\}_i$ is then the required eigenvector. C_i is the normalizing factor and can be shown to converge the smallest eigenvalue Ω_1 as $\{w\}$ converges.

3 Discussion of Results

The applicability of the method is demonstrated through treatment of two sets of plates with different flexural and membrane boundary conditions. The solutions presented extend the range of published amplitudes. A third set of solutions for rectangular plates serves to demonstrate the influence of aspect ratios on large-amplitude vibrations. Figures 1 and 2 show the large-amplitude frequencies of square plates with stress free and immovable boundary conditions, respectively. The results from the present analysis yield higher frequencies compared to the available solutions. However, the agreement is close for most practical purposes. Figure 3 represents large-amplitude natural frequencies of simply supported and rotationally fixed rectangular plates of different aspect ratios. The large-amplitude frequency for any given amplitude may be evaluated by simply dividing the given small-amplitude frequency (Ω_s) through the measured ordinate of the curve at the selected amplitude. Note that the solutions presented apply equally to the small vibrations of plates undergoing large deflections under a uniformly distributed loading to a static deflection equal to the large amplitude given herein.

Acknowledgment

The author wishes to thank Professor A. K. Basu, Chariman, Civil Engineering Department, Indian Institute of Technology, for his valuable discussions.

References

1 Aalami, B., and Williams, D. G., *Thin Plate Design for Transverse Loading*, Wiley, New York, 1977.

2 Chu, H. N., and Herrmann, G., "Influence of Large Amplitudes on Free Flexural Vibrations of Rectangular Plates," ASME Journal of Applied Mechanics, Vol. 23, Dec. 1956, pp. 532–540.

3 Yamaki, N., "Influence of Large Amplitude on Flexural Vibrations of Elastic Plates," *ZAMM*, Vol. 41, No. 12, 1961, pp. 501–510.

4 Herrmann, G., "Influence of Large Amplitudes on Flexural Motions of Elastic Plates," NACA TN 3578, 1955.

5 Von Karman, T., "Festigkeitsprobleme im Maschinenbau," *Encyklopaedie der Mathematischen Wissenschaften*, Vol. 4, 1910, p. 349.

6 Prabhakara, M. K., and Chai, C. Y., "Nonlinear Flexural Vibrations of Orthotropic Plates," *Journal of Sound and Vibration*, Vol. 52, No. 4, 1977, pp. 511–518.

7 Vendhan, C. P., "An Investigation into Nonlinear Vibrations of Thin Plates," *International Journal of Nonlinear Mechanics*, Vol. 12, 1977, pp. 209–221.

8 Aalami, B., "Large Deflection of Rectangular Plates Under Patch Loading," *Journal of Structural Division*, ASCE, Nov. 1972, pp. 261–269.

9 Ramachandran, J., "Large Amplitude Vibrations of Elastically Restrained Rectangular Plates," ASME Journal of Applied Mechanics, Vol. 40, Sept. 1973, pp. 881–813.

10 Wah, Y., "Large Amplitude Flexural Vibrations of Rectangular Plates," *Int. J. Mech. Sci.*, Vol. 5, 1963, pp. 425–438.

11 Mei, C., "Finite Element Displacement Method for Large Amplitude Free Flexural Vibrations of Beams and Plates," *Journal of Computers and Structures*, Vol. 3, 1973, pp. 163–174.

Inviscid Steady Flow Past Turbofan Mixer Nozzles

W. C. Chin[1]

Introduction

The thrust and noise benefits mixer nozzles offer are well known in aircraft engine design. Analytical viscous studies

[1] President, Applied AeroNalysis, 7703 Meadowbriar Lane, Houston, Texas 77063. Mem. ASME.

Manuscript received by ASME Applied Mechanics Division, December, 1983; final revision, February, 1984.

have been pursued, for example, as in reference [1], to simulate experimental results. Still, an understanding of the mixing process is incomplete since mixer geometries are marked by rapid streamwise and azimuthal change. What mechanisms and nondimensional parameters really control mixing?

Steady inviscid solutions may be relevant in a sense. For flows producing steady wakes, these results initialize shear layer "marching" calculations, viscosity being of secondary importance. And for unstable wakes, steady inviscid results "start" rollup calculations, which induce additional mixing; eventually, diffusion end effects predominate as flow gradients due to vortex sheet spiralling become important. This Note addresses the boundary conditions only for "cold" and "hot" core flow wake interaction with different reference conditions. Thus, for our purposes, we neglect compressibility and nonlinearity (for flows with shocks, choked nozzles may throttle the internal flow and solutions may or may not exist for arbitrary ambient conditions); also, simple mixers with weak undulations are assumed.

Analytical Formulation

We consider irrotational flows with different external and internal reference pressures, speeds, and densities P^e, U^e, ρ^e, and P^i, U^i, ρ^i. The total potentials $\phi^{e,i}$ satisfy $\nabla^2\phi = \phi^{e,i}_{xx} + \phi^{e,i}_{rr} + \phi^{e,i}_r/r + \phi^{e,i}_{\theta\theta}\ (x,\ r,\ \theta)/r^2 = 0$ in cylindrical coordinates. Tangency conditions apply on the mixer surfaces $r^{e,i} = R + f^{e,i}(x,\ \theta)$ and on the shroud $r = R_s + s(x)$, R and R_s being mean radii. Hence, $\phi^{e,i}_r = \phi^{e,i}_x f^{e,i}_x + \phi^{e,i}_\theta f^{e,i}_\theta/(R+f^{e,i})^2$ and $\phi^e_r = \phi^e_x s'(x)$, with $\nabla\phi^{e,i} \sim U^{e,i}\hat{i}$ far upstream; also, pressure continuity holds through the trailing edge slipstream, where all the vorticity is concentrated (the semi-infinite geometry of Fig. 1 is assumed). Now expand $f = \epsilon f_1 + \epsilon^2 f_2 + \ldots$, $s = \epsilon s_1 + \epsilon^2 s_2 + \ldots$, $\phi^{e,i} = U^{e,i}x + \epsilon\,\phi_1^{e,i} + \epsilon^2\,\phi_2^{e,i} + \ldots$, with $\epsilon << 1, f_1, f_2, s_1, s_2 \sim 0(R)$, and $\phi^{e,i}_{1,2} \sim 0(U^{e,i}x)$. To $0(\epsilon)$, $\nabla^2\phi^{e,i}_1 = 0$, $\phi^{e,i}_{1_r}\ (x, R\pm) = U^{e,i}f^{e,i}_{1_x}\ (x,\ \theta)$, $\phi^e_{1_r}\ (x,\ R_s) = U^e s_1'(x)$ and $\phi^i_{1_r}(x, 0) = 0$, with $\nabla\phi^{e,i}_1 \sim 0$ upstream. Pressure matching on $r = R$ yields $\rho^e U^e \phi^e_{1_x} - \rho^i U^i \phi^i_{1_x} = \Delta P = (P^e - P^i)/\epsilon \sim 0(1)$. The solution is difficult because velocities in addition to potential jump through the trailing edge "*te*" wake: spatial difference formulas *must* include these jumps in any direct approach. Here, normalized variables are used to make this unnecessary; we take the usual formulas, assuming continuity of all "'potential' derivatives," yet allow the required jumps, thus simplifying the numerics and bringing out the governing nondimensional parameters. If $\bar{x} = x/R$, $\bar{r} = r/R$, $\bar{\phi}^{e,i}_1\ (\bar{x},\ \bar{r},\ \theta) = \phi^{e,i}_1\ (x, r, \theta)/U^{e,i}R$, then $\rho^e U^{e2}\,\bar{\phi}_{1\,\bar{x}}^{\,e} - \rho^i U^{i2}\,\bar{\phi}_{1\,\bar{x}}^{\,i} = \Delta P$ shows how both dynamic heads appear. Setting $\bar{\phi}_{\rm avg} = ½(\bar{\phi}_1{}^e + \bar{\phi}_1{}^i)$ and $[\bar{\phi}] = \bar{\phi}_1{}^e - \bar{\phi}_1{}^i$, we obtain $[\bar{\phi}] = [\bar{\phi}]_{(\bar{x}_{te})} + C_1(\bar{x} - \bar{x}_{te}) + C_2(\bar{\phi}_{\rm avg}(\bar{x}, 1, \theta) - \bar{\phi}_{\rm avg}(\bar{x}_{te},\ 1,\ \theta))$ where $C_1 = \Delta P/½(\rho^e U^{e2} + \rho^i U^{i2})$ and $C_2 = (\rho^i U^{i2} - \rho^e U^{e2})/½(\rho^e U^{e2} + \rho^i U^{i2})$, measuring static pressure and dynamic head differences relative to an average head, similar to the powered engine flow boundary conditions in references [2, 3]. $[\bar{\phi}]$ is *not* a true potential jump, since $\bar{\phi}_1{}^e$ and $\bar{\phi}_1{}^i$ are normalized differently; this normalization will also allow simple airfoil code modification.

Since mixer flowfields are periodic, we set $\bar{\phi}_1{}^{e,i}(\bar{x},\ \bar{r},\ \theta) = g(\theta)h^{e,i}(\bar{x},\ \bar{r})$ so that $g_{\theta\theta} + p^2 g = 0$ and $h_{\bar{x}\bar{x}} + h_{\bar{r}\bar{r}} + h_{\bar{r}}/\bar{r} - p^2 h/\bar{r}^2 = 0$. For traces with antisymmetric crests and troughs, $g_n(\theta) = \cos nN\theta$, $n = 0, 1, 2, \ldots, N$ being the lobe number, a lobe consisting of a crest and a trough ($\phi_\theta/r = 0$ at the θ planes bisecting crests and troughs) and, $h^{e,i}_{n_{\bar{x}\bar{x}}} + h^{e,i}_{n_{\bar{r}\bar{r}}} + h^{e,i}_{n_{\bar{r}}}/\bar{r} - n^2N^2h^{e,i}_n/\bar{r}^2 = 0$. If $f^{e,i}_1(x,\theta) = R\sum_{n=0}^{\infty} B^{e,i}_n\ (\bar{x})\ \cos nN\theta$, then, $h^{e,i}_{n_{\bar{r}}}(\bar{x}, 1\pm) = B^{e,i}_{n_{\bar{x}}}(\bar{x})$. Taking the shroud as $s_1(x) = R\bar{s}_1(\bar{x})$, we find $h^e_{0_{\bar{r}}}(\bar{x},\ R_s/R) = \bar{s}_{1_{\bar{x}}}(\bar{x})$, $h^e_{n_{\bar{r}}}\ (\bar{x},\ R_s/R) = 0$ for $n>0$, and $h^i_{n_{\bar{r}}}\ (\bar{x}, 0) = 0$. With $\bar{\phi}^{e,i}_1(\bar{x}, \bar{r}, \theta) = \sum_{n=0}^{\infty} h^{e,i}_n \cos nN\theta$, Kutta's condition implies $h^e_n(\bar{x},\ 1+) - h^i_n(\bar{x},\ 1-) = h^e_n(\bar{x}_{te}, 1+) - h^i_n(\bar{x}_{te}, 1-) + ½C_2(h^e_n(\bar{x}, 1+) + h^i_n(\bar{x}, 1-) - h^e_n(\bar{x}_{te}, 1+) - h^i_n(\bar{x}_{te}, 1-))$ for $n>0$, and, $h^e_0(\bar{x}, 1+) - h^i_0(\bar{x}, 1-) = h^e_0(\bar{x}_{te}, 1+) - h^i_0(\bar{x}_{te}, 1-) + C_1(\bar{x} - \bar{x}_{te}) + ½C_2(h^e_0(\bar{x}, 1+) + h^i_0(\bar{x}, 1-) - h^e_0(\bar{x}_{te}, 1+) - h^i_0(\bar{x}_{te}, 1-))$ for $n = 0$. C_1 appears only in the latter and is unimportant in three-dimensional effects; thus we consider C_2 alone. Both modes may be unstable. The $n = 0$ "jet" may represent an unstable circular vortex sheet; the $n > 0$ modes are additionally marked by downstream shed vortices due to θ variations (probable self-induced motion causes rollup, which distorts the axisymmetric flow described, enhancing mixing).

Calculated Results and Closing Remarks

Our normalizations simplify the column relaxation. In airfoil theory, the speed ϕ_n normal to the "wake" or "branch cut" is continuous; the usual "ϕ_r" and "ϕ_{rr}" forms are used with nonzero $[\phi]$'s easily accounted in the differencing. For mixer and powered engine flows, the branch cut must be placed accurately and not arbitrarily, since it separates distinctly different flows. Differencing through this wake is subtle since $\phi^e_{1_r}(x,\ R+,\ \theta) \neq \phi^i_{1_r}(x,\ R-,\ \theta)$. A potential "obviously" defined by $\phi = \phi^e_1, \phi^i_1$ for $r \gtrless R$ and differenced using standard formulas would need to include a cumbersome and unknown velocity jump. But the choice $\bar{\phi}_1 = \bar{\phi}^e_1\ (\bar{x}, \bar{r}, \theta)$, $r > R$ and $\bar{\phi}_1{}^i\ (\bar{x}, \bar{r}, \theta)$, $r < R$ removes this difficulty: the usual formulas hold with only a potential jump subtracted out, i.e., $\phi_{r_j} = (\phi_{j+1} - \phi_{j-1} - [\phi])/(r_{j+1} - r_{j-1})$, the slipstream slopes $\bar{\phi}_{1\,\bar{r}}^{\,e} = \phi^e_{1_r}/U^e$ and $\bar{\phi}_{1\,\bar{r}}^{\,i} = \phi^i_{1_r}/U^i$ having been

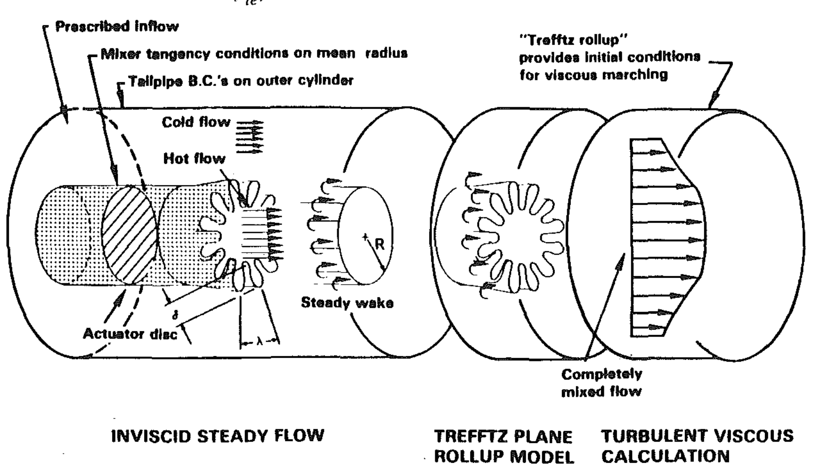

Fig. 1 Flow mixing mechanism and numerical modeling

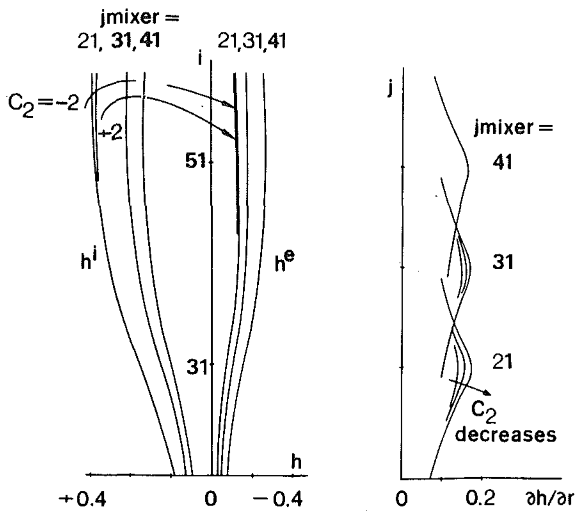

Fig. 2 Surface $h^{e,i}$'s and trailing edge plane $\partial h/\partial r$

implicitly and correctly assumed continuous. This simplifies computations because airfoil codes apply with slight change.

A box with streamwise and radial meshes $\Delta\bar{x}_i = 0.05$, $1 \le i \le 81$, and $\Delta\bar{r}_j = 0.033$, $1 \le j \le 61$, was used, assuming a $N = 4$, $n = 1$ mixer with $B^e_{n\bar{x}}(\bar{x}) = 0$ deg, $1 \le i \le 30$ and 10 deg, $31 \le i \le 51$, 51 being the trailing edge. Mean radii R, where tangency and Kutta conditions apply, were assumed at $j$mixer = 21, 31, and 41; R_s was taken at $j = 61$ along $1 \le i \le 81$. For each case, $C_1 = 0$, but C_2 ranged -2, 0, $+2$. The "h potential" formulation, not purely Neumann, also requires $h^{e,i} = 0$ far upstream where θ variations vanish. This is needed in calculating ϕ_θ/r, which is proportional to h, and hence velocity slip. Converged results were obtained at 1000 sweeps of the box. Figure 2 shows surface $h^{e,i}$'s with $C_2 = -2$, 0, $+2$ for each mixer. Again h measures ϕ_θ/r, while $h_{\bar{x}}$, weak here, measures streamwise speed. The dependence on C_2 is very slight, but that on "$j$mixer" is strong; also, $h^e < 0$, $h^i > 0$, with $h^{e,i}$ taking their largest values at the trailing edge exit plane. The jump $h^i - h^e$, somewhat related to azimuthal velocity slip, decreases with increases in $j$mixer. Also shown are exit plane $h_{\bar{r}}$'s versus $\bar{r}$. Proportional to the radial velocity, $h_{\bar{r}} = 0$ on $j = 1$ and at R_s; it has its maximum on the surface and is continuous in $\bar{r}$ as required (actual velocities are not, again, and some dependence on C_2 is noted). Our limited results show that C_2 is less important than R in producing flows with high azimuthal slip; mixer effectiveness, of course, also depends on $U^{e,i}$, R and R_s as they affect the shear layer. It may be that shed vorticity distribution is more significant if wake rollup controls an essentially inviscid process. These speculative ideas aim at stimulating discussion only; our work addresses mainly appropriate slipstream boundary conditions, numerical stability, and qualitative results. Extension of these results to realistic geometries and at high Mach numbers remains.

References

1 Anderson, B. H., and Povinelli, L. A., "The Effects of Macro Vortex Interactions on the Characteristics of Turbofan Forced Mixer Nozzles," AIAA Paper No. 81-0274, Jan. 1981.

2 Chin, W. C., "Superpotential Solution for Jet Engine External Potential and Internal Rotational Flow Interaction," ASME JOURNAL OF APPLIED MECHANICS, Vol. 51, June 1983, pp. 259–264.

3 Chin, W. C., "Engine Power Simulation for Transonic Flow-Through Nacelles," AIAA Journal, Oct. 1983, pp. 1471–1472.

The Energy-Release Rate in the Growth of a One-Dimensional Delamination

W.-L. Yin[1] and J. T. S. Wang[1]

Introduction

The growth of a buckled delamination in a compressively loaded homogeneous plate has been studied by Kachanov [1] and Chai et al. [2] on the basis of a Griffith-type fracture criterion. The latter work was concerned with the growth of a one-dimensional delamination; the associated energy-release rate, G, was computed by evaluating the total potential energy of the plate and differentiating the result with respect to the variable length of delamination, l. The nature of the function $G(l)$ determines the stability characteristics of delamination growth. In this Note, we use the J-integral method to obtain an *algebraic* expression of G in terms of the postbuckling solution of the delaminated plate. In three special cases, our formula reduces to previously known analytical expressions.

Analysis

Consider a homogeneous orthotropic plate of a linearly elastic material whose orthotropic axes coincide with the longitudinal, normal, and transverse directions of the plate (the x, y, z or x_1, x_2, x_3 directions, respectively). The plate contains a one-dimensional delamination and is in a buckled stated under a sufficiently large axial load. In Fig. 1, we show a segment of the plate containing the delamination front (crack tip). A cross section of the plate ahead of the crack tip carries compressive axial force P_1, shearing force V_1, and bending moment M_1, per unit width of the plate. Behind the crack tip, two cross-sections below and above the delamination carry loads P_2, V_2, M_2, and P_3, V_3, M_3, respectively. It is assumed that these forces and moments have already been determined from the postbuckling solution of the plate. Then the normal and shearing stresses across the three cross sections can be calculated on the basis of classical plate theory. Evaluation of the J-integral along the boundary curve of Fig. 1 yields the energy-release rate associated with the growth of delamination [3]. Since the portion of the strain energy due to the shearing force is generally small as compared to the bending energy or the energy of membrane compression, the effects of the shearing forces V_1, V_2, and V_3 may be ignored. In the following analysis, we consider only the effects of the axial forces and bending moments.

Equilibrium of the segment shown in Fig. 1 requires that

$$P_1 = P_2 + P_3,\ M_1 = M_2 + M_3 + P_3\,H/2 - P_2\,h/2, \qquad (1)$$

where h is the thickness of the delaminated layer and $t = H + h$ is the total thickness of the laminate. We decompose the system of loads in Fig. 1 into two subsystems:

$$M_i = M_i{}' + M_i'',\ P_i = P_i{}' + P_i'', \quad (i = 1, 2, 3) \qquad (2)$$

where with the notation $\bar{h} = h/t$, the first subsystem $\{P_i{}', M_i{}'\}$ is defined by

$$P_1{}' = 0,\ P_2{}' = -P_3{}' = \bar{h}\{P_1 + 6(1-\bar{h})M_1/t\} - P_3,$$
$$M_1{}' = 0,\ M_2{}' = M_2 - M_1(1-\bar{h})^3,\ M_3{}' = M_3 - M_1\bar{h}^3 \qquad (3)$$

The second subsystem $\{P_i''$ and $M_i''\}$ produces a non singular stress field near the delamination front:

$$\sigma_x = -P_1/t - 12M_1 y/t^3,\ \tau_{xy} \approx 0(-t/2 \le y \le t/2).$$

The mode I and mode II stress intensity factors associated with this subsystem of loading vanish. Consequently, the

[1]Associate Professor, and Professor, respectively, School of Engineering Science and Mechanics, Georgia Institute of Technology, Atlanta, 30332.

Manuscript received by the Applied Mechanics Division, June, 1983; final revision, May, 1984.

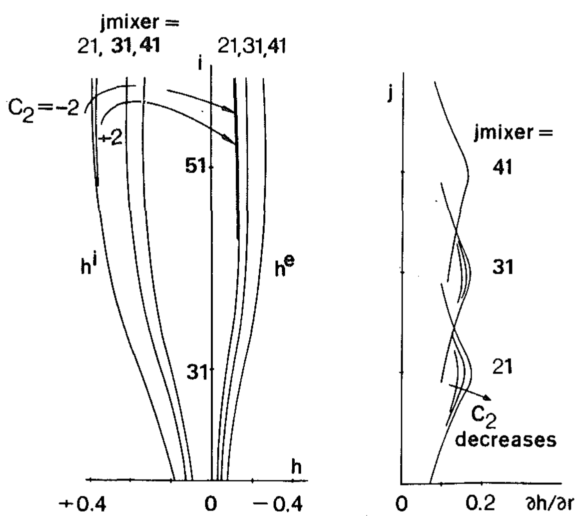

Fig. 2 Surface $h^{e,i}$'s and trailing edge plane $\partial h/\partial r$

implicitly and correctly assumed continuous. This simplifies computations because airfoil codes apply with slight change.

A box with streamwise and radial meshes $\Delta\bar{x}_i = 0.05$, $1 \le i \le 81$, and $\Delta\bar{r}_j = 0.033$, $1 \le j \le 61$, was used, assuming a $N = 4$, $n = 1$ mixer with $B^e_{n\bar{x}}(\bar{x}) = 0$ deg, $1 \le i \le 30$ and 10 deg, $31 \le i \le 51$, 51 being the trailing edge. Mean radii R, where tangency and Kutta conditions apply, were assumed at $j$mixer = 21, 31, and 41; R_s was taken at $j = 61$ along $1 \le i \le 81$. For each case, $C_1 = 0$, but C_2 ranged -2, 0, $+2$. The "h potential" formulation, not purely Neumann, also requires $h^{e,i} = 0$ far upstream where θ variations vanish. This is needed in calculating ϕ_θ/r, which is proportional to h, and hence velocity slip. Converged results were obtained at 1000 sweeps of the box. Figure 2 shows surface $h^{e,i}$'s with $C_2 = -2$, 0, $+2$ for each mixer. Again h measures ϕ_θ/r, while $h_{\bar{x}}$, weak here, measures streamwise speed. The dependence on C_2 is very slight, but that on "$j$mixer" is strong; also, $h^e < 0$, $h^i > 0$, with $h^{e,i}$ taking their largest values at the trailing edge exit plane. The jump $h^i - h^e$, somewhat related to azimuthal velocity slip, decreases with increases in $j$mixer. Also shown are exit plane $h_{\bar{r}}$'s versus $\bar{r}$. Proportional to the radial velocity, $h_{\bar{r}} = 0$ on $j = 1$ and at R_s; it has its maximum on the surface and is continuous in $\bar{r}$ as required (actual velocities are not, again, and some dependence on C_2 is noted). Our limited results show that C_2 is less important than R in producing flows with high azimuthal slip; mixer effectiveness, of course, also depends on $U^{e,i}$, R and R_s as they affect the shear layer. It may be that shed vorticity distribution is more significant if wake rollup controls an essentially inviscid process. These speculative ideas aim at stimulating discussion only; our work addresses mainly appropriate slipstream boundary conditions, numerical stability, and qualitative results. Extension of these results to realistic geometries and at high Mach numbers remains.

References

1 Anderson, B. H., and Povinelli, L. A., "The Effects of Macro Vortex Interactions on the Characteristics of Turbofan Forced Mixer Nozzles," AIAA Paper No. 81-0274, Jan. 1981.

2 Chin, W. C., "Superpotential Solution for Jet Engine External Potential and Internal Rotational Flow Interaction," ASME JOURNAL OF APPLIED MECHANICS, Vol. 51, June 1983, pp. 259–264.

3 Chin, W. C., "Engine Power Simulation for Transonic Flow-Through Nacelles," AIAA Journal, Oct. 1983, pp. 1471–1472.

The Energy-Release Rate in the Growth of a One-Dimensional Delamination

W.-L. Yin[1] and J. T. S. Wang[1]

Introduction

The growth of a buckled delamination in a compressively loaded homogeneous plate has been studied by Kachanov [1] and Chai et al. [2] on the basis of a Griffith-type fracture criterion. The latter work was concerned with the growth of a one-dimensional delamination; the associated energy-release rate, G, was computed by evaluating the total potential energy of the plate and differentiating the result with respect to the variable length of delamination, l. The nature of the function $G(l)$ determines the stability characteristics of delamination growth. In this Note, we use the J-integral method to obtain an *algebraic* expression of G in terms of the postbuckling solution of the delaminated plate. In three special cases, our formula reduces to previously known analytical expressions.

Analysis

Consider a homogeneous orthotropic plate of a linearly elastic material whose orthotropic axes coincide with the longitudinal, normal, and transverse directions of the plate (the x, y, z or x_1, x_2, x_3 directions, respectively). The plate contains a one-dimensional delamination and is in a buckled stated under a sufficiently large axial load. In Fig. 1, we show a segment of the plate containing the delamination front (crack tip). A cross section of the plate ahead of the crack tip carries compressive axial force P_1, shearing force V_1, and bending moment M_1, per unit width of the plate. Behind the crack tip, two cross-sections below and above the delamination carry loads P_2, V_2, M_2, and P_3, V_3, M_3, respectively. It is assumed that these forces and moments have already been determined from the postbuckling solution of the plate. Then the normal and shearing stresses across the three cross sections can be calculated on the basis of classical plate theory. Evaluation of the J-integral along the boundary curve of Fig. 1 yields the energy-release rate associated with the growth of delamination [3]. Since the portion of the strain energy due to the shearing force is generally small as compared to the bending energy or the energy of membrane compression, the effects of the shearing forces V_1, V_2, and V_3 may be ignored. In the following analysis, we consider only the effects of the axial forces and bending moments.

Equilibrium of the segment shown in Fig. 1 requires that

$$P_1 = P_2 + P_3,\ M_1 = M_2 + M_3 + P_3 H/2 - P_2 h/2, \qquad (1)$$

where h is the thickness of the delaminated layer and $t = H + h$ is the total thickness of the laminate. We decompose the system of loads in Fig. 1 into two subsystems:

$$M_i = M_i' + M_i'',\ P_i = P_i' + P_i'', \quad (i = 1, 2, 3) \qquad (2)$$

where with the notation $\bar{h} = h/t$, the first subsystem $\{P_i', M_i'\}$ is defined by

$$P_1' = 0,\ P_2' = -P_3' = \bar{h}\{P_1 + 6(1-\bar{h})M_1/t\} - P_3,$$
$$M_1' = 0,\ M_2' = M_2 - M_1(1-\bar{h})^3,\ M_3' = M_3 - M_1\bar{h}^3 \qquad (3)$$

The second subsystem $\{P_i''$ and $M_i''\}$ produces a non singular stress field near the delamination front:

$$\sigma_x = -P_1/t - 12M_1 y/t^3,\ \tau_{xy} \approx 0(-t/2 \le y \le t/2).$$

The mode I and mode II stress intensity factors associated with this subsystem of loading vanish. Consequently, the

[1] Associate Professor, and Professor, respectively, School of Engineering Science and Mechanics, Georgia Institute of Technology, Atlanta, 30332.

Manuscript received by the Applied Mechanics Division, June, 1983; final revision, May, 1984.

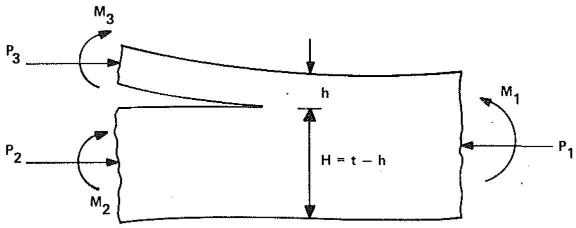

Fig. 1

stress intensity factors and the energy release rates associated with the total loading system are the same as those associated with the first subsystem of loading.

The subsystem of loading given by equation (3) leaves the undelaminated portion in Fig. 1 free from axial force and bending moment. Under this loading, the two cross-sections on the left side carry equal and opposite axial forces

$$P^* = \bar{h}\{P_1 + 6(1-\bar{h})M_1/t\} - P_3. \tag{4}$$

The bending moments in the two layers are given, respectively, by

$$M^* = M_3 - M_1\bar{h}^3 \tag{5}$$

and $M_2{}' = P^*t/2 - M^* = M_2 - M_1(1-h)^3$, as shown in Fig. 2. Hence the first subsystem of loading contains only two independent load parameters P^* and M^*. The stress intensity factors and the energy release rates are functions of these two load parameters.

The stresses in the cross section of the thinner delaminated layer produced by the tensile load P^* and bending moment M^* are

$$\sigma_x = P^*/h - 12M^*\,\eta/h^3.\ \sigma_y \approx \tau_{xy} \approx 0(-h/2 \le \eta \le h/2). \tag{6}$$

where η is the normal coordinate measured from the midplane of this layer. In Fig. 2, the cross section of the laminate ahead of the delamination front is subjected to vanishing stress and strain. In the region behind the delamination front, we have $\epsilon_z = 0$. It follows that

$$\sigma_z = \nu_{13}\sigma_x,\ \epsilon_x = (\sigma_x - \nu_{31}\sigma_z)/E_1 = (1-\nu_{31}\nu_{13})\sigma_x/E_1, \tag{7}$$

where E_1, ν_{13}, and ν_{31} stand for the appropriate elastic moduli of the orthotropic material. Hence the following expression holds along a vertical path across the thinner delaminated layer:

$$\begin{aligned} dJ &\equiv (1/2)\sigma_{ij}\,\epsilon_{ij}\,dy - \sigma_{ij}\,\eta_j(\partial u_i/\partial x)ds \\ &= (1/2)(\sigma_x\,\epsilon_x + \sigma_z\,\epsilon_z)dy + \sigma_x\epsilon_x\,ds = (1/2)(\sigma_x\epsilon_x - \sigma_z\epsilon_z)\,ds \\ &= \frac{1-\nu_{13}\nu_{31}}{2E_1}\left(\frac{P^*}{h} - \frac{12M^*\eta}{h^3}\right)d\eta,\ (-h/2 \le \eta \le h/2). \end{aligned}$$

The contribution to the J-integral from this layer is

$$\int_{-h/2}^{h/2} dJ = \frac{1-\nu_{13}\nu_{13}}{2E_1 h}\{(P^*)^2 + 12(M^*/h)\}.$$

Similarly, the thicker delaminated layer contributes the following term to the J-integral

$$\int_{-H/2}^{H/2} dt = \frac{1-\nu_{13}\nu_{31}}{2E_1 H}\left\{(P^*)^2 + 12\left(\frac{P^*t/2 - M^*}{H}\right)^2\right\}.$$

The sum of the last two integrals delivers the energy-release rate since the remaining portions of the path make no contribution to the J-integral:

$$G = \frac{1-\nu_{13}\nu_{31}}{2E_1 t^3}\left\{\frac{(tP^*)^2}{\bar{h}(1-\bar{h})} + \frac{12(M^*)^2}{\bar{h}^3} + \frac{12(tP^*/2 - M^*)^2}{(1-\bar{h})^3}\right\}. \tag{8}$$

Here P^* and M^* are defined by equations (4) and (5) in terms of the axial forces and bending mements shown in Fig. 1.

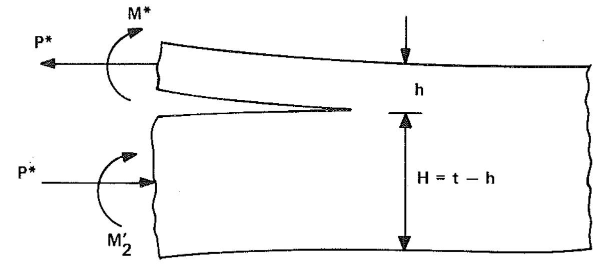

Fig. 2

Thin Film, Thick Column, and Symmetric Split Models

If the moment M_1 produces negligible bending of the laminate, then the laminate has a small curvature compared to the delaminated layer and the maximum bending strain in the laminate is negligible compared to the membrane strain. Consequently.

$$M_1 t^{-3} << M_3 h^{-3}, \quad 6M_1/t^2 << P_1/t.$$

Under these conditions equations (4) and (5) reduce, respectively, to

$$P^* = \bar{h}P_1 - P_3, \quad M^* = M_3. \tag{9}$$

Since the two ends of the thin delaminated layer remain horizontal after buckling, the Euler buckling load of the layer is $P_3 = P_{cr} = E_1 h\,\epsilon_{cr}$ where

$$\epsilon_{cr} = \frac{\pi^2}{3(1-\nu_{13}\nu_{31})}\left(\frac{h}{l}\right)^2. \tag{10}$$

Let $D = E_1 h^3/\{12(1-\nu_{13}\ \nu_{31})\}$ denote the bending stiffness per unit width of the layer. Then the transverse deflection and the bending moment of the buckled layer are given by

$$w(x) = \frac{w_0}{2}\left(1+\cos\frac{2\pi x}{l}\right),\ M(x) = -\frac{Dw_0}{2}\left(\frac{2\pi}{l}\right)^2\cos\frac{2\pi x}{l},$$

$$\left(-l/2 \le x \le \frac{l}{2}\right). \tag{11}$$

Here the amplitude w_0 depends on the *average* compressive strain ϵ_0 in the laminate. The amplitude may be determined by observing that the curve length of the buckled layer exceeds the projected length by an amount due to the difference of the compressive axial strain ϵ_{cr} in the buckled layer and the compressive strain ϵ_2 in the portion of the laminate beneath the layer:

$$w_0{}^2 = (1-\nu_{13}\nu_{31})(2l/\pi)^2(\epsilon_2 - \epsilon_{cr}).$$

In the present case, it is found that

$$\frac{P_1}{E_1 t} = \frac{(1-\bar{h})\epsilon_0 + \bar{h}\bar{l}\epsilon_{cr}}{1-\bar{h}+\bar{h}\bar{l}},\ \frac{P_3}{E_1 t} = \bar{h}\,\epsilon_{cr}, \tag{12a}$$

and

$$\epsilon_2 = [\{1-\nu_{13}\nu_{31}\bar{h}(1-\bar{l})\}\epsilon_0 - (1-\nu_{13}\nu_{31})\bar{h}(1-\bar{l})\epsilon_{cr}]$$

$$/(1-\bar{h}+\bar{h}\bar{l}), \tag{12b}$$

where $\bar{l}$ denotes the ratio of delamination length to the total length of the laminate. Now the bending moment M_3 can be obtained by evaluating equation (12b) at the end points. This yields

$$\left(\frac{M_3}{E_1 t^2}\right)^2 = \frac{\bar{h}^4}{3}\,\frac{1-\nu_{13}\nu_{31}\bar{h}(1-\bar{l})}{1-\bar{h}+\bar{h}\bar{l}}\,\epsilon_{cr}(\epsilon_0 - \epsilon_{cr}). \tag{13}$$

Substituting equations (12) and (13) into equations (9) and (8), we finally obtain

$$G = \frac{(1-\nu_{13}\nu_{31})E_1 h}{2(1-\bar{h}+\bar{h}\bar{l})^2}(1-\bar{h})(\epsilon_0-\epsilon_{cr}) \left[\epsilon_0+\epsilon_{cr}\left\{3+4\frac{\bar{h}\,\bar{l}}{1-\bar{h}}\right\}\right]. \quad (14)$$

This formula for G becomes identical to equation (29) of Chai et al. [2] when the orthotropic moduli are replaced by the corresponding moduli of an isotropic elastic material. In the limit $h \rightarrow 0$. equation (14) immediately reduces to the following formula for a "thin film model":

$$G = (1-\nu_{13}\nu_{31})E_1 h(\epsilon_0-\epsilon_{cr})\,(\epsilon_0+3\epsilon_{cr})/2. \quad (15)$$

Finally, for a "symmetric split model" we have

$$\bar{h}=1/2, M_1=0, P^*=0, M^*=M_3.$$

Hence equation (8) reduces to

$$G=\{12(1-\nu_{13}\nu_{31})/Eh^3)\}(M_3)^2=(M_3)^2/D. \quad (16)$$

This is familiar formula for the energy release rate of a symmetric double cantilever beam-plate.

Acknowledgments

Partial support of this research by Lockhead Georgia Company, Under Grant No. CY48335 to Georgia Institute of Technology, is gratefully acknowledged. The authors wish to thank Mr. John N. Dickson for his effort in initiating the project and his generous an sustained help.

References

1 Kachanov, L. M., "Separation Failure of Composite Materials," *Polymer Mechanics*, Vol. 12, 1976, pp. 812–815.

2 Chai, H., Babcock, C. D., and Knauss, W. G., "One-Dimensional Modelling of Failure in Laminated Plates by Delamination Buckling," *Int. J. Solids Structures*, Vol. 17, No. 11, 1981, pp. 1069–1083.

3 Budiansky, B., and Rice, J. R., "Conservation Laws and Energy Release Rates," ASME JOURNAL OF APPLIED MECHANICS, Vol. 40, 1973, pp. 201–203.

Liapunov's Direct Method Applied to the Buckling of Rotating Beams

D. C. Kammer[1] and A. L. Schlack, Jr.[2]

Introduction

The buckling of rotating beams caused by compressive axial stresses due to centrifugal effects has interested several investigators [1–3] in the last 10 years. In their investigations the critical spin rate for buckling in the plane of rotating was found as a function of the parameter α, where α is the ratio of hoop radius to beam length. However, agreement is lacking in results presented in the literature for the critical spin rate.

White, Kvaternik, and Kaza [1] cited convergence problems at high spin rates as the cause of the discrepancies and therefore resorted to an exact numerical integration technique to avoid the problem. The method put forth in this paper utilizes Liapunov's direct method to derive conditions that are sufficient for stability in the plane of rotation in terms of the parameters of the system. Liapunov's method provides a significant advantage in that the conditions for stability can be obtained without explicitly solving the equations of motion.

[1]Project Engineer, Structural Dynamics Research Corporation (SDRC, Inc.), 1105 Roselle Street, San Diego, Calif. 92121.

[2]Professor, Department of Engineering Mechanics, University of Wisconsin, Madison, Wis. 53706.

Manuscript received by ASME Applied Mechanics Division, February, 1984; final revision, June, 1984.

Theoretical Formulations

The configuration investigated in this Brief Note consists of a uniform Euler beam clamped to the inside of a rigid hoop (a partial spoke, for example) which is assumed to spin at a constant rate ω. If the end of the beam $x = L$ is assumed to be free from stress, the axial load is given by

$$P(x)=1/2m\ \omega^2[(L^2-x^2)-2L\alpha(L-x)] \quad (1)$$

where α is the ratio of hoop radius R to beam length L and m is the mass per unit length. For $\alpha > 1/2$, compressive stresses exist within the beam.

Vibrations in the plane of rotation are governed by the equation [1]

$$m[-v_{,tt}+\omega^2 v]+[Pv_{,x}]_{,x}-[EI_z v_{,xx}]_{,xx}=0. \quad (2)$$

According to Theorem 6.9.4, page 247 of reference [4], the stability of the system can be determined by testing the positive definiteness of the dynamic potential function [5] $U' = V - T_0$, where V is the potential energy and T_0 is that portion of the kinetic energy that is a function of displacement. The form of the function U' is given by

$$U'=1/2\ EI_z\int_0^L v_{,xx}{}^2dx+1/2\int_0^L[Pv_{,x}{}^2-m\omega^2v^2]dx. \quad (3)$$

An appropriate modal expansion [6] is assumed for the inplane displacement v of the form

$$v=\sum_{i=1}^n v_i\Phi_i \quad (4)$$

where Φ_i are either admissible or comparison functions. When the preceding expansion is substituted into the dynamic potential, the function U' can be represented to within a certain order of accuracy by the quadratic form

$$1/2\sum_{i=1}^n\sum_{j=1}^n U'_{,q_iq_j}|_e q_iq_j=1/2\{q\}^T[H]_e\{q\} \quad (5)$$

where $[H]_e$ is the associated Hessian matrix evaluated at the equilibrium position. Terms within the Hessian matrix are of the form

$$H_{ij}=EI_z\int_0^L \Phi_{i,xx}\Phi_{j,xx}dx + \int_0^L[P\ \Phi_{i,x}\Phi_{j,x}-m\omega^2\Phi_i\Phi_j]dx. \quad (6)$$

The positive-definiteness of the Liapunov function U' may then be determined by applying Sylvester's Theorem to the Hessian matrix. The result is a set of necessary and sufficient conditions for the quadratic form to be positive-definite. The conditions are that all the principal minor determinants corresponding to the symmetric Hessian matrix be positive.

In the present investigation [7], it was found that for this class of problem the determinant of the Hessian matrix being positive is a necessary and sufficient condition for all the principal minor determinants to be positive. Therefore, the system will be stable if the determinant of the Hessian matrix, evaluated at the equilibrium position, is positive [8].

The equation of the curve that separates the regions of stability and instability is derived by setting the determinant of the Hessian matrix equal to zero. This results in an nth-order polynomial equation in the square of the critical spin rate parameter of the form

$$A\ \lambda_c^n+B\lambda_c^{n-1}+\ldots C\lambda_c+D=0 \quad (7)$$

where $\lambda_c = m\omega^2L^4/EI$.

The coefficients A, B, etc. are functions of the parameter α. Therefore, equation (7) can be solved for n roots λ_{ci} as functions of α. The derived root λ_{ci} represents the square of

$$G = \frac{(1-\nu_{13}\nu_{31})E_1 h}{2(1-\bar{h}+\bar{h}\bar{l})^2}(1-\bar{h})(\epsilon_0-\epsilon_{cr})$$

$$\left[\epsilon_0+\epsilon_{cr}\left\{3+4\frac{\bar{h}\,\bar{l}}{1-\bar{h}}\right\}\right]. \tag{14}$$

This formula for G becomes identical to equation (29) of Chai et al. [2] when the orthotropic moduli are replaced by the corresponding moduli of an isotropic elastic material. In the limit $h \to 0$. equation (14) immediately reduces to the following formula for a "thin film model":

$$G=(1-\nu_{13}\nu_{31})E_1 h(\epsilon_0-\epsilon_{cr})\,(\epsilon_0+3\epsilon_{cr})/2. \tag{15}$$

Finally, for a "symmetric split model" we have

$$\bar{h}=1/2,\, M_1=0,\, P^*=0,\, M^*=M_3.$$

Hence equation (8) reduces to

$$G=\{12(1-\nu_{13}\nu_{31})/Eh^3)\}(M_3)^2=(M_3)^2/D. \tag{16}$$

This is familiar formula for the energy release rate of a symmetric double cantilever beam-plate.

Acknowledgments

Partial support of this research by Lockhead Georgia Company, Under Grant No. CY48335 to Georgia Institute of Technology, is gratefully acknowledged. The authors wish to thank Mr. John N. Dickson for his effort in initiating the project and his generous an sustained help.

References

1 Kachanov, L. M., "Separation Failure of Composite Materials," *Polymer Mechanics*, Vol. 12, 1976, pp. 812–815.

2 Chai, H., Babcock, C. D., and Knauss, W. G., "One-Dimensional Modelling of Failure in Laminated Plates by Delamination Buckling," *Int. J. Solids Structures*, Vol. 17, No. 11, 1981, pp. 1069–1083.

3 Budiansky, B., and Rice, J. R., "Conservation Laws and Energy Release Rates," ASME Journal of Applied Mechanics, Vol. 40, 1973, pp. 201–203.

Liapunov's Direct Method Applied to the Buckling of Rotating Beams

D. C. Kammer[1] and A. L. Schlack, Jr.[2]

Introduction

The buckling of rotating beams caused by compressive axial stresses due to centrifugal effects has interested several investigators [1–3] in the last 10 years. In their investigations the critical spin rate for buckling in the plane of rotating was found as a function of the parameter α, where α is the ratio of hoop radius to beam length. However, agreement is lacking in results presented in the literature for the critical spin rate.

White, Kvaternik, and Kaza [1] cited convergence problems at high spin rates as the cause of the discrepancies and therefore resorted to an exact numerical integration technique to avoid the problem. The method put forth in this paper utilizes Liapunov's direct method to derive conditions that are sufficient for stability in the plane of rotation in terms of the parameters of the system. Liapunov's method provides a significant advantage in that the conditions for stability can be obtained without explicitly solving the equations of motion.

[1] Project Engineer, Structural Dynamics Research Corporation (SDRC, Inc.), 1105 Roselle Street, San Diego, Calif. 92121.

[2] Professor, Department of Engineering Mechanics, University of Wisconsin, Madison, Wis. 53706.

Manuscript received by ASME Applied Mechanics Division, February, 1984; final revision, June, 1984.

Theoretical Formulations

The configuration investigated in this Brief Note consists of a uniform Euler beam clamped to the inside of a rigid hoop (a partial spoke, for example) which is assumed to spin at a constant rate ω. If the end of the beam $x = L$ is assumed to be free from stress, the axial load is given by

$$P(x)=1/2m\ \omega^2[(L^2-x^2)-2L\alpha(L-x)] \tag{1}$$

where α is the ratio of hoop radius R to beam length L and m is the mass per unit length. For $\alpha > 1/2$, compressive stresses exist within the beam.

Vibrations in the plane of rotation are governed by the equation [1]

$$m[-v,_{tt}+\omega^2 v]+[Pv,_x],_x-[EI_z v,_{xx}],_{xx}=0. \tag{2}$$

According to Theorem 6.9.4, page 247 of reference [4], the stability of the system can be determined by testing the positive definiteness of the dynamic potential function [5] $U' = V - T_0$, where V is the potential energy and T_0 is that portion of the kinetic energy that is a function of displacement. The form of the function U' is given by

$$U'=1/2\ EI_z\int_0^L v,_{xx}{}^2dx+1/2\int_0^L[Pv,_x{}^2-m\omega^2v^2]dx. \tag{3}$$

An appropriate modal expansion [6] is assumed for the inplane displacement v of the form

$$v=\sum_{i=1}^n v_i\Phi_i \tag{4}$$

where Φ_i are either admissible or comparison functions. When the preceding expansion is substituted into the dynamic potential, the function U' can be represented to within a certain order of accuracy by the quadratic form

$$1/2\sum_{i=1}^n\sum_{j=1}^n U',_{q_iq_j}|_e q_iq_j=1/2\{q\}^T[H]_e\{q\} \tag{5}$$

where $[H]_e$ is the associated Hessian matrix evaluated at the equilibrium position. Terms within the Hessian matrix are of the form

$$H_{ij}=EI_z\int_0^L\Phi_i,_{xx}\Phi_j,_{xx}dx$$

$$+\int_0^L[P\ \Phi_i,_x\Phi_j,_x-m\omega^2\Phi_i\Phi_j]dx. \tag{6}$$

The positive-definiteness of the Liapunov function U' may then be determined by applying Sylvester's Theorem to the Hessian matrix. The result is a set of necessary and sufficient conditions for the quadratic form to be positive-definite. The conditions are that all the principal minor determinants corresponding to the symmetric Hessian matrix be positive.

In the present investigation [7], it was found that for this class of problem the determinant of the Hessian matrix being positive is a necessary and sufficient condition for all the principal minor determinants to be positive. Therefore, the system will be stable if the determinant of the Hessian matrix, evaluated at the equilibrium position, is positive [8].

The equation of the curve that separates the regions of stability and instability is derived by setting the determinant of the Hessian matrix equal to zero. This results in an nth-order polynomial equation in the square of the critical spin rate parameter of the form

$$A\ \lambda_c^n+B\lambda_c^{n-1}+\ldots C\lambda_c+D=0 \tag{7}$$

where $\lambda_c = m\omega^2L^4/EI$.

The coefficients A, B, etc. are functions of the parameter α. Therefore, equation (7) can be solved for n roots λ_{ci} as functions of α. The derived root λ_{ci} represents the square of

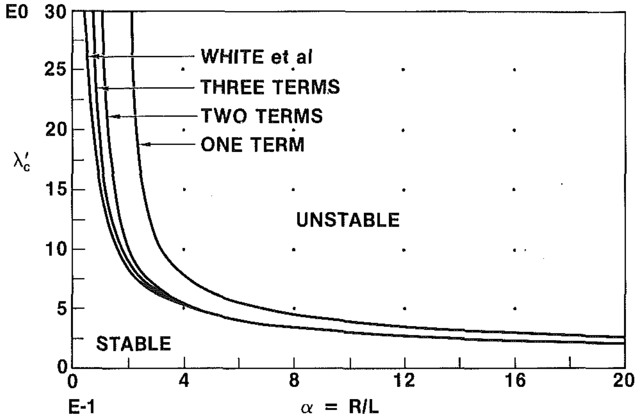

Fig. 1 Inplane buckling of mode one

the spin rate parameter required to buckle a particular mode [9]. When $\lambda_{ci} > 0$, the mode represented by λ_{ci} can buckle at a finite spin rate. If $\lambda_{ci} < 0$, the mode cannot buckle for the corresponding value of α. Separating the preceding two cases is the requirement of an infinite spin rate necessary to buckle the particular mode. This situation occurs when α takes on the critical value α_{ci} corresponding to the ith mode. The critical value is a zero of the leading coefficient A in equation (7).

Numerical Results

The theory set forth is applied to the uniform cantilevered beam described in the foregoing. Results are presented for the case of inplane buckling using admissible functions in expansion (4) of the form $\Phi_i = x^{i+1}$. These functions satisfy the geometric boundary conditions of zero deflection and slope at the root of the beam.

A one-term approximation results in the following relation between λ'_c and α:

$$\lambda'_c = \left[\frac{4}{\frac{1}{3}\alpha - \frac{1}{15}} \right]^{1/2} \tag{8}$$

where $\lambda'_c = \lambda_c^{1/2}$.

Equation (8) gives the critical spin rate required to buckle the beam inplane as a function of α. The critical value of α at which an infinite spin rate is required for buckling is given by $\alpha_{c1} = 0.2$.

For a two-term approximation, equation (7) will be a second-order polynomial possessing two roots, one for each mode. The critical value of α corresponding to the first mode has been reduced to $\alpha_{c1} = 0.094$ by the addition of a second term in the assumed displacement expansion. Adding a third term introduces a third buckled state and further reduces the value of α_{c1} to 0.055.

The one, two, and three-term approximations to the buckling curve for the first mode (along with the curve derived by White, et al.) are plotted in the λ'_c, α plane for fixed beam length L and variable radius R in Fig. 1. Through the first three approximations, the value of α_{c1} has monotonically converged toward the value widely accepted in the literature for the inplane case, $\alpha_{c1} = 0.0$. This trend continues as still more terms are added to the assumed deflection expression [7].

Conclusion

Buckling criteria have been derived as a function of system parameters for a radially mounted beam spinning at a constant rate using Liapunov's direct method. A critical value of the ratio $\alpha = R/L$ was determined, below which the beam cannot buckle for a finite spin rate.

Admissible functions were used to show that the derived solution converges to the solution found in the literature. The success of the present method of solution in predicting the correct relation between the critical spin rate parameter λ'_{c1} and the radius-to-length ratio α has demonstrated that recourse need not be made to the solution of the equations of motion to solve the stability problem. Liapunov's direct method provides an efficient method for determining stability boundaries for this class of problems. It is also readily adaptable to systems with nonuniform physical properties and geometries and different boundary conditions.

References

1 White, W. F., Kvaternik, R. G., and Kaza, K. R. V., "Buckling of Rotating Beams," *International Journal of Mechanical Sciences*, Vol. 21, 1979, pp. 739–745.

2 Lakin, W. D., and Nachman, A., "Unstable Vibrations and Buckling of Rotating Flexible Rods," *Quarterly of Applied Mathematics*, Vol. 35, Jan. 1978, pp. 479–493.

3 Peters, D. A., and Hodges, D. H., "In-Plane Vibration and Buckling of a Rotating Beam Clamped Off the Axis of Rotation," ASME Journal of Applied Mechanics, Vol. 47, June 1980, pp. 398–402.

4 Meirovitch, L., *Methods of Analytical Dynamics*, McGraw-Hill, New York, 1970.

5 Pringle, R., "On the Stability of a Body With Connected Moving Parts," *AIAA Journal*, Vol. 4, No. 8, Aug. 1966, pp. 1395–1404.

6 Meirovitch, L., "A Stationarity Principle for the Eigenvalue Problem for Rotating Structures," *AIAA Journal*, Vol. 14, No. 10, Oct. 1976, pp. 1387–1394.

7 Kammer, D. C., "Dynamic Response of Rotating Beams With Nonconstant Angular Velocity," Ph.D. Thesis, University of Wisconsin, Madison, 1983.

8 Langhaar, H. L., *Energy Methods in Applied Mechanics*, Wiley, New York, 1962, pp. 324–327.

9 Fox, C. H. J., and Burdess, J. S., "The Natural Frequencies of a Thin Rotating Cantilever With Offset Root," *Journal of Sound and Vibration*, Vol. 65, No. 2, 1979, pp. 151–158.

Material Frame-Indifference in Turbulence Modeling

C. G. Speziale[1]

In a recent paper, Lumley [1] addressed an all too often neglected feature of turbulence modeling: the invariance of the closure relations. In fact, before the work of Donaldson, et al. [2], there was a considerable amount of turbulence modeling that did not satisfy even rudimentary invariance requirements under a change of coordinates (such invariance is, of course, guaranteed by simply writing all equations in tensor form). Lumley [1] asserts that the principle of material frame-indifference, which would require that the closure relations that tie the Reynolds stress tensor to the mean velocity field be form invariant under a change of frame, is unequivocally not applicable to turbulent flows and criticizes the arguments made in Speziale [3, 4]. However, several subsequent articles [5, 6] have been published on this subject which strongly indicate that material frame-indifference is applicable to turbulence modeling in, at least, a limiting sense. The purpose of this paper is to present this alternative position in more detail.

In Speziale [3, 4] no objection to the method of moments was raised (moment equations are a rigorous consequence of

[1] Department of Mechanical Engineering, Stevens Institute of Technology, Hoboken, N.J. 07030.

Manuscript received by ASME Applied Mechanics Division, March, 1984; Final revision, July, 1984.

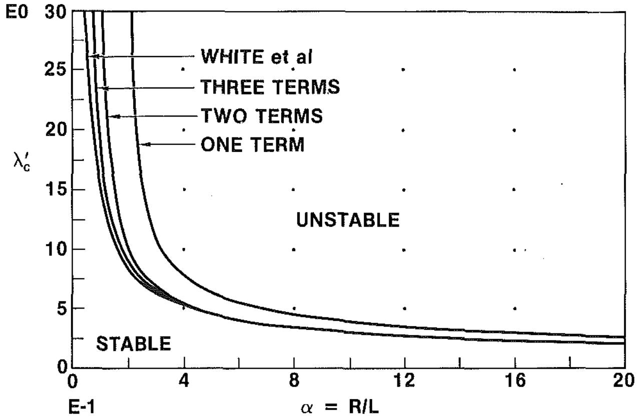

Fig. 1 Inplane buckling of mode one

the spin rate parameter required to buckle a particular mode [9]. When $\lambda_{ci} > 0$, the mode represented by λ_{ci} can buckle at a finite spin rate. If $\lambda_{ci} < 0$, the mode cannot buckle for the corresponding value of α. Separating the preceding two cases is the requirement of an infinite spin rate necessary to buckle the particular mode. This situation occurs when α takes on the critical value α_{ci} corresponding to the ith mode. The critical value is a zero of the leading coefficient A in equation (7).

Numerical Results

The theory set forth is applied to the uniform cantilevered beam described in the foregoing. Results are presented for the case of inplane buckling using admissible functions in expansion (4) of the form $\Phi_i = x^{i+1}$. These functions satisfy the geometric boundary conditions of zero deflection and slope at the root of the beam.

A one-term approximation results in the following relation between λ'_c and α:

$$\lambda'_c = \left[\frac{4}{\frac{1}{3}\alpha - \frac{1}{15}} \right]^{1/2} \tag{8}$$

where $\lambda'_c = \lambda_c^{1/2}$.
Equation (8) gives the critical spin rate required to buckle the beam inplane as a function of α. The critical value of α at which an infinite spin rate is required for buckling is given by $\alpha_{c1} = 0.2$.

For a two-term approximation, equation (7) will be a second-order polynomial possessing two roots, one for each mode. The critical value of α corresponding to the first mode has been reduced to $\alpha_{c1} = 0.094$ by the addition of a second term in the assumed displacement expansion. Adding a third term introduces a third buckled state and further reduces the value of α_{c1} to 0.055.

The one, two, and three-term approximations to the buckling curve for the first mode (along with the curve derived by White, et al.) are plotted in the λ'_c, α plane for fixed beam length L and variable radius R in Fig. 1. Through the first three approximations, the value of α_{c1} has monotonically converged toward the value widely accepted in the literature for the inplane case, $\alpha_{c1} = 0.0$. This trend continues as still more terms are added to the assumed deflection expression [7].

Conclusion

Buckling criteria have been derived as a function of system parameters for a radially mounted beam spinning at a constant rate using Liapunov's direct method. A critical value of the ratio $\alpha = R/L$ was determined, below which the beam cannot buckle for a finite spin rate.

Admissible functions were used to show that the derived solution converges to the solution found in the literature. The success of the present method of solution in predicting the correct relation between the critical spin rate parameter λ'_{c1} and the radius-to-length ratio α has demonstrated that recourse need not be made to the solution of the equations of motion to solve the stability problem. Liapunov's direct method provides an efficient method for determining stability boundaries for this class of problems. It is also readily adaptable to systems with nonuniform physical properties and geometries and different boundary conditions.

References

1 White, W. F., Kvaternik, R. G., and Kaza, K. R. V., "Buckling of Rotating Beams," *International Journal of Mechanical Sciences*, Vol. 21, 1979, pp. 739–745.

2 Lakin, W. D., and Nachman, A., "Unstable Vibrations and Buckling of Rotating Flexible Rods," *Quarterly of Applied Mathematics*, Vol. 35, Jan. 1978, pp. 479–493.

3 Peters, D. A., and Hodges, D. H., "In-Plane Vibration and Buckling of a Rotating Beam Clamped Off the Axis of Rotation," ASME Journal of Applied Mechanics, Vol. 47, June 1980, pp. 398–402.

4 Meirovitch, L., *Methods of Analytical Dynamics*, McGraw-Hill, New York, 1970.

5 Pringle, R., "On the Stability of a Body With Connected Moving Parts," *AIAA Journal*, Vol. 4, No. 8, Aug. 1966, pp. 1395–1404.

6 Meirovitch, L., "A Stationarity Principle for the Eigenvalue Problem for Rotating Structures," *AIAA Journal*, Vol. 14, No. 10, Oct. 1976, pp. 1387–1394.

7 Kammer, D. C., "Dynamic Response of Rotating Beams With Nonconstant Angular Velocity," Ph.D. Thesis, University of Wisconsin, Madison, 1983.

8 Langhaar, H. L., *Energy Methods in Applied Mechanics*, Wiley, New York, 1962, pp. 324–327.

9 Fox, C. H. J., and Burdess, J. S., "The Natural Frequencies of a Thin Rotating Cantilever With Offset Root," *Journal of Sound and Vibration*, Vol. 65, No. 2, 1979, pp. 151–158.

Material Frame-Indifference in Turbulence Modeling

C. G. Speziale[1]

In a recent paper, Lumley [1] addressed an all too often neglected feature of turbulence modeling: the invariance of the closure relations. In fact, before the work of Donaldson, et al. [2], there was a considerable amount of turbulence modeling that did not satisfy even rudimentary invariance requirements under a change of coordinates (such invariance is, of course, guaranteed by simply writing all equations in tensor form). Lumley [1] asserts that the principle of material frame-indifference, which would require that the closure relations that tie the Reynolds stress tensor to the mean velocity field be form invariant under a change of frame, is unequivocally not applicable to turbulent flows and criticizes the arguments made in Speziale [3, 4]. However, several subsequent articles [5, 6] have been published on this subject which strongly indicate that material frame-indifference is applicable to turbulence modeling in, at least, a limiting sense. The purpose of this paper is to present this alternative position in more detail.

In Speziale [3, 4] no objection to the method of moments was raised (moment equations are a rigorous consequence of

[1] Department of Mechanical Engineering, Stevens Institute of Technology, Hoboken, N.J. 07030.

Manuscript received by ASME Applied Mechanics Division, March, 1984; Final revision, July, 1984.

the Navier-Stokes equations). The issue addressed in [3] is whether or not a Reynolds stress closure of sufficient generality can be achieved by truncating the infinite hierarchy of moment equations at the second moment and basing closure *solely* on this equation. It was argued that the disparity in the invariance properties between the Reynolds stress tensor, which is frame-independent, and the transport equation for the Reynolds stress tensor, which is not, casts serious doubts on the potential generality of such closures (especially since there exists a subset of the hierarchy of moment equations that are frame-independent [3]). While this argument was somewhat speculative when published, recent work on the limiting case of two-dimensional turbulence supports this position [5, 6]. Although two-dimensional turbulence is, strictly speaking, a pseudoturbulence, it does constitute a real approximation to turbulence in the upper atmosphere (or in any rapidly rotating framework sufficiently far from solid boundaries) and has thus been of interest to geophysicists. In Speziale [5, 6] it was proven, as a rigorous consequence of the Navier-Stokes equations, that the Reynolds stress tensor in a two-dimensional turbulence *must* satisfy the principle of material frame-indifference. This results from the fact that for a two-dimensional turbulence the fluctuating vorticity transport equation in an arbitrary noninertial frame of reference takes the invariant form [5]

$$\frac{\partial \xi}{\partial t} + \bar{\mathbf{v}} \cdot \nabla \xi = -\mathbf{u} \cdot \nabla \bar{\omega} - \mathbf{u} \cdot \nabla \xi + \overline{\mathbf{u} \cdot \nabla \xi} + \nu \nabla^2 \xi \qquad (1)$$

where ξ is the fluctuating vorticity, $\bar{\omega}$ is the mean vorticity, $\mathbf{u}$ is the fluctuating velocity, $\bar{\mathbf{v}}$ is the mean velocity, and ν is the kinematic viscosity of the fluid. As a direct consequence of (1), the evolution of a velocity fluctuation will be unaffected by the state of rotation of the mean velocity $\bar{\mathbf{v}}$ and, hence, material frame-indifference will rigorously apply. However, in such a turbulence, the Reynolds stress transport equation is still frame-dependent [6] (it contains Coriolis terms), and, hence, it is clear that the invariance properties of this equation do not have a direct bearing on the issue of material frame-indifference.

To obtain a second-order closure that is consistent with the Navier-Stokes equations in two dimensions it is necessary to alter the transformation properties of the Reynolds stress transport equation during the course of the modeling [6]. There are direct and irrevocable consequences of such an occurrence. To be specific, when a modeled equation has different transformation properties than the original equation on which it is based, it can be concluded that this model will only apply to a restricted class of processes that are not closed with respect to this group of transformations [7]. In physical terms, this means that if a second-order closure model applies to a particular turbulent flow it will not, in general, apply to the same turbulent flow when it is subjected to an *arbitrary* rigid body rotation unless there is an ad hoc modification of the empirical constants [6].

In Speziale [3] it was proven that the fluctuating velocity $\mathbf{u}$ based on an ensemble mean is a frame-indifferent vector, i.e., it transforms as

$$\mathbf{u}^* = \mathbf{u}$$

under arbitrary *time-dependent* rotations and translations of the spatial frame of reference and, hence, is independent of the observer. In physical terms, this means that two different observers whose motions differ by an arbitrary rigid body motion would measure the same fluctuating velocity field for a given turbulent flow. Of course, this would not be true of all tensors that enter in the turbulent field equations. For instance, the mean spin tensor $\bar{\omega}$ given by

$$\bar{\omega}_{kl} = \frac{1}{2}\left(\frac{\partial \bar{v}_k}{\partial x_l} - \frac{\partial \bar{v}_l}{\partial x_k}\right) \qquad (2)$$

(where $\bar{\mathbf{v}}$ is the mean velocity) is certainly a tensor but it is *not* a frame-indifferent one. Under a change of frame, equation (2) transforms as

$$\bar{\omega}^* = \bar{\omega} + \text{dual } \mathbf{\Omega} \qquad (3)$$

and is thus not invariant [3] (here, dual $\mathbf{\Omega}$ is the antisymmetric tensor formed from the angular velocity $\mathbf{\Omega}$ of the framing). Furthermore, it should be noted that it is possible to construct fluctuating velocities $\mathbf{u}$ that are *not* independent of the observer. For instance, we can decompose the velocity vector $\mathbf{v}$ into a mean and fluctuating part, respectively,

$$\mathbf{v} = \bar{\mathbf{v}} + \mathbf{u} \qquad (4)$$

where the mean velocity constitutes a variable interval time average [8, 9] given by

$$\bar{\mathbf{v}}(\mathbf{x},t) = \frac{1}{2T}\int_{-\infty}^{\infty} G(t'-t)\mathbf{v}(\mathbf{x},t')dt' \qquad (5)$$

$$G(t'-t) = \begin{cases} 1, & |t'-t| \le T \\ 0, & |t'-t| > T \end{cases}$$

Here, T is some time period, which is usually quite large compared with the time scale of the turbulent fluctuations. It is a simple matter to show that for this case, $\mathbf{u}$ transforms as

$$\mathbf{u}^* = \mathbf{u} + \left[\frac{1}{2T}\int_{-\infty}^{\infty} G(t'-t)\mathbf{\Omega}(t')dt' - \mathbf{\Omega}(t)\right] \times \mathbf{x} \qquad (6)$$

under a time-dependent rotation of the framing and, hence, the fluctuating velocity based on a variable interval time average is frame-dependent unlike that which is constructed from an ensemble mean. However, both fluctuating velocities are tensors! It is extremely important to distinguish ordinary tensors from frame-indifferent tensors since such information can have a crucial impact on the allowable form of models.

Since the fluctuating velocity based on an ensemble mean is a frame-indifferent vector, it follows that the corresponding Reynolds stress tensor is a frame-indifferent tensor [3]. It is true that this does not *automatically* mean that the Reynolds stress tensor must satisfy the principle of material frame-indifference since it is possible for the relationship between frame-indifferent tensors to be frame-dependent (some of the statements made in Speziale [3] are too strong in this regard). However, it is incorrect to argue that since the Navier-Stokes equations are frame-dependent, this necessarily means that material frame-indifference cannot be applied to turbulence modeling. The Reynolds stress tensor that is modeled represents a *special solution* of the Navier-Stokes equations: it is the mean of the outer product of the fluctuating velocity with itself under the conditions that certain stochastic requirements be met and that there only be a limited dependence on initial and boundary conditions. It is a well-established fact that special solutions of an equation can have a larger invariance group than general solutions [10]. The case of two-dimensional turbulence (where material frame-indifference is a rigorous consequence of the Navier-Stokes equations) illustrates this phenomenon and, furthermore, provides a scenario for how material frame-indifference could follow from the Navier-Stokes equations, in an approximate sense, for three-dimensional turbulence sufficiently far from solid boundaries. For such flows, at moderate to rapid rotation rates, the large eddies of turbulence tend to align themselves with the axis of rotation (this is a consequence of the Taylor-Proudman theorem [11]) and thus become two-dimensional for which material frame-indifference rigorously applies. Furthermore, inertial effects on the small scales of turbulence in such a case are much less pronounced and they have been successfully modeled in the large-eddy simulations by using the Smagorinsky model, which is frame-indifferent [12].

Turbulence in a rotating frame is certainly quite different than turbulence in an inertial frame of reference. The critical issue, however, is whether or not this difference in turbulence structure arises from inertial effects on the mean velocity history described by the mean momentum equation or from the failure of material frame-indifference (material frame-indifference, of course, does not say that if an experiment is subjected to a rigid body rotation the motion will be left unchanged). Although it is possible, in principle, to test the validity of material frame-indifference by experiment, such an experiment would be quite difficult to carry out. To directly establish the failure of material frame-indifference in the laboratory it is necessary to produce the *same* mean velocity history in an inertial frame of reference and in an arbitrary noninertial frame of reference and show by measurement that the values of the Reynolds stresses are different in the two cases. A nonconservative body force field would, in general, have to be applied to suppress inertial effects on the mean velocity. Considering these difficulties, it is clear why to the best of my knowledge there exist no published experimental papers that bear conclusively on the issue of material frame-indifference (reference [13] cited in Lumley [1] actually constitutes a "numerical experiment").

The applicability of material frame-indifference to general turbulent flows remains an open question which will only be resolved by rigorous mathematical or experimental proof. However, it is interesting to note that the two most popular turbulent closure models within the general areas of Reynolds stress modeling and subgrid scale stress modeling (large-eddy simulations) satisfy material frame-indifference identically. To be more specific, the widely used k-ϵ or $k-l$ model of turbulence is frame-indifferent and so is the Smagorinsky model which is used to model the small scales of turbulence in the large-eddy simulations. While these models do have serious limitations, in my opinion, there is no conclusive evidence to support the contention that these limitations arise from their frame-indifferent properties. Furthermore, unlike these models, the commonly used frame-dependent, second-order closure models [14, 15] are inconsistent with the Navier-Stokes equations in the limit of two-dimensional turbulence. As a direct consequence of the Taylor-Proudman theorem, this limit is approached by any turbulence in a rapidly rotating framework (i.e., for $\Omega t_0 >> 1$ where t_0 is the time scale of the turbulent fluctuations) that is sufficiently far from solid boundaries. It is a simple matter to show that, for such a turbulence, the second-order closure models of Lumley [14] and Launder, et al. [15] reduce to the equation

$$\epsilon_{3\alpha\lambda}\ \tau_{\lambda\beta}+\epsilon_{3\beta\lambda}\ \tau_{\lambda\alpha}=0 \tag{7}$$

where ϵ is the permutation tensor, τ is the Reynolds stress tensor, and all Greek indices take on the range of values 1, 2 which correspond to the x_1, x_2-coordinates that are perpendicular to the axis of rotation. Equation (7) is obtained by taking the limit as $\Omega\rightarrow\infty$ of the modeled Reynolds stress transport equation [14, 15] in a rotating frame (only the Coriolis terms survive; c.f. [6]). It is clear that equation (7) has the unique solution

$$\tau_{11}=\tau_{22},\tau_{12}=0 \tag{8}$$

which would thus require a state of isotropy for *any* such two-dimensional turbulence. This, of course, is not consistent with the Navier-Stokes equations in two-dimensions for which the state of rotation of the fluid has no effect on the evolution of a velocity fluctuation [6] and, thus, cannot place any constraints on the Reynolds stress tensor (let alone require it to be isotropic). Since the limiting case of two-dimensional turbulence *must* satisfy material frame-indifference, such frame-dependent, second-order closure models [14, 15] that are not invariant in the two-dimensional limit are much more likely to incorporate spurious physics in the description of rotating flows than the more simple frame-indifferent models.

References

1 Lumley, J. L., "Turbulence Modeling," ASME Journal of Applied Mechanics, Vol. 50, 1983, pp. 1097–1103.

2 Donaldson, C. duP., and Rosenbaum, H., "Calculation of Turbulent Shear Flows Through Closure of the Reynolds Equation by Invariant Modeling," ARAP Report No. 127, 1968.

3 Speziale, C. G., "Invariance of Turbulent Closure Models," *Phys. Fluids*, Vol. 22, 1979, pp. 1033–1037.

4 Speziale, C. G., "Closure Relations for the Pressure-Strain Correlation of Turbulence," *Phys. Fluids*, Vol. 23, 1980, pp. 459–463.

5 Speziale, C. G., "Some Interesting Properties of Two-Dimensional Turbulence," *Phys. Fluids*, Vol. 24, 1981, pp. 1425–1427.

6 Speziale, C. G., "Closure Models for Rotating Two-Dimensional Turbulence," *Geophys. Astrophys. Fluid Dynamics*, Vol. 23, 1983, pp. 69–84.

7 Wang, C. C., "On the Concept of Frame-Indifference in Continuum Mechanics and in the Kinetic Theory of Gases," *Arch. Rat. Mech. Anal.*, Vol. 58, 1975, pp. 381–393.

8 Hinze, J. O., *Turbulence*, McGraw-Hill, New York, 1975.

9 Kim, J., "On the Structure of Wall-Bounded Turbulent Flows," *Phys. Fluids*, Vol. 26, 1983, pp. 2088–2097.

10 Rosen, G., "Restricted Invariance of the Navier-Stokes Equations," *Phys. Review A*, Vol. 22, 1980, pp. 313–314.

11 Chandrasekhar, S., *Hydrodynamic and Hydromagnetic Stability*, Oxford University Press, 1961.

12 Moin, P., and Kim, J., "Numerical Investigation of Turbulent Channel Flow," *J. Fluid Mech.*, Vol. 118, 1982, pp. 341–377.

13 Bardina, J., Ferziger, J. H., and Rogallo, R. S., "Effect of Rotation on Isotropic Turbulence: Computation and Modeling," submitted to *J. Fluid Mech.*, 1983.

14 Lumley, J. L., "Computational Modeling of Turbulent Flows," in *Advances in Applied Mechanics*, Vol. 18, Yih, C. S., ed., Academic Press, New York, 1978, pp. 124–176.

15 Launder, B. E., Reece, G., and Rodi, W., "Progress in the Development of a Reynolds Stress Turbulence Closure," *J. Fluid Mech.*, Vol. 68, 1975, pp. 537-566.

Journal of Applied Mechanics

Discussion

Nonlinear Bending and Collapse of Long, Thin, Open Section Beams and Corrugated Panels[1]

F. A. Emmerling.[2] The basic assumptions in this work raise some doubts. In particular, the longitudinal stress is assumed "proportional to the vertical distance from the neutral axis" and the bending moment is found "from the classical beam-equilibrium equation $M_z = E_Z I\kappa$" where the area moment of inertia I is calculated for deformed section. But redistribution of longitudinal stress in the cross section constitutes the *main* effect of the initial curvature. This has been known since the linear analysis of Th. V. Karman [1]. (But the work is clearly intended to encompass initially curved beams.) This fact has been confirmed in the nonlinear theory of tubes and open-section beams (initially straight or curved). Regrettably, most of the relevant literature has been overlooked. The review paper by E. L. Axelrad mentioned by the author refers to work [23, 35, 37, 39] treating the problems in question. There are also more recent publications [2].

References

1 Karman, Th., V., Über die Formänderung dünnwandiger Rohre, insbesondere federnder Ausgleichsrohre," *Zeitschr, VDI*, Vol. 55, 1911, pp. 1889–1895.

2 Emmerling, F. A., "Nonlinear Bending of Slit Walled Tubes," (in German), *ZAMM*, Vol. 62, 1982, pp. 345–348.

Author's Closure

Professor Emmerling raises a valid point about the effect of initial curvature on the form of the longitudinal moment-curvature relationship, and I will try to address the issue as best I can in this short space. The neglected terms give rise to two manifestations of error: one associated with the cross section as a whole, and another associated with the deformation of the cross section. Compared to terms retained, the former effect is of order of magnitude $\bar{y}(\kappa+\kappa_0)$, and the latter is of the order of magnitude $(\Delta\bar{y}\kappa_0)/(\bar{y}\kappa)$. Here $\bar{y}$, κ, and κ_0 are as defined (dimensionally) in the paper under discussion, and $\Delta\bar{y}$ is the displacement of the neutral axis from its original location. In the limit as κ and $\Delta\bar{y}$ approach zero, the first effect is the source of greater possible error, and as κ and $\Delta\bar{y}$ become larger, the second effect is of greater importance. Neither of these would I label as the "main effect of the initial curvature." That I would reserve for the importance of κ_0 in the equation $\rho = (\kappa_0 + \kappa)N$, which relates the longitudinal load, N, to the distorting load of the cross section, ρ.

Nevertheless, the neglected effects can be important if κ_0 is too great, and some strictures are needed to judge the appropriateness of the model. I had supposed that when classical beam theory was invoked, the reader would take, as one of the implications, that the depth of the cross section was very much smaller that the radius of curvature of the bend (i.e., that $\bar{y} \ll \kappa_0 + \kappa$). Such would directly address the first source of error described in the foregoing, and is important whether or not $\kappa_0 = 0$. Since the second source of error is tied to the deformation of the cross section, the test for its significance (i.e., the ratio given previously) must be made a posteriori. Of course, if κ_0 is identically zero then the ratio will also be identically zero. In retrospect, I see that it would have been helpful to have incorporated the elements of this Discussion in the original paper. I thank Prof. Emmerling and the Journal for providing the present opportunity for discussion.

On the subject of "relevant literature," there is no reason to assume that because a particular article was unused it was "overlooked." As clearly stated in the paper, the primary purpose was to put forth a versatile solution scheme that was not tied to a particular cross-sectional geometry. The point of comparison to Ashwell [7], Rimrott [9], and Mech [10] was to demonstrate the ability to regenerate trusted and independently obtained results. Other sources could well have been used, including some of the German and Russian articles that Prof. Emmerling cites. My purposes being otherwise served, I *chose* not to. This in no way casts aspersions on these other fine papers or makes my selection "regrettable." The reader seeking additional publications was well served by the reference to Axelrad [11]—the one entry on the reference list without substitute.

[1] By R. C. Benson, and published in the March, 1984 issue of the JOURNAL OF APPLIED MECHANICS, Vol. 51, pp. 141–145.

[2] Professor, Dr.-Ing., Hochschule der Bundeswehr Munchen.

Journal of Applied Mechanics

Book Reviews

Mathematical Foundations of Elasticity. By Jerrold E. Marsden and Thomas J. R. Hughes. Prentice-Hall, Englewood Cliffs, N. J., 1983. 556 Pages. Price $42.95.

REVIEWED BY D. E. CARLSON[1]

The preface begins with the following statement: "This book treats parts of the mathematical foundations of three-dimensional elasticity using modern differential geometry and functional analysis. It is intended for mathematicians, engineers, and physicists who wish to see this classical subject in a modern setting and to see some examples of what newer mathematical tools have to contribute." Given these worthy intentions and the scientific stature of the authors, the book must be taken in earnest by every serious student of elasticity.

The book begins with a preliminary chapter that provides a brief and informal survey of some standard topics in elasticity from a classical point of view. The text proper then redoes these topics in modern terms. Chapter 1 is devoted to the geometry and kinematics of bodies. It starts conventionally with bodies as open sets in three-dimensional Euclidean space and builds up to a description in terms of manifolds. Chapter 2 is on the general balance laws and inequalities of continuum thermomechanics. Chapter 3 gives a fairly general treatment of constitutive theory with special attention paid to elasticity and thermoelasticity. Chapter 4 provides a modern approach to linearization including a general discussion of linearization stability. Chapter 5 develops and applies the theory of Hamiltonian systems to elasticity. In Chapter 6 functional analysis is used to address such questions as existence, uniqueness, and stability. Chapter 7 introduces bifurcation theory and considers applications to both elastostatics and elastodynamics.

The book is aimed at the beginning graduate level. A good background in advanced calculus and a willingness to work are the prerequisites. The reader is helped considerably by the authors' device of using boxes to summarize important formulas in both abstract and component notation and to isolate optional material such as the consequences of the invariance of energy balance under superposed rigid motion. Guides throughout the text indicate how various notions will be used later and what the reader needs to review before proceeding. The many references to the literature are also useful.

It is refreshing to sense that while the authors take their difficult subject very seriously they do not take themselves too seriously. In an amusing disclaimer early in the preface the reader is warned that Kirchhoff has two h's in it. This amusement is heightened by the discovery that often in the text von Karman is spelled as von Karmen.

Do the authors succeed? Recall that the book is intended for mathematicians, engineers, and physicists who wish to see elasticity in a modern setting and to see what kinds of results newer mathematical tools have to contribute. The power of the newer methods comes through clearly; for example, as early as Chapter 1 the thorny old subject of objective rates is disposed of once and for all through use of the Lie derivative. Mathematicians who are trained in modern geometry will find the book to be a valuable introduction to continuum mechanics. Physicists who are trained in general relativity will be pleased to see that the concept of covariance permeates the development. Engineers will probably have the most difficult time with the book, which really is for those *who wish to see* elasticity in a modern setting. Those who wish this enough to work at it will find this to be a very worthwhile book.

[1] Professor, Department of Theoretical and Applied Mechanics, University of Illinois, Urbana, Ill. 61801.

Theory of Shell Structures. By C. R. Calladine. Cambridge University Press, New York, 1983. 763 Pages. Price $135.00.

REVIEWED BY J. L. SANDERS, JR.[2]

This is an unusual book on shells. The work begins with a chapter that is philosophical in tone rather than the more conventional brief introduction to differential geometry. Nowhere in the book is there any version of the system of equations according to what is generally called the first approximation theory of thin shells. The book is tutorial in nature. The dominant theme is to develop a thorough understanding of the behavior of shell structures. The author goes about this by drawing on the readers' presumed understanding of simpler structures such as beams on an elastic foundation, flat plates, or pin-jointed trusses. Some really difficult problems are successfully handled by idealizing the structure to the point where the problem can be solved by relatively simple mathematics without losing essential features or losing too much accuracy in the numerical results. There are several chapters (particularly the one on cylindrical shell roofs) with a definite design orientation. The mathematical methods employed include simple boundary layer theory (but not singular perturbation theory), Fourier series (but not

[2] Professor, Division of Applied Sciences, Harvard University, Cambridge, Mass. 02138. Fellow, ASME.

Fourier integrals), variational methods, and the like. On those occasions when further development of a topic is beyond the limits of such an approach the author furnishes appropriate references to the literature. The author has a "pet" concept which he pushes in what I would regard as an inoffensive manner, namely his two-surface model of a shell. There is an "*S*" (for stretching) surface and a "*B*" (for bending) surface with appropriate distributions of certain internal loads required to ensure that they deform together. The reader can take this or leave it; I happen to leave it. This is definitely an engineer's book on the subject, but one that those with a very mathematical view of structural mechanics could well read with profit.

A wide variety of topics is included. Throughout the text there is ample discussion of the practical implications of the results. The historical background of a problem is occasionally given, and there are numerous references to the literature. The list of topics is more or less as follows: the membrane theory, its advantages and limitations; analysis of cylindrical shells, the influence of length, boundary conditions, and type of loading; the analysis and design of cylindrical shell roofs, including the effects of edge beams; pressure vessels and junction problems, i.e., torispherical heads, etc.; flexibility of axially symmetric bellows, mostly by energy methods; curved tubes and pipe bends including the effects of reinforcing rings; buckling of cylindrical shells under various loadings and with various boundary conditions by the classical bifurcation analysis including the effect of stiffening elements; post-buckling analysis and imperfection sensitivity; the Brazier effect in the buckling of bent tubes; vibrations of cylindrical shells; plastic analysis, generalized yield surfaces, plastic collapse, upper and lower bound methods applied to limit analysis of pressure vessels.

Nonlinear Oscillations Dynamical Systems, and Bifurcations of Vector Fields. By John Guckenheimer and Philip Holmes. Springer-Verlag, New York, 1983. 453 Pages.

REVIEWED BY M. SLEMROD[3]

In recent years there has been a growing trend in the sciences and engineering to apply the powerful tools of the geometric theory of differential equations. Early examples were the adaption of the direct method of Liapunov in nonlinear stability analysis and the use of bifurcation theory to study the branching of solutions. More recently the realization that rather simple-looking, finite-dimensional deterministic systems may behave in a "chaotic" randomlike fashion has caused new interest among some physicists, biiologists, and engineers as to the implications of this aspect of geometric theory in their respective disciplines. The goal of the book of Guckenheimer and Holmes is in the authors' words to provide "a user's guide to the rapidly growing field of knowledge" in dynamical systems theory in general and chaos in particular.

In specific terms the book serves two roles. First it gives the reader (depending on his or her sophistication) either an introduction or review of the main features of the qualitative theory of differential equations. This is accomplished in Chapter 1 and to a lesser extent in Chapter 3.

My belief is that if one feels uncomfortable with this introductory material: linear systems theory, invariant manifolds, Poincare maps, etc., then this book will be tough-going since everything builds on the tools introduced at the beginning. Let us assume the reader does either the necessary groundwork to master these introductory concepts or knew them already. Then we are ready to get down to business. Chapter 2 presents four striking and simple examples that exhibit chaos and their behavior is studied (partially with the aid of computer simulations). Specifically the examples are the forced van der Pol and Duffing equations, the Lorenz equations, and the equations governing the dynamics of bouncing ball. Chapter 3 stresses bifurcation theory and provides an introduction to the important role of the center manifold theorem in nonlinear stability theory. Chapter 4 introduces the Mel'nilcov method which (1) is actually capable of *proving* "chaos" and (2) (in my opinion) can be mastered by many potential appliers. Chapter 5 discusses strange attractors and the geometric theory of the Lorenz attractor. In my view this material is a quantum jump harder than the preceding chapter. Nonetheless the material is accessible. Finally, the book concludes with Chapters 6 and 7 on global bifurcations and local codimension two bifurcations of flows.

As I have noted to some degree earlier, I view the book as "pyramiding." We build up knowledge from chapter to chapter and apply it to problems in nonlinear oscillations as we go along. It does give a seemingly complex and diverse set of ideas a beautiful unity. Furthermore as I have also mentioned earlier the motivated reader willing to work *can* master the ideas and tools presented here. In summary this is a well-written, first-rate book by two first-rate researchers. I recommend it enthusiastically.

[3] Professor, Department of Mathematical Sciences, Rensselaer Polytechnic Institute, Troy, N.Y. 12181.

Fracture Mechanics of Ceramics: Volume 5 **Surface Flaws, Statistics, and Microcracking,** and Volume 6 **Measurements, Transformations, and High-Temperature Fracture.** Edited by R. C. Bradt, A. G. Evans, D. P. H. Hasselman, and F. F. Lange. Plenum Press, New York, 1983. 692 and 674 Pages. Price $89.50 and $89.50.

REVIEWED BY J. W. HUTCHINSON[4]

These two volumes contain a total of 78 papers that were presented at an international symposium on fracture of ceramics held at The Pennsylvania State University in July, 1981. The volumes represent much more than the usual collection of symposium papers. For one thing, the field of fracture mechanics of ceramics is at an exciting stage with several new developments holding out promise for tougher ceramics, and the books reflect this. The leading contributors to the field have papers in the volumes. While the volumes focus on the fracture of ceramics, they are otherwise quite comprehensive in their coverage. Most of the contributions are research papers, with a healthy mix of theory, experiment, and materials design, but there are also well-written survey papers on a variety of topics including indentation mechanics, statistical aspects of design with ceramics, testing techniques, and toughening mechanisms. A partial listing of some of the other topics dealt with includes: dynamic fracture, surface flaws, multiple crack interactions, microcrack toughening mechanisms, porous and cellular ceramics, compressive fracture, phase transformation toughening, microstructural design, *R*-curve behavior, high-temperature fracture, thermal shock resistance, crack healing, and subcritical crack growth. The volumes are obviously relevant to materials scientists, particularly to ceramicists, but there is also a high content of interesting mechanics here. Some of it is in a fairly rudimentary state, which makes it all the more interesting.

[4] Professor, Division of Applied Sciences, Harvard University, Cambridge, Mass. 02138. Fellow ASME.

Theoretical Glaciology. By Kolumban Hutter. D. Reidel, Mass., *1983*. *510* Pages. Price $*104.00*

REVIEWED BY T. J. HUGHES[5]

This is a most impressive book. Most shortcomings cited in this review reflect on Hutter's decision to limit the scope of his study, not the study itself, which is extremely thorough and well presented. His writing is lucid despite the fact that English is not has native tongue.

The book is organized into seven chapters. Chapter one presents the fundamentals of continuum mechanics, with detailed treatments of the balance equations, the response of the material to environmental conditions, an application of the entropy principle to stress and temperature fields, and phase changes as one important material response. Chapter two examines several constitutive equations as they relate to the mechanical properties imposed by the hexagonal symmetry of ice single-crystals, the isotropic symmetry of randomly oriented polycrystalline ice, and phase transformations that involve brine in sea ice. These considerations constitute Part I of the book, which unites continuum mechanics and materials science in a framework within which glaciers can be studied.

Part II provides numerous glaciological applications of the principles developed in Part I. Chapter three gives the basic practical application; the flow of ice masses under the force of gravity, masses that range from small valley glaciers to continental ice sheets. Two-dimensional flow is examined in terms of stress and temperature field equations, and the stress and thermal boundary conditions that prevail when the bed and surface slopes are nearly identical. Chapter four examines the velocity field of these slabs as a consequence of temperature-stress feedback. It begins by stating the basic boundary-value problem, reduces it to linear form, and then provides solutions of zero and first-order, with numerical results for steady-state solutions and an examination of surface waves on glaciers. These chapters present what might be called classical glaciology.

The remainder of Part II concentrates on new developments, many by Hutter himself. Chapter five treats cases where the surface and bed slopes are substantially unequal; what Hutter calls the shallow-ice approximation. The basal shear stress formulation is modified for this situation, and steady-state solutions are presented for ice flow and surface profiles that result from variable bed topography. Ice divides of ice sheets are examined and an appendix examines higher-order stress solutions in the shallow-ice approximation. Chapter six analyzes the response of valley glaciers and continental ice sheets to seasonal and climatic change, including the motion of kinematic waves and other surface waves on glaciers. Chapter seven concludes the book by expanding the two-dimensional treatments for ice sheets to three dimensions, and by focusing on the effect of varying cross sections of valley glaciers. Variational principles are introduced to treat local phenomena such as ice falls and calving ice cliffs. Some finite-element solutions to these problems are examined.

The book has hundreds of equations and a corresponding number of mathematical errors. Although these errors do not seem to invalidate the mathematical treatments, the reader should carefully work through every derivation before applying the final equations.

[5] Professor, Department of Geological Sciences, University of Maine, Orono, ME 04469

Mechanical Behavior of Anisotropic Solids. Edited by Jean-Paul Boehler. Martinus Nijhoff, The Hague, *1982*. *927* Pages. Price $120.00.

REVIEWED BY Y. F. DAFALIAS[6]

This volume contains the 54 invited contributions of 84 authors from 15 different countries to an international colloquium organized by J. P. Boehler and A. Sawczuk at Villard de-Lans, France, in June 1979. In the 927 pages of the handsomely printed volume the reader can find almost every aspect of anisotropy not only as it pertains to the mechanical behavior of solids, but also to a number of nonmechanical properties. The overall trend is the identification, measurements, and analytical modeling of anisotropic properties at various scales and from different perspectives, rather than the solution to problems where anisotropy plays a role (although a few contributions address the latter).

The volume is organized into 12 sessions, some of which are preceded by one of the five general lectures presented. The title and a brief description of the content of each session is given in the following

Session 1: Invariant Formulation of Constitutive Equations

This session contains six communications and one general lecture entitled, "The Formulation of Constitutive Equations for Anisotropic Solids," written by A. J. M. Spencer. The general content is the mathematical theory of invariant representations for quantities of different tensorial orders associated with elastic, plastic, creep, and fracture processes, with the emphasis placed on the mathematical aspects.

Session 2: Physical Propertis of Anisotropic Materials

The session contains six communications focusing on physical properties and their implicit use for characterizing anisotropic mechanical properties. Magnetic anisotropy for metals, electrical conductivity anisotropy for saturated granular media, structural modeling of pseudo-elastic bodies, anisotropy in liquid crystals, thermoelasticity in conjunction with electrical measurements, and birefringence in finitely deformed materials are the particular topics.

Session 3: Changes of Macroscopic Anisotropy in Metals

Following the general lecture entitled "Experimental Plasticity on the Anisotropy of Metals," written by K. Ikegami with an extensive bibliography, four communications are presented of both a theoretical and experimental nature on the macroscopic description of the response of metals with initial or induced anisotropy.

Session 4: Anisotropy of Metallic Polycrystals

The emphasis of the general lecture, "Relations entre Textures et Comportement Mécanique Anisotrope des Métaux," by P. Parniére and two of the three communications that follow it are on the description and relation between microscopic mechanicms and macroscopic anisotropic response of polycrystalline metals, supported by analytical development and experimental observations of a metallurgical nature. The third communication is a theoretical and experimental study of plastic wave propagation under combined stresses and nonproportional loading paths.

Session 5: Analytical and Numerical Methods for the *Determination of Mechanical Properties of Composites*

The general lecture, "Mechanical Properties of Com-

[6] Associate Professor, Department of Civil Engineering, University of California, Davis, Calif. 95616. Mem. ASME.

posites," by G. J. Dvorak, as well as its three following contributions concentrate on the determination of macroscopic, anisotropic mechanical properties of heterogeneous media from the properties of their constituents, with emphasis on elasticity, plasticity, and viscoelasticity of fiber-reinforced or layered composites.

Session 6: Strength of Composites

The three contributions of this section address specifically the problems of composite strength, either from the point of view of a failure surface or the delamination failure mode, supplementing the theory with experimental data.

Session 7: Mechanics of Anisotropic Rocks

The comprehensive general lecture, "anisotropie Mecaniqué des Roches," is written by P. M. Sirieys. The emphasis of the lecture and its following three communications is on the anisotropy of rock masses. In addition to the general considerations, features particularly important for rocks, such as the response of joints and the thermically induced anisotropic fissuration, are examined.

Session 8: Anisotropy of Consolidated Clays and of Materials With Internal Friction

The four contributions address the question of the effect of initial or induced by consolidation anisotropy on the mechanical response of pressure-sensitive materials with emphasis on clays and sands. Failure and yield criteria for such media are presented.

Session 9: Vibrations, Waves' Propagation, and Induced Anisotropy

The common feature of the give contributions is the effect (and detection) of anisotropy on the propagation of waves. Different kinds of waves are treated, such as magnetic, acoustic, electroacoustic, etc., for different materials and from both theoretical and experimental points of view.

Session 10: Damage and Creep

Two of the four communications focus on the development of anisotropic internal damage and its macroscopic effect on elastic and viscoplastic properties of metals. The other two concentrate on creep characteristics of eutectic composite and polycrystalline glass.

Session 11: Experimental Investigations and Interpretation of Mechanical Tests

While emphasizing experimental aspects supported by proper theoretical development the five contributions present a plethora of experimental data indicating the mechanical effect of anisotropy on diverse materials such as perforated plates, rocks, clays, epoxy/carbon, and graphite/epoxy.

Session 12: Problems of Civil Engineering

The three communications of the last session present problems associated with the effect of mechanical anisotropy on the loading of large-scale structures, such as rock mass and oil shale, with methods of analysis ranging from the practical to the theoretical.

It is clear from the foregoing synopsis of the contents that the volume is addressed to the specialist not only on anisotropy in general, but also on different subjects of mechanical behavior. The English-speaking reader should also consider the fact that 15 of the 54 contributions are written in French. Nevertheless, we believe that this volume is extremely useful for the serious researcher on anisotropy, and the diversity of the subjects in many respects helps in integrating the general concept. It must also be mentioned that this volume is followed by two others in press (corresponding colloquia in 1981 and 1983) with emphasis on more specific aspects of anisotropy.

The long period that elapsed from the time of the first colloquium (1979) to the publication of the present volume (1982) is compensated for by the excellent appearance and quality of the volume as well as the uniformity of the presentations, much of which should be attributed to the effort of the editor in preparing the guidelines for the authors and in carefully reviewing the proofs.

An Introduction to Continuum Mechanics. By M. E. Gurtin. Academic Press, New York, 1981. 265 Pages. Price $34.50.

REVIEWED BY W. J. DRUGAN[7]

For students, practitioners, and researchers in the many areas of solid and fluid mechanics that are of importance today, a clear, precise understanding of the fundamental principles of continuum mechanics is indispensible. Professor Gurtin's book is an exemplary source for such an understanding: it is lucid, concise, and rigorous.

As befits the "Mathematics in Science and Engineering" series of which this book is a volume, the presentation is fairly mathematical: the reader's minimal background should include finite-dimensional vector spaces and advanced calculus from a mathematical (as opposed to pure applications) perspective so that the book's terminology and methods of proof are familiar. The benefits of requiring this level of mathematical literacy are that crucial concepts can be stated and proved rigorously, and that a number of elegant modern results and perspectives can be accurately conveyed. I found these to be among the book's most attractive features: every important result is clearly stated (as a theorem or proposition) together with all necessary assumptions, and every result is either proved or accompanied by a reference to a proof. Thus, a number of important concepts that are taken for granted in many texts on the subject are explicitly stated and proved here; this philosophy should be particularly valuable to students new to continuum mechanics.

The striking conciseness of the book enables the reader to acquire a clear broad perspective on the subject and its principal concepts; Professor Gurtin has evidently worked hard to effect a lucid, direct approach. Students may find the book difficult in places due to this terseness, but I feel the extra effort required will be well rewarded.

Regarding the specific content, the book begins with two chapters on tensor algebra and analysis, which are notable for the development of a very general notion of differentiation applicable to tensor functions of arbitrary rank, and for simple, clear interpretations of such concepts as divergence and curl. These chapters (the entire book, for that matter) employ direct—as opposed to component—notation exclusively. Many concepts and results do provide more insight when viewed in direct notation, but I feel that students of continuum mechanics should also be exposed to index notation, as it often provides the simplest approach for proofs and manipulations of tensor quantities.

Chapters 3–5 deal with the fundamental topics of kinematics, mass, momentum, and force. The introduction to deformations and the discussions and interpretations of finite strain and rate of deformation tensors are among the clearest

[7] Assistant Professor, Department of Engineering Mechanics, University of Wisconsin, Madison, Wisc. 53706. Assoc. Mem. ASME.

and cleanest I have seen. A nice feature of these sections is the demonstration of how these deformation quantities relate to length changes of arbitrary material curves. I do wish proofs of the theorems for converting volume and surface integrals from current to reference configurations were provided rather than referenced, as these results are extremely important and are employed repeatedly throughout the text. In the chapter on force, I was surprised to see the assumption that the traction vector (stress vector) is a smooth function of position in the body, introduced even before the statement of the integral forms of the momentum balance laws. This deprives the reader of an appreciation of the full generality of these laws (e.g., they permit the existence of stress discontinuities), and fosters the limiting notion that they are equivalent to the differential forms of momentum balance. Indeed, this equivalence is proved in the text via the smooth traction assumption, which is misleadingly referred to as a "property of force systems."

The discussion of constitutive equations and some complete theories for describing the behavior of certain material classes comprises the remainder of the book. This discussion is very nicely developed. It begins with the basic example of inviscid fluids in Chapter 6, followed by a general analysis in Chapter 7 of changes of observer and the axiom of observer independence of material response. This general formulation is then applied in Chapter 8 to derive constitutive equations for Newtonian fluids, and in Chapter 9 to derive constitutive equations for elastic materials at finite strain. Chapter 10 shows how a systematic linearization of finite elasticity theory results in the classical theory of linear elasticity. Thus these chapters provide rigorous derivations of the governing equations for the classical theories of ideal, compressible and viscous fluids, and linear and nonlinear elasticity, while giving a very interesting brief tour of some important specific results in these theories. Also notable is the inclusion of uniqueness and stability theorems for the Navier-Stokes equations, together with careful proofs which illustrate some nice mathematics; uniqueness theorems for linear elastostatics and elastodynamics; and valuable comparisons between the linear and finite elasticity theories, such as differences in the requirements for existence of solutions, and a comparison of solutions for the problem of simple shear. I would like to have seen at least brief sections on a few other important theories of material behavior that currently receive much attention in research and in practice, such as plasticity and viscoelasticity.

One section that could be improved is a confusing definition and discussion of hyperelastic materials, giving a relation between the Piola-Kirchhoff stress tensor and the derivative of strain energy density which is inconsistent with earlier definitions of derivative and tensor. There are also a few cases of undefined notation. Otherwise, I found the book to be remarkably free of errors (except for very few trivial misprints), for which both the author and publisher are to be highly commended.

Additional features of the book include: two appendices, a brief one on the exponential function (of a tensor), and a detailed one on isotropic functions; a substantial set of hints for some of the exercises which appear in the text; and a valuable list of modern references on continuum mechanics and related mathematics.

This book is a major contribution to the modern continuum mechanics literature by one of the subject's best expositors. The minor constructive criticisms noted in the foregoing should not obscure this fact.

Elastic Wave Propagation in Transversely Isotropic Media. By Robert G. Payton. Martinus Nijhoff, The Netherlands, 1983. 192 pages. Price $42.50.

REVIEWED BY J. G. HARRIS[8]

This book describes the propagation of elastic waves in transversely isotropic media. In particular, transient wave motion problems are solved in two dimensions (plane strain) and three dimensions for both the full space and the half space. The emphasis is placed on finding explicit representations for the displacement fields. Asymptotic or numerical solutions are not considered and no effort is made to consider experimental aspects of the subject. This book will interest mainly those who are interested both in anisotropic wave propagation and in the mathematical techniques used to investigate such wave motion.

Chapters 1 and 2 provide essential background information for the rest of the book. Chapter 1, in addition to introducing the equations of linear elasticity, describes the constraints on the elastic constants necessary for wave motion and describes the uncoupled equations of motion. Chapter 2 provides the reader with the first real insight into why anisotropic wave motion is interesting. This chapter discusses the nature of the normal (slowness) curve and the wave front curve. The uninitiated reader might first want to read the book by Musgrave listed among the references or that by Auld [1]. Though it is unfortunate that in Figs. 16–26 the normal curve and the wave front curve do not appear on the same page, the discussion of these two curves is handled very well.

Chapter 3, which is the most important chapter, is concerned with calculating the two-dimensional (plane strain) and the three-dimensional Green's tensor for the displacement field in a full space using integral transforms. In the two-dimensional case the expressions for the displacement field are reduced to a sum of residues. To make further progress the author must consider points of observation along the symmetry axis or points near the wave fronts. The reviewer was surprised to learn of the presence of lacunas, in two dimensions, which move with time, and was particularly interested in the wave front approximations near their cuspidal points. In the three-dimensional case explicit expressions for the displacements are calculated for arbitrary observation points subject to a restriction on the elastic constants, and for observation points along the symmetry axis without any restriction on the elastic constants. Closing the chapter, a formula (the Herglotz-Petrowski formula) expressing the displacement field as an integral over the entire slowness surface is derived and used to examine briefly the displacement behavior near the wave fronts.

Chapters 4 and 5 are concerned with the excitation of the transversely isotropic half space where the axis of symmetry is perpendicular to the traction-free surface. In Chapter 4 the displacement of the surface of a two-dimensional half space, excited by a point load applied at the surface, is calculated. In Chapter 5 the displacement of the epicenter of a three-dimensional half space, excited by a buried point force, is calculated. The Betti-Rayleigh reciprocal theorem is then used to calculate the epicentral-axis motion caused by a point force applied at the surface. Chapter 5 closes with a very brief discussion of the body force equivalents to internal discontinuities in an anisotropic solid.

The reviewer found no serious misprints; the proofreading, which is quite important in a book like this, has been careful and thorough. While he is not aware of all the literature in this field, the reviewer believes that this book contains the most

[8] Assistant Professor, Department of Theoretical and Applied Mechanics, 216 Talbot Laboratory, 104 S. Wright St., University of Illinois, Urbana, Ill. 61801. Assoc. Mem. ASME.

and cleanest I have seen. A nice feature of these sections is the demonstration of how these deformation quantities relate to length changes of arbitrary material curves. I do wish proofs of the theorems for converting volume and surface integrals from current to reference configurations were provided rather than referenced, as these results are extremely important and are employed repeatedly throughout the text. In the chapter on force, I was surprised to see the assumption that the traction vector (stress vector) is a smooth function of position in the body, introduced even before the statement of the integral forms of the momentum balance laws. This deprives the reader of an appreciation of the full generality of these laws (e.g., they permit the existence of stress discontinuities), and fosters the limiting notion that they are equivalent to the differential forms of momentum balance. Indeed, this equivalence is proved in the text via the smooth traction assumption, which is misleadingly referred to as a "property of force systems."

The discussion of constitutive equations and some complete theories for describing the behavior of certain material classes comprises the remainder of the book. This discussion is very nicely developed. It begins with the basic example of inviscid fluids in Chapter 6, followed by a general analysis in Chapter 7 of changes of observer and the axiom of observer independence of material response. This general formulation is then applied in Chapter 8 to derive constitutive equations for Newtonian fluids, and in Chapter 9 to derive constitutive equations for elastic materials at finite strain. Chapter 10 shows how a systematic linearization of finite elasticity theory results in the classical theory of linear elasticity. Thus these chapters provide rigorous derivations of the governing equations for the classical theories of ideal, compressible and viscous fluids, and linear and nonlinear elasticity, while giving a very interesting brief tour of some important specific results in these theories. Also notable is the inclusion of uniqueness and stability theorems for the Navier-Stokes equations, together with careful proofs which illustrate some nice mathematics; uniqueness theorems for linear elastostatics and elastodynamics; and valuable comparisons between the linear and finite elasticity theories, such as differences in the requirements for existence of solutions, and a comparison of solutions for the problem of simple shear. I would like to have seen at least brief sections on a few other important theories of material behavior that currently receive much attention in research and in practice, such as plasticity and viscoelasticity.

One section that could be improved is a confusing definition and discussion of hyperelastic materials, giving a relation between the Piola-Kirchhoff stress tensor and the derivative of strain energy density which is inconsistent with earlier definitions of derivative and tensor. There are also a few cases of undefined notation. Otherwise, I found the book to be remarkably free of errors (except for very few trivial misprints), for which both the author and publisher are to be highly commended.

Additional features of the book include: two appendices, a brief one on the exponential function (of a tensor), and a detailed one on isotropic functions; a substantial set of hints for some of the exercises which appear in the text; and a valuable list of modern references on continuum mechanics and related mathematics.

This book is a major contribution to the modern continuum mechanics literature by one of the subject's best expositors. The minor constructive criticisms noted in the foregoing should not obscure this fact.

Elastic Wave Propagation in Transversely Isotropic Media. By Robert G. Payton. Martinus Nijhoff, The Netherlands, 1983. 192 pages. Price $42.50.

REVIEWED BY J. G. HARRIS[8]

This book describes the propagation of elastic waves in transversely isotropic media. In particular, transient wave motion problems are solved in two dimensions (plane strain) and three dimensions for both the full space and the half space. The emphasis is placed on finding explicit representations for the displacement fields. Asymptotic or numerical solutions are not considered and no effort is made to consider experimental aspects of the subject. This book will interest mainly those who are interested both in anisotropic wave propagation and in the mathematical techniques used to investigate such wave motion.

Chapters 1 and 2 provide essential background information for the rest of the book. Chapter 1, in addition to introducing the equations of linear elasticity, describes the constraints on the elastic constants necessary for wave motion and describes the uncoupled equations of motion. Chapter 2 provides the reader with the first real insight into why anisotropic wave motion is interesting. This chapter discusses the nature of the normal (slowness) curve and the wave front curve. The uninitiated reader might first want to read the book by Musgrave listed among the references or that by Auld [1]. Though it is unfortunate that in Figs. 16–26 the normal curve and the wave front curve do not appear on the same page, the discussion of these two curves is handled very well.

Chapter 3, which is the most important chapter, is concerned with calculating the two-dimensional (plane strain) and the three-dimensional Green's tensor for the displacement field in a full space using integral transforms. In the two-dimensional case the expressions for the displacement field are reduced to a sum of residues. To make further progress the author must consider points of observation along the symmetry axis or points near the wave fronts. The reviewer was surprised to learn of the presence of lacunas, in two dimensions, which move with time, and was particularly interested in the wave front approximations near their cuspidal points. In the three-dimensional case explicit expressions for the displacements are calculated for arbitrary observation points subject to a restriction on the elastic constants, and for observation points along the symmetry axis without any restriction on the elastic constants. Closing the chapter, a formula (the Herglotz-Petrowski formula) expressing the displacement field as an integral over the entire slowness surface is derived and used to examine briefly the displacement behavior near the wave fronts.

Chapters 4 and 5 are concerned with the excitation of the transversely isotropic half space where the axis of symmetry is perpendicular to the traction-free surface. In Chapter 4 the displacement of the surface of a two-dimensional half space, excited by a point load applied at the surface, is calculated. In Chapter 5 the displacement of the epicenter of a three-dimensional half space, excited by a buried point force, is calculated. The Betti-Rayleigh reciprocal theorem is then used to calculate the epicentral-axis motion caused by a point force applied at the surface. Chapter 5 closes with a very brief discussion of the body force equivalents to internal discontinuities in an anisotropic solid.

The reviewer found no serious misprints; the proofreading, which is quite important in a book like this, has been careful and thorough. While he is not aware of all the literature in this field, the reviewer believes that this book contains the most

[8]Assistant Professor, Department of Theoretical and Applied Mechanics, 216 Talbot Laboratory, 104 S. Wright St., University of Illinois, Urbana, Ill. 61801. Assoc. Mem. ASME.

systematic treatment of boundary value problems in anisotropic elastodynamics that is available. Moreover, he admires the patience and hard work that has gone into this study.

References

1 Auld, B. A., *Acoustic Fields and Waves in Solids*, Vol. 1, Wiley, New York, 1973.

Mechanics of Material Behavior, The Daniel C. Drucker Anniversary Volume. Edited by George J. Dvorak and Richard T. Shield. Elsevier, The Netherlands, 1984. 383 Pages. Price $94.25.

REVIEWED BY L. B. FREUND[9]

This book is a collection of papers that were included in a Symposium on the Mechanics of Material Behavior which was held at the University of Illinois in Urbana in June of 1983. The main purpose of the Symposium was to recognize the technical contributions made by Daniel C. Drucker to the field of mechanics of material behavior on the occasion of his 65th birthday. The volume includes a summary of Drucker's professional activities and achievements to date (including mention of his service as Technical Editor of the JOURNAL OF APPLIED MECHANICS from 1956 to 1968), and a list of his technical publications. This is followed by complete texts of 22 technical papers on metal plasticity, creep and viscoplasticity, structural dynamics, composite materials, soil mechanics, micromechanics, experimental mechanics, and elasticity. The esteem with which Drucker is held within the applied mechanics community is reflected in the number of contributions to the volume from colleagues who themselves are major contributors to the field, and the broad impact of Drucker's work is conveyed through the range of topics included in the Symposium.

[9]Professor, Division of Engineering, Brown University, Providence, R.I. 02912. Fellow, ASME.

systematic treatment of boundary value problems in anisotropic elastodynamics that is available. Moreover, he admires the patience and hard work that has gone into this study.

References

1 Auld, B. A., *Acoustic Fields and Waves in Solids*, Vol. 1, Wiley, New York, 1973.

Mechanics of Material Behavior, The Daniel C. Drucker Anniversary Volume. Edited by George J. Dvorak and Richard T. Shield. Elsevier, The Netherlands, 1984. 383 Pages. Price $94.25.

REVIEWED BY L. B. FREUND[9]

This book is a collection of papers that were included in a Symposium on the Mechanics of Material Behavior which was held at the University of Illinois in Urbana in June of 1983. The main purpose of the Symposium was to recognize the technical contributions made by Daniel C. Drucker to the field of mechanics of material behavior on the occasion of his 65th birthday. The volume includes a summary of Drucker's professional activities and achievements to date (including mention of his service as Technical Editor of the JOURNAL OF APPLIED MECHANICS from 1956 to 1968), and a list of his technical publications. This is followed by complete texts of 22 technical papers on metal plasticity, creep and viscoplasticity, structural dynamics, composite materials, soil mechanics, micromechanics, experimental mechanics, and elasticity. The esteem with which Drucker is held within the applied mechanics community is reflected in the number of contributions to the volume from colleagues who themselves are major contributors to the field, and the broad impact of Drucker's work is conveyed through the range of topics included in the Symposium.

[9]Professor, Division of Engineering, Brown University, Providence, R.I. 02912. Fellow, ASME.